

XVII International Workshop on
Neutrino Factories and
Future Neutrino Facilities

NUFACT

15

RIO DE JANEIRO
BRAZIL

AUGUST 10-15

PROCEEDINGS



XVII International Workshop on Neutrino factories and Future Neutrino Facilities NuFact15

Rio de Janeiro, Brazil, August 10-15 2015

NuFact15 was the seventeenth in a series that started in 1999 as an important yearly workshop with emphasis on future neutrino projects. This was the first edition in Latin America, showing the scientific growth of this field.

The main goals of the workshop were to review the progress on studies of future facilities able to improve on measurements of the properties of neutrinos and charged lepton flavor violation as well as new phenomena searches beyond the capabilities of presently planned experiments. Since such progress in the neutrino sector could require innovation in neutrino beams, the role of a neutrino factory within future HEP initiatives was addressed.

The workshops are not only international but also interdisciplinary in that experimenters, theorists and accelerator physicists from the Asian, American and European regions share expertise with the common goal of designing the next generation of experiments. **NuFact15** has brought together 125 physicists from all over the world to discuss this exciting field and to set the path to be followed in the years to come.

The NuFact15 workshop was divided into four Working Groups covering the following topics:

- Working Group 1: Neutrino Oscillation Physics
- Working Group 2: Neutrino Scattering Physics
- Working Group 3: Accelerator Physics
- Working Group 4: Muon Physics

NuFact15 was followed by the International Neutrino Summer* School (INSS 2015) that was held in São Paulo, Brazil, from 17 to 28 August 2015.

We thank all members of the National Organizing Committee, Scientific Program Committee, Working Group Conveners and all speakers and participants that have made this workshop a great success.

NuFact15 was made possible by the support of Centro Brasileiro de Pesquisas Físicas (CBPF), Conselho Nacional de Desenvolvimento Científico e Tecnológico (CNPq), Coordenação de Aperfeiçoamento de Pessoal do Ensino Superior (CAPES), Fundação Carlos Chagas Filho de Amparo à Pesquisa do Estado do Rio de Janeiro (FAPERJ) and Fundação de Amparo à Pesquisa do Estado de São Paulo (FAPESP) from Brazil.

Editors of NuFact15 proceedings

Hélio da Motta (CBPF)
Jorge Morfín (Fermilab)

***Northern Hemisphere Summer**

TABLE OF CONTENTS

Preface	i
National Organizing Committee.....	vii
Scientific Program Committee.....	vii
Working Groups and Conveners.....	vii
Timetable.....	viii
Posters.....	xiv
WG 1- Neutrino Oscillation Physics	
Atmospheric neutrinos: Status and prospects.....	1
Results and Prospects from T2K.....	11
Stopping pion experiments in the sterile neutrino field.....	21
Status of atmospheric neutrino oscillation measurements in IceCube and PINGU	31
RENO & RENO-50.....	41
Flavor-Universal Expressions of Neutrino Oscillation Probabilities in Matter.....	51
Last results from Double Chooz.....	61
DUNE Physics	70
MeV gauge boson and secret interaction of sterile neutrinos	80
Probing Neutrino-Scalar Couplings	85
Sensitivity of CP Majorana phases using the synergy between cosmological and neutrinoless double beta decay data at high precision era of measures	90

The impact of neutrino decay on medium-baseline reactor neutrino oscillation experiments	95
Baksan Experiment on Sterile Transitions (BEST)	100
Can Neutrinos Decay?	105
The Angra neutrino experiment	110
Revisiting T2KK and T2KO physics potential and $\nu_{\mu} - \nu_{\mu}$ beam ratio	114
WG 2-Neutrino Sacttering Physics	
Experimental status of neutrino scattering	119
The ANDES Underground Laboratory	129
Neutrino Event Generators	139
Recent developments in neutrino-nucleus scattering theory	149
Status of the Angra Neutrino Project	159
Charged Current Quasielastic Analysis from MINERvA	165
The BONuS Experiment: New Results and Future Plans	173
CC0π Results From T2K	183
Relativistic description of meson-exchange currents and SuperScaling predictions in charged-current neutrino reactions	193
Relativistic Green's Function Model and Optical Potential	203
CAPTAIN, NuMI and Low Energy Physics Programs	213

Charged current resonant and coherent single meson production results from T2K (on and off-axis).....	221
Pion and Kaon Production at MINERvA	231
Neutrino-induced meson productions in resonance region	241
QRPA-based calculations for neutrino scattering and electroweak excitations of nuclei	251
Correlations in neutrino-nucleus scattering	261
Coherent elastic scattering between neutrinos and nuclei	271
Understanding CCQE events in MicroBooNE	276
QCD dynamic effects in the neutrino absorption by the Earth's interior at IceCube neutrino energies and above	281
Computation of atmospheric neutrino production	286
WG 3-Accelerator Physics	
Fermilabs Neutrino Beamlines, a Short History and the Current Status	291
The status of nuSTORM and its production of non-conventional ν_{μ} beams	301
The European Spallation Source Neutrino Super Beam for CP Violation discovery	311
Prospects for Precision Neutrino Cross Section Measurements	320
MICE Demonstration of Ionization Cooling	330
Neutrinos from Plon Beam Line, nuPIL	340
MICE: The Trackers and Magnets	348

LBNF Neutrino Beam	358
A non-conventional neutrino beamline for the measurement of the electron neutrino cross section	368
Studies on pion/muon capture at MOMENT	378
Cosmological bounds of sterile neutrinos in a $SU(3)_C \otimes SU(3)_L \otimes SU(3)_R \otimes U(1)_N$ model as dark matter candidates	388
Progress on Cherenkov Reconstruction in MICE	393
WG 4-Muon Physics	
Connections between $g - 2$, EDMs, CLFV and LHC	398
Update on the AICap Experiment	408
An Overview of the COMET Experiment and Its Recent Progress	418
Searches for Charged Lepton Flavor Violation with the ATLAS Detector at the LHC	428
The Muon $g - 2$ Experiment at Fermilab	438
The Mu2e Experiment at Fermilab	449
The MuLan Experiment: Measuring the muon lifetime to 1 ppm	460
$g-2$ J-PARC (E34)	471
Recent results on lepton flavor violation from CMS	481
Allowed rare pion and muon decays as tests of the Standard Model	491
Search for the decay $\mu^+ \rightarrow e^+e^-e^+$	501
The Multiple Muon Charge Ratio in MINOS Far Detector	509

Development of Muon LINAC for the Muon g-2/EDM Experiment at J-PARC	514
Forbush event detected by CARPET on 2012 March	519
List of Participants.....	524

CHAIRS

J.G. Morfin (Fermilab), H. Da Motta (CBPF) **NATIONAL ORGANIZING COMMITTEE**

H. da Motta	CBPF - Rio de Janeiro	O. Peres	UNICAMP – Campinas
J. Anjos	CBPF - Rio de Janeiro	H. Nunokawa	PUC - Rio de Janeiro
G. Alves	CBPF - Rio de Janeiro	R. Gomes	UFG – Goiás
F. Caruso	CBPF - Rio de Janeiro	V. Pleitez	UNESP - São Paulo
C. Escobar	UNICAMP – Campinas		

SCIENTIFIC PROGRAM COMMITTEE

A. Blondel	U. Geneva, Switzerland	N.K. Mondal,	TIFR, India
A. Bross	FERMILAB, USA	J. Morfin	FERMILAB, USA
A. Bogacz	Jefferson Lab, USA	C. Moore	FERMILAB, USA
A. Cervera	IFIC, Spain	H. da Motta	CBPF, Brazil
M. Dracos	IN2P3, France	J. Nelson.	William and Mary C., USA
S. Geer	FERMILAB, USA	K. Nishikawa	KEK, Japan
M. Goodman	ANL, USA	V. Palladino	U. Napoli, Italy
D. Harris	FERMILAB, USA	P. Soler	U. Glasgow, UK
T. Hasegawa	KEK, Japan	J. Strait	FERMILAB, USA
P. Huber	Virginia Tech, USA	S. Svoboda	U.C. Davis, USA
E. Kemp	UNICAMP, Brazil	F. terranova	Milano-Bicoca, Italy
H. Kirk	BNL, USA	Y. Wang	IHEP, China
Y. Kuno	Osaka Japan	M. Zisman	LBNL, USA
K. Long	Imperial C., UK		

NuFact15 WORKING GROUPS AND CONVENERS

WG1: neutrino oscillation physics	Alex Sousa (U. Cincinnati, USA) Mark Hartz (Kavli IPMU, Japan) Francesca Di Lodovico (Queen Mary U. of London, UK)
WG2: neutrino scattering physics	Kendall Mahn (MSU, USA) Hide-Kazu Tanaka (ICRR, Japan) Marco Martini (Gent/Saclay, France)
WG3: accelerator physics	Pavel Snopok (IIT, USA) Jingyu Tang (IHEP, China) Chris Densham (STFC, UK)
WG4: muon physics	Andrew Norman (FERMILAB, USA) Haibo Li (IHEP, China) Angela Papa (PSI, Switzerland)

TIMETABLE

MONDAY AUGUST 10

08:30 – 08:55	Registration	
08:55 – 09:30	Opening	
Plenary session 1		
09:30 – 09:45	WG1: plans and questions	
09:45 – 10:00	WG2: plans and questions	
10:00 – 10:15	WG3: plans and questions	
10:15 – 10:30	WG4: plans and questions	
10:30 – 11:00	Coffee break	
Plenary session 2		
11:00 – 11:30	Theoretical Status of Neutrino Physics	Mu-Chum Chen (UC Irvine)
11:30 – 12:00	Atmospheric Neutrino Status and Prospects	Justin Evans (Manchester)
12:00 – 12:30	Experimental status of neutrino scattering	Sara Bolognesi (John Hopkins)
12:30 – 13:00	Generator status	Hugh Gallagher (Tufts)
13:00 – 14:30	Lunch	
WG1 session		
14:30 – 14:54	Mass model summary	Mu-Chu Chen (UC Irvine)
14:54 – 15:18	CP violation	Suprabh Prakash (Harish-Chandra)
15:18 – 15:42	NSI	Sushant Raut (Physical research Laboratory)
15:42 – 16:06	DUNE Physics	James Strait (Fermilab)
16:06 – 16:30	HK Physics	Tom Feusels (British Columbia)
WG2 session		
14:30 – 15:10	T2K CC0pi results	Andrew Furmanski (Manchester)
15:10 – 15:50	Quasi-elastic measurements at MINERvA	Anushree Ghosh (CBPF)
15:50 – 16:30	NOvA ND	Jonathan Paley (Fermilab)
WG3 session		
14:30 – 15:00	MICE construction	Colin Whyte (Strathclyde)
15:00 – 15:25	MICE Step IV	Milorad popovic (Fermilab)
15:25 – 15:50	MICE cooling demonstration preparation	Jean-Baptiste Lagrange (Imperial College/Fermilab)
15:50 – 16:20	MICE trackers and magnets	Melissa Uchida (Imperial College)
16:20 – 16:30	Discussion	

WG4 session		
14:30 – 15:00	MEG	Dmitri Grigoriev (Budker Institute)
15:00 – 15:30	MEG Upgrades	Angela Papa (Paul Scherrer Institute)
15:30 – 16:00	Mu3e	Roman Gredig (Physik Institute UZH)
16:00 – 16:30	EDMs at PSI	Elise Wursten (Leuven)
16:30 – 16:50	Coffee break	
Round table		
16:50 – 17:20	Physics potential of non-conventional neutrino beams: Neutrino Factory +	Alan Bross (Fermilab)
17:20 – 18:20	Round table: Developing an International Strategy toward a Neutrino Factory	Daniel Cherdack (Colorado) Takashi Kobayashi (KEK) Kenneth Long (Imperial College) Mark Palmer (Fermilab) Jingyu Tang (IHEP)
18:20 – 20:00	Welcome cocktail	

TUESDAY AUGUST 11

Plenary session 3		
09:00 – 09:30	Global Neutrino Oscillation Fits	Renata Zukanovich (USP)
09:30 – 10:00	MOMENT synergies with other projects	Jingyu Tang (IHEP)
10:00 – 10:30	MAP/MICE	Mark Palmer (Fermilab)
10:30 – 11:00	Coffee break	
Joint WG1 – WG2 session		
11:00 – 11:24	T2K Near Detector Experience	Kendal Mahn (Michigan)
11:24 – 11:48	T2K and HK future near detectors	Akihiro Minamino (Kyoto)
11:48 – 12:12	DUNE near detectors	Kirk McDonald (Princeton)
12:12 – 12:36	CAPTAIN+LAriat	Jason St. John (Cincinnati)
12:36 – 13:00	ANNIE	Mayly Sanchez (Iowa)
WG3 session		
11:00 – 11:24	MOMENT as multiple neutrino sources	Ye Yuan (IHEP)
11:24 – 11:48	Studies on pion/muon capture at MOMENT	Nikolaos Vassilopoulos (IPHC)
11:48 – 12:12	Cooling structure at the MOMENT target	Jianfei Tong (IHEP)
12:12 – 12:36	Protons after bombarding the target at MOMENT	Cai Meng (IHEP)
12:36 – 13:00	Studies on charge selection at MOMENT	Yingpeng Song (IHEP)

WG4 session		
11:00 – 11:30	COMET	Ben Krikler (Imperial College)
11:30 – 12:00	DeeMee	Masaharu Aoki (Osaka)
13:00 – 14:30	Lunch	
WG1 session		
14:30 – 14:54	Compact formulas for neutrino oscillation probabilities in matter	Hisakazu Minataka (USP)
14:54 – 15:18	Super-K	Jun Kamada (Tokyo)
15:18 – 15:42	IceCube/PINGU	João Pedro Athayde Marcondes de André (Penn State)
15:42 – 16:06	INO	Sanjeev Kumar Verma (Delhi)
16:06 – 16:30	CHIPS	João Coelho (Tufts)
WG2 session		
14:30 – 15:00	Relativistic description of meson-exchange currents and SuperScaling predictions in charged-current neutrino reactions	Guillermo Daniel Megias Vazquez (Seville)
15:00 – 16:30	The relativistic Green's function Model and the Optical Potential	Carlota Giusti (Pavia)
15:30 – 16:00	CRPA and NN correlations	Tom van Cuyck (Ghent)
16:00 – 16:30	QRPA-based calculations for neutrino scattering and electroweak excitations of nuclei	Arturo Samana (Santa Cruz)
WG3 session		
14:30 – 15:00	NuSTORM overview	Alan Bross (Fermilab)
15:00 – 15:25	Decay ring design for long baseline NF a la NuMAX	Jaroslav Pasternak (Imperial College/RAL-STFC)
15:25 – 15:50	Neutrinos from pion beam line	Jean-Baptiste Lagrange (Imperial College/Fermilab)
15:50 – 16:30	Muon acceleration for NF/MC	Alex Bogacz (Jefferson Lab)
WG4 session		
14:30 – 14:54	g-2 FNAL	Kevin Lynch (York/CUNY)
14:54 – 15:18	g-2 JPARK	Masashi Otani (KEK)
15:18 – 15:42	LHC LFV Atlas	Craig Blocker (Brandeis)
15:42 – 16:06	Belle LFV	Claudia Cecchi (Perugia/INFN)
16:06 – 16:30	LHC LFV CMS	Alexander Nehrkorn (Aachen)
16:30 – 17:00	Coffee break	
Plenary session 4		
17:00 – 17:30	Results and Prospects from NOvA	Mayly Sanchez (Iowa)
17:30 – 18:00	Results and Prospects from T2K	Kirsty Duffy (Oxford)
18:00 – 20:00	Happy hour with posters (see page 9 for posters)	

WEDNESDAY AUGUST 12

Plenary session 5		
09:00 – 09:30	Precision Muon Physics and EDMs (Experimental Overview)	Brendan Kiburg (Fermilab)
09:30 – 10:00	CLFV and Future Facilities (Experimental Overview)	Yoshi Uchida (Imperial College)
10:00 – 10:30	Recent developments of neutrino-nucleus scattering theory	Marco Martini (Ghent)
10:30 – 11:00	Coffee break	
WG1 session		
11:00 – 11:30	MINOS/MINOS+	João Coelho (Tufts)
11:30 – 12:00	OPERA	Chiara Sirignano (Padova/INFN)
12:00 – 12:30	Heavy Neutrinos	Nicola Serra (UZH)
WG2 session		
11:00 – 11:45	Pion and kaon production at MINERvA	Mateus Carneiro (CBPF)
11:45 – 12:30	T2K CC1pi+CC coherent results (on and off axis)	Marti Nirkko (Bern)
WG3 session		
11:00 – 11:25	High-intensity and high-brightness muon beams	Pavel snopok (IIT/Fermilab)
11:25 – 11:50	Hybrid cooling channel	Diktys Stratakis (Brookhaven)
11:50 – 12:15	Final cooling	Mark Palmer (Fermilab)
12:15 – 12:30	Discussion	
WG4 session		
11:00 – 11:23	PIBETA/PEN	Dinko Pocanic (Virginia)
11:23 – 11:46	alcap	Ben Krikler (Imperial College)
11:46 – 12:09	Mulan	Kevin Lynch (York/CUNY)
12:09 – 12:32	mucap	Brendan Kiburg (Fermilab)
12:32 – 14:00	Lunch	
Tour		

THURSDAY AUGUST 13

Plenary session 6		
09:00 – 09:30	Sterile neutrino searches	Bryce Littlejohn (UW-Madison)
09:30 – 10:00	Neutrinoless Double Beta Decay Results and Prospects	Yury Kolomensky (LBNL)
10:00 – 10:30	Connections between g-2, EDMs, CLFV and LHC (Theory Overview)	Paride Paradisi (Padua)
10:30 – 11:00	Coffee break	

Joint WG1-WG2-WG3 session		
11:00 – 11:30	Impact of systematic uncertainties on DUNE	Daniel Cherdack (Colorado)
11:30 – 12:00	Impact of systematic uncertainties on Hyper-K	Mark Hartz (Kavli IPMU/Tokyo/TRIUMF)
12:00 – 12:30	Prospects for reducing beam flux uncertainties with hadron production experiments over the next 10 years	Alessandro Bravar (Geneva)
12:30 – 13:00	Prospects for precision of neutrino cross-section measurements over the next 10 years	Deborah Harris (Fermilab)
13:00 – 14:30	Lunch	
WG1 session		
14:30 – 14:52	Theia Experiment	Gabriel Orebi Gann (UC Berkeley/LBNL)
14:52 – 14:14	Double CHOOZ	Guillaume Pronost (Subatech)
15:14 – 15:36	RENO/RENO-50	Kyung Kwang Joo (Chonnam)
WG2 session		
14:30 – 15:00	Neutrino-induced meson productions in resonance region	Satoshi Nakamura (Kyoto)
15:00 – 15:30	NEUT model improvements, external data fit comparisons	Tom feusels (British Columbia)
15:30 – 16:00	CAPTAIN (BNB and the CAPTAIN/MINERvA physics programs)	Aaron Higuera (Houston)
Joint WG3-WG4 session		
14:30 – 14:53	PRISM	Jaroslav Pasternak (Imperial College/RAL-STFC)
14:53 – 15:16	Mu2e	Vladimir Nagaslaev (Pbar)
15:16 – 15:38	J-PARC high intensity neutrino beam	Tetsuro Sekiguchi (KEK)
15:38 – 16:00	Muon beam line for COMET	Ye Yang (Kyushu/KEK)
16:00 – 16:30	Coffee break	
Plenary session 7		
16:30 – 17:00	Reactor Neutrino Oscillation Results and Prospects - Daya Bay/JUNO	Wei Wang (William and Mary)
17:00 – 17:30	Current Status of the Fermilab Neutrino Beamlines	Craig Moore (Fermilab)
19:00 – 21:00	Workshop dinner	

FRIDAY AUGUST 14

Plenary session 8		
09:30 – 10:00	The ANDES project	Claudio Dib (Federico Santa Maria)
10:00 – 10:30	The Angra neutrino project	Pietro Chimenti (UFABC)
10:30 – 11:00	Coffee break	
WG2 session		
11:00 – 11:30	Deep inelastic scattering at MINERvA	Alessandro Bravar (Geneva)
11:30 – 12:00	The BONuS Experiment: Recent Results and Future Plans	Gail Dodge (Old Dominion)
WG3 session		
11:00 – 11:30	ESS-SB	Marcos Dracos (IPHC-IN2P3/CNRS)
11:30 – 11:59	MTA status and progress	Derun Li (LBNL)
Joint WG1-WG4 session		
11:00 – 11:30	Fermilab SBN Program(includes MicroBooNE)	Kazuhiro Terao (Columbia)
11:30 – 12:00	NA61 (focused on pion yields)	Alessandro Bravar (Geneva)
Joint WG2-WG3 session		
12:00 – 12:30	A novel neutrino beamline for the measurement of the electron neutrino cross section	Francesco Terranova (Milano-Bicocca/INFN)
12:30 – 14:00	Lunch	
WG1 session		
14:00 – 14:30	Source Experiments	Chiara Ghiano (Genova)
14:30 – 15:00	Decay at rest experiments	Eito Iwai (KEK)
15:00 – 15:30	SBL Reactor Experiments	David Martinez Caicedo (IIT)
WG2 session		
14:00 – 14:30	CONNIE	Carla Bonifazi (UFRJ)
14:30 – 15:00	COHERENT	Bjorn Scholz (Chicago)
15:00 – 15:30	Discussion	
WG3 session		
14:00 – 14:30	Latest results on in-beam W powder target at CERN	Ottone Caretta RAL)
14:30 – 15:00	Targets for high-intensity muon sources	Kirk McDonald (Princeton)
15:00 – 15:30	LBNF neutrino beams	James Strait (Fermilab)
15:30 – 16:00	Coffee break	
WG1-WG2-WG3-WG4 summary preparation		
17:30 – 19:30	SPC meeting	
20:00 – 22:00	SPC dinner	

SATURDAY AUGUST 15

Plenary session 9		
09:00 – 09:25	WG1 summary	
09:25 – 09:50	WG2 summary	
09:50 – 10:15	WG3 summary	
10:15 – 10:40	WG4 summary	
10:40 – 11:10	Coffee break	
11:10 – 11:50	Future Accelerator-based Neutrino Physics in Asia	Takashi Kobayashi (KEK)
11:50 – 12:40	Future Accelerator-based Neutrino Physics in America and Europe	Kenneth Long (Imperial College)
Closing		

HAPPY HOUR WITH POSTERS TUESDAY AUGUST 11 (18:00 – 20:00)

#/WG	Title	Presenter
1/1	Baksan Experiment on Sterile Transitions	Yury Malyskin (PUC-Chile)
2/1	Calibration and energy reconstruction at Daya Bay	Yury Malyskin (PUC-Chile)
3/1	Constraining Majorana CP Phase in Precision Era of Cosmology and Double Beta Decay Experiment	Alexander Quiroga (PUC-Rio)
4/1	Constraint on Neutrino Decay with Medium-Baseline Reactor Neutrino Oscillation Experiments	Alexander Quiroga (PUC-Rio)
5/1	Decoherence and Relaxation in Long Baseline Neutrino Experiments	Roberto Oliveira (UNICAMP)
6/1	MeV gauge boson and secret interaction of sterile neutrinos	Orlando Peres (UNICAMP)
7/1	Parameter Limits for Neutrino Oscillation with Decoherence in KamLAND	Guilherme Gomes (UNICAMP)
8/1	Revisiting T2KK and T2KO physics potential and ν_μ - anti- ν_μ beam ratio	Yoshitaro Takaesu (Tokyo)
9/1	The Neutrinos Angra experiment	Stefan Wagner (CBPF)
10/1	Can Neutrinos Decay?	Renan Picoreti (UNICAMP)
11/1	Probing Neutrino-Scalar Couplings	Pedro Pasquini (UNICAMP)
12/2	CCQE-like events in MicroBooNE	Andrew Furmanski (Manchester)
13/2	Computation of atmospheric neutrinos production	Gabriela Vitti Stenico (UNICAMP)
14/2	Neutrino Nucleon Cross Sections at High Energies	Mike Kroll (Ruhr-Uni Bochum)
15/2	Neutrinos generating events for intranuclear cascade in CRISP code	Ms. Danaisis Vargas (Santa Cruz), Arturo Rodolfo Samana (Santa Cruz)

16/2	Phenomenology of single spin asymmetries in inclusive reactions involving photons and leptons	Carlos Javier Solano Salinas (UNI)
17/2	Searching for QCD effects in the neutrino absorption by the Earth's interior at ultra high neutrino energies	Diego Gratieri (UFF)
18/2	Study of the impact of using directionality to investigate geophysical models via the $\bar{\nu}_e + e^-$ elastic scattering interaction	Roger Galindo Orjuela (Santa Maria)
19/2	Test and Characterization of the PMT and the Front-end Circuit for the Neutrinos Angra Experiment	Pietro Chimenti (UFABC)
20/3	Cosmological bounds of sterile neutrinos in a $SU(3)_C \otimes SU(3)_L \otimes SU(3)_R \otimes U(1)_N$ model as dark matter candidates	Cesar Peixoto Ferreira (UNICAMP)
21/3	HTS Pion Capture Solenoid for Next Generation Muon Beam Line	Ye Yang (Kyushu/KEK)
22/3	Progress on Cherenkov Reconstruction for MICE	Daniel Kaplan (IIT)
23/4	Development of muon LINAC for the muon g-2/EDM experiment at J-PARC	Masashi Otani (KEK)
24/4	The Multiple Muon Charge Ratio in the MINOS Far Detector	Cesar Manuel Castromonte (UFG)

Atmospheric neutrinos: Status and prospects*

João Pedro Athayde Marcondes de André†

Michigan State University

(Dated: March 25, 2016)

Abstract

Atmospheric neutrinos are produced in the showers created by the interaction of cosmic rays in the Earth's atmosphere. Neutrino oscillations were discovered in 1998 by Super-Kamiokande using atmospheric neutrinos, and since then they have been continuously used as a tool to measure neutrino oscillations. Status of current measurements of active neutrino oscillations, as well as prospects of future experiments using atmospheric neutrinos are discussed here.

INTRODUCTION

This year, 2015, the Nobel prize was awarded to the discovery of neutrino oscillations [1]. The prize was split between T. Kajita (Super-Kamiokande) and A. B. McDonald (SNO) for discovering neutrino oscillations in the atmospheric neutrino flux in 1998 [2] and the solar neutrino flux in 2002 [3], respectively. Since these two detections, neutrino oscillations have also been measured using neutrinos produced in nuclear reactors and particle accelerators. All these observations provide a consistent picture and most of the parameters describing the 3-flavour standard neutrino oscillation have been measured with varying precision (see [4] and references therein). The remaining open questions in the standard neutrino framework are the value of CP violating phase (δ_{CP}), the neutrino mass hierarchy (the sign of Δm_{32}^2) and the octant of the mixing angle θ_{23} .

The atmospheric neutrino flux is produced from decays of π and K mesons produced by cosmic ray interactions in the Earth's atmosphere and the subsequent shower development [4]. The ν flux produced this way is roughly isotropic, with twice as many $\nu_\mu + \bar{\nu}_\mu$ than $\nu_e + \bar{\nu}_e$ and a similar content of neutrinos and anti-neutrinos. This is a particularly good description at lower energies where π decay dominates ($\pi^+ \rightarrow \mu^+ + \nu_\mu$ with a $\mu^+ \rightarrow e^+ + \nu_e + \bar{\nu}_\mu$ following, and their conjugate processes), nevertheless a full treatment of shower development and meson decays has been performed by several groups [5–7] with typical uncertainties on the overall flux of 10-30% below 100 GeV, and better than 10% precision on relative composition of neutrinos and anti-neutrinos or electron and muon neutrinos.

While it is possible to utilize this relatively well understood flux to probe neutrino oscillations and answer these currently open questions, the current generation of detectors is only able to provide hints as to their values. Future proposed detectors [8–12] have a good potential to measure the neutrino mass hierarchy and octant of θ_{23} . While a significantly

improved detector would be required to envisage measuring δ_{CP} directly with atmospheric neutrinos [13], the determination of the mass hierarchy using atmospheric oscillations could help disentangling the δ_{CP} and the neutrino mass hierarchy effects which are degenerate in $\text{NO}\nu\text{A}$ for in some cases [14].

NEUTRINO OSCILLATIONS

There is currently overwhelming experimental evidence for neutrino oscillation [4]. Theoretically that is described by a difference in the mass (ν_1, ν_2, ν_3) and flavor (ν_e, ν_μ, ν_τ) eigenstates of neutrinos, which will produce changes in the flavor composition of a neutrino flux depending on the energy of the neutrinos (E) and their propagation distance (L). That phenomena is described in vacuum by Eq. (1) and has an oscillation period that depends also on the difference of the mass squared between mass eigenstates ($\Delta m_{jk}^2 = m_j^2 - m_k^2$) and an amplitude that depends on the mixing matrix U . The standard decomposition of U , assuming three neutrino flavors, is shown in Eq. (2) where $c_{ij} = \cos \theta_{ij}$ and $s_{ij} = \sin \theta_{ij}$, with θ_{ij} mixing angles and δ_{CP} is the CP violating phase.

$$P(\nu_\alpha \rightarrow \nu_\beta) = \delta_{\alpha\beta} - 4 \sum_{j>k} \text{Re}(U_{\beta j} U_{\alpha j}^* U_{\beta k}^* U_{\alpha k}) \sin^2 \left(\frac{\Delta m_{jk}^2 L}{4E} \right) + 2 \sum_{j>k} \text{Im}(U_{\beta j} U_{\alpha j}^* U_{\beta k}^* U_{\alpha k}) \sin \left(\frac{\Delta m_{jk}^2 L}{2E} \right) \quad (1)$$

$$U = \begin{pmatrix} 1 & 0 & 0 \\ 0 & c_{23} & s_{23} \\ 0 & -s_{23} & c_{23} \end{pmatrix} \times \begin{pmatrix} c_{13} & 0 & s_{13} e^{-i\delta_{CP}} \\ 0 & 1 & 0 \\ -s_{13} e^{i\delta_{CP}} & 0 & c_{13} \end{pmatrix} \times \begin{pmatrix} c_{12} & s_{12} & 0 \\ -s_{12} & c_{12} & 0 \\ 0 & 0 & 1 \end{pmatrix} \quad (2)$$

As mentioned previously, the value of δ_{CP} and the sign of Δm_{32}^2 (mass hierarchy) have not yet been measured. The two possible cases for the neutrino mass hierarchy are the third mass eigenstate is the heaviest (positive Δm_{32}^2) which is referred to as ‘‘normal hierarchy’’ (NH), or it is the lightest (negative Δm_{32}^2) which is referred to as ‘‘inverted hierarchy’’ (IH).

In order to study neutrino oscillations using atmospheric neutrinos it is essential to reconstruct both the energy and direction of the neutrinos (the zenith direction is needed to calculate L) to be able to map the oscillation as a function of L and E ; the neutrinos are produced with energies spanning many orders of magnitude and are available at varying

values of L (from about 10 km to 13 Mm). For neutrinos travelling through the Earth's core the first maximum ν_μ disappearance happens around 25 GeV.

One notable correction that needs to be taken into account to calculate the oscillation probabilities for atmospheric neutrinos is the fact that neutrinos are propagating through matter and not in vacuum [4, 15, 16]. This impacts the neutrino oscillation because ν_e and $\bar{\nu}_e$ interact with the electrons in the medium differently than the other neutrino and anti-neutrino flavors, given only ν_e and $\bar{\nu}_e$ can scatter off an electron with a W^\pm boson as mediator. For neutrinos propagating through the Earth, this creates the resonance condition shown in Eq. (3) where N_e is the electron density. The \pm in Eq. (3) depends if ν (+) or $\bar{\nu}$ (-) are propagating through matter, and therefore the resonance condition can only happen in the NH for ν and in the IH for $\bar{\nu}$, as those are the only cases where E is positive in Eq. (3). In the mantle, such condition happens for $E \sim 7$ GeV and while trajectories crossing only the mantle are not long enough to have the maximal resonant effect, it is close enough to significantly affect the oscillation probabilities. In core-crossing trajectories the formulations are more complicated [4] but also result in resonance conditions for ν in the NH case or $\bar{\nu}$ in the IH case, which will impact the oscillation probabilities. The effect of oscillation in vacuum and matter, in the presence of resonances, as a function of E and L is shown in Fig. 1. It is through the measure of these resonances that future experiments plan to determine the neutrino mass hierarchy using atmospheric neutrinos.

$$E = \frac{\Delta m_{31}^2 \cos 2\theta_{13}}{\pm N_e 2\sqrt{2}G_F}, \text{ + for } \nu \text{ and } - \text{ for } \bar{\nu} \quad (3)$$

CURRENT RESULTS

Of all detectors currently capable of studying the atmospheric neutrino flux, Super-Kamiokande [18] is certainly the one that has been in operation for the longest time and that has produced the most varied results in oscillations using the atmospheric neutrino flux. Since the discovery of neutrino oscillations by Super-Kamiokande [2], it has continued to collect data and improve the precision of the key parameters (θ_{23} and $|\Delta m_{32}^2|$) describing the neutrino oscillation of the atmospheric neutrino flux, as shown in Fig. 2.

The IceCube Neutrino Observatory, using its denser sub-array DeepCore [23], has also started to perform precise measurements of θ_{23} and $|\Delta m_{32}^2|$, which are also shown in Fig. 2.

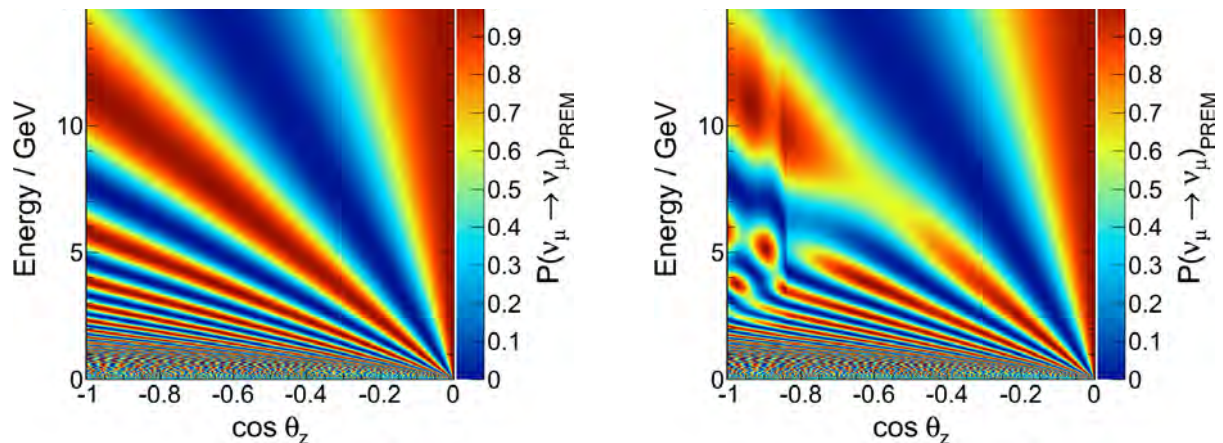


Figure 1: Oscillation probability for $\nu_\mu \rightarrow \nu_\mu$ as a function of the neutrino energy (E) and zenith angle ($\cos\theta_z \sim -L/2R$, with R being the Earth's radius). In the left is shown the ν_μ survival probability in the absence of matter induced resonances (IH for ν) while on the right is shown the same thing when resonances are accounted for (NH for ν). $\cos\theta_z \sim -0.84$ corresponds to the mantle-core transition which correspond to a large change in the medium electron density [17] and therefore produce the discontinuity seen in the right figure.

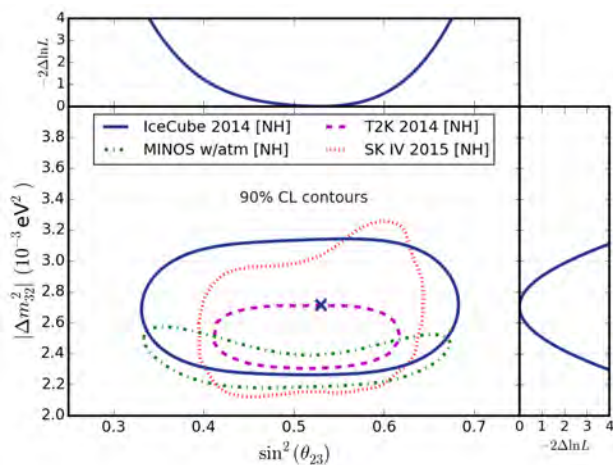


Figure 2: Current precision on the measure of θ_{23} and $|\Delta m_{32}^2|$, assuming NH is true. Of these results, Super-Kamiokande [19] (dotted line) and IceCube [20] (solid line) were produced using exclusively atmospheric neutrinos, MINOS [21] (dash-dotted line) uses both accelerator and atmospheric neutrinos, and T2K [22] (dashed line) uses exclusively accelerator neutrinos.

While currently the best limits to θ_{23} and $|\Delta m_{32}^2|$ were obtained by long baseline accelerator experiments, looking for oscillations at a specific L and E , it is worth noting that the atmospheric neutrino measurements were done using a wide range of L and E which allow for the check of the validity of the neutrino oscillation framework over a larger parameter space. Also, notably the L and E ranges probed by Super-Kamiokande and IceCube are different as each detector is more sensitive at different energy ranges.

Besides these two detectors, there are currently several other detectors capable of measuring the atmospheric neutrino flux. For example, MINOS uses their measurement of atmospheric neutrinos jointly with their accelerator neutrinos to produce their results on θ_{23} and $|\Delta m_{32}^2|$ [21], also shown in Fig. 2, and ANTARES is mostly sensitive to the atmospheric neutrino flux at higher energies and has obtained weaker constraints to those parameters [24].

Besides measuring θ_{23} and $|\Delta m_{32}^2|$, Super-Kamiokande has also looked for ν_τ appearance created from $\nu_\mu \rightarrow \nu_\tau$ oscillation to test the 3-flavor neutrino oscillation framework and observed it with a significance of 3.8σ [25]. Additional studies from Super-Kamiokande [26] also preliminarily provide $\sim 1 \sigma$ preference for NH, the second octant of θ_{23} and $\delta_{CP} \in [\pi, 2\pi]$. Going beyond the three neutrino flavors paradigm, Super-Kamiokande has also put constraints in the sterile neutrino phase space [27].

A more in-depth discussion of the results from Super-Kamiokande and IceCube are found in other contributions to this conference [26, 28].

FUTURE DETECTORS AND EXPECTED SENSITIVITIES

As discussed previously, the current experiments measuring the neutrino atmospheric flux are not likely to answer the remaining open questions in the standard neutrino oscillations framework, however several proposed experiments are able to determine at 3σ the neutrino mass hierarchy and have potential to determine the octant of θ_{23} .

In order to measure the neutrino mass hierarchy with atmospheric neutrinos it is essential to distinguish if the resonances happen for ν or $\bar{\nu}$, as that changes for each hierarchy. In order to make this distinction, INO proposes to use a magnetized iron calorimeter and directly separate ν_μ and $\bar{\nu}_\mu$ achieving the measurement of the neutrino mass hierarchy at 3σ with 7-13 years of data [29]. All other experiments use a different approach to the problem, as suggested by [30, 31], in which the difference in the neutrino and anti-neutrino cross-section produces a slightly different $E \times \cos \theta_z$ pattern for neutrinos and anti-neutrinos, without relying in any capability for the detector to be able to individually distinguish between neutrino and anti-neutrino events. Using this technique PINGU [12] and ORCA [11] can reach 3σ sensitivity to the mass hierarchy for any value for θ_{23} with 3-5 years of data, while it would take Hyper-Kamiokande [9] and the far detector of DUNE [8] about 10 years

of full detector lifetime to reach such precision using atmospheric neutrinos. Note that DUNE will also be able to measure at 3σ the neutrino mass hierarchy using accelerator neutrinos with 6 years of lifetime with a 1.2 MW beam for all values of δ_{CP} [8]. Fig. 3 shows the neutrino mass hierarchy sensitivity as a function of time for the above mentioned atmospheric neutrino experiments.

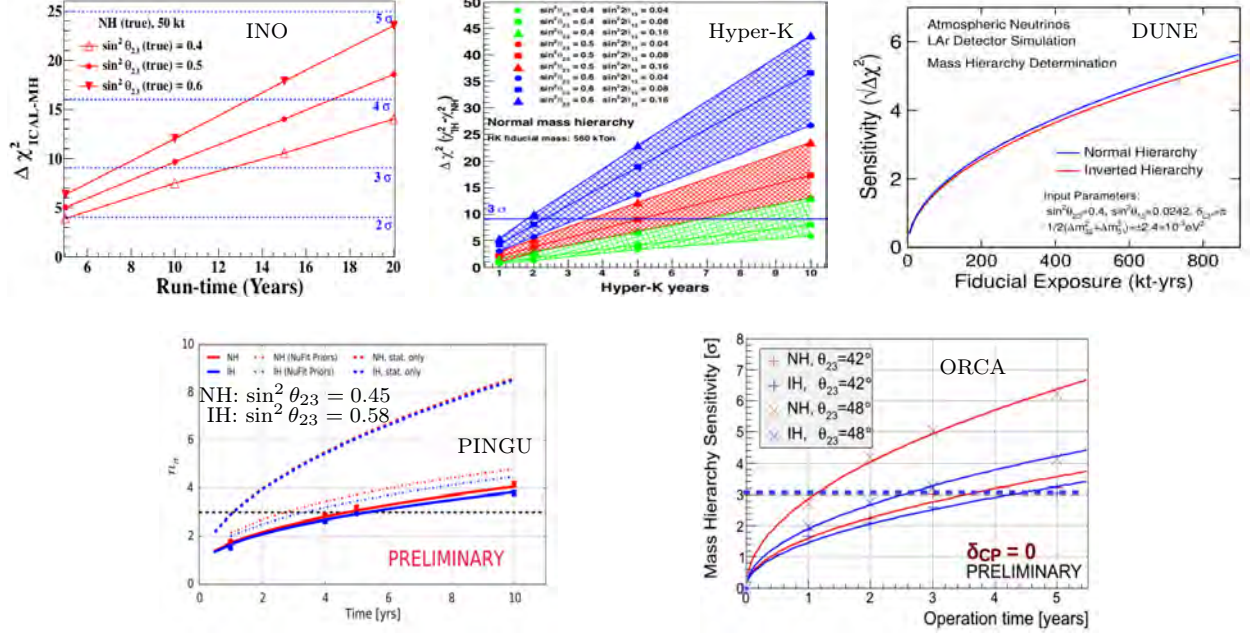


Figure 3: Sensitivity to the neutrino mass hierarchy for INO [29], Hyper-Kamiokande [9], DUNE [8] PINGU [28], and ORCA [11] as a function of time.

These experiments also have good sensitivity to θ_{23} and $|\Delta m_{32}^2|$ (see Fig. 4 for PINGU and INO) and could determine the octant of θ_{23} if it's not too close to maximal (see Fig. 5 for Hyper-Kamiokande and DUNE). Besides those results, they are also expected to provide improved limits on several of the results mentioned above from Super-Kamiokande, such as ν_τ appearance and sterile neutrino searches.

A more in-depth discussion about the capabilities of Hyper-Kamiokande, PINGU and INO to measure atmospheric neutrinos are found in other contributions to this conference [28, 32, 33].

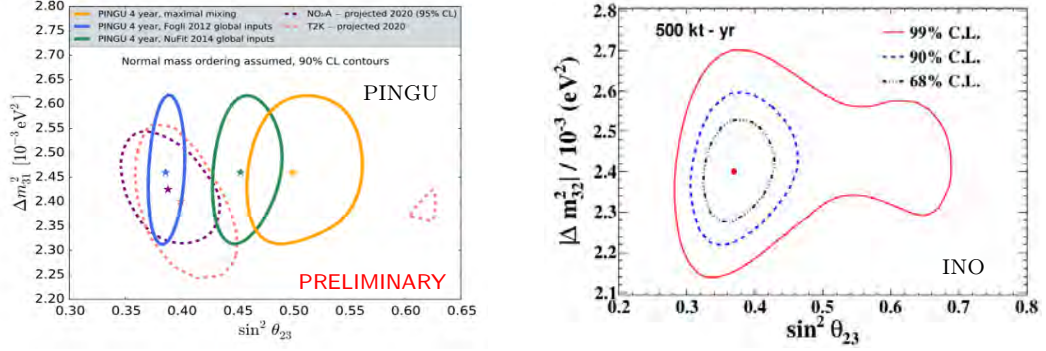


Figure 4: Sensitivity to θ_{23} and $|\Delta m^2|$ for PINGU [28] and INO [10] for 4 and 10 years of lifetime, respectively.

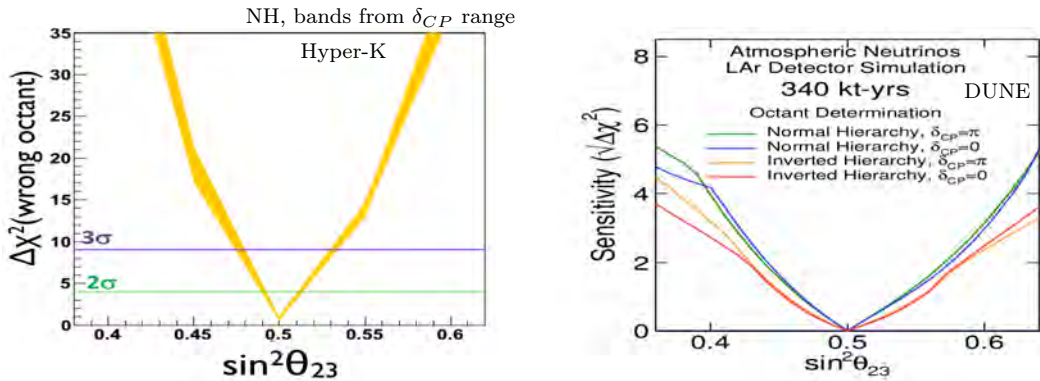


Figure 5: Sensitivity to the octant of θ_{23} , using exclusively atmospheric neutrinos, for Hyper-Kamiokande [32], and DUNE [8] as a function of the true value of θ_{23} for 10 years of lifetime, in both cases.

SUMMARY

Atmospheric neutrinos were fundamental to the discovery of neutrino oscillations. Since then they have continued to provide quality measurements of neutrino oscillations on a wide L and E ranges, in particular measurements of θ_{23} and $|\Delta m_{32}^2|$, searches for sterile neutrinos and ν_τ appearance searches.

The next generation of experiments is expected to further improve on these measurements, may determine the octant of θ_{23} , depending on the true value of that mixing angle, and will be able to measure the neutrino mass hierarchy at 3σ in as few as 3-5 years for some experiments.

* Presented at NuFact15, 10-15 Aug 2015, Rio de Janeiro, Brazil [C15-08-10.2]

† jpa14@icecube.wisc.edu; Speaker

- [1] *The nobel prize in physics 2015*, Nobelprize.org, Nobel Media AB 2014. http://www.nobelprize.org/nobel_prizes/physics/laureates/2015/, accessed: dec 2015.
- [2] Y. Fukuda et al. (Super-Kamiokande), *Phys. Rev. Lett.* **81**, 1562 (1998), hep-ex/9807003.
- [3] Q. R. Ahmad et al. (SNO), *Phys. Rev. Lett.* **89**, 011301 (2002), nucl-ex/0204008.
- [4] K. A. Olive et al. (Particle Data Group), *Chin. Phys.* **C38**, 090001 (2014).
- [5] M. Honda et al., *Phys. Rev.* **D92**, 023004 (2015), 1502.03916.
- [6] G. D. Barr et al., *Phys. Rev.* **D74**, 094009 (2006), astro-ph/0611266.
- [7] G. Battistoni, A. Ferrari, T. Montaruli, and P. R. Sala, *Astropart. Phys.* **19**, 269 (2003).
- [8] C. Adams et al. (LBNE), arXiv:1307.7335 (2013), URL <http://www.osti.gov/scitech/biblio/1128102>.
- [9] K. Abe et al., arXiv:1109.3262 (2011).
- [10] S. Ahmed et al. (ICAL), arXiv:1505.07380 (2015).
- [11] J. Brunner et al. (KM3NeT), PoS(ICRC2015)1092 (2015).
- [12] M. G. Aartsen et al. (IceCube PINGU), arXiv:1401.2046 (2014).
- [13] S. Razzaque and A. Yu. Smirnov, *JHEP* **05**, 139 (2015), 1406.1407.
- [14] *Nova collaboration homepage*, http://www-nova.fnal.gov/plots_and_figures/plot_and_figures.html, accessed: dec 2015.
- [15] L. Wolfenstein, *Phys. Rev.* **D17**, 2369 (1978).
- [16] S. P. Mikheev and A. Yu. Smirnov, *Sov. J. Nucl. Phys.* **42**, 913 (1985).
- [17] A. M. Dziewonski and D. L. Anderson, *Phys. Earth Planet. Interiors* **25**, 297 (1981).
- [18] Y. Fukuda et al. (Super-Kamiokande), *Nucl. Instrum. Meth.* **A501**, 418 (2003).
- [19] R. Wendell (Super-Kamiokande), *AIP Conf. Proc.* **1666**, 100001 (2015), 1412.5234.
- [20] M. Aartsen et al. (IceCube), *Phys. Rev.* **D91**, 072004 (2015), 1410.7227.
- [21] P. Adamson et al. (MINOS), *Phys. Rev. Lett.* **110**, 251801 (2013), 1304.6335.
- [22] K. Abe et al. (T2K), *Phys. Rev. Lett.* **112**, 181801 (2014), 1403.1532.
- [23] R. Abbasi et al. (IceCube), *Astropart. Phys.* **35**, 615 (2012), 1109.6096.
- [24] S. Adrian-Martinez et al. (ANTARES), *Phys. Lett.* **B714**, 224 (2012), 1206.0645.

- [25] K. Abe et al. (Super-Kamiokande), *Phys. Rev. Lett.* **110**, 181802 (2013), 1206.0328.
- [26] J. Kameda et al. (Super-Kamiokande), *Super-kamiokande: Recent results on atmospheric neutrinos*, presented at NuFact 2015 (2015).
- [27] K. Abe et al. (Super-Kamiokande), *Phys. Rev.* **D91**, 052019 (2015), 1410.2008.
- [28] J. P. A. M. de André et al. (IceCube-Gen2), *Status of atmospheric neutrino oscillation measurements in icecube and pingu*, in these proceedings (2015).
- [29] M. M. Devi et al., *JHEP* **10**, 189 (2014), 1406.3689.
- [30] O. Mena, I. Mocioiu, and S. Razzaque, *Phys. Rev.* **D78**, 093003 (2008), 0803.3044.
- [31] E. K. Akhmedov et al., *JHEP* **02**, 082 (2013).
- [32] T. Feusels et al. (Hyper-Kamiokande), *Hk physics*, presented at NuFact 2015 (2015).
- [33] S. K. Verma et al. (ICAL), *Ino*, presented at NuFact 2015 (2015).

Results and Prospects from T2K*

Kirsty Duffy[†]

University of Oxford

(Dated: April 1, 2016)

Abstract

As measurements of the neutrino oscillation parameters improve it is becoming more interesting to study antineutrino oscillations, to investigate CP and CPT violation in the lepton sector and nonstandard matter effects. We present the most recent T2K antineutrino oscillation results, from data collected using a $\bar{\nu}_\mu$ -enhanced neutrino beam corresponding to 4.01×10^{20} protons on target. The first analysis of $\bar{\nu}_e$ appearance on T2K is presented, as well as world-leading measurements of the dominant oscillation parameters for $\bar{\nu}_\mu$ disappearance. T2K measures $\sin^2 2\bar{\theta}_{23} = 0.46_{-0.06}^{+0.14}$ and $\Delta\bar{m}_{32}^2 = 2.50_{-0.2}^{+0.3} \times 10^{-3} \text{ eV}^2$, which is consistent with previous T2K measurements of the neutrino oscillation parameters and existing antineutrino measurements.

THE T2K EXPERIMENT

T2K is a long-baseline neutrino oscillation experiment located in Japan, which uses the 30 GeV proton beam from the J-PARC accelerator to create a muon neutrino beam. The proton beam is directed onto a graphite target, and the resulting pions focussed by magnetic horns (which can select either π^+ , for a beam composed mainly of ν_μ , or π^- , for a beam composed mainly of $\bar{\nu}_\mu$), into a 96 m decay tunnel. The neutrino beam is measured by two near detectors located 280 m from the target, and a far detector, Super-Kamiokande. The far detector and one of the near detectors are placed 2.5° off-axis with respect to the neutrino beam, which results in a quasi-monochromatic neutrino energy spectrum that is sharply peaked around 0.6 GeV. The baseline between neutrino production and the far detector, 295 km, is carefully chosen to correspond to the first minimum in the ν_μ survival probability at the peak energy. T2K can measure neutrino oscillation in two channels: ν_μ disappearance (which is dominated by the oscillation parameters $\sin^2 \theta_{23}$ and Δm_{32}^2) and ν_e appearance (which is sensitive to $\sin^2 \theta_{13}$ and δ_{CP}).

T2K has been taking data since 2010, and has so far collected 1.1×10^{21} protons on target (POT). The beam power has been steadily increasing, and stable running at 345 kW was achieved in 2015, with a maximum beam power of 371 kW. Since mid-2013 the beam has been running in antineutrino mode, where the horn currents are reversed to select π^- instead of π^+ , resulting in a beam that is mostly composed of antineutrinos. Sensitivity studies show that T2K may, depending on the value of δ_{CP} , be sensitive to δ_{CP} when roughly equal amounts of neutrino-mode and antineutrino-mode data are collected, with the full predicted data set of 7.8×10^{21} POT. In addition, measurements of antineutrino oscillations will allow us to test the PMNS framework and search for CP violation (if $P(\bar{\nu}_\mu \rightarrow \bar{\nu}_e) \neq P(\nu_\mu \rightarrow \nu_e)$) or CPT violation or non-standard matter effects (if $P(\bar{\nu}_\mu \rightarrow \bar{\nu}_\mu) \neq P(\nu_\mu \rightarrow \nu_\mu)$). 4.011×10^{20} POT have been collected in antineutrino mode, which is roughly one third of the total data set. However, the event rates in antineutrino mode are significantly lower than in the neutrino-mode beam, due to both pion multiplicity and the difference between ν and $\bar{\nu}$ cross

sections.

The near detectors: ND280 and INGRID

T2K has two near detectors, shown in figure 1: INGRID, which is on-axis with respect to the neutrino beam, and ND280, which is at the same off-axis angle as Super-Kamiokande. Both detectors have a rich program of physics which has been covered in other presentations at this conference; here we will focus on their use in the oscillation analysis.

The on-axis detector, INGRID, is an array of 7+7 iron/scintillator detectors arranged in a cross shape centered on the beam axis. It is used to measure the beam stability, profile, and direction, and has shown that the beam direction is stable to within 0.4 mrad.

The off-axis detector, ND280, is used directly in the oscillation fits to reduce the flux and cross-section uncertainties. It is made up of many subdetectors, but only the central Fine-Grained Detectors (FGDs) and Time Projection Chambers (TPCs) are used for this analysis. ND280 contains two FGDs, which provide a target for neutrino interactions with excellent vertexing capabilities at the interaction point. The current oscillation fits use only FGD1, for which the target material is carbon. The TPCs are then used to measure the interaction products, and give very good momentum resolution and particle identification. ND280 is contained in the repurposed UA1 magnet, which enables the TPC information to distinguish positive and negative charged leptons from $\bar{\nu}$ and ν interactions.

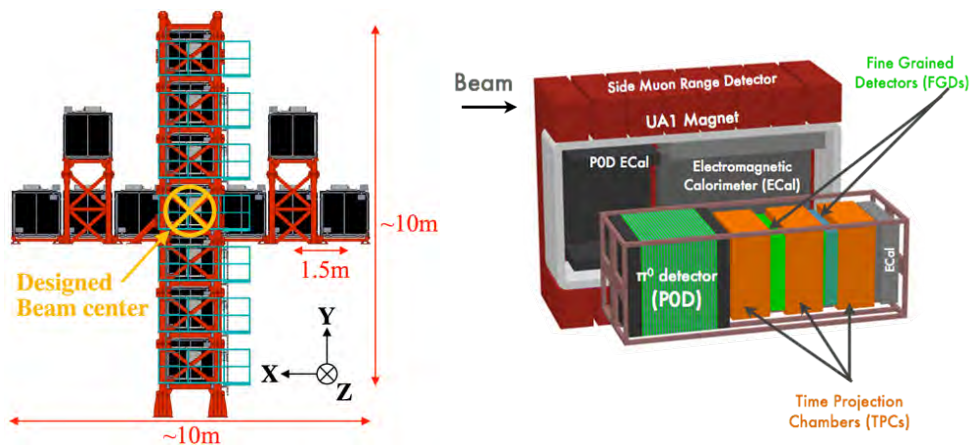


FIG. 1: The T2K near detectors: INGRID (**left**) and ND280 (**right**).

The far detector: Super-Kamiokande

The far detector, Super-Kamiokande, is a 50kton water Cherenkov detector (22.5kton fiducial mass). It has no magnetic field so cannot distinguish between neutrino and antineu-

trino interactions, but is capable of very good μ/e separation by the pattern of light from the charged lepton ($<1\%$ of μ events are misidentified).

OSCILLATION ANALYSIS STRATEGY

The analysis strategy for the oscillation results presented here is similar to previous T2K results [1]: data samples of charged current (CC) interactions are fit at ND280 to provide a tuned prediction of the unoscillated spectrum at the far detector and its associated uncertainty. This is then compared to the data at the far detector, where μ -like or e -like data samples are fit to estimate the oscillation parameters.

Near detector (ND280) fit

The near detector fit takes inputs from theoretical flux, cross section, and detector models, each of which has its own uncertainties.

The flux model uses information from measurements by INGRID and the beam monitors, as well as external data from the NA61/SHINE experiment. It is used to constrain the prediction at the far detector through correlations between the neutrino flux at both detectors, as predicted by beam simulations.

The predictions at both ND280 and Super-Kamiokande use the same cross-section model, so the ND280 fit can reduce the cross-section uncertainty in the Super-Kamiokande prediction by fitting parameter values in the underlying models. Information from external data (from the MINER ν A and MiniBooNE experiments) are also included as a prior for the ND280 fit. It is not possible to constrain all the cross-section parameters because of the different target materials in the near detector (carbon) and far detector (primarily oxygen), as the relative errors between interactions on carbon and oxygen are not always well understood. Separate parameters are used for Fermi momentum, binding energy, multinucleon event normalisation and CC coherent pion production normalisation on oxygen, which are not well constrained by the near detector. We use a conservative (100% error, with no correlation with multinucleon events on carbon) ansatz for the multinucleon normalisation on oxygen.

The near detector fit also estimates correlations between the flux and cross-section parameters at Super-Kamiokande.

The data in the near detector are fit in the momentum and angle of the outgoing lepton from the neutrino interaction. Data from the neutrino-mode beam as well as antineutrino mode are used to ensure that the model parameters are consistent between neutrinos and antineutrinos, and provide a constraint on the wrong-sign background (ν in the $\bar{\nu}$ beam). In total 5.82×10^{20} POT of data in neutrino mode and 0.43×10^{20} POT of data in antineutrino

mode are used, split into seven samples. The antineutrino-mode data are split into ‘ ν_μ CC 1 track’, ‘ ν_μ CC >1 track’, ‘ $\bar{\nu}_\mu$ CC 1 track’, and ‘ $\bar{\nu}_\mu$ CC >1 track’ samples. The ‘1 track’ samples are dominated by CC quasielastic (CCQE) interactions ($\nu_\mu + n \rightarrow \mu^- + p$ or $\bar{\nu}_\mu + p \rightarrow \mu^+ + n$, the ‘signal’ at Super-Kamiokande), and the ‘>1 track’ samples are used to estimate the background from other interactions. The neutrino-mode data are divided into three subsamples according to the number of measured pions associated with the interaction: ‘ ν_μ CC0 π ’, ‘ ν_μ CC1 π^+ ’, and ‘ ν_μ CC other’, which are dominated by CCQE, CC resonant pion production, and deep inelastic scattering interactions respectively.

Figure 2 shows some of the flux and cross-section parameters with their associated uncertainties before and after the near detector fit. The predicted flux at Super-Kamiokande is generally increased by the fit, although the uncertainty is decreased. Some of the cross-section parameters fit to values which are significantly different to their prior predictions, particularly the multinucleon event normalisation parameter on carbon (“CC 2p-2h ^{12}C ”). The uncertainties on the parameters which the near detector is sensitive to are generally decreased in the fit, but there is not much change to the uncertainties of the oxygen-specific parameters.

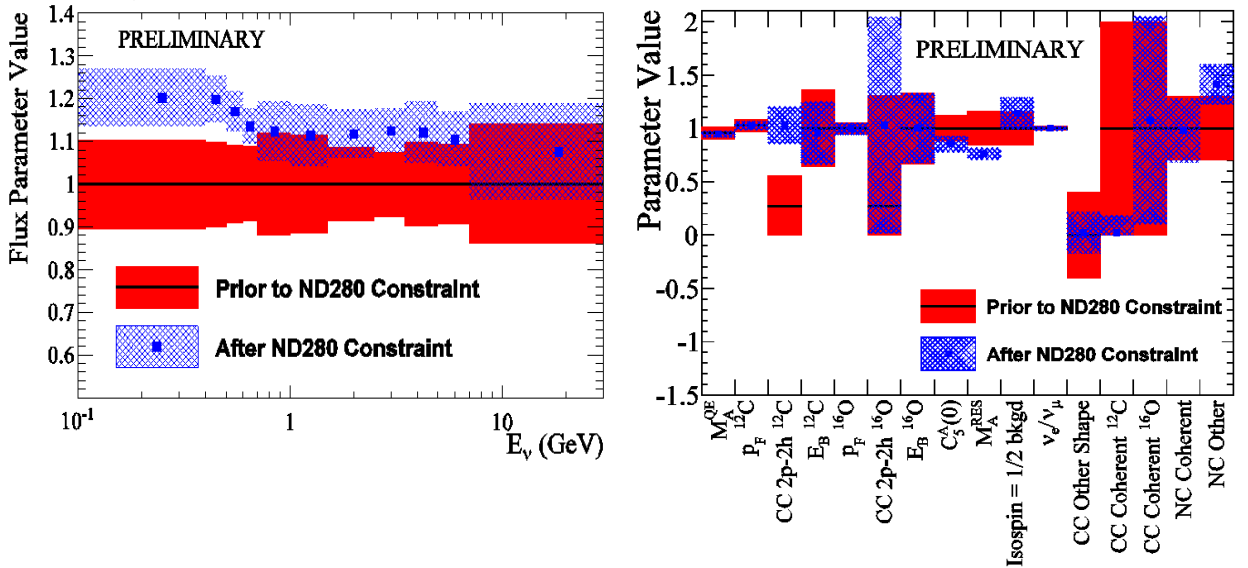


FIG. 2: Some flux and cross-section systematic parameters with uncertainties before and after the near detector fit. **Left:** flux parameters for $\bar{\nu}_\mu$ flux in the antineutrino-mode beam. **Right:** underlying parameters for the cross-section models.

Table I shows the uncertainty in the predicted number of $\bar{\nu}_\mu$ events at Super-Kamiokande due to each source of systematic error. The near detector fit reduces the error due to the parameters that it can constrain from 9.2% to 3.4%. However, the overall error is dominated by the cross-section parameters which are not constrained by the near detector (in particular

TABLE I: Fractional error in the number of $\bar{\nu}_\mu$ events predicted at Super-Kamiokande (SK) due to different sources of systematic error, before and after the near detector (ND) fit.

Systematic	$\frac{\Delta N_{SK}}{N_{SK}}$ without ND	$\frac{\Delta N_{SK}}{N_{SK}}$ with ND
All common to ND/SK	9.2%	3.4%
Multinucleon effect on oxygen	9.5%	
All oxygen cross-section	10.0%	
Final state interaction/secondary interaction at SK	2.1%	
SK detector	3.8%	
Total	14.4%	11.6%

the multinucleon event normalisation systematic, which alone produces a 9.5% uncertainty).

Far detector fit

The result of the near detector fit is propagated to the far detector. This is used as a prior for the far detector fit, which includes additional uncertainties from a Super-Kamiokande detector model. Two different analyses are described in the following sections, which both use the same near detector fit results but different assumptions and data samples at the far detector.

NEW RESULTS FROM ANTINEUTRINO RUNNING

$\bar{\nu}_e$ appearance analysis

The aim of this analysis is to look for anti-electron neutrino appearance, separately from electron neutrino appearance (which has already been observed with a significance of 7.3σ at T2K [2]). In order to test whether or not our data indicate the presence of $\bar{\nu}_e$ appearance, we introduce a new parameter β which modifies the $\bar{\nu}_e$ appearance probability:

$$P(\bar{\nu}_\mu \rightarrow \bar{\nu}_e) = \beta \times P_{PMNS}(\bar{\nu}_\mu \rightarrow \bar{\nu}_e) \quad (1)$$

Aside from this, CPT symmetry is assumed (so the same oscillation parameters are used for neutrino and antineutrino oscillations). In this parameterisation, $\beta = 1$ corresponds to $\bar{\nu}_e$ appearance in accordance with the PMNS prediction (which allows for CP violation if $\delta_{CP} \neq 0$). $\beta = 0$ corresponds to no $\bar{\nu}_e$ appearance.

The analysis uses a marginal likelihood, which is integrated over all parameters other than β :

$$\mathcal{L}(\beta) = \int \int \prod_{SKbins} \mathcal{L}_{Poisson,bin}(\beta, \vec{\sigma}, \vec{f}) \times \pi_{syst.}(\vec{f}) \times \pi_{osc.}(\vec{\sigma}) d\vec{\sigma} d\vec{f} \quad (2)$$

where $\vec{\sigma}$ are the oscillation parameters, \vec{f} are the systematic parameters, $\pi_{syst.}(\vec{f})$ is the prior probability density for the systematic parameters (taken from the near detector fit), and $\pi_{osc.}(\vec{\sigma})$ is the prior probability density for the oscillation parameters. $\mathcal{L}_{Poisson,bin}$ is the Poisson likelihood in each bin given the number of data events and number of predicted events at Super-Kamiokande. The Super-Kamiokande data and prediction are binned in either reconstructed (anti-)neutrino energy (E_{rec}) or momentum and angle (with respect to the incoming neutrino direction) of the measured lepton ($p - \theta$), and the product runs over all bins. The oscillation priors are taken from the posterior of the T2K joint ν_μ and ν_e fit [1], which have a peak value for $\delta_{CP} \sim -\pi/2$.

We report the significance for $\beta = 1$ in two ways: a p-value and a Bayes factor.

The p-value relies on a test statistic $-2\Delta \ln \mathcal{L} = -2(\ln \mathcal{L}(\beta = 1) - \ln \mathcal{L}(\beta = 0))$, which compares the marginal likelihoods from two fits assuming $\beta = 1$ and $\beta = 0$. This is then compared to the same test statistic calculated from an ensemble of test experiments on fake data generated with $\beta = 0$, to characterise how anomalous our data are with respect to the $\beta = 0$ hypothesis.

The Bayes factor is simply the likelihood ratio:

$$B_{10} = \frac{\mathcal{L}(Data|\beta = 1)}{\mathcal{L}(Data|\beta = 0)} \quad (3)$$

and describes how much our data favours $\beta = 1$ over $\beta = 0$.

The current data set contains 3 events in the e -like sample at Super-Kamiokande. At the T2K best-fit parameter values from neutrino analyses (given in table III) we expect ~ 1.3 events if $\beta = 0$ and ~ 3.7 events if $\beta = 1$. Examining the full range $\delta_{CP} = [-\frac{\pi}{2}, \frac{\pi}{2}]$ and both mass hierarchies, we predict between 3.7 and 5.3 events for $\beta = 1$. Events are selected according to the following criteria: they must be fully contained within the fiducial volume of the detector, have only one reconstructed ring, and have electron-like particle identification. The lepton momentum must be greater than 100 MeV, and the reconstructed (anti-)neutrino energy smaller than 1.25 GeV. The event must pass the π^0 rejection cuts used in the Super-Kamiokande software and there can be no decay electrons.

Table II shows the test statistic ($-2\Delta \ln \mathcal{L}$), the p-value, and the Bayes factor for the data fit. The p-value is greater than 15% for both the E_{rec} and $p - \theta$ fit, which shows no disagreement between the data and the $\beta = 0$ hypothesis. The Bayes factor is 1.1 for the E_{rec} fit and 0.6 for the $p - \theta$ fit (which is equivalent to a Bayes factor of ~ 1.7 in favour of $\beta = 0$ over $\beta = 1$). Neither of these show strong enough evidence to support $\beta = 1$ over $\beta = 0$, so with the current data set we cannot conclude that we have observed $\bar{\nu}_e$ appearance with statistical significance.

TABLE II: Test statistics, p-values, and Bayes factors from T2K $\bar{\nu}_e$ appearance analysis

Super-Kamiokande binning	$-2\Delta \ln \mathcal{L}$	p-value	B ₁₀
$\bar{\nu}E_{rec}$	0.16	0.16	1.1
Lepton $p - \theta$	-1.16	0.34	0.6

TABLE III: Oscillation parameters used for the $\bar{\nu}_\mu$ disappearance analysis. Fixed values are taken from the output of the T2K $\nu_\mu + \nu_e$ joint fit [1] and the 2014 edition of the Particle Data Booklet [3].

	Value for neutrinos	Value for antineutrinos
$\sin^2 \theta_{23}$	0.527	0–1
$\Delta m_{32}^2 (\times 10^{-3} \text{eV}^2)$	2.51	0–20
$\sin^2 \theta_{13}$		0.0248
δ_{CP} (rad.)		-1.55
$\sin^2 \theta_{12}$		0.304
$\Delta m_{21}^2 (\times 10^{-5} \text{eV}^2)$		7.53

$\bar{\nu}_\mu$ disappearance analysis

This analysis uses the antineutrino-mode data to measure the antineutrino oscillation parameters, so CPT invariance is not assumed. We fit the oscillation parameters that dominate $\bar{\nu}_\mu$ disappearance, $\sin^2 \bar{\theta}_{23}$ and $\Delta \bar{m}_{32}^2$, in the ranges given in table III. All other antineutrino and neutrino oscillation parameters are fixed such that $\theta_{12} = \bar{\theta}_{12}$, $\theta_{13} = \bar{\theta}_{13}$, $\Delta m_{12}^2 = \bar{\Delta} m_{12}^2$, and $\delta_{CP} = \bar{\delta}_{CP}$.

The Super-Kamiokande fit maximises a marginal likelihood \mathcal{L} with respect to $\sin^2 \bar{\theta}_{23}$ and $\Delta \bar{m}_{32}^2$:

$$\mathcal{L}(\vec{\sigma}) = \int \prod_{SKbins} \mathcal{L}_{Poisson,bin}(\vec{\sigma}, \vec{f}) \times \pi_{syst.}(\vec{f}) d\vec{f} \quad (4)$$

where all symbols are as previously defined. In this analysis the Super-Kamiokande data was binned only in reconstructed (anti-)neutrino energy.

There are 34 events in the μ -like sample from antineutrino beam data. The event selection is similar to that used in the e -like selection: events must be fully contained in the fiducial volume and may only have one reconstructed ring. However, in this case the event must be consistent with a muon-like particle identification, there must be one or fewer decay electrons, and the outgoing lepton momentum must be greater than 200 MeV.

Figure 3 shows the predicted reconstructed energy spectrum under the no-oscillation hypothesis, and the best-fit spectrum from the data fit, along with the data. The right-hand plot shows the ratio of both data and best-fit spectrum to the unoscillated prediction, which

shows the characteristic ‘oscillation dip’ that is clear evidence of $\bar{\nu}_\mu$ oscillation. The binning shown in the plot is coarser than the binning used for the data fit.

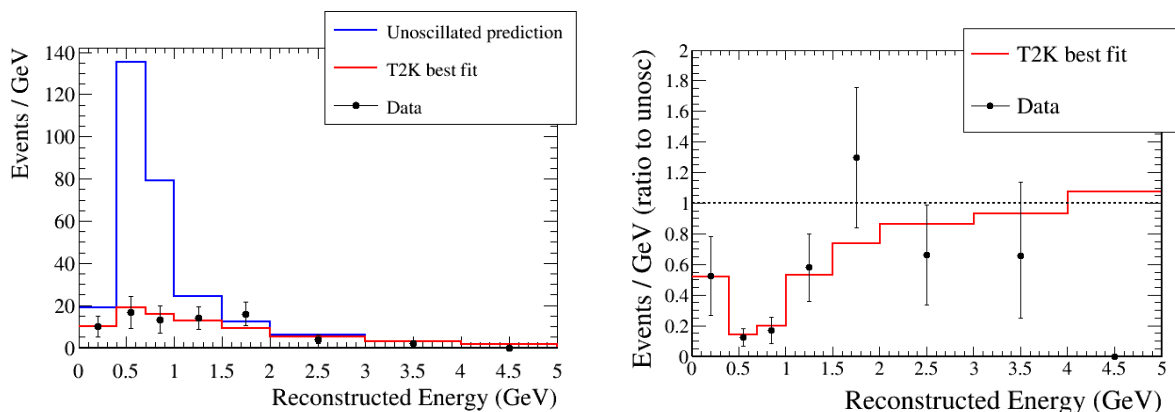


FIG. 3: **Left:** Predicted reconstructed energy spectrum in the case of no oscillations, and best-fit reconstructed energy spectrum after the data fit. Data is overlaid in black, with statistical errors shown. **Right:** Ratio of best-fit energy spectrum and data to prediction without oscillations.

The left hand side of figure 4 shows the 68% and 90% credible interval contours in $\sin^2 \bar{\theta}_{23}$ – $\Delta \bar{m}_{32}^2$ compared to the contours from the T2K $\nu_\mu + \nu_e$ joint fit [1]. The antineutrino analysis has much larger contours because it has much lower statistics than the neutrino analysis, but the results are consistent: we see no evidence for CPT violation. Projecting the posterior onto one dimension gives best-fit estimates with 1σ errors:

$$\sin^2 \bar{\theta}_{23} = 0.46_{-0.06}^{+0.14}$$

$$\Delta \bar{m}_{32}^2 = 2.50_{-0.2}^{+0.3} \times 10^{-3} \text{ eV}^2$$

The right hand side of figure 4 shows the contours from this analysis overlaid with the 90% contours from $\bar{\nu}_\mu$ disappearance analyses in MINOS [4] and Super-Kamiokande using atmospheric neutrinos [5]. The results from all three experiments are in agreement.

SUMMARY AND FUTURE PROSPECTS

We have presented here the first T2K results based on antineutrino data, including analyses of $\bar{\nu}_e$ appearance and $\bar{\nu}_\mu$ disappearance.

For $\bar{\nu}_e$ appearance we calculate a p-value greater than 15% and a Bayes factor ~ 1 , so there is not sufficient evidence to claim observation of $\bar{\nu}_e$ appearance in the current data set.

The 1D best-fit values from the measurement of $\bar{\nu}_\mu$ disappearance at T2K are $\sin^2 2\bar{\theta}_{23} = 0.46_{-0.06}^{+0.14}$ and $\Delta \bar{m}_{32}^2 = 2.50_{-0.2}^{+0.3} \times 10^{-3} \text{ eV}^2$. The 2D contours are in agreement with T2K neutrino-mode fits and antineutrino results published by MINOS and Super-Kamiokande.

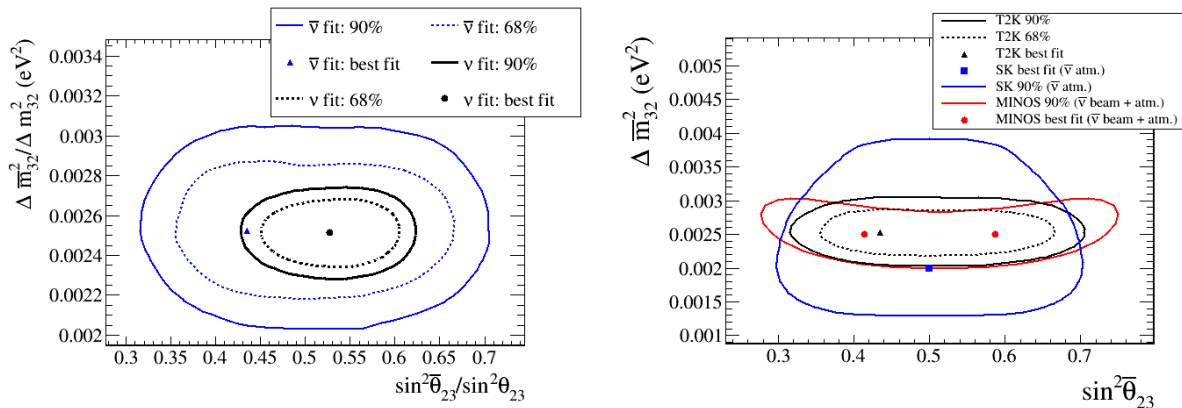


FIG. 4: 68% and 90% credible intervals in $\sin^2 \bar{\theta}_{23} - \Delta \bar{m}_{32}^2$ from the $\bar{\nu}_\mu$ disappearance analysis. **Left:** overlaid with contours from the T2K $\nu_\mu + \nu_e$ joint fit [1]. **Right:** overlaid with contours from similar analyses by MINOS (using antineutrino-mode beam and atmospheric data) [4] and Super-Kamiokande (using atmospheric data only) [5]. The MINOS contour was originally presented in terms of $\sin^2 2\bar{\theta}_{23}$ and had to be unfolded (hence the two best-fit points).

Both analyses are statistics-limited and T2K is continuing to run with an antineutrino beam which will provide additional data to improve both measurement.

* Presented at NuFact15, 10-15 Aug 2015, Rio de Janeiro, Brazil [C15-08-10.2]

† kirsty.duffy@physics.ox.ac.uk; Speaker

- [1] K. Abe, J. Adam, H. Aihara, T. Akiri, C. Andreopoulos, S. Aoki, A. Ariga, S. Assylbekov, D. Autiero, M. Barbi, et al. (T2K Collaboration), Phys. Rev. D **91**, 072010 (2015), URL <http://link.aps.org/doi/10.1103/PhysRevD.91.072010>.
- [2] K. Abe, J. Adam, H. Aihara, T. Akiri, C. Andreopoulos, S. Aoki, A. Ariga, T. Ariga, S. Assylbekov, D. Autiero, et al. ((T2K Collaboration)), Phys. Rev. Lett. **112**, 061802 (2014), URL <http://link.aps.org/doi/10.1103/PhysRevLett.112.061802>.
- [3] K. A. Olive et al. (Particle Data Group), Chin. Phys. **C38**, 090001 (2014).
- [4] P. Adamson, I. Anghel, C. Backhouse, G. Barr, M. Bishai, A. Blake, G. J. Bock, D. Bogert, S. V. Cao, C. M. Castromonte, et al. (MINOS Collaboration), Phys. Rev. Lett. **110**, 251801 (2013), URL <http://link.aps.org/doi/10.1103/PhysRevLett.110.251801>.
- [5] K. Abe, Y. Hayato, T. Iida, M. Ikeda, K. Iyogi, J. Kameda, Y. Koshio, Y. Kozuma, M. Miura, S. Moriyama, et al. (Super-Kamiokande Collaboration), Phys. Rev. Lett. **107**, 241801 (2011), URL <http://link.aps.org/doi/10.1103/PhysRevLett.107.241801>.

Stopping pion experiments in the sterile neutrino field*

Eito Iwai[†]

KEK, Tsukuba, JAPAN

(Dated: March 24, 2016)

Abstract

Experiments to search for a sterile neutrinos using decay-at-rest neutrinos have a similar approach to the LSND experiment, which first indicated the sterile neutrino. The feature of the experimental method is described, and the JSNS² experiment [1, 2] at the J-PARC Material and Life science Facility (MLF) and the OscSNS experiment [3] at the Oak Ridge National Laboratory (ORNL) are introduced as on-going projects. The experimental setup, sensitivity and the current status of the experiments are described.

INTRODUCTION

Sterile neutrino

In the last twenty years, the LSND [4] and other experiments [5–7] reported neutrino phenomena, which cannot be explained by the standard three neutrino scheme, with more than 3σ significance. A sterile neutrino was introduced to explain such phenomena. It is a new kind of lepton, which has neither electromagnetic nor weak interactions, and can be observed only by neutrino oscillations.

Searching for a sterile neutrino is one of the hottest topics in the neutrino field, and various new experiments are proposed and prepared in the world. Designing a experiment with small systematic uncertainties is crucial.

Experiments to search for a sterile neutrino

Experiments to search for a sterile neutrino can be classified by their neutrino sources: reactor, radio-active source, accelerator using decay-in-flight and decay-at-rest neutrinos. We discuss the decay-at-rest neutrino experiments in the following sections. A proton beam hits a target and produces pions, muons and kaons. They stop and decay at the target or surrounding materials. The decay-at-rest neutrino experiment uses such neutrinos as a probe. We introduce two experiments: the JSNS² at the J-PARC MLF and the OscSNS at the ORNL as the decay-at-rest experiments. First, we describe the common features of those experiments and then move on to each experiment.

Principle of measurement

The main channel to search in these two experiments is $\bar{\nu}_\mu$ to $\bar{\nu}_e$ oscillation via the fourth (or more) mass eigenstate. Figure 1 shows the schematic of the experiment. The $\bar{\nu}_\mu$ is from μ^+ decay-at-rest. The $\bar{\nu}_e$ from μ^- decay (beam intrinsic $\bar{\nu}_e$) is suppressed by three orders of magnitude by π^-/μ^- captures. The inverse beta decay (IBD: $\bar{\nu}_e + p \rightarrow e^+ + n$) is utilized to detect $\bar{\nu}_e$. The neutron from the IBD is observed as gamma(s) from neutron capture by gadolinium (Gd) or hydrogen. By detecting the neutron from the IBD, delayed coincidence

method can be used: a positron makes the prompt signal and a captured neutron makes the delayed signal.

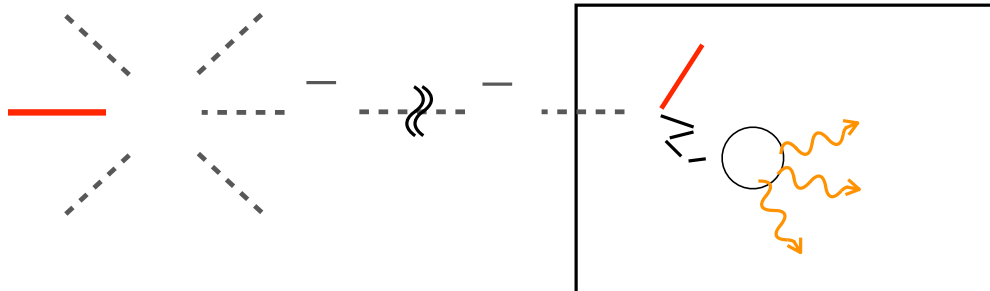


FIG. 1: Schematic of the experiment. In this figure, neutrons from the IBD are captured by gadolinium.

Signal events can be distinguished from the dominant background, another neutrino process: $\bar{\nu}_e$ from μ^- decay, by using the difference of energy distributions as shown in Fig. 2.

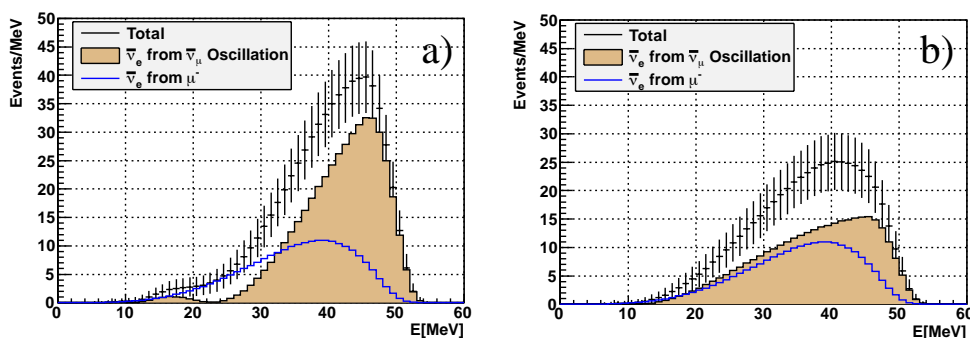


FIG. 2: Expected energy distributions of signal and dominant background for the JSNS² experiment [8]; a) JSNS² best sensitivity: $(\Delta m^2, \sin^2 2\theta) = (2.5 \text{ eV}^2, 0.003)$, b) LSND best fit: $(\Delta m^2, \sin^2 2\theta) = (1.2 \text{ eV}^2, 0.003)$.

Because of these features described above, the two experiments have the following advantages over other sterile neutrino oscillation experiments.

- Low duty factor:

Because we use neutrinos made by the short pulsed proton beam, neutrinos come within short period. It is a big advantage to reject beam-unrelated backgrounds, such as fast neutron from cosmic rays, compared with the reactor and the radio-active source experiments.

- Small contamination of beam intrinsic $\bar{\nu}_e$:

The ratio of $\bar{\nu}_e$ from μ^- decays to $\bar{\nu}_\mu$ from μ^+ decays is one order of magnitude smaller than that of the decay-in-flight experiments ($\sim 1\%$). Moreover signals can be directly

distinguished from the beam intrinsic $\bar{\nu}_e$ by using the difference of energy distributions as described above.

- Well-understood neutrino energy spectrum:

We use neutrinos from muon decay-at-rest, and the neutrino energy spectrum is well-known as the Michel spectrum. This is also a big advantage over other decay-in-flight experiments.

- Absence of nuclear effects:

Neutrinos interact with free protons and the incident neutrino energy from the muon decay-at-rest is up to 50 MeV. The neutrino energy is thus reconstructed easily: $E_\nu \sim E_e + 1.8$ MeV.

- Well-understood neutrino flux:

The number of μ^+ decay can be directly measured together by detecting $\nu_e + {}^{12}\text{C} \rightarrow e^- + {}^{12}\text{N}_{\text{gs}}$.

- Well-known neutrino cross section:

The inverse beta decay process is utilized to detect oscillation signals. The cross section of the IBD is measured with a precision of a few % [9].

J-PARC E56: JSNS² EXPERIMENT

The JSNS² stands for "J-PARC Sterile Neutrino Search at J-PARC Spallation Neutrino Source". The Japan Proton Accelerator Research Complex (J-PARC) consists of three accelerators: 400 MeV Linac, 3 GeV rapid cycling synchrotron (RCS) and 50 GeV (currently 30 GeV) main ring (MR). Most of the protons from the RCS are delivered to the MLF. The JSNS² detector is placed in the third floor of the MLF.

Neutrino source and apparatus

The mercury target placed in the MLF is hit by protons from the RCS to produce neutrons for material and life science. Not only the neutrons but also a large number of neutrinos are emitted from the target at the same time. The JSNS² experiment uses these neutrinos for the sterile neutrino search.

The design power of the RCS is 1 MW and 500 kW continuous beam was delivered so far in spring 2015. The beam from the RCS has 2-bunch structure and the repetition rate is 25 Hz. Fig. 3 shows the timing distribution of neutrinos from pions, muons and kaons. By selecting neutrinos coming after 1 μs from the beam, pure neutrinos from stopped muons can be observed.

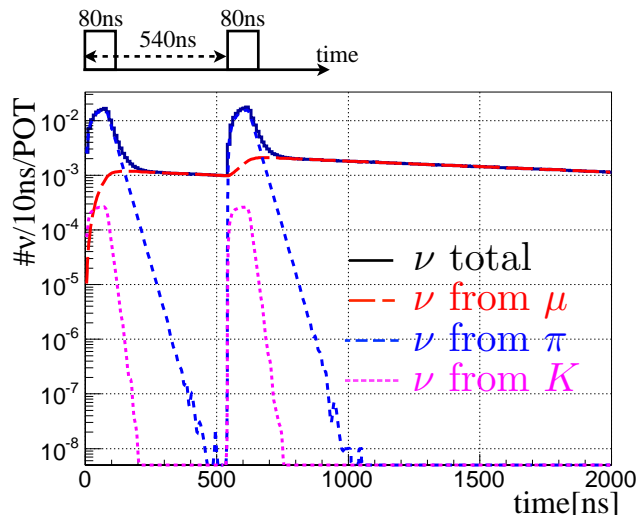


FIG. 3: Timing distribution of neutrinos from pions, muons and kaons [1].

To detect neutrinos, two liquid scintillator (LS) detectors will be placed. The baseline is 24 m from the target. The fiducial volume is 50 tonnes in total. The Gd-loaded LS is used to detect neutrons from IBD. By loading Gd in LS, a neutron from IBD is detected as 8 MeV gammas in total. The LS also has e/n separation capability by using Cherenkov emission and/or Pulse Shape Discrimination technique. A new beamline and a new building for the detector are NOT necessary. Because the detector technology is well-established and some experts of such detector belong to the JSNS² collaboration, just 1.5 years is necessary from grand breaking to physics runs. The construction cost is estimated to be 2 million dollars per detector and 4 million dollars in total.

Sensitivity

Fig. 4 shows the expected sensitivity of the JSNS² experiment for 5 years \cdot MW exposure. Most of the parameter region indicated by the LSND experiment can be explored with 5 σ significance.

Status

Followings are the brief history and status of the JSNS² experiment. In late 2012, some of us began consideration of the experiment. In spring 2013, we held a background measurement at the MLF first floor. Based on the measurement result, we submitted an experiment proposal [1] at the 17th J-PARC PAC in September 2013. In spring 2014, we held a background measurement at the MLF third floor, which is the candidate detector location of the

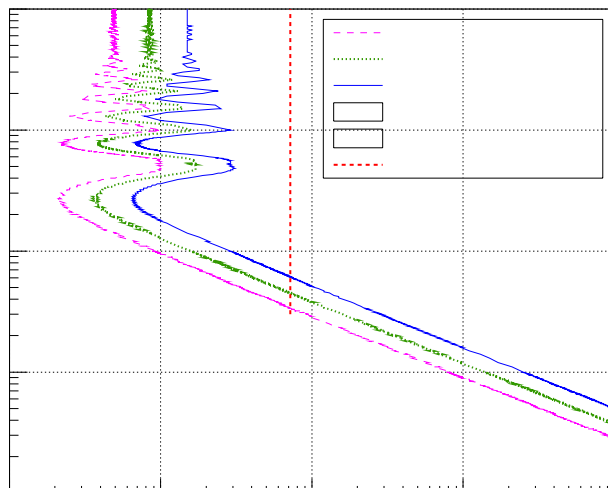


FIG. 4: Expected sensitivity of the JSNS² experiment for 5 years · MW exposure [8]. The green and blue lines correspond to 3σ and 5σ significance, respectively.

experiment, according to the recommendation of the J-PARC PAC. Based on the measurement in 2014, we submitted the status report [8] at the 19th J-PARC PAC and requested Stage-1 approval. In January 2015, we received Stage-1 approval from the J-PARC. After receiving the Stage-1 approval, the R&D budget toward coming Technical Design Report (TDR) and Stage-2 approval is officially supported by J-PARC/KEK.

For the RCS proton beam, 1 MW trial was held in December 2014. The accelerator group tuned the configuration specially for the trial, and achieved 1 MW beam in short period. Toward the continuous 1 MW operation, the power supplies of the Radio Frequency (RF) cavity are upgraded in summer 2015.

In the topics described above, we briefly describe about the background measurement at the candidate location, the MLF third floor.

Background measurement at the candidate location

One of the main purposes of this measurement is to directly measure one of backgrounds induced by beam fast neutrons at the candidate location for the detectors. The background was indicated by the previous background measurement in 2013. Fig. 5 shows the definitions of "signal" and "background" of this measurement. Based on the Geant4 [10] based Monte Carlo simulation studies, beam induced fast neutrons hit our detector and produce pions, these pions then decay into Michel electrons ($n + p(\text{or } C) \rightarrow X + \pi^+$, then $\pi^+ \rightarrow \mu^+ \rightarrow e^+$). The incident neutron is captured in the detector. These sequential process can mimic the IBD.

	beam-on	beam-off	comment
signal		×	delayed signal is not required for this measurement
backgrounds		○	huge, rejected by charged veto
		○	rejected by charged activity coming earlier (Parent muon)
		○	accidental coincidence

FIG. 5: The definition of "signal" and "backgrounds" of the background measurement. Signal is Michel electrons induced by beam fast neutrons.

Fig. 6 shows the schematic view of the 500 kg plastic scintillator detector for this measurement. The 500 kg scintillator detector was surrounded by two layers of charged vetoing system.

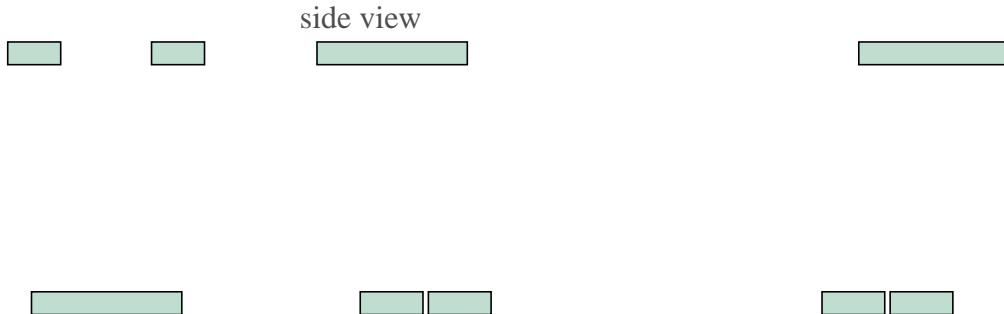


FIG. 6: Schematic view of the 500 kg plastic scintillator detector for the background measurement at the candidate location. (left: front view, right: side view)

Fig. 7 shows the energy distribution for the beam-ON and the beam-OFF events, before and after applying the charged veto cut. The numbers of events both consistent between the beam-ON and the beam-OFF data either with or without applying the charged veto cut. After applying all the cuts, we set the upper limit of the background level. The backgrounds for prompt and delayed signal are also evaluated. We confirmed the background level is manageable and smaller than the dominant background: $\bar{\nu}_e$ from μ^- decay. The detail of this background measurement is described in this article [8, 11].

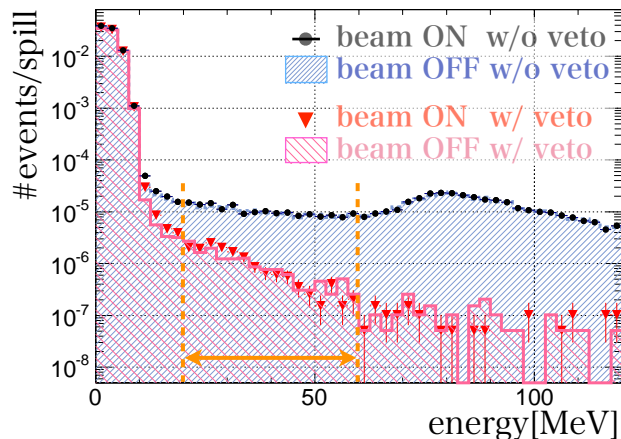


FIG. 7: Energy distribution of the events taken with beam-ON and beam-OFF, before and after applying charged veto cut [11].

OSCSNS EXPERIMENT AT ORNL

The OscSNS is another decay-at-rest experiment to search for a sterile neutrino at the ORNL. The OscSNS has similar approach to the JSNS² and we briefly introduce the experiment based on the description in this article [3].

There are three neutron sources at the ORNL, and the Spallation Neutron Source (SNS) is one of them. The mercury target placed in the SNS is hit by 1 GeV protons to produce neutrons and neutrinos as well. The OscSNS uses these neutrinos for the search. The beam power is 1.4 MW and the repetition rate is 60 Hz.

The OscSNS detector is 20.5 m long cylindrical shape, and its diameter is 8 m. The fiducial volume of the detector is 450 tonnes. This detector is placed 60 m from the mercury target. They plan to use hydrogen (free proton) to capture neutrons from the IBD, but loading Gd option is also under consideration. The construction cost is estimated to be 22 million dollars in total.

Fig. 8 shows the expected sensitivity of the OscSNS experiment for 6 calendar years exposure. The parameter region indicated by the LSND experiment is fully covered with more than 5σ significance. Their unique feature is that the L/E oscillation pattern can be observed in their detector depending on Δm^2 as shown in Fig. 9 because of the 20.5 m long cylindrical shape of the OscSNS detector.

The OscSNS collaboration visited the SNS and first showed their physics plan in April 2013, and then submitted their R&D proposal and white paper to the Department of Energy (DOE). The R&D funding from the DOE will start the detailed design of the experiment. They estimate it takes 3 years from grand breaking to start the experiment.

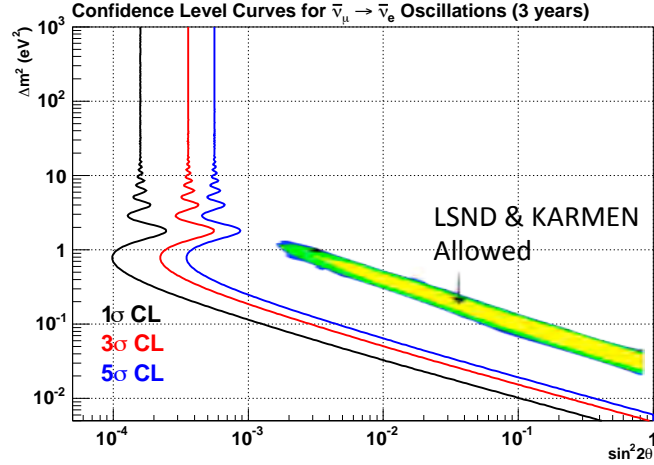


FIG. 8: Expected sensitivity of the OscSNS experiment for 6 calendar years exposure [3]. The red and blue lines correspond to 3σ and 5σ significance, respectively.

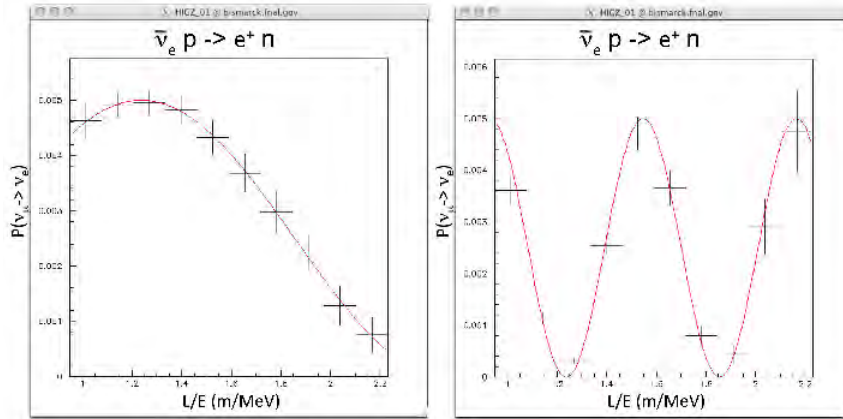


FIG. 9: The oscillation probability as a function of L/E for 10 calendar years of data collection for $\Delta m^2 = 1 \text{ eV}^2$ (left) and 4 eV^2 (right) [3].

COMPARISON

The JSNS² and the OscSNS have similar concepts to search for a sterile neutrino, but each of them has its own features as shown in Table I. The beam power is similar (1 MW for the JSNS², 1.4 MW for the OscSNS), but their beam energy is different. The larger beam energy of 3 GeV provides larger π and μ production rate for the JSNS², on the other hand the lower beam energy of 1 GeV provides less beam intrinsic $\bar{\nu}_e$ background rate for the OscSNS. The longer baseline of 60 m and the larger fiducial volume of 450 tonnes of the OscSNS provide the capability of the fully-covered exploration of the allowed parameter regions, but also require higher cost and longer start-up time. The compact detector of the

JSNS² just requires relatively reasonable cost, and NO new dedicate building is necessary. It leads to the rapid start of the exploration of the parameter region of $\Delta m^2 > \text{eV}^2$ with 5 σ sensitivity.

TABLE I: Comparison of features of the JSNS² experiment and the OscSNS experiment.

	JSNS ²	OscSNS	Notes
fiducial vol.	50 t	450 t	
base line	24 m	50 m	LSND: 30 m
beam energy	3 GeV	1 GeV	JSNS ² : larger π/μ production rate OscSNS: less beam intrinsic $\bar{\nu}_e$
beam power	1 MW	1.4 MW	
delayed signal	Gd(8 MeV, 30 μs)	H(2.2 MeV, 220 μs)	OscSNS: Gd option?
cost	4 M dollars	22 M dollars	

SUMMARY

We described decay-at-rest neutrino experiments in the sterile neutrino field, and introduced two experiments: the JSNS² at the J-PARC MLF and the OscSNS at the ORNL as on-going projects. They adopt a similar approach to the LSND experiment, which first indicated the sterile neutrino. They are thus direct and complete test of the LSND result. The common features of those experiments lead to many advantages over other sterile neutrino experiments. The experimental setup, sensitivity and the current status of the experiments were described, and their individual unique features were also mentioned.

* Presented at NuFact15, 10-15 Aug 2015, Rio de Janeiro, Brazil [C15-08-10.2]

† `eito@post.kek.jp`; Speaker

- [1] M. Harada et al., arXiv:1310.1437 [physics.ins-det].
- [2] <http://research.kek.jp/group/mlfnu/>
- [3] OscSNS Collaboration, arXiv:1307.7097 [physics.ins-det].
- [4] A. Aguilar et al., Phys. Rev. D **64**, 112007 (2001).
- [5] A.A.Aguilar-Arevalo et al. [MiniBooNE Collaboration], Phys.Rev.Lett. **110**.161801 (2013).
- [6] C. Giunti and M. Laveder, Phys.Rev.C **83**, 065504 (2011).
- [7] Th. A. Mueller et al., Phys.Rev.C **83**, 054615 (2011). P. Huber, Phys.Rev.C **84**, 024617 (2011).
- [8] M. Harada et al., arXiv:1507.07076 [physics.ins-det].
- [9] P. Vogel and J. F. Beacom, Physical Review D **60** 053003 (1999).
- [10] J. Allison et al., IEEE Transactions on Nuclear Science **53** No. 1 270-278 (2006); S. Agostinelli et al., Nuclear Instruments and Methods A **506** 250-303 (2003).
- [11] S. Ajimura et al., Prog. Theor. Exp. Phys. (2015) 063C01.

**Status of atmospheric neutrino oscillation measurements in
IceCube and PINGU***

João Pedro Athayde Marcondes de André[†]

Michigan State University

for the IceCube-Gen2 Collaboration[‡]

(Dated: December 20, 2015)

Abstract

The IceCube Neutrino Observatory, located at the South Pole, is the world's largest neutrino detector. DeepCore, the low energy extension for IceCube, with a threshold of about ten GeV is well suited to study neutrino oscillations using neutrinos produced in the Earth's atmosphere and traveling distances as large as the Earth's diameter before being detected. Using these neutrinos DeepCore makes measurements of the neutrino oscillation parameters θ_{23} and $|\Delta m_{32}^2|$ with precisions approaching that of dedicated experiments. PINGU, a proposed low energy extension to IceCube, would further reduce the detector's energy threshold to a few GeV to allow the measurement of the neutrino mass hierarchy at the 3σ level with 3-5 years of data, in addition to significant improvements to the determination of the parameters already being studied by DeepCore. Current results from DeepCore and PINGU sensitivity to θ_{23} , $|\Delta m_{32}^2|$ and the neutrino mass hierarchy are discussed here.

INTRODUCTION

Neutrino oscillations were discovered by Super-Kamiokande in 1998 [1] through the measurement of atmospheric neutrinos, and SNO in 2002 [2] through the measurement of solar neutrinos. Since then neutrino oscillation has also been observed in various experiments using other neutrino sources, such as particle accelerators and reactors. The parameters describing the standard 3-flavor neutrino oscillation have been measured with varying precision by these experiments (see [3] and references therein) with the exception of the CP-violating phase (δ_{CP}) and the mass hierarchy. For the latter, the case where the third mass eigenstate is heaviest (positive Δm_{32}^2) is referred to as “normal” (NH), while when it is the lightest (negative Δm_{32}^2) it is referred to as “inverted” (IH). The amplitude of the neutrino flavor oscillation is determined by the elements of the mixing matrix, which is described by the mixing angles (θ_{12} , θ_{13} , and θ_{23}) and δ_{CP} , while its oscillation period in vacuum depends on $|\Delta m_{32}^2|L/E$ and $|\Delta m_{21}^2|L/E$, where E is the neutrino energy and L is the distance it traveled between its production and interaction points.

Atmospheric neutrinos are particularly interesting for studying neutrino oscillations because they are produced with energies spanning many orders of magnitude and are available at varying values of L (up to the Earth's diameter of about 12700 km). For neutrinos traveling through the Earth's core, the first maximum ν_μ disappearance happens around 25 GeV, which makes its measurement possible for large-volume neutrino detectors. In particular, the IceCube/DeepCore energy threshold of around ten GeV allows it to map this first maximum of ν_μ disappearance [4] as a function of L and E and therefore measure the parameters

$|\Delta m_{32}^2|$ and θ_{23} .

A recent measurement [5] of a relatively large mixing angle between the first and third mass eigenstates (θ_{13}) has made it possible to determine the neutrino mass hierarchy using atmospheric neutrinos with megaton-scale detectors such as the proposed Precision IceCube Next Generation Upgrade (PINGU). This is possible due to matter effects [6, 7], that depend on the sign of Δm_{32}^2 , affecting neutrinos propagating through the Earth's core and mantle which produce a resonant effect changing the event rates in the detector as a function of L and E around 5-15 GeV [8, 9]. PINGU will also contribute to improving the precision measurement of ν_μ disappearance among several other topics discussed in detail in [10].

THE ICECUBE/DEEPCORE AND PINGU DETECTORS

The IceCube Neutrino Observatory [11] is the world's largest neutrino detector, with a total volume of about 1 km³ in the deep glacier near the South Pole Station, Antarctica, and is instrumented with 5160 digital optical modules (DOMs). The observatory was designed to detect high-energy neutrinos and look for an extraterrestrial component to the observed neutrino flux, for which it successfully provided first evidence recently [12].

The original detector design was augmented by creating a region close to the center of the detector with a higher density of optical sensors in the deep, clearest ice, therefore increasing the photocathode coverage in that volume. This volume with increased photocathode density, called DeepCore [13], was added with the objective of lowering the energy threshold of the IceCube detector from hundreds to about ten GeV and thus make it possible to perform competitive measurements of neutrino oscillations and dark matter searches.

With the goal of further lowering the energy threshold of the IceCube Neutrino Observatory, PINGU [10] is being proposed. It achieves that goal by further increasing the density of optical modules in the DeepCore region, as shown in Fig. 1. This increased photocathode density will effectively lower the energy threshold of the detector by an order of magnitude.

Background rejection

The main background in IceCube/DeepCore to observing ν oscillations consists of the atmospheric μ co-produced in the cosmic ray showers. In DeepCore analyses, this background is rejected by looking in the surrounding IceCube strings for signals indicating that the event could have in fact originated outside DeepCore and propagated into its volume. In addition to rejecting atmospheric μ events, some of these algorithms are also used to

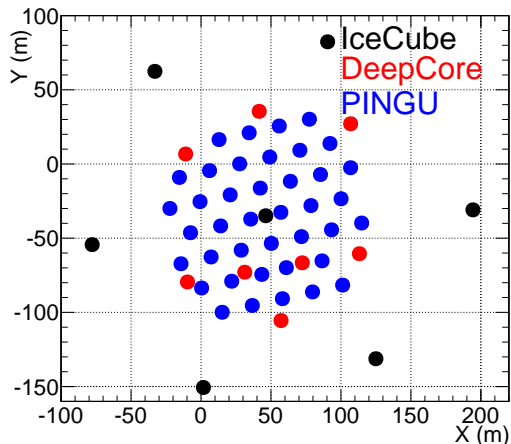


Figure 1: A top view of the proposed PINGU detector geometry used for the studies presented in this proceeding. The location of existing IceCube strings are shown in black, DeepCore in red and PINGU in blue.

extract a sample used to estimate the shape of the distribution of this background in the final sample. Besides these veto criteria, atmospheric μ are down-going and signal ν are up-going, therefore restricting the final sample only to events reconstructed as up-going further reduces the atmospheric μ background.

Another non-negligible background to analyses in DeepCore are events produced by the detector self-triggering due to the presence of noise in the DOMs. Such events are rejected by requiring a minimum number of photons in the event that are consistent with a Cherenkov wavefront propagating in the ice in which the detector is embedded and by requiring a minimal quality to the event reconstruction.

In PINGU, while we have not performed extensive atmospheric μ background and dedicated detector self-triggering simulations, we expect to be able to reject these two backgrounds using the same techniques that are already successfully in use in DeepCore, and given the low rates of these backgrounds in the DeepCore they are currently neglected in PINGU analyses.

Reconstruction of events

The signal for the 3-flavor ν oscillation analysis are neutrinos with energy less than about 50 GeV. Given the detector threshold for both DeepCore and PINGU, most of the interactions are produced via deep inelastic scattering (DIS) which produce for ν charged current (CC) interactions a lepton of the same flavor as the neutrino and a hadronic shower, which are to a good approximation collinear.

The lepton produced by the ν interaction will either produce a track in the detector if there is a μ in the final state, or a shower otherwise. Given the detector granularity, the lepton induced showers and the hadronic showers produced by the DIS interactions will

have a similar topology, while a μ track can be distinguished more easily from the showers. Because of that, the general hypothesis used for reconstructing events is of DIS ν_μ CC interactions. Using this hypothesis, the other interactions (with the exception of ν_τ CC interactions with a μ produced by the τ decay) will resemble a ν_μ CC interaction with a low energy μ produced, and given the similarities in the different shower topologies they are still reconstructed reasonably well. Additionally, looking for a μ in the final state is also used to either select mainly ν_μ CC events for ν_μ disappearance analyses, as shown in Fig. 2, or to classify events between tracks and cascades for the neutrino mass hierarchy analysis.

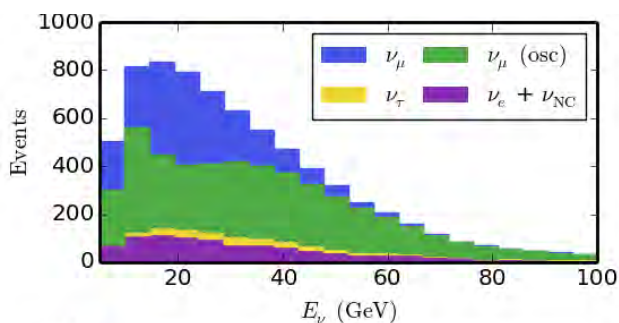


Figure 2: Composition of sample used for the ν_μ disappearance analysis [4] as a function of true neutrino energy. The blue shaded area shows the expected size of the oscillation effect reducing the event rate, while the purple and yellow region show the contamination of the sample by events that are not ν_μ CC (green).

Typically only a few tens of photons produced in these low energy neutrino interactions will be detected in DeepCore and some of those will have scattered multiple times before being detected. The latest results from DeepCore [4] relied on identifying unscattered photons and using them to reconstruct the direction of the event that produced them, following [14]. The identification of unscattered, or direct, photons is performed by requiring a specific pattern of their arrival time and location. In order for the directional reconstruction to perform well it is required for the event to have at least 5 unscattered photons identified, which reduces significantly the size of the available sample that can be used in the analysis as only 30% of the events have the required number of direct photons. After the direction of the event is reconstructed using only the unscattered photons, the energy and vertex of the neutrino are reconstructed using all the observed photons in the event, without allowing the reconstructed direction to change.

A new reconstruction method has matured in the last few years to make possible the reconstruction of events that do not have a large number of unscattered photons. This new reconstruction estimates simultaneously the interaction vertex, the neutrino direction, and energy by maximizing the likelihood of the tested hypothesis to yield the observed light distribution in the detector, both in terms of its position, time, and charge. In order to estimate the expected light distribution, the optical properties of the South Pole ice are accounted for based on the in-situ measurements of its properties [15]. This new method

achieves a precision comparable to the one described above, while at the same time being able to reconstruct nearly all neutrino events. This new reconstruction is currently being tested in DeepCore with the goal of creating the next generation of oscillation analysis and is also the main reconstruction used in PINGU.

Neutrino mass hierarchy signature in PINGU

For neutrino energies around 5-15 GeV, the MSW effect changes the survival probabilities for neutrinos and anti-neutrinos differently, depending on the ordering of the mass states. The difference between the cross-section of neutrinos and anti-neutrinos makes it possible to use atmospheric neutrinos to measure the neutrino mass hierarchy without an explicit discrimination between ν and $\bar{\nu}$ as proposed by [8, 9]. This is possible by comparing the observed rate of neutrinos as a function of E and L (measured by reconstructing the neutrino direction) with the expected distributions from the NH and IH hypothesis. The expected difference between these two cases, shown in Fig. 3, while small, creates a pattern that is measurable and helps reduce the effects of various systematics.

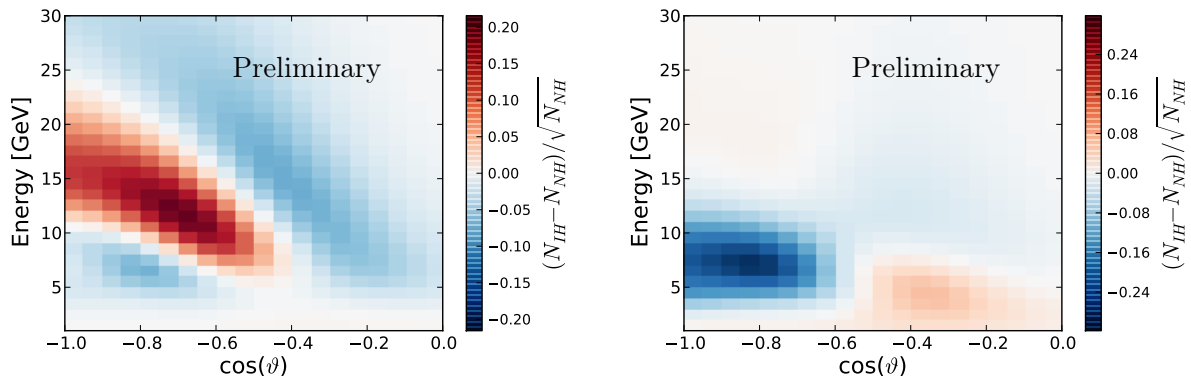


Figure 3: Distinguishability metric for track-like (left) and cascade-like (right) events for the neutrino mass hierarchy as defined in [9] for one year of simulated PINGU data.

ANALYSIS METHOD AND SYSTEMATICS

The current oscillation analysis in DeepCore aims at measuring θ_{23} and $|\Delta m_{32}^2|$. To extract those parameters, the simulation is fit to the data under both hierarchy assumptions and both results are reported. A likelihood ratio method is used both for the fitting and

to estimate the uncertainty of the measurement using a χ^2 approximation. In those fits θ_{13} is allowed to vary in the region allowed by the global fit to data [3], while δ_{CP} is fixed to 0 and θ_{12} and Δm_{21}^2 are fixed to their best fit value [3], as DeepCore is insensitive to these last parameters. Besides the neutrino oscillation parameters, the fitting procedure also minimizes over several nuisance parameters accounting for the current knowledge of the atmospheric ν and μ flux, neutrino interactions and detector related effects. Table I lists all the parameters considered.

Table I: Nuisance parameters used in DeepCore ν_μ disappearance analysis [4].

Nuisance parameters		Nominal value	Variation
Atmospheric flux	overall ν normalization		Free
	atm. flux spectral index	Honda 2015 [16]	$\pm 5\%$
	ν_e/ν_μ flux ratio		$\pm 20\%$
	overall μ normalization	from data	Free
Neutrino interactions	QE axial mass		
	RES axial mass	GENIE [17]	from GENIE
	DIS Bodek-Yang parameters		
Detector	DOM angular acceptance	flashers [15]	from range of models
	DOM overall efficiency	flashers and μ	$\pm 10\%$
	Bulk ice surrounding detector	flashers	compared 2 models
	Hadronic energy scaling	Geant4[18]	$\pm 5\%$

For PINGU analyses, the data is replaced either by an ensemble of pseudo-experiments or by an average experiment in the fitting procedure described above. The sensitivity to the neutrino mass hierarchy, in the case where an ensemble of pseudo-experiments is used, is estimated by computing the probability to reject the other hierarchy for the median experiment using the likelihood ratio between fitting each hierarchy; alternatively in the case where an average experiment is used, the sensitivity is estimated by computing the $\Delta\chi^2$ obtained with from fitting either hierarchy and assuming the value is distributed as a χ^2 with 1 degree of freedom [19]. In both cases the “wrong hierarchy” parameters tested are chosen to minimize the difference to the “true hierarchy” being tested. The sensitivity to $|\Delta m_{32}^2|$ and θ_{23} is estimated using the same procedure as for the average experiment, however it is compared to a χ^2 with 2 degrees of freedom.

The nuisance parameters considered in PINGU analysis are similar to those used for DeepCore for the atmospheric ν flux, neutrino interactions and ν oscillations. An additional

uncertainty of 10% on the $\nu/\bar{\nu}$ ratio has been added and the range of variation allowed for the atmospheric ν flux parameters was re-evaluated based on [20]. The neutrino interaction uncertainties as well as a more detailed description of the atmospheric ν flux uncertainties have only been accounted for with the χ^2 method and were shown to have a small impact in the results. The detector uncertainties accounted for in DeepCore are not currently considered in PINGU, however an energy scale uncertainty of 10% is used in PINGU as a proxy for the DOM efficiency uncertainty. $|\Delta m_{32}^2|$ and θ_{23} are free nuisance parameters for the neutrino mass hierarchy analyses and are found to be the parameters with the largest impact in its significance.

RESULTS

The latest published ν_μ disappearance analysis in DeepCore [4] was obtained using 3 years of data. The events selected with reconstructed energy between 6 and 56 GeV were used to measure $\sin^2 \theta_{23} = 0.53^{+0.09}_{-0.12}$ and $|\Delta m_{32}^2| = 2.72^{+0.19}_{-0.20} \times 10^{-3} \text{eV}^2$. The best fit point and 90% confidence regions as a function of these oscillation parameters are shown in Fig. 4.

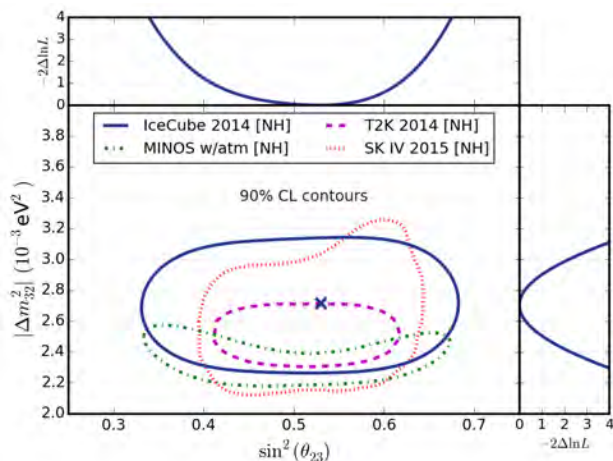


Figure 4: Latest DeepCore ν_μ disappearance results [4] (blue) compared with other experiments [21–23].

The PINGU sensitivity to the neutrino mass hierarchy depends strongly on the value of θ_{23} as shown in the left of Fig. 5. Assuming the best fit values for θ_{23} and Δm_{32}^2 quoted by the global fit [24], a 3σ determination of the neutrino mass hierarchy is expected with 5 years of data as shown in the right of Fig. 5. Using current information provided by global fits [24] the time to reach 3σ is reduced to about 3 years. This is a somewhat pessimistic scenario as the global best fits for $\sin^2 \theta_{23}$ are close to the minimal sensitivities expected as a function of θ_{23} . PINGU's capability to measure θ_{23} and $|\Delta m_{32}^2|$ is shown in Fig. 6.

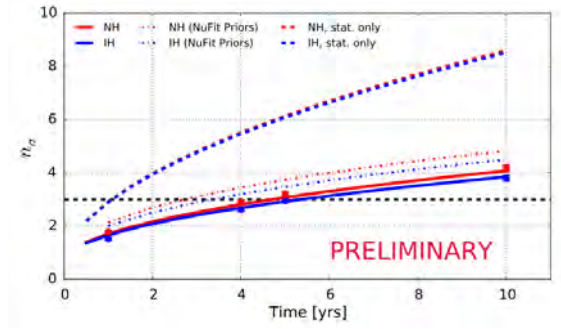
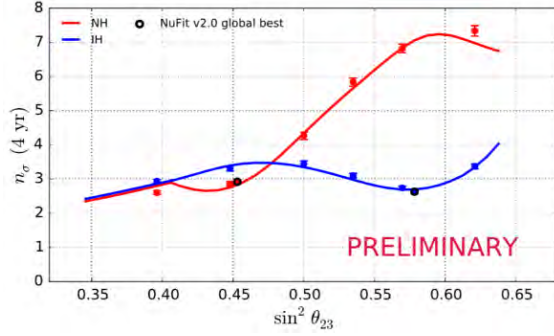


Figure 5: PINGU sensitivity to the neutrino mass hierarchy using ensembles of pseudo-experiments (points) and average experiments (lines) as a function of $\sin^2 \theta_{23}$ for 4 years on the left, and as a function of time for θ_{23} from [24] on the right. On the right figure, in addition to the base analysis where all systematics are accounted and no external information is used to constrain θ_{23} and $|\Delta m_{32}^2|$ (solid lines and points) the cases where we use current knowledge on oscillation parameters from [24] (dotted lines) or assume statistical only errors (dashed lines) are also shown.

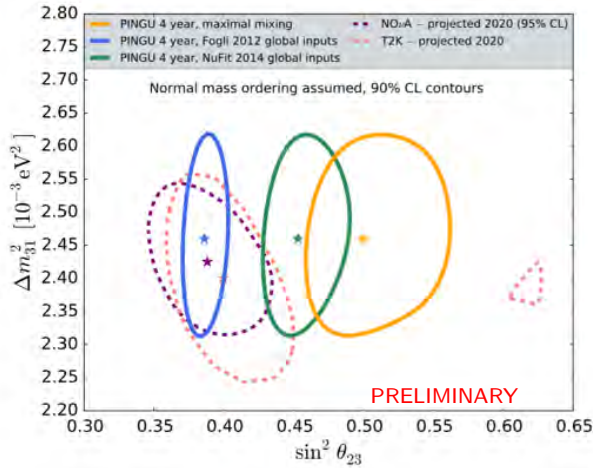


Figure 6: PINGU sensitivity to θ_{23} and $|\Delta m_{32}^2|$ assuming NH for different assumed true parameters [24, 25] (solid lines) compared to projected T2K [26] and $\text{NO}\nu\text{A}$ [27] results.

CONCLUSIONS

Despite being used for almost 20 years since the discovery of neutrino oscillations, atmospheric neutrinos are still a valuable tool to study this phenomenon; recent results obtained with DeepCore have started to approach the sensitivities obtained by dedicated experiments, and the proposed low-energy extension to IceCube, PINGU, will have capability of measuring at 3σ the neutrino mass hierarchy with 3-5 years of data in addition to significantly improving the measurement of θ_{23} and $|\Delta m_{32}^2|$.

* Presented at NuFact15, 10-15 Aug 2015, Rio de Janeiro, Brazil [C15-08-10.2]

† jpa14@icecube.wisc.edu; Speaker

‡ URL: <http://icecube.wisc.edu/collaboration/collaborators>

- [1] Y. Fukuda et al. (Super-Kamiokande), Phys. Rev. Lett. **81**, 1562 (1998), hep-ex/9807003.
- [2] Q. R. Ahmad et al. (SNO), Phys. Rev. Lett. **89**, 011301 (2002), nucl-ex/0204008.
- [3] K. A. Olive et al. (Particle Data Group), Chin. Phys. **C38**, 090001 (2014).
- [4] M. Aartsen et al. (IceCube), Phys. Rev. **D91**, 072004 (2015), 1410.7227.
- [5] F. P. An et al. (Daya Bay), Phys. Rev. Lett. **112**, 061801 (2014), 1310.6732.
- [6] L. Wolfenstein, Phys. Rev. **D17**, 2369 (1978).
- [7] S. P. Mikheev and A. Yu. Smirnov, Sov. J. Nucl. Phys. **42**, 913 (1985).
- [8] O. Mena, I. Mocioiu, and S. Razzaque, Phys. Rev. **D78**, 093003 (2008), 0803.3044.
- [9] E. K. Akhmedov et al., JHEP **02**, 082 (2013).
- [10] M. G. Aartsen et al. (IceCube PINGU), arXiv:1401.2046 (2014).
- [11] *Icecube collaboration homepage*, <http://icecube.wisc.edu>, accessed: dec 2015.
- [12] M. G. Aartsen et al. (IceCube), Science **342**, 1242856 (2013), 1311.5238.
- [13] R. Abbasi et al. (IceCube), Astropart. Phys. **35**, 615 (2012), 1109.6096.
- [14] J. A. Aguilar et al. (ANTARES), Astropart. Phys. **34**, 652 (2011), 1105.4116.
- [15] M. G. Aartsen et al. (IceCube), Nucl. Instrum. Meth. **A711**, 73 (2013), 1301.5361.
- [16] M. Honda et al., Phys. Rev. **D92**, 023004 (2015), 1502.03916.
- [17] C. Andreopoulos et al., Nucl. Instrum. Meth. **A614**, 87 (2010), 0905.2517.
- [18] S. Agostinelli et al. (GEANT4), Nucl. Instrum. Meth. **A506**, 250 (2003).
- [19] M. Blennow, P. Coloma, P. Huber, and T. Schwetz, JHEP **03**, 028 (2014), 1311.1822.
- [20] G. D. Barr et al., Phys. Rev. **D74**, 094009 (2006), astro-ph/0611266.
- [21] P. Adamson et al. (MINOS), Phys. Rev. Lett. **110**, 251801 (2013), 1304.6335.
- [22] K. Abe et al. (T2K), Phys. Rev. Lett. **112**, 181801 (2014), 1403.1532.
- [23] R. Wendell (Super-Kamiokande), AIP Conf. Proc. **1666**, 100001 (2015), 1412.5234.
- [24] M. C. Gonzalez-Garcia, M. Maltoni, and T. Schwetz, JHEP **11**, 052 (2014), 1409.5439.
- [25] G. L. Fogli et al., Phys. Rev. **D86**, 013012 (2012), 1205.5254.
- [26] K. Abe et al. (T2K), PTEP **2015**, 043C01 (2015), 1409.7469.
- [27] *Nova collaboration homepage*, http://www-nova.fnal.gov/plots_and_figures/plot_and_figures.html, accessed: dec 2015.

RENO & RENO-50*

K. K. Joo[†]

*Institute for Universe and Elementary Particles, Department of Physics,
Chonnam National Univeristy, Gwangju, 500-757, Korea*

(Dated: December 19, 2015)

Abstract

This paper briefly describes development, recent progress of RENO and future prospect of the reactor neutrino oscillation experiment, RENO-50. The RENO experiment has measured θ_{13} and provided clean information on $\sin^2 2\theta_{13}$. It gives rich programs of neutrino properties, detector development, nuclear monitoring and application. Using reactor neutrinos, a future reactor neutrino experiment, RENO-50, will search for more precise measurement of θ_{12} , Δm_{12}^2 and mass hierarchy, etc.

RENO

Experimental setup

RENO (Reactor Experiment for Neutrino Oscillation) is a reactor-based neutrino oscillation experiment to measure the smallest neutrino mixing angle (θ_{13}) using electron anti-neutrinos emitted from the Yonggwang (new name: Hanbit) nuclear power plant in Korea. It is located on the west coast of southern part of Korea, about 400 km from Seoul. The power plant consists of six pressurized water reactors producing a total thermal power of 16.4 GW_{th} . The six reactors with each maximum thermal output of 2.8 GW_{th} (reactors 3, 4, 5 and 6) or 2.66 GW_{th} (reactors 1 and 2) are lined up in roughly equal distances and span ~ 1.3 km. The RENO uses two identical near and far detectors to reduce the systematic uncertainties. The near and far detectors are placed roughly 290 m and 1.4 km away from the center of the reactor array, respectively. The near detector (ND) is located underground a 70 m high hill with an overburden of ~ 110 mwe and the far detector (FD) is placed underground a 260 m high mountain with an overburden ~ 450 mwe [1, 2].

Detector

The RENO detector consists of four concentric cylindrical layers: the target, the γ -catcher, the buffer, and the veto [2, 3]. The acrylic vessel holding the target liquid is surrounded by the γ -catcher. The target is filled with 16 mass tons of linear alkyl benzene ($\text{C}_n\text{H}_{2n+1}-\text{C}_6\text{H}_5$, $n = 10\sim 13$)-based 0.1% gadolinium (Gd)-loaded liquid scintillator (GdLS) [4–6]. The γ -catcher holds 28 mass tons of unloaded liquid scintillator (LS). Outside the

γ -catcher, a 70 cm thick buffer layer is filled with 76 mass tons of a non-scintillating liquid, mineral oil (MO, C_nH_{2n+2} , $n=11\sim 44$). This provides shielding from radioactivity in the surrounding rocks and in the 354 10-inch Hamamatsu R7081 photomultiplier tubes (PMTs) that are mounted on the inner wall of the stainless steel buffer container [2, 7]. The outermost layer is the 1.5 m thick veto system and filled with highly purified water. This layer provides events coming from outside by Cherenkov radiation and also shields against ambient cosmic-rays and neutrons from the surrounding rocks. Sixty-seven 10-inch R7081 water-proof PMTs are mounted on the wall of the veto vessel [2, 7]. The whole surfaces of veto layer are covered with Tyvek sheets to increase the light collection.

The detection principle of reactor neutrinos

The reactor antineutrinos are detected through the inverse beta decay process (IBD, $\bar{\nu}_e + p \rightarrow e^+ + n$) followed by neutron capture. The prompt positron annihilates and yields 1~8 MeV of visible energy. The neutron is captured by a hydrogen, and it gives off a gamma with an energy of 2.2 MeV. On the other hand, the delayed neutron capture signal can produce several gammas with a higher total energy of ~ 8 MeV approximately 30 μ s later if LS is loaded with a small amount of Gd, having a large neutron capture cross section. Therefore, GdLS significantly increases the efficiency of identifying the delayed signal against the low energy backgrounds [8, 9]. The coincidence of a prompt positron signal and a delayed signal from neutron capture by Gd provides the distinctive signature of IBD.

Data sample and backgrounds

RENO began data-taking from August, 2011. For about 500 days data-taking period between August 2011 to January 2013, the near (far) detector accumulated 290775 (31541) electron antineutrino candidate events [10]. This is about twice more data collected compared with the previous result published in 2012 [1]. Event rates of the observed IBD candidates and the estimated background at ND/FD are summarized in Table I [10]. Systematic uncertainties are classified into two categories related to reactor and detection. All systematic uncertainties have been significantly reduced since the first measurement

Detector	Near detector	Far detector
Selected events	290775	31541
Accidental rate (per day)	6.89 ± 0.09	0.97 ± 0.03
${}^9\text{Li}/{}^8\text{He}$ rate (per day)	8.36 ± 0.82	1.54 ± 0.23
Fast neutron rate (per day)	2.28 ± 0.04	0.48 ± 0.02
${}^{252}\text{Cf}$ contamination rate (per day)		0.14 ± 0.03

TABLE I: Event rates of the observed IBD candidates and the estimated backgrounds at $1.2 < E_p < 8.0$ MeV, where E_p is IBD prompt energy.

presented in [1].

Results and summary

Based on the number of events at the near detector and assuming no oscillation, RENO finds a clear deficit with a far-to-near ratio. Therefore, a clear disappearance of reactor antineutrinos is observed. The best-fit value thus obtained is $\sin^2 2\theta_{13} = 0.087 \pm 0.009(\text{stat.}) \pm 0.007(\text{syst.})$, where the world average value of $|\Delta m_{ee}^2|$ is used [11]. Therefore, currently RENO has measured $\sin^2 2\theta_{13}$ at $\sim 11\%$ precision level. Within 3 years, the mixing angle of θ_{13} expects to be measured to $\sim 5\%$ precision level [12]. Fig. 1 shows that the observed spectrum of IBD prompt signals in the far detector is compared to non-oscillation expectations based on measurements in the near detector [10]. This disagreement of the spectra provides further evidence of neutrino oscillation.

RENO-50

After RENO experiment, RENO collaboration plans to construct an underground detector of RENO-50. At ~ 50 km from the reactor center, the neutrino oscillation due to θ_{12} takes place at maximum. An experiment with the baseline of ~ 50 km could be a natural extension of current RENO θ_{13} experiment. The main goals of RENO-50 are to measure the most accurate (1%) value of θ_{12} and to attempt determination of the neutrino mass hierarchy. The RENO-50 is expected to detect neutrinos from nuclear reactors, the Sun,

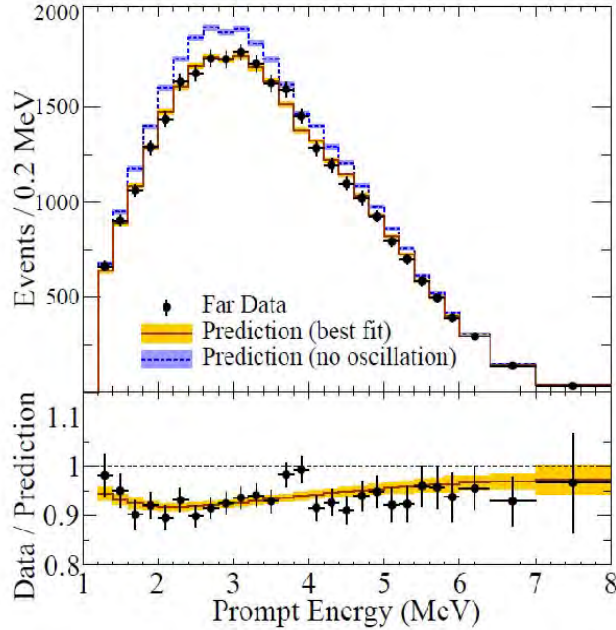


FIG. 1: Observed spectrum of the prompt signals in the FD with the no-oscillation prediction obtained from the measurement in the ND.

Supernova, the Earth, any possible stellar object and a J-PARC neutrino beam [13]. It could be acting as a neutrino telescope. RENO-50 needs \$100M for 5 year's construction. Facility and detector construction will be scheduled from 2016 to 2021. Operation and experiment will be started from 2020. Currently funding for RENO-50 is applied. Fig. 2 shows $\bar{\nu}_e$ disappearance probability as a function of L/E with the current best values of Δm^2 and $\sin^2 2\theta_{12}$, and $\sin^2 2\theta_{13}$ at the upper bound [13]. There is large θ_{12} neutrino oscillation effect at ~ 50 km. The KamLAND experiment has observed a 40% disappearance of ν_e at the baseline of 180 km [14].

Currently KamLAND energy resolution is $\sim 6\%$ level. In order to achieve 3% energy resolution, RENO-50 will use high transparency liquid scintillator. Through careful purification and using better quality of PPO, attenuation length will be increased from 15 m to 25 m. Using 15,000 20-inch PMTs will provide a large photocathode coverage from 34% to 67%. In addition, Hamamatsu 20-inch PMTs having an enhanced QE from 20% to 35% will be used.

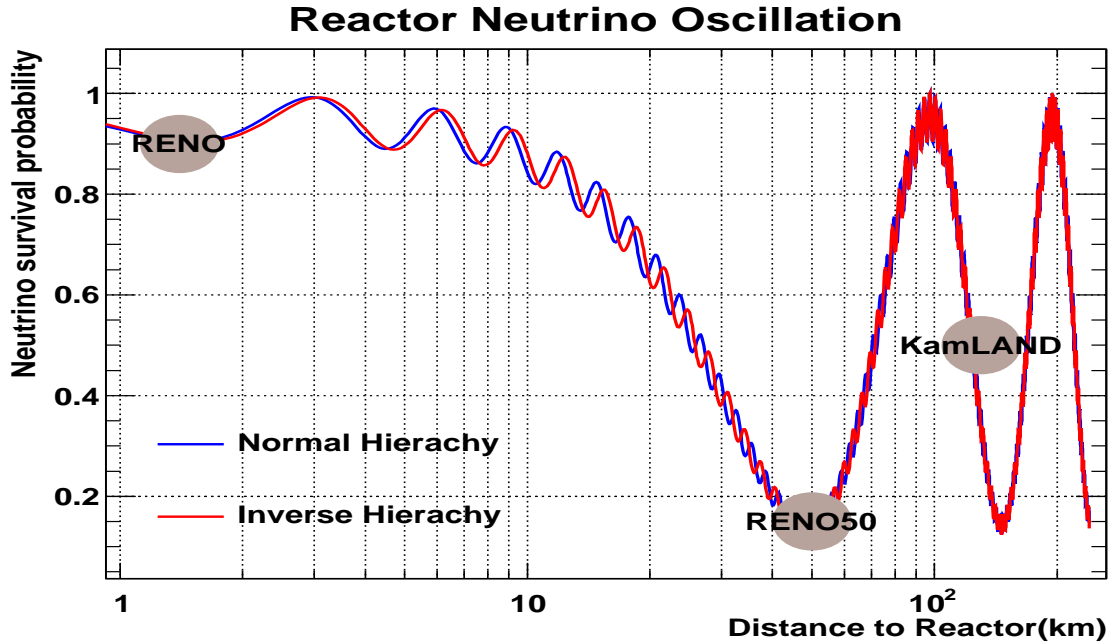


FIG. 2: The survival probability of $\bar{\nu}_e$ as the ratio of the distance to the neutrino energy (L/E). Normal hierarchy and inverted hierarchy are drawn.

Experimental site and RENO-50 detector

There are four nuclear reactor power plant sites (Ulchin, Wolsung, Kori and Yonggwang) in Korea. RENO-50 is dedicated to the Yonggwang nuclear power plant. A contribution from other nuclear power plants can be negligible. In RENO-50, RENO will be used as near detectors, so that precise reactor neutrino fluxes can be measured. Careful survey on candidate site for RENO-50 has been performed. An optimal candidate site is found at the 450 meter high Mt. Guemseong located at the city of Naju, ~ 50 km from the Hanbit nuclear power plant. RENO-50 is considering an inclined tunnel to obtain a deeper location. This corresponds to ~ 900 mwe overburden.

RENO-50 detector will use 18000 tons ultra-low-radioactive liquid scintillator (LS). Diameter is 30 m and height is 30 m. It is 18 times bigger than KamLAND detector. It consists of three layers: from the inner to outer, it is target, MO layer, and water veto layer. Total 15000 20-inch high efficiency PMTs will be installed and this will provide 67% surface coverage. Table II shows the comparison between RENO-50 and KamLAND.

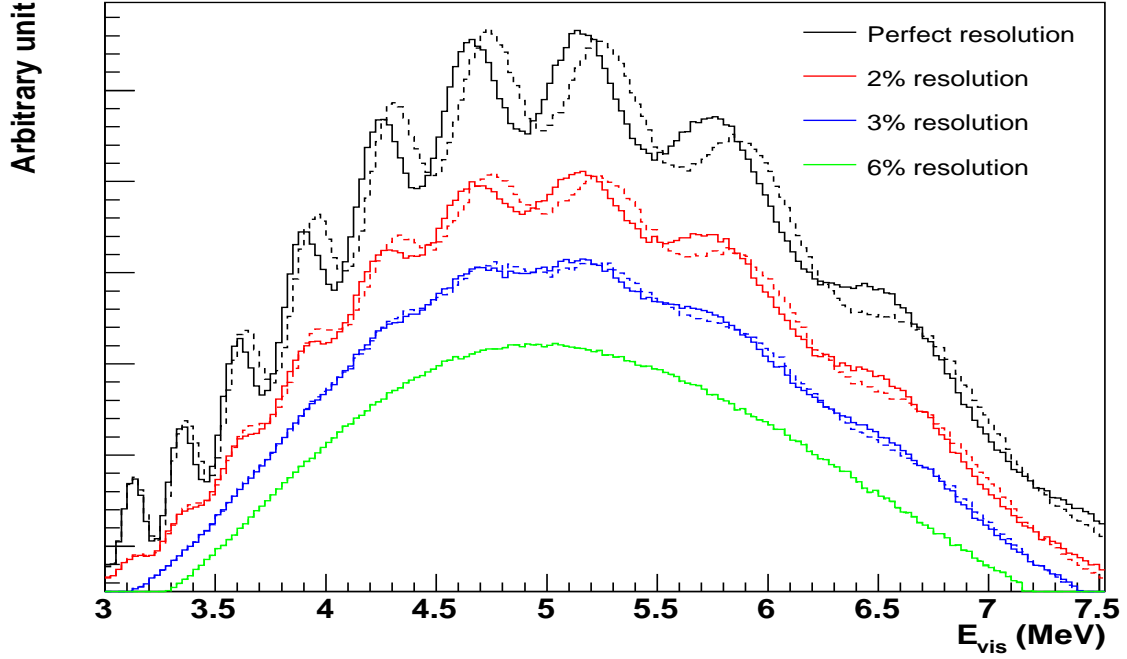


FIG. 3: Survival probability with different energy resolution. Solid line is normal hierarchy and dashed line is inverted hierarchy.

Experiment	Oscillation reduction	Reactor flux	Detector size	Sys. error (flux)	Error on $\sin^2 2\theta_{12}$
KamLAND	40%	53	1 kton	3%	5.4%
RENO-50	77%	6×14.7	18 kton	~ 0.3	0.4%

TABLE II: Comparison between RENO-50 and KamLAND.

Physics with RENO-50

1. Mass hierarchy

Reactor experiments can determine the neutrino mass hierarchy (MH). Advantage of reactor neutrino experiments is to determine MH independently from CP phase and matter effects. However, in RENO-50 case, determination of MH is challenging. It requires extremely good energy resolution better than 3%, as shown in Fig. 3 [13]. By using 18

ton detector, RENO-50 will get $\sim 3\sigma$ significance with 3 years data-taking.

2. Precise measurement of mixing parameter θ_{12}

In RENO-50, the near and far detectors of RENO could be used as near detectors, and thus would reduce relevant systematic uncertainties significantly. For baselines longer than 50 km, the reactor antineutrino oscillations due to Δm_{31}^2 average out and the survival probability becomes

$$P = \cos^4 \theta_{13} \left[1 - \sin^2 2\theta_{12} \sin \left(\frac{\Delta m_{21}^2 L}{4E} \right) \right].$$

The oscillations due to θ_{12} and Δm_{21}^2 were observed in the KamLAND experiment [14]. Because the antineutrino survival probability becomes minimal for $\sin^2 \left(\frac{\Delta m_{21}^2 L}{4E} \right) \approx 1$, the optimal baseline for measuring θ_{12} is about 50 \sim 70 km. Namely, $P \approx 1 - \sin^2 2\theta_{12}$ is very sensitive to the value of θ_{12} . RENO-50 detector is expected to improve the error of the θ_{12} value. Current value of $\frac{\delta \sin^2 \theta_{12}}{\sin^2 \theta_{12}}$ is $\sim 5.4\%$ level [15]. RENO-50 will improve this value to $\sim 1.0\%$ (1σ) in 1 year. Furthermore, $\frac{\delta \Delta m_{12}^2}{\Delta m_{12}^2}$ will be improved from current 2.6% to $\sim 1.0\%$ (1σ) in 2 year.

3. Neutrino burst from a supernova

RENO-50 detector filled with LS will be sensitive to a burst of neutrinos of all flavors from a Galactic supernova in the energy range of a few to tens of MeV. The time scale of the burst is tens of seconds. The background in the RENO-50 detector in a 10 second period is low enough for an observation of the neutrino signals from supernova burst. The RENO-50 detector would observe ~ 6000 events from a supernova at 8 kpc [16, 17].

4. Solar neutrinos

With ultra low activity liquid scintillator such as Borexino level, RENO-50 will search for matter effect on neutrino oscillation [18, 19]. Therefore the center of the Sun can be probed. Furthermore, the standard solar model would be examined and tested.

5. Reactor neutrino physics

The RENO and RENO-50 detectors will detect an order of million neutrino events per

year. They will measure the flux and energy distribution of the reactor neutrinos with a greater accuracy than ever. This information would lead to meaningful comparison of thermal power and reactor fuel loading between measurements and calculations. In addition, a precise determination of the reactor neutrino spectrum might be useful for reducing the flux uncertainty. Therefore reactor neutrinos could be used as an application for the direct check of nuclear non-proliferation treaties.

6. Other physics topics

J-PARC beams with off-axis angle ($\sim 3^\circ$) can reach RENO-50 detector at the level of ~ 400 per year. Furthermore, RENO-50 will test on non-standard physics such as sterile neutrino physics. While recent neutrino oscillation results are understood in the framework of 3 active neutrino mixing, they do not completely exclude admixture of sterile neutrinos [20, 21].

In the mean while, a scalar field of acceleron associated with the dark energy of the universe provides an idea if mass varying neutrinos. Possible couplings of acceleron to matter fields could introduce a very different feature of neutrino oscillation parameters. RENO-50 may test a possible effect due to the mass varying neutrinos because of different path lengths in air and matter.

Summary of RENO-50

RENO-50 is a long term operational and multi-purpose detector. Determining mass hierarchy is very challenging but not impossible with very good energy resolution better than 3% level. In addition, neutrino oscillation parameters, θ_{12} and Δm_{12}^2 , will be precisely measured less than 0.5% level, which can constraint new physics. In summary, RENO-50 reactor experiment with longer baseline of ~ 50 km is under pursuit to perform high-precision measurements of θ_{12} , Δm_{21}^2 , and Δm_{31}^2 , and to determine the mass hierarchy.

Acknowledgements

This work was supported by the Korea Neutrino Research Center, which was established with a grant from the National Research Foundation of Korea (NRF) funded by

the Korean government (MSIP) (No. 2012-0001176), the Basic Science Research program through the National Research Foundation of Korea (NRF) funded by the Ministry of Education (2012M2B2A6030210), Samsung Science & Technology Foundation (SSTF-BA1402-06), Chonnam National University (2014).

* *Presented at NuFact15, 10-15 Aug 2015, Rio de Janeiro, Brazil*

† `kkjoo@chonnam.ac.kr`; Speaker

- [1] J. K. Ahn *et al.*, (RENO Collaboration), *Phys. Rev. Lett.* **108**, 191802 (2012).
- [2] J. K. Ahn *et al.*, (RENO Collaboration), arXiv:hep-ex/1003.1391 (2010).
- [3] K. S. Park *et al.*, (RENO Collaboration), *Nucl. Instrum. Methods A***686**, 91 (2012).
- [4] J. K. Park *et al.*, (RENO Collaboration), *Nucl. Instrum. Methods A***707**, 45 (2013).
- [5] I. S. Yeo *et al.*, *J. of the Korean Phys. Soc.* **62**, 22 (2013).
- [6] S. H. So *et al.*, *J. of the Korean Phys. Soc.* **62**, 26 (2013).
- [7] K. J. Ma *et al.*, (RENO Collaboration), *Nucl. Instrum. Methods A***629**, 93 (2011).
- [8] A. Piepke, V. Novikov and W. Moser, *Nucl. Instrum. Methods A***432**, 39 (1999).
- [9] P. K. Lightfoot. *et al.*, *Nucl. Instrum. Methods A***522**, 439 (2004).
- [10] J. H. Choi *et al.*, (RENO Collaboration), arXiv:hep-ex/1511.05849 (2015).
- [11] K. A. Olive *et al.*, (Particle Data Group), *Chin. Phys. C***38**, 090001 (2014).
- [12] K. K. Joo, *J. of the Korean Phys. Soc.* **63**, 1489 (2013).
- [13] C. D. Shin and K. K. Joo, *Adv. High. Ene. Phys.* **2014**, 327184 (2014).
- [14] K. Eguchi *et al.* (KamLAND Collaboration), *Phys. Rev. Lett.* **90**, 021802 (2003).
- [15] T. Araki *et al.* (KamLAND Collaboration), *Phys. Rev. Lett.* **94**, 081801 (2005).
- [16] K. Scholberg, “Supernova neutrino detection”, arXiv:astro-ph/070108v1 (2007).
- [17] L. Cadonati, F. P. Calaprice, and M. C. Chen, “Supernova Neutrino Detection in Borexino,” *Astropart. Phys.* **16**, 361-372 (2002).
- [18] G. Alimonti *et al.* (Borexino Collaboration), *Nucl. Instrum. Method. A***440**, 360 (2000).
- [19] S. N. Ahmed *et al.* (SNO Collaboration), *Phys. Rev. Lett.* **87**, 011301 (2002);
- [20] G. Mention *et al.* hep-ex/1101.2755v3 (2011).
- [21] Th. A. Muller *et al.* hep-ex/1101.2663v1 (2011).

Flavor-Universal Expressions of Neutrino Oscillation Probabilities in Matter*

Hisakazu Minakata^{a,b†}

^a*Instituto de Física, Universidade de São Paulo,
C. P. 66.318, 05315-970 São Paulo, Brazil*

^b*Yachay Tech University, School of Physical Sciences and
Nanotechnology, San Miguel de Urcuquí, Ecuador ‡*

(Dated: January 18, 2016)

Abstract

We construct a new perturbative framework to describe neutrino oscillation in matter with the unique expansion parameter ϵ , which is defined as $\Delta m_{21}^2 / \Delta m_{\text{ren}}^2$ with the renormalized atmospheric $\Delta m_{\text{ren}}^2 \equiv \Delta m_{31}^2 - s_{12}^2 \Delta m_{21}^2$. It allows us to derive the maximally compact expressions of the oscillation probabilities in matter to order ϵ in the form akin to those in vacuum. This feature allows immediate physical interpretation of the formulas, and facilitates understanding of physics of neutrino oscillations in matter. Moreover, quite recently, we have shown that our three-flavor oscillation probabilities $P(\nu_\alpha \rightarrow \nu_\beta)$ in all channels can be expressed in the form of universal functions of L/E . The ν_e disappearance oscillation probability $P(\nu_e \rightarrow \nu_e)$ has a special property that it can be written as the two-flavor form which depends on the single frequency. This talk is based on the collaborating work with Stephen Parke [1].

INTRODUCTION

Do we understand neutrino oscillation? Most experimentalists and most theorists would agree to answer “*Yes we do*”. There is a simple way to derive, in vacuum and in matter, the oscillation probability and apparently it describes well the available experimental data.

However, I want to point out that not every aspect of theory of neutrino oscillation has been tested experimentally. For example, to my knowledge,

- No one observed neutrinos directly in their mass eigenstates as a whole.¹ It probably requires detection of neutrinos by gravitational effects, and in this context, cosmological observation is likely to be the first runner to achieve the goal, see e.g., [2].
- Nobody observed the effect of neutrino’s wave packet. See for example [3] for a recent treatment. If someone could develop technology which has sensitivity to the size or shape of the wave packet, then it would become possible to see it. If the time resolution of detector is improved dramatically, in principle, it may allow us to detect the effect of superluminal neutrinos due to oscillation-driven modification of shape of the wave packet in flight [4].

I said in the above that “there is a simple way to derive the oscillation probability in vacuum and in matter”. In fact, this comment is only true for the regime in which single- Δm^2 dominance approximation applies, and the things are quite different beyond it. Now, the various neutrino experiments entered into the regime where the three-flavor effects become important. Or, precision of measurement became so high that it has sensitivity to the sub-leading effects. See e.g., [5, 6]. The accelerator neutrino experiment [7, 8] is the best example for the former because the CP phase effect, not only $\sin \delta$ but also $\cos \delta$ effect, is the genuine

¹ One may argue that observation of ^8B solar neutrinos detect ν_2 in a good approximation. But, it still detects ν_e component of ν_2 if one uses CC reaction. Detection by NC reaction does not alter this situation, because a particular component of ν_2 causes the reaction in each time.

three-flavor effect. This is best understood by the general theorems derived in Refs. [9, 10] ($\sin \delta$ terms) and [11] ($\cos \delta$ terms).

Let us focus on the accelerator neutrino experiment because it will play a major role in observing the CP phase effect in a robust way [12, 13]. In the regime where the three-flavor effect is important our theoretical understanding of the neutrino oscillation probability is not quite completed in my opinion. Let me first try to convince the readers on this point. For pedagogical purpose, I start from neutrino oscillation in vacuum. If you want to know the key point go directory to section .

THE OSCILLATION PROBABILITY IN VACUUM IS SIMPLE

The neutrino oscillation probability in vacuum is simple. If only two generations of neutrinos (ν_e and ν_μ) exist it takes the form

$$P(\nu_\mu \rightarrow \nu_e) = \sin^2 2\theta \sin^2 \left(\frac{\Delta m^2 L}{4E} \right) \quad (1)$$

where θ denotes the mixing angle and $\Delta m^2 = m_2^2 - m_1^2$. The variable $\frac{\Delta m^2 L}{2E}$ in the sine function is nothing but the phase difference between the mass eigenstates ν_2 and ν_1 which is developed when neutrinos travelled a distance L . Whereas the strength of the oscillation is determined by the transition amplitude $\sin 2\theta$.

In nature the three-generation neutrinos exist, ν_α ($\alpha = e, \mu, \tau$) in the flavor basis and ν_i ($i = 1, 2, 3$) in the mass eigenstate basis. Let us define the MNS lepton flavor mixing matrix [14] as $\nu_\alpha = U_{\alpha i} \nu_i$. Then, the neutrino oscillation probability has richer structure with more terms with different characteristics:

$$\begin{aligned} P(\nu_\beta \rightarrow \nu_\alpha) = & \delta_{\alpha\beta} - 4 \sum_{j>i} \text{Re}[U_{\alpha 1} U_{\beta 1}^* U_{\alpha 2}^* U_{\beta 2}] \sin^2 \frac{\Delta m_{ji}^2 L}{4E} \\ & + 8 \text{Im}[U_{\alpha 1} U_{\beta 1}^* U_{\alpha 2}^* U_{\beta 2}] \sin \frac{\Delta m_{32}^2 L}{4E} \sin \frac{\Delta m_{21}^2 L}{4E} \sin \frac{\Delta m_{31}^2 L}{4E}. \end{aligned} \quad (2)$$

In addition to the proliferation of the conventional term that appear in (1) due to the three mass-squared differences, there arises a universal CP and T violating term, the last one in (2). The term is suppressed by the two small factors, the Jarlskog factor [15] $\text{Im}[U_{\alpha 1} U_{\beta 1}^* U_{\alpha 2}^* U_{\beta 2}] = c_{12} s_{12} c_{23} s_{23} c_{13}^2 s_{13} \sin \delta < 0.035$, and $\frac{\Delta m_{21}^2 L}{4E} \sim \frac{\Delta m_{21}^2}{\Delta m_{31}^2} \simeq 0.03$ assuming that $\frac{\Delta m_{31}^2 L}{4E} \sim 1$. They both indicates that the CP violation is a genuine three flavor effect.

THE OSCILLATION PROBABILITY IN MATTER IS COMPLICATED

It is well known that under the constant matter density approximation the neutrino oscillation probability in matter can be expressed in the form in (2), but with replacement

$$\Delta m_{ji}^2 \rightarrow \lambda_j - \lambda_i, \quad U_{\alpha i} \rightarrow V_{\alpha i}, \quad (3)$$

where $V_{\alpha i}$ is the mixing matrix in matter defined as $\nu_\alpha = V_{\alpha i} \nu_i^m$ with ν_i^m ($i = 1, 2, 3$) being the mass eigenstate in matter. $\frac{\lambda_i}{2E}$ denote the eigenvalues of the Hamiltonian in matter,

$$H = \frac{1}{2E} \left\{ U \begin{bmatrix} 0 & 0 & 0 \\ 0 & \Delta m_{21}^2 & 0 \\ 0 & 0 & \Delta m_{31}^2 \end{bmatrix} U^\dagger + \begin{bmatrix} a & 0 & 0 \\ 0 & 0 & 0 \\ 0 & 0 & 0 \end{bmatrix} \right\}, \quad (4)$$

where $a \equiv 2\sqrt{2}G_F N_e E$ is the Wolfenstein matter potential [16] with electron number density N_e and the Fermi constant G_F . The Hamiltonian governs the evolution of neutrino states as $i \frac{d}{dx} \nu = H \nu$.

Then, you may say that the oscillation probability in matter, Eq. (2) with the replacement (3), is structurally very simple. It is true. Even more amazingly one can obtain the exact expressions of the V matrix elements [17, 18]. However, you will be convinced if you look into the resulting expressions by yourself that they are terribly complicated, and it is practically impossible to read off some physics from the expressions. Sorry, I have no space here to introduce you the beautiful method for calculating the V matrix elements introduced in Ref. [18], and demonstrate the complexity of the resultant expression.

We need perturbation theory, but it is *not* enough

Here is a natural question you may raise: “Isn’t it possible to compute the eigenvalues λ_i and $V_{\alpha i}$ perturbatively?² If you take this way you must be able to obtain much simpler analytic expressions of the oscillation probabilities.” Yes, of course you can. But, when you engage this business you discover that the eigenvalues λ_i receives the first order corrections. When you expand by the small parameters your formulas for the oscillation probabilities do not remain to the structure-revealing form (2). Usually you obtain proliferation of terms, and the situation becomes much worse when you go to higher orders. This is the characteristic feature of the expressions obtained by the perturbative frameworks so far examined, to our understanding.³

Since it is very hard to collect all the relevant references in which the various perturbative frameworks are developed, please look at the bibliography in [1, 11, 19] for an incomplete list of references, from which you can start your own search.

Then, the immediate question would be “Can’t you construct perturbation theory in which the first order corrections to the eigenvalues λ_i are absent?”. If we can, the prolifer-

² In fact, it is a highly nontrivial question why the expansion of the exact expression of λ_i and V matrix elements by the small parameter does not work. This question is briefly addressed in [1].

³ I hope you understand that this comment is not to hurt the previous authors’ efforts devoted to understand the neutrino oscillations by developing the various perturbative schemes. In talking about the proliferation of terms, in fact, the present author was very good at producing lengthy formulas: He is proud of deriving the longest formula for $P(\nu_e \rightarrow \nu_\mu)$ expanded to third order in $\varepsilon \equiv \frac{\Delta m_{21}^2}{\Delta m_{31}^2}$, $\sin \theta_{13}$, and even including the NSI parameters to the same order, which spanned 3 pages when it is explicitly written. See arXiv version 1 of [19]. If you are interested in seeing the other (but much less pronounced) examples see section 3.3.6 in Ref. [1].

ation of terms is avoided and the simple structure of the oscillation probabilities in (2) is maintained to first order in the expansion parameter. The answer to the above question is *Yes* and this is what we did in Ref. [1].

THE OSCILLATION PROBABILITY IN MATTER CAN BE MADE EXTREMELY SIMPLE AND COMPACT

The next question we must ask is then: How can we make the first order correction to the eigenvalues λ_i vanishes? There is a simple way to make it happen. That is, if we choose the decomposition of the Hamiltonian into the unperturbed and the perturbed parts correctly, then it is automatic. For concreteness I want to describe how it happens in the perturbative framework we have developed in [1].

We first go to the tilde basis $\tilde{H} = U_{23}^\dagger H U_{23}$. Then, we decompose \tilde{H} as $\tilde{H}(x) = \tilde{H}_0(x) + \tilde{H}_1(x)$:

$$\tilde{H}_0(x) = \frac{\Delta m_{\text{ren}}^2}{2E} \left\{ \left[\begin{array}{ccc} \frac{a}{\Delta m_{\text{ren}}^2} + s_{13}^2 & 0 & c_{13}s_{13} \\ 0 & 0 & 0 \\ c_{13}s_{13} & 0 & c_{13}^2 \end{array} \right] + \epsilon \left[\begin{array}{ccc} s_{12}^2 & 0 & 0 \\ 0 & c_{12}^2 & 0 \\ 0 & 0 & s_{12}^2 \end{array} \right] \right\}, \quad (5)$$

$$\tilde{H}_1(x) = \epsilon c_{12}s_{12} \frac{\Delta m_{\text{ren}}^2}{2E} \left[\begin{array}{ccc} 0 & c_{13} & 0 \\ c_{13} & 0 & -s_{13} \\ 0 & -s_{13} & 0 \end{array} \right], \quad (6)$$

where

$$\Delta m_{\text{ren}}^2 \equiv \Delta m_{31}^2 - s_{12}^2 \Delta m_{21}^2, \quad \text{and} \quad \epsilon \equiv \Delta m_{21}^2 / \Delta m_{\text{ren}}^2. \quad (7)$$

The vanishing diagonal terms in the perturbed Hamiltonian (6) guarantees the absence of the first-order corrections to the eigenvalues. Then, we can obtain the structure-revealing form of the oscillation probabilities in matter, Eq. (2) with the replacement (3), to first order in ϵ . Notice that use of the renormalized Δm_{ren}^2 defined in (7) makes the form of the tilde-Hamiltonian very neat. Because of the use of the unique expansion parameter ϵ provided by nature, we have named our perturbative framework as “renormalized helio-perturbation theory” [1].

UNIVERSAL FORM OF NEUTRINO OSCILLATION PROBABILITIES IN MATTER

This is not the end of the story. We have observed the following two “unexpected” new features. If we write down the disappearance oscillation probability $P(\nu_e \rightarrow \nu_e)$ in our renormalized helio-perturbation theory, it is extremely simple. To order ϵ it reads

$$P(\nu_e \rightarrow \nu_e) = 1 - \sin^2 2\phi \sin^2 \frac{(\lambda_+ - \lambda_-)L}{4E} \quad (8)$$

where λ_- , λ_0 , λ_+ denote the three eigenvalues of $2E\tilde{H}_0$. ϕ , the mixing θ_{13} in matter, is given by

$$\begin{aligned}\cos 2\phi &= \frac{\Delta m_{\text{ren}}^2 \cos 2\theta_{13} - a}{\lambda_+ - \lambda_-}, \\ \sin 2\phi &= \frac{\Delta m_{\text{ren}}^2 \sin 2\theta_{13}}{\lambda_+ - \lambda_-}.\end{aligned}\quad (9)$$

Compare the expression in (8) to the vacuum formula in (1). So similar! Notice that, though extremely compact, it contains all-order contributions of both s_{13} and a .

The leading order ϵ^0 term in the appearance channel probability $P(\nu_e \rightarrow \nu_\mu)$ calculated to order ϵ is also governed by the particular frequency $\lambda_+ - \lambda_-$:

$$\begin{aligned}P(\nu_e \rightarrow \nu_\mu) &= \left[s_{23}^2 \sin^2 2\theta_{13} + 4\epsilon J_r \cos \delta \left\{ \frac{(\lambda_+ - \lambda_-) - (\Delta m_{\text{ren}}^2 - a)}{(\lambda_+ - \lambda_0)} \right\} \right] \left(\frac{\Delta m_{\text{ren}}^2}{\lambda_+ - \lambda_-} \right)^2 \sin^2 \frac{(\lambda_+ - \lambda_-)L}{4E} \\ &+ 8\epsilon J_r \frac{(\Delta m_{\text{ren}}^2)^3}{(\lambda_+ - \lambda_-)(\lambda_+ - \lambda_0)(\lambda_- - \lambda_0)} \sin \frac{(\lambda_+ - \lambda_-)L}{4E} \sin \frac{(\lambda_- - \lambda_0)L}{4E} \cos \left(\delta - \frac{(\lambda_+ - \lambda_0)L}{4E} \right)\end{aligned}\quad (10)$$

where J_r , the reduced Jarlskog factor, is defined as

$$J_r \equiv c_{12}s_{12}c_{23}s_{23}c_{13}^2s_{13}.\quad (11)$$

This expression (10) is quite compact, despite that it contains all-order contributions of s_{13} and a . In particular, it keeps the similar structure as the one derived by the Cervera *et al.* [20], which retains terms of order ϵ^2 but is expanded by s_{13} only up to second order.

Furthermore, quite recently, we have observed that the first-order formulas for the oscillation probabilities have the flavor-universal (up to θ_{23} -dependent coefficient) expressions. Namely, $P(\nu_\alpha \rightarrow \nu_\beta)$ (including the ν_e sector) can be written in a universal form:

$$\begin{aligned}P(\nu_\alpha \rightarrow \nu_\beta) &= \delta_{\alpha\beta} \\ &+ 4 \left[\{A_{+-}^{\alpha\beta}\} s_\phi^2 c_\phi^2 + \epsilon \{B_{+-}^{\alpha\beta}\} (J_r \cos \delta) \frac{(\Delta m_{\text{ren}}^2)^2 \{(\lambda_+ - \lambda_-) - (\Delta m_{\text{ren}}^2 - a)\}}{(\lambda_+ - \lambda_-)^2 (\lambda_+ - \lambda_0)} \right] \sin^2 \frac{(\lambda_+ - \lambda_-)L}{4E} \\ &+ 4 \left[\{A_{+0}^{\alpha\beta}\} c_\phi^2 + \epsilon \{B_{+0}^{\alpha\beta}\} (J_r \cos \delta / c_{13}^2) \frac{\Delta m_{\text{ren}}^2 \{(\lambda_+ - \lambda_-) - (\Delta m_{\text{ren}}^2 + a)\}}{(\lambda_+ - \lambda_-)(\lambda_+ - \lambda_0)} \right] \sin^2 \frac{(\lambda_+ - \lambda_0)L}{4E} \\ &+ 4 \left[\{A_{-0}^{\alpha\beta}\} s_\phi^2 + \epsilon \{B_{-0}^{\alpha\beta}\} (J_r \cos \delta / c_{13}^2) \frac{\Delta m_{\text{ren}}^2 \{(\lambda_+ - \lambda_-) + (\Delta m_{\text{ren}}^2 + a)\}}{(\lambda_+ - \lambda_-)(\lambda_- - \lambda_0)} \right] \sin^2 \frac{(\lambda_- - \lambda_0)L}{4E} \\ &+ 8\epsilon J_r \frac{(\Delta m_{\text{ren}}^2)^3}{(\lambda_+ - \lambda_-)(\lambda_+ - \lambda_0)(\lambda_- - \lambda_0)} \sin \frac{(\lambda_+ - \lambda_-)L}{4E} \sin \frac{(\lambda_- - \lambda_0)L}{4E} \\ &\quad \times \left[\{C^{\alpha\beta}\} \cos \delta \cos \frac{(\lambda_+ - \lambda_0)L}{4E} + \{S^{\alpha\beta}\} \sin \delta \sin \frac{(\lambda_+ - \lambda_0)L}{4E} \right].\end{aligned}\quad (12)$$

	$\nu_e \rightarrow \nu_e$	$\nu_e \rightarrow \nu_\mu$ $\nu_\mu \rightarrow \nu_e$	$\nu_e \rightarrow \nu_\tau$ $\nu_\tau \rightarrow \nu_e$	$\nu_\mu \rightarrow \nu_\tau$ $\nu_\tau \rightarrow \nu_\mu$	$\nu_\mu \rightarrow \nu_\mu$	$\nu_\tau \rightarrow \nu_\tau$
Order ϵ^0 : $A_{+-}^{\alpha\beta}$ $A_{+0}^{\alpha\beta} = A_{-0}^{\alpha\beta}$	-1 0	$\sin^2 \theta_{23}$ 0	$\cos^2 \theta_{23}$ 0	$-\sin^2 \theta_{23} \cos^2 \theta_{23}$ $\sin^2 \theta_{23} \cos^2 \theta_{23}$	$-\sin^4 \theta_{23}$ $-\sin^2 \theta_{23} \cos^2 \theta_{23}$	$-\cos^4 \theta_{23}$ $-\sin^2 \theta_{23} \cos^2 \theta_{23}$
Order $\epsilon \cos \delta$: $B_{+-}^{\alpha\beta} = C^{\alpha\beta}$ $B_{+0}^{\alpha\beta} = B_{-0}^{\alpha\beta}$	0 0	1 0	-1 0	$-\cos 2\theta_{23}$ $-\cos 2\theta_{23}$	$\cos 2\theta_{23} - 1$ $\cos 2\theta_{23}$	$\cos 2\theta_{23} + 1$ $\cos 2\theta_{23}$
Order $\epsilon \sin \delta$: $S^{\alpha\beta}$	0	± 1	∓ 1	± 1	0	0

TABLE I: The values for the 5 coefficients for all oscillation channels, $\nu_\alpha \rightarrow \nu_\beta$ and $\bar{\nu}_\alpha \rightarrow \bar{\nu}_\beta$ to be used in conjunction with eq. (12). Note that they are 0, ± 1 or simple functions of θ_{23} .

The eight coefficients $A_{ij}^{\alpha\beta}$, $B_{ij}^{\alpha\beta}$, $C^{\alpha\beta}$ and $S^{\alpha\beta}$ are given in Table I. Notice that they are 0, ± 1 , or the simple functions of θ_{23} . The antineutrino oscillation probabilities $P(\bar{\nu}_\alpha \rightarrow \bar{\nu}_\beta)$ can be easily obtained from the neutrino oscillation probabilities as $P(\bar{\nu}_\alpha \rightarrow \bar{\nu}_\beta : E) = P(\nu_\alpha \rightarrow \nu_\beta : -E)$. See Ref. [1] for explanation.

We observe in Table I the existence of three equalities between the coefficients

$$A_{-0}^{\alpha\beta} = A_{+0}^{\alpha\beta}, \quad B_{-0}^{\alpha\beta} = B_{+0}^{\alpha\beta} \quad \text{and} \quad B_{+-}^{\alpha\beta} = C^{\alpha\beta} \quad (13)$$

which hold due to the invariance of the oscillation probabilities under the following transformation

$$\phi \rightarrow \pi/2 + \phi \quad \text{and} \quad \lambda_+ \leftrightarrow \lambda_- \quad (14)$$

The invariance (14) must hold because the two cases in (14) are both equally valid two ways of diagonalizing the zeroth-order Hamiltonian. Look at (9) to observe that the defining equations of ϕ are invariant under (14). Then, the former two identities in (13) trivially follow, but the last one requires use of the kinematic relationship

$$\sin \Delta_{+-} \sin \Delta_{+0} \cos \Delta_{-0} = \sin \Delta_{+-} \sin \Delta_{-0} \cos \Delta_{+0} + \sin^2 \Delta_{+-}$$

where $\Delta_{ji} \equiv \frac{(\lambda_j - \lambda_i)L}{4E}$. Notice that the relation $B_{+-}^{\alpha\beta} = C^{\alpha\beta}$ needs to be satisfied only to order ϵ^0 because these terms are already suppressed by ϵ .

The two new features of the oscillation probabilities, the flavor-universal expressions of the oscillation probabilities $P(\nu_\alpha \rightarrow \nu_\beta)$ in (12), and the extremely compact disappearance oscillation probability $P(\nu_e \rightarrow \nu_e)$ in (8) is the most remarkable outcome of our renormalized helio-perturbation theory examined to order ϵ .

HOW ACCURATE ARE OUR FORMULAS?

After hearing so much advertisement such as “structure-revealing” or “extremely compact”, you probably want to ask the question “how accurate are the formulas for the oscillation probabilities?”. It is certainly a legitimate question. In Fig. 1 we present the contours of equal probability for the exact (solid blue) and the approximate (dashed red) solutions for the channels $\nu_e \rightarrow \nu_\mu$, $\nu_e \rightarrow \nu_e$ and $\nu_\mu \rightarrow \nu_\mu$. The right (left) half plane of each panel of Fig. 1 corresponds to the neutrino (anti-neutrino) channel.

Overall, there is a good agreement. For large values of the matter potential, $|a| > \frac{1}{3}|\Delta m_{\text{ren}}^2|$ we have no restrictions on L/E to have a good approximation to the exact numerical solutions. Whereas for small values of the matter potential, $|a| < \frac{1}{3}|\Delta m_{\text{ren}}^2|$, we still need the restriction $L/E \lesssim 1000$ km/GeV. The agreement between the exact and approximate formulas is worst at around the solar resonance, which is actually close to the vacuum case. The reasons for this behavior and how to interpret the drawback are discussed in [1]. In the $\nu_\mu \rightarrow \nu_\mu$ channel the agreement is almost perfect due to the presence of order unity term in the oscillation probability.

SUMMARY AND REMARKS

- We have developed a new perturbative framework which allows us to derive the formulas for the oscillation probabilities in matter to order $\epsilon \equiv \frac{\Delta m_{21}^2}{\Delta m_{\text{ren}}^2} \simeq \frac{\Delta m_{21}^2}{\Delta m_{31}^2}$ in the form akin to the ones in vacuum. The correct way of decomposing the Hamiltonian into the unperturbed and perturbed parts is the key to make this property hold.
- As a remarkable outcome of our machinery we have obtained the two new features of the three-flavor oscillation probabilities in matter: (i) the flavor-universal expressions of the oscillation probabilities $P(\nu_\alpha \rightarrow \nu_\beta)$ in (12), and (ii) the extremely compact disappearance probability $P(\nu_e \rightarrow \nu_e)$ in (8).
- The obvious next goal of this investigation is to extend our results to order ϵ^2 . Since the vacuum-like form of the oscillation probabilities hold at order ϵ and in all orders we have speculated that this property prevails to higher orders.
- We have discussed in [1] the issue of incorrect feature of the level crossing of the eigenvalues at the solar resonance, which appears to be a universal fault in all perturbative framework which involve ϵ . I hope that we can resolve this issue in our investigation of the renormalized helio-perturbation theory to order ϵ^2 .

This talk is based on the collaborating work with Stephen Parke to whom the author thanks for enjoyable collaboration. He is grateful to Theory Group of Fermilab for supports and warm hospitalities during his visits. The author thanks Universidade de São Paulo for the great opportunity of stay under “Programa de Bolsas para Professores Visitantes Internacionais na USP”. He is supported by Fundação de Amparo à Pesquisa do Estado de São Paulo (FAPESP) under grant 2015/05208-4. He thanks the support of FAPESP funding grant 2015/12505-5 which allowed him to participate in NuFact 2015.

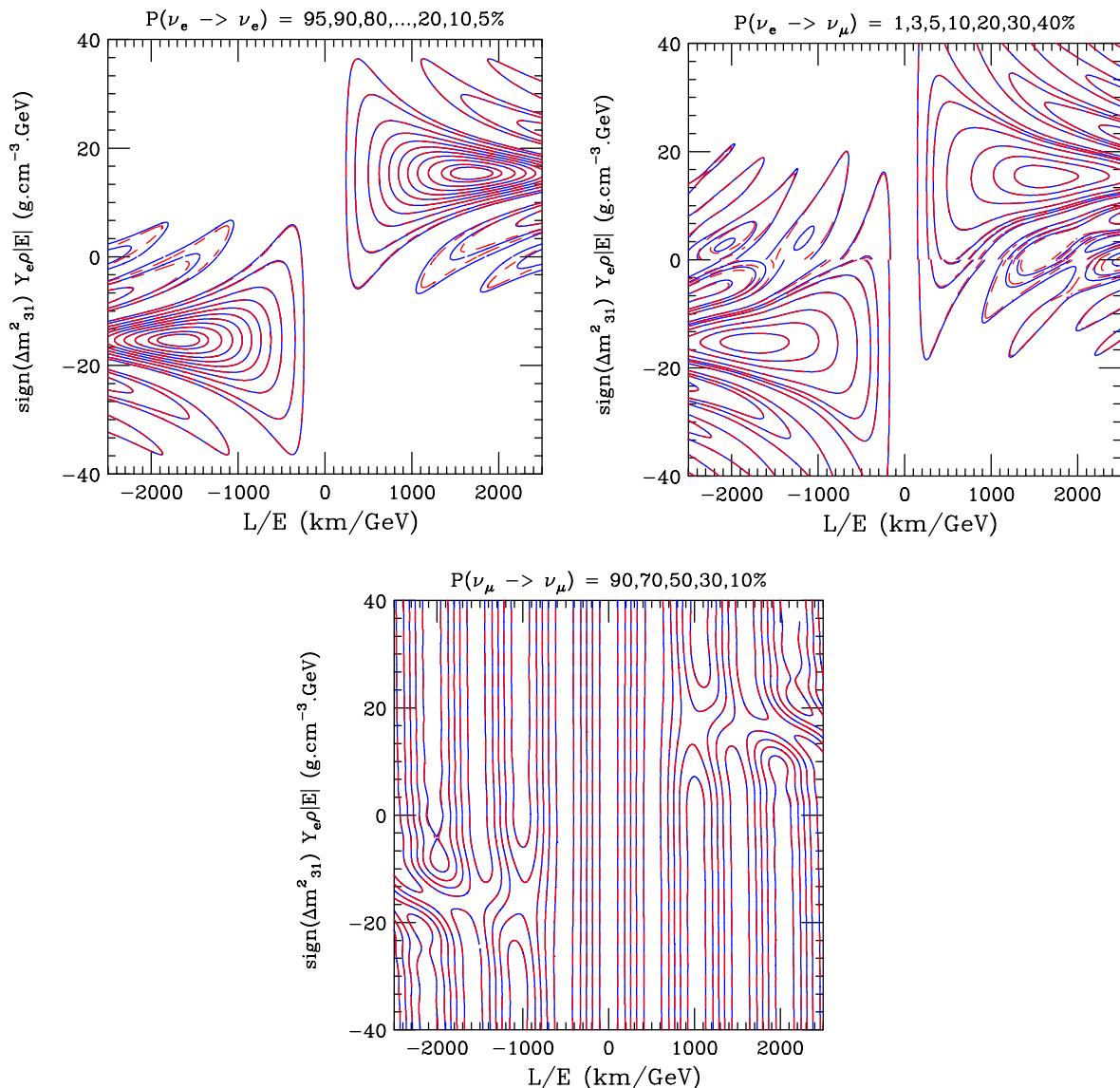


FIG. 1: The iso-probability contours for the exact (solid blue) and approximate (dashed red) oscillation probabilities for upper left, $\nu_e \rightarrow \nu_e$, upper right, $\nu_e \rightarrow \nu_\mu$ and lower, $\nu_\mu \rightarrow \nu_\mu$. The upper (lower) half plane is for normal ordering (inverted ordering), whereas positive (negative) L/E is for neutrinos (antineutrinos). For treatment of antineutrinos, see section . The order of the contours given in the title is determined from the line $L/E=0$. The discontinuities at $L/E=0$ are because we are switching mass orderings at this point. In most of parameter space the approximate and exact contours sit on top of one another so the lines appear to alternate blue-red dashed. Note that, for $L/E > 1000$ km/GeV and $|Y_e \rho E| < 5$ g cm $^{-3}$ GeV, the difference between the exact and approximate contours becomes noticeable at least for $\nu_e \rightarrow \nu_e$ and $\nu_e \rightarrow \nu_\mu$.

* Written version of the talk presented at NuFact15, 10-15 Aug 2015, Rio de Janeiro, Brazil [C15-08-10.2] under the title "Compact Formulas for Neutrino Oscillation Probabilities in

Matter”.

† hisakazu.minakata@gmail.com

‡ Address after April 2016

- [1] H. Minakata and S. J. Parke, “Simple and Compact Expressions for Neutrino Oscillation Probabilities in Matter,” arXiv:1505.01826 [hep-ph].
- [2] P. A. R. Ade *et al.* [Planck Collaboration], “Planck 2015 results. XIII. Cosmological parameters,” arXiv:1502.01589 [astro-ph.CO].
- [3] E. Akhmedov, D. Hernandez and A. Y. Smirnov, *JHEP* **1204** (2012) 052 doi:10.1007/JHEP04(2012)052 [arXiv:1201.4128 [hep-ph]].
- [4] H. Minakata and A. Y. Smirnov, *Phys. Rev. D* **85** (2012) 113006 doi:10.1103/PhysRevD.85.113006 [arXiv:1202.0953 [hep-ph]].
- [5] A. Gando *et al.* [KamLAND Collaboration], *Phys. Rev. D* **88** (2013) 3, 033001 doi:10.1103/PhysRevD.88.033001 [arXiv:1303.4667 [hep-ex]].
- [6] K. Okumura, *Phys. Procedia* **61** (2015) 619. doi:10.1016/j.phpro.2014.12.061
- [7] K. Abe *et al.* [T2K Collaboration], *Phys. Rev. D* **91** (2015) 11, 112002 doi:10.1103/PhysRevD.91.112002 [arXiv:1503.07452 [hep-ex]].
- [8] J. Bian [NOvA Collaboration], arXiv:1510.05708 [hep-ex].
- [9] V. A. Naumov, *Int. J. Mod. Phys. D* **1** (1992) 379. doi:10.1142/S0218271892000203
- [10] P. F. Harrison and W. G. Scott, *Phys. Lett. B* **476** (2000) 349 doi:10.1016/S0370-2693(00)00153-2 [hep-ph/9912435].
- [11] K. Asano and H. Minakata, *JHEP* **1106** (2011) 022 doi:10.1007/JHEP06(2011)022 [arXiv:1103.4387 [hep-ph]].
- [12] K. Abe *et al.* [Hyper-Kamiokande Proto-Collaboration], *PTEP* **2015** (2015) 053C02 doi:10.1093/ptep/ptv061 [arXiv:1502.05199 [hep-ex]].
- [13] T. Akiri *et al.* [LBNE Collaboration], arXiv:1110.6249 [hep-ex].
- [14] Z. Maki, M. Nakagawa and S. Sakata, *Prog. Theor. Phys.* **28** (1962) 870. doi:10.1143/PTP.28.870
- [15] C. Jarlskog, *Phys. Rev. Lett.* **55** (1985) 1039. doi:10.1103/PhysRevLett.55.1039
- [16] L. Wolfenstein, *Phys. Rev. D* **17** (1978) 2369. doi:10.1103/PhysRevD.17.2369
- [17] H. W. Zaglauer and K. H. Schwarzer, *Z. Phys. C* **40** (1988) 273. doi:10.1007/BF01555889
- [18] K. Kimura, A. Takamura and H. Yokomakura, *Phys. Rev. D* **66** (2002) 073005 doi:10.1103/PhysRevD.66.073005 [hep-ph/0205295].
- [19] T. Kikuchi, H. Minakata and S. Uchinami, *JHEP* **0903** (2009) 114 doi:10.1088/1126-6708/2009/03/114 [arXiv:0809.3312 [hep-ph]].
- [20] A. Cervera, A. Donini, M. B. Gavela, J. J. Gomez Cadenas, P. Hernandez, O. Mena and S. Rigolin, *Nucl. Phys. B* **579** (2000) 17 [Nucl. Phys. B **593** (2001) 731] doi:10.1016/S0550-3213(00)00221-2 [hep-ph/0002108].

Last results from Double Chooz*

Guillaume Pronost^{1,†}

(for the Double Chooz collaboration)

¹*SUBATECH, CNRS/IN2P3, Université de Nantes,
Ecole des Mines de Nantes, 44307 Nantes, France*

(Dated: December 22, 2015)

Abstract

The Double Chooz collaboration presents an updated measurement of $\sin^2(2\theta_{13})$ using reactor $\bar{\nu}_e$ detected through the inverse beta decay reaction in which the neutron is captured on hydrogen. This measurement is based on the far detector-only 2 years data-set, which contains about twice as much data as in the previous hydrogen analysis. The H-based sample allows for an independent data-set, additional to the Gd-based sample. This sample is normally contaminated by an overwhelming accidentals background due to radioactivity (hence the need for gadolinium) and is affected by different detector response systematics. Thanks to new methods for both background rejection and detection systematics, Double Chooz was able to measure $\sin^2(2\theta_{13}) = 0.098^{+0.038}_{-0.039}$, consistent with the value measured in the Gd-based sample: $\sin^2(2\theta_{13}) = 0.090^{+0.032}_{-0.029}$. This demonstrates that the H-based IBD analysis is as good as the Gd-based one for high precision physics. The H and Gd analyses were also combined in order to measure $\sin^2(2\theta_{13})$ and the spectral distortion above 4 MeV observed in the Gd analysis.

INTRODUCTION

The Double Chooz (DC) experiment aims at the measurement of the θ_{13} mixing angle from the oscillation of reactor $\bar{\nu}_e$. It consists in two identical liquid-scintillator Gd-loaded detectors located at 400 m (Near detector (ND)) and 1050 m (Far detector (FD)) from the two reactor cores of the CHOOZ nuclear power plant (Ardenne, France). The design of both detectors is presented in FIG. 1. θ_{13} can be extracted from the measurement of an $\bar{\nu}_e$ deficit and of an energy distortion in the FD due to ν oscillations.

Reactor neutrinos are detected by a delayed coincidence technique through the inverse β -decay (IBD) reaction on protons: $\bar{\nu}_e + p \rightarrow e^+ + n$. The positron is observed as the prompt signal with an energy related to the neutrino energy as: $E_{signal} \simeq E_\nu - 0.8$ MeV. The neutron is captured after its thermalization, either on Gd or H in liquid scintillator with high efficiency. Gd captures occur after a mean time of ~ 30 μ s and emit a few γ -rays with a total energy of 8 MeV, which is well above the energy of natural radioactivity. In addition, DC was the first experiment to publish a measurement of θ_{13} using IBD neutron captures on H [1], in which the released γ -ray carries only 2.2 MeV, an energy well within the range of natural radioactivity thus leading to sizable background. Two IBD analyses are performed in DC, one with Gd neutron captures and the other with H neutron captures. Since the ND

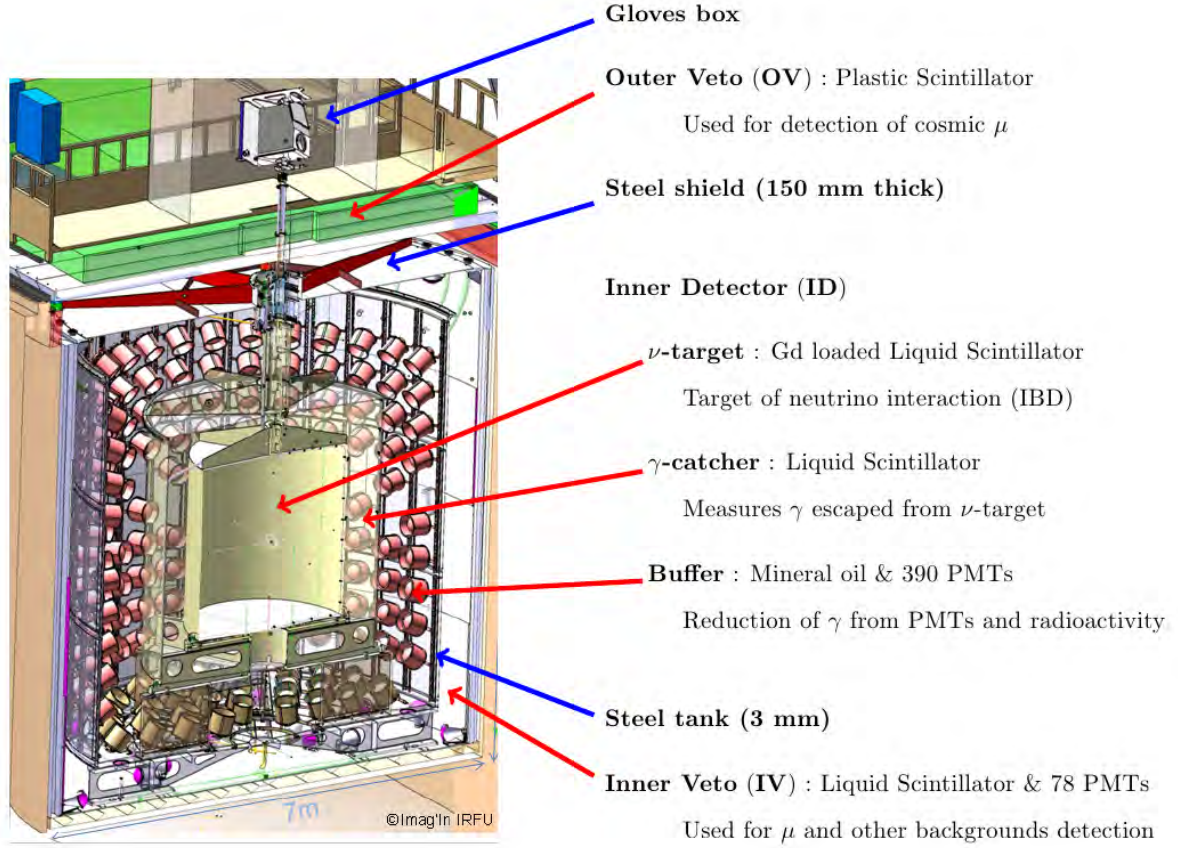


FIG. 1: Double Chooz detector design

was not completed for the last analyses, θ_{13} was extracted from the comparison between the $\bar{\nu}_e$ flux and spectrum from a MC simulation and from the FD.

The Gd analysis, published in [2], allowed to measure $\sin^2(2\theta_{13}) = 0.090_{-0.029}^{+0.032}$ and showed a distortion in the ratio of the background-subtracted data to the prediction above a prompt signal energy of 4 MeV. The present H analysis has been performed in order to cross-check the results of the Gd analysis with an independent data-set, and demonstrates the capability of precise measurement of reactor $\bar{\nu}_e$ without Gd loading.

ENERGY RECONSTRUCTION

The Double Chooz visible energy (E_{vis}) is computed from the number of photoelectrons (PE) N_{PE} . It is calculated and calibrated independently for data and Monte Carlo (MC),

following the same sequence of steps, and treating the MC like a second detector. The following equations show the relation between the E_{vis} and the total number of PE:

$$E_{vis}^{0,m} = N_{PE}^m \times f_u(\rho, z) \times f_{MeV} \quad (1)$$

$$E_{vis}^{data} = E_{vis}^{0,data} \times f_s^{data}(E_{vis}^{0,data}, t) \quad (2)$$

$$E_{vis}^{MC} = E_{vis}^{0,MC} \times f_{nl}^{MC}(E_{vis}^{0,MC}) \quad (3)$$

where $E_{vis}^{0,m}$ is a notation for the visible energy before the application of the stability correction or of the non-linearity corrections. m refers to either *data* or *MC*, $f_u(\rho, z)$ is the correction coming from the uniformity of the detector response, with (ρ, z) the reconstructed event position in the detector in cylindrical coordinates. f_{MeV} is the conversion factor from PE to MeV, extracted from the Hydrogen capture peak of neutron coming from a ^{252}Cf source deployed at the center of the detector, during a long calibration run. $f_s^{data}(E_{vis}^{0,data}, t)$ is the correction coming from the stability of the detector response, with t the reconstructed event's time. Finally, $f_{nl}^{MC}(E_{vis}^{0,MC})$ is the correction coming from the non-linearities of the detector response. These non-linearities are the charge non-linearity (QNL), which is associated with the modeling of the readout system, and the light non-linearity (LNL), which arises from the scintillator modeling, which is particle dependent.

NEUTRINO SELECTION

The selection of Hydrogen neutrino candidates is performed on an energy depositions data-set taken between April 2011 and January 2013. The single energy deposition data-set is obtained after application of a 1.25 ms muon veto and some cuts to reject spontaneous light emission from the photomultipliers (called *light noise*). The prompt and the delayed signals are selected with cuts on the energy, the multiplicity and the delayed coincidence. In order to reject the different backgrounds affecting the sample, several other cuts are applied. The different selection cuts applied in the H selection are listed in TAB. I.

Three different backgrounds contaminate the sample: $\beta - n$ emitters, like ^9Li and ^8He , which are long live-time cosmogenic radio-isotope ; correlated energy deposition due to fast

μ veto	$E_{vis}(\text{ID}) > 20 \text{ MeV}$ or $Q(\text{IV}) > 30k \text{ a.u.}$
μ dead time	1250 μs
Light noise cut	yes
E_{vis} (prompt)	[1, 20] MeV
Delayed coincidence	Multivariate analysis: ANN cut (New) Relaxed cuts: E_{vis} (delayed) $\in [1.3, 3] \text{ MeV}$ $\Delta t (e^+ - n) \in [0.5, 800] \mu\text{s}$ and $\Delta d (e^+ - n) < 1200 \text{ mm}$
Multiplicity cuts	$[-0.8, 0.9] \text{ ms}$ (relative to prompt)
OV veto	yes
IV veto (prompt)	yes
IV veto (delayed)	yes (New)
FV veto	yes
Li+He veto	yes
MPS veto	yes (New)

TABLE I: Selection cuts applied in the H analysis for neutrino candidates. The label (**New**) indicates the new methods developed for the H analysis.

neutrons proton-recoil and capture on H nuclei, and to stopping- μ decaying with the emission of a Michel electron ; and accidental background due to random coincidence between two single energy depositions, mainly due to natural radioactivity. In this H analysis, this last background is the dominant one since the delayed signal energy is well within the range of the natural radioactivity.

The delayed coincidence cuts were relaxed with respect to the previous H selection [1] in order to reduce the systematic uncertainties on the detection efficiency. This was allowed thanks to the development of new powerful background rejection methods which lead to an efficient rejection of background with a low inefficiency (i.e. low rejection of IBD events). These new rejection methods are the Artificial Neural Network cut (ANN cut), the Inner Veto veto (IV veto) and the Multiple Pulse Shape veto (MPS veto).

The ANN cut has been developed to reduce the accidental background by exploiting the different relations between the delayed energy, the space correlation, Δd , and the time

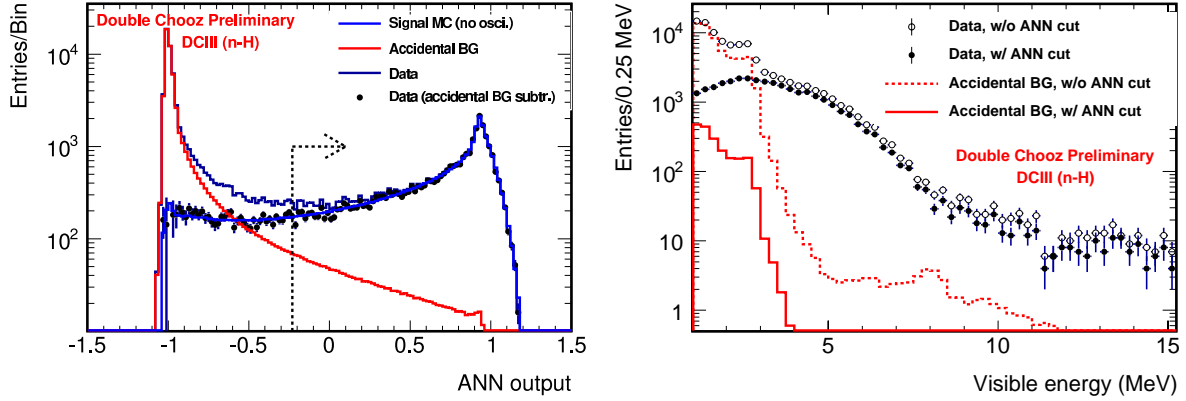


FIG. 2: *Left*: Output of ANN for H neutrino candidates (gray), accidental (blue), signal MC (red) and neutrino candidates after accidental BG subtraction (points). *Right*: Prompt energy spectrum of neutrino candidates (black) and accidental events (red) before and after application of ANN cut.

correlation, Δt , for the accidental background and the IBD events. A multivariate analysis has been performed using an Artificial Neural Network (ANN). FIG. 2 (left) illustrated the output of this ANN for on-time and off-time delayed coincidence data. With the application of this cut, the IBD efficiency only decreased by $\sim 6\%$ whereas the signal to accidental background ratio has been improved by more than a factor of 10 with respect to the previous H analysis [1]. The data sample after application of the ANN cut, shown in FIG. 2 (right), clearly demonstrating its effectiveness.

The IV veto method tags and rejects events triggered by the ID energy deposition and exhibiting energy deposition in the IV detector within the same *flash*-ADC window (256 ns). In contrast to the last Gd analysis [2], where the main target of the IV veto was the fast neutron background, the IV veto main target in the H analysis is the accidental background which can be reduced by tagging multiple Compton scattering of γ s in the IV and ID. In this new analysis, the IV veto has been applied on both the prompt and the delayed signal, allowing to reject $\sim 27\%$ of the remaining accidental background after the ANN cut, in addition to also reject fast neutron and stopping- μ .

The MPS cut method tags and rejects events triggered by their pulse shape distribution. Multiple fast neutrons are expected to be produced by μ spallations. Therefore, multiple simultaneous fast neutron interactions in the detector can be expected. Looking at pulse shape composed by a main pulse and multiple additional pulses within a *flash*-ADC window,

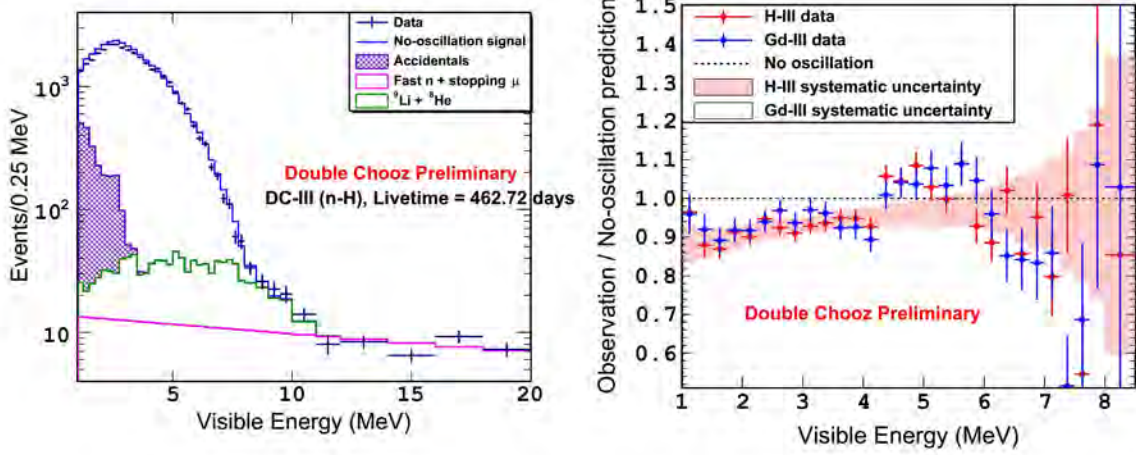


FIG. 3: *Left*: Prompt energy spectrum of neutrino candidates (black) with the the three stacked background components and non-oscillated prediction. *Right*: Ratio of the observation to the prediction for Gd (published in [2]) and H analysis.

MPS can tag and reject 25% of the fast neutron events.

RESULTS

FIG. 3 (left) shows the prompt energy spectrum of the H IBD candidates, together with the measured background components and the expected spectrum in the non-oscillation hypothesis. 31898 IBD candidates have been obtained in the data sample, with estimated background rates of 4.34 ± 0.02 accidental background events per day, 1.55 ± 0.15 fast neutron and stopping- μ background events per day and $0.95^{+0.57}_{-0.33}$ ^9Li and ^8He background events per day. FIG. 3 (right) is the ratio of the background-subtracted data to the prediction. It demonstrates a clear spectral deficit of $\bar{\nu}_e$ due to oscillations. In addition, a distortion between 4 and 6 MeV is present. This is a confirmation of the distortion already observed in the Gd analysis with an independent data sample of IBD events.

The θ_{13} value was extracted using a reactor rate modulation method (RRM) [3] which consists in the comparison between the observed and the expected rate of IBD candidates for different reactor power. This method allows to measure an independent value of θ_{13} and of the background rate. As shown on FIG. 4, the best-fit values are obtained for $\sin^2(2\theta_{13}) = 0.098^{+0.038}_{-0.039}$ and 7.29 ± 0.49 background events per day. Due to the observed,

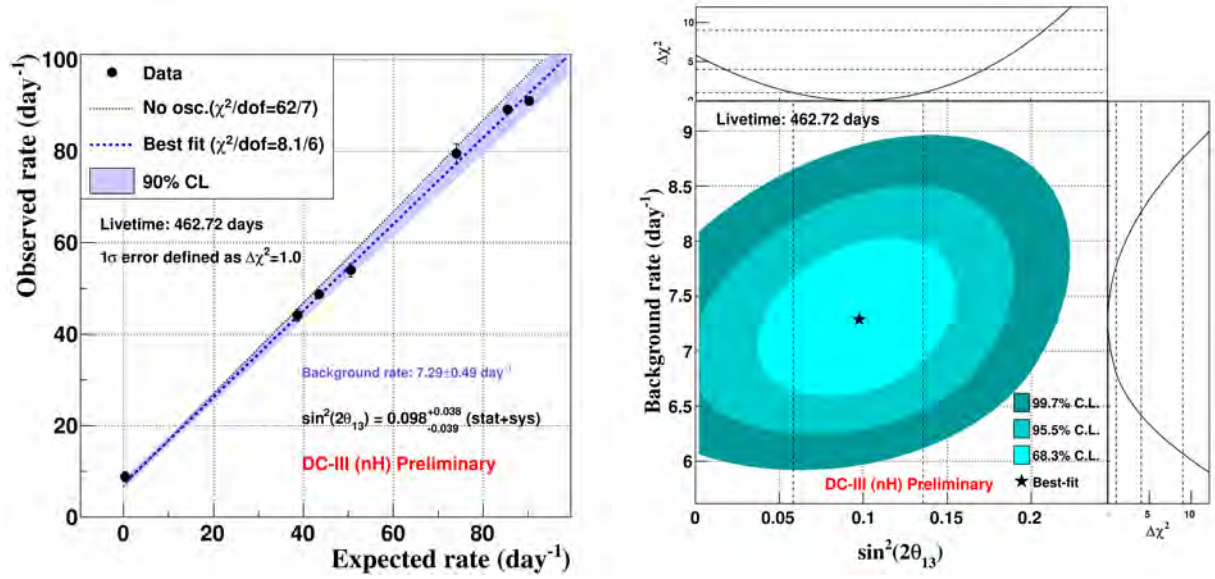


FIG. 4: Reactor rate modulation analysis in H channel: observed rate of neutrino candidates in function of expected rate from reactor flux (left) and best fit results on $\sin^2(2\theta_{13})$ and background rate (right).

and not yet understood, distortion, this result is considered the main H result. A cross-check has been performed with a rate+shape method and gave $\sin^2(2\theta_{13}) = 0.124^{+0.030}_{-0.039}$. A combined RRM fit of the data samples from the last Gd analysis [2] and from this H analysis has also been performed. It gave a result of $\sin^2(2\theta_{13}) = 0.90 \pm 0.033$. Thanks to the higher statistics, this improved the Gd-only RRM result ($\sin^2(2\theta_{13}) = 0.090^{+0.034}_{-0.035}$).

CONCLUSIONS

A new measurement of $\sin^2(2\theta_{13})$ has been released by the Double Chooz collaboration with a H analysis. Several novel background rejection methods have been developed for this analysis, allowing to reach a predicted signal to background ratio of 10.2, one order a magnitude larger than in the previous H analysis [1]. The RRM analysis of H IBD candidates measured a value of $\sin^2(2\theta_{13}) = 0.098^{+0.038}_{-0.039}$. This analysis is a demonstration of the capability of precise measurement of reactor $\bar{\nu}_e$ without Gd loading. The spectral distortion between 4 and 6 MeV observed in the Gd analysis has been confirmed with this independent analysis. This analysis has been published in [4].

The near detector of Double Chooz started to take data since early 2015. The near

detector + far detector analysis would allow to reduce the current large uncertainties on the neutrino flux and detection efficiency to below 0.1%. Double Chooz is expected to reach a final precision of 10% on $\sin^2(2\theta_{13})$ in this next phase.

* *Presented at NuFact15, 10-15 Aug 2015, Rio de Janeiro, Brazil [C15-08-10.2]*

† `guillaume.pronost@subatech.in2p3.fr`

- [1] Y. Abe et al. (Double Chooz), Phys. Lett. **B723**, 66 (2013), 1301.2948.
- [2] Y. Abe et al. (Double Chooz), JHEP **10**, 086 (2014), [Erratum: JHEP02,074(2015)], 1406.7763.
- [3] Y. Abe et al. (Double Chooz), Phys. Lett. **B735**, 51 (2014), 1401.5981.
- [4] T. Abrahao et al. (Double Chooz) (2015), 1510.08937.

DUNE Physics*

James Strait[‡]

Fermi National Accelerator Laboratory[‡]

P.O. Box 500, Batavia,

IL 60510-0500, USA

on behalf of the DUNE Collaboration

(Dated: January 20, 2016)

[‡] Operated by Fermi Research Alliance, LLC under Contract No. De-AC02-07CH11359 with the United States Department of Energy

Abstract

The Deep Underground Neutrino Experiment is a worldwide effort to build a next-generation long-baseline neutrino experiment with a neutrino beam and near detector at Fermilab and a far detector at the Sanford Underground Research Facility 1,300 km from Fermilab. It is a merger of previous efforts and other interested parties to build, operate and exploit a staged 40-kt liquid argon detector and a high precision near detector exposed to a high-power, broad-band neutrino beam. The goals of the experiment are precision oscillation measurements, including CP violation and neutrino mass hierarchy determination, search for nucleon decay, and neutrino astrophysics, as well as precision neutrino physics at the near site.

INTRODUCTION

The DUNE Collaboration[1] plans to address a number of the fundamental open questions in particle physics and astroparticle physics utilizing a massive liquid argon time-projection chamber (LAr TPC) located at a depth of 4,300 meters water equivalent at the Sanford Underground Research Facility (SURF) in Lead, South Dakota; a high-power, broad band, sign-selected ν_μ beam at Fermilab with a baseline distance from source to detector of 1,300 km; and a precision neutrino detector located on the Fermilab site[2]. The primary science objectives[3] include: neutrino oscillation physics to search for CP is violation in the leptonic sector, determine the ordering of the neutrino mass eigenstates, make precision measurements of oscillation parameters, test the three-neutrino paradigm; searches for baryon number violating processes (nucleon decay); and neutrino astrophysics, most notably precision measurements of neutrinos from a core-collapse supernova within the Galaxy, should one occur during the multi-decade lifetime of the experiment.

DUNE is a newly formed international collaboration, with strong representation from the previous LBNE, LBNO and other collaborations. As of the time of *NuFact15*, DUNE had 776 collaborators from 144 institutions located in 26 different countries on five continents. The DUNE Collaboration will design, build, commission and operate the near and far detectors[4] and is responsible for carrying out the scientific program utilizing them.

Facilities necessary to mount this experiment[5], including the neutrino beam[6], the cryostats and cryogenics systems to house the LAr TPC far detector, and conventional facilities at both Fermilab and SURF will be designed, built and commissioned by the Long-

Baseline Neutrino Facility (LBNF) Project. A new, broad-band and tunable neutrino beam is being designed, optimized for the Fermilab-SURF baseline. It will be driven by a 1.2 MW proton beam provided by the PIP-II upgrade[7], and is designed to accommodate future beam power upgrades to 2.4 MW. The design of the beam is still being optimized, and physics results are presented below for different options currently under study. LBNF is a U.S. Project based at Fermilab with contributions from a number of international partners.

THE DUNE DETECTORS

The far detector[4] is a 40 kt fiducial mass (~ 70 kt total mass) LAr TPC, located deep underground at SURF. The detector is divided into four independent 10 kt modules, each housed in its own cavern, as shown in Fig. 1. The detectors are placed in cryostats each of inner dimension 15 m wide \times 14 m high \times 62 m long. This arrangement allows for a staged construction and gives flexibility for evolution of the LAr TPC technology. While the cryostats will be identical, the LAr TPC detectors may not be, allowing lessons learned from the construction of the first module or information gleaned from the DUNE or other R&D programs to be incorporated in subsequent modules.

The reference design is a single-phase LAr TPC, which is an evolution of the successful ICARUS design[8] and in which alternating anode and cathode planes divide the liquid volume into four 3.6 m drift regions. The reference design is supported by development programs at Fermilab (the DUNE 35 t prototype, MicroBooNE[9], the Fermilab Short-Baseline Neutrino Program[10], and LArIAT[11]) and at CERN (ICARUS/WA104[12] and the DUNE Single-Phase Prototype[13]). Dual-phase readout technology, which is being developed by the WA105 Collaboration[14], is a potential alternate design that if demonstrated could form the basis for the second or subsequent 10 kt modules.

The DUNE near detector must constrain the systematic uncertainties for the oscillation analysis, which requires it to have the capability to precisely measure exclusive neutrino interactions of all four species in the beam: $\nu_\mu, \bar{\nu}_\mu, \nu_e,$ and $\bar{\nu}_e$. This naturally results also in a self-contained non-oscillation neutrino physics program that exploits the intense LBNF beam. The reference design is a NOMAD-inspired[15] Fine-Grained Tracker (FGT)[4] illustrated in Fig. 2. It consists of a central straw-tube tracker with embedded nuclear targets, including high-pressure argon-filled tubes and calcium ($A=40$) targets, and a lead-scintillator

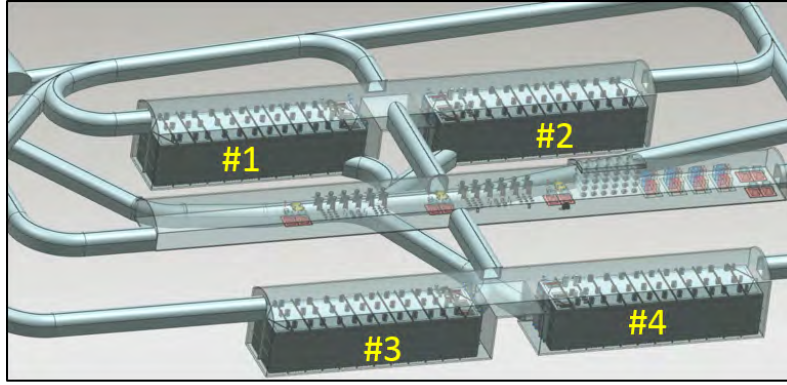


FIG. 1: Layout of the four caverns that will house the four 10-kt fiducial mass LAr TPC DUNE detectors at the Sanford Underground Research Facility

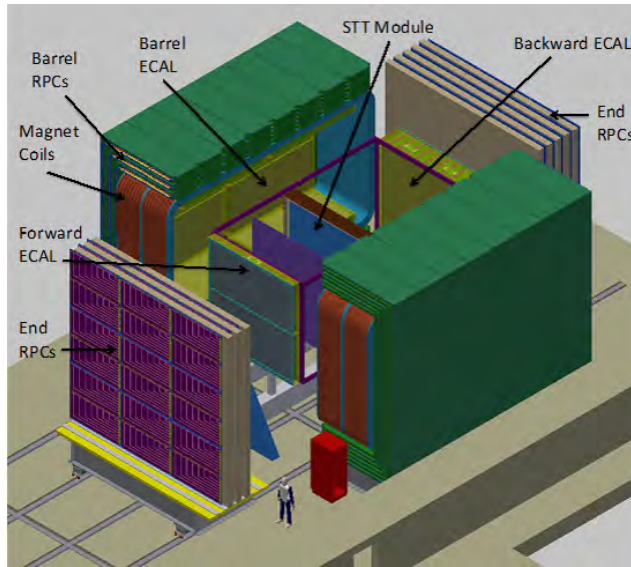


FIG. 2: The DUNE near detector reference design.

sampling electromagnetic calorimeter, both inside a large-aperture dipole magnet. An RPC-based muon identification system is embedded in the magnet yoke and in steel walls up- and down-stream of the magnet. DUNE has established a task force to perform an end-to-end physics study of the FGT capabilities to support the long-baseline analysis and to quantify the potential benefits of augmenting it with a LAr TPC or high-pressure gaseous argon TPC. Further details about the DUNE near detector can be found in [16].

THE DUNE SCIENCE PROGRAM

The primary scientific program of LBNF/DUNE addresses key science questions highlighted in the P5 report[17]. This program focuses on three areas: 1) Neutrino oscillation physics to probe CP violation (CPV) in the leptonic sector, determine the neutrino mass hierarchy (MH), and make precision measurements of oscillation parameters to test the three-neutrino paradigm; 2) Search for nucleon decay, particularly in modes such as $p \rightarrow K^+ \bar{\nu}$ which are difficult for existing experiments to access; and 3) Supernova burst physics, exploiting the sensitivity of an LAr TPC to ν_e (as opposed to $\bar{\nu}_e$). Any of these would represent a major discovery. It is these science objectives that drive the design of LBNF and DUNE.

In addition, there is a high-priority ancillary science program that is enabled by the intense LBNF beam, the very long baseline, and the precision DUNE detectors. This program includes: 1) Other oscillation physics with beyond-the-Standard-Model sensitivity such as non-standard neutrino interactions, sterile neutrinos, or measurements of ν_τ appearance; 2) Oscillation physics with atmospheric neutrinos; 3) Neutrino physics with the near detector such as neutrino cross-sections, electroweak physics, nuclear and QCD physics; and 4) Searches for signatures of dark matter.

DUNE will exploit the high-intensity, broad-band LBNF neutrino beam and the 1,300 km baseline to make a comprehensive set of neutrino oscillation measurements to determine the MH, probe CPV, determine the θ_{23} octant, test the 3-flavor paradigm, and search for ν non-standard interactions in a single experiment. The long-baseline and wide-band beam allow measurement of oscillation effects over a broad range of energies, covering more than one full oscillation cycle as illustrated in Fig. 3. With a 1,300 km baseline, matter effects are at the 40% level, which allows for an efficient determination of the mass ordering and clean separation of CP violating effects from the matter effect.

Sensitivities for determining oscillation parameter are evaluated using a fast Monte Carlo[18], GLOBES[19] and GENIE[20]. The fast MC simulates detector response by smearing energies and angles at the final-state particle level based on measurements by ICARUS[8] and ArgoNeuT[21]. It "reconstructs" the neutrino energy, uses a kNN-based multivariate technique for ν_e "reconstruction," and generates parameterized efficiencies for input to GLOBES. Examples of the fast MC results are shown in Fig. 4.

Sensitivities for CPV and MH determination are shown in Fig. 5 as a function of the

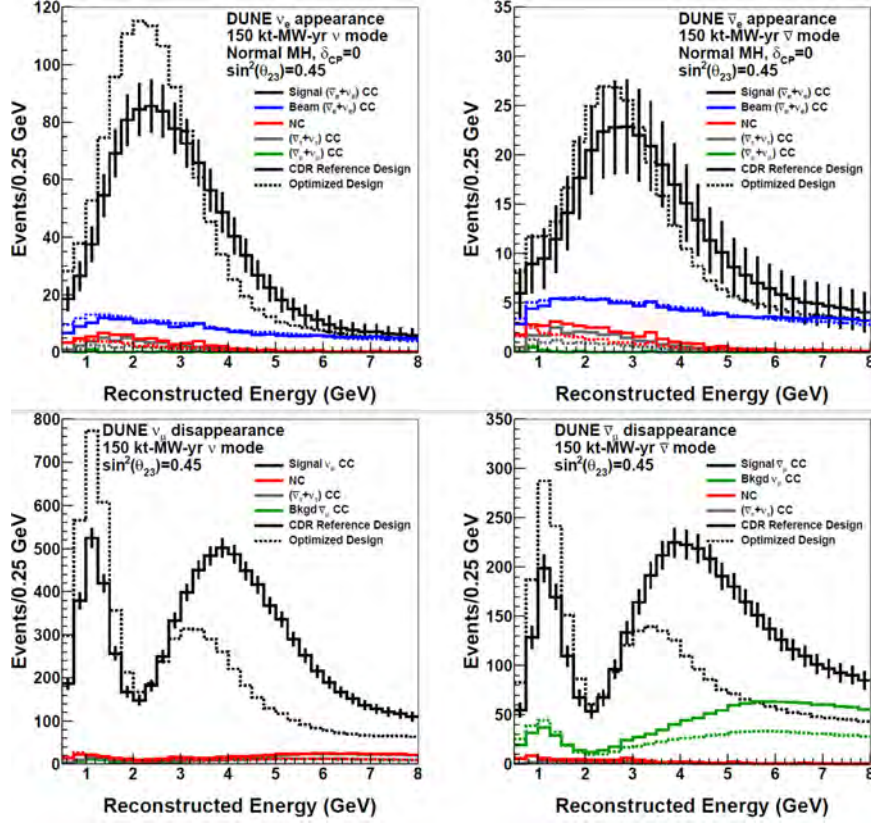


FIG. 3: ν_e appearance (top) and ν_μ disappearance (bottom) spectra in the LBNE ν (left) and $\bar{\nu}$ (right) beams. Spectra are shown for two different target-horn systems[6].

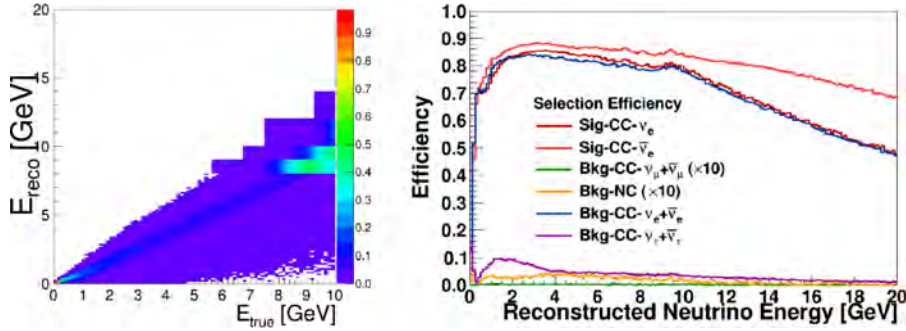


FIG. 4: Reconstructed versus true neutrino energy for charged-current ν_e events (left) and selection efficiencies for ν_e appearance events and principle backgrounds (right).

product of detector mass \times beam power \times time. Sensitivities are estimated the normal MH, but the MH and θ_{23} octant assumed to be unknown. CPV discovery sensitivity is expressed as the minimum significance over 50% of δ_{CP} values for determining that $\delta_{CP} \neq 0$ or π . Results are shown for two different beam designs and for a range of systematic errors[22]

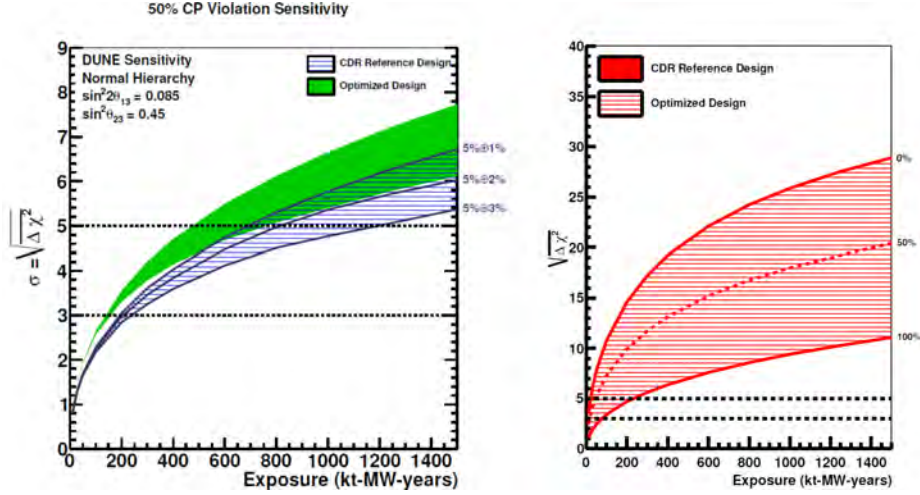


FIG. 5: Minimum significance for CPV discovery for 50% of the range of δ_{CP} as a function of exposure for two different beam designs and a range of systematic errors (left). Minimum significance for MH determination for different fractions of the range of δ_{CP} and the optimized beam design (right).

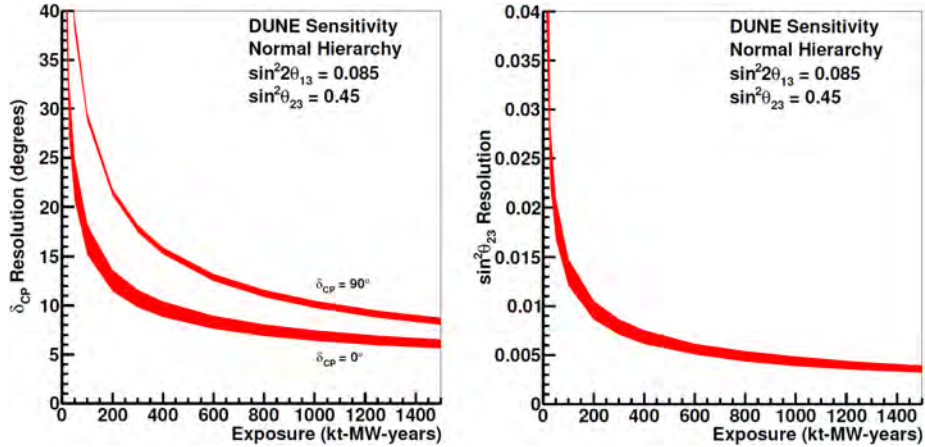


FIG. 6: Resolution for measuring δ_{CP} (left) and $\sin^2\theta_{23}$ (right) as a function of exposure.

that is compatible with expectations utilizing the DUNE near detector. The importance of good control of systematic errors is evident, as is the advantage of further beam optimization. With tight systematic errors and the optimized beam, a 5σ discovery of CPV over 50% of the δ_{CP} range requires an exposure of about 500 kt-MW-years.

Sensitivity MH determination is shown for the optimized beam design. This measurement is mainly limited by statistical errors. In the best case, the MH can be determined to $>5\sigma$ with very small exposure, while an exposure of about 250 kt-MW-years is required to cover

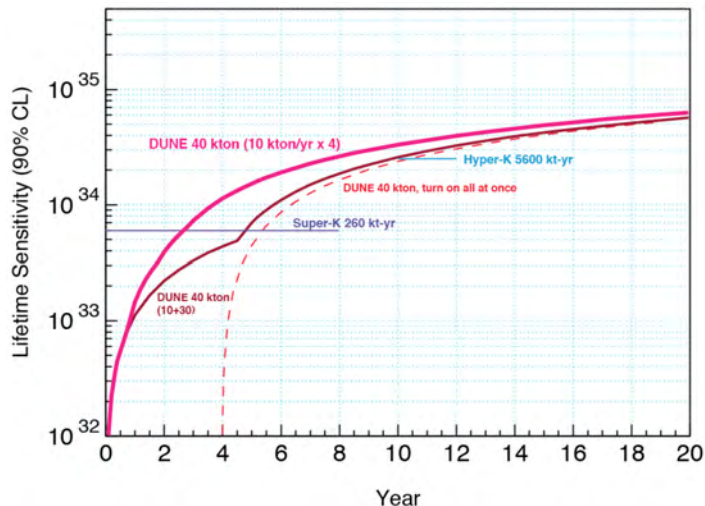


FIG. 7: Expected 90% limit on the lifetime for $p \rightarrow K^+\bar{\nu}$ as a function of time for several staging scenarios for the DUNE LAr TPC detector.

the full δ_{CP} range.

Resolutions for measuring δ_{CP} and $\sin^2\theta_{23}$ are shown in Fig. 6. The width of the bands shows the sensitivity to different neutrino beam designs. For large exposures the measurement resolution for δ_{CP} is better than 10° and approaches 5° if δ_{CP} is near 0. The asymptotic resolution for $\sin^2\theta_{23}$ is less than 0.005.

A unique capability of a LAr TPC is its high detection efficiency and strong background rejection for observing potential nucleon decay modes involving kaons, such as $p \rightarrow K^+\bar{\nu}$, which are difficult to observe in water Cherenkov detectors. The signature is an isolated K^+ of the appropriate energy, which can be cleanly identified by its dE/dx pattern and its subsequent decay into easily identified modes such as $K^+ \rightarrow \mu^+ \rightarrow e^+$ or $K^+ \rightarrow \pi^+\pi^0$. The expected detection efficiency is $>95\%$ with essentially no background (<0.5 event for a 10 year exposure of a 40 kt detector), allowing a single event to provide evidence for proton decay. The lifetime limit grows essentially linearly with time for many years, as shown in Fig. 7, which also shows the current limit from Super-K[23] and a projected limit for Hyper-K assuming similar efficiencies as Super-K.

The DUNE LAr TPC also provides unique capabilities for the measurement of neutrinos from a core-collapse supernova. It is mainly sensitive to ν_e , through the reaction $\nu_e + {}^{40}\text{Ar} \rightarrow e^- + {}^{40}\text{K}^*$, while existing water and liquid scintillator detectors are mainly sensitive to $\bar{\nu}_e$ through the inverse beta decay reaction. In addition to providing complemen-

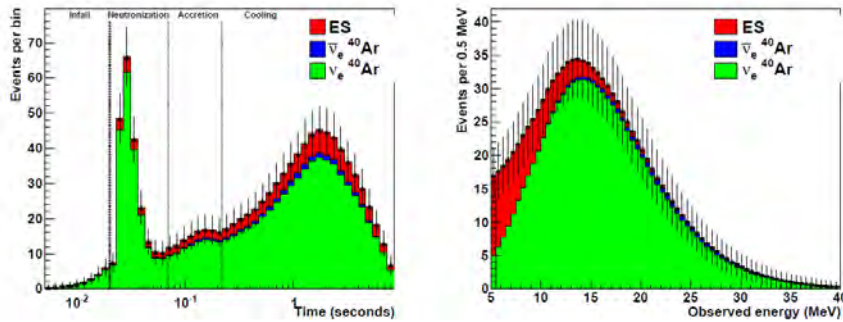


FIG. 8: Expected time-dependent signal in a 40 kt LAr TPC for an electron-capture supernova at 10 kpc (left) and the time-integrated energy spectrum (right).

tary information over the full time-scale of the supernova explosion, DUNE provides a clean measurement of the neutronization burst. Figure 8 shows both the time evolution of the neutrino signal and the time-integrated energy spectrum for an electron-capture supernova[24] computed using SNoWGLoBES[25].

SUMMARY

DUNE has an advanced design for a world-leading experiment focused on fundamental open questions in particle physics and astroparticle physics: long-baseline oscillation physics to determine CPV and MH, make precision measurements of oscillation parameters, test the three-neutrino paradigm, and look for physics beyond the standard model; search for nucleon decay in modes to which current detectors are comparatively insensitive; and neutrino astrophysics, especially measurements of supernova neutrinos. A clear scientific strategy has been established, and the construction project is moving forward with a plan for first data from the far detector in the middle of the next decade.

* Presented at NuFact15, 10-15 Aug 2015, Rio de Janeiro, Brazil [C15-08-10.2]

† strait@fnal.gov; Speaker

[1] <http://www.dunescience.org>.

[2] LBNF/DUNE Collaboration, *Conceptual Design Report, Volume 1: The LBNF and DUNE Projects*, Tech. Rep. DUNE-doc-180 (2015).

- [3] LBNF/DUNE Collaboration, *Conceptual Design Report, Volume 2: The Physics Program for DUNE at LBNF*, Tech. Rep. DUNE-doc-181, arXiv:1512.06148 (2015).
- [4] LBNF/DUNE Collaboration, *Conceptual Design Report, Volume 4: The DUNE Detectors at LBNF*, Tech. Rep. DUNE-doc-183, arXiv:1601.02984 (2015).
- [5] LBNF/DUNE Collaboration, *Conceptual Design Report, Volume 3: Long-Baseline Neutrino Facility for DUNE*, Tech. Rep. DUNE-doc-182 (2015).
- [6] J. Strait *et al.*, “LBNF Neutrino Beam,” *Presented at the XVII International Workshop on Neutrino Factories and Future Neutrino Facilities*, (2015).
- [7] P. Derwent *et al.*, *Proton Improvement Plan-II*, Tech. Rep. Project X-doc-1232 (2013).
- [8] C. Rubbia *et al.*, JINST **6**, P07011 (2011).
- [9] <http://www-microboone.fnal.gov>.
- [10] <http://sbn.fnal.gov>.
- [11] <http://lariat.fnal.gov/>.
- [12] M. Bonesini (ICARUS/WA104), J. Phys. Conf. Ser. **650**, 012015 (2015).
- [13] M. A. Leigui de Oliveira *et al.*, Tech. Rep. SPSC-P-351 (CERN, 2015).
- [14] I. D. Bonis *et al.*, Tech. Rep. SPSC-TDR-004 (CERN, 2014) arXiv:1409.4405 .
- [15] F. Vannucci, Adv. High Energy Phys. **2014**, 129694 (2014).
- [16] K. McDonald, “DUNE Near Detectors,” *Presented at the XVII International Workshop on Neutrino Factories and Future Neutrino Facilities*, (2015).
- [17] Particle Physics Project Prioritization Panel, “Building for Discovery: Strategic Plan for U.S. Particle Physics in the Global Context,” http://science.energy.gov/~media/hep/pdf/May-2014/FINAL_P5_Report_053014.pdf (2014).
- [18] C. Adams *et al.* (LBNE) (2013) arXiv:1307.7335[hep-ex] .
- [19] P. Huber, M. Lindner, and W. Winter, Comput. Phys. Commun. **167**, 195 (2005).
- [20] C. Andreopoulos *et al.*, Nucl. Instrum. Meth. **A614**, 87 (2010).
- [21] R. Acciarri *et al.*, Phys. Rev. **D89**, 112003 (2014).
- [22] D. Cherdack, “Impact of systematic uncertainties on DUNE,” *Presented at the XVII International Workshop on Neutrino Factories and Future Neutrino Facilities*, (2015).
- [23] <http://pdg.lbl.gov>.
- [24] L. Hudepohl *et al.*, Phys. Rev. Lett. **104**, 251101 (2010).
- [25] <http://www.phy.duke.edu/~schol/snowglobes>.

MeV gauge boson and secret interaction of sterile neutrinos*

Zahra Tabrizi[†]

School of Particles and Accelerators,

Institute for Research in Fundamental Sciences (IPM),

P.O.Box 19395-1795, Tehran, Iran and

Instituto de Física Gleb Wataghin - UNICAMP, 13083-859, Campinas, SP, Brazil

O. L. G. Peres[‡]

Instituto de Física Gleb Wataghin - UNICAMP, 13083-859, Campinas, SP, Brazil

Abdus Salam International Centre for Theoretical Physics, ICTP, I-34010, Trieste, Italy and

School of Particles and Accelerators,

Institute for Research in Fundamental Sciences (IPM), P.O.Box 19395-1795, Tehran, Iran

(Dated: January 5, 2016)

Abstract

Sterile neutrinos can have secret interactions that have consequences in cosmology and in laboratory experiments. We use the constraints from cosmology and from laboratory experiments: such as $g - 2$ measurement and the MINOS neutrino experiment to find out the constraints on the existence of secret interactions of sterile neutrinos.

INTRODUCTION

Light sterile neutrinos did not fit in the simplest formulation to explain the neutrino oscillations observed in most of the experiments [1]. There are hints of sterile neutrino presence in the electron neutrino appearance in LSND and Mini-BooNe experiments [2] and for the electron neutrino disappearance in reactor experiments [3]. These hints can be fitted if we add one additional light sterile neutrino.

The existence of light sterile neutrino have deep consequences in cosmology in the nucleosynthesis, cosmic microwave background and large scale structure formation. Results from Planck [4] are compatible with three lightest neutrinos and with the total mass of neutrinos $\sum m_\nu < 0.17$ eV disfavouring the presence of light sterile neutrino with mass difference $\Delta m_{41}^2 \sim 1$ eV².

We can evade the cosmological constraints on sterile neutrinos if we can effectively decouple it from evolution in early Universe. Recently it was proposed that a large coupling of sterile neutrino with MeV gauge boson can suppress the sterile neutrino oscillations decoupling from other neutrinos [5, 6].

We proposed to investigate the possibility of the sterile neutrino states interacting with a new gauge boson X , with mass \sim MeV, which has couplings with the sterile neutrinos and the charged leptons in the SM [7]. This new interaction of the sterile neutrinos was first mentioned in [8]. The " ν_s **Secret Interaction**" (ν_s SI) model produces a neutral current (NC) matter potential for the sterile states proportional to G_X , where G_X is the field strength of the new interaction. The NC matter potential in the ν_s SI model changes the oscillation probability of neutrinos and anti-neutrinos drastically. Therefore, using the data of a neutrino oscillation experiment such as the MINOS experiment [9], we can test the ν_s SI model.

Phenomenology of ν_s SI model

We enlarge the SM with one extra species of the sterile neutrinos which do not couple with the SM gauge bosons, but have interactions with a new $U_X(1)$ gauge symmetry (the ν_s SI model). The new gauge boson couples to the sterile neutrinos and charged leptons with coupling constants g'_s and g'_l , respectively, where for simplicity, we have assumed equal coupling constants for the charged leptons. The strength of this new interaction is given by

$$\frac{G_X}{\sqrt{2}} = \frac{g'_s g'_l}{4M_X^2}, \quad (1)$$

where M_X is the mass of the new gauge boson.

We are going to study the consequences of this model for

1. longbaseline neutrino experiments such as MINOS [9] that observe oscillations of neutrinos and antineutrinos
2. $(g - 2)_\mu$ discrepancy: a light gauge boson with mass \sim MeV can be used as a novel explanation for the 3.6σ discrepancy between the experimental measurement and the SM prediction of the muon anomalous magnetic moment, $(g - 2)_\mu$ [10].
3. CCFR experiment on measurement of the neutrino trident cross-section [11] can test the existence of light gauge bosons

To study the consequences for longbaseline experiments we should write down the neutrino evolution equation in the ν_s SI model,

$$i \frac{d}{dr} \begin{pmatrix} \nu_e \\ \nu_\mu \\ \nu_\tau \\ \nu_s \end{pmatrix} = \left[\frac{1}{2E_\nu} U M^2 U^\dagger + V^{\nu_s \text{SI}}(r) \right] \begin{pmatrix} \nu_e \\ \nu_\mu \\ \nu_\tau \\ \nu_s \end{pmatrix}, \quad (2)$$

where U is the 4×4 PMNS matrix [1], which is parametrized by the active-active mixing angles $(\theta_{12}, \theta_{13}, \theta_{23})$ as well as 3 active-sterile mixing angles $(\theta_{14}, \theta_{24}, \theta_{34})$. The matrix of the mass squared differences $M^2 = \text{diag}(0, \Delta m_{21}^2, \Delta m_{31}^2, \Delta m_{41}^2)$. The matter potential matrix in the ν_s SI model will be (after subtracting the constant $V_{NC}(r) \times \mathbb{I}$)

$$V^{\nu_s \text{SI}}(r) = \sqrt{2} G_F N_e(r) \text{diag}\left(1, 0, 0, \frac{(1-\alpha)}{2}\right). \quad (3)$$

The same evolution equation applies to anti-neutrinos with the replacement $V^{\nu_s \text{SI}}(r) \rightarrow -V^{\nu_s \text{SI}}(r)$. We consider the ν_s SI model with $\alpha > 0$.

Results

We put together all results in Fig. (1) . From the MINOS experiment we arrive to the the black dashed curve shown for the MINOS analysis and the purple shaded region ishows the favored 2σ region from $(g - 2)_\mu$ discrepancy and red solid curve represents the results of the constrains from CCFR experiment on measurement of the neutrino trident cross-section [11].

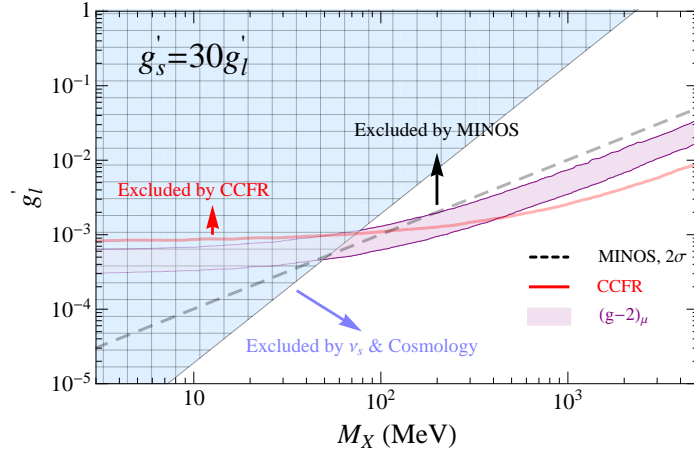


FIG. 1: We have shown the region of interest for the ν_s SI model with a light gauge boson with mass M_X and couplings g'_l and $g'_s = \gamma g'_l$. The result of the analysis of the ν_s SI model with the MINOS data is shown by the black dashed curve with 2σ C.L. (for $\gamma = 30$). The purple shaded region is the region favored by the $(g - 2)_\mu$ discrepancy, while the red curve is the CCFR [11] measurement of the neutrino trident cross-section [12]. The blue shaded region is where the tension between the sterile neutrino and cosmology is relieved.

CONCLUSIONS

We have investigated the possibility that the light sterile neutrinos as suggested by the reactor anomaly have hidden interaction with an "MeV scale" gauge boson. In the Secret Interaction (ν_s SI) model, the sterile neutrinos have neutral current matter potential. Therefore, we can use the data of the neutrino experiments to constrain this model and probe other new physics scenarios. The field strength of this model is described by G_X . In this work we studied the ν_s SI model using the MINOS experiment and showed that the values above $G_X/G_F = 92.4$ are excluded.

One consequence of the ν_s SI model is constraining other new physics scenarios such as explaining the $(g-2)_\mu$ discrepancy with a light gauge boson. We showed that using the ν_s SI model, the $(g-2)_\mu$ region is entirely ruled out for $M_X \lesssim 100\sqrt{\gamma/30}$ MeV by the MINOS data. Also, the secret interaction of sterile neutrinos which is introduced in the literature to solve the tension between the sterile neutrinos and cosmology is excluded by MINOS for $g'_i > 5.3 \times 10^{-4}$ for any value of M_X . We can use the data of the future neutrino oscillation experiments such as DUNE [13] to further test the ν_s SI model and get a definite answer on the presence of the light gauge boson.

Z. T. thanks the hospitality of UNICAMP and O. L. G. P thanks the hospitality of IPM. O. L. G. P. thanks the support of FAPESP funding grant 2012/16389-1 and 2015/12505-5.

* *Presented at NuFact15, 10-15 Aug 2015, Rio de Janeiro, Brazil [C15-08-10.2]*

† Electronic address: `tabrizi.physics@ipm.ir`

‡ Electronic address: `orlando@ifi.unicamp.br`

- [1] K. N. Abazajian et al. (2012), arXiv:1204.5379.
- [2] A. A. Aguilar-Arevalo et al. (MiniBooNE Collaboration), Phys. Rev. Lett. **105**, 181801 (2010).
- [3] G. Mention et al., Phys. Rev. D **83**, 073006 (2011).
- [4] P. A. R. Ade et al. (Planck) (2015), 1502.01589.
- [5] S. Hannestad, R. S. Hansen, and T. Tram, Phys.Rev.Lett. **112**, 031802 (2014).
- [6] B. Dasgupta and J. Kopp, Phys.Rev.Lett. **112**, 031803 (2014).
- [7] Z. Tabrizi and O. L. G. Peres (2015), 1507.06486.
- [8] M. Pospelov, Phys.Rev. **D84**, 085008 (2011).
- [9] P. Adamson et al. (MINOS Collaboration), Phys. Rev. Lett. **110**, **251801** (2013).
- [10] M. Pospelov, Phys. Rev. **D80**, 095002 (2009).
- [11] S. R. Mishra et al. (CCFR), Phys.Rev.Lett. **66**, 3117 (1991).
- [12] W. Altmannshofer, S. Gori, M. Pospelov, and I. Yavin, Phys.Rev.Lett. **113**, 091801 (2014).
- [13] J. M. Berryman, A. de Gouvêa, K. J. Kelly, and A. Kobach, Phys. Rev. **D92**, 073012 (2015).

Probing Neutrino-Scalar Couplings*

P. S. Pasquini[†]

Instituto de Física Gleb Wataghin - UNICAMP,

13083-859, Campinas SP, Brazil and

AHEP Group, Institut de Física Corpuscular – C.S.I.C./Universitat de València. C/Catedrático José Beltrán, 2 E-46980 Paterna (València) - SPAIN

O. L. G. Peres

Instituto de Física Gleb Wataghin - UNICAMP,

13083-859, Campinas SP, Brazil and

The Abdus Salam International Centre for Theoretical Physics,

Strada Costiera 11, 34014 Trieste, Italy.

(Dated: December 5, 2015)

Abstract

Motivated by discovery of scalar particles at the LHC, we revisit the bounds from Yukawa couplings of scalar particles with neutrinos. Using data from meson decays and including for the first time the spectrum from meson decays we manage to put the following constraints for massless scalars: $|g_e|^2 < 1.9 \times 10^{-6}$, $|g_\mu|^2 < 1.9 \times 10^{-7}$ at 90%C.L. and we get bounds on massive scalars up to 100 MeV.

PACS numbers: 13.15.+g, 14.60.Lm, 14.60.St

Keywords: Neutrinos, Scalar Couplings, Yukawa couplings

INTRODUCTION

Neutrino masses may imply new interactions to scalar particles with several mass scales. One should ask how strong can be those interactions to be accommodate into currently data. Thus, we probe phenomenologically motivated neutrino Yukawa Couplings of the form,

$$-\mathcal{L}_{\text{int}} = \frac{1}{2}g_{\alpha\beta}\bar{\nu}_\alpha\nu_\beta\chi_1 + \frac{i}{2}h_{\alpha\beta}\bar{\nu}_\alpha\gamma_5\nu_\beta\chi_2 \quad (1)$$

$\chi_1(\chi_2)$ is a (pseudo-) scalar particle. This interactions can change meson decay,

$$P^- \rightarrow l + \bar{\nu}, \quad (2)$$

by adding a new possible reaction that also emits a scalar particle χ ,

$$P^- \rightarrow l + \bar{\nu}_m + \chi \quad (3)$$

that is experimentally indistinguishable from Eq. (2). Notice that now in ν_m , $m = e, \mu, \tau$ not only $m = l$. This new contribution was calculated by [1] and can be parametrized as,

$$\Gamma(P \rightarrow l + \text{Anything}) = \Gamma_{\text{SM}} + |g_l|^2\Gamma' \quad (4)$$

where $\Gamma' = \Gamma'(m_l, m_\nu, m_\chi, m_P)$ changes the usual two-body decay due to this new interaction and

$$|g_l|^2 = \sum_m |g_{lm}|^2 + |h_{lm}|^2 \quad (5)$$

ANALYSIS AND RESULTS

We used recent data from [2–5] of leptonic decay rates of π, K, D, D_s and B meson considered the standard model prediction of Γ , this was possible only because of recent calculations of f_p in lattice QCD [6]. By taking a χ^2 of the form,

$$\chi^2 = \sum_i \frac{(\Gamma_{\text{exp}}^{(i)} - \Gamma_{\text{teo}}^{(i)})^2}{\sigma_i^2} \quad (6)$$

we extracted new limits for masses ranging from zero to 300 MeV, the full description of the analysis can be found in [7], results for zero scalar mass are presented in Table I and for non-zero masses in Figure 1

Constants	Ref. [8]	Ref. [9]	Our Results
$ g_e ^2$	$< 4.4 \times 10^{-5}$	$< (0.8 - 1.6) \times 10^{-5}$	< 4.4 (4.4) $\times 10^{-5}$
$ g_\mu ^2$	$< 3.6 \times 10^{-4}$		< 4.5 (3.6) $\times 10^{-6}$
$ g_\tau ^2$	$< 2.2 \times 10^{-1}$		< 40 (8)

TABLE I: Comparison between previous bounds [8, 9] with our results with $m_\chi = 0$, using the rates of the meson decay at 90% C.L. In Black the bounds marginalizing V_{CKM} in Red, taking the central value of uncorrelated measurements.

We also used heavy neutrino search [10, 11] to constraining even further the bounds. It was possible due to the fact that the virtual neutrino ν_x of the decay of Eq. (3) can acquire a virtual mass m_x that mimics a continuum spectrum of heavy neutrinos ν_H that was probed in those searches. Thus, setting $m_x = m_H$ into the differential decay rate of the decay $P \rightarrow l\bar{\nu}\chi$, we can translate point to point previous bounds of the mixing $|U_{lH}|$ of the heavy neutrino to the lepton into bounds to the Yukawa coupling between scalar and the SM neutrino, the allowed region of the parameter space can be found on Figure 1.

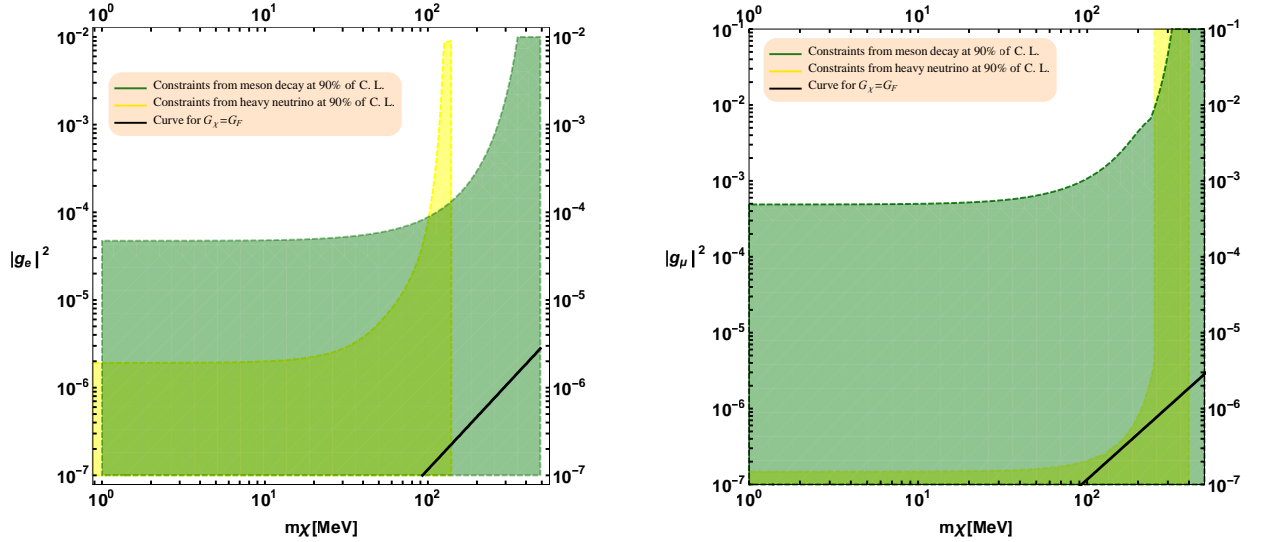


FIG. 1: Bounds on $|g_l|^2$ at 90% C.L. The Green part comes from meson decay and the Yellow part from heavy neutrino search. The black line are interactions weaker than the weak interaction.

CONCLUSION

We recalculated bounds for Yukawa interactions between Neutrinos and Hypothetical scalar particles χ using recent data and decay rates rather than branching fractions for two cases, (I) $m_\chi = 0$ and obtaining $|g_e|^2 < 1.9 \times 10^{-6}$ and $|g_\mu|^2 < 1.9 \times 10^{-7}$ at 90% C.L., which is an improvement on previous results in literature and (II) $m_\chi \neq 0$ showing that those bounds can be safely used up to 100 MeV scales and no bounds can be put for masses $m_\chi \gtrsim 300$ MeV.

ACKNOWLEDGEMENTS

O. L. G. P thanks the support of FAPESP funding grant 2012/16389-1. P. S. P. thanks the support of FAPESP funding grant 2014/05133-1 and 2015/16809-9.

* Presented at NuFact15, 10-15 Aug 2015, Rio de Janeiro, Brazil [C15-08-10.2]

† Electronic address: pasquini@ifi.unicamp.br;orlando@ifi.unicamp.br

[1] V. D. Barger, W.-Y. Keung, and S. Pakvasa, Phys. Rev. **D25**, 907 (1982).

- [2] K. A. Olive et al. (Particle Data Group), *Chin. Phys.* **C38**, 090001 (2014).
- [3] M. Ablikim et al. (BESIII Collaboration), *Phys. Rev.* **D89**, 051104 (2014).
- [4] R. M. White (BaBar Collaboration), *J. Phys. Conf. Ser.* **347**, 012026 (2012).
- [5] A. Zupanc et al. (Belle Collaboration), *JHEP* **09**, 139 (2013).
- [6] S. Aoki et al., *Eur. Phys. J.* **C74**, 2890 (2014).
- [7] P. S. Pasquini and O. L. G. Peres (2015), 1511.01811.
- [8] A. P. Lessa and O. L. G. Peres, *Phys. Rev.* **D75**, 094001 (2007).
- [9] J. Albert et al. (EXO-200 Collaboration), *Phys. Rev.* **D90**, 092004 (2014).
- [10] D. I. Britton et al., *Phys. Rev.* **D46**, 885 (1992).
- [11] A. V. Artamonov et al. (E949 Collaboration), *Phys. Rev.* **D91**, 052001 (2015), [Erratum: *Phys. Rev.* **D91**, 059903(2015)].

**Sensitivity of CP Majorana phases using the synergy between
cosmological and neutrinoless double beta decay data at high
precision era of measures**

Alexander A. Quiroga*

Departamento de Física, Pontifícia Universidade Católica do Rio de Janeiro

C. P 38071, 22451-970, Rio de Janeiro, Brazil.

(Dated: April 2, 2016)

Abstract

We study the detectability of Majorana phase of neutrinos through the precision data of the sum of neutrino masses by cosmological observations, lifetime of neutrinoless double beta decay in ton-scale experiments and the effective neutrino mass measured from single beta decay experiments. We found there is a synergy when data of the three experiments is combined, this allow to constraint one of the Majorana phase (α_{21}) by excluding 10–40% the phase space at the 2σ level of confidence for the lowest neutrino mass of 0.1 eV.

INTRODUCTION

In spite that we are in a era where the oscillation parameters are measured with a high precision [1–3], there are some questions in the neutrino sector that remain open. In this work we want to study one of these open questions, it is the CP Majorana neutrino phases [4, 5]. In order to analyze these phases we need to assume that neutrinos are Majorana particles. We are motivated to analyze these parameters because, nowadays, through an unprecedented precision that observables are being measured by experiments, is possible to get valuable information of the parameters when the data of three observables are combined [6]. In order to quantify our results, we have used a function called “exclusion fraction function” (f_{CPX}) which is defined as a fraction of the CP Majorana phase space that can be excluded with a certain C.L when the inputs parameters are given [7–9].

THE OBSERVABLES

The efective neutrino mass ($m_{0\nu\beta\beta}$) is measured through the half-life time $T_{1/2}^0$ in the neutrinoless double beta decay experiments. Unfortunately this measure have the largest uncertainty in the nuclear matrix element (NME) which introduces an uncertainty with a factor between 2 – 4 [10] in the $m_{0\nu\beta\beta}$. The efective neutrino mass can be related to the oscillation parameters as:

$$m_{0\nu\beta\beta} = |m_1 c_{13}^2 c_{12}^2 + m_2 c_{13}^2 s_{12}^2 e^{i\alpha_{31}} + m_3 s_{13}^2 e^{i\alpha_{31}}|, \quad (1)$$

where m_i is the neutrino masses and $c_{ij} = \cos \theta_{ij}$, $s_{ij} = \sin \theta_{ij}$ whereas α_{31} , α_{32} represents the CP Majorana phases in the MNS matrix mixing neutrino [11]. The prevision on future neutrinoless double beta decay experiments is that will cover the inverted mass hierarchy band which means $m_{0\nu\beta\beta} \approx 10 \text{ meV}$.

The absolute neutrino mass (Σ) is related the oscillation parameters as:

$$\Sigma = m_1 + m_2 + m_3. \quad (2)$$

In recent observations by the Planck Collaboration when baryon acoustic oscillation (BAO) is added they obtained the most severe upper bound $\Sigma < 0.23\text{eV}$ (Planck + WMAP + highL+BAO) at 95% C.L [12]. However, we must be careful with those results coming from cosmological analysis because depend on a particular model, in our work we assume that the ‘‘Standard Model of Cosmology’’ is well described by the Λ CDM model.

The effective neutrino mass m_β , through the single beta decay process can be measured with the distortion caused by $m_\beta \neq 0\text{eV}$ in the end point of the electron energy spectrum in the Kurie plot. The effective neutrino mass measured by this technique can be written as:

$$m_\beta^2(\nu_e) = c_{12}^2 c_{13}^2 m_1^2 + s_{12}^2 c_{13}^2 m_2^2 + s_{13}^2 m_3^2. \quad (3)$$

Currently the best upper limit on m_β comes from Mainz [13] and Troitsk [14] each experiment found a limit of $m_\beta < 2.3\text{eV}$ and $m_\beta < 2.05\text{eV}$ respectively at 95% CL. There is an experiment called ‘‘KATRIN’’ [15] that will improve these bound by one order of magnitude, the upper bound expected with KATRIN is $m_\beta < 0.2\text{eV}$ at 90% C.L.

ANALYSIS METHOD

We analyze the CP Majorana phases minimizing the χ^2 function which is defined as:

$$\chi^2 \equiv \min \left\{ \left[\frac{\Sigma^{(0)} - \Sigma^{\text{fit}}}{\sigma_\Sigma} \right]^2 + \left[\frac{m_\beta^{(0)} - m_\beta^{\text{fit}}}{\sigma_\beta} \right]^2 + \left[\frac{\xi m_{0\nu\beta\beta}^{(0)} - m_{0\nu\beta\beta}^{\text{fit}}}{\sigma_{0\nu\beta\beta}} \right]^2 \right\}, \quad (4)$$

where we have assumed that each observable have a central value ($\Sigma^0, m_\beta^0, m_{0\nu\beta\beta}^0$) and 1σ of uncertainty ($\sigma_\Sigma = 0.05\text{eV}, \sigma_\beta = 0.06\text{eV}, \sigma_{0\nu\beta\beta} = 0.01\text{eV}$) (for more details see Appendix A in [9]) whereas the functions $\Sigma^{\text{fit}}(m_0), m_\beta^{\text{fit}}(m_0), m_{0\nu\beta\beta}^{\text{fit}}(m_0, \alpha_{12}, \alpha_{13})$ must be fitted varying the parameters m_0, α_{13} and α_{12} . In this work is imperative a special attention to the NME uncertainty which is represented by ξ in the equation (4) and is quite similar to the one in [16]. See also [9]. We explore four different values of NME uncertainty parameter, $r_{\text{NME}} = 1.1, 1.3, 1.5, 2.0$ where ξ is bounded as $1/\sqrt{r_{\text{NME}}} \leq \xi \leq \sqrt{r_{\text{NME}}}$. In order to quantify our results, we have used ‘‘the exclusion fraction function’’ see FIG. 1, it is a useful function which shows us how much the parameters can be excluded

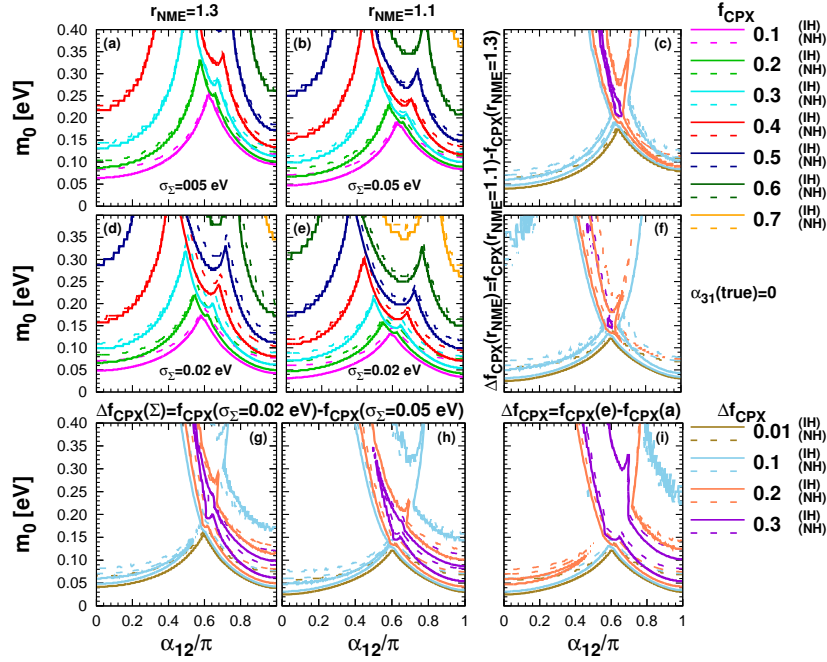


FIG. 1. In (a), (b), (d), (e) Contours of f_{CPX} determined at 3σ C.L for the Inverted and Normal Hierarchy (IH, NH). (1 DOF) projected into the plane of the true values of α_{21}/π and the lightest neutrino mass m_0 for the cases where true value of $(\sigma_\Sigma, r_{\text{NME}}) =$ (a) (0.05 eV, 1.3), (b) (0.05 eV, 1.1), (d) (0.02 eV, 1.3) and (e) (0.02 eV, 1.1) are shown. In (c) and (f), we show, respectively, for $\sigma_\Sigma = 0.05$ eV and 0.02 eV, the iso-contours of $\Delta f_{\text{CPX}}(r_{\text{NME}}) \equiv f_{\text{CPX}}(r_{\text{NME}} = 1.1) - f_{\text{CPX}}(r_{\text{NME}} = 1.3)$ whereas in (g) and (h), we show, respectively, for $r_{\text{NME}} = 1.3$ and 1.1, the iso-contours of $\Delta f_{\text{CPX}}(\Sigma) \equiv f_{\text{CPX}}(\sigma_\Sigma = 0.02 \text{ eV}) - f_{\text{CPX}}(\sigma_\Sigma = 0.05 \text{ eV})$. In (i) we show the iso-contours of $\Delta f_{\text{CPX}}(\Sigma, r_{\text{NME}}) \equiv f_{\text{CPX}}(\sigma_\Sigma = 0.02 \text{ eV}, r_{\text{NME}} = 1.1) - f_{\text{CPX}}(\sigma_\Sigma = 0.05 \text{ eV}, r_{\text{NME}} = 1.3)$.

SUMMARY AND REMARKS

- The dependence of $m_{0\nu\beta\beta}$ on α_{13} is very weak due to the small value of s_{13}^2 and there is a very weak dependence between α_{12} and α_{13} . *For more details see [9]*,
- The best and worse sensitivities to α_{12} is when the true value of α_{12} are 0 or π and $3\pi/2$ respectively. See figure (1),
- The sensitivity to α_{12} increase to low values of true m_0 in the inverted ordering case, whereas for larger values of m_0 there is an increase of the sensitivity for any value of NME. See figure (1),

- The sensitivity to α_{12} increases when the uncertainty of the NME decreases and also when the uncertainty of the Σ decreases, See figure (1). In this point, we expect that in the near future, with the cosmological data coming with an unprecedented precision, the interest of the Cosmology on the neutrino sector be renewed,
- There is a synergy between $m_{0\nu\beta\beta}$ and Σ data which play a interesting role to constraint the CP Majorana phase α_{12} . As we can see in the equation (2) even without dependence of Σ on α_{12} , we found that when the cosmological data are added to equation (4) the sensitivity to α_{12} increases. *For more details see [9].*

Acknowledgments

This work was supported by the Brazilian Funding Agencies, Conselho Nacional de Ciência e Tecnologia (CNPq) and Coordenação de Aperfeiçoamento de Pessoal de Nível Superior (CAPES).

* alarquis@fis.puc-rio.br, Presenter

- [1] T. Kajita, Adv. High Energy Phys. **2012**, 504715 (2012).
- [2] A. B. McDonald, New J. Phys. **6**, 121 (2004) [astro-ph/0406253].
- [3] K. Inoue, New J. Phys. **6**, 147 (2004).
- [4] J. Schechter and J. W. F. Valle, Phys. Rev. D **22**, 2227 (1980).
- [5] S. M. Bilenky, J. Hosek and S. T. Petcov, Phys. Lett. B **94**, 495 (1980).
- [6] G. L. Fogli, *et al* Phys. Rev. D **70**, 113003 (2004) [hep-ph/0408045].
- [7] P. Machado, H. Minakata, H. Nunokawa and R. Funchal, JHEP **1405**, 109 (2014).
- [8] W. Winter, Phys. Rev. D **70**, 033006 (2004) [hep-ph/0310307].
- [9] H. Minakata, H. Nunokawa and A. A. Quiroga PTEP **033B03** 2015, 2015 [arXiv:1402.6014].
- [10] V. A. Rodin, A. Faessler, F. Simkovic and P. Vogel, Phys. Rev. C **68**,044302 (2003).
- [11] Z. Maki, M. Nakagawa and S. Sakata, Prog. Theor. Phys. **28**, 870 (1962).
- [12] P. A. R. Ade *et al.* [Planck Collaboration], Astron. Astrophys. **571**, A16 (2014).
- [13] C. Kraus *et al.*, Eur. Phys. J. C **40**, 447 (2005) [hep-ex/0412056].
- [14] V. N. Aseev *et al.* [Troitsk Collaboration], Phys. Rev. D **84**, 112003 (2011).
- [15] J. Wolf [KATRIN Collaboration], Nucl. Instrum. Meth. A **623**, 442 (2010).
- [16] S. Pascoli, S. T. Petcov and T. Schwetz, Nucl. Phys. B **734**, 24 (2006) [hep-ph/0505226].

**The impact of neutrino decay on medium-baseline reactor
neutrino oscillation experiments**

Alexander A. Quiroga*

*Departamento de Física, Pontifícia Universidade Católica do Rio de Janeiro,
C. P 38071, 22451-970, Rio de Janeiro, Brazil.*

(Dated: April 2, 2016)

Abstract

In this work we use the fact that JUNO has the best opportunity to put the most stringent constraint on ν_3 lifetime over other experiments which utilize artificial neutrinos source. If there is a neutrino decay into invisible states, we find, by studying the χ^2 function that ν_3 decay lifetime can be constrained to $\tau_3/m_3 \geq 7.5 (5.5) \times 10^{-11} s/eV$ at 95% (99%) C.L by JUNO by 100kt.years of exposure. We also discuss the effect of ν_3 decay on the determination of neutrino mass ordering as well as the precision of oscillation parameters to be measured by JUNO.

INTRODUCTION

Nowadays there are bounds on the lifetime of ν_2 and ν_1 [1–6], however the state of the art of neutrino decay shows us there is not a strong constraint on ν_3 decay by using either astrophysical or supernova neutrinos. In order to constraint the lifetime of ν_3 , perhaps, the best method is to use the neutrino oscillation phenomenon because is possible to research by choosing a specific flavor oscillation or energy scale where this quantum phenomenon is most sensitive to ν_3 [7, 8]. We assume a ν_3 decay into invisible final states and in order to constraint the lifetime neutrino decay, we analyze the deformation of the expected event distribution curves which data will be collected, in the future, through medium baseline neutrino reactor as JUNO [9] and RENO-50 [10]. We argue that JUNO could get the best bound on ν_3 because it is the unique artificial neutrino source which can measure the atmospheric-scale neutrino oscillation at the baseline around the solar-scale oscillation *a detailed picture can be found in Ref [11]*, this means a severer bound on lifetime by a factor of $\Delta m_{13}^2/\Delta m_{12}^2 \approx 30$. Also in this work we study the possibility of a confuse measure of the mass ordering as well as lost of sensitivity to constraint the mixing parameters by JUNO due to the ν_3 decay effect.

THE OSCILLATION PROBABILITY

The neutrino decay effect changes the survival probability oscillation which now can be written as:

$$P(\bar{\nu}_e \rightarrow \bar{\nu}_e) = 1 - c_{13}^4 \sin^2 2\theta_{12} \sin^2 \left(\frac{\Delta m_{21}^2 L}{4E} \right) - s_{13}^4 \left(1 - e^{-\Gamma_3 L} \right) - \frac{1}{2} \sin^2 2\theta_{13} \left[1 - \cos \left(\frac{\Delta m_{\text{atm}}^2 L}{2E} \right) e^{-\frac{\Gamma_3 L}{2}} \right], \quad (1)$$

where $c_{ij} = \cos \theta_{ij}$ and $s_{ij} = \sin \theta_{ij}$, for derivation see appendix A in [11]. As we can see in eq (1) there is an attenuation on the oscillation amplitude due to the term $e^{-\frac{\Gamma_3 L}{2}}$ which affect the atmospheric scale. Also there is a decrease of the probability introduced by the factor $(1 - e^{-\Gamma_3 L})$.

As the oscillation probability is directly related to the expected events distribution, therefore there are effects through ν_3 decay that must be discussed. The first impact is that neutrino decay smooth out the small waves which are related to the atmospheric-scale, however, this effect could be mimic by a reduction on θ_{13} . Fortunately, this misunderstand is avoid with a precision measurement of θ_{13} by short baseline reactor neutrino experiments [12]. The reduction of the oscillation amplitude also can be due to a low energy resolution of the experiment, however, 3% of energy resolution will be reached by JUNO and RENO-50 [13]. We also want to study how much the ν_3 decay could confuse the determination of the mass ordering by JUNO and how much the sensitivity to the mixing parameters is affected by ν_3 decay. We are going to answer these two important questions at the end of this work.

ANALYSIS METHOD

In this work we need to built the χ^2 fuction as $\chi^2 = \chi_{\text{stat}}^2 + \chi_{\text{param}}^2 + \chi_{\text{sys}}^2$ [14, 15], each term is defined as:

$$\chi_{\text{stat}}^2 \equiv \int_0^{E_{\text{vis}}^{\text{max}}} dE_{\text{vis}} \left(\frac{\frac{dN^{\text{obs}}}{dE_{\text{vis}}} - \sum_{i=\text{react, U, Th}} (1 + \xi_i) \frac{dN_i^{\text{fit}}}{dE_{\text{vis}}}}{\sqrt{\frac{dN^{\text{obs}}}{dE_{\text{vis}}}}} \right)^2, \quad (2)$$

where $dN^{\text{obs}}/dE_{\text{vis}}$ is the event distribution of the signal that we have simulated and denoted as: “observed”, ξ_i is the parameter that normalizes the flux of the reactor neutrinos. The second term is defined as: $\chi_{\text{param}}^2 \equiv \sum_{i=1}^4 \left(\frac{\bar{x}_i - x_i^{\text{fit}}}{\sigma(x_i)} \right)^2$, where \bar{x}_i represents the inputs and x_i^{fit} are the fitted values, each index denote the mixing parameters where $x_1 \equiv \sin^2 \theta_{12}$, $x_2 \equiv \Delta m_{21}^2$, $x_3 \equiv \sin^2 \theta_{13}$, $x_4 \equiv \Delta m_{31}^2$. For the values of $\sigma(x_i)$ we have used the current uncertainty in [16]. The third term is defined as: $\chi_{\text{sys}}^2 \equiv \left(\frac{\xi_{\text{react}}^{\text{fit}}}{\sigma_{\xi_{\text{react}}}} \right)^2 + \left(\frac{\xi_{\text{U}}^{\text{fit}}}{\sigma_{\xi_{\text{U}}}} \right)^2 + \left(\frac{\xi_{\text{Th}}^{\text{fit}}}{\sigma_{\xi_{\text{Th}}}} \right)^2 + \left(\frac{\eta^{\text{fit}}}{\sigma_{\eta}} \right)^2$ where $\sigma_{\xi_{\text{react}}} = 3\%$ for reactor neutrinos following [17], and the other uncertainties are $\sigma_{\xi_{\text{U}}} = \sigma_{\xi_{\text{Th}}} = 20\%$ for geoneutrinos [15]. We also include the uncertainty of the energy resolution by using a pull term with $\sigma_{\xi_{\eta}} = 10\%$. With respect to the energy resolution we have used the stochastic term $\sigma_E/E = 0.03(1 + \eta)/\sqrt{E/\text{MeV}}$. The bound on the decay timelife by

JUNO is shown in the FIG 1, we can see that after 5 (15) years of data taking the constraint is $\tau_3/m_3 \geq 5.5 (8.5) \times 10^{-11}$ s/eV at 99% C.L.

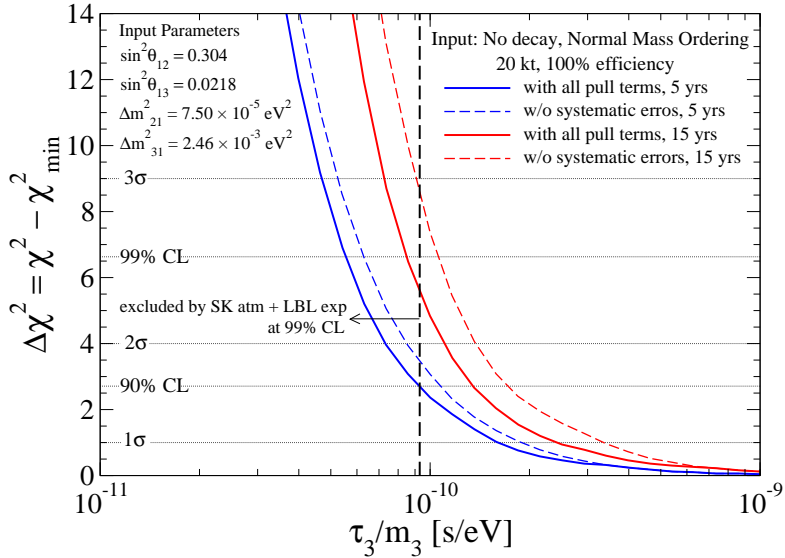


FIG. 1. $\Delta\chi^2 \equiv \chi^2 - \chi_{\min}^2$ is shown by the red (blue) curves for 5 (15) years of data taking, as a function of the fitted value of τ_3/m_3 calculated for the JUNO detector placed at $L = 52.5$ km from a reactor with 35.8 GW thermal power, assuming 5 years of exposure and 100% detection efficiency. We have taken that the true (input) value of τ_3/m_3 is infinite (stable ν_3). The solid curves correspond to the results obtained by using our full χ^2 whereas the dashed ones correspond to the case without assuming systematic errors. The contributions from the reactors at Daya Bay and Huizhou as well as those from geoneutrinos are taken into account. The bound comes from the SK atmospheric neutrinos plus long-baseline oscillation experiment obtained is indicated by the vertical black dashed line.

SUMMARY AND REMARKS

- We found that the bound on the decay lifetime of the massive neutrino state ν_3 is $\tau_3/m_3 \geq 7.5 (5.5) \times 10^{-11}$ s/eV at 95% (99%) C.L can be obtained by JUNO with 5 years of exposure at 100% efficiency. *See figure 1,*
- After 15 years running, the expected bound we found is $\tau_3/m_3 \geq 11 (8.5) \times 10^{-11}$ s/eV. *See figure 1,*
- After 15 years running JUNO the bound on the decay can be constrained to the level of the current atmospheric neutrinos experiment. *See [7],*

- There is an impact of the decay on the mass ordering determination by a reduction of $\Delta\chi^2$ in five units, but only in the case where the decay is allowed in both the input and the fit. *For details see [11]*,
- Regarding to the impact of the decay on the determination of the oscillation parameters by JUNO, we found there is a small effect of the decay. However for Δm_{31}^2 when the decay effect is allowed in both the input and the fit the uncertainty of Δm_{31}^2 would be 30% larger. *For details see [11]*.

Acknowledgments

This work was supported by the Brazilian Funding Agencies, Conselho Nacional de Ciência e Tecnologia (CNPq) and Coordenação de Aperfeiçoamento de Pessoal de Nível Superior (CAPES).

* alarquis@fis.puc-rio.br, Presenter

- [1] J. F. Beacom and N. F. Bell, Phys. Rev. D **65** (2002) 113009.
- [2] A. S. Joshipura, E. Masso and S. Mohanty, Phys. Rev. D **66** (2002) 113008.
- [3] A. Bandyopadhyay, S. Choubey and S. Goswami, Phys. Lett. B **555** (2003) 33.
- [4] J. M. Berryman, A. de Gouvea and D. Hernandez, arXiv:1411.0308 [hep-ph].
- [5] R. Picoreti, M. M. Guzzo, P. C. de Holanda and O. L. G. Peres, arXiv:1506.08158 [hep-ph].
- [6] J. A. Frieman, H. E. Haber and K. Freese, Phys. Lett. B **200** (1988) 115.
- [7] M. C. Gonzalez-Garcia and M. Maltoni, Phys. Lett. B **663** (2008) 405.
- [8] R. Wendell *et al.* [Super-Kamiokande Collaboration], Phys. Rev. D **81** (2010) 092004.
- [9] M. He [JUNO Collaboration], arXiv:1412.4195 [physics.ins-det].
- [10] J. Park, PoS Neutel **2013** (2013) 076.
- [11] T. Abrahao, H. Minakata, H. Nunokawa, A. A. Quiroga JHEP **11**, 001 (2015),
- [12] F. P. An *et al.* [Daya Bay Collaboration], arXiv:1505.03456 [hep-ex].
- [13] L. Zhan, Talk at XVI International Workshop on Neutrino Telescopes, Venice, Italy, 2015.
- [14] S. F. Ge, K. Hagiwara, N. Okamura and Y. Takaesu, JHEP **1305**, 131 (2013).
- [15] F. Capozzi, E. Lisi and A. Marrone, Phys. Rev. D **89**, 013001 (2014).
- [16] M. C. Gonzalez-Garcia, M. Maltoni and T. Schwetz, JHEP **1411** (2014) 052.
- [17] P. Huber, Phys. Rev. C **84**, 024617 (2011) [Phys. Rev. C **85**, 029901 (2012)].

Baksan Experiment on Sterile Transitions (BEST)*

Yury Malyskin,^{1,2,†} Bruce Cleveland,³ Sergei Danshin,¹ Vladimir Gavrin,¹
Valery Gorbachev,¹ Tatiana Ibragimova,¹ Anatoly Kalikhov,¹
Tatiana Knodel,¹ Yulia Kozlova,¹ Victor Matveev,¹ Ilya Mirmov,¹
Jeff Nico,⁴ Alexander Shikhin,¹ Evgeny Veretenkin,¹ Steven Elliott,⁵
Hamish Robertson,⁶ David Sinclair,⁷ and John Wilkerson⁸

¹*Institute for Nuclear Research RAS, Russia*

²*Pontifical Catholic University of Chile*

³*SNOLAB, Canada*

⁴*National Institute of Standards and Technology, USA*

⁵*Los Alamos National Laboratory, USA*

⁶*University of Washington, USA*

⁷*SNO Lab, Canada*

⁸*University of North Carolina, USA*

(Dated: December 17, 2015)

Abstract

A discrepancy between the results and their theoretical predictions is observed in radiochemical calibration experiments SAGE and GALLEX in measurements with artificial radioactive sources. This discrepancy can be explained by neutrino transitions to a hypothetical sterile state on a short baseline, corresponding to the squared mass difference of the order of 1 eV^2 . A new underground experiment BEST to search for this type of neutrino transition is planned to be carried out at the Baksan Neutrino Observatory on the Gallium-Germanium Neutrino Telescope, which has been used in the solar neutrino experiment SAGE. The idea is to observe the neutrino capture rate at two distances from the source. A Ga target is divided in two concentric zones in a way that the neutrino path lengths in each zone are equal. A statistically significant difference of the neutrino capture rates in these zones, as well as a considerable deficiency of the average rate in both zones in comparison with the expected rate, will indicate the existence of the neutrino oscillation on a short baseline. The key features of this experiment are the intense compact neutrino source, which provides a high flux of monochromatic neutrinos, low backgrounds (including solar neutrinos), and a well established during decades technique of neutrino detection. The experiment allows to put constraints on squared mass difference and mixing angle corresponding to the oscillations to the hypothetical sterile neutrinos.

INTRODUCTION

In addition to three known neutrino species (ν_e , ν_μ and ν_τ) there can exist one or more neutrino flavor eigenstates. However, only three neutrino flavors with mass less than the Z^0 boson mass can participate in the electro-weak interactions [1]. This gives the name ‘sterile’ to other hypothetical neutrinos.

Nowadays the possibility of existence of sterile neutrinos is one the most attractive questions. Up to date there is neither clear evidence of sterile neutrino observation, nor any evidence of their non-existence. A set of unexplained experimental results (ν_e appearance in a pure ν_μ beam [2, 3], reactor anomaly [4], gallium anomaly [5, 6], and some others) can be interpreted as an indication of sterile neutrinos with $\Delta m^2 \sim 1 \text{ eV}^2$. However, there are other experimental results making constraints on sterile neutrino parameters, e.g. [7–9]. The significance of data *in favor of* and *in contradiction to* the hypothesis of sterile neutrino existence is more than 2.5σ [10]. This situation requires a clarification through dedicated researches.

GENERAL IDEA

The idea of Baksan Experiment on Sterile Neutrino Transitions (BEST) is to observe transitions of active electron neutrino from an intensive ^{51}Cr source to sterile states on their passage through a Ga metal target. The probability of non-disappearance can be written in the following form:

$$P_{ee} \rightarrow 1 - \sin^2 2\theta \sin \left(1.27 \frac{\Delta m^2 (\text{eV}^2) L (\text{m})}{E_\nu (\text{MeV})} \right),$$

where θ is sterile neutrino mixing angle, Δm^2 is mass difference, L is distance from the source, and E_ν is neutrino energy.

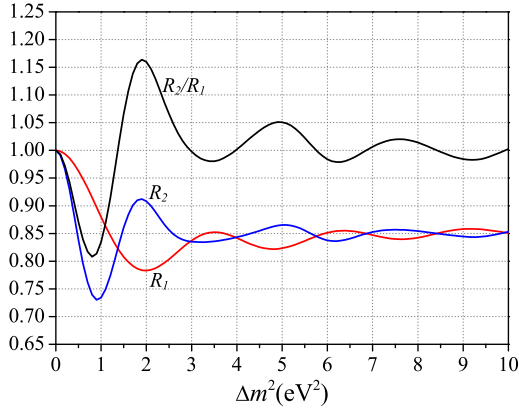


FIG. 1: Ratios of measured ν capture rates to expected ones in the absence of sterile neutrino transitions in the inner zone (R_1), in the outer zone (R_2), and their ratio (R_2/R_1) as a function of Δm^2 for mixing angle $\theta = 0.3$.

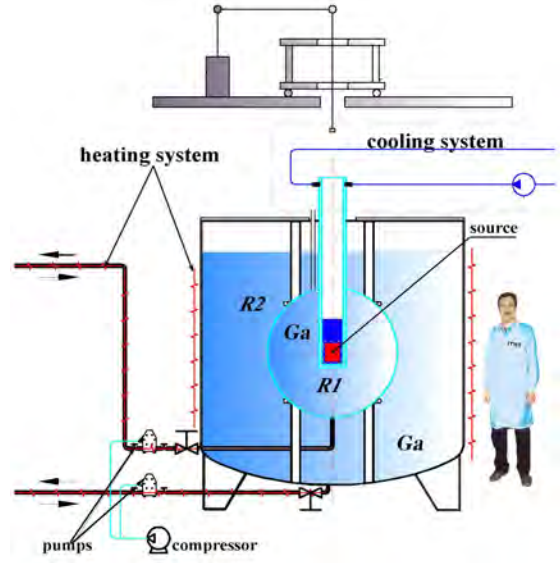


FIG. 2: Scheme of BEST experimental setup.

The Ga detector is sensitive to only active electron flavors, therefore neutrinos oscillated to a sterile flavor are invisible for it. This leads to a decrease of neutrino detection rate. Since neutrino transition to sterile state has a sinusoidal character, the detection rate depends on the distance from the source.

The source will be placed at the center of a two-zone Ga target. The zones are completely independent and have different base-lines. This configuration makes it possible to observe transitions to sterile neutrino in two ways:

- comparing measured and expected rates under assumption of no sterile neutrino transitions,
- comparing detection rates in two zones.

The first method requires an accurate knowledge of the source activity and neutrino reaction cross section. The second does not rely on this information, however it is not conclusive for some Δm^2 values when the rates in both zones are close to each other. Fig. 1 illustrates this, showing the expected capture rates R_1 and R_2 depending on Δm^2 (here and below the rates $R_{1,2}$ are normalized to ones without sterile neutrino transitions). One can see that $R_1/R_2 = 1$ does not necessarily mean the absence of oscillations. Indeed, $R_1 = R_2$ for some Δm^2 , however the rates R_1 and R_2 are lower than it is expected in the absence of transitions to sterile neutrino.

Finally, it is worth to mention, that the mixing angle θ defines the amplitudes of the oscillations. Fig. 1 shows the case when $\theta = 0.3$.

DETECTION SYSTEM

The scheme of the BEST experimental setup is shown in Fig. 2. A compact high intensity 3 MCi ^{51}Cr neutrino source is planned to be placed at the center of a 50-t target of liquid

Ga metal that is divided into independent inner and outer zones, and neutrino capture rates in each zone are measured simultaneously. The zones are specially constructed so that the average neutrino path lengths (55 cm) in each zone are nearly the same. This means that the observed neutrino capture rates in both volumes are the same if there are no transitions to a sterile state. As it has been already mentioned, the transition of electron neutrino to sterile states will lead to decrease of the detected capture rates and, for certain Δm^2 values, to their difference. The zones' baselines are optimized for the highest sensitivity at $\Delta m^2 \sim 1\text{eV}^2$.

The detection technique to be used in BEST is exactly the same as was used in the SAGE experiments for decades [11]. Neutrinos are detected via decay of ^{71}Ge produced in charge-current reaction $\nu_e + ^{71}\text{Ga} \rightarrow ^{71}\text{Ge} + e^-$ in the 50 t Ga target. The method has shown its reliability and we will not go into details here.

The biggest challenges for the BEST experiment are a production of a highly radioactive neutrino source and a precise measurement of its activity. The source is planned to be produced in research nuclear reactor SM-3 (RIAR) by exposing by neutrons of 3.5 kg of ^{50}Cr enriched to 97%. Produced by this way ^{51}Cr nuclei will serve as a source emitting almost monochromatic neutrinos: 90% of neutrinos have energy of 750 keV and other 10% – 430 keV. Their capture fractions are 95% and 5% respectively. Relatively small size of the source ($\text{Ø}8.6 \times 9.5$ cm) will allow to get a practically pure oscillation sinusoid, which gives a better sensitivity and makes the results interpretation more straightforward.

The source activity is planned to be measured by two independent methods and their uncertainties are expected to be within 1%. The first method is based on precise measurements of thermal heat released from the source due to ^{51}Cr decay [12]. A 3 MCi source will emit about 650 W of heat. The second method is based on measuring with PHGe the continuous spectrum of gammas emitted by the source [13].

EXPECTED RESULTS

The source with initial activity of 3 MCi placed at the center of the concentric tanks will produce a mean of 65 atoms of ^{71}Ge per day in each zone at the beginning of measurements. The background is mostly from the Sun (0.16 and 0.83 atoms/day in the inner and the outer zones respectively) and is negligible in comparison with the signal from the source. Expected statistical and systematic uncertainties are 3.7% and 2.6% respectively, giving the total uncertainty of 4.5%.

Sterile neutrino transitions can be observed via certain combinations of measured to predicted capture rates under assumption of absence of oscillations in two zones R_1 and R_2 . Possible positive outcomes are:

- R_1 and R_2 differ significantly from each other,
- $R_1 \simeq R_2$ but the average rate in both zones is considerably below the expected rate.

The improvement of the SAGE+GALLEX sensitivity by adding BEST results is shown in Fig. 3. Region of $\sin 2\theta > 0.1$ can be excluded with a 3σ significance for $1\text{ eV} < \Delta m^2 < 10\text{ eV}$.

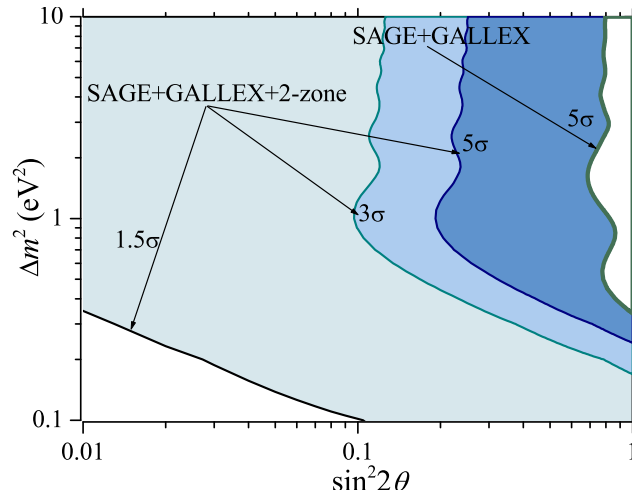


FIG. 3: Sensitivity of the 2-zone experiment

SUMMARY

A new experiment BEST searching for an evidence of sterile neutrino transitions is under preparation at the Baksan Neutrino Observatory. The baseline is ~ 1 m and the experiment is most sensitive to $\Delta m^2 \sim 1\text{eV}^2$. The well established technique used in the SAGE experiment will be used for neutrino detection. High source activity (3 MCi) will provide rich statistic and high signal-to-backgrounds ratio. Almost monochromatic neutrino energy and the compactness of the source will allow to observe a pure sinusoidal oscillation and to simplify the results interpretation. The experiment will start as soon as the source will be ready and the measurements will take about a year.

* Presented at NuFact15, 10-15 Aug 2015, Rio de Janeiro, Brazil [C15-08-10.2]

† malyshkin@inr.ru; Speaker

- [1] D. E. Groom et al. (Particle Data Group), Eur. Phys. Jour. **C15**, 1 (2000).
- [2] A. Aguilar-Arevalo et al. (LSND), Phys. Rev. D **64**, 112007 (2001), hep-ex/0104049.
- [3] A. Aguilar-Arevalo et al. (MiniBooNE Collaboration), Phys. Rev. Lett. **110**, 161801 (2013).
- [4] G. Mention, M. Fechner, T. Lasserre, T. A. Mueller, D. Lhuillier, M. Cribier, and A. Letourneau, Phys. Rev. D **83**, 073006 (2011).
- [5] C. Giunti and M. Laveder, Phys. Rev. D **82**, 053005 (2010).
- [6] V. N. Gavrin, V. V. Gorbachev, E. P. Veretenkin, and B. T. Cleveland (2010), arXiv:1006.2103.
- [7] A. Aguilar-Arevalo et al. (MiniBooNE Collaboration), Phys. Rev. Lett. **102**, 101802 (2009).
- [8] B. Armbruster et al. (KARMEN), Phys. Rev. D **65**, 112001 (2002), hep-ex/0203021.
- [9] P. Astier et al. (NOMAD), Nucl. Phys. **B611**, 3 (2001), hep-ex/0106102.
- [10] K. N. Abazajian et al. (2012), arXiv:1204.5379.
- [11] J. N. Abdurashitov et al. (SAGE), Phys. Rev. C **80**, 015807 (2009).
- [12] E. P. Veretenkin, V. N. Gavrin, S. N. Danshin, T. V. Ibragimova, Y. P. Kozlova, and I. N. Mirmov, Phys. Atom. Nucl. **77**, 1 (2015).
- [13] V. V. Gorbachev and Y. M. Malyshkin, Instrum. Exp. Tech. **58**, 418 (2015).

Can Neutrinos Decay?*

Renan Picoreti,[†] M. M. Guzzo, and P. C. de Holanda

Instituto de Física Gleb Wataghin - UNICAMP, 13083-859, Campinas SP, Brazil.

O. L. G. Peres

Instituto de Física Gleb Wataghin - UNICAMP,

13083-859, Campinas SP, Brazil. and

The Abdus Salam International Centre for Theoretical Physics,

Strada Costiera 11, 34014 Trieste, Italy.[‡]

(Dated: December 19, 2015)

Abstract

We consider the possibility of solar neutrino decay as a sub-leading effect on their propagation between production and detection. Using current oscillation data, we set a new lower bound to ν_2 lifetime $\tau_2/m_2 \geq 7.2 \times 10^{-4} \text{ s} \cdot \text{eV}^{-1}$ at 99% C.L.. Also, we show how seasonal variations in the solar neutrino data can give interesting additional information about neutrino lifetime.

INTRODUCTION

The LMA-MSW solution for the Solar Neutrino Problem, in combination with the measurement of the other oscillation parameters by experiments designed for atmospheric, reactor and long-baseline neutrinos, established the scenario of three massive light neutrinos that mix [1]. With precise measurements of the standard oscillation parameters, it is possible to investigate new phenomena such as the neutrino decay scenario, $\nu' \rightarrow \nu + X$, as a sub-leading effect in the propagation of solar neutrinos and set limits to their lifetime using the most recent experimental data. For solar neutrinos, the current bound to ν_2 lifetime for invisible non-radiative decays [2] is $\tau_2/m_2 \geq 8.7 \times 10^{-5} \text{ s} \cdot \text{eV}^{-1}$ at 99% C.L..

FORMALISM

After production in the solar core, neutrinos propagate outwards undergoing flavor oscillation and resonant flavor transition due to the solar matter potential. After emerging from the solar matter, they travel across the interplanetary medium until they reach the Earth's surface where they can be detected.

For the current limits to their lifetime, neutrinos do not decay inside the Sun and it is sufficient to only consider their decay on the way to Earth. For the scenario in which all the final products are invisible, the decay survival probability of a neutrino mass-eigenstate i , with energy E_ν , after propagating a distance L , is

$$P_i^{\text{surv}} = \exp \left[- \left(\frac{\alpha_i}{E_\nu} \right) L \right], \text{ with } \alpha_i = \frac{m_i}{\tau_i}, \quad (1)$$

where m_i is the eigenstate's mass, τ_i is the eigenstate's lifetime and L is the Sun-Earth distance.

For the assumption that only the ν_2 mass-eigenstate is unstable, the electron neutrino survival probability including decay and oscillation for three neutrino families is

$$P(\nu_e \rightarrow \nu_e) = c_{13}^4 \left[P_{e1}^\ominus P_{1e}^\oplus + P_{e2}^\ominus (P_2^{\text{surv}}) P_{2e}^\oplus \right] + s_{13}^4, \quad (2)$$

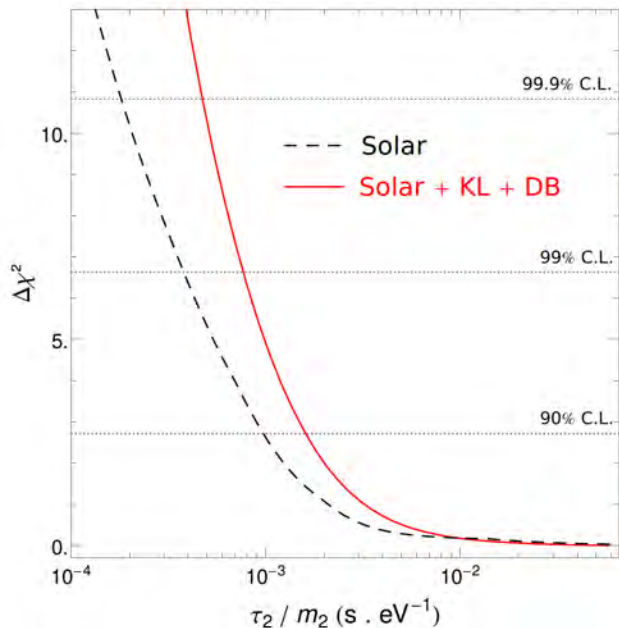


Figure 1: $\Delta\chi^2$ as a function of ν_2 lifetime τ_2/m_2 . The continuous curve shows the results for the analysis using only solar data while the dashed curve shows results for the combined data analysis.

where $s_{ij} = \sin\theta_{ij}$ and $c_{ij} = \cos\theta_{ij}$, P_i^{surv} is given in Eq. (1), P_{ei}^\odot is the probability of the produced ν_e to be found as a ν_i at the surface of the Sun, and $P_{i\alpha}^\oplus$ is the probability of a ν_i to be detected as a ν_α on Earth.

In this scenario, one interesting point is that the sum over all probabilities is not equal to 1, as explicitly we have $\sum_{\alpha=e,\mu,\tau} P(\nu_e \rightarrow \nu_\alpha) = 1 - c_{13}^2 P_{e2}^\odot (1 - P_2^{\text{surv}})$. This non-unitary evolution was discussed in Ref. [3].

ANALYSIS AND RESULTS

For the analysis of ν_2 decay over the Earth-Sun distance and how it affects the expected rate for each solar neutrino experiment, we numerically calculate the neutrino survival probabilities under the assumption of adiabatic evolution inside the Sun [4]. Then, we compute the expected event rate for each relevant experiment and compare it to their data [5–10].

We can add complementary information from the reactor experiments KamLAND [11] and Daya Bay [12] and their detection of $\bar{\nu}_e$ oscillations. These reactor experiments give precise constraints on Δm_{21}^2 and $\sin^2\theta_{13}$ and for their typical baselines, and the currently allowed values of τ_2/m_2 , decay can be neglected and their standard neutrino analysis can also be used for decay scenario.

We write a combined χ^2 function for solar, KamLAND and Daya Bay data and from the complete marginalization over the standard parameters, we can extract a lower limit to the ν_2 eigenstate lifetime $\tau_2/m_2 \geq 7.7 \times 10^{-4} \text{ s} \cdot \text{eV}^{-1}$, at 99% C.L., as shown in Fig. 1 for $\Delta\chi^2$ as a function of τ_2/m_2 .

Experiment	$(\epsilon_{\text{exp}} \pm \sigma_{\text{exp}}) / \epsilon_0$
Borexino [13]	2.38 ± 0.61
SuperK-I [14]	1.51 ± 0.43
SNO Phase I [15]	0.86 ± 0.51

Table I: Experimental best-fit values and errors for Earth's orbital eccentricity ϵ for different solar neutrino experiments. We also show the ratio between the fitted values and the Earth's eccentricity ϵ_0 .

SEASONAL EFFECT

In the absence of decay, the neutrino flux arriving on Earth is given by $\phi_{\nu}^{\oplus} = \phi_{\nu}^{\odot} / (4\pi r^2)$, where r is the time-dependent Earth-Sun distance. The ratio between maximum (perihelion) and minimum (aphelion) fluxes is $R_0 = (1 + \epsilon_0)^2 / (1 - \epsilon_0)^2$, where $\epsilon_0 = 0.0167$ is Earth's orbital eccentricity. Decay modifies the ratio between maximum and minimum neutrino fluxes and hence also the eccentricity ϵ measured from the neutrino data as given by

$$R = R_0 \frac{N(r_{\min})}{N(r_{\max})} = \frac{(1 + \epsilon)^2}{(1 - \epsilon)^2}, \quad (3)$$

where $r_{\max}(r_{\min})$ is the aphelion (perihelion) distance and N is the number of events calculated from the adequate probabilities and cross sections for each experiment. Since $N(r_{\min}) > N(r_{\max})$ due to P_2^{surv} dependence on the orbital distance, $R > R_0$ for any neutrino energy and thus, for any neutrino decay scenario, an enhancement in the seasonal variation of the solar neutrino flux is to be expected, which in turn would lead to $\epsilon > \epsilon_0$.

In fact, some experiments have measured an eccentricity different from the standard value, albeit still compatible with ϵ_0 , as shown in Table (I). The eccentricity measured with neutrinos ϵ as it would be measured by different experiments as a function of the neutrino

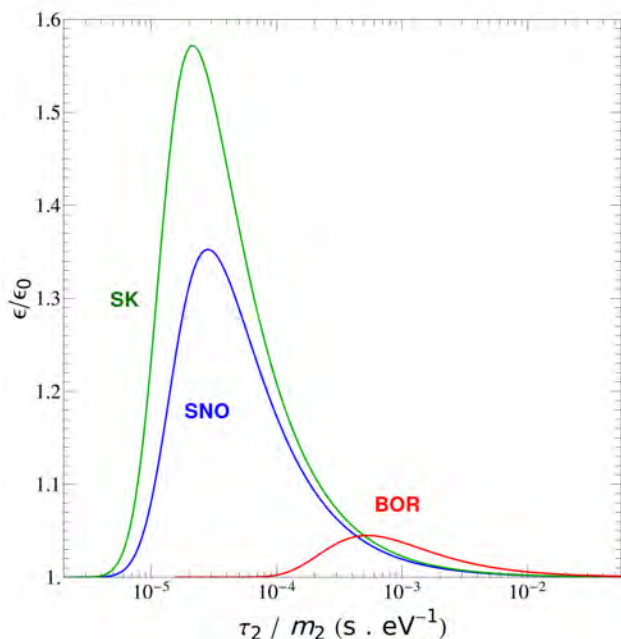


Figure 2: Dependence of the orbital eccentricity ϵ with the neutrino lifetime τ_2/m_2 as it would be measured by different experiments — the ${}^7\text{Be}$ line in Borexino (BOR), Super-Kamiokande (SK), and Sudbury Neutrino Observatory (SNO).

lifetime τ_2/m_2 is shown in Fig. 2.

Including the eccentricity data in the analysis with a penalty function added to the χ^2 for each experiment $\chi_{\text{seasonal}}^2 = (\epsilon_{\text{exp}} - \epsilon)^2 / (\sigma_{\text{exp}})^2$ results in a slightly lower value

$$\tau_2 / m_2 \geq 7.2 \times 10^{-4} \text{ s} \cdot \text{eV}^{-1}, \text{ at 99\% C.L.} \quad (4)$$

due to the fact that the current eccentricity measurements and errors will favor lower, already excluded, lifetimes, for which the enhancement in the seasonal variation (and hence measured eccentricity) is higher.

CONCLUSION

From our analysis, we have obtained a new upper bound to the ν_2 eigenstate lifetime $\tau_2 / m_2 \geq 7.2 \times 10^{-4} \text{ s} \cdot \text{eV}^{-1}$ at 99% C.L.. which is almost one order higher than the previous established bound [2] at $\tau_2 / m_2 \geq 8.7 \times 10^{-5} \text{ s} \cdot \text{eV}^{-1}$ at 99% C.L..

* *Presented at NuFact15, 10-15 Aug 2015, Rio de Janeiro, Brazil [C15-08-10.2]*

† `picoreti@ifi.unicamp.br`

‡ The authors would like to thank FAPESP, CNPq and CAPES for several financial supports.

O.L.G.P. thanks the support of FAPESP funding grants 2012/16389-1 and 2015/12505-5.

- [1] M. C. Gonzalez-Garcia and Y. Nir, *Rev.Mod.Phys.* **75**, 345 (2003).
- [2] A. Bandyopadhyay, S. Choubey, and S. Goswami, *Phys.Lett.* **B555**, 33 (2003).
- [3] J. M. Berryman, A. de Gouvêa, D. Hernández, and R. L. N. Oliveira, *Phys.Lett.* **B742**, 74 (2015).
- [4] P. C. de Holanda and A. Y. Smirnov, *Phys.Rev.* **D83**, 113011 (2011).
- [5] B. T. Cleveland et al., *Astrophys.J.* **496**, 505 (1998).
- [6] F. Kaether, W. Hampel, G. Heusser, J. Kiko, and T. Kirsten, *Phys.Lett.* **B685**, 47 (2010).
- [7] J. N. Abdurashitov et al. (SAGE Collaboration), *Phys.Rev.* **C80**, 015807 (2009).
- [8] J. Hosaka et al. (Super-Kamiokande Collaboration), *Phys.Rev.* **D73**, 112001 (2006).
- [9] B. Aharmim et al. (SNO Collaboration), *Phys.Rev.* **C88**, 025501 (2013).
- [10] C. Arpesella et al. (Borexino Collaboration), *Phys.Rev.Lett.* **101**, 091302 (2008).
- [11] A. Gando et al. (KamLAND Collaboration), *Phys.Rev.* **D83**, 052002 (2011).
- [12] F. P. An et al. (Daya Bay Collaboration), *Phys.Rev.Lett.* **112**, 061801 (2014).
- [13] G. Bellini et al. (Borexino Collaboration), *Phys. Rev. D* **89**, 112007 (2014).
- [14] M. B. Smy et al. (Super-Kamiokande Collaboration), *Phys.Rev.* **D69**, 011104 (2004).
- [15] B. Aharmim et al. (SNO Collaboration), *Phys.Rev.* **D72**, 052010 (2005).

The Angra neutrino experiment*

Stefan Wagner,^{1,†} T.A. Alvarenga,² J.C. Anjos,¹ G. Azzi,¹ A.S. Cerqueira,²
P. Chimenti,³ J.A. Costa,³ T.I. Dornelas,² P.C.M.A. Farias,² G.P. Guedes,⁴
L.F.G. Gonzalez,⁵ E. Kemp,⁵ H.P. Lima Jr.,¹ R. Machado,¹ R.A. Nóbrega,² H.
Nunokawa,⁶ I.M. Pepe,⁷ D.B.S. Ribeiro,⁷ E.F. Simas Filho,⁷ and G.A. Valdivieso⁸

(Neutrinos Angra collaboration)

¹*Centro Brasileiro de Pesquisas Físicas, Rio de Janeiro, Brazil*

²*Universidade Federal de Juiz de Fora, Juiz de Fora, Brazil*

³*Universidade Federal do ABC, Santo André, Brazil*

⁴*Universidade Estadual de Feira de Santana, Feira de Santana, Brazil*

⁵*Universidade Estadual de Campinas, Campinas, Brazil*

⁶*Pontifícia Universidade Católica do Rio de Janeiro, Rio de Janeiro, Brazil*

⁷*Universidade Federal da Bahia, Salvador, Brazil*

⁸*Universidade Federal de Alfenas, Poços de Caldas, Brazil*

(Dated: December 20, 2015)

Abstract

The *Neutrinos Angra* detector is a demonstrator experiment to measure the antineutrino flux from nuclear reactors for nuclear safeguards and non-proliferation purposes. The 1 m³ Gd-loaded water Cherenkov detector will be installed at 25 m from the 4 GW_{th} Angra-II reactor core and detect $\approx 5 \cdot 10^3$ neutrinos per day. The detector is now completely assembled and is being extensively tested at the CBPF. Preliminary analyses with data from the detector were used to assess the electronics and PMT characteristics, as well as to study the muon flux and background rate. The detector will soon be shipped to its destination at the Angra dos Reis nuclear power plant and begin taking neutrino data.

CONCEPT

The *Neutrinos Angra* experiment aims to measure antineutrinos from the Angra-II reactor block of the Angra dos Reis nuclear power plant. Main objective of the experiment is to determine the reactor power from the measured antineutrino flux and, by doing so, demonstrate the possibility of using small-scale neutrino detectors for safeguards and nuclear non-proliferation. For this purpose the detector is designed to be safe, compact, cost-effective, and easily deployable in agreement with recommendations of the International Atomic Energy Agency [1].

DETECTOR DESIGN

The Neutrino Target consists of a volume of 1 m³ of water doped with Gadolinium (ca. 0.3 %). Antineutrinos from the reactor are detected via the inverse beta decay (IBD) reaction $\nu_e + p \rightarrow e^+ + n$. The positron instantly deposits its energy and annihilates producing a prompt signal. The neutron thermalizes and is then captured on a Gadolinium nucleus. The deexcitation of the nucleus releases several gammas and yields a delayed signal. The coincidence to a previous prompt event creates a characteristic signature for IBD events. The short coincidence time of $\approx 10^{-8}$ s and high deexcitation energy of ≈ 8 MeV sets antineutrino reactions apart from most accidental background events. The Cherenkov light produced in the Target is observed by 32 PMTs (8 inch Hamamatsu R5912) at the top and bottom walls of the vessel. To increase the light yield the Target walls are covered with

highly reflective material [2].

The Target is surrounded by active Veto volumes, which are filled with pure water and are equipped with a total of 12 PMTs to observe the Cherenkov light created by cosmic muons. In addition to the active Veto volumes there is a lateral layer of 25 cm of pure water as a passive shielding protecting the fiducial volume from external radioactivity and neutrons induced by cosmic rays.

The experiment will be installed at the Almirante Álvaro Alberto nuclear power plant at Angra dos Reis, Rio de Janeiro. The detector will be placed at a close distance of 25 m from the core of the Angra-II reactor. With 4 GW thermal power of the reactor the expected number of observed antineutrino events is of the order of $5 \cdot 10^3$ events per day. The measurement of the antineutrino flux at this very short baseline also provides a further data point for the investigation of the so-called reactor anomaly. Unlike most other neutrino experiments, the Angra detector will be placed above ground and be exposed to a high rate of cosmic muons and muon-induced backgrounds. Their rejection is an important challenge for the experiment and special attention is paid to the efficient handling of the background. Several analysis techniques are being developed and evaluated to identify and reject background events.

CURRENT STATUS

The detector is now completely assembled at the CBPF and is taking data. Currently, the detector performance and stability is being intensively tested. Acquired physics data has already been used to characterize the PMTs and readout electronics and to study the detector response [3]. It also allows to measure the cosmic muon flux and the rate of further background, which helps to improve the Monte Carlo simulations of the experiment. A calibration campaign is also envisaged. After the tests are concluded the detector will be fully commissioned and shipped to its destination at the nuclear power plant in Angra dos Reis, Rio de Janeiro.

ACKNOWLEDGMENTS

This work is supported by several Brazilian agencies through a number of funding projects. The *Neutrinos Angra* collaboration acknowledges the support of the Ministério da Ciência, Tecnologia e Inovação (MCTI), the Conselho Nacional para o Desenvolvimento Científico e Tecnológico (CNPq), the Financiadora de Estudos e Projetos (FINEP) and the state funding agencies FAPESP, FAPEMIG and FAPERJ. The collaborators also like to thank the universities and institutes listed on the author page.

* *Presented at NuFact15, 10-15 Aug 2015, Rio de Janeiro, Brazil [C15-08-10.2]*

† `swagner@cbpf.br`; Presenter

- [1] J. A. et al., Nucl. Phys. B, Proc. Suppl. (2015).
- [2] J. A. et al., Nucl. Part. Phys. Proc. (2015).
- [3] J. A. et al., Nucl. Instr. Meth. A (2015).

Revisiting T2KK and T2KO physics potential and $\nu_\mu - \bar{\nu}_\mu$ beam ratio*

Kaoru Hagiwara

*Theory Center, KEK, 1-1 Oho, Tsukuba, Ibaraki 305-0801, Japan and
Department of Accelerator Science, Sokendai,
1-1 Oho, Tsukuba, Ibaraki 305-0801, Japan*

Pyungwon Ko

*School of Physics, KIAS, 85 Hoegi-ro,
Dongdaemun-gu, Seoul 130-722, Korea*

Naotoshi Okamura

*Department of Radiological Sciences,
International University of Health and Welfare,
2600-1 Kitakanemaru, Ohtawara, Tochigi 324-8501, Japan*

Yoshitaro Takaesu[†]

Department of Physics, University of Tokyo, Tokyo 113-0033, Japan

(Dated: December 19, 2015)

Abstract

We revisit the sensitivity study of a Tokai-to-Kamioka-and-Korea (T2KK) and Tokai-to-Kamioka-and-Oki (T2KO) proposals where a 100 kton detector is placed in Korea ($L = 1000$ km) and Oki island ($L = 653$ km) in Japan, respectively, in addition to the Super-Kamiokande (SK) for determination of the neutrino mass hierarchy and leptonic CP phase (δ_{CP}). We systematically study the ν_μ and $\bar{\nu}_\mu$ focusing beam ratio and find that the T2KK and T2KO experiments can improve their sensitivity to both the mass hierarchy determination and leptonic CP phase measurement simultaneously, using ν_μ and $\bar{\nu}_\mu$ focusing beams with 3 : 2 - 2.5 : 2.5 beam ratio.

INTRODUCTION

Determination of the neutrino mass hierarchy and CP violating phase in the Maki-Nakagawa-Sakata (MNS) mixing matrix has been next targets in the neutrino physics. Ideas of extending the Tokai-to-Kamioka (T2K) experiment with additional water Čerenkov detectors placed in Korea (Tokai-to-Kamioka-and-Korea: T2KK) [1–12] or in Oki island (Tokai-to-Kamioka-and-Oki: T2KO) [11, 13] as well as at Super-Kamiokande (SK) site has been proposed to address those questions. It has been shown that the T2KK experiment with a 100 kton fiducial-volume detector in Korea in addition to the SK detector is an appealing proposal. In this presentation, we revisit the sensitivity study of the T2KK [8, 10] and T2KO [11] experiments for the neutrino mass hierarchy and CP phase, studying the dependence of the sensitivities on the ν_μ and $\bar{\nu}_\mu$ focusing beam ratio systematically with dedicated estimation of backgrounds. Especially, the treatment of the NC π^0 backgrounds is improved in this analysis.

SENSITIVITY ANALYSES AND RESULTS

We use the ν_μ and $\bar{\nu}_\mu$ focusing beam fluxes from the J-PARK with the proton energy of 40 GeV [14]. The baseline length from the J-PARK to the SK, Oki and Korea detectors are taken to be 295 km, 653 km and 1000 km, respectively. The averaged matter densities, $\bar{\rho}$, along the baseline between J-PARK and SK, Oki and Kr detectors have been evaluated in Refs. [10, 11] and taken to be 2.60, 2.75 and 2.90 g/cm³, respectively. NC single- π^0 events can be a substantial background source for ν_e and $\bar{\nu}_e$ appearance modes and affect the sensitivity to the mass hierarchy and CP phase significantly [8]. We consider the uncertainties of the background due to the π^0 rejection [15] and axial masses of the single pion production processes, assigning the 11% normalization uncertainty for the total NC single- π^0 backgrounds and 13% and 15% normalization uncertainties for the NC resonant and coherent single- π^0 backgrounds, respectively.

In Fig. 1, the sensitivity of the T2KK experiments to the mass hierarchy determination is shown. The true value of $\sin^2 \theta_{23}$ is assumed to be 0.5. It is shown that including $\bar{\nu}_\mu$ focusing beam can improve the sensitivity, especially in high sensitivity regions. Although there are reduction of sensitivities in some δ_{CP} regions by including $\bar{\nu}_\mu$ focusing beams, the reduction is minimized with the $\nu_\mu : \bar{\nu}_\mu = 4 : 1$ beam ratio for both OAB cases. On the other

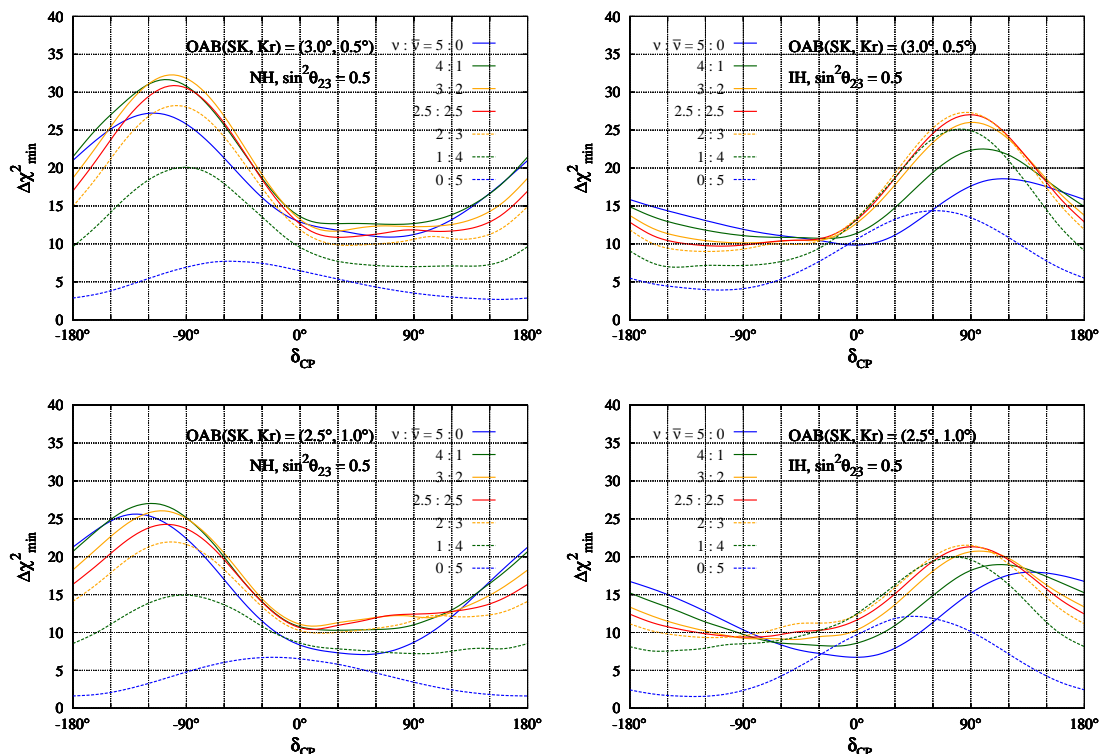
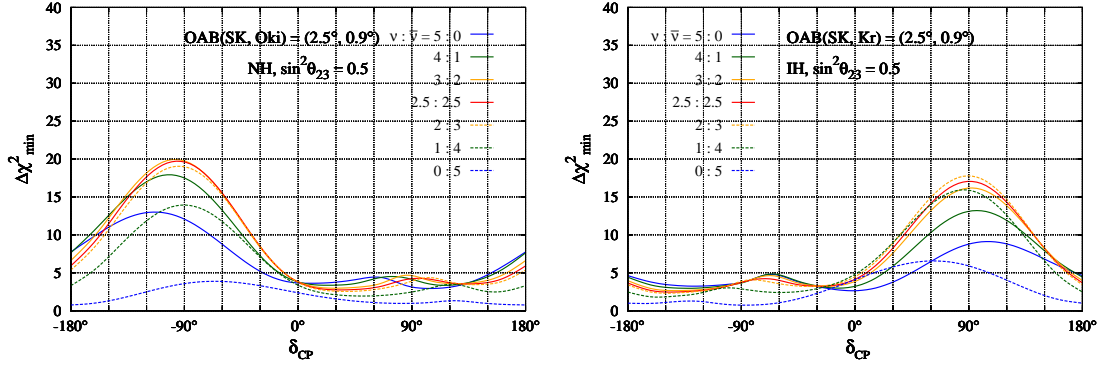
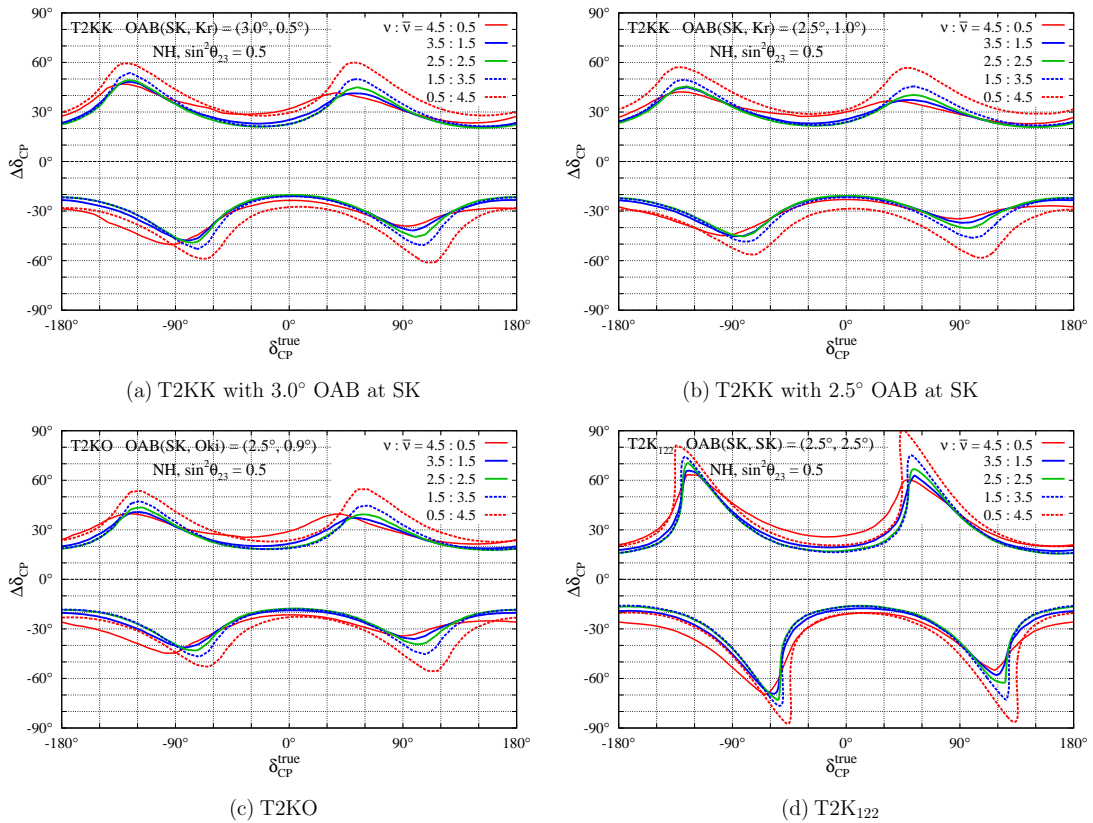


FIG. 1: The $\Delta\chi^2$ minimum for the T2KK experiment to reject the wrong mass hierarchy as a function of the leptonic CP phase, δ_{CP} . The left and right plots are for the normal and inverted hierarchy cases, while the upper and lower plots are for the 3.0° (0.5°) and 2.5° (1.0°) off-axis beam at SK (Kr) detector, respectively.

hand, comparing the lowest $(\Delta\chi^2)_{\text{min}}$ in the whole $\bar{\nu}$ range of the CP phase, the ν_μ and $\bar{\nu}_\mu$ focusing beam ratio of 4:1 is the best for the 3.0° OAB at SK, and 3:2 - 2:3 are best for the 2.5° OAB at SK. In terms of the highest sensitivity, 4:1, 3:2 and 2.5:2.5 beam ratios give comparable sensitivity for the normal hierarchy, but 3:2 and 2:3 are significantly better than 4:1 for the inverted hierarchy case. Thus, around 3:2 - 2.5:2.5 would be a preferred choice for both OAB cases.

In Fig. 2, we show the sensitivities of the T2KO experiment. The improvement by including $\bar{\nu}_\mu$ focusing beam is significant in the high sensitivity region, while the sensitivities in the low sensitivity region does not change so much, preferring the running ratio of 3:2 - 2:3. Comparing to the T2KK, the sensitivity is lower by 30% - 70% in $(\Delta\chi^2)_{\text{min}}$. The lower sensitivity in the T2KO is basically due to the smaller matter effects.

Next, let us discuss the sensitivity to the CP phase measurements. In Fig. 3, we show the 1σ uncertainties of CP phase measurements as functions of the CP phase for the four experiments: (a) T2KK with 3.0° OAB at SK, (b) T2KK with 2.5° OAB at SK, (c) T2KO and (d) T2K₁₂₂, where a 100 kton detector is placed at the Kamioka site along with SK detectors with the total detector volume of 122.5 kton. The uncertainty of the CP phase measurement is smallest around $\delta_{\text{CP}} \sim 0^\circ$ and $\sim 180^\circ$, while the sensitivity is worst around $\delta_{\text{CP}} \sim \pm 60^\circ$ and $\sim \pm 120^\circ$ as clearly seen in the T2K₁₂₂. This low sensitivity reflects the


 FIG. 2: Same as Fig. 1, but for the T2KO experiment with the 2.5° (0.9°) OAB at SK (Oki).

 FIG. 3: The 1σ uncertainty of CP phase measurements as functions of the CP phase when $\sin^2 \theta_{23} = 0.5$, and mass hierarchy is known to be the normal hierarchy.

degeneracy between δ_{CP} and $\pi - \delta_{\text{CP}}$ in the $\sin \delta_{\text{CP}}$ term in the $\nu_\mu(\bar{\nu}_\mu) \rightarrow \nu_e(\bar{\nu}_e)$ oscillation probability, and we need information of $\cos \delta_{\text{CP}}$ to resolve it. The accuracy of the CP phase measurement around these low sensitivity regions with the T2KK and T2KO is significantly better than that with the T2K₁₂₂. The T2KK and T2KO observe up to the second peak of the $\nu_\mu \rightarrow \nu_e$ oscillation and are more sensitive to the $\cos \delta_{\text{CP}}$ term, allowing more accurate measurements of the CP phase around those low sensitive regions.

As for the ν_μ and $\bar{\nu}_\mu$ focusing beam ratio, the ratio between 3.5:1.5 and 1.5:3.5 give the smaller uncertainty in most of the CP phases, except for the low sensitivity region, where the ratio of 4.5 : 0.5 gives the best accuracy. Using the 2.5:2.5 beam ratio, the three experiments measure the CP phase with the uncertainty of $\sim 20^\circ - 50^\circ$ (T2KK with 3.0° OAB), $\sim 20^\circ - 45^\circ$ (T2KK with 2.5° OAB and T2KO) and $\sim 15^\circ - 70^\circ$ (T2K₁₂₂), depending on the CP phase. For the inverted hierarchy case, the uncertainties show similar dependences on the ν_μ and $\bar{\nu}_\mu$ focusing beam ratio as the normal hierarchy case.

CONCLUSION

As discussed in this presentation, the T2KK and T2KO experiments can improve their sensitivity to both the mass hierarchy determination and leptonic CP phase measurement using ν_μ and $\bar{\nu}_\mu$ focusing beams with 3:2 - 2.5:2.5 beam ratio. The T2KK experiment allows us to determine the mass hierarchy and measure the leptonic CP phase simultaneously. The T2KO experiment also has sensitivity to the CP phase measurement, while its physics potential for the mass hierarchy determination is not as good as the T2KK experiment.

K.H. and Y.T. wish to thank the KIAS, where part of this work was done. This work is in part supported by the Grant in Aid for Scientific Research (No.60322997) from MEXT, Japan, and KNRC through National Research Foundation of Korea Grant (Y.T.).

* Presented at NuFact15, 10-15 Aug 2015, Rio de Janeiro, Brazil [C15-08-10.2]

† takaesu@hep-th.phys.s.u-tokyo.ac.jp; Speaker

- [1] K. Hagiwara, Nucl.Phys.Proc.Suppl. **137** (2004) 84.
- [2] M. Ishitsuka, T. Kajita, H. Minakata and H. Nunokawa, Phys.Rev. **D72** (2005) 033003.
- [3] K. Hagiwara, N. Okamura and K.-i. Senda, Phys.Lett. **B637** (2006) 266.
- [4] K. Hagiwara, N. Okamura and K.-i. Senda, Phys.Rev. **D76** (2007) 093002.
- [5] T. Kajita, H. Minakata, S. Nakayama and H. Nunokawa, Phys.Rev. **D75** (2007) 013006.
- [6] K. Hagiwara and N. Okamura, JHEP **0801** (2008) 022.
- [7] P. Huber, M. Mezzetto and T. Schwetz, JHEP **0803** (2008) 021.
- [8] K. Hagiwara and N. Okamura, JHEP **0907** (2009) 031.
- [9] F. Dufour, T. Kajita, E. Kearns and K. Okumura, Phys.Rev. **D81** (2010) 093001.
- [10] K. Hagiwara, N. Okamura and K. Senda, JHEP **1109** (2011) 082.
- [11] K. Hagiwara, T. Kiwanami, N. Okamura and K.-i. Senda, [arXiv:1209.2763](https://arxiv.org/abs/1209.2763) (2012).
- [12] F. Dufour, [arXiv:1211.3884](https://arxiv.org/abs/1211.3884) (2012).
- [13] A. Badertscher, T. Hasegawa, T. Kobayashi, A. Marchionni, A. Mereaglia *et al.*, [arXiv:0804.2111](https://arxiv.org/abs/0804.2111) (2008).
- [14] A.K. Ichikawa, private communication.
- [15] T. Barszczak, Ph.D. thesis, University of California, Irvine (2005).

Experimental status of neutrino scattering*

Sara Bolognesi[†]

IRFU, CEA Saclay, Gif-sur-Yvette, France

(Dated: March 23, 2016)

Abstract

After highlighting the importance of neutrino cross section modeling for neutrino oscillation measurements, the most recent neutrino cross section measurements are presented. New preliminary results are available from T2K for the measurement of charged current interactions on carbon without pions in the final state, single pion production in water, coherent pion production in carbon and charged current inclusive interactions in carbon as a function of neutrino energy. Few other results already published by the MINER ν A and T2K collaborations are also discussed.

NEUTRINO CROSS SECTION MEASUREMENTS

Precise knowledge of the neutrino interaction cross section is crucial for present and future long baseline neutrino oscillation experiments. The parameters describing neutrino oscillations are extracted by comparing the rate of neutrino interactions at near and far detectors placed on the neutrino beamline. The near detector is sensitive to the convolution of flux and neutrino cross section, this measurement is used to constrain the neutrino spectrum expected at the far detector in absence of oscillations. In T2K the uncertainty on this measurement is $\sim 8\%$ for ν and $\sim 11\%$ for $\bar{\nu}$, highly dominated by uncertainty on neutrino cross section. In future long baseline experiments like DUNE [1] and HyperKamiokande [2], such uncertainty has to be kept below 2% to avoid spoiling the sensitivity to CP-violation phase of the PMNS matrix of neutrino oscillation.

The extrapolation of the neutrino interaction rate from the near to the far detector is not straightforward for various reasons:

- neutrinos at near and far detectors have different neutrino energy distributions mainly because the neutrino spectrum, for a given neutrino flavor, is changed by the oscillation;
- the near detector mainly measures ν_μ and $\bar{\nu}_\mu$, which dominate the flux produced by the accelerator, while at the far detector also ν_e and $\bar{\nu}_e$, produced by oscillation, have to be measured;
- near and far detectors have different acceptance for the outgoing particles produced in neutrino interactions;
- near and far detectors may have different elemental composition and therefore neutrino may interact with different nuclear targets in the two detectors.

To perform the extrapolation from near to far detector, the neutrino cross section needs thus to be known as a function of neutrino energy, for different neutrino flavors and for anti-neutrinos, for different nuclear targets and the distribution of the kinematics of the outgoing particles has to be known (or, in other terms, exclusive cross sections computation are necessary).

On the other hand, the measurement of neutrino cross section is experimentally complicated since the neutrino energy is not known event by event. The neutrino energy can be inferred from the kinematics of the particles produced in the interaction but such approach

is limited by the detector precision: low energy particles can be reconstructed only above a given threshold, the angular acceptance may be limited, the recoiling nucleus is mostly undetected and neutrons are typically not detectable. As a consequence there are large model uncertainties which are introduced in the unfolding of detector effects to compute the signal efficiency and to estimate backgrounds. Best practices to address these issues include quoting cross section measurements only in limited phase space with large and constant detector efficiency, cross-checking results between different selections and analysis strategies and using control regions to constrain the backgrounds from data.

Finally, the produced neutrino energy spectrum and rate is known through the flux modeling, which is based on a detailed simulation of the beam-line and, possibly, constrained by external hadro-production measurements. The flux uncertainties are typically the largest systematics ($\sim 10\%$) on the cross section overall normalization. To avoid such large uncertainties, cross section ratios (between different nuclear targets, different neutrino species) can be measured.

In the following, the most recent cross section measurements, at the time of NuFact15 conference, are reviewed.

QUASI-ELASTIC-LIKE INTERACTIONS

The Charged Current Quasi-Elastic (CCQE) interaction is the dominant one in the T2K neutrino energy spectrum, peaked around 0.6 GeV. In the events selected at the far detector for oscillation measurements, the neutrino energy is computed from the angle and momentum of the outgoing lepton, assuming CCQE kinematics. Such energy reconstruction from the lepton kinematics relies on assumptions on the nuclear model in the initial state (and on the distribution of the outgoing nucleon in the final state if this is below threshold). Since the oscillation parameters are extracted from the neutrino energy spectrum thus reconstructed, it is crucial to have a very precise modeling of CCQE interactions to avoid biases on the measurement of oscillation parameters.

The Monte Carlo simulations of the CCQE process rely on parametrizations that are tuned to data. In particular, the axial mass in the dipole form factor of the interaction (M_A^{QE}) is tuned to old bubble-chamber data of neutrino interaction on deuterium. Additional nuclear effects in the nuclear targets, heavier than deuterium, used in modern experiments (typically carbon, water or argon) are implemented relying on a Relativistic Fermi Gas approximation to describe the nucleus (including corrections for Pauli blocking and binding energy). In 2010 MiniBooNE's measurement of CCQE cross section [3] has shown a large discrepancy with respect to this simplified model. New models have been developed [4–7] which include long-range correlation between nucleons (computed in Random Phase Approximation, RPA) and neutrino interactions with correlated nucleon-nucleon pairs (called 2p2h). Such models have shown to describe successfully the MiniBooNE results. A good agreement with MiniBooNE measurements can also be obtained by tuning effective nuclear parameters (eg: $M_A^{QE} \sim 1.2$ GeV) but at the expense of disagreement with bubble-chamber data [8] (which give an axial mass $M_A^{QE} \sim 1$ GeV).

The nuclear effects have to be taken into account not only in the initial state but also on

the final state (FSI). Neutrino interactions which produce a pion then absorbed in the nuclear medium by FSI cannot be distinguished experimentally from pure CCQE interactions. The interactions measured experimentally are therefore called Charged-Current Zero-Pions (CC0 π) and consist of: pure CCQE interactions on single nucleon, interactions through the 2p2h channel (which includes Δ pion-less decay) and single pion production from Δ resonance where the pion get absorbed by FSI effects (without affecting the muon kinematics). It should be noted that the separation between FSI and Δ pion-less decay is somehow arbitrary and can lead to double counting, a correct treatment (as in [9]) should consider the two contributions together in the computation of the cross section. The cited models including 2p2h are fully analytic and do not include FSI effects. On the other hand, long- and short-range correlations between nucleons have been recently included in Monte Carlo generator like NEUT [10], GENIE [11] and NuWro [12], which include FSI effects through intranuclear cascade models. Still these generators are tuned from data with effective parameters in order to get a satisfactory agreement with the neutrino interaction measurements today available.

A new CC0 π measurement on carbon with the off-axis T2K near detector (ND280) is available. The analysis has been designed to be solid against model-dependent assumptions. The selection requires events with only one reconstructed muon or a muon and a proton, special care has been taken to increase the efficiency to high angle and low momentum muons, the background prediction is tuned using control regions and the result is presented as flux-integrated double-differential cross section as a function of muon momentum and angle. A second analysis, based on different selection and cross section extraction method, has also been performed. The agreement between the results from the two analyses proves the robustness of the measurement against the effects due to signal and background modeling. The results are compared in Fig.1 to the predictions from Martini et al [4, 5] and Nieves et al [6, 7], with and without including multi-nucleons effects. Even if these models do not include FSI effects, the impact of CC1 π events with pion absorption is very small (few %) in the intermediate angular and momentum region shown in Fig.1. The results are also compared to Monte Carlo simulation including FSI effects but without nucleon-nucleon correlations. The data prefer the presence of 2p2h contribution with respect pure CCQE with RPA corrections but the precision is not good enough yet to distinguish between different models.

Measuring also the proton(s) angle and momentum may enhance the capability of distinguishing between different models. On the other hand exclusive measurements are more model dependent, as the MINER ν A analysis in [13] and the T2K on-axis INGRID analysis in [14]. To overcome such problem, it is interesting to look into variables as much as possible near to the actual experimental measurement, with minimal corrections for detector effects and acceptance. This is the case of the vertex energy distribution published by MINER ν A in [15, 16] and shown in Fig.2. Considering that MINER ν A detector is sensitive to proton but not to neutrons, the excess at high vertex energy in neutrino data but not in anti-neutrino data, is an indication for the presence of 2p2h events ($\nu_{\mu}np \rightarrow \mu^{-}pp$, while $\bar{\nu}_{\mu}np \rightarrow \mu^{+}nn$ are undetectable). Unfortunately this kind of variables can only be compared with Monte Carlo prediction fully embedded with detector simulation and the available models have today very poor predictive power for the kinematics of the outgoing proton.

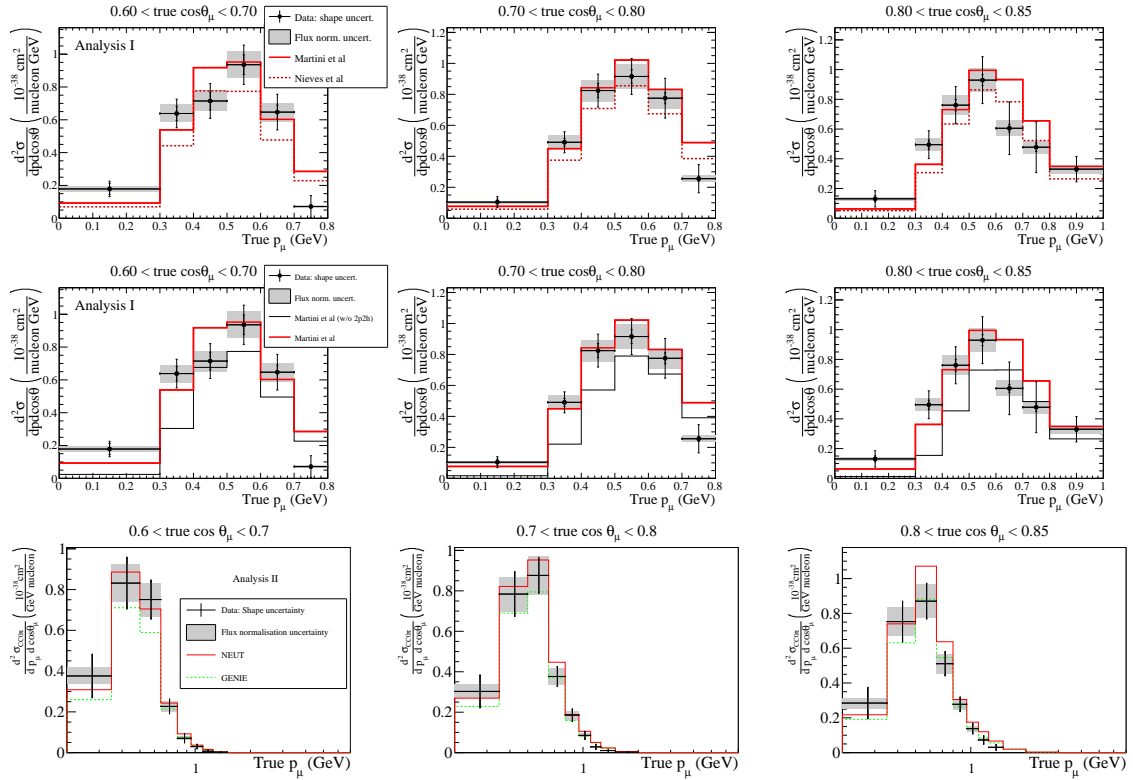


FIG. 1. Results of CC0 π measurement from T2K compared with the model of Martini et al and Nieves et al (top row) and with the model from Martini et al with and without 2p2h contribution (middle row). Results of the same measurement with an alternative analysis strategy (bottom row), compared to NEUT (v.5.1.4.2, $M_A^{QE} \sim 1.2$ GeV) and GENIE (v2.6.4, $M_A^{QE} \sim 1.2$ GeV) simulations without 2p2h.

The most informative and still model-independent measurement would be a cross section fully differential both in muon and proton angle and momentum, limited to the phase space of high proton and muon reconstruction efficiency.

PION PRODUCTION

The production of single pion in neutrino interaction is mainly due to Δ resonance production and decay. FSI may then modify the kinematics of the pion, absorb it, change its charge, and/or produce other pions. It is well known that MiniBooNE [17] and MINER ν A [18] results are in disagreement: beyond overall normalization issues, the differences between the two experiments in the shape of the differential cross section as a function of the outgoing pion energy cannot be described by any model (see, for instance, [19]). Since interaction cross section and FSI have different dependence on the number of nucleons, the two contributions can be disentangled by measuring CC1 π on different targets. T2K has new preliminary results for CC1 π^+ on water with ND280 data. The signal includes events with only one

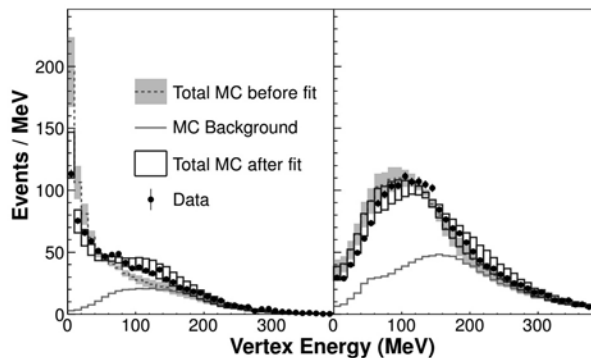


FIG. 2. Comparison between MINERνA data and simulation for the distribution of energy around the interaction vertex in CCQE events for neutrinos (left) and anti-neutrinos (right).

pion and with positive charge. The target detector is composed of passive layers of water alternating with two active layers of scintillator (CH). In order to be reconstructed, the outgoing pion in water interactions must reach the first downstream active layer, therefore the acceptance is limited to relatively high pion momentum (> 200 MeV). In the first carbon active layer both carbon and water interactions are reconstructed while the interactions reconstructed in the second layer are mainly due to carbon. Interactions on the second carbon layer are used to constraint the contribution of CC1 π on carbon on the first layer and thus extract the cross section due to water interactions only. A control sample is used to constrain the background with multiple pions. The results are shown in Fig.3: GENIE tends to overestimate the overall rate while NEUT is in good agreement with the data; given the present uncertainties, the shape is well reproduced by both generators, even if a hint of suppression is visible for very forward pions. This region is dominated by interactions where the neutrino scatters coherently from an entire nucleus, leaving the nucleus unchanged in its ground state. These interactions are characterized by very small momentum transferred to the nucleus $|t| = \sqrt{(q - p_\pi)^2}$ and no hadronic activity (no nucleons is ejected). Such channel has been investigated recently by ArgoNeuT, MINERνA and T2K. The reconstructed $|t|$ and the deposited energy around the vertex are used to select coherent interactions in data. Sidebands in both $|t|$ and vertex energy distributions are used to tune the background. It is indeed difficult to have a precise simulation of the background in the selected phase-space because the vertex energy depends on the details of the detector response to very low energy deposits (near detector threshold and below) and the model of non-coherent CC1 π , especially for the selected kinematics, is not yet precisely constrained. Previous results from MINERνA showed a suppression with respect to the Rein-Sehgal model [20] at low pion energy and large pion angle, while ArgoNeuT statistics is not sufficient for a differential measurement but provide the first integrated measurement on argon [21]. At low neutrino energy, where only upper limits (from K2K [22] and SciBooNE [23]) were available, T2K has a new preliminary result (Fig.3): the coherent signal is observed with 2.2σ significance and the results are in good agreement with a new microscopic model from Alvarez-Ruso [24], better suited for low energy.

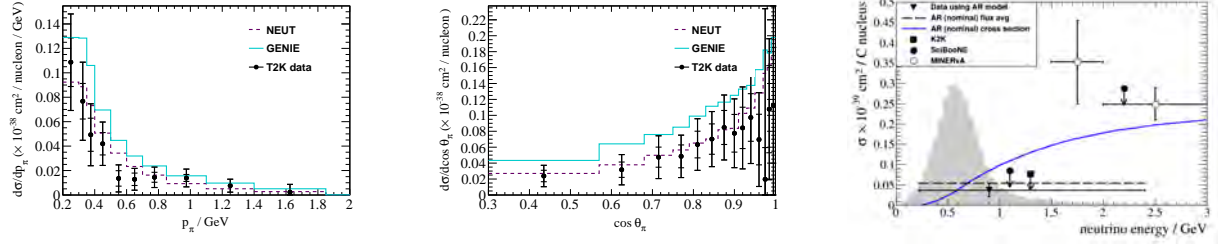


FIG. 3. T2K preliminary measurement of $CC1\pi^+$ cross section as a function of pion momentum (left) and angle (middle), compared to NEUT and GENIE simulation. T2K measurement of coherent pion production (right) compared with expectation from Alvarez-Ruso model.

DEPENDENCE OF THE CROSS SECTION ON NEUTRINO ENERGY, NUCLEAR TARGET AND NEUTRINO FLAVOR

As previously discussed, in the oscillation analysis to extrapolate the near detector constraints to the far detector, the energy dependence of the neutrino interaction cross section has to be known. Typically, the neutrino energy can only be reconstructed from the kinematics of the outgoing particles relying on model-dependent assumptions which introduce large theory systematics. T2K has presented the first measurement [25] which do not rely on such assumptions for the reconstruction of the neutrino energy. The idea is based on the geometry of the on-axis near detector: the INGRID detector is cross-shaped with the beam impinging in the center. Different modules are placed at different off-axis angles and therefore see different neutrino energy spectra, as shown in Fig. 4. The dependence on neutrino energy can then be extracted by combining the neutrino interaction rate measured in different modules (the NuPRISM detector proposal [26] is based on the same concept). In this approach the uncertainties in the flux modeling become the dominant systematics. Results are shown in Fig.4: data suggest a suppression of the cross section at high energy.

If the near and the far detector have different elemental composition (as in T2K), it is crucial to know the cross section dependence on the nuclear target. Comparing the cross section for different nuclear targets is also useful to isolate and measure nuclear effects. The ratio between cross sections on different targets has the advantage of canceling the flux uncertainties as well as most of the systematics related with model-dependent assumptions on the signal efficiency and background estimation. To maximize such cancellation, it is crucial to impose the same phase space for the particles outgoing from interactions on both the nuclear targets. This has been done in the T2K measurement of the CC-inclusive, per nucleon, cross section ratio between iron and carbon in INGRID [27]:

$$\frac{\sigma_{CC}^{Fe}}{\sigma_{CC}^{CH}} = 1.047 \pm 0.007(stat.) \pm 0.035(syst.), \quad (1)$$

where the acceptance of outgoing muons for events both on carbon and on iron, has been limited with kinematics cut only in the region accessible for carbon (small muon

angle). The total cross-sections are then corrected to the full phase space but the theory systematics due to this correction mostly cancel out in the ratio.

An interesting measurement of ratio between targets has been presented by MINER ν A in the region dominated by Deep Inelastic Scattering (DIS) [28]. A recent update, after background subtraction and correction for detector effects, of lead over carbon cross section ratio as a function of Bjorken x , shown in Fig.4, suggests slightly larger nuclear screening effects for low x than what is in the GENIE simulation. In these measurements on different nuclear targets, as for the CC1 π measurement in water by T2K previously discussed, the interactions may happen on carbon in the scintillator region or in relatively thin layers of passive material, made of different nuclear targets, surrounded by scintillator. In order to reconstruct the interaction, the outgoing particles must exit from the passive layer and reach the downstream scintillator module. Extrapolating two or more tracks to their common starting point, the event vertex may be assigned to the passive layers but the procedure is limited by the tracking precision. There is also the possibility that backward going particles leak into the scintillator region upstream of the passive layer which may confuse the vertex reconstruction algorithm. As a consequence, there could be migration of events: interactions which have the real vertex in the passive layer may be reconstructed as scintillator interactions and viceversa. This is the main systematics common to the available measurements on nuclear targets which are not active detectors. Since the modeling of backward nucleons is not well known theoretically, the control of this event migration must be done from data using control regions of interactions in the scintillator.

Finally for future long baseline experiments, which will dispose at the far detector of large statistic samples of ν_e appearance, is particularly important to measure the cross section for electron neutrino. At the near detector the flux of ν_e is very small with respect to ν_μ ($\Phi_{\nu_e}/\Phi_{\nu_\mu} < 1\%$), so this measurements are mainly limited by statistics. T2K has measured the CC-inclusive cross section on carbon as a function of the electron momentum and angle [29], as shown in Fig. 5. T2K has also measured the ratio between data and NEUT simulation of the total rate of electron neutrino CC-inclusive interactions in water [30]:

$$R_{on-water} = 0.87 \pm 0.33(stat.) \pm 0.21(syst.). \quad (2)$$

CONCLUSION

For long baseline neutrino oscillation measurements it is crucial to know the neutrino-nucleus interaction cross section with high precision in order to perform an unbiased extrapolation of the near detector constraints to the far detector. Considering the accuracy expected at future experiments (DUNE, Hyper-Kamiokande), the present uncertainty on the neutrino cross sections would be the limiting systematics.

For future neutrino cross section measurements, in view of the poor knowledge of the nuclear effects involved in the neutrino-nucleus interactions, it is particular important to design analyses as much as possible solid against model-dependent assumptions. The cross section measurements are always affected by initial and final state interactions which are difficult to disentangle. In order to reach a detailed understanding of the different effects, it

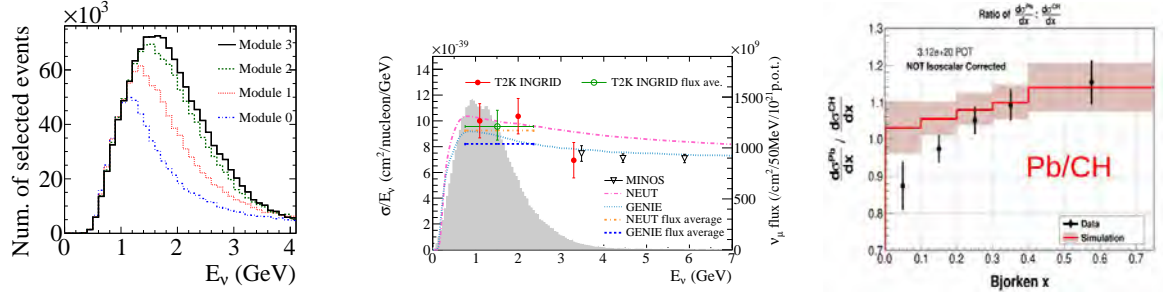


FIG. 4. Neutrino energy spectrum for events selected on different INGRID modules (left). CC-inclusive cross section measurement as a function of neutrino energy in INGRID (right). Ratio between lead and carbon DIS cross section as a function of Bjorken x measured by MINER ν A, compared to GENIE simulation (right).

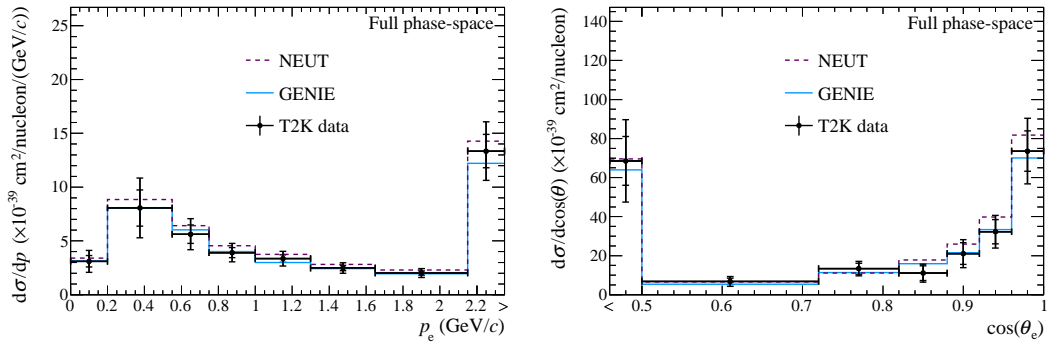


FIG. 5. Measurement of CC-inclusive electron neutrino cross section on carbon at T2K as a function of electron momentum (left) and angle (right).

is crucial to compare measurements from different interaction processes, at different neutrino energies, on different nuclear targets and for different neutrino species. On the experimental point of view, it is important to compare results from various experiments which are limited by different systematics and to cross-check results from different neutrino fluxes, the flux uncertainty being the dominant systematics on the cross section normalization.

Due to the complexity of the problem and in view of the importance for future long baseline experiments, it is fundamental to maintain a long term effort for neutrino interactions measurements based on a strict collaboration between different experiments and with the theory community.

* Presented at NuFact15, 10-15 Aug 2015, Rio de Janeiro, Brazil [C15-08-10.2]

† sara.bolognesi@cea.fr; Speaker

- [1] C. Adams *et al.* (LBNE) (2013) arXiv:1307.7335 [hep-ex].
- [2] K. Abe *et al.*, (2011), arXiv:1109.3262 [hep-ex].
- [3] A. A. Aguilar-Arevalo *et al.* (MiniBooNE), Phys. Rev. **D81**, 092005 (2010), arXiv:1002.2680 [hep-ex].
- [4] M. Martini, M. Ericson, G. Chanfray, and J. Marteau, Phys. Rev. C **80**, 065501 (2009).
- [5] M. Martini, M. Ericson, G. Chanfray, and J. Marteau, Phys. Rev. C **81**, 045502 (2010).
- [6] J. Nieves, I. R. Simo, and M. V. Vacas, Phys. Lett. B **707**, 72 (2012).
- [7] J. Nieves, F. Sanchez, I. Ruiz Simo, and M. Vicente Vacas, Phys.Rev. **D85**, 113008 (2012), arXiv:1204.5404 [hep-ph].
- [8] V. Bernard, L. Elouadrhiri, and U.-G. Meissner, J. Phys. **G28**, R1 (2002), arXiv:hep-ph/0107088 [hep-ph].
- [9] A. M. Ankowski, O. Benhar, and M. Sakuda, Phys. Rev. **D91**, 033005 (2015), arXiv:1404.5687 [nucl-th].
- [10] Y. Hayato, Nucl. Phys. Proc. Suppl. **112**, 171 (2002).
- [11] C. Andreopoulos *et al.*, Nucl. Instrum. Meth. **A614**, 87 (2010), arXiv:0905.2517 [hep-ph].
- [12] C. Juszczak, Acta Phys.Polon. **B40**, 2507 (2009), arXiv:0909.1492 [hep-ex].
- [13] T. Walton *et al.* (MINERvA), Phys. Rev. **D91**, 071301 (2015), arXiv:1409.4497 [hep-ex].
- [14] K. Abe *et al.* (T2K), Phys. Rev. **D91**, 112002 (2015), arXiv:1503.07452 [hep-ex].
- [15] G. A. Fiorentini *et al.* (MINERvA), Phys. Rev. Lett. **111**, 022502 (2013), arXiv:1305.2243 [hep-ex].
- [16] L. Fields *et al.* (MINERvA), Phys. Rev. Lett. **111**, 022501 (2013), arXiv:1305.2234 [hep-ex].
- [17] A. A. Aguilar-Arevalo *et al.* (MiniBooNE), Phys. Rev. **D83**, 052007 (2011), arXiv:1011.3572 [hep-ex].
- [18] B. Eberly *et al.* (MINERvA), Phys. Rev. **D92**, 092008 (2015), arXiv:1406.6415 [hep-ex].
- [19] J. T. Sobczyk and J. Zmuda, Phys. Rev. **C91**, 045501 (2015), arXiv:1410.7788 [nucl-th].
- [20] D. Rein and L. Sehgal, Nucl. Phys. **B223** (1983).
- [21] R. Acciarri *et al.* (ArgoNeuT), Phys.Rev.Lett. **113**, 261801 (2014), arXiv:1408.0598 [hep-ex].
- [22] M. Hasegawa *et al.* (K2K), Phys. Rev. Lett. **95**, 252301 (2005), arXiv:hep-ex/0506008 [hep-ex].
- [23] K. Hiraide *et al.* (SciBooNE), Phys. Rev. **D78**, 112004 (2008), arXiv:0811.0369 [hep-ex].
- [24] L. Alvarez-Ruso, L. S. Geng, S. Hirenzaki, and M. J. Vicente Vacas, Phys. Rev. **C75**, 055501 (2007), [Erratum: Phys. Rev.C80,019906(2009)], arXiv:nucl-th/0701098 [nucl-th].
- [25] K. Abe *et al.* (T2K), (2015), arXiv:1509.06940 [hep-ex].
- [26] S. Bhadra *et al.* (nuPRISM), (2014), arXiv:1412.3086 [physics.ins-det].
- [27] K. Abe *et al.* (T2K), Phys. Rev. **D90**, 052010 (2014), arXiv:1407.4256 [hep-ex].
- [28] B. G. Tice *et al.* (MINERvA), Phys. Rev. Lett. **112**, 231801 (2014), arXiv:1403.2103 [hep-ex].
- [29] K. Abe *et al.* (T2K), Phys. Rev. Lett. **113**, 241803 (2014), arXiv:1407.7389 [hep-ex].
- [30] K. Abe *et al.* (T2K), Phys. Rev. **D91**, 112010 (2015), arXiv:1503.08815 [hep-ex].

The ANDES Underground Laboratory*

Claudio O. Dib[†]

*CCTVal and Department of Physics,
Universidad Técnica Federico Santa María, Valparaíso, Chile*

Xavier Bertou[‡]

Centro Atómico Bariloche - Instituto Balseiro, CNEA/CONICET, Argentina

Oswaldo Civitarese[§]

*Department of Physics, University of La Plata,
c.c. 67 (1900), La Plata, Argentina*

Juan Carlos D'Olivo[¶]

Universidad Nacional Autónoma de México, Mexico D.F., Mexico

João C. dos Anjos^{**}

*Centro Brasileiro de Pesquisas Físicas,
Rio de Janeiro, RJ, 22290-180, Brazil*

(Dated: November 17, 2015)

Abstract

ANDES (Agua Negra Deep Experiment Site) is a proposed underground laboratory to be built inside the Agua Negra road tunnel under the Andes Mountains at the border between Argentina and Chile. It will be the 3rd deepest underground lab in the world and the first in the Southern Hemisphere. ANDES is expected to host experiments from world level collaborations in Particle and Astroparticle Physics, Seismology, Geology, Geophysics and Biology. Here we present the general features of the laboratory, the expected science program and the current status of the proposal.

INTRODUCTION

ANDES (Agua Negra Deep Underground Site) is a proposed underground laboratory to be built inside the Agua Negra road tunnel (<http://andeslab.org>). The proposal takes advantage of the planned construction of this road tunnel which will join Argentina and Chile across the Andes mountains between the San Juan Province (Argentina) and the Coquimbo Region (Chile). As of today, ANDES will be the first underground laboratory of this kind in the Southern Hemisphere.

ANDES is proposed to be located at the deepest point in the tunnel, 1750 m vertical below the surface, becoming the third deepest underground lab in the world and providing an attenuation of 10^{-7} for the atmospheric muon flux. This level of shielding will provide the sensitivity required for unique experiments in Physics such as Dark matter searches and Neutrino physics, and other sciences as Geophysics, Seismology, Biology, environmental studies, cosmic radiation impact on instrumentation and more.

The lab is planned to host experiments from collaborations worldwide. The selection of experiments will be based on their scientific value and their relevance to the member nations, and shall fulfill aspects of safety and environmental impact. In addition to the underground site, there will be two Support Laboratories on the surface, one near the city of La Serena (Chile) and the other in the town of Rodeo (Argentina).

The laboratory will be managed by a Latin American consortium, CLES (Consortio Latinoamericano de Estudios Subterráneos), an entity formed among the participating countries. The current participants leading this proposal are Argentina, Brazil, Chile and Mexico. It is expected that further nations will join in. The following sections describe the Agua Negra Tunnel, the Lab conceptual design, preliminaries for the organization, and a summary.

THE AGUA NEGRA TUNNEL

The Agua Negra tunnel across the Andes mountains is part of the new international road that will connect the Province of San Juan, Argentina with the Region of Coquimbo, Chile, at latitude 30.19° S and longitude 69.82° W, providing a year-long access between the countries. The current pass, at 4780 m a.s.l., is closed most of the year due to poor weather conditions. It will be a system of two parallel tunnels 14 km long with two lanes each, running nearly 100 m apart and connected every 500 m with galleries for pedestrians

and every 1500 m for emergency vehicles. The Chilean entrance will be at an altitude of 3600 m a.s.l. and the Argentinian entrance at 4080 m a.s.l., thus providing a 3% slope for natural ventilation and drainage. The total power consumption for the tunnel, including emergency ventilation, is estimated to be near 15 MW.

THE LABORATORY

If the rock conditions are adequate, the underground laboratory will be located at about 4 km from the Chilean entrance, on the south side of the eastbound tunnel, where the mountain is higher, providing a vertical coverage near 1750 m of rock and an omnidirectional shield not less than 1670 m (Fig. 1). The exact location will depend mainly on the geomechanical condition of the rock that assures stability, and then on the depth of the site. A 1750 m of vertical rock overburden, 4500 m water equivalent, will place ANDES as the third deepest lab in the world, after Jin Ping, China (2400 m) [1] and SNOLAB, Canada (2070 m) [2]. See Fig. 2.

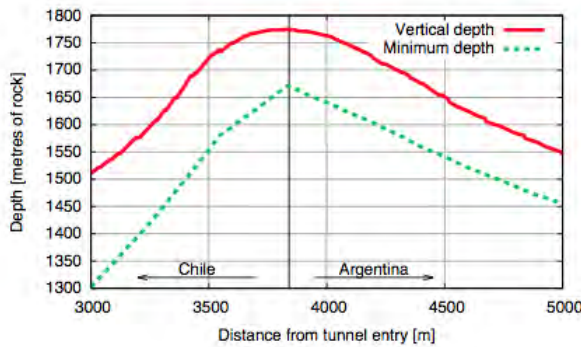


FIG. 1: Vertical and omnidirectional coverage of the rock vs. lab location in meters from the Chilean entrance.

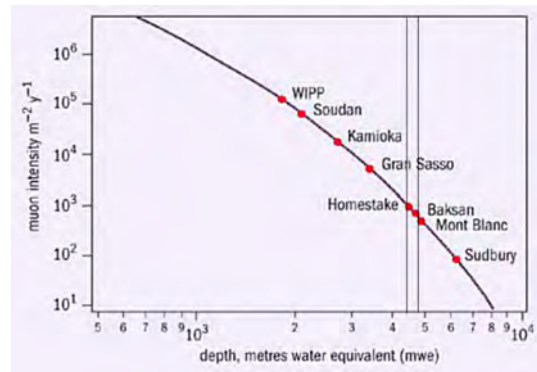


FIG. 2: Muon flux crossing a horizontal section vs. depth, expected at ANDES (vertical band). Muon flux at sea level is near 100 [$1/m^2s$].

To date there are no rock samples at the expected depth, but 9 samples from 8 perforations done at 600 m deep were analyzed, showing basalt, andesite and rhyolites, with activities that range within 2 - 15 [Bq/kg] for U-238, 0.9 - 5.7 [Bq/kg] for Th-232, and 45 - 60 [Bq/kg] for K-40. These figures can be compared to 4.5 - 30 [Bq/kg] for U-238, 8.5 - 76 [Bq/kg] for Th-232 and 4.5 - 30 [Bq/kg] for K-40 at the Canfranc Laboratory, Spain.

To date, all deep underground laboratories are in the Northern Hemisphere. ANDES would be the first of its kind in the Southern Hemisphere. A southern location will be valuable for several reasons[3], e.g. Dark Matter search at a southern site may help eliminate possible season-induced backgrounds on the observed yearly modulations in experiments in the north [4, 5]. An additional site in the south will also be valuable to test whether neutrinos from an eventual supernova oscillate as they travel through the inside of the earth.

Other special features of the ANDES site are the low neutrino background from nuclear reactors and its location on the earth's crust near the subduction of the Pacific and Continental tectonic plates, issues that could be relevant for geoneutrino studies. The nearest nuclear reactors are in Argentina: one 2.1 GWth reactor in Embalse, 560 km away, and two other reactors, Atucha I of 1.2 GWth and Atucha II of 2.1 GWth, 1080 km away. The next nearest reactors are in Angra dos Reis, Brazil, about 2660 km away.

Science at ANDES

ANDES is expected to host experiments at the frontier in the fields of astro and particle physics in the next decades. It should also host experiments in other sciences, such as Geology, Geophysics and Biology. The southern Andes mountain range is one of the most active seismic regions in the world, and an underground facility like ANDES will provide a valuable site for seismological studies and monitoring. As a low-background facility it should also provide services for high sensitivity measurements in environmental studies and for development in state-of-the art instrumentation and electronics. The preliminary scientific program at ANDES then considers:

Neutrino Physics: these experiments are flagship in many underground laboratories. At ANDES there is a proposal to install a 3 kton liquid scintillator neutrino detector, for studies of geoneutrinos and neutrinos from supernovae, among other sources [6]. This major size detector would be located inside the large pit. In addition, there are proposals for installing neutrinoless double beta nuclear decay experiments, most of which of considerably smaller size, to be located in some of the other caverns.

Dark Matter Searches: the particles that compose the dark matter in the universe is one of the most outstanding questions in Cosmology and Astroparticle Physics. Many experimental techniques exist so far and further techniques are being proposed. Different techniques are sensitive to different ranges of masses of the hypothetical dark matter particles, so this diversity in techniques is still necessary. Some experiments have claimed to see signals that modulate with a year period, possibly due to the variation of the dark matter wind as the earth goes around the sun [4, 5]. To rule out possible backgrounds from seasonal effects, similar detections could be done in a southern site such as ANDES. New Dark Matter detection techniques should also find space at ANDES, as they are expected to fit in the proposed caverns.

Nuclear Astrophysics: the low radiation environment of the ANDES site also allows studies of low energy nuclear physics [7]. These experiments require low energy accelerators in low background environments to study ion collisions of the type that occur in stars.

Geophysics/Geology/Seismology: the Andes mountain range is an active tectonic site in the planet, with plenty of seismic activity. This constitutes a challenge for the design of the experimental equipment. On the other hand it is an opportunity to do underground research and monitoring of the seismic activity. ANDES should at least be part of a seismograph network within Chile and Argentina. Moreover, taking advantage of the high sensitivity instrumentation at ANDES, several studies of correlation between seismic activity or rock burst and other signals such as radon release can be performed.

Biology: underground sites provide special environments for studies of biological systems in extreme media, in low radiation conditions and the like. ANDES expects to host experiments in these sciences as well.

Low radiation measurements: low background instrumentation in underground sites have been finding new applications and services for the industry and for measurements of traces of indicators and contaminants applied to environmental studies. ANDES will be a unique site in South America for these new types of measurements.

The underground caverns

Here we describe the caverns in its current status, according to the New Conceptual Design done by Lombardi S.A.[8]. This new design considers longer access tunnels from previous designs to improve rock stability. It includes four full size alternatives depending on the quality of the rock found on site, and two reduced size options as well. The preferred option is the deepest point, located at the frontier between the countries, on the south side of the eastbound Agua Negra tunnel, near km 4 from the Chilean entrance. See Fig. 3.

The access to and exit from the lab will be through detention bays in the tunnel, including traffic lights for flow control. The main access gallery be about 100 long, 3.5 m wide by 4.5 m high, able to fit up to 40 ft container trucks. In the central transit area the gallery will have two lanes for vehicles to cross or park. The emergency room/cafeteria will be located in this sector. There will also be a 470 m long, 3 m wide and 3.5 m high, emergency gallery for light vehicles connecting to the opposite tunnel.

A main gate will be kept closed to limit access to the complex, and further along a second barrier will be closed when the main gate is open.

The laboratory spaces (technical room, secondary cavern and pit, main cavern and main pit, in that order) will be located along a gallery 200 m long, 3.5 x 4.5 m cross section, with enough space for all cables, supply and ventilation ducts required for the lab. For the purpose of rock stability, the minimal spacing between the caverns is estimated to be 40-60 m. The bottom of the main pit will be accessed through another gallery, 250 m long 3.5 m wide, 4.0 m high, with a 12% slope. We now describe the caverns according to Fig. 3.

Service rooms

In the new conceptual design the services are separated in different rooms, for practical purposes. The following rooms are located outside the experimental area:

- The ventilation and air filtering room will be located by the access gallery, connecting to the ventilation gallery; the ventilation equipment should be able to renew the full volume of the lab air every hour and to filter the existing radon in the air. A slight overpressure inside the lab area should be maintained. Air conditioning should keep the lab at 21°C even at the 2 MW peak consumption, and should also control the relative humidity to guarantee operation of the equipment and human hygrothermal comfort.

conditioning and the other half will be available to the experiments. This cavern will include an equipped workshop. It will also include fire control systems, monitoring and safety systems tightly integrated to the Agua Negra tunnel safety system.

- A clean room with controlled environment parameters for experimental work will be located in the central part of the experimental area.

The Secondary Cavern

The originally proposed three secondary caverns are merged into a single excavation 14 m long, 16 m wide, 14 m high, which may be subdivided by concrete walls if several independent spaces are necessary. This area will host smaller size experiments, offices, laboratories, and services for the lab personnel and visitors.

The Secondary Pit

Located at the end of the secondary cavern. It is 9 m diameter by 15 m total depth, dedicated to ultra low background measurements. It is accessed by a central corridor at 10 m above the bottom. It will have a suitable vessel for low radiation measurements, properly supported to prevent flotation in the case the pit is flooded with water for further shielding. A sealed system for power lines, data, and monitoring should reach the interior of the vessel.

The Main Cavern

It shall be 50 m long, 21 m wide and 23 m high, with oval profile for structural stability. A 40 ton bridge crane on the ceiling will slide longitudinally on rails, reaching the loading area. The total use of space is achieved by making the main beams of the bridge crane having the curvature of the roof of the cavern. Lateral displacement of the load should be done by a zipper mechanism. The area for experimental equipment shall be rectangular 35 m by 19 m. The equipment area shall have a drainage system that channels fluid leaks into lateral gutters, and a pumping system according to the drain thereof. Collected fluid should be directed to the service cavern. Conveniently distributed panels for power supply, low power lines, communication networks, compressed air, water and services shall be included.

The Main Pit

It will be 30 m in diameter and 38 m deep (instead of the 42 m originally proposed). Located at the end of the lab gallery, accessed at a point 30 m above the bottom. An additional access with a 12% slope will reach the bottom. The pit will host a single large size neutrino experiment of high sensitivity. As a shield from ambient radiation, the pit could be filled with water to a height of 30 m from the bottom, after the experiment is installed. A pump system for the filling and emptying of the well is therefore required. The

pump system may also connect to the fire safety network, so that the pit can be used as an additional water reservoir for fire fighting. A 20 ton bridge crane should be installed in the ceiling in order to move equipment inside the pit.

Support Laboratories

In addition to the underground site, ANDES, as most underground laboratories, requires infrastructure at surface level as well in order to provide all the services related to administration, reception of equipment, preparation of experiments, office and meeting space, data processing and connectivity, and outreach to the public.

Since the underground site lies at high altitude (near 3800 m a.s.l.) in a relative isolated place, two support labs are proposed. The current proposed sites are one in La Serena, a city of 230,000 inhabitants and port at the Pacific coast in Chile, 200 km from the tunnel, and one in Rodeo, a town of 2,400 inhabitants in Argentina, 90 km from the tunnel. La Serena is a city with universities and a technical infrastructure that supports major astronomy observatories in the region, so that this support laboratory is envisioned as hosting most of the administrative and long term equipment construction and assembly. The support laboratory at Rodeo, which is closer to the tunnel, should be used for more frequent installation and operations of the experiments.

An important activity of the support laboratories should be the outreach to the public. The support laboratories should consider 100 to 200 m² for office space, 200 to 400 m² for equipment and laboratory space, and 100 to 200 m² for an adequate visitor center.

ORGANIZATION

Since ANDES will be the first international laboratory of its kind in Latin America, groundbreaking steps at the highest political levels of the participating nations will be required. Notwithstanding the foreseen efforts, the proposal has received widespread support.

The current proposal is that ANDES will be managed by an international institution called *Consortio Latinoamericano de Estudios Subterráneos* or CLES (Latinamerican Consortium for Underground Studies). The organization of CLES is still under discussion, but it should: (i) conduct, through the concurrence of the interested parts, the administrative organization of ANDES and its integration to the scientific communities of the region; (ii) define and coordinate the areas of scientific interest; (iii) coordinate the division of the different sciences; (iv) form the external scientific advisory boards, and the internal committees that oversee the operation of the experiments; (v) establish the rules and protocols for the selection and setup of the experimental proposals; (vi) coordinate the academic integration with other institutions, including the participation of researchers and students; (vii) identify the regular sources of financing for ANDES, establish the financing mechanisms, define the budgets and the rules for support and overheads of the experiments; (viii) organise scientific events, such as conferences and workshops; (ix) promote the outreach of the laboratory activities; (x) establish the long term plans for the ANDES laboratory, including expansion

and upgrades.

The ANDES initiative can be thought of as the experimental branch of a broader scientific organization, aimed at strengthening the links between the laboratory and academic communities in Latin America. CLES can be envisioned as an institution analogous to CERN in Europe, in its role as coordinator of scientific endeavours. As such, the existence of CLES should enable not only the definition of the management and organizational structures for ANDES, but also as an instrument for the creation of the appropriate environment for regional integration in science and culture.

The participating nations in the initial proposal at the scientific level are Argentina, Brazil, Chile and Mexico. Further Latin American countries are expected to join. In particular, Colombia has already expressed interest in being part of the ANDES proposal.

SUMMARY

ANDES (Agua Negra Deep Experiment Site) is a proposed underground laboratory to be built inside the Agua Negra tunnel, the latter a tunnel which is part of an international road that will connect Argentina and Chile, between the province of San Juan (Argentina) and the region of Coquimbo (Chile). The laboratory will be set at the deepest point, 1750 m vertical under the rock, at an altitude of approximately 3,800 m a.s.l. It will include a large cylindrical pit 38 m deep and 30 m diameter to host a large neutrino experiment, a main cavern 50 m long, 21 m wide and 23 m high for other large experiments, a secondary cavern of smaller size, an ultra low background pit, and several smaller service caverns, including an emergency room. Due to its location, it will be third deepest underground lab in the world and the first to be built in the Southern Hemisphere.

The scientific programme of the laboratory should include experiments in particle and astroparticle physics, in particular Neutrino and Dark Matter experiments, and other experiments in Nuclear Physics, Biology, Geophysics, Geology and Seismology. It should also provide services of ultra low background measurements and applications to instrumentation development and industry.

The underground site will be accompanied by two support laboratories at surface level at the most convenient places. One of them could be set in the city of La Serena, Chile and the other in the town of Rodeo, Argentina.

The laboratory will be managed by an international Consortium formed by scientists and representatives of the participating Latinamerican nations, called CLES (Consortio Latinoamericano de Estudios Subterranos). This consortium, besides managing the ANDES laboratory, should constitute a seed for further integration of the sciences and culture in the continent.

The speaker thanks the organizers for the hospitality and support, and acknowledges partial support from Fondecyt, Chile, grant 1130617.

* Presented at NuFact15, 10-15 Aug 2015, Rio de Janeiro, Brazil [C15-08-10.2]

† claudio.dib@usm.cl; Speaker

‡ bertou@gmail.com; General coordinator

§ osvaldo.civitarese@fisica.unlp.edu.ar

¶ dolivo@nucleares.unam.mx

** janjos@on.br

- [1] Y.-C. Wu et al., Chin. Phys. **C37**, 086001 (2013), 1305.0899.
- [2] N. J. T. Smith, Eur. Phys. J. Plus **127**, 108 (2012).
- [3] T. Kajita, private communication.
- [4] R. Bernabei et al., in *Proceedings, 15th Workshop on What Comes Beyond the Standard Models?* (2013), pp. 1–9, [1(2012)], 1301.6243.
- [5] C. E. Aalseth et al. (CoGeNT) (2014), 1401.3295.
- [6] P. A. N. Machado, T. Muhlbeier, H. Nunokawa, and R. Zukanovich Funchal, Phys. Rev. **D86**, 125001 (2012), 1207.5454.
- [7] A. Formicola, G. Imbriani, M. Junker, D. Bemmerer, R. Bonetti, C. Brogini, C. Casella, P. Corvisiero, H. Costantini, G. Gervino, et al., Nucl. Instr. Meth. **507**, 609 (2003).
- [8] Lombardi, S.A., www.lombardi.ch.

Neutrino Event Generators*

Hugh Gallagher[†]

Tufts University, Medford, MA, USA, 02155

(Dated: March 24, 2016)

Abstract

For the world-wide neutrino community, neutrino event generators provide one of the key interfaces between theory and experiment. In this note I will describe improvements to four generators that simulate neutrino interactions in the few-GeV regime: GENIE, GiBUU, NEUT, and NuWRO. I will conclude with some thoughts on how research in this area has evolved over the past decade, and what some of the outstanding challenges are.

I. INTRODUCTION

This paper will have two objectives. The first is to describe briefly recent developments in the four main neutrino event generators that are in use around the world: NEUT, GiBUU, NuWRO, and GENIE. At the same time, I will use a somewhat wider lens, and examine how this tool has evolved over the past decade, and where it might be headed. This will highlight, I believe, recent successes as well as some significant challenges.

For experimentalists, generators need no introduction. They play a number of roles in the analysis of data and the production of our scientific results. If one is performing a cross section analysis, the goal is to produce a result that is as model (i.e. generator)-independent as possible, often achieved by making data-based corrections. Nonetheless generators, combined with full detector simulations, are used for background estimation, acceptance corrections, and connecting true to observed quantities (typically encoded in an unfolding matrix). These necessarily introduce systematic errors associated with the generators and the models they contain.

For oscillation experiments, the role played by generators is less obvious, since these measurements typically involve near/far comparisons. In this case, generators are often tuned to near detector data, and residual uncertainties on model parameters then impact the precision of oscillation results. In this context, of primary concern to the experiment is the question of how wrong the model could potentially be.

I would point out that while generators are indeed used in other branches of physics, in particular electron scattering and collider physics, neutrino generators are unique in a number of ways. They lack of a simple factorization of hard and soft processes that allows simplifications in collider simulations, and many of the quantities that we are attempting

**Presented at NuFact15, 10-15 Aug 2015, Rio de Janeiro, Brazil [C15-08-10.2]*

[†]Hugh.Gallagher@tufts.edu; Supported by U. S. Department of Energy grant DE-SC-0007866. The author would like to thank C. Andreopoulos, T. Golan, Y. Hayato, U. Mosel, and J. Sobczyk for their thoughts and contributions.

to calculate are, from a theoretical perspective, extremely complicated, requiring relativistic nuclear many-body theory for an accurate *ab initio* treatment.

A. The Components

If we view an Event Generator as a piece of software, than its inputs are a neutrino (of specified flavor and energy) and a nucleus, and the output is a set of outgoing particle four vectors. These codes typically attempt to (imprecisely) factorize the task:

1. The initial nuclear model which describes the energy-momentum distributions of nucleons in the target nucleus.
2. Models for the fundamental nucleon-level scattering processes.
3. For inclusive interactions, the generator runs an appropriate hadronization algorithm, many of which are tuned to free nucleon data.
4. The effect of the nuclear medium on final state hadrons is computed.

In all cases, one has a range of options for the modeling, often going from the very simple (Relativistic Global Fermi Gas), to the extremely complicated, and one of the practical challenges in developing this software is balancing the computational requirements against the desire for detailed microscopic calculations. This factorization relies on the applicability of the Impulse Approximation - a valid approach for scattering at GeV energies, however relying entirely on this assumption is incorrect, as it neglects the important role played by 2p-2h scattering processes. Generators are benchmarked against a wide range of data, including electron scattering, neutrino scattering - from the bubble chamber era as well as experiments from the past decade - and hadron probes.

II. RECENT PROGRESS

In this section we will review recent improvements in four of the most widely used generators in the few-GeV regime: GENIE, GiBUU, NEUT, and NuWRO.

A. NuWRO

NuWRO was the first neutrino event generator to be developed by a theory group (Wroclaw University)[1]. Careful attention is paid to making smooth transitions between models, for instance in the treatment of the transition region between resonance production and

DIS, or in the transition between low mass hadronization and PYTHIA. The final models are benchmarked against data, and good agreement is shown [1, 2]. The NuWRO collaboration has investigated the difficult and important problem of hadronization in nuclei, an area where generators apply very different approaches [3].

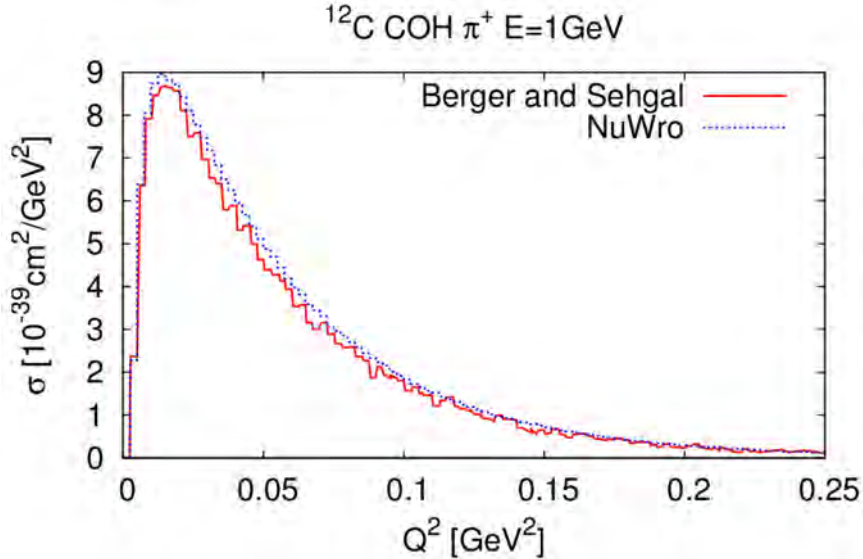


FIG. 1: Berger-Sehgal calculation (red) and NuWRO prediction (blue) of the Q^2 distribution of muon neutrino CC coherent interactions off carbon at $E_\nu=1$ GeV.

Recently, several improvements have been made. The Berger-Sehgal model for coherent production [4], in both NC and CC channels, has been added. Figure 1 shows the good agreement between the NuWRO implementation and the original theory calculation for the Q^2 distribution of CC coherent interactions on carbon at 1 GeV. Modifications have been made to the angular distribution of pions in delta decays, which are now based on ANL/BNL bubble chamber measurements. Another major development has been eWRO - the ability to run the NuWRO models in electron scattering mode, which makes possible a wide variety of comparisons to electron scattering data. One example is shown in Figure 2.

B. GiBUU

The Giessen Boltzmann-Uehling-Uhlenbeck (GiBUU) model is a semiclassical transport model in coupled channels [6] that takes into account numerous nuclear effects: the local density approximation, mean-field and Coulomb potentials, off-shell particle transport, 2p2h excitations, and in-medium spectral functions. It is the only generator that uses transport theory, the others all rely on intranuclear cascade Monte Carlos. It has been extensively

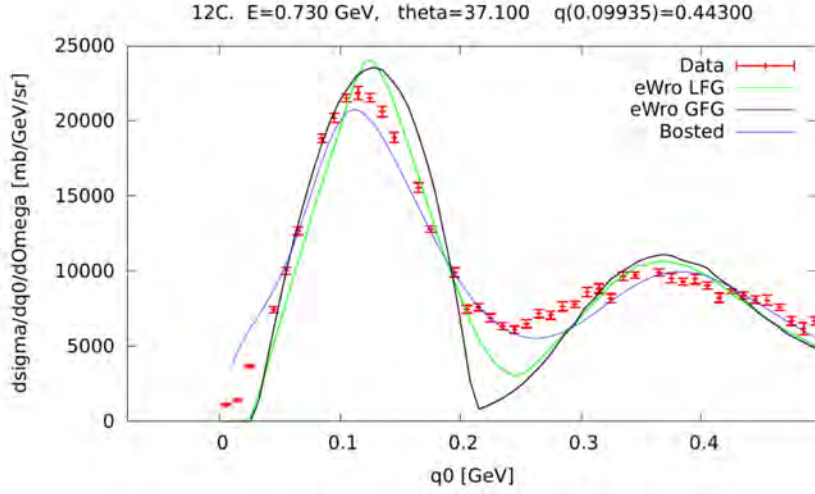


FIG. 2: Electron inclusive scattering comparison using eWRO. Shown are results from a global fermi gas (black), local Fermi gas (green), and using the Bosted parametrization of the inclusive response [5].

checked against data for heavy-ion collisions, electron scattering, photo-production, and hadron-nucleus collisions. GiBUU describes a wide range of data with a single, self-consistent microscopic model, ensuring consistency between nuclear effects in the initial state (such as Fermi motion, Pauli blocking, hadron self-energies, and medium-modified cross sections) and the final state (such as particle reinteractions). GiBUU is best viewed as a theoretical framework, which has now found application in photo-, electron-, neutrino-, pion-, nucleon-, and heavy-ion reactions, giving it considerably broader scope than most neutrino generators.

GiBUU has been used extensively over the past several years to illuminate areas where nuclear effects can play significant roles in experimental analyses [7–9]. These papers have described the issues generally, discussing the model choices in GiBUU, for instance, while also studying their implications in the context of specific experimental programs and measurements. As an example, the consequences for experiment of 2p2h scattering and final-state interactions, in terms of neutrino energy reconstruction, kinematic reconstruction, usefulness of topological separation based on final state observables, and others, have been explored. By providing fast turnaround for implementation of new theoretical ideas, theory-led generator groups are able to quickly provide tools to assess the impact on experiment. This stands in contrast with generators developed by experimentalists, which incorporate new theory more slowly, and are most often used as the front end to full Monte Carlo simulations. This is often a slow process, but one that is needed for experiments to assess exactly how their measurements are impacted. In this way, generators developed by theory- and experiment-led teams play complementary roles.

C. GENIE

The GENIE [10] neutrino event generator utilizes a software design which emphasizes extensibility, modularity, and flexibility. This design lowers the bar to development work, and over the past two years the collaboration has been re-organized to better facilitate model contributions by the broader community to GENIE. Fermilab has also taken on a larger role in GENIE activities, serving to support the large user base at the lab and acting as a hub for GENIE work. GENIE also has a new release strategy, where major releases (the next being GENIE 3.0) incorporate changes to the default set of models, and minor releases (the most recent being 2.10) incorporate new models as optional elements.

GENIE 2.10 offered a number of enhancements, which are described in detail elsewhere [11]. They include improvements to the intranuclear rescattering simulation to better characterize the A dependence of rescattering processes, the inclusion of an Effective Spectral Function model [12] that combines a new nuclear model based on super-scaling phenomenology with modeling of multi-nucleon scattering processes, the inclusion of a model for neutrino production of single kaons [13], and extensions to run to TeV scales, among others. Results from the new intranuclear rescattering model are shown in Figure 4, and the muon energy distribution from 1.5 GeV CC reactions producing single kaons is shown in Figure 3.

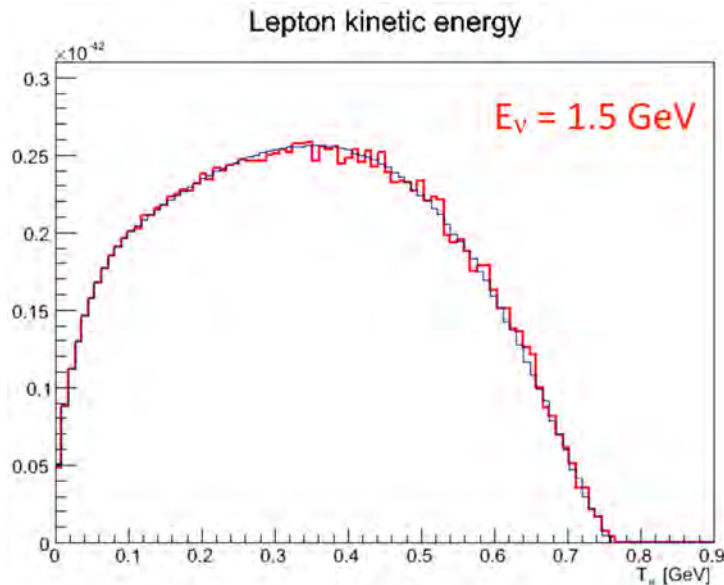


FIG. 3: Muon energies from 1.5 GeV CC $\Delta S = 1$ single pion reactions. The predictions from the full theory calculation [13] are shown (blue), together with a standalone C++ implementation that is identical to the GENIE prediction (red).

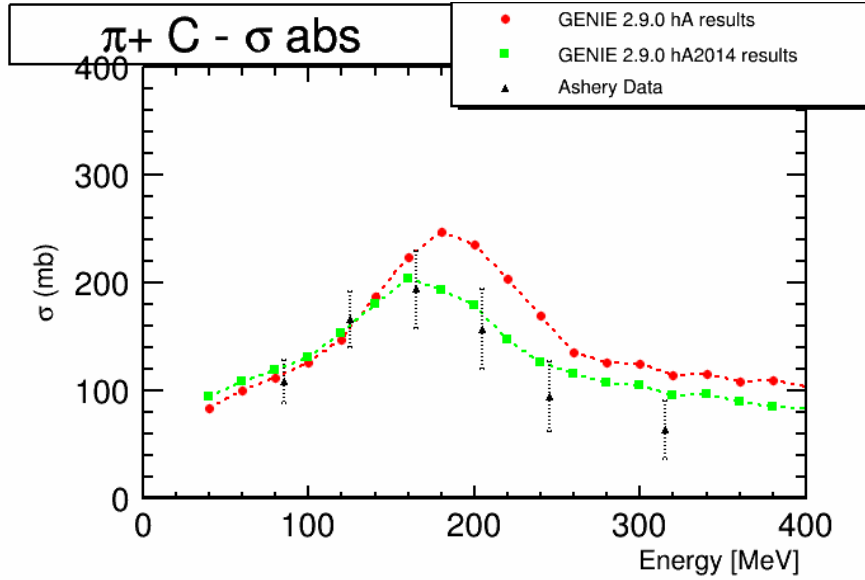


FIG. 4: Pion absorption on carbon, data compared with the GENIE default model (red) and the new intranuke model (green).

D. NEUT

The NEUT neutrino event generator was originally developed for the Kamiokande experiment, and has been used by the Super-Kamiokande, K2K, SciBoone, T2K, and Hyper-Kamiokande collaborations [14]. The primary goal of NEUT development is to meet the needs of this experimental program. Recent additions to NEUT include the Nieves model for multi-nucleon production [15] and a returning of the single pion cross sections to the ANL/BNL data [16], both of which are on by default. In addition, the Nieves calculation of RPA correction [17] is available as a reweightable option, and radiative CCQE is also available as an optional process. Figure 5 shows the effect of including the RPA corrections on the CCQE cross section, and Figure 6 shows the multi-nucleon scattering cross sections. An extensive campaign of retuning using T2K near detector data, together with data from previous experiments in the same energy range, was carried out as part of their oscillation analyses, and is described elsewhere in these proceedings [19]. Other ongoing work includes re-tuning to pion multiplicity distributions, incorporation of the full CCQE model of Nieves, and improvements to the coherent model. More information about recent NEUT upgrades can be found in [19].

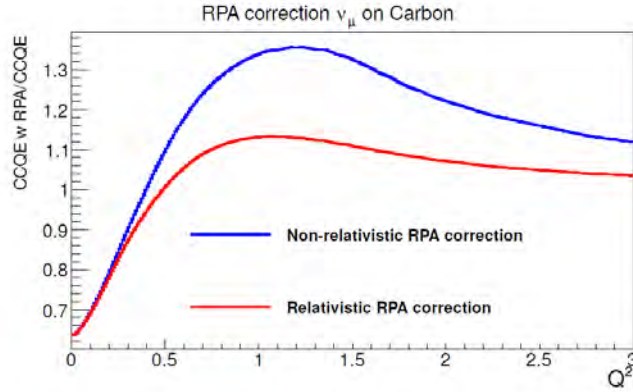


FIG. 5: Effect of relativistic (red) and non-relativistic (blue) RPA corrections on the shape of the Q^2 distribution for CCQE interactions (NEUT).

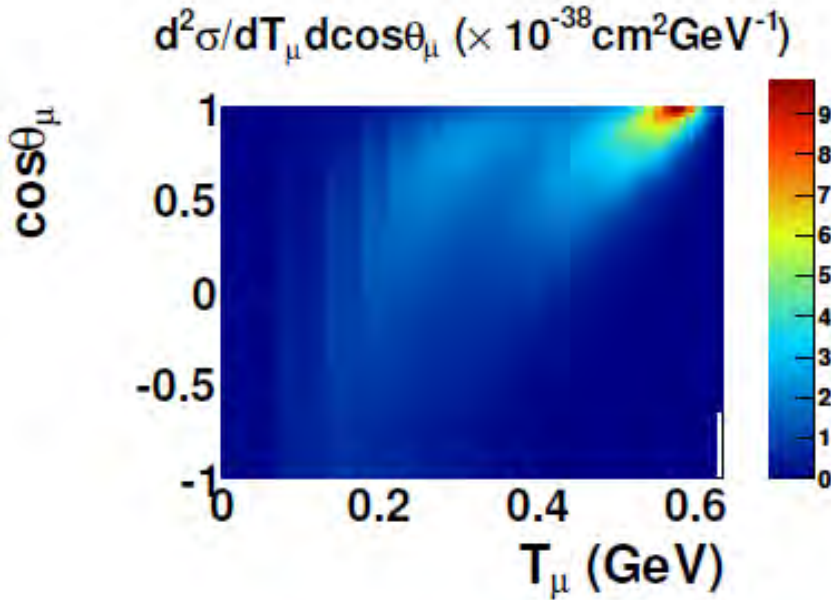


FIG. 6: Doubly differential distribution of $E_\nu = 0.65$ GeV QE-like interactions from oxygen, including 2p2h excitations (NEUT).

III. PROGRESS MADE AND CHALLENGES AHEAD

Experimentalists are fortunate to have access to four neutrino generators that are under active development. They have different emphases and perspectives, and play somewhat complementary roles, as they straddle the experiment/theory divide. Having multiple generators available to an experiment can be very helpful. For instance, being able to run multiple generators is a simple and (possibly) effective way to evaluate generator-related

systematic errors, but ONLY when: they incorporate different models and/or assumptions, are tuned to and constrained by relevant data, and the reasons for differences between the generators are well-understood (more work is needed here).

Over the past five years there has been continued and marked progress in the development and usage of neutrino generators. There has been a continuation of a trend towards open source, publicly available generator codes. Worldwide, there is an active theory community, and a number of theorists now work directly with experiments or generator developers. These direct experiment-theory conversations have produced new ideas about how to incorporate sophisticated (but slow) calculations into generators [18], and more experiments are now in a position to compare their results to multiple generators, and a variety of models within generators. Across the field there is now a broad recognition of the importance of close experiment-theory collaborations for progress in this area. Over the coming years, these efforts will naturally lead into conversations about the assignment of generator-related systematic errors, which can often be a difficult topic.

One of the largest challenges our field faces at the moment is in digesting the large amount of data that has been produced over the past decade, and building from it a consistent model of neutrino-nucleus interactions. To start with, there is a huge volume of data (γA , νA , eA , πA , pA), in principle. Deciding upon a strategy for incorporating this data into a coherent and consistent generator can in itself be a challenge, particularly as it has become clear that it is not possible to fit the entirety of the world's data using the models that are currently on the market. Progress often requires detailed understanding of an experiment's systematic errors, including correlations. Generator tuning campaigns, which also produce estimates of systematic errors, require large amounts of effort and require close collaboration between theorists, experimentalists, and generator authors.

Another challenge for generator developers stems from one of the largest theory challenges - how to correctly (or effectively) incorporate sophisticated nuclear physics into the needed calculations for neutrinos with energies around 1 GeV. There are a number of modeling issues that remain to be fully resolved, most significantly calculations related to np-nh processes, which for the purposes of generators, need to include modeling of the hadronic final state. And as always, trying to merge models that have applicability in separate kinematic domains will continue to be a challenge, as new models emerge.

Success in this area requires people working together across boundaries in our field: experiment/theory, particle/nuclear, High- vs. Medium- energy, and the neutrino-, electron-, and hadron-scattering communities. There are often challenges of geography, as the main experimental facilities in this field are currently running in Japan and the U.S., while the largest theory community is in Europe. These boundaries, unfortunately, define many of the funding mechanisms of our field, and finding creative ways to fund these collaborative

initiatives will be important. New ideas, effort, and collaborative structures will be required in order to make the feedback loop between theory and experiment, in which generators play an important role, operate more effectively in the coming years.

-
- [1] C. Juszczak, J. A. Nowak, and J. T. Sobczyk, Nucl.Phys.Proc.Suppl. **159**, 211 (2006), hep-ph/0512365.
 - [2] J. A. Nowak and J. T. Sobczyk, Acta Phys. Polon. **B37**, 2371 (2006), hep-ph/0608108.
 - [3] T. Golan, C. Juszczak, and J. T. Sobczyk, Phys.Rev. **C86**, 015505 (2012), 1202.4197.
 - [4] C. Berger and L. M. Sehgal, Phys. Rev. **D79**, 053003 (2009), 0812.2653.
 - [5] M. E. Christy and P. E. Bosted, Phys. Rev. **C81**, 055213 (2010), 0712.3731.
 - [6] O. Buss, T. Gaitanos, K. Gallmeister, H. van Hees, M. Kaskulov, O. Lalakulich, A. B. Larionov, T. Leitner, J. Weil, and U. Mosel, Phys. Rept. **512**, 1 (2012), 1106.1344.
 - [7] O. Lalakulich, K. Gallmeister, and U. Mosel, Phys. Rev. **C86**, 014614 (2012), [Erratum: Phys. Rev.C90,no.2,029902(2014)], 1203.2935.
 - [8] U. Mosel, O. Lalakulich, and K. Gallmeister, Phys. Rev. **D89**, 093003 (2014), 1402.0297.
 - [9] U. Mosel, in *Topical Research Meeting on Prospects in Neutrino Physics (NuPhys2014) London, UK, December 15-17, 2014* (2015), 1504.08204, URL <http://inspirehep.net/record/1365544/files/arXiv:1504.08204.pdf>.
 - [10] C. Andreopoulos, A. Bell, D. Bhattacharya, F. Cavanna, J. Dobson, et al., Nucl.Instrum.Meth. **A614**, 87 (2010), 0905.2517.
 - [11] M. Alam et al. (2015), 1512.06882.
 - [12] A. Bodek, M. Christy, and B. Coopersmith, Eur.Phys.J. **C74**, 3091 (2014), 1405.0583.
 - [13] M. Rafi Alam, I. Ruiz Simo, M. Sajjad Athar, and M. Vicente Vacas, Phys.Rev. **D82**, 033001 (2010), 1004.5484.
 - [14] Y. Hayato, Nucl. Phys. Proc. Suppl. **112**, 171 (2002).
 - [15] J. Nieves, I. Ruiz Simo, and M. J. Vicente Vacas, Phys. Rev. **C83**, 045501 (2011), 1102.2777.
 - [16] C. Wilkinson, P. Rodrigues, S. Cartwright, L. Thompson, and K. McFarland, Phys. Rev. **D90**, 112017 (2014), 1411.4482.
 - [17] J. Nieves, J. E. Amaro, and M. Valverde, Phys. Rev. **C70**, 055503 (2004), [Erratum: Phys. Rev.C72,019902(2005)], nucl-th/0408005.
 - [18] J. Schwehr, D. Cherdack, and R. Gran (2016), 1601.02038.
 - [19] T. Feusels, *These Proceedings* (2016).

Recent developments in neutrino-nucleus scattering theory*

Marco Martini[†]

Department of Physics and Astronomy, Ghent University,

Proeftuinstraat 86, B-9000 Gent, Belgium and

ESNT, CEA-Saclay, DSM, IRFU, Service de Physique Nucléaire,

F-91191 Gif-sur-Yvette Cedex, France

(Dated: March 23, 2016)

Abstract

In the present and future accelerator-based neutrino oscillation experiments nuclear targets (such as C, O, Ar and Fe) are involved. Hence the knowledge of neutrino-nucleus scattering is very important. In particular it is crucial for the determination of the neutrino energy which enters the expression of the oscillation probability. The status of the different theoretical approaches treating the open channels in the few-GeV region, i.e. the quasielastic, the pion production and the multinucleon emission, is reviewed. Special emphasis is devoted to the multinucleon emission channel, which turned to be crucial to explain the unexpected behavior of the charged current quasielastic measurement performed by MiniBooNE. The theoretical and experimental interest towards these multinucleon excitations continues to increase.

INTRODUCTION

Neutrino physics has undergone a spectacular development in the last decade, following the discovery of neutrino oscillations. In the present and future accelerator-based neutrino oscillation experiments nuclear targets, such as ^{12}C , ^{16}O , ^{40}Ar or ^{56}Fe , are involved, hence the knowledge of neutrino-nucleus scattering is very important. In particular it is crucial for the determination of the neutrino energy which enters the expression of the oscillation probability. In accelerator-based experiments the neutrino beams (at difference with respect to electron beams, for example) are not monochromatic but they span a wide range of energies, hence the incoming neutrino energy is reconstructed from the final states of the reaction. This determination is typically done through the charged current quasielastic (CCQE) events, commonly defined as those in which the emission product only includes one charged lepton. The reconstructed energy hypothesis used to obtain the neutrino energy from the measured charged lepton variables (energy and scattering angle) via a two-body formula is that the neutrino interaction in the nuclear target takes place on a nucleon at rest. The identification of the reconstructed neutrino energy with the real one is too crude. Several nuclear effects such as Pauli blocking, Fermi motion, collective aspects of the nuclear response and, very important, multinucleon emission, need to be taken into account. Furthermore, the fact that in the accelerator-based experiments the incoming neutrino beam exhibits a wide spectrum of energies implies that not only the quasielastic but also other reaction mechanisms, such as for example the pion production, contribute to the neutrino nucleus

cross section. The status of the different theoretical approaches treating the open channels in the few-GeV region, i.e. the quasielastic, the pion production and the multinucleon emission, is here reviewed, devoting special emphasis to the multinucleon emission channel.

QUASIELASTIC AND MULTINUCLEON EMISSION

The multinucleon emission channel in connection with the quasielastic has attracted a lot of attention in these last years. In fact, as illustrated in Fig. 1, the inclusion of this channel in the quasielastic cross section was suggested [1, 2] to be the possible explanation of the MiniBooNE CCQE total cross section on carbon [3], apparently too large with respect to many theoretical predictions employing the standard value of the axial mass. Since the MiniBooNE experiment, as well as other experiments involving Cherenkov detectors, defines a charged current “quasielastic” event as the one in which only a final charged lepton is detected, the ejection of a single nucleon (a genuine quasielastic event) is only one possibility, and one must in addition consider events involving a correlated nucleon pair from which the partner nucleon is also ejected, as discussed first in Ref. [4]. This leads to the excitation of 2 particle-2 hole (2p-2h) states; 3p-3h excitations are also possible. The inclusion in the quasielastic cross section of events in which several nucleons are ejected (np-nh excitations), leads to an excess over the genuine quasielastic value. Martini *et al.* [1, 2] have argued that this is the likely explanation of the MiniBooNE anomaly showing that their evaluation can account for the excess in the cross section without any modification of the axial mass. After this suggestion the interest of the neutrino scattering and oscillation communities on the multinucleon emission channel rapidly increased. Indeed this channel was not included in the generators used for the analyses of the neutrino cross sections and oscillations experiments. Today there is an effort to include this np-nh channel in several Monte Carlo. Concerning the theoretical situation, nowadays several calculations agree on the crucial role of the multinucleon emission in order to explain the MiniBooNE neutrino [3] and antineutrino [5] data. Nevertheless there are some differences on the results obtained for this np-nh channel by the different theoretical approaches. The aim of this section is to review the current theoretical status on this subject.

The theoretical calculations of np-nh excitations contributions to neutrino-nucleus cross sections are presently performed essentially by three groups. There are the works of Martini

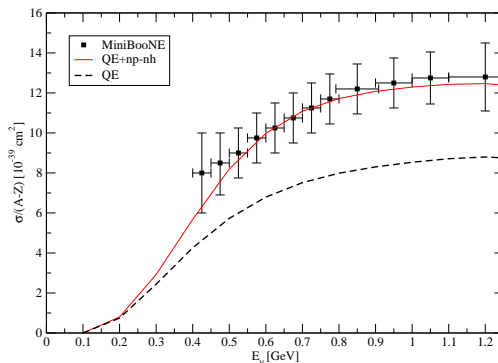


FIG. 1: Charged current “Quasielastic” cross section on carbon measured by MiniBooNE [3] compared to Martini *et al.* calculations. The figure is taken from Ref. [1].

et al. [1, 2, 6–11], the ones of Nieves *et al.* [12–16] and the ones of Amaro *et al.* [17–23]. The np-nh channel is taken into account through more phenomenological approaches in the so called Transverse Enhancement Model (TEM) [24] and in GiBUU [25–27]. In the 2p-2h sector, the three microscopic approaches mentioned above are based on the Fermi gas. We remind that there exist several two-body current contributions. We have first of all the Meson Exchange Currents (MEC), given by the pion-in-flight term, the contact term and the Δ -intermediate state or Δ -MEC term. Furthermore in the independent particle models, such as the Fermi gas, the nucleon-nucleon (NN) correlations must be taken into account. It is possible by including an additional two-body current, the correlation current. Even in the simple Fermi gas model, an exact relativistic calculation of all the two-body current contributions is difficult for several reasons. First of all it involves the computation of 7-dimensional integrals for a huge number of 2p-2h response Feynman diagrams. Second divergences in the NN correlations sector and in the angular distribution of the ejected nucleons [20, 21] may appear and need to be regularized. Furthermore the calculations should be performed for all the kinematics compatible with the experimental neutrino flux. For these reasons an exact relativistic calculation is computationally very demanding and as a consequence different approximations are employed by the different groups in order to reduce the dimension of the integrals and to regularize the divergences. The choice of subset of diagrams and terms to be calculated presents also important differences. In this connection Amaro *et al.* explicitly add to the genuine quasielastic only the MEC contributions and not the NN correlations-MEC interference terms. MEC contributions, NN correlations and NN

correlations-MEC interference are present both in Martini *et al.* and Nieves *et al.* even if Martini *et al.* consider only the Δ -MEC. On the other hand the treatment of Amaro *et al.* is fully relativistic as well as the one of Nieves *et al.* while the results of Martini *et al.* are related to a non-relativistic reduction of the two-body currents. The interference between direct and exchange diagrams is neglected by Martini *et al.* and Nieves *et al.* Another important difference is that Amaro *et al.* consider the 2p-2h contribution only in the vector sector while Martini *et al.* and Nieves *et al.* also in the axial one. Fully relativistic calculations of Amaro *et al.* for the axial sector are in progress but not published. In this connection, some preliminary results have been presented for the first time by Megias at this conference [23]. Taking into account the existence of all these differences, is not surprising that these models produce different final results. This point is illustrated in Fig. 2 where the MiniBooNE neutrino and antineutrino flux folded double differential CCQE-like cross sections calculated in the different approaches are displayed. For sake of illustration the results are given for $0.8 < \cos \theta < 0.9$ as function of the muon kinetic energy. The complete theoretical results in the different bins for neutrinos and antineutrinos are given in Refs. [6, 9] for Martini *et al.*, in Refs. [13, 15] for Nieves *et al.* and in Refs. [17, 19] for Amaro *et al.* An updated version of the last results is given by Megias *et al.* in Ref. [22] from which we take the results reported in the last two panels of Fig. 2. As one can observe from Fig. 2 the results of Martini *et al.* are in good agreement with the experimental data. In the case of Nieves *et al.* and Amaro *et al.* there is a tendency to underestimate the MiniBooNE data. The preliminary results shown by Megias [23] including also the axial contributions are in a better agreement with the MiniBooNE data. An important point is that the relative role of the multinucleon contribution is different for neutrino and antineutrino in the different approaches. The nuclear cross-section difference for neutrinos and antineutrinos stands as a potential obstacle in the interpretation of experiments aimed at the measurement of the CP violation angle, hence has to be fully mastered. As discussed in Refs. [2, 11, 19] the difference between the neutrino and antineutrino results is due to the presence in the neutrino-nucleus cross section expression of the vector-axial interference term, which changes sign between neutrino and antineutrino, the basic asymmetry which follows from the weak interaction theory. Due to this vector-axial interference term, the relative weight of the different nuclear responses is different for neutrino and antineutrino. As a consequence also the relative weight of the np-nh contributions is different for neutrino

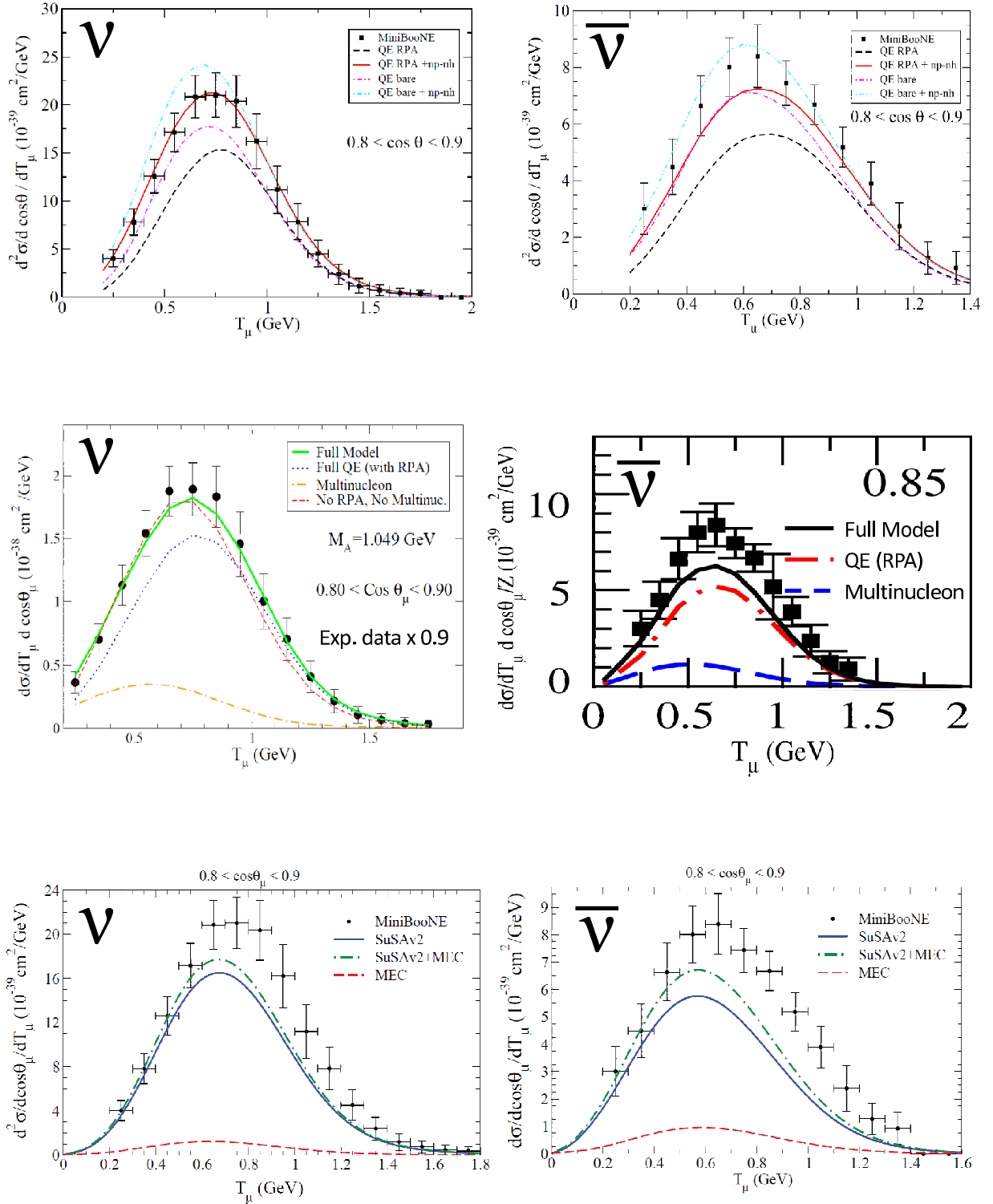


FIG. 2: MiniBooNE flux integrated neutrino (left panels) and antineutrino (right panels) CCQE-like double differential cross section on carbon per active nucleon for $0.8 < \cos \theta < 0.9$ as a function of the muon kinetic energy. Top panels: Martini *et al.* [6, 9] results. Middle panels: Nieves *et al.* [13, 15] results. Bottom panels: Megias *et al.* [22] results representing an update of the Amaro *et al.* [17, 19] results.

and antineutrino. For example the fact that np-nh contributions are larger for antineutrinos with respect to neutrinos in the case of Amaro *et al.* is due to the fact that Amaro *et al.* consider the np-nh contributions only in the vector sector, hence not in the vector-axial interference term. In order to investigate the multinucleon content of the vector-axial interference term, Ericson and Martini have recently considered [11] the difference between the neutrino and antineutrino MiniBooNE quasielastic-like double-differential cross sections. They have shown that the model of Martini *et al.*, which includes the np-nh excitations in the vector-axial interference term, gives a good fit for the difference of the MiniBooNE cross sections reproducing well the data in the full range of muon energy and emission angle. This result represents an important test for the presence of the multinucleon component in the vector-axial interference term. A similar conclusion on a relevant two-body current contribution in the vector-axial interference term has been recently obtained by Lovato *et al.* [28, 29] who calculated the neutral weak current two-body contributions to sum rules and Euclidean responses in ^{12}C .

Up to now we have discussed the theoretical models in connection with the MiniBooNE cross sections. For the moment the theoretical calculations for the np-nh excitations are restricted to the relatively small energy and momentum transfer, prevalent in the MiniBooNE and T2K experiments. Concerning T2K, the measurement performed by this collaboration of charged-current double differential cross sections on carbon with zero pions in the final state ($\text{CC}0\pi$) has been presented for the first time at this conference [30]. These experimental results have also been compared with the theoretical predictions of Martini *et al.* and Nieves *et al.* Also in this case a good agreement with data is obtained adding to the genuine quasielastic cross section calculated in RPA the multinucleon contributions.

How the np-nh processes behave at large energy and momentum transfer is still an open question. Nevertheless, Megias *et al.* in Ref. [22] applied the model of Amaro *et al.*, which includes only vector MEC contributions, to neutrino energies of up to 100 GeV and compared their predictions also with NOMAD [31] and MINER ν A neutrino [32] and antineutrino [33] CCQE data. Preliminary comparison with NOMAD total CCQE cross sections including in the theoretical calculations also axial two-body current contributions have been presented for the first time by Megias at this conference [23]. Gran *et al.* [16] applied the model of Nieves *et al.* to neutrino energies of up to 10 GeV. However they placed a cut on the three-momentum transfer of 1.2 GeV. They compared their results with the MINER ν A neutrino

and antineutrino CCQE Q^2 distribution. A similar comparison has been performed also by Mosel *et al.* [27] using GiBUU. As a general remark, by comparing the results of Refs. [16, 22, 27] with MINER ν A data, one can observe that the MINER ν A Q^2 distributions can be reproduced also without the inclusion of np-nh excitations. This is not the case of the MiniBooNE Q^2 distributions [6, 9, 22]. A reasonable simultaneous agreement with the MiniBooNE and MINER ν A Q^2 distributions is obtained by Meucci and Giusti [34] using the relativistic Green's function model with a complex optical potential.

PION PRODUCTION AND INCLUSIVE CROSS SECTIONS

In this section we rapidly discuss the present situation for the pion production and inclusive cross sections. In the one pion production channel some questions are still open. For instance, theoretical calculations [10, 35, 36] of CC $1\pi^+$ single and double differential cross sections as a function of muon variables are in agreement with the MiniBooNE data [37]. On the contrary theoretical works [36, 38] on the MiniBooNE differential cross sections function of the final pion variables display a reshaping of the differential cross section due to the inclusion of pion final state interaction which suppresses the agreement with the MiniBooNE data. More recently the MINER ν A experimental results appear [39]. Nowadays there is a general tendency of theoretical calculations and Monte Carlo results to underestimate the MiniBooNE data [37, 40] and to overestimate the MINER ν A ones [39]. This is discussed for example in Refs. [41, 42]. Further investigations are needed. We remind the different energies of MiniBooNE and MINER ν A neutrino beams.

The inclusive ν_μ CC double differential cross section on carbon has been published by T2K in Ref. [43]. The inclusive measurements are important because they are less affected by background subtraction with respect to exclusive channels measurements. Martini and Ericson have compared their predictions with the T2K experimental results in Ref. [10]. In this paper they have shown that in order to obtain an agreement with the T2K inclusive data one needs to consider not only the genuine quasielastic and the one pion production channels but also the multinucleon excitations. These results represent the first successful test of the necessity of the multinucleon emission channel in an experiment with another neutrino flux with respect to the one of MiniBooNE. This conclusion, using the same theoretical model, has been recently reached also in connection with the T2K CC 0π results mentioned

above and the ν_e charged-current inclusive differential cross sections on carbon [44]. This agreement with both ν_μ and ν_e CC inclusive T2K flux folded differential cross sections is not systematically obtained in other approaches. For instance the SuSAv2 model by Ivanov et al *et al.* [45] reproduces well the CC inclusive T2K flux folded ν_μ double differential cross section but underestimates the CC inclusive T2K flux folded ν_e single differential cross section. A comparison with these quantities has also been performed by Meucci and Giusti using the Relativistic Green's function model which turned to underestimate the ν_μ and ν_e CC inclusive T2K data [46]. Finally, interesting differences between the T2K flux folded ν_μ results obtained by the various theoretical approaches appear in particular in the forward direction where low-lying giant resonance contributions can be non-negligible, as pointed out in Ref. [10], and explicitly shown in Ref. [47].

* *Presented at NuFact15, 10-15 Aug 2015, Rio de Janeiro, Brazil [C15-08-10.2]*

† `martini.marco@gmail.com`; Speaker

- [1] M. Martini, M. Ericson, G. Chanfray and J. Marteau, Phys. Rev. C **80**, 065501 (2009).
- [2] M. Martini, M. Ericson, G. Chanfray and J. Marteau, Phys. Rev. C **81**, 045502 (2010).
- [3] A. A. Aguilar-Arevalo *et al.* [MiniBooNE Collaboration], Phys. Rev. D **81**, 092005 (2010).
- [4] J. Marteau, J. Delorme and M. Ericson, Nucl. Instrum. Meth. A **451**, 76 (2000).
- [5] A. A. Aguilar-Arevalo *et al.* [MiniBooNE Collaboration], Phys. Rev. D **88**, 032001 (2013).
- [6] M. Martini, M. Ericson and G. Chanfray, Phys. Rev. C **84**, 055502 (2011).
- [7] M. Martini, M. Ericson and G. Chanfray, Phys. Rev. D **85**, 093012 (2012).
- [8] M. Martini, M. Ericson and G. Chanfray, Phys. Rev. D **87**, 013009 (2013).
- [9] M. Martini and M. Ericson, Phys. Rev. C **87**, 065501 (2013).
- [10] M. Martini and M. Ericson, Phys. Rev. C **90**, 025501 (2014).
- [11] M. Ericson and M. Martini, Phys. Rev. C **91**, no. 3, 035501 (2015).
- [12] J. Nieves, I. Ruiz Simo, M. J. Vicente Vacas, Phys. Rev. **C83**, 045501 (2011).
- [13] J. Nieves, I. Ruiz Simo and M. J. Vicente Vacas, Phys. Lett. B **707**, 72 (2012).
- [14] J. Nieves, F. Sanchez, I. Ruiz Simo and M. J. Vicente Vacas, Phys. Rev. D **85**, 113008 (2012).
- [15] J. Nieves, I. Ruiz Simo and M. J. Vicente Vacas, Phys. Lett. B **721**, 90 (2013).
- [16] R. Gran, J. Nieves, F. Sanchez and M. J. Vicente Vacas, Phys. Rev. D **88**, 113007 (2013).

- [17] J. E. Amaro, M. B. Barbaro, J. A. Caballero *et al.*, Phys. Lett. **B696**, 151-155 (2011).
- [18] J. E. Amaro, M. B. Barbaro, J. A. Caballero *et al.*, Phys. Rev. D **84**, 033004 (2011).
- [19] J. E. Amaro, M. B. Barbaro, J. A. Caballero *et al.*, Phys. Rev. Lett. **108**, 152501 (2012).
- [20] I. Ruiz Simo, C. Albertus, J. E. Amaro *et al.*, Phys. Rev. D **90**, no. 3, 033012 (2014).
- [21] I. R. Simo, C. Albertus, J. E. Amaro *et al.*, Phys. Rev. D **90**, no. 5, 053010 (2014).
- [22] G. D. Megias, T. W. Donnelly, O. Moreno *et al.* Phys. Rev. D **91**, no. 7, 073004 (2015).
- [23] G. D. Megias, talk presented at NuFact15.
- [24] A. Bodek, H. S. Budd and M. E. Christy, Eur. Phys. J. C **71**, 1726 (2011).
- [25] O. Lalakulich, K. Gallmeister and U. Mosel, Phys. Rev. C **86**, no. 1, 014614 (2012).
- [26] O. Lalakulich, U. Mosel and K. Gallmeister, Phys. Rev. C **86**, 054606 (2012).
- [27] U. Mosel, O. Lalakulich and K. Gallmeister, Phys. Rev. D **89**, no. 9, 093003 (2014).
- [28] A. Lovato, S. Gandolfi, J. Carlson *et al.*, Phys. Rev. Lett. **112**, 182502 (2014).
- [29] A. Lovato, S. Gandolfi, J. Carlson *et al.*, Phys. Rev. C **91**, 062501 (2015).
- [30] S. Bolognesi; A. Furmanski, talks presented at NuFact15.
- [31] V. Lyubushkin *et al.* [NOMAD Collaboration], Eur. Phys. J. C **63**, 355 (2009).
- [32] G. A. Fiorentini *et al.* [MINERvA Collaboration], Phys. Rev. Lett. **111**, 022502 (2013).
- [33] L. Fields *et al.* [MINERvA Collaboration], Phys. Rev. Lett. **111**, no. 2, 022501 (2013).
- [34] A. Meucci and C. Giusti, Phys. Rev. D **89**, no. 11, 117301 (2014).
- [35] M. V. Ivanov, J. M. Udias, A. N. Antonov *et al.*, Phys. Lett. B **711**, 178 (2012).
- [36] O. Lalakulich and U. Mosel, Phys. Rev. C **87**, 014602 (2013).
- [37] A. A. Aguilar-Arevalo *et al.* [MiniBooNE Collaboration], Phys. Rev. D **83**, 052007 (2011).
- [38] E. Hernandez, J. Nieves and M. J. V. Vacas, Phys. Rev. D **87**, 113009 (2013).
- [39] B. Eberly *et al.* [MINERvA Collaboration], arXiv:1406.6415 [hep-ex].
- [40] A. A. Aguilar-Arevalo *et al.* [MiniBooNE Collaboration], Phys. Rev. D **81**, 013005 (2010).
- [41] J. T. Sobczyk and J. Zmuda, Phys. Rev. C **91**, 045501 (2015).
- [42] U. Mosel, Phys. Rev. C **91**, 065501 (2015).
- [43] K. Abe *et al.* [T2K Collaboration], Phys. Rev. D **87**, 092003 (2013).
- [44] K. Abe *et al.* [T2K Collaboration], Phys. Rev. Lett. **113**, no. 24, 241803 (2014).
- [45] M. V. Ivanov, G. D. Megias, R. Gonzalez-Jimenez *et al.*, arXiv:1506.00801 [nucl-th].
- [46] A. Meucci and C. Giusti, Phys. Rev. D **91**, no. 9, 093004 (2015).
- [47] V. Pandey, N. Jachowicz, T. Van Cuyck *et al.*, Phys. Rev. C **92**, 024606 (2015).

Status of the Angra Neutrino Project*

Chimenti, P.[†]

Universidade Federal do ABC - UFABC

Anjos, J.C., Azzi, G., Castromonte, C., Lima Jr,
H.P., Machado, R., Rocha, O., and Souza, M.J.N.

Centro Brasileiro de Pesquisas Físicas - CBPF

Cerqueira, A.S. and Nóbrega, R.A.

Universidade Federal de Juiz de Fora - UFJF

Farias, P.C.M.A., Pepe, I.M., Ribeiro, D.B.S., and Simas Filho, E.F.

Universidade Federal de Bahia - UFBA

Guedes, G.P.

Universidade Estadual de Feira de Santana - UEFES

Gonzales, L.F.G., Kemp, E., and Rodrigues, O.B.

Universidade Estadual de Campinas - UNICAMP

Nunokawa, H. and Wagner, S.

Pontifícia Universidade Católica de Rio de Janeiro - PUC-Rio

Valdivieso, G.A.

Universidade Federal de Alfenas - UNIFAL-MG

(Dated: March 24, 2016)

Abstract

The Angra Neutrino Project aims at measuring neutrinos from the Angra-II power plant for monitoring purposes. The water Cherenkov detector, with a fiducial volume of about 1.4 ton filled with a solution of GdCl_3 , is under construction in Rio de Janeiro. All parts are already constructed and are being assembled and tested first at CBPF to be installed in Angra later this year. The current status of simulations, construction and tests is presented. This will be the first neutrino detector entirely designed, constructed and operated in Brazil.

INTRODUCTION

The possibility to use anti-neutrinos emitted by a nuclear power plant for monitoring and non-proliferation purposes was noted long ago (see [1] for a recent overview of the subject). Only recently however advances in detector technology permitted the actual realization of this original idea. Along this line of research the Angra Neutrino Project [2] (ANP for short) aims at developing a low budget detector to monitor the Angra-II power plant as a proof of concept.

Most recent efforts in this field were focused on the application of scintillators, either plastic or liquid, as detection technology. Due to budget consideration and safety requirements we focused our effort on the development of a Water Cherenkov detector employing a $\text{H}_2\text{O} - \text{GdCl}_3$ solution (0.3% in mass of Gd) to increase the signal-over-noise ratio. Indeed good quality plastic scintillators are relatively expensive and liquid scintillators are flammable with a flash point considered too low for a safe operation in a nuclear power plant environment. Moreover past experiments were placed in a site with an overburden of some meters of rock water equivalent. Neutrinos Angra would provide the first measurement at surface (no overburden).

It must be emphasized that the development of local small scale experiment is extremely important to train students and young researchers to experimental particle physics and to boost local technologies. Indeed this will be the first neutrino experiment completely designed, built and operated in Brazil. In this sense the Angra Neutrino Experiment has a usefulness extending much longer its scientific goal.

DESIGN

The Angra-II power plant is a Pressurized-Water reactor with a nominal thermal power of 4 GW. The detection channel is the inverse beta decay: an electron anti-neutrino interact on a proton yielding a neutron and a positron. The neutron is subsequently captured by a gadolinium nucleus dissolved in water resulting in a cascade of deexcitation gammas. The interaction signature is therefore a prompt event given by the positron and a delayed event generated by the neutron.

The position of closest approach where a detector could be installed is at about 30 m from the reactor core. In order to have a sizable event rate (more than about 10^3 day^{-1}) a detector with a fiducial mass of about 1 ton must be built. The detector also has to be installed inside the neutrino laboratory: a standard high cube 12 m container installed near the reactor dome. This sets important geometrical requirements.

In order to reduce the background rate, the detector has to be shielded. Again the technology of choice for this purpose was based on water tanks: water, being an excellent neutron moderator, is very efficient in reducing the amount of environmental neutrons entering the detector. Moreover the water shield tanks can be instrumented to act as an active veto against cosmic rays.

The detector design as implemented in the Geant4 simulation is illustrated in Fig. 1.

MECHANICS AND ELECTRONICS

The mechanical design is implemented with stainless steel containers for both the veto volumes and as support to the polyethylene vessel containing the Water-Gadolinium solution. Indeed this solution is corrosive and if in contact with metallic surfaces would degrade the water transparency. Internal surfaces of the tanks are folded with tyvek or gore-tex in order to increase the light collection efficiency. Photons are detected by the classic 8 inches Hamamatsu R5912 Photomultiplier tube with waterproof base. Water is recirculated through microfilters and UV lights to maintain transparency.

PMTs are powered by a CAEN SY4527 H.V. system. Their signals are pre-amplified and discriminated by a custom front-end electronic NIM module and finally read-out by a FADC board entirely designed at CBPF. Pre-amplified signals exhibit rise time of order 20 ns, fall

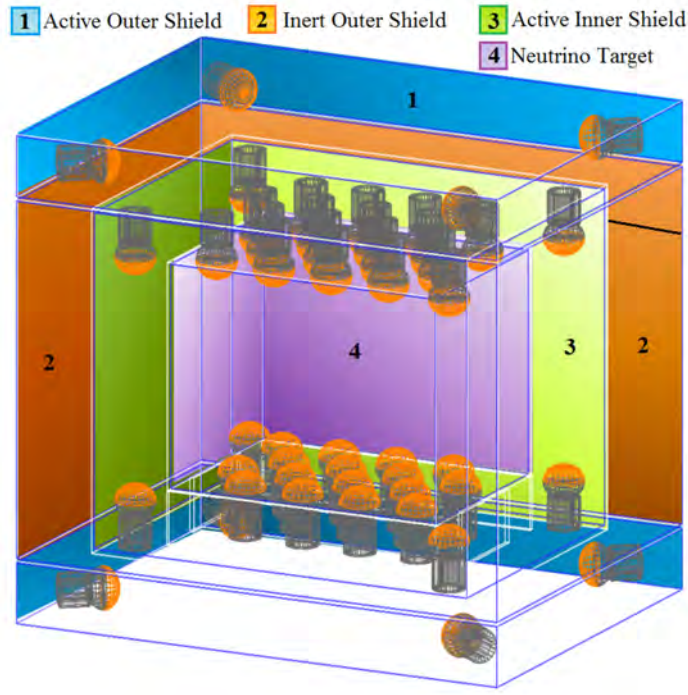


FIG. 1: Design of the Angra Neutrino Detector.

time of order 80 ns and pulse height of about $37 \text{ mV}/p.e.$ at nominal PMT gain of 10^7 . Front-end electronics saturates at about 52 p.e.. Pedestals and discrimination thresholds can be tuned remotely by an on board I2C controller.

Pre-amplified signals are sampled by custom boards (DAQs) assembling both FADCs and TDCs combining good signal charge and time reconstruction. FADCs have $2 V_{pp}$ dynamic range, 10 bits of effective resolution and work at 125 MHz. TDCs have 81 ns resolution and $9.8 \mu\text{s}$ range. Onboard FPGAs implement optimal filters and control communication with read-out boards both through USB or VME interfaces. DAQ boards include a CAN controller for remote configuration.

Signals are finally acquired on PC by a VME bus single board computer (MVME3100 by Emerson Network Power).

All mechanical and electronic elements have been built or purchased and are being assembled and tested at CBPF [3].

SIMULATION

The simulation code is divided in to four domains with well defined interfaces:

- **Primary Generators:** this code provides samples of neutrino and background primary interactions in the detector. It collects all the available information on primary particle distribution. Primary interaction samples are stored in text files with HepEVT formatting.
- **Geant4 [4] Simulation:** the responsibility of this domain is to simulate the propagation and interaction of primary particle with the detector. Results are stored (after post-processing) in root files containing information about photoelectrons generated in each PMT by each event. Time at this stage is relative to the primary interaction.
- **Mixer:** this domain distributes simulated events of both neutrino interactions and background according to poisson distribution in the right time order.
- **Front-end simulation:** this domain simulate the response of both electronics and trigger logic producing output files equivalent to the one produced in a real data acquisition.

The first three domains are in an advanced phase of development. A first prototype of the last domain has been also implemented.

First simulation, not yet tuned against detector calibrations, indicate antineutrino detection efficiency between 50% and 80%, depending on selection criteria. Also we foresee the possibility of detecting reactor on/off with high significance in a day of data acquisition. The results however heavily depend on precise estimation of backgrounds [5].

FIRST TESTS AND CONCLUSIONS

First tests are being performed with the inner detector filled with water and half equipped with PMTs. In this configuration we verified the capability of detecting single p.e. generated by Cherenkov. Also the light yield is about as expected by simulation. Light yield however strongly depend on water transparency, which has to be carefully monitored during the experiment lifetime.

In conclusion the experimental results expected by the Angra Neutrino Experiment are still interesting and well placed within the international effort to provide a nuclear safeguard

technology employing neutrinos. The project is ongoing and results of preliminary tests of the equipment are according to expectations.

The Angra Collaboration acknowledges the support of Ministério de Ciência, Tecnologia e Inovação (MCTI), the Conselho Nacional para o Desenvolvimento Científico e Tecnológico (CNPq), Financiadora de Estudos e Projetos (FINEP) and the following state research agencies: FAPESP, FAPMIG and FAPERJ. P.Chimenti thanks the support of FAPESP funding grant 2015/12505-5.

* *Presented at NuFact15, 10-15 Aug 2015, Rio de Janeiro, Brazil [C15-08-10.2]*

† `pietro.chimenti@ufabc.edu.br`; Speaker

- [1] M. Cribier, J. Phys. Conf. Ser. **593**, 012004 (2015).
- [2] J. C. Anjos et al., Nucl. Part. Phys. Proc. **267-269**, 108 (2015).
- [3] T. A. Alvarenga et al. (2016), manuscript submitted for publication.
- [4] S. Agostinelli et al. (GEANT4), Nucl. Instrum. Meth. **A506**, 250 (2003).
- [5] P. Chimenti et al. (2014), angra Internal Note.

Charged Current Quasielastic Analysis from MINER ν A*

Anushree Ghosh[†]

CBPF - Centro Brasileiro de Pesquisas Físicas,

Rua Dr. Xavier Sigaud 150,

Urca, Rio de Janeiro,

Rio de Janeiro, 22290-180, Brazil

on behalf of the MINER ν A Collaboration

(Dated: April 12, 2016)

Abstract

The MINER ν A detector situated in Fermilab, is designed to make precision cross-section measurements for scattering processes on various nuclei. In this proceeding, the results of the charged current quasi-elastic (CCQE) analysis using lepton kinematics and with proton kinematics have been presented. Comparison of these with theoretical models suggested that further studies are required to include the additional nuclear effects in the current simulations. The first direct measurement of electron-neutrino quasielastic-like scattering in the few-GeV region of incident neutrino energy has also been presented. All three analyses, discussed here, are carried out on hydrocarbon target.

MINER ν A DETECTOR

The MINER ν A experiment [1], located at Fermilab, is dedicated to making precise measurement of neutrino-nucleus cross sections in the few-GeV region, which are relevant for neutrino oscillation experiments. The MINER ν A detector is situated in the NuMI beamline at Fermilab, along with the MINOS and NO ν A experiments. NuMI provides an intense beam of neutrinos and antineutrinos, resulting from the decay of mesons produced by 120 GeV protons impinging on a carbon target. All the results discussed here were generated from data taken between 2010 and 2012 in the low-energy beam configuration, with a peak neutrino energy of about 3 GeV. During this period data from 3.98×10^{20} protons on target were collected in the neutrino mode, and 1.7×10^{20} protons were collected in the antineutrino mode. Since the summer of 2013 MINER ν A has been taking data in the NuMI medium energy configuration, with a peak neutrino energy of about 6 GeV.

The central tracking region of the MINER ν A detector is constructed from 120 planes of parallel triangular strips of plastic scintillator, arranged almost perpendicular to the beam axis. Each strip contains a wavelength-shifting fiber, which delivers light generated by charged particles to photomultiplier tubes. Targets of water, carbon, iron, and lead are embedded between scintillating strips upstream of the central detector, and a liquid helium target is placed upstream of the main detector. The central detector is surrounded by an electromagnetic and hadronic calorimetry. The magnetized MINOS near detector sits downstream of MINER ν A and serves as a muon spectrometer. The results presented in this paper are based on an analysis of interactions in the central, fully-active tracking region.

CCQE INTERACTION

The quasielastic interaction is defined as the process in which a neutrino scatters from a nucleon bound in the nucleus via the exchange of a W^\pm boson, thereby emitting a charged lepton and nucleon, with no meson production and minimal energy transfer to spectator nucleons. If the neutrino scatters quasi-elastically from a stationary nucleon, the neutrino energy (E_ν) and momentum transfer Q^2 can be calculated from the polar angle and the momentum of the final state lepton. Alternatively, one can also reconstruct the neutrino energy and the momentum transfer from the final state proton kinematics.

Quasielastic scattering from a bound nucleon is generally modeled as scattering on free nucleons in a relativistic Fermi gas (RFG), with the nucleon axial form factor that measured in neutrino-deuterium quasielastic scattering [2][3]. The RFG model [4] assumes that the initial state nucleons act independently in the mean field of the nucleus and does not include effects due to nucleon-nucleon correlations, as well as interactions of the final state particles within the nucleus, which significantly modify the Fermi gas picture, and thereby affect the neutrino energy reconstruction in oscillation experiments. The hadrons produced in the neutrino-nucleus interactions are subject to final-state interactions (FSI) while propagating through the nucleus. As a result, the inelastic processes with a quasi-elastic-like final state (i.e., no final state mesons) and nucleon-nucleon correlations contribute to the measured quasielastic (QE) cross section having different kinematics and final state hadron content for the same neutrino energy. These processes are particularly important when reconstruction is done using proton kinematics instead of lepton kinematics.

This paper presents the results of a CCQE analysis using both lepton kinematics and proton kinematics on a hydrocarbon target.

CCQE INTERACTION USING LEPTON KINEMATICS

MINER ν A has previously measured both neutrino and antineutrino differential cross sections in the fully active central tracking region [5][6]. The neutrino energy and the square of the four momentum transferred to the nucleus, Q_{QE}^2 , are estimated from the muon momentum and angle using the quasielastic hypothesis:

$$E_\nu^{QE} = \frac{m_n^2 - (m_p - E_b)^2 - m_\mu^2 + 2(m_p - E_b)E_\mu}{2(m_p - E_b - E_\mu + p_\mu \cos \theta_\mu)} \quad (1)$$

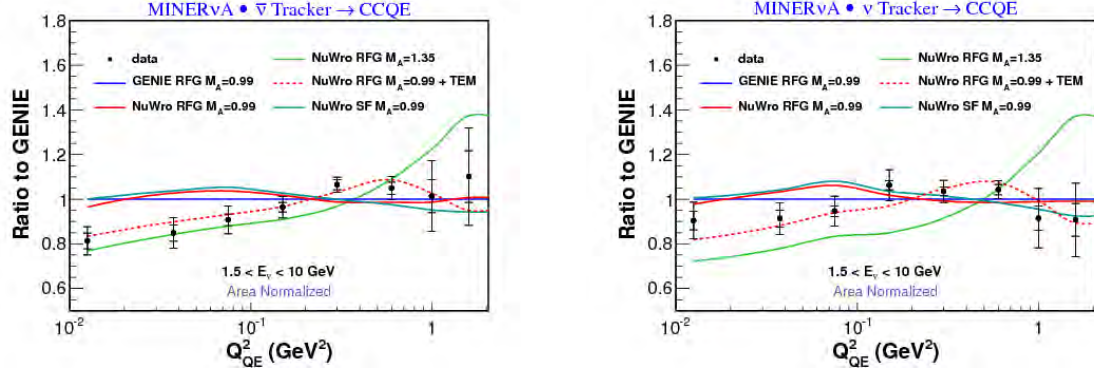


FIG. 1: Left: antineutrino CCQE differential cross-section. Right: neutrino CCQE differential cross section. The events are reconstructed using muon kinematics

$$Q_{QE}^2 = 2E_\nu^{QE}(E_\mu - p_\mu \cos \theta_\mu) - m_\mu^2, \quad (2)$$

where E_μ and p_μ are the muon energy and momentum, θ_μ is the muon angle with respect to the beam and m_n , m_p and m_μ are the masses of the neutron, proton and muon, respectively. A selection has been made on the energy and direction of a tracked proton in order to remove the events modified by the FSI or caused by the non-QE processes and hence, increase the QE purity of the sample.

Figure 1 shows the shape-only measured differential cross section distribution as a ratio to the GENIE [7] 2.6.2 Monte Carlo prediction and compared to various theoretical models and M_A values from the NuWro generator [8]. GENIE uses an RFG model, with $M_A = 0.99$ GeV/ c^2 . Figure 1 also shows the comparison with NuWro generator's RFG models with M_A of 0.99 GeV and 1.35 GeV, as well as with its modeling of nuclear effects using spectral functions (SF) and transverse enhancement (TEM). At high Q^2 , our data disfavor $M_A = 1.35$ GeV/ c^2 as extracted from fits of the MiniBooNE neutrino quasielastic data. There is very little difference if the RFG nuclear model is replaced with a spectral function (SF) model [9]. For both the neutrino and antineutrino cases, the best agreement is obtained using the lower value of $M_A = 0.99$, along with the empirical transverse enhancement model (TEM), motivated by electron-carbon scattering data [10], which gives an indication of the correlation effects in initial state nucleus.

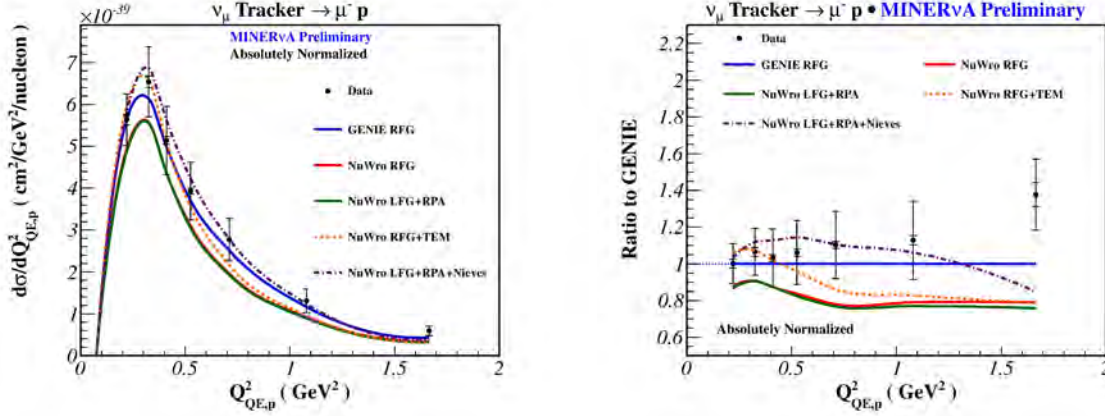


FIG. 2: Neutrino CCQE-like differential cross section. The events are reconstructed using proton kinematics.

CCQE INTERACTION USING PROTON KINEMATICS

The other CCQE analysis [11] presented here uses a sample of CCQE-like events where both the muon and proton are identified. In this analysis, Q^2 is reconstructed using proton kinematics. This eliminates the need for the muon to enter the MINOS detector, which in turn increase angular acceptance. Proton tracks are distinguished from pions by putting a cut on energy deposition rate dE/dx . The events with Michel electrons from the decay of a pion to a muon, which itself decays at rest, are also rejected. The CCQE-like differential cross section as a function of Q_p^2 , along with the prediction from GENIE and NuWro using RFG Model, is shown in Fig. 2 (left panel). Various extensions to the NuWro QE RFG prediction are shown, where each prediction represents the sum over all reactions with at least one proton above 110 MeV and no other hadron in the final state. Figure 2 (right panel) shows the comparison of the shape of $\frac{d\sigma}{dQ_p^2}$ between prediction and data. In contrast to the previous analysis, which favored TEM, this analysis shows closest agreement to the RFG with no other modifications. However, there are several important differences between the two analyses. Unlike the one track analysis, in this case, due to the requirement for a trackable proton with a kinetic energy > 110 MeV, the low Q^2 range is restricted. Also, FSI modeling is important here, as the final state proton may be affected by FSI interaction as mentioned before.

ELECTRON NEUTRINO SCATTERING

Next, I present the results of the direct measurement of the CCQE-like electron neutrino scattering on nucleons in the central tracker region at an average ν_e energy of 3.6 GeV, which is one of the dominant reaction mechanisms at most energies of interest to oscillation experiments [12]. This analysis focuses on a search for CCQE-like events, i.e., events with either an electron or positron, no other leptons or photons, any number of nucleons, and no other hadrons. Candidate events are selected from the data based on three major criteria. First, a candidate must contain a reconstructed cone object of angle 7.5° ; must originate in the fiducial volume, and must be identified as a candidate electromagnetic cascade by a multivariate PID algorithm. Second, electrons and positrons are distinguished from photons by eliminating events in which the energy deposition at the upstream end of the cone is consistent with two particles rather than one. Third, CCQE-like interactions are selected using a classifier called the “extra energy fraction”, Ψ . An event’s visible energy not associated with the electron candidate or a sphere of radius 30 cm centered around the cone vertex is denoted as “extra energy”, defined as:

$$\Psi = \frac{E_{extra}}{E_{electron}} \quad (3)$$

Figure 3 shows the differential ν_e CCQE-like cross sections versus electron energy and angle for both the data and the POT-normalized Monte Carlo samples. The similar distribution in Q_{QE}^2 is presented in Fig. 4 (left panel). The simulation procedure appears to underestimate the width of the electron production angle, thereby exhibiting a harder spectrum in Q_{QE}^2 . However, these differences are reduced after taking into account the Q^2 dependent correlated errors such as the error in the electromagnetic energy scale.

We also compare the measured differential cross section for ν_e and ν_μ on carbon as a function of Q_{QE}^2 , as shown in Fig. 4 (right panel). The data for the differential cross section for ν_e CCQE interactions agree within the errors with that for ν_μ CCQE interactions. Considering the Q^2 dependent correlated errors, the data is consistent with the GENIE prediction within 1σ .

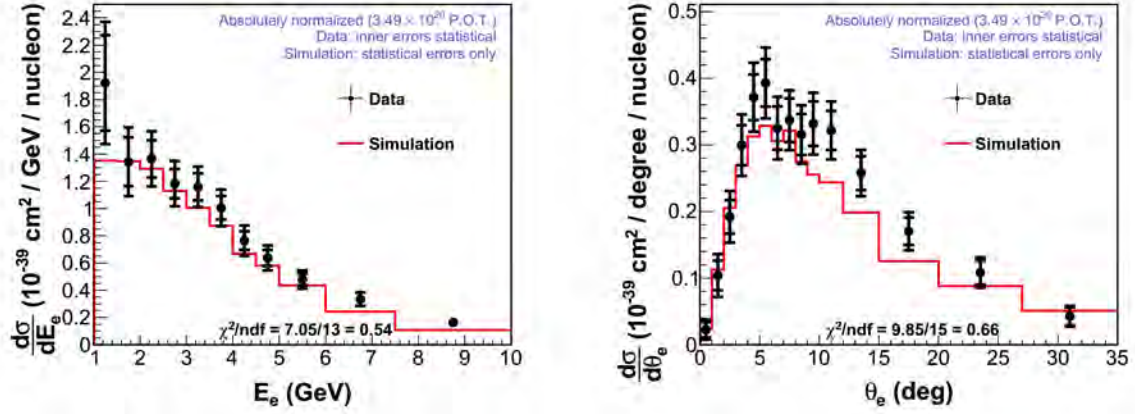


FIG. 3: Left: differential ν_e CCQE-like cross section verses electron energy. Right: differential ν_e CCQE-like cross section verses electron angle.

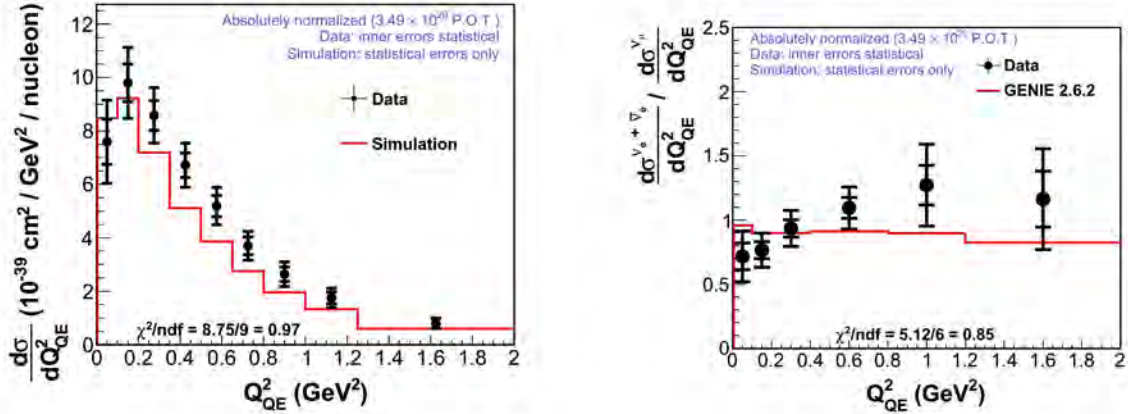


FIG. 4: Left: Differential ν_e CCQE-like cross section verses Q^2_{QE} . Right: ratio of the MINER ν A ν_e CCQE differential cross section as a function of Q^2_{QE} to the analogous result from MINER ν A for ν_μ .

Acknowledgment

This work was supported by the Fermi National Accelerator Laboratory under US Department of Energy contract No. DE-AC02-07CH11359 which included the MINER ν A construction project. Construction support also was granted by the United States National Science Foundation under Award PHY-0619727 and by the University of Rochester. Support for participating scientists was provided by NSF and DOE (USA) by CAPES and CNPq (Brazil), by CoNaCyT (Mexico), by CONICYT (Chile), by CONCYTEC, DGI-PUCP and

IDI/IGI-UNI (Peru), by Latin American Center for Physics (CLAF) and by RAS and the Russian Ministry of Education and Science (Russia). We thank the MINOS Collaboration for use of its near detector data. Finally, we thank the staff of Fermilab for support of the beamline and the detector.

* *Presented at NuFact15, 10-15 Aug 2015, Rio de Janeiro, Brazil [C15-08-10.2]*

† `Anushree@cbpf.br`; Speaker

- [1] L. Aliaga et al. (MINERvA), Nucl. Instrum. Meth. **A743**, 130 (2014), 1305.5199.
- [2] A. Bodek, S. Avvakumov, R. Bradford, and H. Budd, Journal of Physics: Conference Series **110**, 082004 (2008), URL <http://stacks.iop.org/1742-6596/110/i=8/a=082004>.
- [3] K. S. Kuzmin, V. V. Lyubushkin, and V. A. Naumov, Eur. Phys. J. **C54**, 517 (2008), 0712.4384.
- [4] R. A. Smith and E. J. Moniz, Nucl. Phys. **B43**, 605 (1972), [Erratum: Nucl. Phys.B101,547(1975)].
- [5] G. A. Fiorentini et al. (MINERvA), Phys. Rev. Lett. **111**, 022502 (2013), 1305.2243.
- [6] L. Fields et al. (MINERvA), Phys. Rev. Lett. **111**, 022501 (2013), 1305.2234.
- [7] C. Andreopoulos, C. Barry, S. Dytman, H. Gallagher, T. Golan, R. Hatcher, G. Perdue, and J. Yarba (2015), 1510.05494.
- [8] T. Golan, C. Juszczak, and J. T. Sobczyk, Phys. Rev. **C86**, 015505 (2012), 1202.4197.
- [9] O. Benhar, A. Fabrocini, S. Fantoni, and I. Sick, Nucl. Phys. **A579**, 493 (1994).
- [10] A. Bodek, H. S. Budd, and M. E. Christy, Eur. Phys. J. **C71**, 1726 (2011), 1106.0340.
- [11] T. Walton et al. (MINERvA), Phys. Rev. **D91**, 071301 (2015), 1409.4497.
- [12] J. Wolcott et al. (MINERvA) (2015), 1509.05729.

The BONuS Experiment: New Results and Future Plans*

Gail E. Dodge[†]

Old Dominion University

CLAS Collaboration

(Dated: April 13, 2016)

Abstract

Knowledge of both neutron and proton structure functions is necessary in order to determine the valence quark distributions in the nucleon. Measurements on the neutron typically use nuclear targets, but the results are complicated by nuclear binding and nucleon off-shell effects. In the BONuS (Barely Offshell Nucleon Structure) experiment at Jefferson Lab, 4.2 and 5.3 GeV electrons were scattered from a gaseous deuterium target. A Radial Time Projection Chamber (RTPC) was used to detect the low energy spectator protons, thus enabling a cleaner investigation of the neutron. Results for the unpolarized neutron structure function F_2^n , as well as the neutron to proton ratio F_2^n/F_2^p are presented. The range of validity of the spectator model is discussed. These results may be important for neutrino-nucleus scattering experiments in order to understand nuclear background processes. We also report on an investigation of the EMC effect in deuterium.

INTRODUCTION

The behavior of parton distribution functions at high Bjorken x is of great interest to the nuclear and particle physics communities. To focus on just one example, the ratio of d and u quark distributions d/u as $x \rightarrow 1$ depends sensitively on the mechanism by which spin-flavor symmetry is broken [1]. An understanding of both neutron and proton structure is important in order to access the underlying u and d valence quark distributions. The ratio of the unpolarized structure function F_2 for the neutron and proton is sensitive to the d/u ratio at high x via

$$\frac{F_2^n}{F_2^p} = \frac{1 + 4d/u}{4 + d/u}.$$

In order to investigate this ratio, one needs data on both proton and neutron targets. Neutron structure information is also needed for the analysis of neutrino-nucleus scattering experiments, such as MiniBooNE, MINERvA, T2K, ND280, etc.

Unfortunately our access to neutron structure functions is limited by the lack of a free neutron target. Experiments on nuclear targets are plagued by the uncertainty inherent in corrections for off-shell and binding effects, which are especially problematic at large x [2].

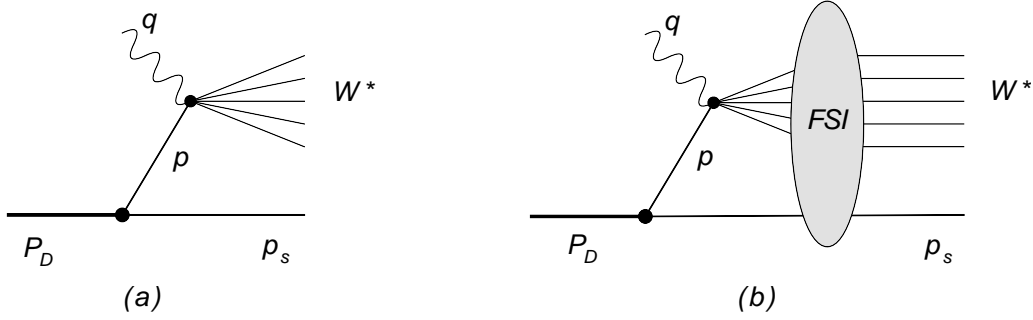


FIG. 1: Schematic of electron scattering from the deuteron, with detection of the spectator proton p_s . Final state interactions are shown in (b) [3].

BONUS EXPERIMENT

To approximate a free neutron target, the BONuS collaboration has successfully used a deuterium target and detected the low energy, recoil proton, which allows us to correct for the initial (Fermi) momentum of the neutron in the deuteron. This spectator tagging technique is illustrated in Fig. 1. Calculations have shown that Final State Interactions (FSI) can be minimized for low momentum spectator protons ($p_s < 100$ MeV/c) recoiling at angles relative to the momentum transfer from the electron, θ_{pq} , greater than 100 degrees [4]. Off-shell effects are similarly negligible for $p_s < 100$ MeV/c [5, 6].

Electrons of energy 2.1, 4.2 and 5.3 GeV were scattered from a 7 atm D_2 target of length 20 cm in Hall B at Jefferson Lab and detected in the CEBAF Large Acceptance Spectrometer (CLAS) [7]. The target was surrounded by a Radial Time Projection Chamber (RTPC) [8], which was designed to minimize the material through which low energy protons had to travel. A schematic of the RTPC is shown in Fig. 2. A longitudinal magnetic field of 3.5 and 4.7 Tesla was provided by a solenoid surrounding the RTPC and enabled the proton momenta to be determined from the radius of curvature of their trajectory. Ionization electrons produced by the proton drifted to the first of three layers of Gaseous Electron Multiplier (GEM) foils at a radius of 6 cm. The electrical signal was amplified in the three layers of GEM foils and then detected on readout pads, which recorded the amplitude of the signal in 114 ns bins. The maximum drift time was about 6 μ s.

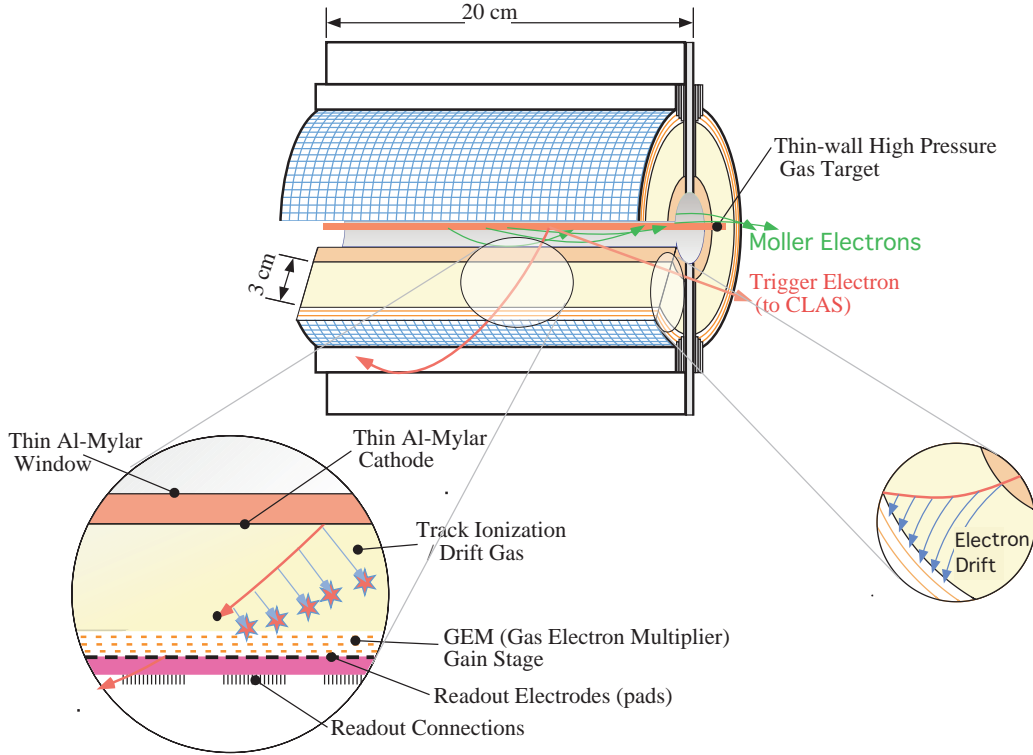


FIG. 2: Schematic of the Radial Time Projection Chamber, which includes three layers of GEM detectors [3].

DATA ANALYSIS

The power of the spectator tagging technique can be seen in Fig. 3, which shows the nucleon resonance region plotted as a function of the invariant mass, W , of the virtual photon plus nucleon (black symbols), which assumes a free nucleon target and is calculated entirely from the initial and scattered electron. If one uses the spectator proton kinematics in order to calculate the true neutron momentum in the deuteron, one finds an invariant mass distribution, W^* (red symbols) that is closer to that of the free proton. In this case, the Fermi momentum of the neutron in the deuteron is properly taken into account. The BONuS data were analyzed in two ways. First a set of Very Important Proton (VIP) events were defined to include protons with momenta less than 100 MeV/c and scattering angles θ_{pq} greater than 100 degrees. These VIP events are ones in which Final State Interactions and other nuclear effects are minimized, as described above. For these events the ratio of tagged to inclusive scattering events was calculated as a function of the various kinematic

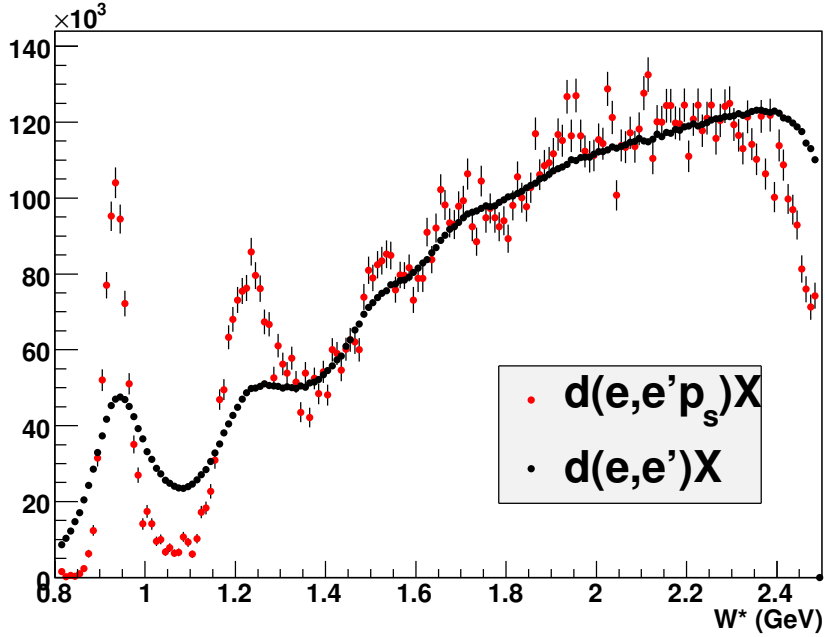


FIG. 3: W^* for inclusive electron scattering on the deuteron (black) and semi-inclusive [9].

variables. After corrections to account for background differences and a single normalization factor determined from a new parametrization of world data by Christy *et al.* [10–12] we found F_2^n/F_2^d . Some of the 5.3 GeV data are shown in Fig. 4 in bins of momentum transfer Q^2 .

A second approach was to use all tagged data (*i.e.* not only the VIP events), and divide by data simulated using the spectator model in every kinematic bin. The resulting ratio, known as $R_{D/S}$, deviates from 1 in bins where the data do not match the Monte Carlo prediction and is therefore an indication of the range of validity of the spectator model. Multiplying by the spectator model for F_2^n results in a model dependent result for the neutron structure function, called $F_2^{n,eff}$. The systematic errors in the two methods of analyzing the data are different, but the results are very similar [3]. Fig. 5 shows an example of the ratio $R_{D/S}$ as a function of θ_{pq} for various ranges in spectator momentum. In general the data are consistent with the spectator model for low proton momenta and backward angles, although there is some deviation even for the 2nd lowest momentum bin. Detailed results from the BONuS experiment can be used to test FSI calculations (see, e.g., Ref. [13]).

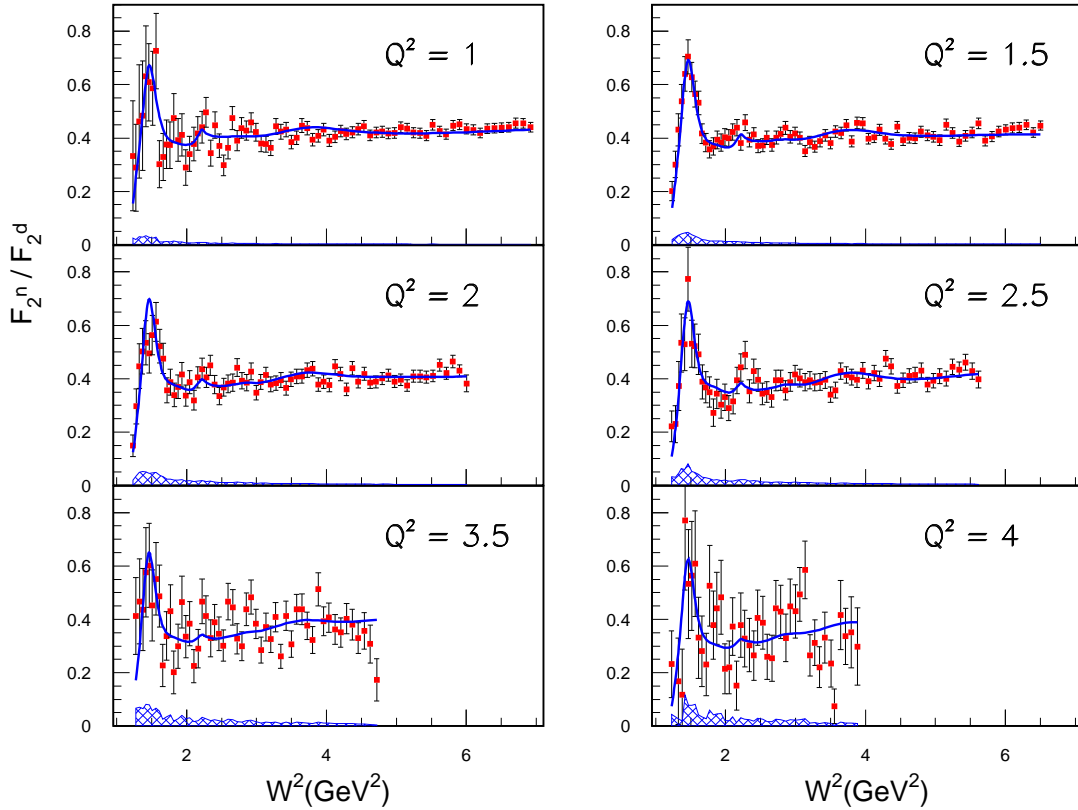


FIG. 4: Ratio of F_2^n to F_2^d for 5.3 GeV data in bins of Q^2 . Results are only for VIP events (see text for details) [3]. The curve is a new parametrization of world data by Christy *et al.*, [12], which was used to normalize the data. The blue hatched band represents the point-to-point systematic uncertainty.

RESULTS

To extract the neutron structure function F_2^n we start with the ratio of tagged to untagged VIP events, as described above (see, e.g., Fig. 4). We multiply these ratios by F_2^d as determined by a new fit to world data from Christy *et al.* [12], which does not include the BONuS data. The resulting values for F_2^n are model dependent, mainly via the normalization factor that comes from the world parametrization. Fig. 6 shows the final result for both the 4.2 and 5.3 GeV data, together with the Christy fit to world data. One can see that the world data parametrization describes the data well, but that it averages out the resonances somewhat, because the fit is based on deuteron data.

Finally, we can take our result for F_2^n/F_2^d and calculate F_2^n/F_2^p using world data for F_2^d

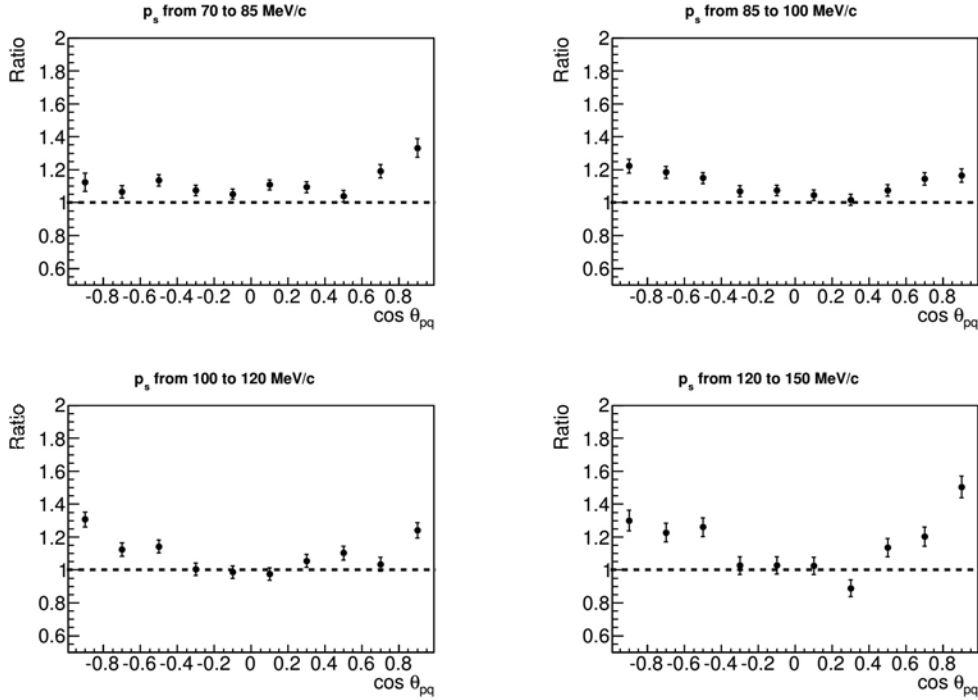


FIG. 5: Ratio of tagged events to events simulated in the spectator model as a function of θ_{pq} for various ranges of spectator proton momentum. These data are for one Q^2 bin ($1.10 - 2.23 \text{ GeV}^2/c^2$) and one W^* bin ($1.35 - 1.6 \text{ GeV}/c^2$). Systematic uncertainties are shown by the shaded band [3].

and F_2^p in deep inelastic scattering (DIS) kinematics to investigate the behavior of u/d as x approaches 1. Our result is shown in Fig. 7. The highest x accessible to our data depends on the lower limit of W^* that is included, but for the safest integration limit our ratio only goes out to $x \approx 0.6$. Data at higher beam energy is needed, and we are now preparing a new BONuS experiment that will use the upgraded beam energy at Jefferson Lab [14].

Another interesting topic that can be investigated with the BONuS data is the possibility of measuring an EMC effect in deuterium [15]. The EMC effect refers to the deviation from 1 of the ratio of the F_2 structure function for a nucleus compared to “free” nucleons, usually taken as F_2^d . The slope of the ratio between $x = 0.3$ and 0.7 is often taken as indicative of the size of the EMC effect in a nucleus. But what about the deuteron itself? One can construct the ratio of F_2^d to the sum of F_2 for the proton and neutron, as shown in Fig. 8. There is a noticeable slope to the ratio, which is consistent with the calculation by Kulagin and Petti [16]. The EMC slope in the deuteron is consistent with the trend that relates the

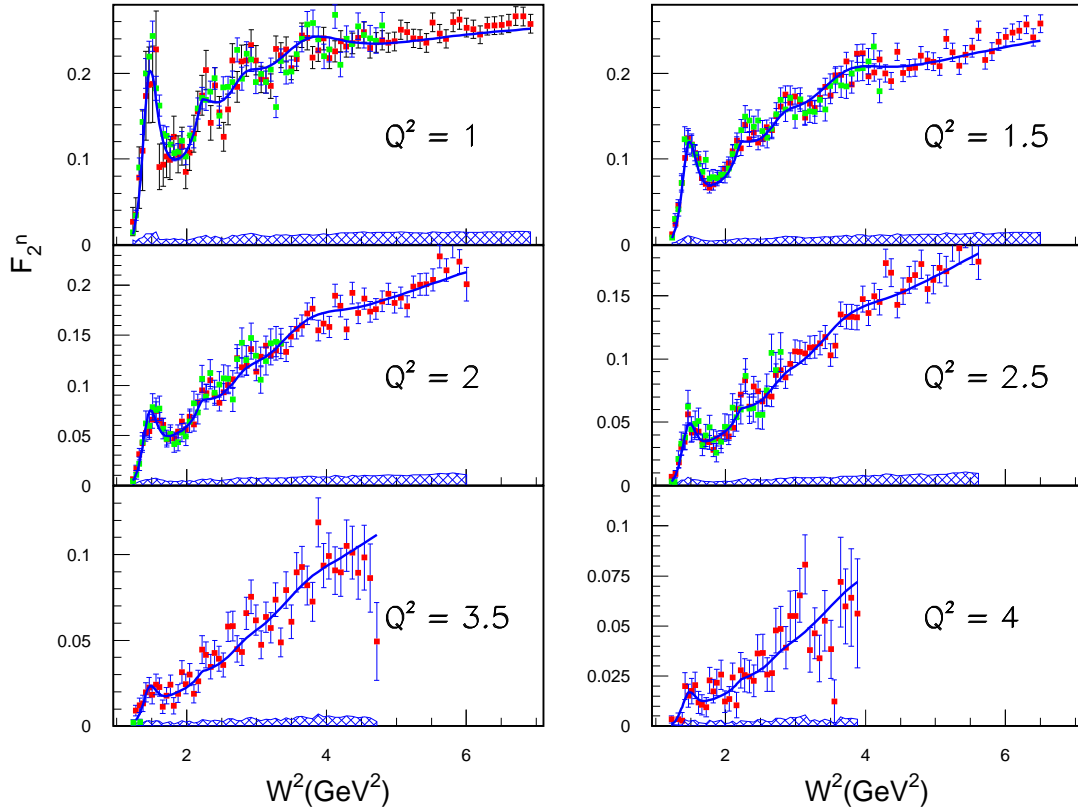


FIG. 6: BONUS result for F_2^n extracted for VIP events (see text). The curve is a new parametrization of world data by Christy *et al.*, [12], which does not include the BONUS data. Results for a beam energy of 4.2 GeV (5.3 GeV) are shown in green (red). The blue hatched band shows the systematic uncertainty for the 5.3 GeV data. The size of the systematic uncertainty for the 4.2 GeV data is similar.

size of the EMC effect to the probability of short range correlations in a nucleus [15, 17].

SUMMARY

In the BONUS experiment at Jefferson Lab 4.2 and 5.3 GeV electrons were scattered off of a gaseous deuterium target. Detection of the low energy recoiling protons in the RTPC enabled us to tag events in which the electron scattered from the neutron in the deuteron. At low spectator momenta and backward angles the events are relatively free from final state and other nuclear effects, which makes it possible to extract the structure function of the neutron F_2^n over a wide kinematic range. These results are useful for understanding

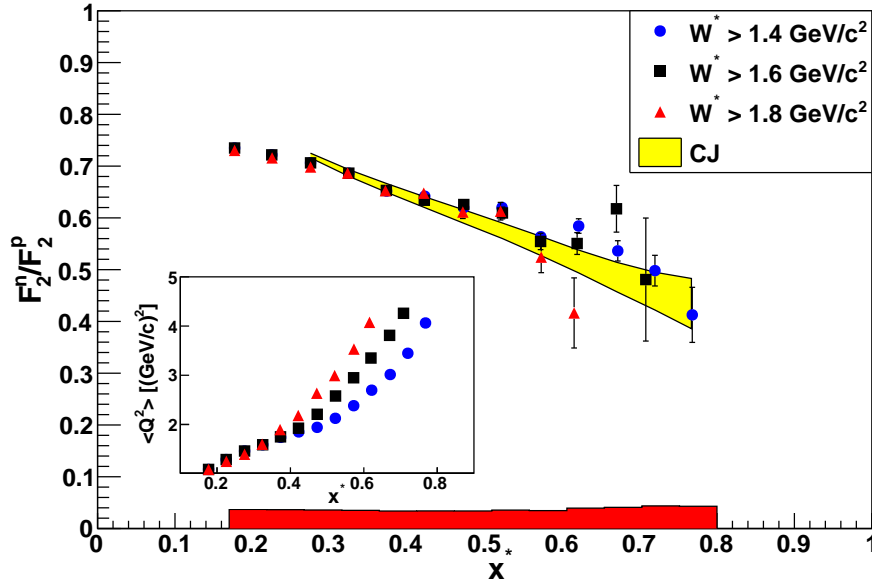


FIG. 7: Ratio of F_2^n/F_2^p as a function of Bjorken x for various integration limits in W^* [3]. The red band indicates the systematic uncertainty. The global parton distribution function fit by Accardi *et al.* [2] is shown as the yellow band.

background events in neutrino-nucleus scattering experiments, and for studying the behavior of the quark distributions d/u at large Bjorken x .

* Presented at NuFact15, 10-15 Aug 2015, Rio de Janeiro, Brazil [C15-08-10.2]

† gdodge@odu.edu; Supported by DOE grant DE-FG02-96ER40960

- [1] W. Melnitchouk and A. W. Thomas, Phys. Lett. **B377**, 11 (1996), nucl-th/9602038.
- [2] A. Accardi, W. Melnitchouk, J. Owens, M. Christy, C. Keppel, L. Zhu, and J. Morfin, Phys. Rev. D **84**, 014008 (2011), 1102.3686.
- [3] S. Tkachenko, N. Baillie, S. Kuhn, et al., Phys. Rev. C **89**, 045206 (2014), ISSN 0556-2813.
- [4] C. Ciofi degli Atti, L. P. Kaptari, and B. Z. Kopeliovich, Eur. Phys. J. **A19**, 145 (2004), nucl-th/0307052.
- [5] W. Melnitchouk, A. W. Schreiber, and A. W. Thomas, Phys. Lett. **B335**, 11 (1994).
- [6] W. Melnitchouk, A. W. Schreiber, and A. W. Thomas, Phys. Rev. **D49**, 1183 (1994).

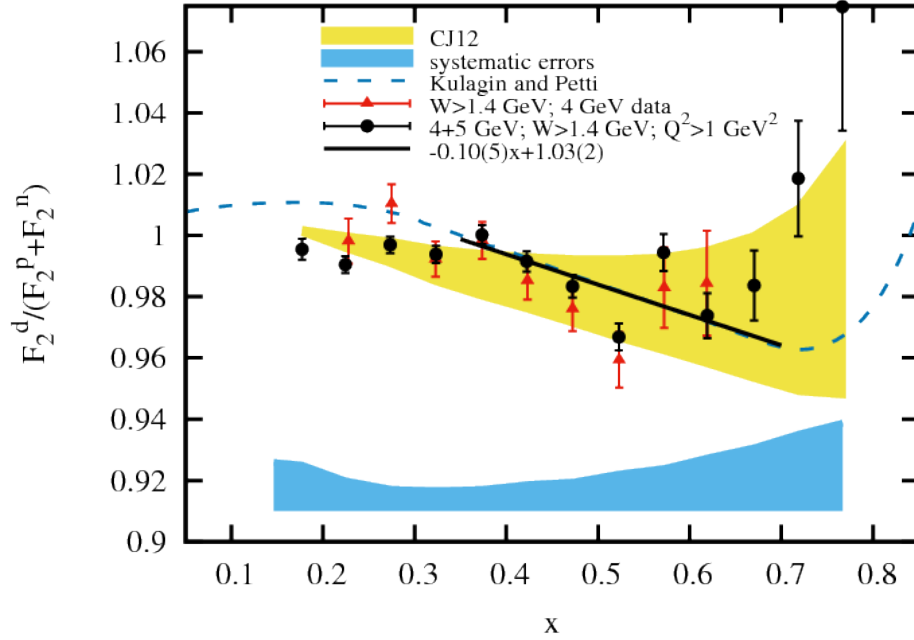


FIG. 8: Ratio of F_2^d to the sum of F_2 for the proton and neutron [15]. The black circles include the 4.2 and 5.3 GeV data. The red triangles are the 4.2 GeV data only. The systematic errors are shown by the blue band. The yellow band represents the range of predictions arising from global fits that use three different nuclear models for deuteron data [18].

- [7] B. Mecking et al., Nucl. Instrum. Meth. **A503**, 513 (2003).
- [8] H. C. Fenker et al., Nucl. Instrum. Meth. **A592**, 273 (2008).
- [9] N. Baillie et al. (CLAS Collaboration), Phys. Rev. Lett. **108**, 199902 (2012), 1110.2770.
- [10] P. E. Bosted and M. E. Christy, Phys. Rev. **C77**, 065206 (2008), 0711.0159.
- [11] M. E. Christy and P. E. Bosted, Phys. Rev. **C81**, 055213 (2010), 0712.3731.
- [12] M. E. Christy, N. Kalantarians, J. J. Ethier, and W. Melnitchouk, in preparation.
- [13] W. Cosyn, W. Melnitchouk, and M. Sargsian, Phys. Rev. **C89**, 014612 (2014), 1311.3550.
- [14] M. Amarian et al., Jefferson Lab Experiment **E12-06-113** (2006).
- [15] K. A. Griffioen et al., Phys. Rev. **C92**, 015211 (2015), 1506.00871.
- [16] S. A. Kulagin and R. Petti, Nucl. Phys. **A765**, 126 (2006), hep-ph/0412425.
- [17] O. Hen, D. W. Higinbotham, G. A. Miller, E. Piasetzky, and L. B. Weinstein, Int. J. Mod. Phys. **E22**, 1330017 (2013), 1304.2813.
- [18] J. F. Owens, A. Accardi, and W. Melnitchouk, Phys. Rev. **D87**, 094012 (2013), 1212.1702.

CC0 π Results From T2K*

Andrew P. Furmanski for the T2K collaboration[†]

University of Warwick and

University of Manchester

(Dated: March 23, 2016)

Abstract

Preliminary CCQE, and CCQE-like measurements from T2K detectors are presented. First, an energy-dependent CCQE measurement on-axis is presented, using the INGRID detector. Secondly, the first model-independent double differential (p_μ, θ_μ) CC0 π measurement using the off-axis detector is presented.

INTRODUCTION

T2K is a long baseline neutrino oscillation experiment based in Japan [1]. Using the main ring accelerator at J-PARC, a neutrino beam with a peak energy around 1.5 GeV is produced. By placing detectors slightly off axis from this beam, they are exposed to a narrow-band flux with a peak energy of 0.6 GeV. The primary goal of T2K, after its measurement of electron neutrino appearance, is to search for anti-electron neutrino appearance, to search for CP violation. Observing a difference in the neutrino and anti-neutrino appearance probabilities would be evidence for CP violation. Charged Current (CC) neutrino interactions on nuclei are used to search for these oscillations at T2K, as well as all other current and planned experiments. Understanding these interactions is crucial for precision measurements of neutrino oscillations. Of particular importance for T2K is the interaction channel where only the lepton is observed at the far detector. The latest measurements in this channel are presented, including measurements in both the T2K on-axis flux and off-axis flux.

THE T2K EXPERIMENT

The T2K beam

T2K utilises an off-axis narrow band beam with a peak energy of around 0.6 GeV. The flux prediction is based on a FLUKA/GEANT3 simulation which has been tuned to NA61/SHINE hadron production measurements. Figure 1 shows the off-axis flux prediction at the near detector. For more detailed information see [2].

T2K near detector suite

The T2K near detector suite is positioned 280 m downstream of the production target. It consists of two detectors, one on-axis and one off-axis, providing a number of different nuclear targets in different neutrino fluxes. The on-axis detector - Interactive Neutrino GRID (INGRID) - is constructed in a large cross shape from 14 identical modules, each built from alternating planes of steel and plastic scintillator. An additional module, the proton module, consists of only scintillator bars, with a finer grained bar used in the central part of the module. This module sits on-axis, between the vertical and horizontal sets of regular modules, and is used as the target in the on-axis measurement described here. The off-axis detector, known simply as ND280, utilises multiple subdetectors and detector technologies. The detector can be broadly divided into the pi-zero detector (P0D), and tracker regions, all of which is surrounded by electromagnetic calorimeters, and placed in the refurbished UA1/NOMAD magnet which provides a 0.2T magnetic field. The tracker region, which is used for the off-axis analyses described here, is formed from a “sandwich” of three argon gas-filled Time Projection Chambers (TPCs) and two plastic scintillator Fine-Grained Detectors (FGDs). The TPCs provide precise measurement of track curvature and dE/dx to provide momentum measurements, charge identification, and PID. Figure 2 shows schematics of the near detectors.

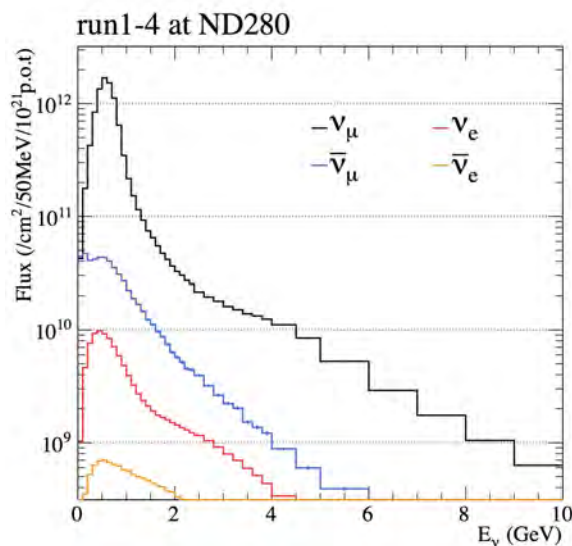


FIG. 1: The flux prediction, separated by neutrino flavour, 2.5° off axis at 280 m.

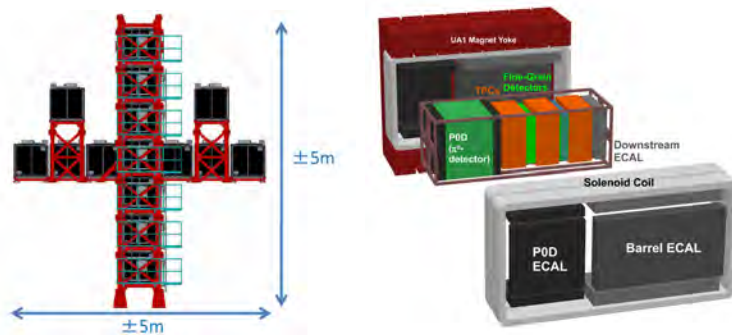


FIG. 2: A schematic of (left) the INGRID detector and (right) the ND280 detector. The INGRID proton module is placed at the centre, between the horizontal and vertical sets of modules.

ON-AXIS CCQE MEASUREMENT

Strategy

This measurement is able to utilise the wide-band nature of the on-axis beam to measure an energy-dependent cross section. The INGRID on axis beam peaks at 1 GeV in the INGRID center modules and decreases 200 MeV at the edge modules [3]. High energy and low energy events are selected using kinematic and topological cuts, and the samples are further divided into “one-track” and “two-track” topologies. The cross section is reported in both the high-energy and low-energy region separately, for the one-track, two-track, and combined samples (which is the sum of both one- and two-track samples). The analysis is described in detail in [4].

Results

Figure 3 shows the resulting cross sections compared with other recent CCQE measurements from MiniBooNE, MINER ν A, NOMAD, and SciBooNE.

By placing kinematic cuts on the data it is understood that model-dependence is introduced. In particular alternate nuclear models affect the muon angular and momentum spectrum, leading to potentially large changes in efficiency from these kinematic cuts. In addition, considering potential MEC events as a background leads to a change in the extracted cross section, meaning that this analysis is not able to distinguish between models that include these effects and those that don't. Nevertheless, the large difference between

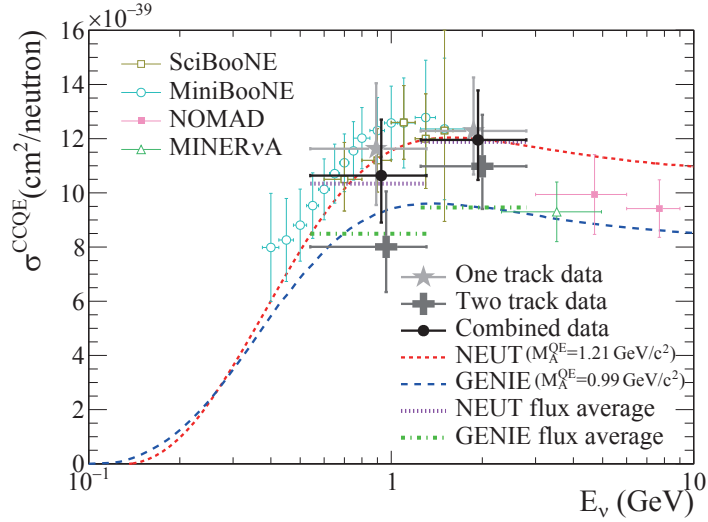


FIG. 3: Results from the INGRID analysis. Data points are slightly offset in energy for clarity. Also shown are the predictions from both NEUT and GENIE [5], measurements from MiniBooNE, SciBooNE, NOMAD, and MINERvA.

the cross sections extracted from the one-track and two-track samples in the low energy region is interesting.

OFF-AXIS DOUBLE DIFFERENTIAL CROSS SECTION MEASUREMENT

Strategy

The off-axis strategy revolves around making measurements that are as independent of the signal model as possible. This means there are no kinematic cuts placed, and the cross section is measured as a function of detector variables (in this case the muon momentum and angle). It also means that the signal is defined in an unambiguous way, in terms of the final-state topology rather than the underlying interaction type. In this case, the topology is denoted “CC0 π ”, and is defined as the presence of a muon, and any number of nucleons but no other hadronic particles. The measurement is a flux-integrated measurement, leading to minimal dependence on the flux model.

An additional measure taken to ensure model-independence is to perform two separate analyses to serve as cross checks of each other. These two analyses utilise different selections, different cross section extraction methods, and different methods of constraining the

backgrounds. They are referred to as “Analysis I” and “Analysis II”.

Event Selections

Pre-selection

Both analyses start by selecting the highest momentum negative track that starts in the first FGD fiducial volume. The track is required to be within the beam spill in time and have more than 18 TPC hits to ensure good quality. This track is the muon candidate, and is required to be muon-like according to dE/dx measurements in the TPC. Additional cuts are then used to reject broken tracks and entering backgrounds.

Analysis I

After the pre-selection, Analysis I counts proton-like tracks and divides the selection into four categories.

- **Selection 1:** one-track events, with a muon in the TPC.
- **Selection 2:** two-track events, with a muon and a single proton in the TPC.
- **Selection 3:** two-track events, with a muon in the TPC and a positive track contained in the FGD.
- **Selection 4:** two-track events, with a proton in the TPC and a negative track in the FGD (which can reach the ECal and SMRD).

In addition, two additional selections are defined to constrain single-pion and multi-pion events which form the largest backgrounds. This is the first measurement from ND280 which has some acceptance at angles above 90 degrees, due to region 4 where the muon can be backwards-going.

Analysis II

After the pre-selection, Analysis II is designed to veto final state pions by searching for pion-like tracks in the TPC and FGD, delayed decay electrons in the FGD, and electron-like

tracks in the TPC which could come from a neutral pion decay photon conversion. The remaining background from misreconstructed pions is constrained by fits to external data sets from MiniBooNE and MINER ν A. This selection is fully proton-inclusive, so events with two detectable final-state protons (from MEC processes, for example) will be included. It does suffer from higher backgrounds than the selection in Analysis I, however it benefits from a higher efficiency.

Cross Section Extraction

In Analysis I, the $CC0\pi$ cross section is extracted by performing a maximum likelihood fit to the observed data as a function of muon kinematics. The fit is performed simultaneously over the signal and background samples.

Analysis II performs a simple subtraction of the expected background, and then relies on a Bayesian unfolding procedure to correct the reconstructed muon kinematic distributions for detector smearing and inefficiencies.

Results

The double differential results for Analysis I are shown in figure 4, compared with two theoretical predictions [6, 7]. In figure 5, the results from both analyses are compared in four bins in true $\cos\theta_\mu$ between 0.6 and 0.9. A very high level of agreement is found, giving confidence in the model-independence of the results.

The total integrated cross section is measured to be:

$$\sigma_{analysisI} = (4.17 \pm 0.47(syst) \pm 0.05(stat)) \times 10^{-39} \text{cm}^2 \text{nucleon}^{-1} \quad (1)$$

which is comparable to the NEUT [8] prediction of $4.39 \times 10^{-39} \text{cm}^2 \text{nucleon}^{-1}$. The result from Analysis II is in very good agreement.

Analysis II does not reconstruct backwards tracks due to the simple selection criteria. For this analysis the efficiency is above 50% only for muons where $\cos\theta_\mu < 0.6$ and $p_\mu > 0.2$. When integrating the cross section only over this high-efficiency region, the restricted phase space (rps) cross section is measured to be:

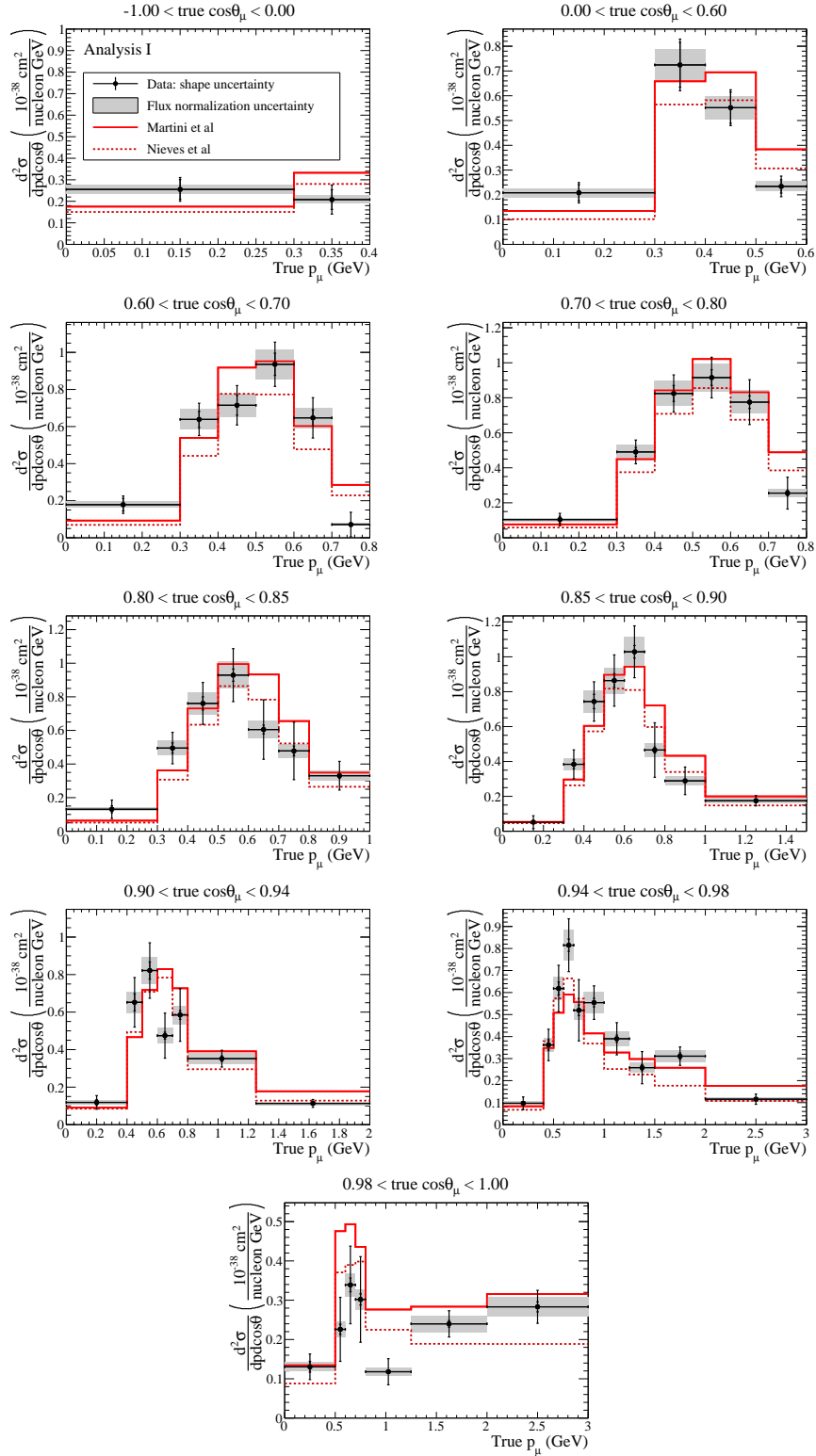


FIG. 4: The preliminary double differential $CC0\pi$ cross section results from Analysis I, shown as a function of momentum for each angular slice. The grey band indicates the fully correlated flux normalisation uncertainty, whilst the inner error bars show the statistical uncertainty and the full error bars show the full statistical and systematic uncertainty (excluding the flux normalisation uncertainty). The results are compared to predictions from the Nieves model [6] (red dashed) and the Martini model [7] (red solid).

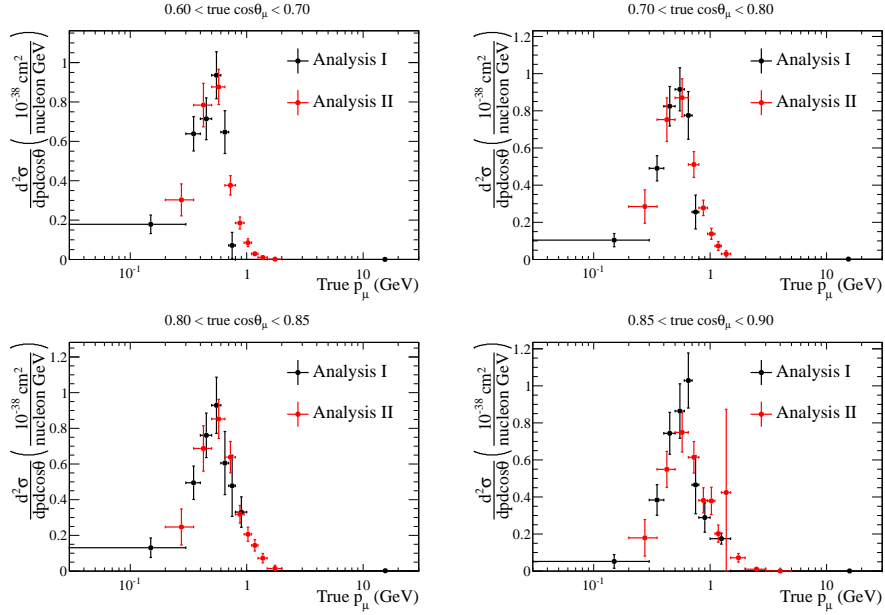


FIG. 5: Analysis I and Analysis II preliminary double differential results compared, in the angular region $0.6 < \cos \theta_\mu < 0.9$. Very good agreement is observed across all bins.

$$\sigma_{rps} = (0.202 \pm 0.0359(\text{syst}) \pm 0.0026(\text{stat})) \times 10^{-38} \text{cm}^2 \text{nucleon}^{-1} \quad (2)$$

which is also comparable to the NEUT prediction of $0.232 \times 10^{-39} \text{cm}^2 \text{nucleon}^{-1}$.

The consistency of the two results is a very good indicator of the model-independence of the results. Furthermore fake data studies for Analysis II have shown that assuming a drastically different prior model for the signal had minimal effect on the result. The results also show some interesting differences when compared to predictions.

CONCLUSIONS

Preliminary T2K results have been presented. They include the ν_μ CCQE cross section on carbon at two different energies using the on-axis near detector. This measurement was performed for one-track events, two-track events, and the combined sample. Interestingly the two-track result is significantly lower than the one-track event. T2K has also measured the double-differential ν_μ CC0 π cross section on carbon as a function of muon momentum and angle using the off-axis near detector. This result is the first model-independent topology-based cross section measurement from T2K, and further work will lead to results which

include information about the hadronic side of the interaction through proton measurements too.

* *Presented at NuFact15, 10-15 Aug 2015, Rio de Janeiro, Brazil [C15-08-10.2]*

† `andrew.furmanski@manchester.ac.uk`; Speaker

- [1] K. Abe et al. (T2K Collaboration) , Nucl. Inst. & Meth. **659**, 106 (2011).
- [2] K. Abe et al. (T2K Collaboration), Phys.Rev. **D87**, 012001 (2013), 1211.0469.
- [3] K. A. et al., Nucl. Instrum. Meth. **A 694**, 211 (2012), ISSN 0168-9002, URL <http://www.sciencedirect.com/science/article/pii/S0168900212002987>.
- [4] K. Abe et al. (T2K Collaboration), Phys.Rev. **D91**, 112002 (2015), 1503.07452.
- [5] C. Andreopoulos et al., Nucl. Instrum. Meth. **A 614**, 87 (2010), 0905.2517.
- [6] J. Nieves, I. R. Simo, and M. J. V. Vacas, Phys. Rev. C **83**, 045501 (2011), URL <http://link.aps.org/doi/10.1103/PhysRevC.83.045501>.
- [7] M. Martini, M. Ericson, G. Chanfray, and J. Marteau, Phys. Rev. C **80**, 065501 (2009), URL <http://link.aps.org/doi/10.1103/PhysRevC.80.065501>.
- [8] Y. Hayato, Nuclear Physics B - Proceedings Supplements **112**, 171 (2002), ISSN 0920-5632, URL <http://www.sciencedirect.com/science/article/pii/S0920563202017590>.

**Relativistic description of meson-exchange currents and
SuperScaling predictions in charged-current neutrino reactions***

Guillermo D. Megias[†] and Juan A. Caballero

*Departamento de Física Atómica, Molecular y Nuclear,
Universidad de Sevilla, 41080 Sevilla, SPAIN*

Jose E. Amaro

*Departamento de Física Atómica, Molecular y Nuclear and
Instituto Carlos I de Física Teórica y Computacional,
Universidad de Granada, 18071 Granada, SPAIN*

Maria B. Barbaro

*Dipartimento di Fisica, Università di Torino,
Sezione di Torino, Via P. Giuria 1, 10125 Torino, ITALY*

T. William Donnelly

*Center for Theoretical Physics, Laboratory for Nuclear Science and Department of Physics,
Massachusetts Institute of Technology,
Cambridge, Massachusetts 02139, USA*

(Dated: March 22, 2016)

Abstract

We present our recent progress on the relativistic modeling of neutrino-nucleus reactions [1–6] and comparisons with high precision experimental data in a wide energy range (0-100 GeV). We compare charged-current quasielastic (CCQE) neutrino and antineutrino cross sections obtained within the phenomenological SuperScaling Approach [7, 8] (SuSA model) which is based on the analysis of electron-nucleus scattering data and has been recently improved with the inclusion of Relativistic Mean Field theory effects (SuSAv2 model [1]). We also evaluate and discuss the impact of meson-exchange currents (2p-2h MEC) on lepton-nucleus interactions through the analysis of two-particle two-hole axial and vector contributions to electroweak response functions in a fully relativistic Fermi gas [5, 9, 10]. Finally, our model is extended beyond the QE nuclear regime by including effects such as Δ contributions [6] associated to the pion production region (i.e. nucleonic resonances) and Deep Inelastic Scattering processes (DIS) where quarks and gluons degrees of freedom are relevant for describing the nuclear structure.

A correct interpretation of current neutrino oscillation experiments strongly relies on our understanding of neutrino-nucleus scattering at intermediate energies (from 0.5 to 10 GeV) and in particular of the nuclear-structure effects involved. One of the simplest descriptions of the nucleus, the relativistic Fermi gas (RFG) model, which is known to be inadequate for inclusive electron scattering in the QE regime, also fails to reproduce recent measurements of QE neutrino and antineutrino scattering cross sections [11–15]. This supports the need for considering mechanisms such as final-state interactions, nuclear correlations or MEC [5, 9, 10, 16, 17].

In this sense, we apply a semi-phenomenological model to describe the QE regime, which is called the superscaling approach (SuSA) [7, 8]. It assumes the existence of universal scaling functions for electromagnetic and weak interactions. Analyses of inclusive (e, e') data have shown that at energy transfers below the QE peak, superscaling is fulfilled rather well [7, 8], which implies that the reduced cross section is largely independent of the momentum transfer (first-kind scaling) and of the nuclear target (second-kind scaling) when expressed as a function of the appropriate scaling variable (ψ). From these analyses a phenomenological scaling function, $f(\psi)$, was extracted from the longitudinal QE electron scattering responses,

and subsequently used to predict neutrino-nucleus cross sections by multiplying it by the single-nucleon weak cross sections. In this work, we employ a recent improved version of the superscaling model, called SuSAv2 [1], that incorporates relativistic mean field (RMF) effects [18–20] in the longitudinal and transverse nuclear responses, as well as in the isovector and isoscalar channels independently. This model also includes in a natural way an enhancement of the transverse response through RMF effects without resorting to inelastic processes or two-particle emission via MEC.

The QE muon neutrino and antineutrino cross sections measured by the MiniBooNE experiment [11, 12], where QE events are characterized by the absence of pions in the final state, have triggered a lot of theoretical work trying to explain the unexpectedly large results, in apparent tension with the higher-energy data from the NOMAD experiment [13]. Several calculations [5, 9, 10, 16, 17] have demonstrated that 2p2h excitations induced by two-body meson-exchange currents (MEC) play a significant role in the interpretation of the QE MiniBooNE data and in the neutrino energy reconstruction, which is therefore model dependent.

In our description [9, 10], this 2p-2h effect includes all the direct-exchange interference terms as well as the vector and axial components arising from the weak current in a fully relativistic way without further approximations. As shown in Fig. 1, our 2p2h MEC predictions are larger in the transverse channel (T and T' components) than in the longitudinal one (CC , CL and LL terms). Moreover, the results displayed in Figs. 2 and 3 show the relevance of the axial and vector transverse MEC responses, where the axial-axial (T_{AA}) contribution is more significant at low momentum transfer (q) than the vector-vector (T_{VV}) one, in contrast to what is observed at higher q values.

In the QE region, the superscaling predictions have been successfully compared with the recent MINER ν A data [14, 15], that have been shown in [1, 2] to be well reproduced without need of invoking large 2p2h contributions. Good agreement is also obtained with the high-energy NOMAD data [13] (see Fig. 4). On the contrary, the MiniBooNE QE data [11, 12] are underpredicted by the model. The inclusion of 2p2h MEC excitations in both vector and axial channels, evaluated using the model of [9, 10], gives results which are in agreement with the MiniBooNE experimental points in both neutrino and antineutrino cases (See Figs. 4 and 5).

Furthermore, an analysis of the relevant kinematic regions in the QE $\nu_\mu - {}^{12}\text{C}$ total cross

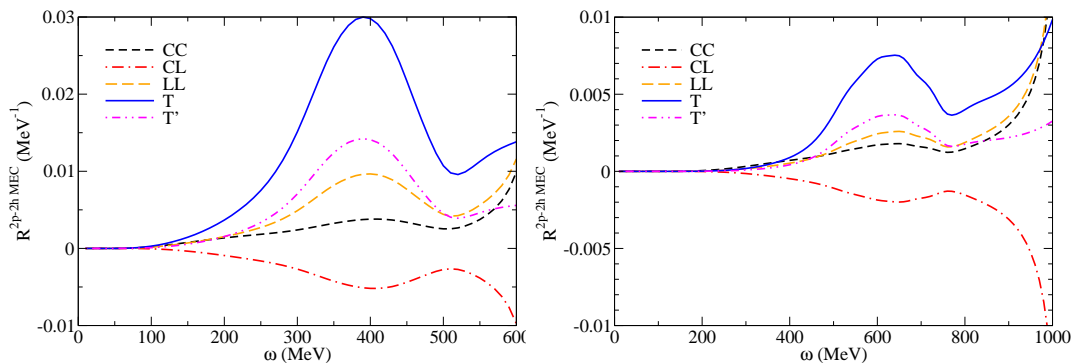


FIG. 1: (Color online) Comparison between the different components (CC, CL, LL, T and T') of the 2p-2h MEC response at different fixed values of the momentum transferred ($q=600 \text{ MeV}/c$ [left panel], $q=1000 \text{ MeV}/c$ [right panel]).

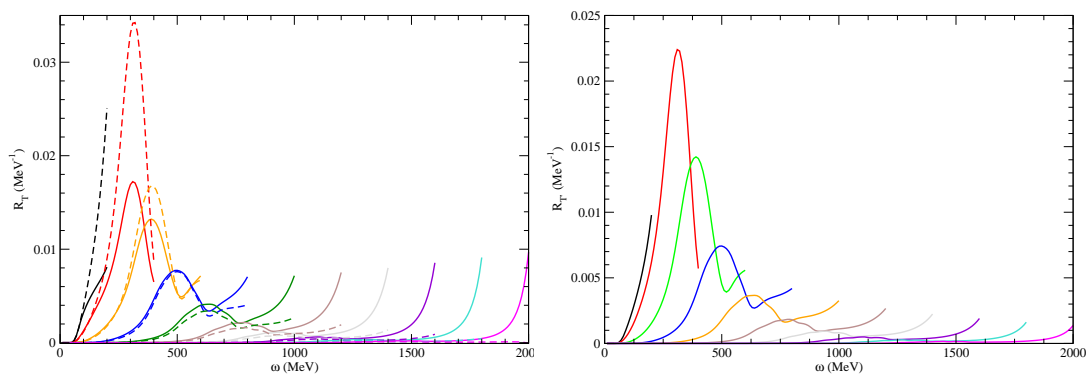


FIG. 2: (Color online) 2p-2h MEC transverse responses in terms of the energy transferred (ω) at different fixed values of the momentum transferred (q) from $q=200 \text{ MeV}/c$ to $q=2000 \text{ MeV}/c$ in steps of $200 \text{ MeV}/c$ (from left to right). Left panel shows the vector-vector (solid lines) and axial-axial (dashed lines) responses whereas the right panel shows the interference vector-axial ones.

section is shown in Fig. 6, where it is observed that the main contribution to the total cross section comes from $\omega < 1000 \text{ MeV}$ and $q < 1000 \text{ MeV}/c$, even at high neutrino energies. The same conclusion can be drawn by analyzing the different kinematics in the total MEC cross section (Fig. 7), although the relevant kinematic region is enlarged slightly to higher kinematics.

The superscaling approach has also been extended from the QE domain into the region where the Δ -excitation dominates. It has been shown [6] that the residual strength in the

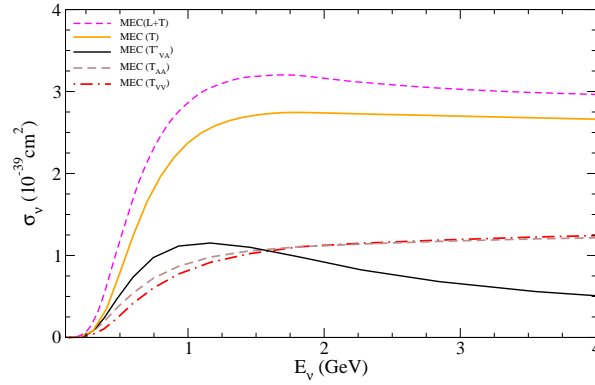


FIG. 3: (Color online) Separation into longitudinal and transverse terms of the total MEC ν_μ - ^{12}C cross section per nucleon displayed versus neutrino energy E_ν . The different components (vector-vector (VV), axial-axial (AA) and vector-axial (VA)) of the transverse MEC response are also shown.

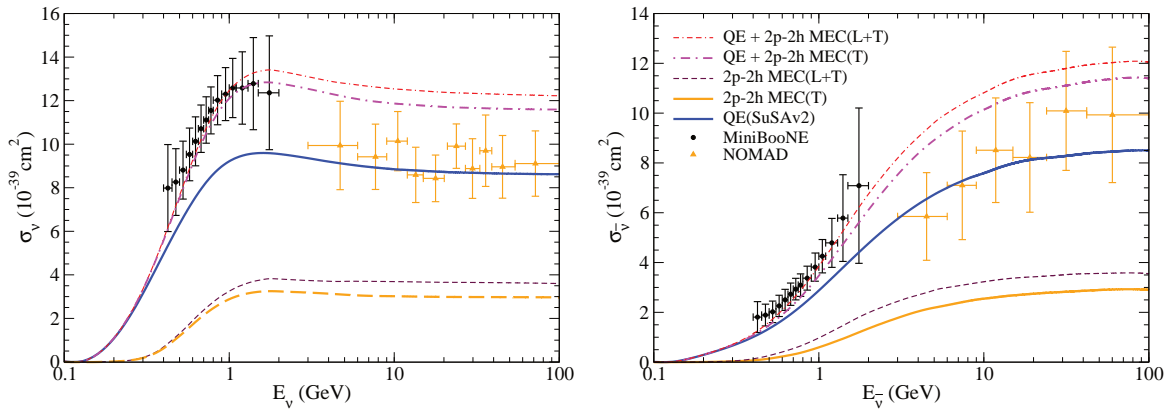


FIG. 4: (Color online) CCQE ν_μ - ^{12}C cross section per nucleon displayed versus neutrino energy E_ν and evaluated using the SuSAv2 and the SuSAv2+MEC approaches (left panel). CCQE $\bar{\nu}_\mu$ - ^{12}C cross section is also shown (right panel). Results are compared with the MiniBooNE [11, 12] and NOMAD [13] experimental data. Also presented for reference are the results excluding the longitudinal MEC contributions.

resonance region, obtained by subtracting the QE+MEC contribution from the total cross section, can be accounted for by introducing a new scaling function f_Δ dominated by the $N \rightarrow \Delta$ and employing a new scaling variable, ψ_Δ , which is suited to the resonance region.

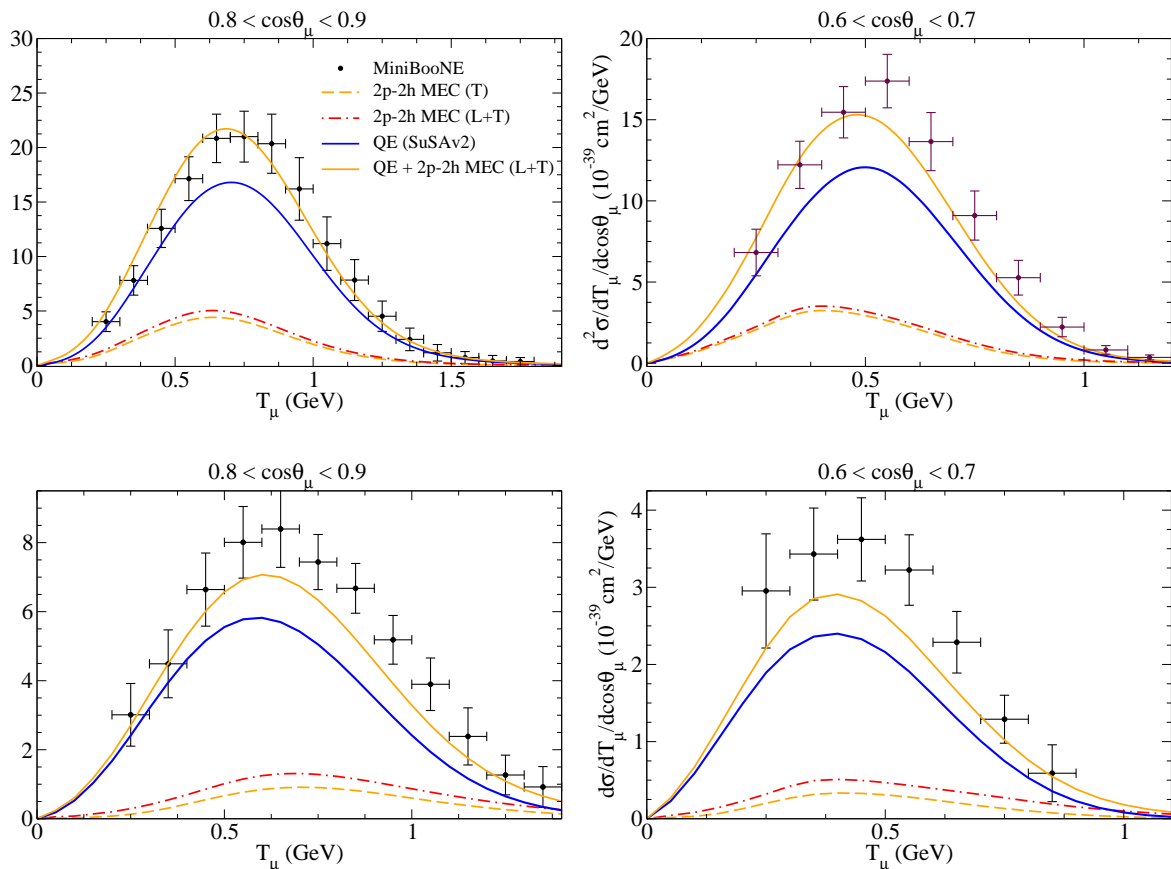


FIG. 5: (Color online) MiniBooNE flux-integrated double-differential cross section per target nucleon for the ν_μ CCQE process on ^{12}C (top panels) and for the $\bar{\nu}_\mu$ one (bottom panels) displayed versus the kinetic energy T_μ for various bins of $\cos\theta_\mu$ obtained within the SuSAv2 and SuSAv2+MEC approaches. MEC results with and without the longitudinal contributions are also shown for reference. The data are from Refs. [11, 12].

This procedure yields a good representation of the electromagnetic response in both the QE and Δ regions, as shown in [6].

Accordingly, charged current inclusive neutrino-nucleus cross sections are evaluated using the superscaling model for quasielastic scattering and its extension to the pion production region as well as the 2p-2h MEC contributions. The results are compared with the inclusive neutrino-nucleus data from the T2K [21, 22] and SciBooNE [23] collaborations (see Figs. 8 and 9, respectively). For neutrino energies around 1 GeV (T2K and SciBooNE experiments), the three mechanisms considered in this work provide good agreement with data. The results

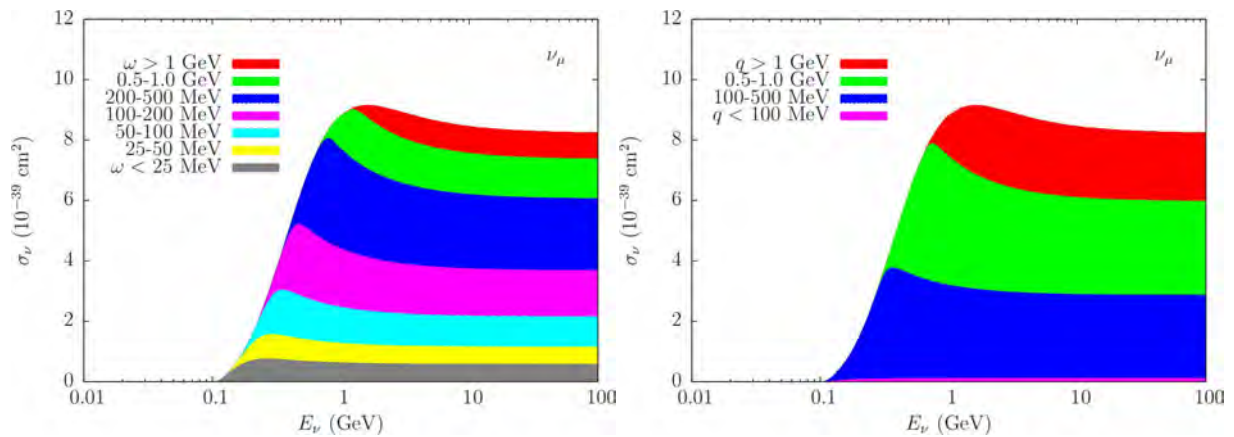


FIG. 6: (Color online) Total CCQE $\nu_\mu-^{12}\text{C}$ cross section per target nucleon evaluated considering different regions of the energy (left panel) and momentum transfer (right panel), as indicated in the figure through different coloured bands.

show that processes induced by vector two-body currents play a minor role in the inclusive cross sections at the kinematics considered, whereas the main contributions to the cross sections are associated with quasielastic (QE) scattering and one pion (1π) production. At higher neutrino energies (see Fig. 8) multiple pion and kaon production, excitation of resonances other than the Δ and deep inelastic channels should also be considered.

Therefore, we have developed a fully relativistic theoretical description of the inelastic spectrum (nucleonic resonances, DIS, etc.) [24] which has been recently improved with the SuSv2 formalism and will be presented in detail in a forthcoming publication. This approach has been successfully tested against (e, e') data (see Fig.10) and work is in progress to include it in the analysis of neutrino-nucleus interactions with the aim of achieving a complete analysis of present and future neutrino oscillation experiments (MINERvA, ArgoNeuT [25, 26], SciBooNE, etc.).

Finally, it is important to remark that the possibility of describing the different nuclear regimes, particularly QE and MEC contributions, through a straightforward parametrization, which is possible with our theoretical models, might be of interest to Monte Carlo neutrino event simulations used in the analysis of neutrino oscillation experiments.

* Presented at NuFact15, 10-15 Aug 2015, Rio de Janeiro, Brazil [C15-08-10.2]

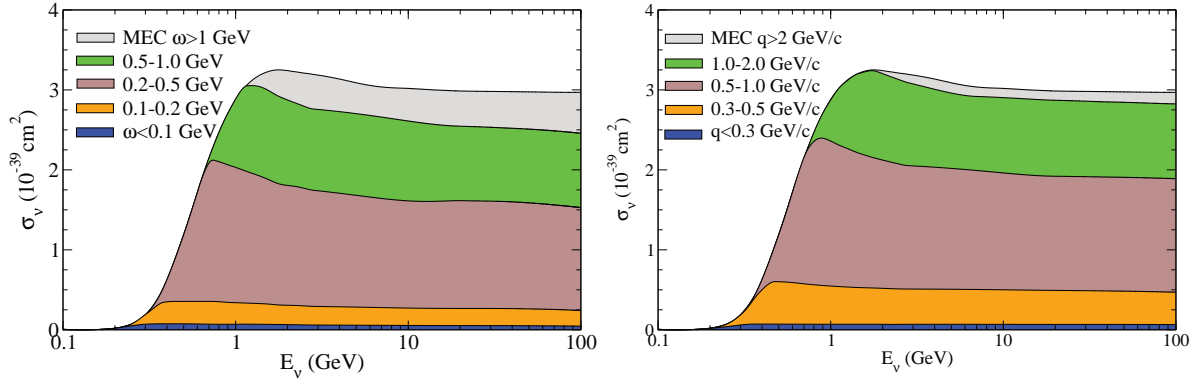


FIG. 7: (Color online) As for Fig. 6, but for the 2p-2h MEC cross section.

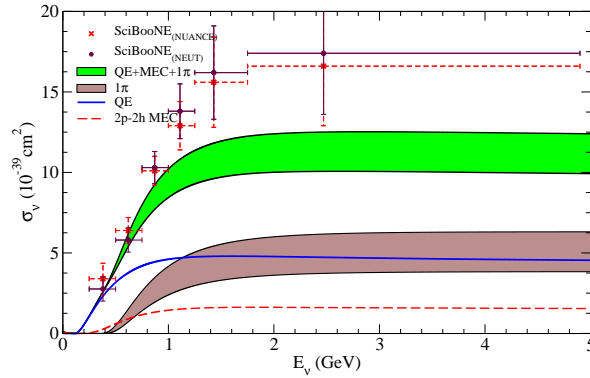


FIG. 8: (Color online) The CC-inclusive ν_μ cross section on a polystyrene target (C_8H_8) per nucleon evaluated in the SuSav2 model as a function of the neutrino (antineutrino) energy and compared with the SciBooNE data [23]. The separate contributions of the QE, 1π and 2p-2h vector MEC are displayed.

† megias@us.es; Speaker

- [1] R. González-Jiménez, G. D. Megias, M. B. Barbaro, J. A. Caballero, and T. W. Donnelly, Phys. Rev. C **90**, 035501 (2014).
- [2] G. D. Megias, M. V. Ivanov, R. González-Jiménez, M. B. Barbaro, J. A. Caballero, T. W. Donnelly, and J. M. Udías, Phys. Rev. D **89**, 093002 (2014).
- [3] M. V. Ivanov, A. N. Antonov, J. A. Caballero, G. D. Megias, et al., Phys. Rev. C **89**, 014607 (2014).
- [4] G. D. Megias, J. E. Amaro, M. B. Barbaro, J. A. Caballero, and T. W. Donnelly, Phys. Lett. B **725**, 170 (2013).
- [5] G. D. Megias, T. W. Donnelly, O. Moreno, C. F. Williamson, J. A. Caballero, R. González-Jiménez, A. De Pace, M. B. Barbaro, W. M. Alberico, M. Nardi, et al., Phys. Rev. D **91**,

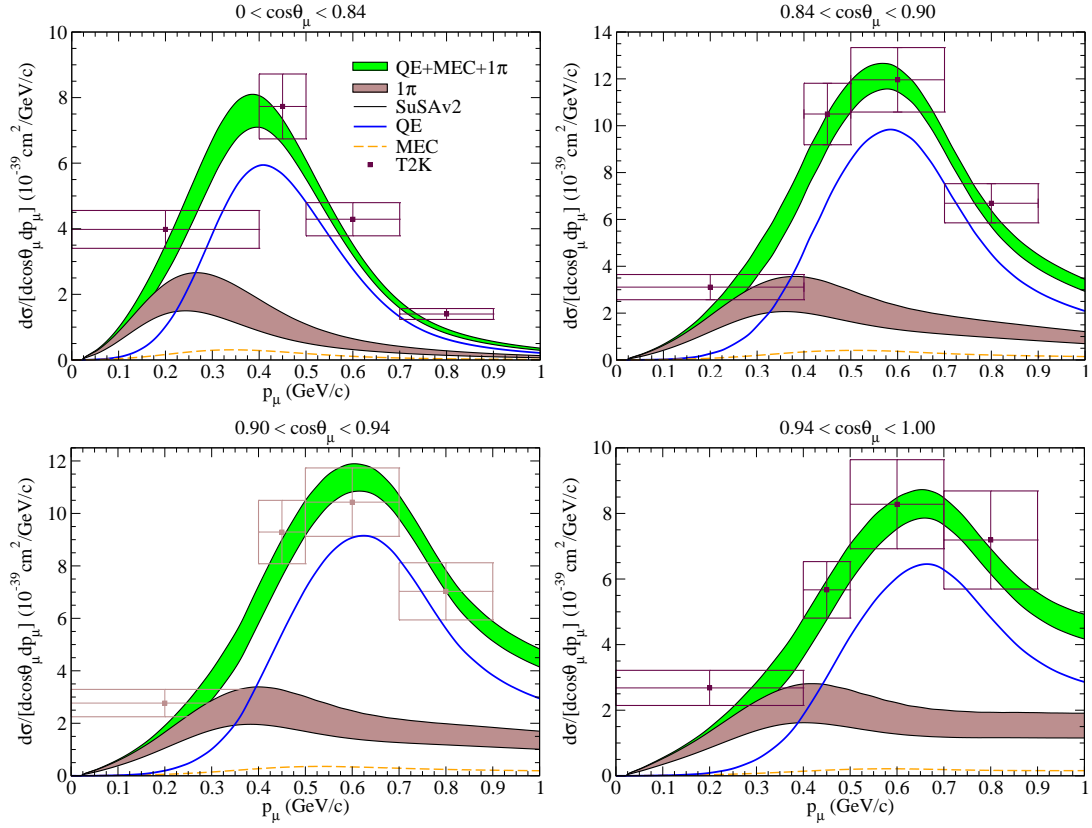


FIG. 9: (Color online) The CC-inclusive T2K flux-folded ν_μ - ^{12}C double-differential cross section per nucleon evaluated in the SuSAv2 model is displayed as a function of the muon momentum for different bins in the muon angle. The separate contributions of the QE, 1π and vector $2p$ - $2h$ vector MEC are displayed. The data are from [21].

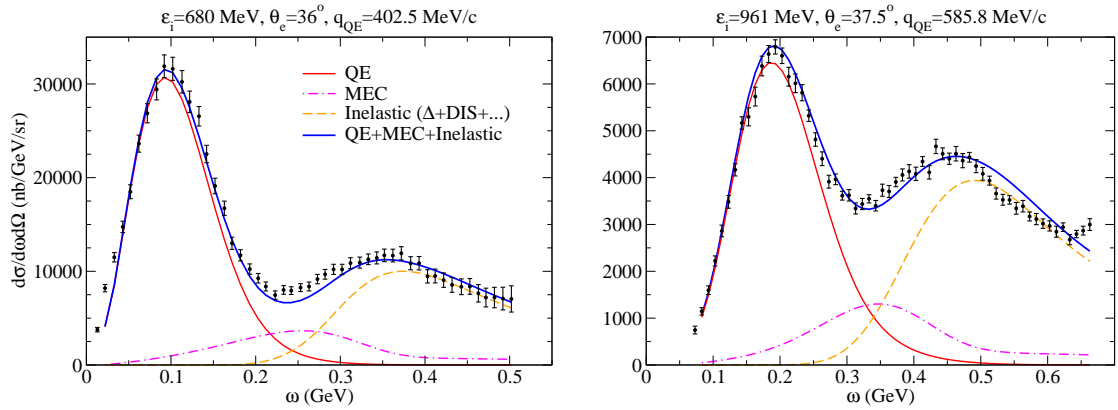


FIG. 10: (Color online) Comparison of inclusive $^{12}\text{C}(e, e')$ cross sections and predictions of the QE(SuSAv2), MEC and Inelastic(SuSAv2) models at different set values of the position of the QE peak (q_{QE}), incident electron energy (ε_i) and the scattering angle (θ_e). Data taken from [27].

- 073004 (2015).
- [6] M. Ivanov, G. D. Megias, et al., arXiv:1411.6264 [hep-ex] (2015).
 - [7] T. W. Donnelly and I. Sick, Phys. Rev. Lett. **82**, 3212 (1999).
 - [8] T. W. Donnelly and I. Sick, Phys. Rev. C **60**, 065502 (1999).
 - [9] I. Ruiz Simo, C. Albertus, J. E. Amaro, M. B. Barbaro, J. A. Caballero, and T. W. Donnelly, Phys. Rev. D **90**, 033012 (2014).
 - [10] I. R. Simo, C. Albertus, J. E. Amaro, M. B. Barbaro, J. A. Caballero, and T. W. Donnelly, Phys. Rev. D **90**, 053010 (2014).
 - [11] A. A. Aguilar-Arevalo et al. (MiniBooNE Collaboration), Phys. Rev. D **81**, 092005 (2010).
 - [12] A. A. Aguilar-Arevalo et al. (MiniBooNE Collaboration), Phys. Rev. D **88**, 032001 (2013).
 - [13] V. Lyubushkin et al. (NOMAD Collaboration), Eur. Phys. J. C **63**, 355 (2009).
 - [14] G. A. Fiorentini et al. (MINER ν A collaboration), Phys. Rev. Lett. **111**, 022502 (2013).
 - [15] L. Fields et al. (MINER ν A collaboration), Phys. Rev. Lett. **111**, 022501 (2013).
 - [16] M. Martini, M. Ericson, G. Chanfray, and J. Marteau, Phys. Rev. C **80**, 065501 (2009).
 - [17] J. Nieves, I. Ruiz Simo, and M. J. Vicente Vacas, Phys. Rev. C **83**, 045501 (2011).
 - [18] J. A. Caballero, J. E. Amaro, M. B. Barbaro, T. W. Donnelly, C. Maieron, and J. M. Udías, Phys. Rev. Lett. **95**, 252502 (2005).
 - [19] J. A. Caballero, Phys. Rev. C **74**, 015502 (2006).
 - [20] J. A. Caballero, J. E. Amaro, M. B. Barbaro, T. W. Donnelly, and J. M. Udías, Phys. Lett. B **653**, 366 (2007).
 - [21] K. Abe et al. (T2K Collaboration), Phys. Rev. D **87**, 092003 (2013).
 - [22] K. Abe et al. (T2K Collaboration), Phys. Rev. Lett. **113**, 241803 (2014).
 - [23] Y. Nakajima et al. (SciBooNE Collaboration), Phys. Rev. D **83**, 012005 (2011).
 - [24] M. B. Barbaro, J. A. Caballero, T. W. Donnelly, and C. Maieron, Phys. Rev. C **69**, 035502 (2004).
 - [25] C. Anderson et al. (ArgoNeuT Collaboration), Phys. Rev. Lett. **108**, 161802 (2012).
 - [26] R. Acciarri et al. (ArgoNeuT Collaboration), Phys. Rev. D **89**, 112003 (2014).
 - [27] O. Benhar, D. Day, and I. Sick, Rev. Mod. Phys. **80**, 189 (2008).

Relativistic Green's Function Model and Optical Potential*

Carlotta Giusti[†]

*Dipartimento di Fisica, Università degli Studi di Pavia and INFN,
Sezione di Pavia, via Bassi 6 I-27100 Pavia, Italy*

Andrea Meucci

*Dipartimento di Fisica Nucleare e Teorica,
Università degli Studi di Pavia and INFN,
Sezione di Pavia, via Bassi 6 I-27100 Pavia, Italy*

Martin V. Ivanov

*Institute for Nuclear Research and Nuclear Energy,
Bulgarian Academy of Sciences, Sofia 1784, Bulgaria*

José Manuel Udías

*Grupo de Física Nuclear, Departamento de Física Atómica,
Molecular y Nuclear, Universidad Complutense de Madrid,
CEI Moncloa, 28040 Madrid, Spain*

(Dated: March 21, 2016)

Abstract

The relativistic Green's function model describes final-state interactions in the inclusive quasi-elastic lepton-nucleus scattering by means of a complex optical potential. The model has been quite successful in the description of data of electron and neutrino-nucleus scattering, but there are some caveats due to the use of phenomenological optical potentials. We discuss the theoretical uncertainties of the model and present results obtained with a new global relativistic folding optical potential.

INTRODUCTION

Accurate predictions of neutrino-nucleus cross sections are needed for use in experimental studies of neutrino oscillations, where nuclei are used as neutrino detectors. A proper analysis of data requires that uncertainties on nuclear effects in the response to neutrino interactions are reduced as much as possible. Several decades of experimental and theoretical work on electron scattering have provided a lot of detailed information on nuclear structure and dynamics [1, 2]. Models developed and successfully tested in comparison with electron-scattering data for electron scattering have been extended to neutrino-nucleus scattering. Although different, the two situations present many similar aspects and the comparison with electron-scattering data represents the first necessary test of a nuclear model. Recently, the MiniBooNE collaboration has produced high-quality data, mostly on a carbon target, for a number of selected channels, in particular, for the Quasi-Elastic (QE) one [3, 4], that is, where no pions are detected in the final state. Within the QE kinematic domain, the nuclear response to the electroweak probe is dominated by the process where, in the Impulse Approximation (IA), the probe directly interacts through a one-body current on a quasi-free nucleon which is then knocked out of the nucleus. A proper description of the Final-State Interactions (FSI) between the emitted nucleon and the residual nucleus is very important for a correct interpretation of the experimental data.

In electron-scattering experiments the emitted nucleon can be detected in coincidence with the scattered electron. Kinematic situations can be envisaged where the residual nucleus is left in a discrete eigenstate and the final state is completely determined. This is the exclusive one-nucleon knockout, that is usually described in the Distorted-Wave IA (DWIA), where FSI are accounted for by a complex Optical Potential (OP) whose absorptive imaginary part gives a reduction that is essential to reproduce $(e, e'p)$ data [1, 2, 5–8]. In the inclusive scattering, where only the scattered electron is detected, all the available final

nuclear states are included in the measured cross section. In this case, a model based on the DWIA, where the cross section is given by the sum, over all the nucleons, of integrated one-nucleon knockout processes and FSI are described by a complex OP with an imaginary absorptive part, is conceptually wrong. The OP describes elastic nucleon-nucleus and its imaginary part accounts for the fact that, if other channels are open besides the elastic one, part of the incident flux is lost in the elastically scattered beam and appears in the inelastic channels which are open. This flux may not contribute to the experimental cross section of the exclusive reaction, where only one channel is considered, and the experimental signal receives contributions mainly from the process where the knocked-out nucleon scatters elastically with the residual nucleus in the considered final state. In contrast, in the inclusive scattering the flux lost in a channel must be recovered in the other channels and in the sum over all the channels the flux can be redistributed but must be conserved. The DWIA does not conserve the flux.

In the Relativistic Green's Function (RGF) model FSI are described in the inclusive QE scattering consistently with the exclusive scattering by the same complex OP, but in the inclusive scattering the imaginary part redistributes and conserves the flux in the sum over all the final-state channels. The model was developed within a nonrelativistic [9, 10] and a relativistic framework [11–14] for the inclusive (e, e') scattering. The relativistic model (RGF) was extended to neutrino-nucleus scattering [15–23]. The formalism can translate the flux lost toward inelastic channels, represented by the imaginary part of the OP, into the strength observed in inclusive reactions. Therefore, the OP becomes a powerful tool to include important contributions not included in other descriptions of FSI based in the IA. The model has been quite successful in the comparison with data: it provides a good description of QE (e, e') data and of the Charged-Current QE (CCQE) MiniBooNE and MINER ν A data, both for ν and $\bar{\nu}$ scattering [3, 4, 17, 19, 23–25], and of Neutral-Current Elastic (NCE) MiniBooNE data [18, 22, 26, 27].

The model is successful but there are some caveats. Available phenomenological OPs make RGF calculations feasible, but do not allow us to disentangle and evaluate the role of a specific contribution: all inelastic contributions are included in the imaginary part of the OP. Phenomenological OPs are obtained through a fit to elastic proton-nucleus scattering data. Available data, however, do not completely constrain the shape and the size of the OP. Different OPs, able to give equivalent descriptions of elastic proton-scattering data, differ, in particular, in their imaginary parts, and therefore their inelastic contributions, and may produce theoretical uncertainties on the numerical predictions of the RGF model.

In this contribution we discuss the uncertainties due to the use of the OP in RGF calculations. In particular, we present results obtained with a new microscopic Global Relativistic Folding OP (GRFOP) [28, 29] generated within the Relativistic IA (RIA) by folding the Horowitz-Love-Franey (HLF) [30, 31] t -matrix with the relevant relativistic mean-field Lorentz densities via the so-called $t\rho$ -approximation. The new results are compared with previous results obtained with phenomenological OPs [32].

RELATIVISTIC GREEN'S FUNCTION MODEL

Lepton-nucleus scattering is usually described in the one-boson exchange approximation, where the cross section is obtained from the contraction between the lepton tensor, which essentially depends on the lepton kinematics, and the hadron tensor $W^{\mu\nu}$, whose components are given by products of the matrix elements of the nuclear current between the initial and final nuclear states.

In the RGF model, with suitable approximations, mainly related to the IA, the components of the hadron tensor are written in terms of the s.p. optical model Green's function and then, exploiting the spectral representation of the s.p. Green's function, in a form containing matrix elements of the same type as the DWIA ones of the exclusive scattering, but where there are eigenfunctions of OP and of its Hermitian conjugate, where the imaginary part has an opposite sign and gives in one case an absorption and in other case a gain of strength. Therefore, in the model the imaginary part of the OP redistributes the flux lost in a channel in the other channels, and in the sum over all the channels the total flux is conserved. In the inclusive scattering, where all elastic and inelastic channels are included, the RGF formalism makes it possible to reconstruct the flux lost into nonelastic channels starting from the complex OP that describes elastic nucleon-nucleus scattering data. The model gives a good description of the experimental (e, e') cross sections in the QE region [11, 13, 14] and is able to describe CCQE and NCE MiniBooNE data and CCQE MINER ν A data [17–19, 22, 23]. In comparison with the MiniBooNE cross sections, the RGF results are usually larger than the results of other models based on the IA, which, in general, underpredict data. The enhancement can be ascribed to the contribution of inelastic channels, which are recovered by the imaginary part of the OP and that are not included in other IA-based models.

The OP can recover contributions beyond direct one-nucleon emission, such as, for instance, rescattering of the outgoing nucleon and some multinucleon processes, which can be included in CCQE measurements. The model, being based on the use of a one-body nu-

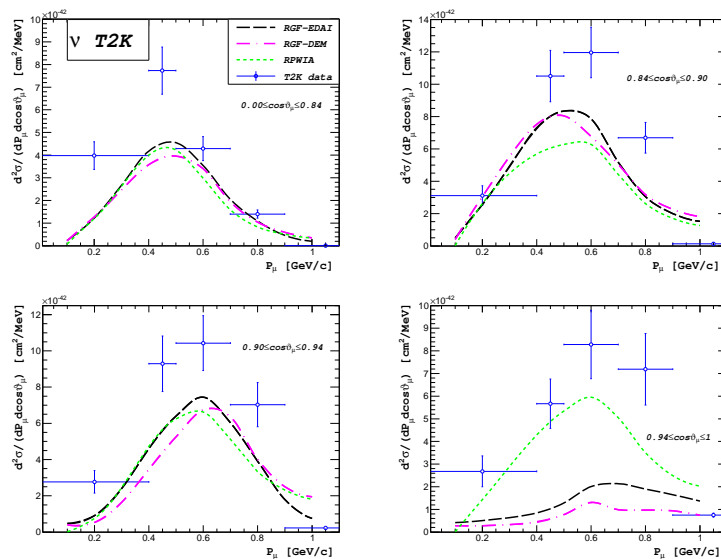


Figure 1: Flux-averaged CC-inclusive double differential ν_{μ} - ^{12}C cross sections per target nucleon as a function of the muon momentum. The data are from T2K [34].

clear current, does not contain meson-exchange-currents mechanisms, that can be included in CCQE data. On the other hand, the OP can include pion-absorption and pion-emission processes, that should have already been subtracted in CCQE data. With a phenomenological OP we cannot disentangle the role of a specific reaction process. It has been written in [33] that the good agreement of the RGF results with the MiniBooNE data “should be interpreted with care” and that “it would be very interesting to confront the RGF results with the fully CC-inclusive data”, where pion production is included.

The comparison with the fully CC-inclusive cross sections on ^{12}C measured by the T2K collaboration [34] is shown in Fig. 1. For the RGF calculations, two different parametrizations for the OP of ^{12}C have been adopted: the Energy-Dependent and A-Independent EDAI OP of [32] and the Democratic (DEM) OP of [35]. EDAI is a single-nucleus parametrization, which is constructed to better reproduce the elastic proton- ^{12}C phenomenology, whereas DEM is obtained through a fit to elastic proton scattering data on a wide range of nuclei. The results of the Relativistic Plane-Wave IA (RPWIA), where FSI are neglected, also shown in the figure, are approximately 50% lower than the data. Both RGF results are also generally lower than the data, although within the error bars for low values of the muon momentum and large angular bins. In the RGF the imaginary part of the OP can include the excitation of multinucleon channels, it may contain some contribution due to pion emission, but the results in Fig. 1 clearly show that this is not enough to reproduce

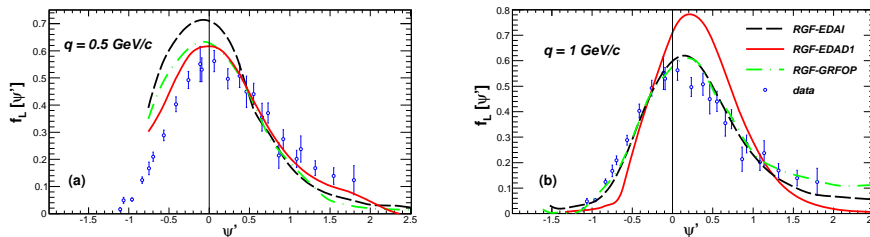


Figure 2: Longitudinal contributions to the scaling function for $q = 500$ and 1000 MeV/ c compared with the averaged experimental scaling function.

CC-inclusive data. [36].

GLOBAL RELATIVISTIC FOLDING OPTICAL POTENTIAL

To reduce the uncertainties on the RGF results due to the use of phenomenological OPs, the need arises to build microscopic OPs. A new relativistic OP has been built for ^{12}C , a nucleus that is often used in neutrino-scattering experiments. The new OP is global, i.e., spanning a large range of kinetic energies of the nucleon, and it has been built within the RIA, by folding [28, 29] the HLF t -matrix [30, 31] with the relativistic mean-field Lorentz densities via the so-called $t\rho$ -approximation. In this way the shape of the OP is severely constrained by the assumed shape of the nuclear density and the strength of the different contributions is essentially dictated by their respective contents in the effective parametrization of the NN scattering amplitudes. The new GRFOP: 1) is derived from all available data of elastic proton scattering on ^{12}C we are aware of; 2) stems from a folding approach, with neutron density fitted to data and proton density taken from electron-scattering experiments; 3) the same nuclear densities are used at all the energies in the range between 20 and 1040 MeV; 4) the imaginary term is built from the effective NN interaction.

The GRFOP reproduces quite well the experimental cross sections and analyzing powers for the elastic proton scattering on ^{12}C in the energy range between 20 and 1040 MeV [29], with an agreement comparable to the one obtained with the EDAI and EDAD1 OPs [32].

The GRFOP has been tested within the RGF for QE electron scattering and $\nu(\bar{\nu})$ -nucleus scattering at MiniBooNE kinematics [29]. In the case of electron scattering, the results are in generally good agreement with the experimental (e, e') cross sections and close to the results obtained with EDAI and EDAD1 [29]. Of particular interest is the comparison with the experimental longitudinal scaling function. The analysis of QE (e, e') world data has

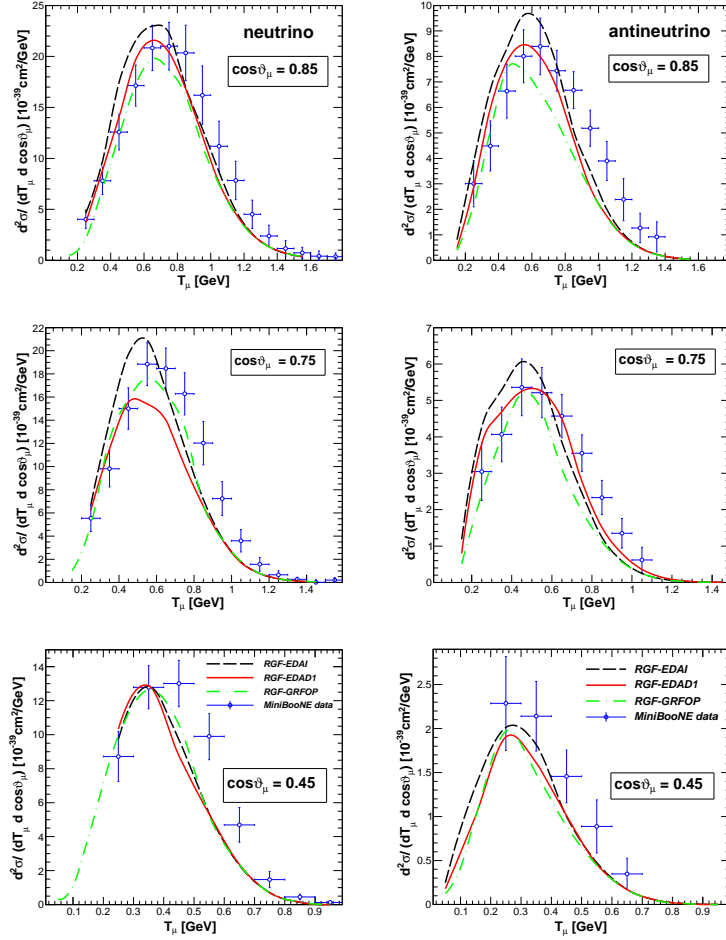


Figure 3: Flux-averaged double-differential cross section per target nucleon for the CCQE $^{12}\text{C}(\nu_\mu, \mu^-)$ (left panels) and $^{12}\text{C}(\bar{\nu}_\mu, \mu^-)$ (right panels) reactions as a function of the muon kinetic energy T_μ for three bins of the muon scattering angle $\cos \vartheta_\mu$ calculated with RGF-GRFOP (dot-dashed lines), RGF-EDAD1 (solid lines) and RGF-EDAI (dashed lines). Experimental data from MiniBooNE [3, 4].

shown that these data, when plotted against a properly chosen scaling variable Ψ' , show a mild dependence on the momentum transfer (scaling of first kind) and almost no dependence on the nuclear target (scaling of second kind). These properties are well satisfied in the longitudinal channel, while violations associated to effects beyond the IA occur mainly in the transverse channel [37, 38]. The scaling function is obtained dividing the longitudinal contribution to the (e, e') cross sections by an appropriate single-nucleon cross section [37, 39]. In Fig. 2 the scaling functions obtained in the RGF with the RGFOP, EDAI, and EDAD1 OPs for two values of the momentum transfer q are compared with the experimental function.

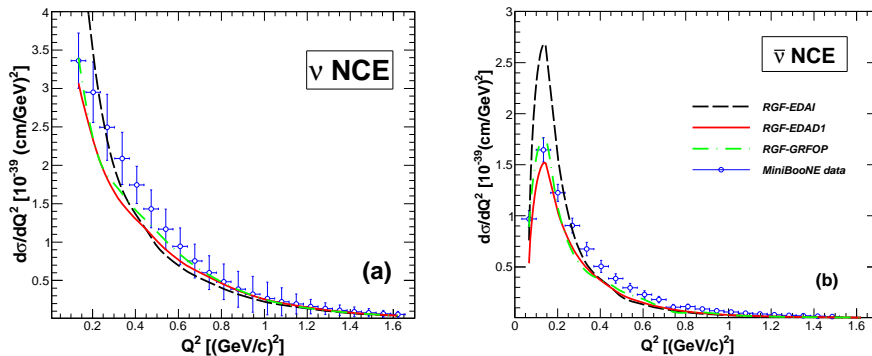


Figure 4: (Neutrino and antineutrino NCE flux-averaged cross section per target nucleon as a functions of Q^2 calculated with RGF-GRFOP (dot-dashed lines), RGF-EDAD1 (solid lines), and RGF-EDAI (dashed lines). Experimental data from MiniBooNE [26, 27].

The asymmetric shape of the experimental function is reproduced by the RGF model. The different dependence on q of the results with the three OPs makes the RGF scaling-function tail less pronounced as the value of q goes up. It is interesting to notice the different behavior as a function of q of the results with EDAI and EDAD1 in comparison with the experimental function: EDAD1 reproduces the experimental function at $q = 0.5$ GeV/ c and overestimates it at $q = 1$ GeV/ c , while with EDAI the experimental function is overestimated at $q = 0.5$ GeV/ c and reproduced at $q = 0.5$ MeV/ c . The RGF results with these two OPs do not scale enough. In contrast, the results with RGFOP scale better, they give a milder dependence on q and a better agreement with the experimental scaling function.

The comparison with the CCQE MiniBooNE data is presented in Fig. 3 for three bins of the muon scattering angle. A good agreement with the shape of the experimental cross sections is generally obtained with all the three OPs. The RGF-EDAD1 and RGF-EDAI results are similar in the bin $0.4 \leq \cos \vartheta_\mu \leq 0.5$. Larger differences, around 20%, are obtained in the peak region for the forward-angle scattering bins, the RGF-EDAI results being larger than the RGF-EDAD1 ones and in somewhat better agreement with the ν -scattering data. In the case of $\bar{\nu}$ scattering, data are slightly overestimated by RGF-EDAI and satisfactorily described by RGF-EDAD1. The RGF-GRFOP results are always smaller than the RGF-EDAI and the RGF-EDAD1 ones for the bin $0.8 \leq \cos \vartheta_\mu \leq 0.9$, while for the bin $0.7 \leq \cos \vartheta_\mu \leq 0.8$ they are larger than the RGF-EDAD1 results and in better agreement with the data. Similar results in comparison with data are produced by the three RGF calculations for the bin $0.4 \leq \cos \vartheta_\mu \leq 0.5$.

The MiniBooNE collaboration has also measured the NCE flux-averaged differential ν and

$\bar{\nu}$ cross section on CH_2 as a function of the four-momentum transferred squared Q^2 [26, 27]. The comparison with the RGF results is shown in Fig. 4. For ν scattering the RGF-EDAI results reproduce the shape and the magnitude of the experimental cross section, but overestimate the first datum at the smallest value of Q^2 ; the RGF-EDAD1 results underestimate the data only at the smallest values of Q^2 ; the RGF-GRFOP calculations generally provide a satisfactory agreement with the data. Also for $\bar{\nu}$ scattering the RGF results are in satisfactory agreement with the data. Close results are obtained with RGF-EDAD1 and RGF-GRFOP, while the RGF-EDAI cross section is enhanced at $Q^2 \approx 0.1 \text{ (GeV/c)}^2$. All the RGF results reproduce the first datum at $Q^2 \approx 0.06 \text{ (GeV/c)}^2$.

The RGF-GRFOP results lie, in general, between the RGF-EDAI and RGF-EDA1 ones and are in many cases in better agreement with the data. The new GRFOP results reduce the uncertainties in the numerical predictions of the RGF model and confirm our previous findings in comparison with data. The RIA can provide successful relativistic OPs with similar fits to elastic nucleon-nucleus scattering data. The GRFOP can be employed as a useful alternative to phenomenological optical potentials.

* Presented at NuFact15, 10-15 Aug 2015, Rio de Janeiro, Brazil [C15-08-10.2]

† carlotta.giusti@pv.infn.it; Speaker

- [1] S. Boffi, C. Giusti, and F.D. Pacati, *Phys. Rep.* **226** (1993) 1-101.
- [2] S. Boffi, C. Giusti, F.D. Pacati, and M. Radici *Electromagnetic Response of Atomic Nuclei* Oxford Studies in Nuclear Physics, Vol. 20, Clarendon Press, Oxford (1996).
- [3] A.A. Aguilar-Arevalo *et al.*, *Phys. Rev.D* **81** (2010) 092005-1-22.
- [4] A.A. Aguilar-Arevalo *et al.*, *Phys. Rev.D* **88** (2013) 032001-1-22.
- [5] J.M. Udías *et al.*, *Phys. Rev. C* **48** (1993) 2731-2739.
- [6] A. Meucci, C. Giusti, and F.D. Pacati, *Phys. Rev.C* **64** (2001) 014604-1-10.
- [7] A. Meucci, C. Giusti, and F.D. Pacati, *Phys. Rev.C* **64** (2001) 064615-1-8.
- [8] C. Giusti *et al.*, *Phys. Rev.C* **84** (2011) 024615-1-12.
- [9] F. Capuzzi, C. Giusti, and F.D. Pacati *Nucl. Phys.A* **524** (1991) 681-705.
- [10] F. Capuzzi *et al.*, *Ann. Phys.* **317** (2005) 492-529.
- [11] A. Meucci *et al.*, *Phys. Rev.C* **67** (2003) 054601-1-12.
- [12] A. Meucci, C. Giusti, and F.D. Pacati *Nucl. Phys. A* **756** (2005) 359-381.
- [13] A. Meucci *et al.*, *Phys. Rev. C* **80** (2009) 024605-1-12.

- [14] A. Meucci *et al.*, *Phys. Rev. C* **87** (2013) 054620-1-14.
- [15] A. Meucci, C. Giusti, and F.D. Pacati *Nucl. Phys. A* **739** (2004) 277-290.
- [16] A. Meucci *et al.*, *Phys. Rev. C* **83** (2011) 064614-1-10.
- [17] A. Meucci *et al.*, *Phys. Rev. Lett.* **107** (2011) 172501-1-5.
- [18] A. Meucci, C. Giusti, and F.D. Pacati, *Phys. Rev. D* **84** (2011) 113003-1-8.
- [19] A. Meucci, and C. Giusti, *Phys. Rev. D* **85** (2012) 093002-1-6.
- [20] A. Meucci, C. Giusti, and M. Vorabbi, *Phys. Rev. D* **88** (2013) 013006-1-7.
- [21] R. González-Jiménez *et al.*, *Phys. Rev. C* **88** (2013) 025502-1-10.
- [22] A. Meucci, and C. Giusti, *Phys. Rev. D* **89** (2014) 057302-1-4.
- [23] A. Meucci, and C. Giusti, *Phys. Rev. D* **88** (2014) 117301-1-5.
- [24] G.A. Fiorentini *et al.*, *Phys. Rev. Lett.* **111** (2013) 022502-1-6.
- [25] L. Fields *et al.*, *Phys. Rev. Lett.* **111** (2013) 022501-1-7.
- [26] A.A. Aguilar-Arevalo *et al.*, *Phys. Rev. D* **82** (2010) 092005-1-16.
- [27] A.A. Aguilar-Arevalo *et al.*, *Phys. Rev. D* **91** (2015) 092005-1-12.
- [28] M.V. Ivanov *et al.*, *Nuclear Theory* **30** (2011) 116-125, eds. A.I. Georgieva and N. Minkov, Heron Press, Sofia.
- [29] M.V. Ivanov *et al.*, *Phys. Rev. C* to be published.
- [30] C.J Horowitz, *Phys. Rev. C* **31** (1985) 1340-1348.
- [31] D.P. Murdock and C.J Horowitz, *Phys. Rev. C* **35** (1987) 1442-1462.
- [32] E.D. Cooper *et al.*, *Phys. Rev. C* **47** (1993) 297-311.
- [33] L. Alvarez-Ruso, Y. Hayato, and J. Nieves, *New. J. Phys* **16** (2014) 075015-1-63.
- [34] K. Abe *et al.*, *Phys. Rev. D* **87** (2013) 092003-1-20.
- [35] E.D. Cooper, S. Hama, and B.C. Clark, *Phys. Rev. C* **80** (2009) 034605-1-5.
- [36] A. Meucci and C. Giusti, *Phys. Rev. D* **91** (2015) 093004-1-6.
- [37] C. Maieron, T.W. Donnelly, and I. Sick, *Phys. Rev. C* **65** (2002) 025502-1-15.
- [38] T.W. Donnelly and I. Sick, *Phys. Rev. Lett.* **82** (1999) 3212-3215.
- [39] J.A. Caballero, *Phys. Rev. C* **74** (2006) 015502-1-12.

CAPTAIN, NuMI and Low Energy Physics Programs*

A. Higuera[†]

Department of Physics, University of Houston, Houston, Texas, USA

(Dated: March 30, 2016)

Abstract

CAPTAIN, Cryogenic Apparatus for Precision Tests of Argon Interactions with Neutrinos is a liquid argon TPC currently being built at Los Alamos National Laboratory (LANL). The CAPTAIN detector is a portable and evacuable cryostat that can hold 7700 liters of liquid argon. Within the CAPTAIN program a prototype detector has been built, Mini-CAPTAIN a smaller liquid argon TPC inside a 1500 liter cryostat. We present the CAPTAIN physics program that includes measuring neutron interactions at Los Alamos Neutron Science Center, the proposal for measuring neutrino interactions at the NuMI (Neutrinos from Main Injector) beamline at energies relevant for DUNE, and the potential for low-energy neutrino measurements at the Booster Neutrino Beam (BNB) and the NuMI absorber. Finally we discuss the status of CAPTAIN and the first demonstration of an ionization track from a laser calibration system in the Mini-CAPTAIN detector, announced in August 2015.

INTRODUCTION

Precise measurements of neutrino cross-sections and nuclear effects are needed in order to have a complete understanding of neutrino oscillations because the neutrino oscillation probability is energy-dependent, the reconstruction of the incoming neutrino energy becomes critical. In addition, there is a consensus that more and precise neutrino cross-section measurements are needed to constrain theoretical models. These are necessary to develop a coherent plan that would contribute to the success of future oscillation measurements. As an example the Deep Underground Neutrino Experiment (DUNE) has proposed to use a liquid argon time project chamber (TPC) detector with a baseline of 1300 km from the Long-Baseline Neutrino Facility (LBNF), which will provide a high-power, wide-band muon neutrino beam [1], and measurements of neutrino-argon interactions in this energy range are crucial for the success of the DUNE. Results on neutrino-argon interactions have been released from ArgoNeuT experiment [3–6] a 170 liter (0.25 ton active volume) liquid argon TPC that took data in the NuMI low-energy beam configuration however these results are statistically limited.

CAPTAIN NUMI PHYSICS PROGRAM

Liquid argon TPCs provide excellent position resolution, energy resolution, and particle identification, enabling precision reconstruction of complex interaction topologies. The CAPTAIN TPC is a hexagonal shape with a 1 m height and 2 m diameter, consisting of three active wire planes with 3 mm pitch and 3 mm wire spacing on a cathode plane, grid plane, and ground plane. CAPTAIN will be equipped with a photon detection system to observe scintillation light produced inside the liquid argon.

To address the studies important for neutrino oscillations, the study of neutrino-argon interactions in the neutrino energy range relevant for long-baseline neutrino oscillation physics is needed. Hence CAPTAIN is designed to conduct studies important for precision measurements of neutrino oscillations and observation of supernova burst neutrinos in a next generation liquid argon neutrino detector.

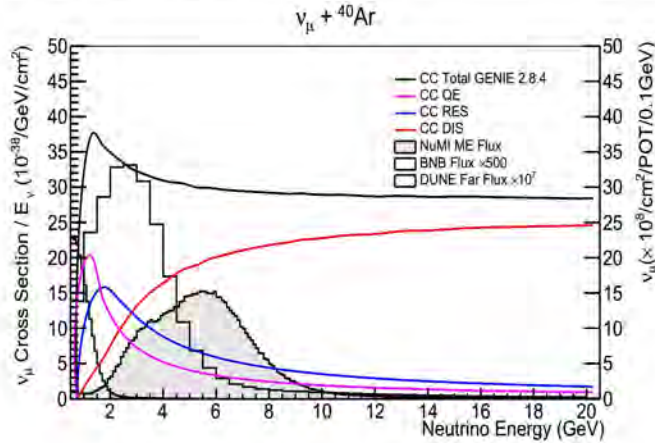


FIG. 1: Unoscillated ν_μ DUNE far flux, BNB flux at MiniBooNE, medium-energy NuMI flux at the MINOS near hall and GENIE cross section on ^{40}Ar .

Figure 1 compares the neutrino flux from the medium-energy NuMI beam at the MINOS near hall, the flux from the Booster Neutrino Beam (BNB) at the location of MiniBooNE, and the proposed flux for DUNE at the DUNE far detector. The NuMI beam medium-energy (ME) configuration overlaps the entire neutrino energy range for DUNE. By placing CAPTAIN in the NuMI beamline there is an opportunity to study neutrino-argon interactions in the neutrino energy range relevant for DUNE's long-baseline neutrino oscillation physics program.

MINERvA is an experiment dedicated to measuring neutrino cross-sections located at the MINOS near hall, in front of the MINOS near detector (ND) and is currently taking data in the NuMI ME configuration. The MINERvA detector consists of a series of nuclear targets followed by a fine-grained scintillator tracking region surrounded by electromagnetic and hadronic calorimeters [7]. The magnetized MINOS ND serves as a downstream muon spectrometer. MINERvA's dataset includes interactions on a variety of nuclei ranging from helium to lead. Combining CAPTAIN and MINERvA would be very beneficial in order to study neutrino-argon interactions in the energy range relevant for long-baseline neutrino oscillation physics, because some particles exiting CAPTAIN, most importantly forward-going muons, can be tracked and their energy measured in MINERvA and/or the MINOS ND, resulting in a far better estimate of the incoming neutrino energy than could be achieved with CAPTAIN alone. In addition, by making measurements of cross section ratios, namely argon to hydrocarbon in the scintillator, stringent tests of the nuclear effect models can be made, since these cross section ratios are not hampered by large flux uncertainties. The simplest way to integrate the CAPTAIN detector into MINERvA is to replace MINERvA's existing liquid helium target with the CAPTAIN detector, and this is our default plan. We performed simulations of neutrino interactions on liquid argon with the CAPTAIN detector geometry placed in the position of MINERvA's existing liquid helium target with the on-axis ME NuMI flux. The simulations predict 12.5M ν_μ CC interactions within the CAPTAIN LAr volume for an exposure of 6×10^{20} protons on target (POT). To study the acceptance of ν_μ CC events in MINERvA and the MINOS ND, neutrino interactions were generated using GENIE Neutrino Monte Carlo Generator [8] version 2.8.4. MINERvA's detector response was simulated with a tuned GEANT4-based simulation. Considering muons that reach MINERvA or the MINOS ND, the overall muon reconstruction efficiency for ν_μ CC events is 64%. Figure 2 shows the muon acceptance as a function of neutrino energy, muon momentum, Q^2 and muon angle with respect to the beam direction. In addition, Figure 2 shows the events where the muon charge sign is reconstructed; this is particularly important for an antineutrino flux configuration to avoid wrong sign contamination. In terms of topologies we expect to collect 916k CCQE-like events, 1953k CC1 π events and 1553k CC1 π^0 [9]. Finally it is important to mention that CAPTAIN-MINERvA will have the unique ability to study event reconstruction for neutrino interactions on argon events with different particle multiplicities and will be the only experiment making high-statistics measurements

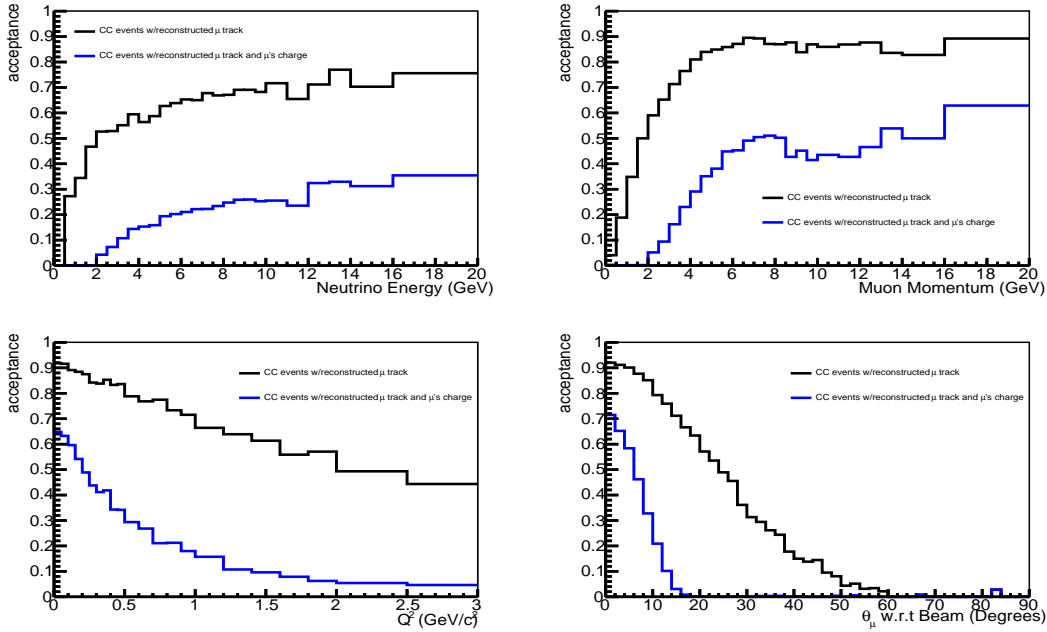


FIG. 2: Muon acceptance for ν_μ CC events as function of neutrino energy, muon track momentum, Q^2 and muon angle with respect to the beam direction for all events with a reconstructed muon track (black) and for the subset of events with reconstructed tracks in which the charge sign is also reconstructed (blue).

of neutrino interactions on argon in the medium energy range before DUNE.

CAPTAIN LOW ENERGY PHYSICS PROGRAM

Measurement of supernova neutrinos (SN) is also an important physics topic for the DUNE experiment [1]. The measurement of the time evolution of the energy and flavor spectrum of neutrinos from supernova can revolutionize our understanding of neutrino properties and SN physics. In order to achieve such measurements it is very important to reject neutron spallation backgrounds. Therefore, it is crucial to have a reliable method to tag neutron-argon interactions. This will also help to improve the neutrino energy reconstruction for neutrino oscillation measurements when neutrons are produced in the final state from the neutrino-argon interaction. The CAPTAIN low energy physics program plans to perform neutron studies at the Weapons Neutron Research Facility (WNR) at LANL. The project plans to place the Mini-CAPTAIN detector in the WNR neutron beam. The

Mini-CAPTAIN detector is a smaller liquid argon TPC inside a 1500 liter cryostat. The CAPTAIN detector and the Mini-CAPTAIN detector are similar, including cryostats, cryogenics, electronics, TPCs, photon detection system and laser calibration system. The design differences between the two detectors are driven by the cryostat sizes and geometries.

During the neutron run at the WNR two runs have been proposed, high-intensity and low-intensity run. The high-intensity run is useful to study neutron production of Cl isotopes that constitute an important background for SN neutrino detection. The low-intensity mode can be used to study the neutrino-like argon reaction: $n + {}^{40}\text{Ar} \rightarrow {}^{40}\text{Ar}^* + n$. Since this interaction is a very good control sample for the neutral-current (NC) interactions, $\nu_x + {}^{40}\text{Ar} \rightarrow {}^{40}\text{Ar}^* + \nu_x$, induced by supernova neutrinos and to study reconstruction capabilities of ${}^{40}\text{Ar}^*$ de-excitation in a LAr TPC.

In addition, as part of the coherent plan relevant for the success of DUNE, it is necessary to understand neutrino-argon interactions at low energies (tens of MeV) in order to demonstrate the capability of a liquid argon detector to search SN neutrinos. The $\nu - \text{Ar}$ cross-section has never been measured for these energies and have theoretical uncertainties around 10-15%. To measure low-energy neutrino-argon interaction we plan to put the CAPTAIN detector close to the target hall at the Booster Neutrino Beam at Fermilab to collect low-energy neutrinos produced by pions that decay at rest. Detailed beam flux studies are underway and require neutron background measurements from SciBath [10] to determine the ideal location and necessary shielding.

Another source for a low-energy neutrino beam is at the NuMI absorber hall. Studies are underway which include a more detailed NuMI flux simulation, measurements of backgrounds in the access tunnel and determination of the amount of shielding.

SUMMARY AND CAPTAIN STATUS

The CAPTAIN cryostat, electronics and field cage are in hand to construct the CAPTAIN detector. Also, the purification system has been delivered. CAPTAIN is currently planned to move to Fermilab by Fall 2016.

The cryostat, cryogenics and TPC of the Mini-CAPTAIN detector have been commissioned. The electronics, TPC and heat load have been tested. The purity monitor is installed and photon detector system will be installed soon. Purification tests for Mini-CAPTAIN

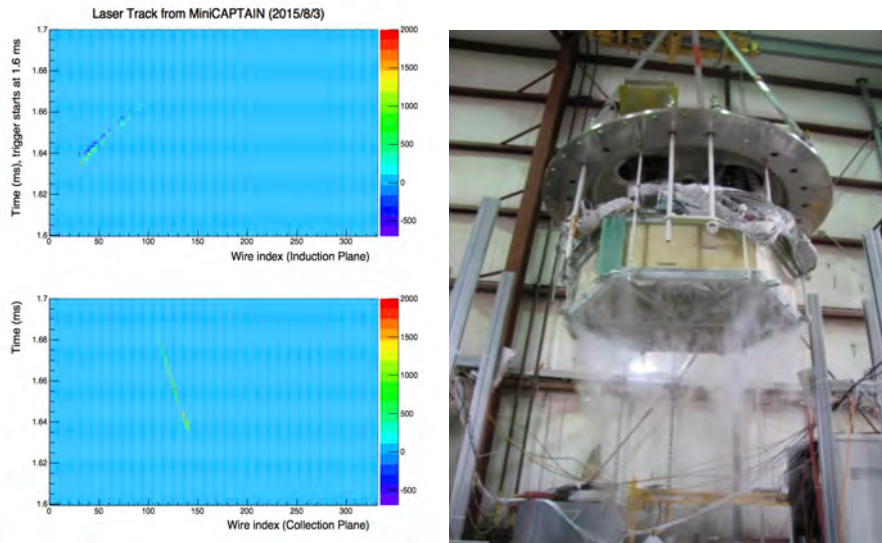


FIG. 3: First laser track observed by the Mini-CAPTAIN TPC on August 3, 2015. The color represents ADC value (left). Mini-Captain Assembly (right).

have been under way since July 2015. On August 3, 2015, the first ionization track from the laser calibration system was observed by the Mini-CAPTAIN TPC. The first image of a UV laser track recorded by a induction and collection plane of the TPC is shown in Figure 3 (left). The observation of the first track demonstrates that the required purity has been achieved. Commissioning of the Mini-CAPTAIN detector is reaching completion and its neutron beam running at WNR will take place in January 2016.

CAPTAIN measurements will provide great benefit to the neutrino oscillation and supernova neutrino programs at DUNE, therefore CAPTAIN will play a significant role to the DUNE R&D program. A full proposal to Fermilab PAC for the CAPTAIN-MINERvA project has been submitted.

* *Presented at NuFact15, 10-15 Aug 2015, Rio de Janeiro, Brazil [C15-08-10.2]*

† ahiguera@central.uh.edu; Speaker

[1] Long-Baseline Neutrino Facility (LBNF) and Deep Underground Neutrino Experiment (DUNE) Conceptual Design Report, June 2015 <http://www.dunescience.org/>.

[2] C. Adams et al. (LBNE Collaboration), arXiv:1307.7335 [hep-ex].

- [3] C. Anderson et al. (ArgoNeuT Collaboration), Phys. Rev. Lett. 108, 161802 (2012).
- [4] R. Acciarri et al. (ArgoNeuT Collaboration), Phys. Rev. D89, 112003 (2014).
- [5] R. Acciarri et al. (ArgoNeuT Collaboration), Phys. Rev. D90, 012008 (2014).
- [6] R. Acciarri et al. (ArgoNeuT Collaboration), Phys. Rev. Lett. 113, 261801 (2014).
- [7] L. Aliaga et al. (MINERvA Collaboration), Nucl. Instrum. Meth. A743 130- 159, (2014).
- [8] C.Andreopoulos, A.Bell, D.Bhattacharya, F.Cavanna, J.Dobson, S.Dytman, H.Gallagher, P.Guzowski, R.Hatcher, P.Kehayias, A.Meregaglia, D.Naples, G.Pearce, A.Rubbia, M.Whalley and T.Yang, Nucl. Instrum. Meth. A614 87-104 (2010).
- [9] CAPTAIN-MINERvA proposal presented to Fermilab PAC, June 2015.
- [10] R. Cooper, L. Garrison, H.-O. Meyer, T. Mikev, L. Rebenitsch and R. Tayloe. arXiv:1110.4432 [hep-ex].

**Charged current resonant and coherent single meson production
results from T2K (on and off-axis)***

M. Nirrko[†]

AEC-LHEP, University of Bern

(Dated: December 23, 2015)

Abstract

It is a truth universally acknowledged that a scientist in possession of a good neutrino oscillation experiment must be in want of a neutrino interaction model. In order to reduce systematic effects, understanding the way neutrinos interact with matter is crucial. Known cross-sections from various experiments show significant discrepancies with common theoretical models within the low energy region ($\sim 1\text{GeV}$). Data taken with the T2K near detectors will cover this critical region, as cross-section measurements for various interaction channels are on the way. This article focuses on the resonant and coherent contributions to neutrino-induced meson production, including proton decay backgrounds, for which various analyses are under way.

PACS numbers: 13.15.+g, 25.30.Pt

INTRODUCTION

Recent cross-section measurements of single pion production ($\text{CC-}1\pi^+$) from MiniBooNE [1] and MINERvA [2] have been reported as differential cross-sections as a function of charged pion kinetic energy. While the data seemed to agree at higher energies, significant discrepancies were seen below 100MeV. More importantly, the Monte-Carlo (MC) models used did not agree well with data in either experiment [2].

Coherent pion production has so far only been measured in the intermediate energy range (1–10GeV) and above. Available data is sparse, and suggests that typical MC generators (GENIE [3], NEUT [4]) are not correctly predicting the cross-section at lower energies [5]. Extending the measurements below 1GeV will be beneficial to presently used models.

With neutrino energies similar to the Booster Neutrino Beam (BNB) used for MiniBooNE and a more sharply peaked flux, T2K [6] will be able to provide complementary measurements of the various pion production channels at low energies, providing comparable results for MINERvA and others [7].

THE T2K EXPERIMENT

The Tokai-to-Kamioka (T2K) experiment is a long-baseline ($L/E \approx 500\text{km/GeV}$) muon-neutrino oscillation experiment located in Japan, shown in Fig. 1. Its main goals are to measure ν_e appearance (determines θ_{13}), ν_μ disappearance (determines θ_{23} and $|\Delta m_{32}^2|$) and CP violation (determines δ_{CP}). Further goals include a search for sterile components in ν_μ disappearance by observing NC events, and making world-leading contributions to neutrino-nucleus cross-section measurements. For more information on neutrino and antineutrino oscillation measurements at T2K, see references [8, 9].

T2K uses Super-Kamiokande [10] as the far detector, which measures neutrino rates at the first oscillation maximum. While the far detector already existed, the beam line and near detector complex were constructed for the T2K experiment. The proton synchrotron located at J-PARC fires 30 GeV protons onto a graphite target, currently providing a beam

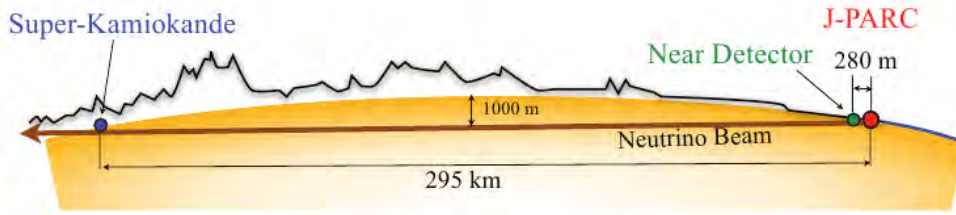


FIG. 1: Neutrinos are produced at J-PARC in Tokai, from which they travel 295km through the Earth before reaching the Super-Kamiokande detector in Kamioka. The near detector site located at J-PARC is used to monitor beam flux as well as measure neutrino interactions.

power up to 400kW. The target beam line is arranged at a 2.5° angle with respect to Super-Kamiokande; this off-axis method produces a narrow neutrino energy spectrum peaked at 0.6GeV.

Near detectors

The on-axis detector (INGRID, see Fig. 2) is constructed from an array of 16 iron/scintillator sandwich modules, and functions as a neutrino flux monitor. The identical modules are arranged in the shape of a plus sign, large enough to measure the beam flux at different off-axis angles. Each module is made from alternating planes of scintillator tracker and iron plates. A similar module consisting purely of scintillators called the proton module is placed upstream and is used for cross section measurements.

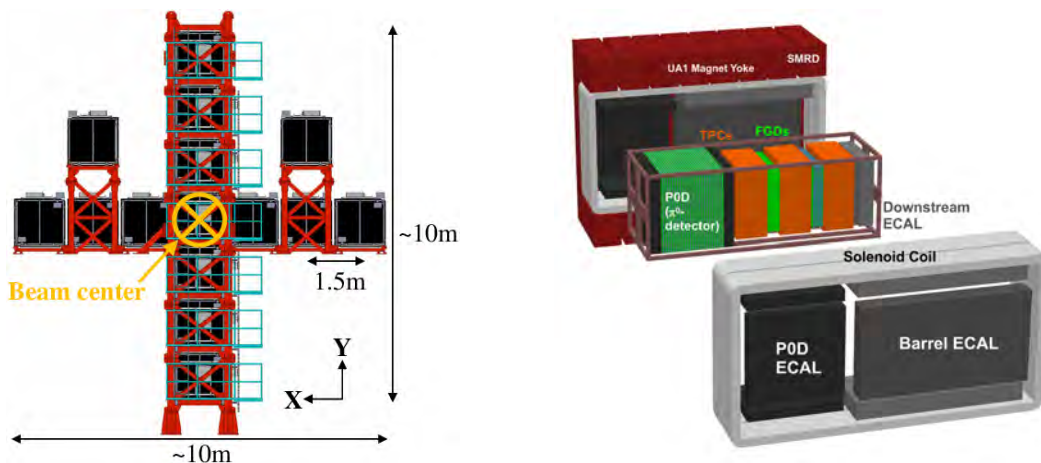


FIG. 2: Schematics of the on-axis (INGRID, left) and off-axis (ND280, right) detectors.

The off-axis detector (ND280, see Fig. 2) is located 280m downstream from the target and serves multiple purposes, from measuring the neutrino flux and energy spectrum as well as the intrinsic beam contamination from electron neutrinos to cross-sections for specific neutrino reactions. It is composed of various sub-detectors: A water-scintillator detector

optimised to detect π^0 's (P0D) is placed at the upstream end. It consists of tracking planes of scintillator bars that alternate with water. Downstream of the P0D lies the tracker, optimised to study CC interactions. It consists of three time-projection chambers (TPCs) and two interspersed fine-grained detectors (FGDs). The TPCs contain an argon-based drift gas and a central cathode to produce a uniform electric field inside the active drift volume. Electrons produced by passing particles drift outward towards the central planes located on each side of the detector. The FGDs serve as massive targets for the neutrinos within the tracker. They consist of scintillator bars arranged in layers perpendicularly to each other. The first FGD consists purely of scintillator material, while the second FGD is interspersed with water layers. An electromagnetic calorimeter (ECAL) surrounds both the P0D and the tracker. The entire detector is magnetised by a 0.2T homogeneous field, allowing the charge and momentum of reconstructed tracks to be determined.

Event topologies

There is no way to directly see what is going on inside the nucleus during a neutrino interaction, but nuclear effects such as Fermi momentum and final state interactions affect the particle composition and kinematics. For instance, one cannot say for certain whether an observed event containing a charged muon was caused by quasi-elastic scattering (CCQE), resonant production (CC-RES), deep inelastic scattering (CC-DIS). For this reason, it is usually preferred to define interactions by final state topology rather than reaction type. The T2K CC-Inclusive sample is split into three topologies (see Fig. 3) according to the number of charged pions exiting the nucleus.

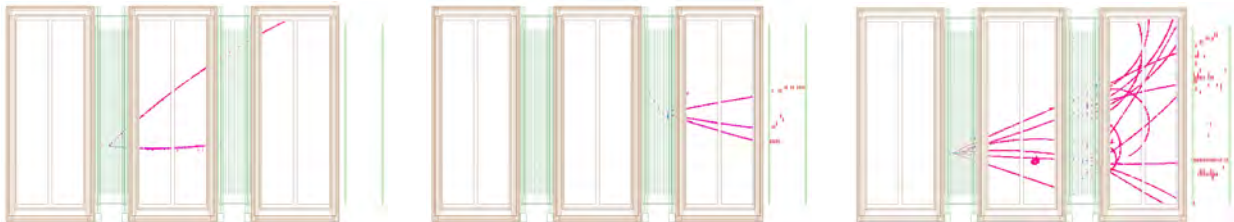


FIG. 3: ND280 tracker event displays for various topologies, from left: CC- 0π , CC- 1π , CC-Other.

The first sample (CC- 0π) rejects pions altogether, and can be described by the reaction $\nu_\mu + N \rightarrow \mu^- + N'$. As one would expect, a large fraction of these events (64%) are “true” CCQE events. The rest is made up of other reactions such as CC-RES, where the outgoing meson is undetected due to reconstruction inefficiencies.

The second sample (CC- 1π) includes all topologies with exactly one positive pion in the final state. Best described by the reaction $\nu_\mu + N \rightarrow \mu^- + \pi^+ + N'$, the dominant reaction is CC-RES, weighing in at 40%. Events in which a pion is produced coherently (CC-COH), leaving the nucleus in exactly the same quantum state, would typically also be categorised as CC- 1π . When specifically selecting CC-COH events, further cuts need to be applied to

ensure no other particles are leaving the nucleus.

All other events are lumped into the third sample (CC-Other), this includes events where negative or neutral pions are produced: $\nu_\mu + N \rightarrow \mu^- + n\pi^{\pm,0} + N'$. Since this sample includes multiple pion events, 68% of events in this sample are CC-DIS.

CROSS-SECTION MEASUREMENTS

This article focuses on some of the more advanced CC- 1π and CC-COH measurements at the T2K near detectors. For information about other cross section analyses, see Ref. [11, 12].

Event selection

All analyses presented here involve charged-current interactions. It is therefore natural to begin any event selection by identifying the outgoing lepton track, in this case a muon. Following some basic data quality cuts, the highest momentum negative track with good quality is selected. It must start within the fiducial volume of the desired sub-detector and is usually associated with the neutrino interaction point. Additionally, Particle Identification (PID) cuts require the track to behave like a Minimally Ionising Particle (MIP). This procedure selects events of which 90% are true CC interactions.

In the case of the ND280 tracker, PID is performed for tracks crossing a TPC. The momentum is obtained from the track curvature within the magnetic field, and the deposited charge inside the gas is related to the deposited energy per unit length dE/dx . Using the Bethe formula that describes the relation between these two variables for different particles, tracks are assigned a likelihood for each particle hypothesis by calculating the pull variables of the expected dE/dx distributions. These are optimised for muons in a specific momentum bin (400–500MeV/c) and perform less well for heavier particles such as kaons or protons.

CC- 1π in water (P0D)

A search for CC- 1π events in water is performed by selecting events with exactly two tracks inside the P0D fiducial volume. The events are split into two samples, depending on whether the muon track is fully contained within the P0D or not. The starting points of both selected tracks are required to be close to the reconstructed vertex. The dE/dx pull variables must match the muon/pion hypothesis. Furthermore, fully contained tracks are required to have a delayed Michel cluster¹ at the end.

An important feature of this measurement is that the water inside the P0D can easily be drained, allowing for different data runs with “water-in” and “water-out” configurations. The background from interactions within the surrounding material (such as scintillators,

¹ Electrons originating in the decay of stopped muons are called Michel electrons.

brass, and lead) is then reduced by subtracting the normalised event rates; one is left with the event rate in water.

Regarding the cross-section, it is interesting to note that the T2K NEUT prediction before FSI agrees with the MiniBooNE data. Results using data are currently under internal review and will be published when approved. The result will be extended into a differential cross-section measurement in the near future. Further efforts will be made to include other topologies (e.g. events with > 2 tracks coming from the interaction vertex).

CC- 1π in water (FGD2)

A similar analysis aims to measure the same quantity using events where the neutrino interacted inside FGD2. Starting with the CC-Inclusive selection (described above), a positive TPC-track with good quality is required. This track must be pion-like (the PID must match the pion hypothesis) and no other pion-like tracks are allowed in the event. Events containing π^0 's are rejected by looking for showers in the ECAL. Since the water is not an active tracking material, the first hits are registered in the first downstream scintillator layer (in which the scintillator bars are arranged horizontally); an intrinsic background from carbon interactions is to be expected. Another important background contribution is from CC interactions other than CC- 1π . In an attempt to constrain these backgrounds, two sidebands are used: A CC- 1π scintillator sample using interactions within the second scintillator layers (bars arranged vertically) describes the intrinsic background from carbon interactions. For the CC non- 1π interactions, a CC-Other water-enhanced sample is used. The MC-predicted background appears to be in good agreement with the data.

The flux-integrated differential cross-section is obtained using the Bayesian unfolding technique [13] to estimate the number of true signal events. Having estimated this number $N_k^{unfolded}$ for each bin k , the integrated neutrino flux Φ , the number of target nucleons $N_{targets}$ and the detection efficiency ϵ_k in a given bin of width ΔX_k , one can calculate the differential cross section for a variable X :

$$\left\langle \frac{\delta\sigma}{\delta X} \right\rangle_k = \frac{N_k^{unfolded}}{\epsilon_k N_{targets} \Phi \Delta X_k}. \quad (1)$$

The results are most interesting when discussed in terms of pion kinematics (Fig. 4): Both generators used (NEUT and GENIE) seem to slightly overestimate this channel. While the total cross section agrees with the NEUT prediction, GENIE over-predicts the cross section by 1.5σ .

CC- 1π in carbon (FGD1)

A related analysis performs a similar selection on carbon, using the FGD1 as an active volume. Apart from investigating standard variables such as momentum p and angle $\cos(\theta)$, this study also attempts to reconstruct neutrino energy E_ν , momentum transfer Q^2 , invariant

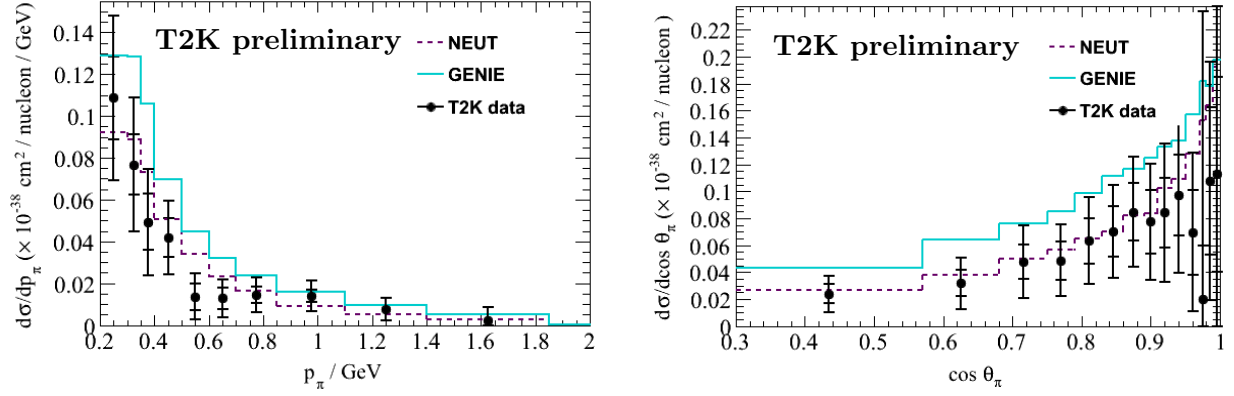


FIG. 4: Differential cross sections for CC-1 π production in water, shown as function of reconstructed pion momentum (left) and angle (right). T2K preliminary results.

mass W and angular variables $\theta_{\mu\pi}$, θ_{planar} , ϕ_{planar} that denote the angle between muon and pion candidates in the lab and the angles in the Adler system², respectively. These planar angles were studied by ANL [14], this study will provide a comparison at lower energies. Angular estimations for the pion candidates within the Rein-Sehgal model [15] were performed using NEUT MC: While the azimuthal angle ϕ_{planar} is presumed to have a flat distribution with a similar shape to ANL, differences are expected for the zenith angle $\cos(\theta_{planar})$. This is because the variable is highly sensitive to nuclear effects (e.g. low momentum pions) that were not an issue for ANL due to the deuterium target used.

CC-COH in carbon (FGD1)

To obtain a decent sample of CC-COH events, exactly one positive track is required after the standard CC-Inclusive cuts. It is required to have a pion-like, but not proton-like PID, and to be associated to the same vertex as the muon candidate. Additional variables are used to discriminate coherent interactions: The Vertex Activity (VA) measured in Photon Equivalent Units (PEU) is required to be low: $VA < 300PEU$. Also, the momentum transfer to the nucleus is required to be low: $|t| = \sqrt{(q - p_\pi)^2} < 0.15GeV$. To restrict the background, each of these two cuts are inverted separately to form two distinct background samples containing mainly CC-RES events. The background parameters and binned signal cross section are simultaneously fitted, yielding an excess of 55 ± 20 CC-COH events (2.7σ) with regard to the null hypothesis.

The cross section was calculated using two coherent production models in GENIE: the Rein-Sehgal (RS) and the Alvarez-Ruso (AR) model [16, 17].

$$\langle \sigma_{CCcoh\pi,C} \rangle_{RS} = (3.8 \pm 1.0(stat) \pm_{1.3}^{1.4}(syst)) \times 10^{-40} \text{ cm}^2/\text{nucleus}$$

² The Adler system refers to the rest frame of the hadronic system, in this case the Δ^{++} .

$$\langle \sigma_{CCcoh\pi,C} \rangle_{AR} = (3.3 \pm 0.9(stat) \pm 1.3_{-1.2}^{+1.3}(syst)) \times 10^{-40} \text{ cm}^2/\text{nucleus}$$

Both models agree with the data obtained so far (see Fig. 5). Currently, this study lacks the statistical power to distinguish between them.

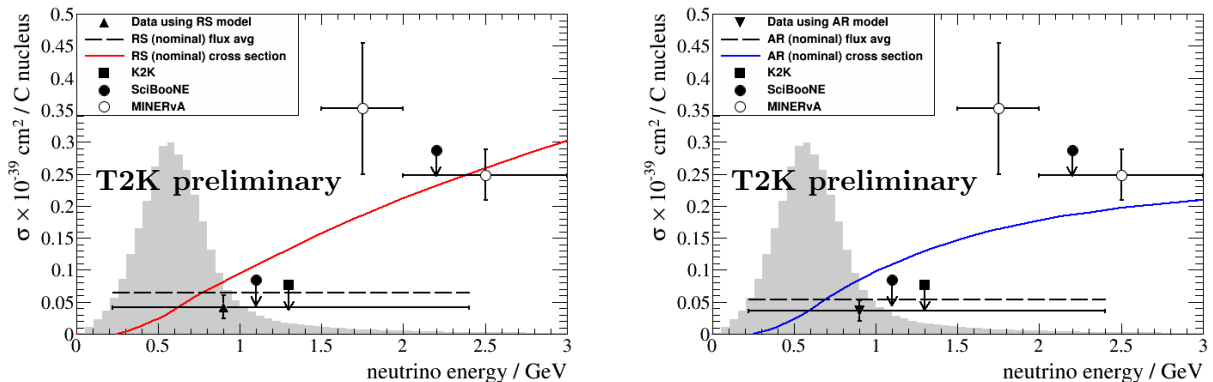


FIG. 5: Total cross section for CC-COH π^+ production in carbon, compared to Rein-Sehgal (left) and Alvarez-Ruso model (right). Previous measurements are shown for comparison. T2K preliminary results.

CC-COH in carbon (INGRID)

Another analysis attempting to measure neutrino-induced CC coherent production in carbon was conducted in the INGRID detector. A typical event is shown in Fig. 6. Exactly two tracks exiting the vertex and matching the muon/pion PID hypotheses are required. The muon must be forward going ($\theta_\mu < 15^\circ$) due to the small Q^2 expected in CC-COH events. Furthermore, the vertex activity (VA), which is defined as the energy deposition around the vertex, must be low ($VA < 34\text{MeV}$) to reject protons below the tracking threshold.

The background for this selection is dominated by CC non-coherent interactions; a background subtraction technique is used to calculate the cross section:

$$\sigma_{CC-COH,\pi} = \frac{N_{sel} - N_{BG}}{\epsilon N_{targets} \Phi}, \quad (2)$$

where the number of signal events is estimated by subtracting the normalised number of background events N_{BG} from the number of selected events N_{sel} . The denominator contains the same variables as in equation 1, but without binning. This method is model-dependent due to the MC-based assumption on the signal purity: The total cross section thus measured is:

$$\sigma_{CCcoh\pi,C} = (1.0267 \pm 0.2455(stat) \pm 0.7028_{-0.6769}^{+0.7028}(syst)) \times 10^{-39} \text{ cm}^2/\text{nucleus}.$$

Due to the large systematic error, the null hypothesis cannot be excluded at this point in time. Therefore, an upper limit (90% C.L.) is calculated:

$$\sigma_{CCcoh\pi,C} < 1.9808 \times 10^{-39} \text{ cm}^2/\text{nucleus}.$$

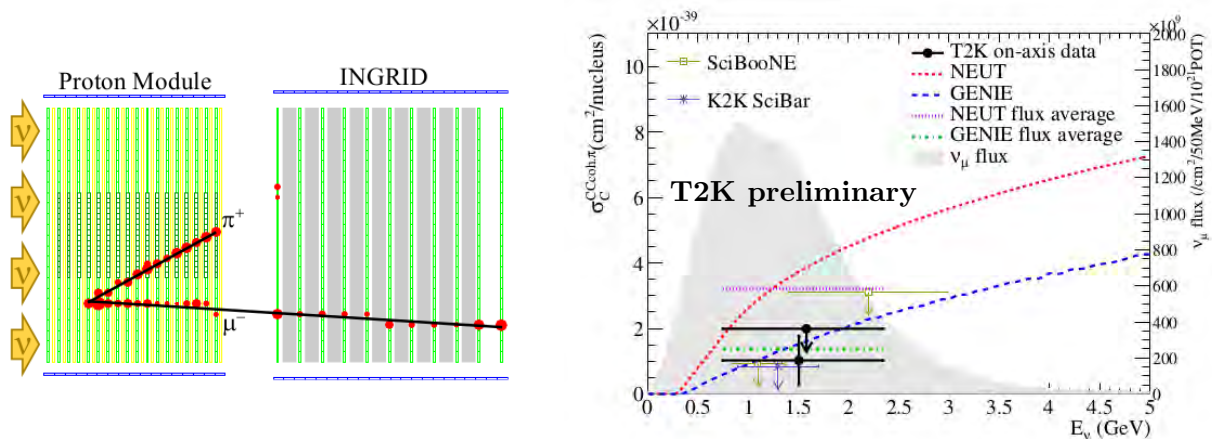


FIG. 6: INGRID search for coherent pion production. Left: Typical event display. Right: Total cross section for this interaction channel. T2K preliminary results.

The result is consistent with the flux average calculated with GENIE, but about 40% below the NEUT prediction (see Fig. 6). The discrepancy is due to generator differences in pion-nucleon cross sections.

CC-1K in carbon (FGD1)

As neutrino energy increases, so do the possibilities for meson production: various CC- $1K^+$ channels exist, where strangeness can be conserved (associated production) or violated (single kaon production). The latter is Cabibbo-suppressed, but nevertheless dominant in the energy region below the threshold for associated production. Very little data is available in the $\sim 1\text{GeV}$ region, with BNL contributing a single data point [18]. First analyses to measure kaon production in modern neutrino beams are on the way at MINERvA [19], with complementary measurements being performed at ND280. These channels represent an important background to proton decay³; future studies of the kaon kinematics may further the development of nuclear models.

The kaon analysis at ND280 uses GENIE with an additional model for single kaon production⁴ [21]. Based on the inclusive CC selection previously described, it uses the TPC PID method within a restricted phase space to select kaons. With a total cross section $\sigma \sim 10^{-40} \text{ cm}^2/\text{nucleus}$ and a rate of 7.2 events per 10^{20}POT predicted by GENIE MC, this analysis is expected to be statistics limited. A result will be reported in 2016.

³ The proton decay mode $p \rightarrow K^+\bar{\nu}$ is favoured by some SUSY-GUT theories, with the current experimental limit for the proton lifetime set by Super-K at $\tau > 5.9 \times 10^{33}\text{y}$ (90% C.L.) [20].

⁴ The `SingleKaon` generator is included as optional model in recent versions of GENIE ($\geq 2.9.0$) [21].

CONCLUSIONS

Cross section measurements provide both fundamental understanding of neutrino-nucleus interactions and valuable inputs to neutrino oscillation experiments. For future oscillation experiments, cross section uncertainties are expected to be among the dominant systematic uncertainties. To improve the various flaws currently present in nuclear models, it will be crucial to provide precision measurements of neutrino cross sections at various energies for different targets, interaction processes and neutrino types. When sufficient statistics are available, differential cross sections should be presented as function of kinematic variables, such as pion momentum. This allows for a better understanding of nuclear effects such as FSI, which distort the outgoing particle composition and kinematics. As the amount of data taken increases, more exotic cross section studies become of interest: Kaon production from neutrino interactions is one of the main backgrounds for proton decay modes predicted by SUSY-GUT theories, which have a fundamental impact on our understanding of the universe.

* *Presented at NuFact15, 10-15 Aug 2015, Rio de Janeiro, Brazil [C15-08-10.2]*

† Speaker (for the T2K collaboration); martti.nirkko@lhep.unibe.ch

- [1] A. Aguilar-Arevalo et al. (MiniBooNE), *Phys. Rev.* **D83**, 052007 (2011), 1011.3572.
- [2] B. Eberly et al. (MINERvA), *Phys. Rev.* **D92**, 092008 (2015), 1406.6415.
- [3] C. Andreopoulos et al., *Nucl. Instrum. Meth.* **A614**, 87 (2010), 0905.2517.
- [4] Y. Hayato, *Acta Physica Polonica B* **40**, 2477 (2009).
- [5] A. Higuera et al. (MINERvA), *Phys. Rev. Lett.* **113**, 261802 (2014), 1409.3835.
- [6] K. Abe et al. (T2K), *Nucl. Instrum. Meth.* **A659**, 106 (2011), 1106.1238.
- [7] O. Lalakulich and U. Mosel, *Phys. Rev.* **C88**, 017601 (2013), 1305.3861.
- [8] K. Abe et al. (T2K), *Phys. Rev. Lett.* **112**, 061802 (2014), 1311.4750.
- [9] K. Abe et al. (T2K) (2015), submitted to PRL, 1512.02495.
- [10] Y. Fukuda et al. (Super-Kamiokande), *Nucl. Instrum. Meth.* **A501**, 418 (2003).
- [11] S. Bolognesi, in *NuFact15 conference proceedings* (2015).
- [12] A. Furmanski, in *NuFact15 conference proceedings* (2015).
- [13] G. D'Agostini, *Nucl. Instrum. Meth.* **A362**, 487 (1995).
- [14] G. M. Radecky et al., *Phys. Rev. D* **25**, 1161 (1982).
- [15] D. Rein and L. M. Sehgal, *Annals Phys.* **133**, 79 (1981).
- [16] D. Rein and L. M. Sehgal, *Nucl. Phys.* **B223**, 29 (1983).
- [17] L. Alvarez-Ruso, L. S. Geng, S. Hirenzaki, and M. J. Vicente Vacas (2007), 0709.0728.
- [18] N. J. Baker et al., *Phys. Rev. D* **24**, 2779 (1981).
- [19] M. Carneiro, in *NuFact15 conference proceedings* (2015).
- [20] K. Abe et al. (Super-Kamiokande), *Phys. Rev. D* **90**, 072005 (2014).
- [21] M. Alam et al. (2015), 1512.06882.

Pion and Kaon Production at MINERvA*

Mateus F. Carneiro[†]

Centro Brasileiro de Pesquisas Físicas,

Rua Dr. Xavier Sigaud 150, Urca,

Rio de Janeiro, Rio de Janeiro, 22290-180, Brazil

on behalf of the MINERvA Collaboration

(Dated: May 23, 2016)

Abstract

The MINERvA (Main INjector ExpeRiment for v-A) detector is situated in Fermilabs NuMI beam, which provides neutrinos and antineutrinos in the 1-20 GeV range. It is designed to make precision cross-section measurements for scattering processes on various nuclei which are important for neutrino oscillation experiments and the probing of the nuclear medium. Presented are recent results from MINERvA on neutral kaon production and various pion production processes.

INTRODUCTION

The MINERvA experiment is a fully active, high resolution detector designed to study neutrino-nucleus scattering in the few-GeV region and provide inputs for neutrino oscillation experiments. The experiment also examines nuclear effects and parton distribution functions (PDFs) using a variety of targets materials. Precision neutrino measurements aiming to determine mass hierarchy, probe CP violation, or look for new physics, require precise knowledge of cross sections, final states, and nuclear effects in neutrino scattering. These experiments need models that will correctly predict the rate and spectrum of events for neutrino interactions, especially using medium-heavy materials such as steel, argon, carbon and oxygen. The relation between true neutrino energy and the final state particles is also a key information for neutrino oscillation physics, since the flavor oscillation probability depends on neutrino energy.

The detector is situated in Fermilab's NuMI beamline [1] along with the MINOS and NOvA experiments. During the period of 2010 through the Spring of 2012 the MINERvA detector took data in the "low energy" mode, in which the peak for the neutrino energy was around 3 GeV. Since then, the NuMI beamline has been working in "medium energy" mode with the neutrino energy peak at 6 GeV.

MINERvA [2] is comprised of 120 hexagonal modules stacked along the beamline. The detector is segmented transversely into: the inner detector, with planes of solid scintillator and passive nuclear target regions of carbon, iron, lead and water; a region of pure scintillator strips; downstream electromagnetic and hadronic calorimeters; and an outer detector composed of a frame of steel with embedded scintillator, which also serves as the supporting structure. The scintillator strips have a triangular shape that permits 3 mm of position resolution and are placed in adjacent planes offset by 60 degrees from each other, enabling a

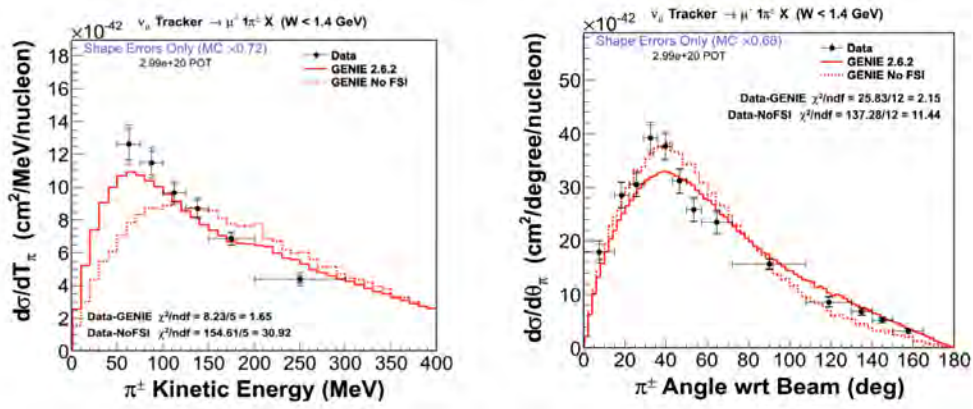


FIG. 1: Differential cross section vs. charged pion kinetic energy (left) and angle (right), in comparison with GENIE with and without FSI.

three-dimensional track reconstruction. The MINOS near detector [3] is situated two meters downstream of the MINERvA detector and serves as a magnetized muon spectrometer.

PION PRODUCTION ANALYSIS

The delta resonance, which decay to a pion and a nucleon, is the main method of pion production. Final state interactions (FSI) can absorb the pion in interactions with nuclear targets, mimicking the quasi-elastic signal and making pion production a major background for detectors that use CCQE as their signal. On the other hand, FSI can produce pions that can contaminate the quasi-elastic signal presenting a indistinguishable topology.

MINERvA has measured the cross section for pion production in two different channels, charged current single charged pion production by neutrino scattering and charged current single pion production by antineutrino scattering. For each channel we present two different analysis: using the hadronic kinematics, which provide information on FSI within the nucleus; and using the leptonic kinematics, which is more sensitive to the initial interaction within the nucleus.

Neutrino Single charged pion production

The main contribution for pion production comes from charged-current processes in which a neutrino scatters from scintillator to produce a muon and a single charged pion ($\nu_\mu A \rightarrow$

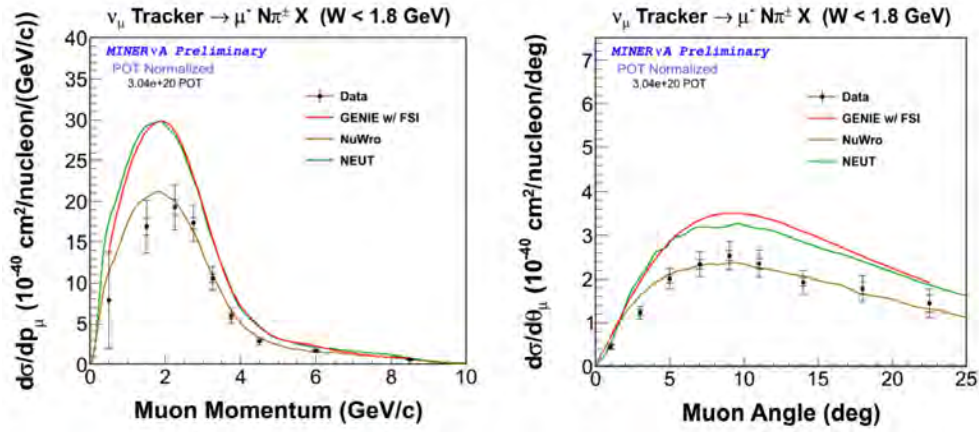


FIG. 2: Differential cross section vs. muon momentum (left) and angle (right), in data and different generators.

$\mu^- \pi^+ A$ or $\nu_\mu A \rightarrow \mu^- \pi^\pm X$ where A is the initial nucleus and X refers to the recoil nucleus which may not be the same as A , plus any other particles that are not pions).

The event selection required a muon that reached the MINOS near detector, and a candidate pion reconstructed inside the MINERvA detector without creating a hadron shower. Pions can be identified in MINERvA by their dE/dx and the presence of a Michel electron from the pion to muon to electron decay chain.

Differential cross sections are measured with respect to the outgoing pion's kinetic energy [4] and the angle between the pion and the neutrino beam. We unfold our signal using GENIE [5], which models pion production using the Rein-Sehgal model [6].

The pion energy plot in Figure 1, in particular, shows the data's clear preference for models including FSI effects, highlighting the importance of these processes to pion energy distributions. The results of this study can be used by generators to constrain both the primary interaction rate for these processes and the FSI parameters.

Figure 2 shows the measurement in term of muon energy and the comparison to GENIE with final-state interactions enabled; to the models used in NuWro [7] and Neut [8]. It's clear that both GENIE and NEUT overestimate the cross section while NuWro provides better prediction.

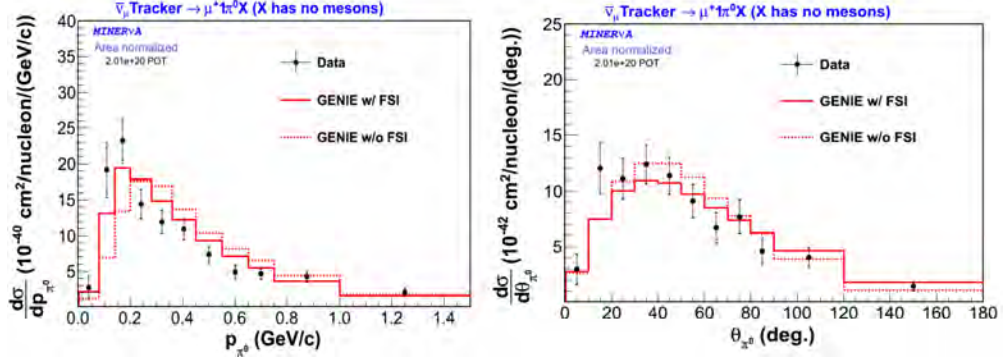


FIG. 3: Differential cross section vs. neutral pion kinetic energy (left) and angle (right), in data and GENIE with and without FSI.

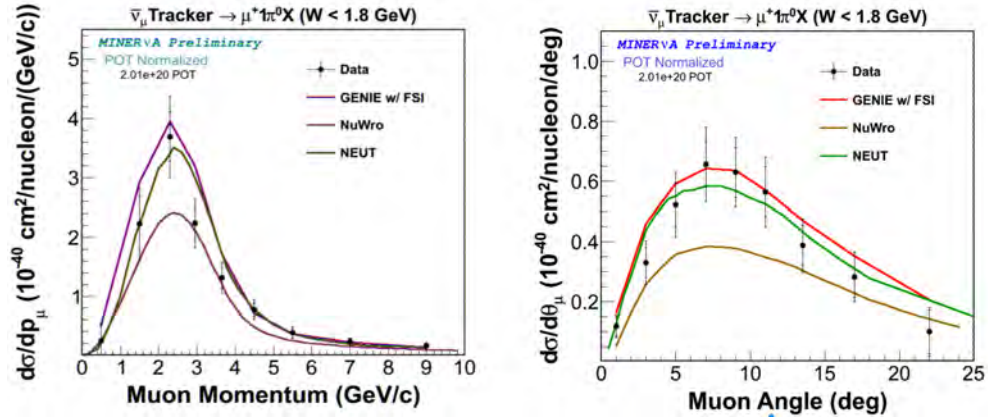


FIG. 4: Differential cross section vs. neutral pion kinetic energy (left) and angle (right), in data and various generators.

Antineutrino Single neutral pion production

The cross section for charged-current neutral pion production from antineutrinos on scintillator ($\bar{\nu}_\mu A \rightarrow \mu^+ \pi^0 X$, where A is the initial nucleus and X refers to the recoil nucleus) is not well-studied, and generators' models vary significantly. It is, however, important to oscillation experiments, as its neutral-current analog ($\bar{\nu}_\mu A \rightarrow \bar{\nu}_\mu \pi^0 X$) can mimic a $\bar{\nu}_e$ appearance signature, due to the electromagnetic shower of the $\pi^0 \rightarrow \gamma\gamma$ decay.

The pion is identified by looking for the two photon showers from its decay. Its energy, and angle are reconstructed from the calorimetrically measured energy and the positions of these photons with respect to the muon vertex [9].

Figure 3 presents the hadronic analysis results and shows differential cross sections with

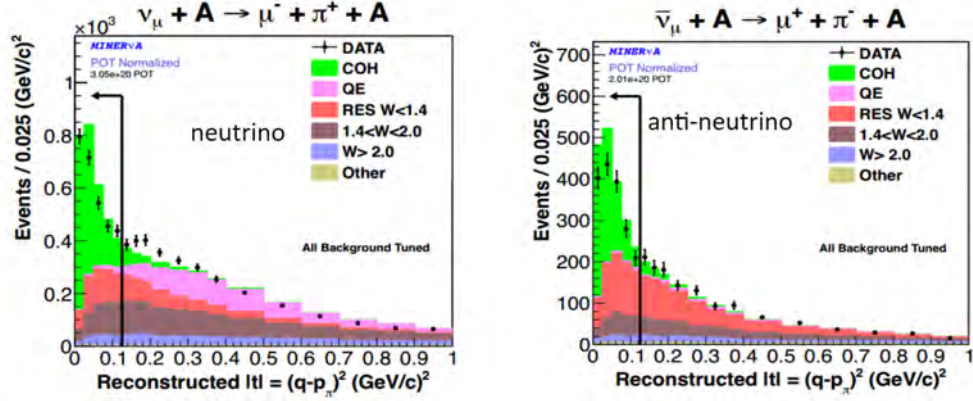


FIG. 5: Reconstructed momentum exchange between the nucleus and the system of the leptons and produced pion ($|t|$) for neutrino and antineutrino.

respect to the kinetic energy and angle of the neutral pion. The plots compare the measured cross section distributions to those predicted by GENIE [5] with and without FSI. Final State Interactions for pions is typically studied in pion beams, and as only charged pion beams are available, π^0 interaction rates must be inferred through isospin relations, leading to significant uncertainties. This measurement will be of use in evaluating the approximations made in generators' models.

Figure 4 shows the result of the new analysis that uses muon variables. The measured cross section distribution are compared with GENIE [5] with FSI, NuWro [7] and Neut [8]. The generators differ in their FSI modeling methods; GENIE and NEUT predictions are similar and higher than NuWro.

Coherent Pion Production

Coherent pion production is the production of a pion after the neutrino scatters off the entire nucleus leaving the nucleus in its ground state. It is characterized by a small momentum exchange between the nucleus and the system formed by leptons and produced pion ($|t|$) defined from the measured muon (p_μ) and pion (p_π) energies and directions as

$$|t| = |(p_\nu - p_\mu - p_\pi)| \approx \left(\sum_{i=\mu,\pi} E_i - p_{i,L} \right)^2 + \left| \sum_{i=\mu,\pi} \vec{p}_{i,T} \right|^2 \quad (1)$$

where the approximation made is that zero energy is transferred to the recoil nucleus and where \vec{p}_T and p_L are the transverse and longitudinal momenta with respect to the known

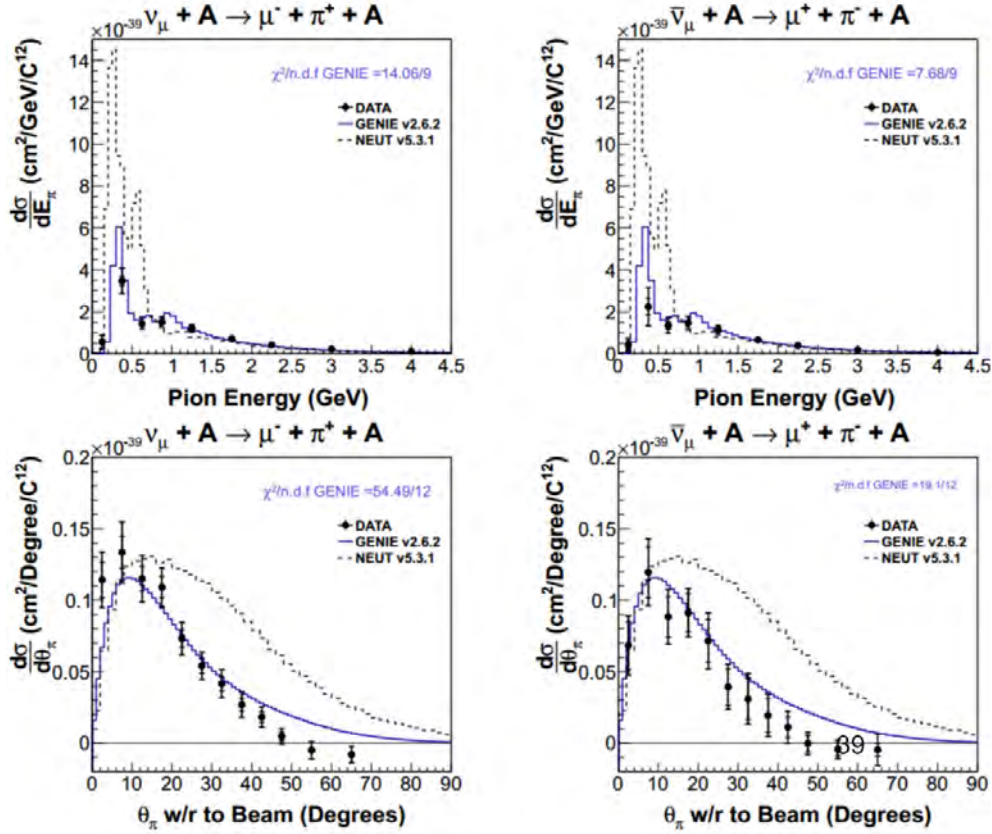


FIG. 6: Cross section distributions in respect of pion energy (top) and pion angle (bottom) for neutrino (left) and antineutrino (right) data.

neutrino beam direction.

The theory in this regime is not well understood, and many different approaches are included in neutrino event generators. Previous experiments have found evidence of this process at neutrino energies of several GeV, but the K2K and SciBooNE experiments made measurements consistent with no coherent pion production around 1 GeV [10, 11]. This process is important in the analysis of accelerator neutrino experiments where this process is a background to the desired quasielastic signal.

Figure 5 shows the distribution of reconstructed $|t|$ for neutrino and antineutrino data, in which the population of coherent events at low $|t|$ is clearly visible [12].

The default simulation overpredicts the backgrounds in the high $|t|$ region, and so we tune the prediction with a fit to pion energy distributions in the $0.2 < |t|/GeV^2 < 0.6$ region. The differential cross sections in pion energy and angle are shown in Figure 6. In

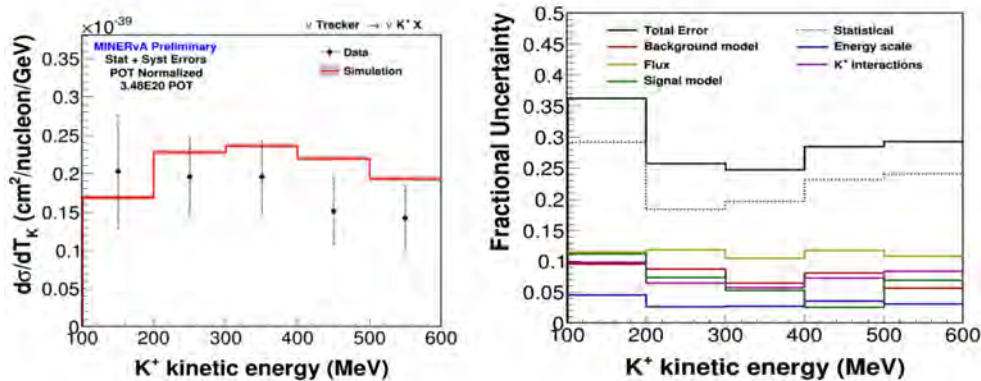


FIG. 7: Preliminary neutral current kaon production cross section with respect to K^+ kinetic energy (left) and the respective fractional uncertainties (right).

both neutrino and antineutrino data, the data favor lower pion angles with respect to the beam, and a lower peak at low pion energies than the prediction of the Rein-Sehgal model, which is used in current neutrino event generators.

KAON PRODUCTION

Neutral Current Kaon

Supersymmetry grand unification models predict proton decay into a K^+ with lifetimes of a few 10^{34} years. For water Cherenkov detector, K^+ is below detection threshold, so the signal consists of the μ^+ from the K^+ decay. The kaon cross section though, is still not well understood.

Strangeness conservation prevents K^+ absorption, and processes like $\pi + n \rightarrow K^+ \Lambda$ inside the nucleus enhance the cross section. For proton decay searches neutral-current reactions like $\nu + p^+ \rightarrow \nu K^+ \Lambda$ and $\nu + n^0 \rightarrow \nu K^+ \Sigma$ are backgrounds. Charged-current reactions are generally not backgrounds because they produce a detectable charged lepton. Neutral current is very important to understand and predict events in future detectors like HyperK. It's also relevant for future Liquid Argon detectors modeling K^+ FSI to understand the signal and any FSI processes that can fake the kaon signal.

Figure 7 shows the preliminary cross section measurement. Neutral current K^+ rate

below water Cherenkov threshold is well modeled by GENIE. This analysis is a work in progress and will be presented soon.

SUMMARY

The MINERvA collaboration is looking into a large range of important neutrino-nucleus cross section measurements which aim to understand, test and improve the model of these processes, and thus reduce systematics in oscillation experiments. The experiment is currently taking a new dataset in the Medium Energy beam configuration that will not only provide higher statistics for these analyses, but will also provide the ability to measure these processes on different nuclei.

This work was supported by the Fermi National Accelerator Laboratory under US Department of Energy contract No. DE-AC02-07CH11359 which included the MINERvA construction project. Construction support also was granted by the United States National Science Foundation under Award PHY-0619727 and by the University of Rochester. Support for participating scientists was provided by NSF and DOE (USA) by CAPES and CNPq (Brazil), by CoNaCyT (Mexico), by CONICYT (Chile), by CONCYTEC, DGI-PUCP and IDI/IGI-UNI (Peru), by Latin American Center for Physics (CLAF) and by RAS and the Russian Ministry of Education and Science (Russia). We thank the MINOS Collaboration for use of its near detector data. Finally, we thank the staff of Fermilab for support of the beamline and the detector.

* *Presented at NuFact15, 10-15 Aug 2015, Rio de Janeiro, Brazil [C15-08-10.2]*

† `mateusc@fnal.gov`; Speaker

- [1] K. Anderson, B. Bernstein, D. Boehnlein, K. R. Bourkland, S. Childress, et al., FERMILAB-DESIGN, 1998, 01, (1998)
- [2] L. Aliaga et al. (The MINERvA Collaboration), *Nucl. Instrum. Methods*, A743, 130, (2014)
- [3] D.G. Michael et al. (MINOS Collaboration), *Nucl. Instrum. Methods*, A596, 190, (2008)
- [4] B. Eberly et al. (The MINERvA Collaboration), arXiv:1406.6415 [hep-ex]
- [5] C. Andreopoulos, et al., *Nucl. Instrum. Methods*, 288A, 87, (2010)
- [6] D. Rein and L. M. Sehgal, *Ann. Phys.*, 133, 79, (1981)

- [7] K. M. Graczyk and J. T. Sobczyk, *Eur. Phys. J*, C31, 177, (2003)
- [8] Y. Hayato, *Acta Phys.Polon.*, B40, 2477-2489, (2009)
- [9] T. Le et al. (The MINERvA Collaboration), arXiv:1503.02107 [hep-ex]
- [10] Hasegawa, M. et al. (K2K Collaboration), *Phys. Rev. Lett*, 95, 25, (2005)
- [11] Hiraide, K. et al. (The SciBooNE Collaboration), *Phys. Rev. D*, 78, 11, (2008)
- [12] A Higuera, A Mislevic et al., (The MINERvA Collaboration), *Phys. Rev. Lett*, 113, 261802, (2014)

Neutrino-induced meson productions in resonance region*

Satoshi X. Nakamura[†]

Department of Physics, Osaka University, Toyonaka, Osaka 560-0043, Japan

(Dated: March 24, 2016)

Abstract

A dynamical coupled-channels (DCC) model for neutrino-nucleon reactions in the resonance region is developed. The DCC model is an extension of what we have previously developed through an analysis of $\pi N, \gamma N \rightarrow \pi N, \eta N, K\Lambda, K\Sigma$ reaction data for $W \leq 2.1$ GeV. In extending the DCC model, we analyze electron-induced reaction data for both proton and neutron targets to determine the vector current form factors up to $Q^2 \leq 3.0$ (GeV/c)². We derive axial-current matrix elements in accordance with the Partially Conserved Axial Current (PCAC) relation to the πN interactions of the DCC model. In this way, the interference pattern between resonant and non-resonant amplitudes can be uniquely fixed. We compare our calculated cross sections for neutrino-induced single-pion productions with available data, and find a reasonable agreement. We also calculate cross sections for the two-pion production in the resonance region, for the first time, with relevant resonance contributions and channel couplings taken into account. We compare the result with the available two-pion production data. The DCC model developed here will be a useful input to a future development of a neutrino-nucleus reaction model and/or a neutrino event generator for analyses of neutrino experiments.

INTRODUCTION

Forthcoming neutrino oscillation experiments will need precise understanding of neutrino-nucleus reactions in order to successfully address the leptonic CP violation and the neutrino mass hierarchy. The neutrino oscillation experiments detect neutrinos in a wide energy range, and thus the neutrino-nucleus reactions with different characteristics need to be understood. For a relatively low-energy neutrino ($E_\nu \lesssim 1$ GeV), the dominant reaction mechanisms are the quasi-elastic knockout of a nucleon, and quasi-free excitation of the $\Delta(1232)$ resonance followed by a decay into a πN final state. For a higher-energy neutrino ($2 \lesssim E_\nu \lesssim 4$ GeV), a large portion of data are from higher resonance excitations and deep inelastic scattering (DIS). In order to understand the neutrino-nucleus reactions of these different microscopic origin, obviously, it is important to combine different expertise. For example, nuclear theorists and neutrino experimentalists recently organized a collaboration at the J-PARC branch of the KEK theory center [1, 2] to tackle this challenging problem.

In this work, we focus on studying the neutrino reactions in the resonance region where the total hadronic energy W extends, $m_N + m_\pi < W \lesssim 2$ GeV; m_N (m_π) is the nucleon (pion) mass. Furthermore we will be concerned with the neutrino reaction on a single nucleon. In the resonance region, particularly between the $\Delta(1232)$ and DIS regions, we are still in the stage of developing a single nucleon model that is a basic ingredient to construct a neutrino-nucleus reaction model. Several theoretical models have been developed for neutrino-nucleon reactions in the resonance region; particularly the $\Delta(1232)$ region has been extensively studied because of its importance. However, there still remain conceptual and/or practical problems in the existing models as follows: First, we point out that reactions in the resonance region are multi-channel processes in nature. However, no existing model takes account of the multi-channel couplings required by the unitarity. Second, the neutrino-induced double pion productions over the entire resonance region have not been seriously studied previously, even though their production rates are expected to be comparable or even more important than those for the single-pion productions around and beyond the second resonance region. Third, interference between resonant and non-resonant amplitudes are not well under control for the axial-current in most of the previous models.

Our goal here is to develop a neutrino-nucleon reaction model in the resonance region

by overcoming the problems discussed above. In order to do so, the best available option would be to work with a coupled-channels model. In the last few years, we have developed a dynamical coupled-channels (DCC) model to analyze $\pi N, \gamma N \rightarrow \pi N, \eta N, K\Lambda, K\Sigma$ reaction data for a study of the baryon spectroscopy [3]. In there, we have shown that the model is successful in giving a reasonable fit to a large amount ($\sim 23,000$ data points) of the data. The model also has been shown to give a reasonable prediction for the pion-induced double pion productions [4]. Thus the DCC model seems a promising starting point for developing a neutrino-reaction model in the resonance region. At $Q^2 = 0$, we already have made an extension of the DCC model to the neutrino sector by invoking the PCAC (Partially Conserved Axial Current) hypothesis [5]. At this particular kinematics, the cross section is given by the divergence of the axial-current amplitude that is related to the πN amplitude through the PCAC relation. However, for describing the neutrino reactions in the whole kinematical region ($Q^2 \neq 0$), a dynamical model for the vector- and axial-currents is needed.

Practically, we need to do the following tasks for extending the DCC model to cover the neutrino reactions. Regarding the vector current, we already have fixed the amplitude for the proton target at $Q^2=0$ in our previous analysis [3]. The remaining task is to determine the Q^2 -dependence of the vector couplings, i.e., form factors. This can be done by analyzing data for the single pion electroproduction and inclusive electron scattering. A similar analysis also needs to be done with the neutron target model. By combining the vector current amplitudes for the proton and neutron targets, we can do the isospin separation of the vector current. This is a necessary step before calculating neutrino processes. As for the axial-current matrix elements at $Q^2=0$, we derive them so that the consistency, required by the PCAC relation, with the DCC πN interaction model is maintained. As a result of this derivation, the interference pattern between the resonant and non-resonant amplitudes are uniquely fixed within our model; this is an advantage of our approach. For the Q^2 -dependence of the axial-current matrix elements, we still inevitably need to employ a simple ansatz due to the lack of experimental information. This is a limitation shared by all the existing neutrino-reaction models in the resonance region.

With the vector- and axial-currents as described above, we calculate cross sections for the neutrino-induced meson productions in the resonance region. We compare our numerical results with available data for single-pion and double-pion productions. Particularly, comparison with the double-pion production data is made for the first time with the relevant resonance contributions and coupled-channels effects taken into account. For a fuller presentation of this work, we refer the readers to Ref. [6].

FORMALISM

The weak interaction Lagrangian for charged-current (CC) processes is given by

$$\mathcal{L}^{\text{CC}} = \frac{G_F V_{ud}}{\sqrt{2}} \int d^3x [J_\mu^{\text{CC}}(x) l^{\text{CC}\mu}(x) + \text{h.c.}] , \quad (1)$$

where G_F is the Fermi coupling constant and V_{ud} is the CKM matrix element. The leptonic current is denoted by l_μ^{CC} , while the hadronic current is

$$J_\mu^{\text{CC}}(x) = V_\mu^+(x) - A_\mu^+(x) , \quad (2)$$

where V_μ^+ and A_μ^+ are the vector and axial currents. The superscript + denotes the isospin raising operator.

Matrix elements of non-resonant currents

As in Eqs. (2), the current consists of the vector and axial currents. Matrix elements of the non-resonant vector current at $Q^2 = 0$ have been fixed through the previous analysis of photon-induced meson-production data [3]. We also need to fix the Q^2 -dependence of the matrix elements to study electron- and neutrino-induced reactions. Regarding the axial current, we take advantage of the fact that most of our $\pi N \rightarrow MB$ (MB : a meson-baryon state) potentials are derived from a chiral Lagrangian. Thus, we basically follow the way how the axial current is introduced in the chiral Lagrangian: an external axial current (a_{ext}^μ) enters into the chiral Lagrangian in combination with the pion field as $\partial^\mu \pi + f_\pi a_{\text{ext}}^\mu$ where f_π is the pion decay constant. Then the tree-level non-resonant axial-current matrix elements are derived from the chiral Lagrangian. By construction, $A_{\text{NP},\text{tree}}^{i,\mu}$ (i : isovector component) and the meson-baryon potential v satisfy the PCAC relation at $Q^2 = -m_\pi^2$: $\langle MB|q \cdot A_{\text{NP},\text{tree}}^i|N\rangle = if_\pi \langle MB|v|\pi^i N\rangle$. The Q^2 -dependence of the axial-coupling to the nucleon is fairly well-known from data analyses of quasi-elastic neutrino scattering and single pion electroproduction near threshold. We employ the conventional dipole form factor, $F_A(Q^2) = 1/(1 + Q^2/M_A^2)^2$, and take a numerical value for the axial mass, $M_A = 1.02$ GeV, from Ref. [7].

Matrix elements of N^* -excitation currents

The hadronic vector current contributes to the neutrino-induced reactions in the finite Q^2 region. In Ref. [3], we have done a combined analysis of $\pi N, \gamma p \rightarrow \pi N, \eta N, K\Lambda, K\Sigma$ reaction data, and fixed matrix elements of the vector current at $Q^2 = 0$ for the proton target. What we need to do is to extend the matrix elements of the vector current of Ref. [3] to the finite Q^2 region for application to the neutrino reactions. This can be done by analyzing data for electron-induced reactions on the proton and the neutron. Then we separate the vector form factors for N^* of $I = 1/2$ (I : isospin) into isovector and isoscalar parts. Regarding N^* of $I = 3/2$ for which only the isovector current contributes, we can determine the vector form factors by analyzing the proton-target data.

Because of rather scarce neutrino reaction data, it is difficult to determine N - N^* transition matrix elements induced by the axial-current. This is in sharp contrast with the situation for the vector form factors that are well determined by a large amount of electromagnetic reaction data. Thus, we need to take a different path to fix the axial form factors. The conventional practice is to write down a N - N^* transition matrix element induced by the axial-current in a general form with three or four form factors. Then the PCAC relation, $\langle N^*|q \cdot A_{\text{NP}}^i|N\rangle = if_\pi \langle N^*|\Gamma|\pi^i N\rangle$, is invoked to relate the presumably most important axial form factor at $Q^2 = -m_\pi^2$ to the corresponding πNN^* coupling. The other form factors are ignored except for the pion pole term. We then assume $A_{\text{NP}}^{i,\mu}(Q^2 = -m_\pi^2) \sim A_{\text{NP}}^{i,\mu}(Q^2 = 0)$. In the present work, we consider the axial currents for bare N^* of the spin-parity $1/2^\pm, 3/2^\pm, 5/2^\pm$ and $7/2^\pm$, and determine their axial form factors at $Q^2 = 0$ using the above procedure. It is even more difficult to determine the Q^2 -dependence of the axial couplings to N - N^* transitions because of the limited amount of data. Thus we assume that the Q^2 -dependence of the axial form factors is the same as that used for the non-resonant axial-current amplitudes.

It is worth emphasizing that a great advantage of our approach over the existing models is that relative phases between resonant and non-resonant amplitudes are made under control within the DCC model. This is possible in our approach by constructing the axial-current amplitudes and πN interactions consistently with the requirement of the PCAC relation.

ANALYSIS OF ELECTRON-INDUCED REACTION DATA

Here we analyze data for electron-induced reactions off the proton and neutron targets to determine the Q^2 dependence of the vector form factors. The data we analyze span the kinematical region of $W \leq 2$ GeV and $Q^2 \leq 3$ (GeV/c)² that is also shared by neutrino reactions for $E_\nu \leq 2$ GeV.

Among data for electron-proton reactions in the resonance region, those for the single pion electroproductions are the most abundant over a wide range of W and Q^2 . Therefore, these are the most useful to determine the Q^2 dependence of the p - N^* transition form factors. The cross sections for $p(e, e'\pi^0)p$ and $p(e, e'\pi^+)n$ have different sensitivities to resonances of different isospin state (1/2 or 3/2). The angular distribution of the pion is useful to disentangle the spin-parity of the resonances. Based on the one-photon exchange approximation, a standard formula of the angular distribution for the single pion electroproduction can be expressed in terms of virtual photon cross sections $d\sigma_\beta(Q^2, W, \cos\theta_\pi^*)/d\Omega_\pi^*$ ($\beta = T, L, LT, TT, LT'$).

The CLAS Collaboration has collected data for the single pion electroproduction off the proton in the kinematical region of our interest. Then they have extracted from the data the virtual photon cross sections. We fit these virtual photon cross sections to determine the Q^2 dependence of the p - N^* transition form factors. The single pion electroproduction data occupy a substantial portion of the relevant kinematical region of W and Q^2 . In some kinematical region, however, we still need more data to fix the vector form factors. In particular, data are missing for the $W \gtrsim 1.4$ GeV and low- Q^2 region, and the $W \gtrsim 1.7$ GeV and $Q^2 \lesssim 2$ (GeV/c)². In those kinematical region, we fit the inclusive structure functions from an empirical model due to Christy and Bosted [8].

We have fitted the data at several Q^2 values where the data are available. All the other parameters in the DCC model are fixed as those determined in Ref. [3]. We have successfully tested the DCC-based vector current model with the data covering the whole kinematical region relevant to neutrino reactions of $E_\nu \leq 2$ GeV. We present a selected result for the analysis of electron-proton reactions. We show a combination of the virtual photon cross sections, $d\sigma_T/d\Omega_\pi^* + \epsilon d\sigma_L/d\Omega_\pi^*$, at $Q^2=0.40$ (GeV/c)² for $p(e, e'\pi^+)n$ from the DCC model in Fig. 1 (left). In the same figure, the corresponding data are also shown for comparison. The DCC model fits the data for both π^0 and π^+ channels reasonably well. We also show in Fig. 1 (right) our DCC-based calculation of differential cross sections of the inclusive electron-proton scattering in comparison with data; the single pion electroproduction cross sections from the DCC model are also presented. In the figure, the range of Q^2 is indicated, and Q^2 monotonically decreases as W increases. The figures show a reasonable agreement between our calculation with the data, and also show the increasing importance of the multi-pion production processes above the $\Delta(1232)$ resonance region. As Q^2 increases, the DCC model starts to underestimate the inclusive cross section towards $W \sim 2$ GeV where the kinematical region is entering the DIS and multi-meson production region.

Regarding the $\gamma n \rightarrow \pi N$ reactions, we analyze unpolarized differential cross sections data from πN threshold to $W = 2$ GeV, and determine the vector nN^* transition strengths at

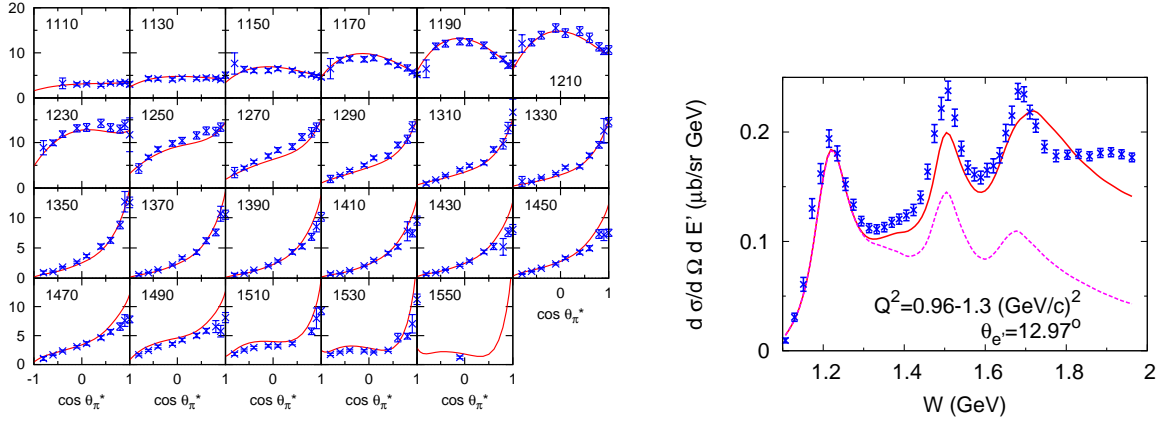


FIG. 1: (Color online) (Left) The virtual photon cross section $d\sigma_T/d\Omega_\pi^* + \epsilon d\sigma_L/d\Omega_\pi^*$ ($\mu\text{b}/\text{sr}$) at $Q^2=0.40$ (GeV/c)² for $p(e, e'\pi^+)n$ from the DCC model. The number in each panel indicates W (MeV). The data are from Ref. [9]. (Right) Comparison of DCC-based calculation with data for inclusive electron-proton scattering at $E_e=5.498$ GeV. The red solid curves are for inclusive cross sections while the magenta dashed-curves are for contributions from the πN final states. The range of Q^2 and the electron scattering angle ($\theta_{e'}$) are indicated in each panel. The data are from Ref. [10].

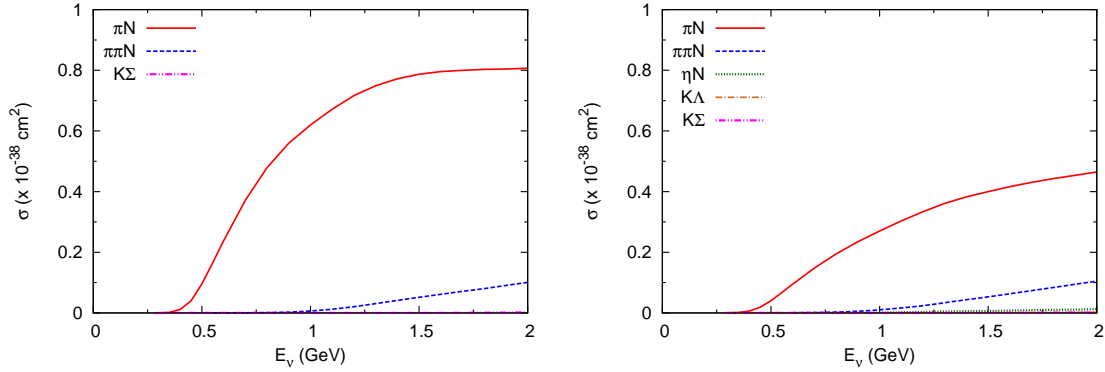


FIG. 2: (Color online) Total cross sections for the CC $\nu_\mu p$ (left) and $\nu_\mu n$ (right) reactions.

$Q^2=0$ for $I=1/2$ N^* states. In the finite Q^2 region, we use empirical inclusive structure functions from Ref. [11, 12] as data to determine the transition vector form factors. We successfully fitted the data by adjusting the vector form factors. See Ref. [6] for numerical results.

RESULTS FOR NEUTRINO REACTIONS

We present cross sections for the $\nu_\mu N$ reactions. With the DCC model, we can predict contributions from all the final states included in our model. Also, the DCC model provides all possible differential cross sections for each channel. Here, we present total cross sections for the CC $\nu_\mu N$ reactions up to $E_\nu = 2$ GeV in Fig. 2. For the proton-target, the single pion

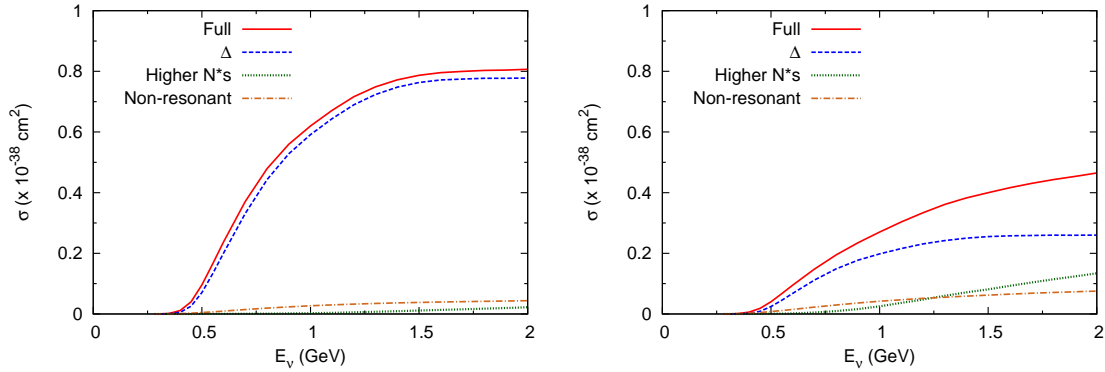


FIG. 3: (Color online) Various mechanisms contributing to $\nu_\mu p \rightarrow \mu^- \pi^+ p$ (left) and $\nu_\mu n \rightarrow \mu^- \pi N$ (right).

production dominates in the considered energy region. For the neutron-target, the single pion production is still the largest, but double-pion production becomes relatively more important towards $E_\nu = 2$ GeV. The ηN and KY production cross sections are $\mathcal{O}(10^{-1}-10^{-2})$ smaller.

Next we examine reaction mechanisms of the $\nu_\mu N$ scattering. In Fig. 3, we break down the single-pion production cross sections into several contributions each of which contains a set of certain mechanisms. For the proton-target process, the contribution from the $\Delta(1232)$ resonance dominates, while the higher N^* contribution is very small. The Δ contribution here is the neutrino cross section calculated with the P_{33} partial wave amplitude that contains the N^* -excitation mechanisms, while the higher N^* contribution is from the resonant amplitude including all partial waves other than P_{33} . The non-resonant cross sections calculated from the non-resonant amplitude is small for the proton-target process. In contrast, the situation is more complex in the neutron-target process where the Δ gives a smaller contribution and both $I=1/2$ and $3/2$ resonances contribute. As can be seen in the right panel of Fig. 3, the Δ dominates for $E_\nu \lesssim 1$ GeV, and higher resonances and non-resonant mechanisms give comparable contributions towards $E_\nu \sim 2$ GeV. This shows an importance of including both resonant and non-resonant contributions with the interferences among them under control. Similarly, we can compare the contribution of resonant and non-resonant amplitudes for the two-pion production reaction. Because $\Delta(1232)$ mainly contributes below the $\pi\pi N$ production threshold and thus gives a small contribution here, the resonant and non-resonant contributions are more comparable. Still, we find that the resonance-excitations are the main mechanism for the double-pion production in the resonance region.

Next we compare the CC neutrino-induced single pion production cross sections from the DCC model with available data from Refs. [13, 14] in Fig. 4. The left panel shows the total cross sections for $\nu_\mu p \rightarrow \mu^- \pi^+ p$ for which $\Delta(1232)$ dominates as we have seen in Fig. 3. If the $\Delta(1232)$ -dominance persists in the neutron-target processes shown in the middle and right panels of Fig. 4, the isospin Clebsch-Gordan coefficients determine the relative strength as $\sigma(\nu_\mu n \rightarrow \mu^- \pi^0 p)/\sigma(\nu_\mu p \rightarrow \mu^- \pi^+ p) = 2/9 \sim 0.22$, and $\sigma(\nu_\mu n \rightarrow \mu^- \pi^+ n)/\sigma(\nu_\mu p \rightarrow \mu^- \pi^+ p) = 1/9 \sim 0.11$. The actual ratios from the DCC model are $\sigma(\nu_\mu n \rightarrow \mu^- \pi^0 p)/\sigma(\nu_\mu p \rightarrow \mu^- \pi^+ p) = 0.28, 0.27, 0.29$, and $\sigma(\nu_\mu n \rightarrow \mu^- \pi^+ n)/\sigma(\nu_\mu p \rightarrow \mu^- \pi^+ p) = 0.13, 0.17, 0.21$ at $E_\nu=0.5, 1, 1.5$ GeV, respectively. The deviations from the naive isospin analysis are due to the non-resonant and higher-resonances contributions mostly in the neutron-target

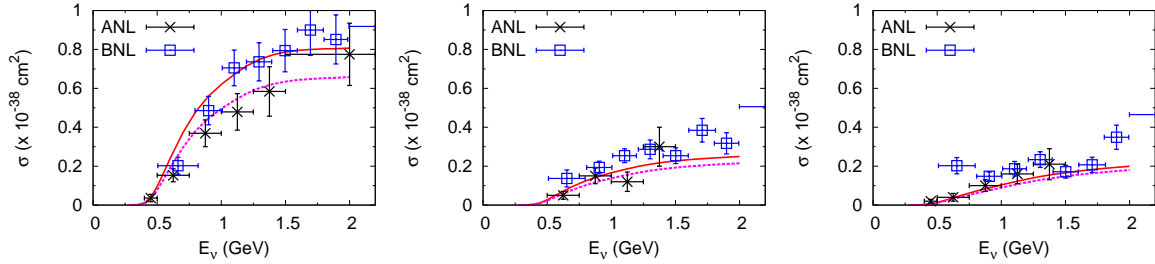


FIG. 4: (Color online) Comparison of the DCC-based calculation (red solid curves) with data for $\nu_\mu p \rightarrow \mu^- \pi^+ p$ (left), $\nu_\mu n \rightarrow \mu^- \pi^0 p$ (middle) and $\nu_\mu n \rightarrow \mu^- \pi^+ n$ (right). The DCC calculation with $0.8 \times g_{AN\Delta(1232)}^{\text{PCAC}}$ is also shown (magenta dashed curve). ANL (BNL) data are from Ref. [13] ([14]).

processes, as we have seen in Fig. 3. The two datasets from BNL and ANL for $\nu_\mu p \rightarrow \mu^- \pi^+ p$ shown in the left panel of Fig. 4 are not consistent as has been well known, and our result is closer to the BNL data [13]. For the other channels, our result is fairly consistent with both of the BNL and ANL data. It seems that the bare axial $N-\Delta(1232)$ coupling constants determined by the PCAC relation are too large to reproduce the ANL data. Because axial $N-N^*$ coupling constants should be better determined by analyzing neutrino-reaction data, it is tempting to multiply the bare axial $N-\Delta(1232)$ coupling constants, $g_{AN\Delta(1232)}^{\text{PCAC}}$, by 0.8, so that the DCC model better fits the ANL data. The resulting cross sections are shown by the dashed curves in Fig. 4. We find that $\sigma(\nu_\mu p \rightarrow \mu^- \pi^+ p)$ is reduced due to the dominance of the $\Delta(1232)$ resonance in this channel, while $\sigma(\nu_\mu n \rightarrow \mu^- \pi N)$ is only slightly reduced. The original data of these two experimental data have been reanalyzed recently [15], and it was claimed that the discrepancy between the two datasets is resolved. The resulting cross sections are closer to the original ANL data. However, the number of data is still very limited, and a new measurement of neutrino cross sections on the hydrogen and deuterium is highly desirable. We also note that the data shown in Fig. 4 were taken from experiments using the deuterium target. Thus one should analyze the data considering the nuclear effects such as the initial two-nucleon correlation and the final state interactions. Recently, the authors of Ref. [16] have taken a first step towards such an analysis. They developed a model that consists of elementary amplitudes for neutrino-induced single pion production off the nucleon [17], pion-nucleon rescattering amplitudes, and the deuteron and final NN scattering wave functions. Although they did not analyze the ANL and BNL data with their model, they examined how much the cross sections at certain kinematics can be changed by considering the nuclear effects. They found that the cross sections can be reduced as much as 30% for $\nu_\mu d \rightarrow \mu^- \pi^+ pn$ due to the NN rescattering. Meanwhile, the cross sections for $\nu_\mu d \rightarrow \mu^- \pi^0 pp$ are hardly changed by the final state interaction. It will be important to analyze the ANL and BNL data with this kind of model to determine the axial nucleon current, particularly the axial $N-\Delta(1232)$ transition strength.

We finally compare our results for double-pion productions with existing data in Fig. 5. Although there exist a few theoretical works on the neutrino-induced double-pion production near threshold [18–20], our calculation for the first time takes account of relevant resonance contributions for this process. The DCC-based prediction is fairly consistent with the data in the order of the magnitude. Particularly, the cross sections for $\nu_\mu p \rightarrow \mu^- \pi^+ \pi^0 p$ from the DCC model are in agreement with data. However, the

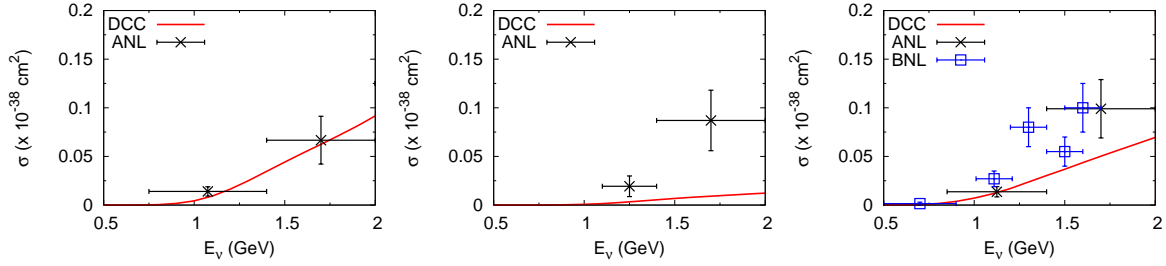


FIG. 5: (Color online) Comparison of the DCC-based calculation with data for $\nu_\mu p \rightarrow \mu^- \pi^+ \pi^0 p$ (left), $\nu_\mu p \rightarrow \mu^- \pi^+ \pi^+ n$ (middle) and $\nu_\mu n \rightarrow \mu^- \pi^+ \pi^- p$ (right). ANL (BNL) data are from Ref. [21] ([14]).

DCC prediction underestimates the $\nu_\mu p \rightarrow \mu^- \pi^+ \pi^+ n$ data. The rather small ratio of $\sigma(\nu_\mu p \rightarrow \mu^- \pi^+ \pi^+ n)/\sigma(\nu_\mu p \rightarrow \mu^- \pi^+ \pi^0 p) \sim 13\%$ at $E_\nu=2$ GeV from our calculation can be understood as follows. Within the present DCC-based calculation, $\pi\pi N$ final states are from decays of the πN and of the $\pi\Delta$, ρN , σN quasi two-body states. For a neutrino CC process on the proton for which hadronic states have $I = 3/2$, the πN , $\pi\Delta$, ρN channels can contribute. Within the current DCC model, we found that the $\pi\Delta$ channel gives a dominant contribution to the double pion productions. Then, retaining only the $\pi\Delta$ contribution, the ratio is given by the isospin Clebsch-Gordan coefficients as, $\sigma(\nu_\mu p \rightarrow \mu^- \pi^+ \pi^+ n)/\sigma(\nu_\mu p \rightarrow \mu^- \pi^+ \pi^0 p) = 2/13 \sim 15\%$, in good agreement with the ratio from the full calculation. With a very limited dataset, we do not further pursue the origin of the difference between our calculation and the data. If the double-pion data are further confirmed, then the model needs to incorporate some other mechanisms and/or adjust model parameters of the DCC model to explain the data.

SUMMARY

In this work, we have developed a dynamical coupled-channels (DCC) model for neutrino-nucleon reactions in the resonance region. Our starting point is the DCC model that we have developed through a comprehensive analysis of $\pi N, \gamma p \rightarrow \pi N, \eta N, K\Lambda, K\Sigma$ data for $W \leq 2.1$ GeV [3]. In order to extend the DCC model of Ref. [3] to what works for the neutrino reactions, we analyzed data for the single pion photoproduction off the neutron, and also data for the electron scattering on both proton and neutron targets. Through the analysis, we determined the Q^2 -dependence of the vector form factors up to $Q^2 \leq 3$ (GeV/c)². We derive the axial-current matrix elements that are linked to the πN potentials of the DCC model through the PCAC relation. As a consequence, relative phases between the non-resonant and resonant axial current amplitudes are uniquely determined within the DCC model.

We have presented cross sections for the neutrino-induced meson productions for $E_\nu \leq 2$ GeV. In this energy region, the single-pion production gives the largest contribution. Towards $E_\nu \sim 2$ GeV, the cross section for the double-pion production is getting larger to become 1/8 (1/4) of the single-pion production cross section for the proton (neutron) target. Because our DCC model has been determined by analyzing the $\pi N, \gamma N \rightarrow \pi N, \eta N, K\Lambda, K\Sigma$ data, we can also make a quantitative prediction for the neutrino cross sections for $\eta N, K\Lambda$, and $K\Sigma$ productions. We found that cross sections for $\eta N, K\Lambda$ and $K\Sigma$ productions are

10^{-2} - 10^{-3} times smaller than those for the single pion production. We have compared our numerical results with the available experimental data. For the single-pion production, our result, for which the axial N - N^* couplings are fixed by the PCAC relation, is consistent with the BNL data for $\nu_\mu p \rightarrow \mu^- \pi^+ p$, while fair agreement with both ANL and BNL data is found for the neutron target data. Through the comparison with the single pion production data for $W \lesssim 1.4$ GeV for which the $\Delta(1232)$ -excitation is the dominant mechanism, we were able to study the strength and the Q^2 -dependence of the axial N - $\Delta(1232)$ coupling. We also calculated double-pion production cross sections by taking account of relevant resonance contributions for the first time, and compared them with the data. We found a good agreement for $\nu_\mu p \rightarrow \mu^- \pi^+ \pi^0 p$ and $\nu_\mu n \rightarrow \mu^- \pi^+ \pi^- p$, but not for $\nu_\mu p \rightarrow \mu^- \pi^+ \pi^+ n$. Because the data for the double-pion productions are statistically rather poor, it is difficult to make a conclusive judgement on the DCC model.

Acknowledgments

The author thanks Hiroyuki Kamano and Toru Sato for their collaboration. This work was supported by Ministry of Education, Culture, Sports, Science and Technology (MEXT) KAKENHI Grant Number 25105010.

* *Presented at NuFact15, 10-15 Aug 2015, Rio de Janeiro, Brazil [C15-08-10.2]*

† `nakamura@kern.phys.sci.osaka-u.ac.jp`; Speaker

- [1] http://nuint.kek.jp/index_e.html; <http://j-parc-th.kek.jp/html/English/e-index.html>.
- [2] S.X. Nakamura, Y. Hayato, M. Hirai, H. Kamano, S. Kumano, M. Sakuda, K. Saito, and T. Sato: AIP Conf. Proc. **1663** (2015) 120010
- [3] H. Kamano, S. X. Nakamura, T.-S. H. Lee, and T. Sato: Phys. Rev. C **88** (2013) 035209
- [4] H. Kamano: Phys. Rev. C **88** (2013) 045203
- [5] H. Kamano, S. X. Nakamura, T.-S. H. Lee, and T. Sato: Phys. Rev. D **86** (2012) 097503
- [6] S. X. Nakamura, H. Kamano, T.-S. H. Lee, and T. Sato: arXiv:1506.03403.
- [7] V. Bernard et al.: J. Phys. **G28** (2002) R1
- [8] M.E. Christy and P. E. Bosted: Phys. Rev. C **81** (2010) 055213
- [9] H. Egiyan et al. (CLAS Collaboration): Phys. Rev. C **73** (2006) 025204
- [10] Preliminary results from JLab E00-002, C. Keppel, M.I. Niculescu, spokespersons. Data files can be obtained at <https://halleweb.jlab.org/resdata/database>.
- [11] P.E. Bosted and M.E. Christy: Phys. Rev. C **77** (2008) 065206
- [12] M.E. Christy, private communication.
- [13] S. J. Barish et al.: Phys. Rev. D **19** (1979) 2521
- [14] T. Kitagaki et al.: Phys. Rev. D **34** (1986) 2554
- [15] C. Wilkinson, P. Rodrigues, S. Cartwright, L. Thompson, and K. McFarland: Phys. Rev. D **90** (2014) 112017
- [16] J.-J. Wu, T. Sato, and T.-S. H. Lee: Phys. Rev. C **91** (2015) 035203
- [17] T. Sato, D. Uno, and T.-S. H. Lee: Phys. Rev. C **67** (2003) 065201
- [18] S. N. Biswas, S. R. Choudhury, A. K. Goyal and J. N. Passi: Phys. Rev. D **18** (1978) 3187
- [19] S. A. Adjei, D. A. Dicus, and V. L. Teplitz: Phys. Rev. D **24** (1981) 623
- [20] E. Hernandez, J. Nieves, S.K. Singh, M. Valverde, and M.J. Vicente Vacas: Phys. Rev. D **77** (2008) 053009
- [21] D. Day et al.: Phys. Rev. D **28** (1983) 2714

QRPA-based calculations for neutrino scattering and electroweak excitations of nuclei*

Arturo R. Samana[†]

*^aDepartamento de Ciências Exatas e Tecnológicas,
Universidade Estadual de Santa Cruz,
Rodovia Jorge Amado km 16, 45650-000 Ilhéus-Ba, Brazil*

Francisco Krmpotić, Alejandro E. Mariano, César A. Barbero
*Departamento de Física, Facultad de Ciencias Exactas,
Universidad Nacional de La Plata, CP 1900 La Plata, Argentina and
Instituto de Física La Plata, CONICET,
115 y 49, CP 1900 La Plata, Argentina*

Carlos A. Bertulani

*Department of Physics, Texas A&M University Commerce,
P.O. Box 3011 Commerce, Texas 75429, USA*

Nils Paar

*Physics Department, Faculty of Science, University of Zagreb,
Bijenicka 32, HR-10002 Zagreb, Croatia*

Abstract

A brief description of nuclear models used in the neutrino-nucleus reactions is performed, describing critically the general features, advantages and disadvantages. We focused on the neutrino-nucleus reactions at low energies due they present extremely subtle physical processes. They involve the weak interaction being very sensitive to the structure of nuclear ground states and excitations. The use of microscopic nuclear structure models in a consistent theoretical framework is therefore essential for a quantitative description of neutrino-nucleus reaction. These microscopic models include the nuclear shell model (SM), the random-phase approximation (RPA), continuum RPA (CRPA), hybrid models (CRPA+SM), quasiparticle RPA (QRPA), relativistic QRPA (RQRPA), and the Fermi gas model. The results with RPA-kind models to describe the nuclear matrix elements involved in neutrino-nucleus reactions, as such as electronic neutrino cross sections, muon capture rates and β^+ and β^- processes are compared. Some implications of QRPA based calculations with another weak processes, as such as the nuclear double beta decay ($\beta\beta$ -decay), are also sketched.

INTRODUCTION

New types of nuclear weak processes have been measured in recent years as such as experimental works involving atmospheric, solar, reactor and accelerator neutrinos [1]. They are based on neutrino and antineutrino interactions with complex nuclei and, rather than being used to study the corresponding cross sections, they are mainly aimed to inquire on possible exotic properties of neutrino, which are not contained in the Standard Model of elementary particles. On the other size, converting an observed neutrino flux into a luminosity requires knowledge of the neutrino-nucleus cross sections for the detector material. In summary, the neutrino-nucleus cross section are strongly important to constrain the properties of neutrinos. In that direction, an accurate description of the nuclear structure of the nuclei involved in the weak interaction is fundamental. This issue demands a giant effort because the nuclear models to be used are dependent of the incident neutrino energy.

Some years ago, we marked the importance of the nuclear structure calculations on the analysis of neutrino oscillation in the LSND experiment [2]. The positive result of this experiment was confronted with the result of Karmen experiment [3], where no oscillation signal was presented. There are two LSND studies of the DIF $\nu_\mu \rightarrow \nu_e$ oscillations [1]. The first analysis was done on the 1993-1995 data sample [1], which gave a transition probability $P_{\nu_\mu \rightarrow \nu_e}^{exp} = (2.6 \pm 1.0 \pm 0.5) \times 10^{-3}$, when the cross-section σ_e predicted by Kolbe et al. within the CRPA is used [4]. The RPA-like models include high-lying one-particle one-hole excitations, but very frequently completely fail to account for the amount and distribution of the GT strength. This is the reason why the CRPA is unable to explain the weak processes (β -decays, μ -capture, and neutrino induced reactions) among the ground states of the triad $\{^{12}\text{B}, ^{12}\text{C}, ^{12}\text{N}\}$ [4]. Thus, it was interesting to reanalyze the LSND results in the framework of the projected QRPA (PQRPA) [2], which is the only RPA model that treats correctly the Pauli principle, explaining in this way the distribution of the GT strength, furnishing satisfactory results not only for the weak processes among the ground states of the triad $\{^{12}\text{B}, ^{12}\text{C}, ^{12}\text{N}\}$, but also for the inclusive weak processes [5]. The left-side of Figure 1 shows a comparison of the CRPA and PQRPA results for $\sigma_e(E_\nu)$, $\sigma_e(E_\nu)\phi_\mu$ and $\sigma_e(E_\nu)\phi_\epsilon$, as a function of E_ν . The neutrino fluxes Φ_{ν_μ} , $\Phi_{\nu_e}^{\pi^+}$ and $\Phi_{\nu_e}^{\mu^+}$ were adopted from the Ref. [1]. So, we have found that the employment of a smaller inclusive DIF ($\nu_e, ^{12}\text{C}$) cross-section, than the one used by the LSND collaboration in the $\nu_\mu \rightarrow \nu_e$ oscillations study of the 1993-1995 data sample, leads to the following consequences: (i) the oscillation probability $P_{\nu_\mu \rightarrow \nu_e}^{exp}$ is increased, and (ii) the previously found consistence between the $(\sin^2 2\theta, \Delta m^2)$ confidence level regions for the $\nu_\mu \rightarrow \nu_e$ and the $\bar{\nu}_\mu \rightarrow \bar{\nu}_e$ oscillations is diminished. These effects are not due to the difference in the uncertainty ranges for the neutrino-nucleus cross-section, but to the difference in the cross-sections themselves.

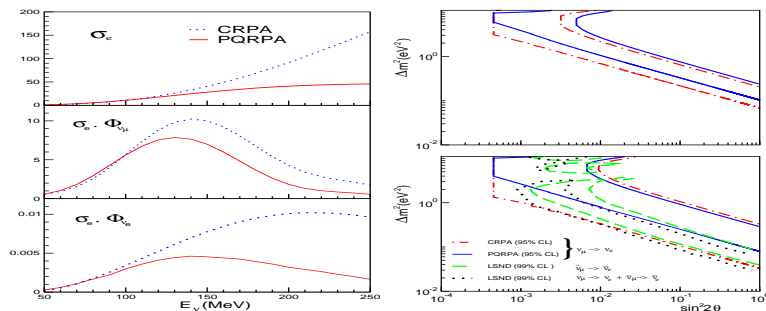


FIG. 1: Left-panel: Comparison between the CRPA and PQRPA results for: $\sigma_e(E_\nu)$ in units of 10^{-40} cm^2 (upper panel), and, in units of $10^{-52} \text{ POT}^{-1} \text{ MeV}^{-1}$, for $\sigma_e(E_\nu)\Phi_{\nu_\mu}$ (middle panel) and $\sigma_e(E_\nu)\Phi_{\nu_e}$ (lower panel). Right-panel: Regions in the neutrino oscillation parameter space. In the upper panel the results for $\nu_\mu \rightarrow \nu_e$ oscillations without the inclusion of the systematic uncertainty are shown, while the lower panel shows those with the uncertainty included [2].

The dynamics of supernova collapse and explosions as well as the synthesis of heavy nuclei are strongly dominated by neutrinos. For example, neutrinos carry away about 99% of gravitational binding energy in the core collapse of a massive star, and only a small fraction ($\sim 1\%$) is transferred to the stalled shock front, creating ejected neutrino fluxes observed in supernova remnants [6]. One important component of the detectors of supernovae neutrinos is ^{56}Fe . The KARMEN Collaboration measured (the only experimental data for a medium-heavy nucleus) the neutrino reaction $^{56}\text{Fe}(\nu_e, e^-)^{56}\text{Co}$ from e^- -bremsstrahlung with the detector surrounding shield [3]. This cross section is important to test the ability of nuclear models in explaining reactions on nuclei with masses around iron, which play an important role in supernova collapse. Experiments on neutrino oscillations such as MINOS [7] use iron as material detector, and future experiments, as such as SNS at ORNL [8]. The theoretical cross section was evaluated in several approximations as SM [9], Hybrid model SM+RPA [10] employed to estimate the number of events from ν - ^{56}Fe reactions in the LVD detector [11], QRPA [12], relativistic QRPA (RQRPA) [13], and projected QRPA [14]. The ν_e - ^{56}Fe cross sections were also described with the gross theory of beta decay (GTBD) [15], phenomenologically-based method of calculation which employs total muon capture rate data to determine the parameters necessary to calculate the inclusive neutrino cross sections [16], or using the local density approximation taking into account Pauli blocking, Fermi motion effects and renormalization of weak transition strengths in the nuclear medium [17].

WEAK-NUCLEAR INTERACTION FORMALISM

The most popular formalism for neutrino-nucleus scattering was developed by the Walecka group [18], where the nuclear transition matrix elements are classified as Coulomb, longitudinal, transverse electric, and transverse magnetic multipole moments related with the theoretical framework of previous electron scattering [19]. We feel that these denominations might be convenient when discussing simultaneously charge-conserving, and charge-exchange processes, but seems unnatural when one considers only the last ones. On the other hand, this terminology is not often used in nuclear β -decay and μ -capture, where one only speaks of vector and axial matrix elements with different degrees of forbiddenness: allowed (GT and Fermi), first forbidden, second forbidden, etc., types. Motivated by this fact, our group developed a proper formalism of weak interaction [5], obtaining new expressions for the transition rates. When studying neutrino induced reactions

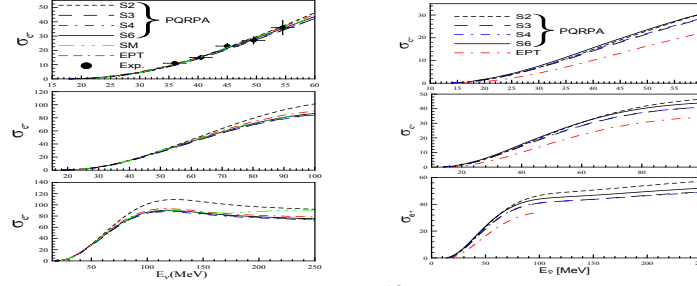


FIG. 2: Left-panel: Comparison of exclusive neutrino- ^{12}C cross sections (in units of 10^{-42} cm^2) evaluated in the PQRPA model [27], the SM [40], and EPT [37] calculations. The experimental data in the DAR region are from Ref. [1]. Right-panel: Similar comparison of nuclear model results for $^{12}\text{C}(\bar{\nu}, e^+)^{12}\text{B}$ cross-sections [27].

[20, 21] it is sometimes preferred to employ the formulation done by Kuramoto *et al.*[22], mainly because of its simplicity. But, the latter formalism does not include the velocity dependent terms in the hadronic current and it does not include the muon capture rates. Therefore, To describe simultaneously the neutrino-nucleus reactions and μ -capture processes it is necessary to resort to additional theoretical developments, such as those of Luyten *et al.* [23] and Auerbach and Klein [24].

In all the cases, the weak Hamiltonian is expressed in the form [18, 25, 26] $H_W(\mathbf{r}) = \frac{G}{\sqrt{2}} J_\alpha l_\alpha e^{-i\mathbf{r}\cdot\mathbf{k}}$, where $G = (3.04545 \pm 0.00006) \times 10^{-12}$ is the Fermi coupling constant (in natural units), the leptonic current $l_\alpha \equiv \{\mathbf{1}, i\mathbf{l}_\emptyset\}$ is given by the Eq. (2.3) in Ref. [5] and the hadronic current operator $J_\alpha \equiv \{\mathbf{J}, iJ_\emptyset\}$ in its nonrelativistic form reads

$$J_\emptyset = g_V + (\bar{g}_A + \bar{g}_{P1})\boldsymbol{\sigma} \cdot \hat{\mathbf{k}} + g_A \frac{i\boldsymbol{\sigma} \cdot \nabla}{M}, \quad (1)$$

$$\mathbf{J} = -g_A \boldsymbol{\sigma} - i\bar{g}_W \boldsymbol{\sigma} \times \hat{\mathbf{k}} - \bar{g}_V \hat{\mathbf{k}} + \bar{g}_{P2}(\boldsymbol{\sigma} \cdot \hat{\mathbf{k}})\hat{\mathbf{k}} - g_V \frac{i\nabla}{M},$$

where $\hat{\mathbf{k}} \equiv \mathbf{k}/|\mathbf{k}|$. The quantity $k = P_i - P_f \equiv \{\mathbf{k}, ik_\emptyset\}$ is the momentum transfer, M is the nucleon mass, and P_i and P_f are momenta of the initial and final nucleon (nucleus). The effective vector, axial-vector, weak-magnetism and pseudoscalar dimensionless coupling constants are, respectively $g_V = 1$, $g_A = 1$, $g_M = \kappa_p - \kappa_n = 3.70$, $g_P = g_A \frac{2Mm_\ell}{k^2 + m_\pi^2}$, where the auxiliary coupling constant $\bar{g}_V, \bar{g}_A, \bar{g}_W, \bar{g}_{P1}, \bar{g}_{P2}$ are defined in [5]. The conserved vector current (CVC) hypothesis, and the partially conserved axial vector current (PCAC) hypothesis are assumed. The finite nuclear size (FNS) effect is incorporated via the dipole form factor with a cutoff $\Lambda = 850 \text{ MeV}$, i.e., $g \rightarrow g [\Lambda^2/(\Lambda^2 + k^2)]^2$.

In performing the multipole expansion of the nuclear operators it is convenient 1) to take the momentum \mathbf{k} along the z axis using the spherical Bessel-Fourier series for $e^{-i\mathbf{k}\cdot\mathbf{r}}$, and 2) to define the operators O_α as

$$O_{\emptyset J} = j_J(\rho) Y_{J0}(\hat{\mathbf{r}}) J_\emptyset \equiv g_V \mathcal{M}_J^V + i g_A \mathcal{M}_J^A + i(\bar{g}_A + \bar{g}_{P1}) \mathcal{M}_{0J}^A, \quad (2)$$

$$O_{mJ} = \sum_L i^{J-L} F_{LJm} j_L(\rho) [Y_L(\hat{\mathbf{r}}) \otimes \mathbf{J}]_J \equiv i(\delta_{m0} \bar{g}_{P2} - g_A + m\bar{g}_W) \mathcal{M}_{mJ}^A + g_V \mathcal{M}_{mJ}^V - \delta_{m0} \bar{g}_V \mathcal{M}_J^V,$$

where $F_{LJm} = (-)^{1+m} (1, -mJm|L0)$, is a Clebsch-Gordan coefficient defined in Ref. [27]. The elementary operators are given by

$$\mathcal{M}_J^V = j_J(\rho) Y_J(\hat{\mathbf{r}}), \quad \mathcal{M}_J^A = M^{-1} j_J(\rho) Y_J(\hat{\mathbf{r}}) (\boldsymbol{\sigma} \cdot \nabla), \quad (3)$$

$$\mathcal{M}_{mJ}^A = \sum_{L \geq 0} i^{J-L-1} F_{LJm} j_L(\rho) [Y_L(\hat{\mathbf{r}}) \otimes \boldsymbol{\sigma}]_J, \quad \mathcal{M}_{mJ}^V = M^{-1} \sum_{L \geq 0} i^{J-L-1} F_{LJm} j_L(\rho) [Y_L(\hat{\mathbf{r}}) \otimes \nabla]_J.$$

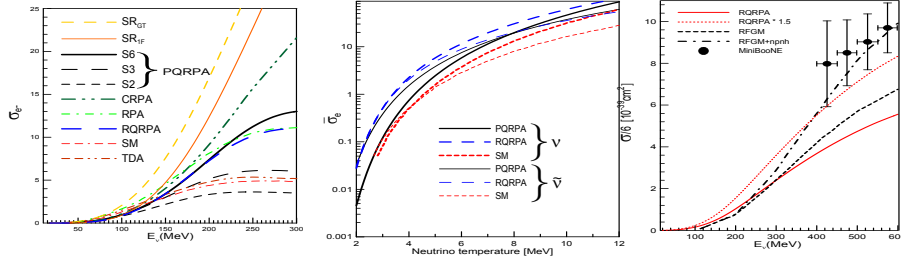


FIG. 3: Left-panel: Inclusive $^{12}\text{C}(\nu, e^-)^{12}\text{N}$ cross-section $\sigma_{e^-}(E_\nu)$ (in units of 10^{-39} cm^2) plotted as a function of the incident neutrino energy E_ν for PQRPA [27], RPA [21], CRPA [10], and RQRPA within S_{20} for $E_{2qp}=100 \text{ MeV}$ [13], SM [21], TDA [18] and global calculations SR_{GT} , and SR_{1F} . Central-panel: Flux-averaged neutrino and antineutrino cross sections $\bar{\sigma}_{e^\pm}$ in ^{12}C with typical supernovae fluxes [27]. Right-panel: RQRPA cross section per neutron (full line) [27] compared with that for the $(\nu_\mu, ^{12}\text{C})$ scattering data measured at MiniBooNE [35], with dotted line is shown the same calculation but renormalized by a factor 1.5, RFGM for pure (1p-1h) excitations (dashed line), and with the inclusion of the np-nh channels (dot-dashed line) [33, 41].

The comparison with the Walecka's formalism-[18] was established in the equation (A.11) of Ref. [27], and where the seven nuclear matrix elements, denoted as: $M_J^M, \Delta_J^M, \Delta_J^M, \Sigma_J^M, \Sigma_J^M, \Sigma_J^M$ and Ω_J^M , are also the elementary operators defined in Equation (3).

The transition amplitude for the neutrino-nucleus reaction at a fixed value of κ , from the initial state $|0^+\rangle$ in the (Z, N) nucleus to the n -th final state $|J_n^\pi\rangle$ in the nucleus $(Z \pm 1, N \mp 1)$, reads $\mathcal{T}_{J_n^\pi}(\kappa) \equiv \sum_{s_\ell, s_\nu} |\langle J_n^\pi | H_W(\kappa) | 0^+\rangle|^2$. The momentum transfer here is $k = p_\ell - q_\nu$, with $p_\ell \equiv \{\mathbf{p}_\ell, iE_\ell\}$ and $q_\nu \equiv \{\mathbf{q}_\nu, iE_\nu\}$, and after some algebra [5] one gets

$$\mathcal{T}_{J_n^\pi}(\kappa) = 4\pi G^2 \left[\sum_{\alpha=\theta, 0, \pm 1} |\langle J_n^\pi | \mathcal{O}_{\alpha J}(\kappa) | 0^+\rangle|^2 \mathcal{L}_\alpha - 2\Re(\langle J_n^\pi | \mathcal{O}_{\theta J}(\kappa) | 0^+\rangle \langle J_n^\pi | \mathcal{O}_{0J}(\kappa) | 0^+\rangle^*) \mathcal{L}_{\theta 0} \right], \quad (4)$$

where $\mathcal{L}_\theta, \mathcal{L}_0, \mathcal{L}_{\pm 1}, \mathcal{L}_{\theta 0}$ are the lepton traces, with $\theta \equiv \hat{\mathbf{q}}_\nu \cdot \hat{\mathbf{p}}_\ell$ being the angle between the incident neutrino and ejected lepton momenta, defined in [27].

The exclusive cross-section (ECS) for the state $|J_n^\pi\rangle$, as a function of the incident neutrino energy E_ν , is

$$\sigma_\ell(J_n^\pi, E_\nu) = \frac{|\mathbf{p}_\ell| E_\ell}{2\pi} F(Z + S, E_\ell) \int_{-1}^1 d(\cos \theta) \mathcal{T}_{J_n^\pi}(\kappa), \quad (5)$$

where E_ℓ is the electron energy, and $\omega_{J_n^\pi} = -k_\theta = E_\nu - E_\ell$ is the excitation energy of the state $|J_n^\pi\rangle$ relative to the state $|0^+\rangle$. Moreover, $F(Z + S, E_\ell)$ is the Fermi function for neutrino ($S = 1$), and antineutrino ($S = -1$), respectively. The inclusive cross-section (ICS) reads, $\sigma_\ell(E_\nu) = \sum_{J_n^\pi} \sigma_\ell(J_n^\pi, E_\nu)$, as well as with folded cross-sections, both exclusive,

$$\bar{\sigma}_\ell(J_n^\pi) = \int dE_\nu \sigma_\ell(J_n^\pi, E_\nu) \Phi_\ell(E_\nu), \quad \bar{\sigma}_\ell = \int dE_\nu \sigma_\ell(E_\nu) \Phi_\ell(E_\nu), \quad (6)$$

and inclusive, respectively, where $\Phi_\ell(E_\nu)$ is the neutrino (antineutrino) normalized flux.

ON NUCLEAR MODELS AND WEAK PROCESSES CALCULATIONS

In a general way, the theoretical models can be divided generically into: (i) models with microscopical formalism with a detailed nuclear structure, solving the microscopic quantum-mechanical Schrodinger or Dirac equation, provides nuclear wave functions and g.s.-shape E_{sp} , J^π nuclear

spin, $\log(ft)$ value, $\tau_{1/2}$ half-life, etc, i.e., Shell Model [28] and RPA-like models as self-consistent Skyrme-HFB+QRPA [29], quasiparticle RPA (QRPA), projected QRPA[30], relativistic QRPA (RQRPA) [31], and density Functional+Finite Fermi System [32]; (ii) models describing overall nuclear properties statistically where the parameters are adjusted to experimental data through polynomial or algebraic expressions and there is no nuclear wave function, for example, Fermi Gas-based Model [33] and Gross Theory of β -decay (GTBD) [34]. It is a difficult task to have one nuclear model that takes into account all the incident neutrinos energy. Several experiments with different sources of neutrinos can adopt one or another model to simulate the neutrino interaction via Monte Carlo and after to measure it in the experiment. For example, present atmospheric and accelerator-based neutrino oscillation experiments involve ^{12}C and operate at neutrino energies $E_\nu \sim 1$ GeV to access the relevant regions of the oscillation parameter space. This is the case of the MiniBooNE detector [35], which uses the light mineral oil containing the CH_2 molecule. Another interval of energy is employed when supernovae neutrinos are studied. The corresponding neutrinos, which carry all flavors were observed in only one occasion (SN1987A), have an energy $E_\nu \lesssim 100$ MeV [36]. For the planned experimental searches of supernovae neutrino signals, which involve ^{12}C as scintillator liquid detector, the precise knowledge of neutrino cross sections of ^{12}N and ^{12}B ground-states (with energies of the order of 10 MeV), *i.e.*, of $\sigma_{e^-}(E_\nu, 1_1^+)$, and $\sigma_{e^+}(E_{\bar{\nu}}, 1_1^+)$ is very important. In fact, in the LVD experiment [11] the number of events detected during the supernova explosion are estimated by convoluting the neutrino supernova flux with: (i) the interaction cross sections, (ii) the efficiency of the detector, and (iii) the number of target nuclei. For the carbon content of the LVD detector have been used so far $\sigma_{e^-}(E_\nu, 1_1^+)$, and $\sigma_{e^+}(E_{\bar{\nu}}, 1_1^+)$, as obtained from the Elementary Particle Treatment (EPT) [37].

So then, we can adopt in low energy region (up to 100 MeV) some accurate shell model (SM) description or RPA-like models and also depending if we are interested to describe exclusive or inclusive quantities. In particular the RPA-like models are by far simpler computationally than the SM. Note that the kind of correlations that these two methods include are not the same. For example, the QRPA makes a large fraction of nucleons to take part in within a large single-particle space, but within a modest configuration space. The shell model, by contrast, deals with a small fraction of the nucleons in a limited single-particle space, but allows them to correlate in arbitrary ways within a large configuration space [38]. It is clear that the nuclear structure descriptions inspired on the Relativistic Fermi Gas Model (RFGM) [39], which do not involve multipole expansions, should only be used for inclusive quantities. A brief report of the nuclear models employed for ^{12}C is presented in Ref.[27].

Now, we describe some results obtained in ^{12}C and ^{56}Fe , nuclei that are using in current neutrino oscillation experiments, and some topics on double beta decay calculations. The PQRPA calculations [5] solved the puzzle found for Volpe et al. [21] related to the collectivity on the ground state in ^{12}C . In Ref. [27] were studied neutrino and antineutrino charge-exchange reactions on ^{12}C using the PQRPA and RQRPA in different configuration spaces to analyze their dependence on the configuration space. Figure 2 shows the exclusive $^{12}\text{C}(\nu, e^-)^{12}\text{N}$ cross-section $\sigma_e(E_\nu, 1_1^+)$, plotted as a function of the incident neutrino energy E_ν . Results for several single-particle spaces S_N , and $t = 0$ for S_2 , and S_3 , $t = 0.2$ for S_4 , and $t = 0.3$ for S_6 , within three different energy intervals, are shown. The SM, and EPT calculations are, respectively, from Refs. [40], and [37]. The experimental data in the DAR region are from Ref. [1]. In similar way, the right-panel of Figure 2 shows the calculated $(\bar{\nu}, ^{12}\text{C})$ cross-section $\sigma_{e^+}(E_{\bar{\nu}}, 1_1^+)$, plotted as a function of the incident antineutrino energy $E_{\bar{\nu}}$ in the same parametrization spaces.

The left-panel of Figure 3 shows the inclusive $^{12}\text{C}(\nu, e^-)^{12}\text{N}$ cross-section $\sigma_{e^-}(E_\nu)$ plotted as a function of the incident neutrino energy E_ν . The PQRPA results within the s.p. spaces S_2 , S_3 , and S_6 , and the same values of $s = t$ [57]. These are compared with two sum rule limits (global calculations): SR_{GT} , and SR_{1F} obtained with average excitation energy $\overline{\omega_{J_n^\pi}}$ of 17.34, and 42 MeV,

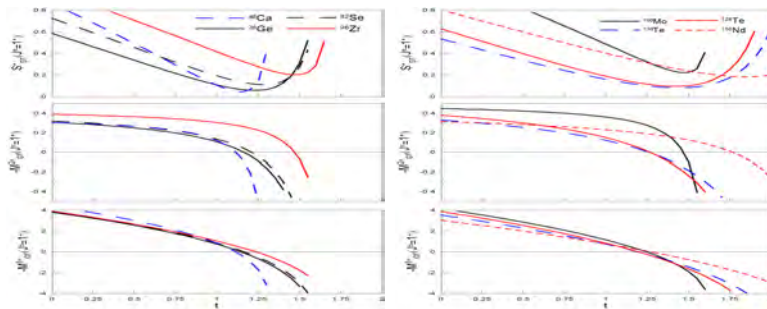


FIG. 4: S_{GT}^+ , $M_{GT}^{2\nu}$, $e M_{GT}^{0\nu}$ as a function of the parameter particle-particle t evaluated in the QRPA [51]

respectively. Several previous RPA-like calculations, namely: RPA [21], CRPA [10], and RQRPA within S_{20} for $E_{2qp}=100$ MeV [13], as well as the SM [21], and the TDA [18] are also shown. The central-panel of Figure 3 shows the flux-averaged neutrino and antineutrino cross sections $\bar{\sigma}_{e\pm}$ in ^{12}C with typical supernovae fluxes showing that in the interval of temperatures $T_\nu = 3 - 5$ MeV: (i) σ for antineutrinos is going larger to similar of σ for neutrinos and, (ii) the results obtained with SM are always smaller than PQRPA and RQRPA calculations [27]. Finally, in the right-panel of Figure 3 shows the calculated RQRPA (within S_{30} and $E_{2qp} = 500$ MeV) quasi-elastic ($\nu_e, ^{12}\text{C}$) cross section per neutron (full line) when is compared with that for the ($\nu_\mu, ^{12}\text{C}$) scattering data measured at MiniBooNE [35]; with dotted line is shown the same calculation but renormalized by a factor 1.5. Also are displayed the calculations done by Martini *et al.* [33, 41] within the RFGM+RPA for pure (1p-1h) excitations (dashed line), and with the inclusion of the np-nh channels (dot-dashed line).

In Ref. [14] were evaluated the inclusive $^{56}\text{Fe}(\nu_e, e^-)^{56}\text{Co}$ cross sections evaluated in QRPA and PQRPA, in the DAR region. They were compared with those obtained with other nuclear structure models: GTBD [15], Hybrid [42], QRPA_S [12], and RQRPA [13]. Table 1 in Ref.[14] shown the comparison of these folded cross section, where all the theoretical models agree with the experimental value due the experimental error in the measured value. The number of events detected for supernova is calculated as,

$$N_\alpha = N_t \int_0^\infty \Phi_\alpha(E_\nu) \cdot \sigma(E_\nu) \cdot \epsilon(E_\nu) dE_\nu, \quad (7)$$

where the index $\alpha = \nu_e, \bar{\nu}_e, \nu_x$ and ($\nu_x = \nu_\tau, \nu_\mu, \bar{\nu}_\mu, \bar{\nu}_\tau$) indicates the neutrino or antineutrino type, N_t is the number of target nuclei, $\Phi_\alpha(E_\nu)$ is the neutrino flux, $\sigma(E_\nu)$ is the neutrino-nucleus cross section, $\epsilon(E_\nu)$ is the detection efficiency, and E_ν is the neutrino energy. Recent calculations by the LVD group [11] estimate that the ($\nu_e + \bar{\nu}_e$) interactions on ^{56}Fe are almost 17% of the total detected signal. The time-spectra can be approximated by the zero-pinned Fermi-Dirac distribution. For the reactions ($\nu_e, ^{56}\text{Fe}$), Ref.[14] calculated N_e and \tilde{N}_e as a function of the neutrino temperatures T_{ν_e} and T_{ν_x} , folding $\sigma_e(E_\nu)$ from different nuclear structure models with the neutrino fluxes $\Phi_{\nu_e}^0(E_\nu, T_{\nu_e})$ and $\Phi_{\nu_x}^0(E_\nu, T_{\nu_x})$, respectively.

We have marked the importance of the semileptonic weak interaction processes in nuclei are very sensitive to detailed properties of nuclear ground states and excitations [43]. Marketin *et al.* [44] performed systematics calculations on muon capture rates for nuclei with $6 \leq Z \leq 94$ using RQRPA. Another RPA systematics calculations were performed by Zinner *et al.*[45]. On the other hand, we have shown that, when the capture of muons is evaluated in the context of the PQRPA, the conservation of the number of particles is very important not only for carbon but in all light nuclei with $A \leq 30$. The consequence of this is the superiority of the PQRPA on the QRPA in this nuclear mass region, where systematic calculations of muon capture rates with these models were performed [46]. One step beyond is made with RQRPA calculations to provide

a self-consistent microscopic description of neutrino-nucleus cross sections involving a large pool of $Z = 8 - 82$ nuclei for the implementation in models of nucleosynthesis and neutrino detector simulations. They performed a large-scale calculations of charged-current neutrino-nucleus cross sections, including those averaged over supernova neutrino fluxes, for the set of even-even target nuclei from oxygen toward lead ($Z = 8 - 82$), spanning $N = 8 - 182$ (O-Pb pool) [47].

We do not until this moment which is the absolute scale mass, and whether the neutrino is a Majorana or Dirac particle. The atomic nuclei are the detectors of the evasive neutrinos and the key of this puzzle is the neutrinoless double beta decay. The three commonly $\beta\beta$ -decay processes are: (i) the two-neutrino $\beta\beta$ -decay ($2\nu\beta\beta$); (ii) the neutrinoless $\beta\beta$ -decay ($0\nu\beta\beta$) and; (iii) the neutrinoless $\beta\beta$ -decay with majoron emission ($0\nu\chi\beta\beta$). The inverse half-life for the $0^+ \rightarrow 0^+$ and nuclear matrix elements (NME's) are related as [38, 48]:

$$T_{1/2}^{-1} = \mathcal{G}(\mathcal{M}\mathcal{F})^2, \quad \mathcal{F} = \begin{cases} 1 & , \text{ for } 2\nu\beta\beta \\ \langle m_\nu \rangle / m_e & , \text{ for } 0\nu\beta\beta \\ \langle g_M \rangle & , \text{ for } 0\nu\chi\beta\beta \end{cases}, \quad (8)$$

where \mathcal{G} is a kinematical factor which depends on the corresponding phase space, \mathcal{M} is the NME and the values in \mathcal{F} are $\langle m_\nu \rangle$ and $\langle g_M \rangle$ respectively the effective neutrino masses and the effective majoron-neutrino coupling. $\mathcal{M}_{2\nu}$ and $\mathcal{M}_{0\nu}$ present many similar features and it can be established that we shall not understand the $0\nu\beta\beta$ -decay unless we understand the $2\nu\beta\beta$ -decay. In other words, if we found an agreement between experimental and theoretical values for $\mathcal{M}_{2\nu}$, it is possible used the same nuclear model (and parametrization) to describe consistently $\mathcal{M}_{0\nu}$. There is an extensive literature on the theoretical estimations of NME of double beta decay using the QRPA model [49, 50]. In a recent work [50], the authors claim to achieve partial restoration of the isospin symmetry and hence fulfillment of the requirement that the $2\nu\beta\beta$ Fermi matrix element $M_F^{2\nu}$ vanishes. But this procedure was used previously in the pioneer work of Krmpotić and S. Sharma [48]. Using that receipt, we reproduce the single GT- β^+ strength (S_{GT}^+), NME for Gamow-Teller of $2\nu\beta\beta$ ($M_{GT}^{2\nu}$), and NME for Gamow-Teller of $0\nu\beta\beta$ ($M_{GT}^{0\nu}$), as a function of the particle-particle parameter t in the residual interaction are shown in Figure 4. These results were obtained using a numerical code that summarizes and gives a new fashion of the formalism presented in Refs. [49] for the $2\nu\beta\beta$ and $0\nu\beta\beta$, based on the Fourier-Bessel expansion of the weak Hamiltonian, adapted for nuclear structure calculations [51].

Another kind RPA formalism for $2\nu\beta\beta$ was proposed some years ago based on the Four Quasiparticle Tamm-Dancoff Approximation (FQTD). Several serious inconveniences found in the QRPA are not present in the FQTD, such as the ambiguity in treating the intermediary states, and further approximations necessary for evaluation of the nuclear matrix elements or, the extreme sensitivity of NME with the ratio between the pn and pp + nn pairings [38]. Some improvements on this model and their extension to open shell nuclei is being studied [52].

SUMMARY

A brief description of nuclear models used in the neutrino-nucleus reactions was performed, describing critically the general features, advantages and disadvantages. We focused on the neutrino-nucleus reactions at low energies due they present extremely subtle physical processes.

We noted that all the formalism to describe weak-nuclear interaction present in the literature are equivalent. Some of the most used formalism were developed by: (i) O'Connell, Donnelly & Walecka [18], where seven irreducible tensor operators (ITO) are obtained and they compose the nuclear matrix elements called by longitudinal, Coulomb, transversal electric, transversal magnetic according to those found in electron scattering formalism [19]; (ii) Kuramoto *et al.* [22], where the

nuclear hamiltonian is expanded up to $(|k|/M)^3$, where $|k|$ is the momentum transfer and M is the mass of nucleon; (iii) Luyten *et al.* [23], developed to evaluate muon capture rates, (iv) Krmpotić *et al.* [5], this uses a notation more familiar to the nuclear β -decay, where one works with allowed, first forbidden, second forbidden, etc transitions.

The microscopic RPA-like models, as such as the QRPA, are extensively used to evaluate weak-nuclear observables. They have some disadvantages, *i.e.*, to work with low energy neutrino regions up to 250 MeV; many of these QRPA are using the Skyrme interaction as residual interaction, but is not good enough to make decisive improvement, and the Gogny interaction is employed to check the Skyrme results; developed essentially for spherical nuclei, and there is a few QRPA model to non-spherical nuclei [53]. The advantages are: a self-consistent treatment, lead to large spaces, excellent agreement with exclusive reaction as well as the SM, with a well description of inclusive reaction and, it is possible to describe reaction up to 600 MeV neutrino energy with relativistic QRPA; a good option for astrophysical systematic calculations and; QRPA is the main tool for double beta decay in the last 30 years. Some improvements are planned through the Universal Nuclear Density Functional - UNEDF [54], and the extension to non-spherical nuclei. The SM is the other microscopical model most widely used. This model has the next disadvantages: only works with magic nuclei ($N = 50, 82, 126$) due they need a great computational effort to open the shells, only treats GT-decay and; to avoid a great computational task, some cut-offs due to configurational space are imposed that could be dangerous violating some sum rules. The advantages of this model is that several essential correlations are included, leading to a correct treatment of even-even and odd isotopes. Some improvements are coming from the ab-initio shell model, where new advances are obtained in nuclei as ^{12}C and ^{16}O [55], ^{48}Ca and ^{124}Sn [56].

Some results with RPA-kind models to describe the nuclear matrix elements involved in neutrino-nucleus reactions were compared. Some implications of QRPA based calculations with another weak processes, as such as the nuclear double beta decay ($\beta\beta$ -decay), were also sketched.

A.R. Samana acknowledges the financial support of the Organizing Committee of NuFact15, in particular to H. da Motta and J. Morfin, UESC and CAPES AUXPE-FAPESB-3336/2014/Processo no: 23038.007210/2014-19.

* Presented at NuFact15, 10-15 Aug 2015, Rio de Janeiro, Brazil [C15-08-10.2]

† arsamana@uesc.br; Speaker

- [1] A. Aguilar *et al.* [LSND collaboration], Phys. Rev. D **64**, 112007 (2001), and references therein.
- [2] A. Samana *et al.* , Phys. Lett. **B642**, 100 (2006).
- [3] KARMEN Collaboration, R. Maschuw, <http://www-ik1.fzk.de/karmen/cc-e.html/article>
- [4] E. Kolbe *et al.* , Phys. Rev. C **49**, 1122 (1994); E. Kolbe *et al.* Nucl. Phys. **A652** (1999) 91.
- [5] F. Krmpotić *et al.* Phys. Rev. C **71**, 044319 (2005).
- [6] H. Duan *et al.* , Phys. Rev. D **74**, 105014 (2006).
- [7] MINOS Collaboration, P. Adamson *et al.*, Phys. Rev. D **76**, 072005 (2007).
- [8] Y. Efremenko, Nucl. Phys. **B138**(Proc. Suppl), 343 (2005)
- [9] E.V. Bugaev *et al.* , Nucl. Phys. **A324**, 350 (1979).
- [10] E. Kolbe *et al.* , Phys. Rev. C **60**, 052801 (1999); E. Kolbe *et al.*, Nucl. Phys. **A652**, 91 (1999).
- [11] N.Yu. Agafonova *et al.*, Astron. Phys. **27**, 254 (2007).
- [12] R. Lazauskas and C. Volpe, Nucl. Phys. **A792**, 219 (2007).
- [13] N. Paar *et al.* , Phys. Rev. C **77**, 024608 (2008).
- [14] A.R. Samana and C.A. Bertulani, Phys. Rev. C **78**, 024312 (2008)
- [15] N. Itoh and Y. Kohyama, Nucl. Phys. **A306**, 527 (1978).

- [16] S. Mintz, J. Phys. G **28**, 451 (2002).
- [17] M.S. Athar *et al.*, Nucl. Phys. **A764**, 551 (2006).
- [18] J.D. Walecka, *Theoretical Nuclear and Subnuclear Physics* (Oxford University Press, New York, 1995) p. 531, and references therein.
- [19] T. de Forest and J.D. Walecka, Adv. in Phys. **15** (1966) 1
- [20] N. Auerbach *et al.*, Phys. Rev. C **56**, R2368 (1997).
- [21] C. Volpe *et al.*, Phys. Rev. C **62**, 015501 (2000).
- [22] T. Kuramoto *et al.*, Nucl. Phys. **A512**, 711 (1990).
- [23] J. R. Luyten *et al.*, H. P. C. Rood, and H. A. Tolhoek, , Nucl. Phys. **41**, 236 (1963).
- [24] N. Auerbach and A. Klein, Nucl. Phys. **A395**, 77 (1983).
- [25] T.W. Donnelly and R. D. Peccei, Phys. Rep. **50**, 1 (1979).
- [26] R.J. Blin-Stoyle and S.C.K. Nair, Advances in Physics **15**, 493 (1966).
- [27] A. R. Samana *et al.*, Phys. Rev. C **83**, 023403 (2011).
- [28] Martinez *et al.*, Phys. Rev. Lett. **83** (1999) 4502.
- [29] J. Engel *et al.*, Rev. C **60**, 14302 (1999).
- [30] F. Krmpotić *et al.*, Phys. Lett. **B319**, 393 (1993).
- [31] N. Paar *et al.*, Phys. Rev. C **69**, 054303 (2004).
- [32] I. N. Borzov and S. Goriely, Phys. Rev. C **62** (2000) 035501.
- [33] M. Martini *et al.*, Phys. Rev. C **80**, 065501 (2009).
- [34] K. Takahashi and M. Yamada, Prog. Theor. Phys. **41**, 1470 (1969).
- [35] A. A. Aguilar-Arevalo *et al.* (MiniBooNE Collaboration), Nucl. Instrum. Methods A **599**, 28 (2009).
- [36] A. Strumia and F. Vissani, arXiv: hep-ph/0606054v2.
- [37] M. Fukugita *et al.*, Phys. Lett. **B12**, 139 (1988).
- [38] F. Krmpotić, Fizika **B14**, 139 (2005).
- [39] M. Valverde *et al.*, Phys. Lett. B **638**, 325 (2006).
- [40] J. Engel *et al.*, Phys. Rev. C **54**, 2740 (1996).
- [41] M. Martini *et al.*, Phys. Rev. C **81**, 045502 (2010).
- [42] E. Kolbe and K. Langanke, Phys. Rev. C **63**, 025802 (2001).
- [43] A. R. Samana *et al.*, New Journal of Physics **10**, 033007 (2008).
- [44] T. Marketin *et al.*, Phys. Rev. C **79**, 054323 (2009).
- [45] N.T. Zinner *et al.*, Phys. Rev. C **74**, 024326 (2006).
- [46] D. Sande Santos *et al.*, Proceedings of Science, <http://pos.sissa.it/archive/conferences/142/120/XXXIV%20BWNP.120.pdf>
- [47] N. Paar *et al.*, Phys. Rev. C **87**, 025801 (2013); N. Paar *et al.*, arXiv:1505.07486 [nucl-th].
- [48] F Krmpotić and S. Shelly Sharma, Nucl. Phys. **A572**, 329 (1994), and references therein.
- [49] C. Barbero *et al.*, Nucl. Phys. **A650** (1999) 485, and references therein.
- [50] F. Simkovic *et al.*, Phys. Rev. C **87**, 045501 (2013).
- [51] C. A. Barbero *et al.* AIP Conference Proceedings **1625**, 169 (2014).
- [52] L. de Oliveira *et al.*, Journal of Physics: Conference Series **630** (2015) 012048
- [53] R. Alvarez-Rodriguez *et al.*, Phys. Rev. C **70**, 064309 (2004)
- [54] UNEDF SciDAC Collaboration, <http://www.unedf.org/>
- [55] James P. Vary *et al.*, arXiv:1507.04693 [nucl-th].
- [56] R.A. Senkov, M. Horoi. Phys. Rev. C **88**, 064312 (2013).
- [57] s is the particle-particle strength parameter for singlet channel, and t is the particle-particle strength parameter for triplet channel for the residual δ -interaction [27].

Correlations in neutrino-nucleus scattering*

T. Van Cuyck,[†] V. Pandey,[‡] N. Jachowicz,[§] R. González-Jiménez,

M. Martini, J. Ryckebusch, and N. Van Dessel

Department of Physics and Astronomy,

Ghent University,

Proeftuinstraat 86,

B-9000 Gent, Belgium

(Dated: March 22, 2016)

Abstract

We present a detailed study of charged-current quasielastic neutrino-nucleus scattering and of the influence of correlations on one- and two-nucleon knockout processes. The quasielastic neutrino-nucleus scattering cross sections, including the influence of long-range correlations, are evaluated within a continuum random phase approximation approach. The short-range correlation formalism is implemented in the impulse approximation by shifting the complexity induced by the correlations from the wave functions to the operators. The model is validated by confronting (e, e') cross-section predictions with electron scattering data in the kinematic region where the quasielastic channel is expected to dominate. Further, the $^{12}\text{C}(\nu_\mu, \mu^-)$ cross sections relevant for neutrino-oscillation experiments are studied. Double differential $^{12}\text{C}(\nu_\mu, \mu^-)$ cross sections, accounting for long- and short-range correlations in the one-particle emission channel and short-range correlations in the two-particle two-hole channel, are presented for kinematics relevant for recent neutrino-nucleus scattering measurements.

INTRODUCTION

One of the major issues in accelerator-based neutrino-oscillation experiments is the need for accurate predictions of neutrino-nucleus scattering cross sections at intermediate (0.01 - 2 GeV) energies. A model where the W boson interacts with a single nucleon, which subsequently leaves the residual nucleus unhindered, does not accurately describe recent experimental measurements of neutrino and antineutrino cross sections. A major complication stems from the fact that typical neutrino-nucleus measurements do not uniquely determine the nuclear final state, as only the energy-momentum of the final muon are measured. In order to explain the discrepancy between theory and experiment, one needs a model that includes nuclear correlations, meson-exchange currents and final-state interactions. In this work, we focus on the influence of nuclear correlations on inclusive quasielastic (QE) cross sections. First we will discuss long-range correlations in a continuum random phase approximation (CRPA) approach, and secondly, the influence of short-range correlations (SRCs). The model described below was used successfully in the description of exclusive electron-scattering processes [1, 2], low-energy and supernova neutrino processes [3–5], and extended to the description of inclusive quasielastic electroweak scattering cross sections at intermediate energies in [6, 7].

QUASIELASTIC NEUTRINO-NUCLEUS SCATTERING CROSS SECTION

In this section, we briefly describe the approach for the calculation of the nuclear response for inclusive electron- and neutrino-nucleus scattering in the QE region. Considering electron scattering off a nucleus, the double differential $A(e, e')$ cross section is written as

$$\frac{d\sigma}{dE_{e'}d\Omega_{e'}} = \left(\frac{\alpha \cos(\theta_{e'}/2)}{2E_e \sin^2(\theta_{e'}/2)} \right)^2 [v_L^e W_{CC} + v_T^e W_T], \quad (1)$$

with α the fine-structure constant and $\theta_{e'}$ the scattering angle of the electron. For CC neutrino-nucleus $A(\nu_\mu, \mu^-)$ interactions, the cross section is expressed as

$$\frac{d\sigma}{dE_\mu d\Omega_\mu} = \left(\frac{G_F \cos(\theta_c) E_\mu}{2\pi} \right)^2 \zeta [v_{CC} W_{CC} + v_{CL} W_{CL} + v_{LL} W_{LL} + v_T W_T - v_{T'} W_{T'}], \quad (2)$$

with G_F the Fermi constant, θ_c the Cabibbo angle and the kinematic factor ζ

$$\zeta = \sqrt{1 - \frac{m_\mu^2}{E_\mu^2}}. \quad (3)$$

The functions v contain the leptonic information and the W are nuclear response functions, they are defined as products of transition matrix elements \mathcal{J}_λ

$$\mathcal{J}_\lambda = \langle \Psi_f | \hat{\mathcal{J}}_\lambda^{\text{nucl}} | \Psi_i \rangle, \quad (4)$$

with $|\Psi_f\rangle$ and $|\Psi_i\rangle$ the final and initial nuclear state and $\hat{\mathcal{J}}_\lambda^{\text{nucl}}$ the spherical components of the nuclear current. The expressions for the v and W can be found in Ref. [7].

HARTREE-FOCK MEAN FIELD MODEL

A key element in the model presented here is the non-relativistic impulse approximation. The Hartree-Fock (HF) single-particle bound-states and the continuum wave functions are obtained by solving the Schrödinger equation using an effective Skyrme interaction. The SkE2 Skyrme parameterization is based on a fit to ground-state and low-lying excited state properties of spherical nuclei [1, 2]. The fact that the outgoing nucleon's wave function is generated in a (real) nuclear potential partially includes final-state interactions, in a natural way. The influence of the spreading width of the particle states is taken into account by a folding procedure [7]. The impact of the Coulomb potential of the nucleus on the outgoing lepton is implemented using a modified effective momentum approach (MEMA) [8]. As the description of the nuclear dynamics is non-relativistic, relativistic corrections are implemented based on the effective scheme proposed in [9].

LONG-RANGE CORRELATIONS

Long-range correlations are introduced using a continuum random phase approximation approach. The CRPA is based on a Green's function formalism, where the CRPA propagator is obtained by the iteration to all orders of the first-order contribution to the particle-hole Green's function

$$\begin{aligned} \Pi^{(RPA)}(x_1, x_2; E_x) &= \Pi^{(0)}(x_1, x_2; E_x) \\ &+ \frac{1}{\hbar} \int dx dx' \Pi^{(0)}(x_1, x; E_x) \tilde{V}(x, x') \Pi^{(RPA)}(x', x_2; E_x), \end{aligned} \quad (5)$$

with \tilde{V} the antisymmetrized Skyrme residual interaction. The same Skyrme SkE2 parameterization that is used to generate the HF single-particle wave functions is used as ph -interaction in the RPA calculation, assuring consistency of the formalism with regards to the nucleon interaction that is used. The Q^2 running of the residual interaction is controlled by a dipole form factor at the nucleon vertices [7]. The CRPA wave-functions $|\Psi_C^{RPA}\rangle$ and transition densities are then related to the unperturbed wave-functions $|ph^{-1}\rangle$ through

$$|\Psi_C^{RPA}\rangle = \sum_{C'} [X_{C,C'} |p'h'^{-1}\rangle - Y_{C,C'} |h'p'^{-1}\rangle], \quad (6)$$

with

$$\begin{aligned} X_{C,C'}(E, \varepsilon_{p'}) &= \delta_{C,C'} \delta(E - \varepsilon_{p'h'}) + \mathcal{P} \int dx_1 \int dx_2 \tilde{V}(x_1, x_2) \\ &\frac{\psi_{h'}(x_1) \psi_{p'}^\dagger(x_1, \varepsilon_{p'})}{E - \varepsilon_{p'h'}} \left\langle \Psi_0 \left| \hat{\psi}^\dagger(x_2) \hat{\psi}(x_2) \right| \Psi_C(E) \right\rangle, \end{aligned} \quad (7)$$

and

$$\begin{aligned} Y_{C,C'}(E, \varepsilon_{p'}) &= \int dx_1 \int dx_2 \tilde{V}(x_1, x_2) \\ &\frac{\psi_{h'}^\dagger(x_1) \psi_{p'}(x_1, \varepsilon_{p'})}{E + \varepsilon_{p'h'}} \left\langle \Psi_0 \left| \hat{\psi}^\dagger(x_2) \hat{\psi}(x_2) \right| \Psi_C(E) \right\rangle, \end{aligned} \quad (8)$$

with C denoting all quantum numbers representing an accessible channel. These equations reflect the fact that RPA wave functions are a superposition of ph - and hp -excitations out of a correlated ground state.

In FIG. 1, the HF and CRPA predictions are compared with double-differential electron-scattering data for three different target nuclei. In view of the fact that our description

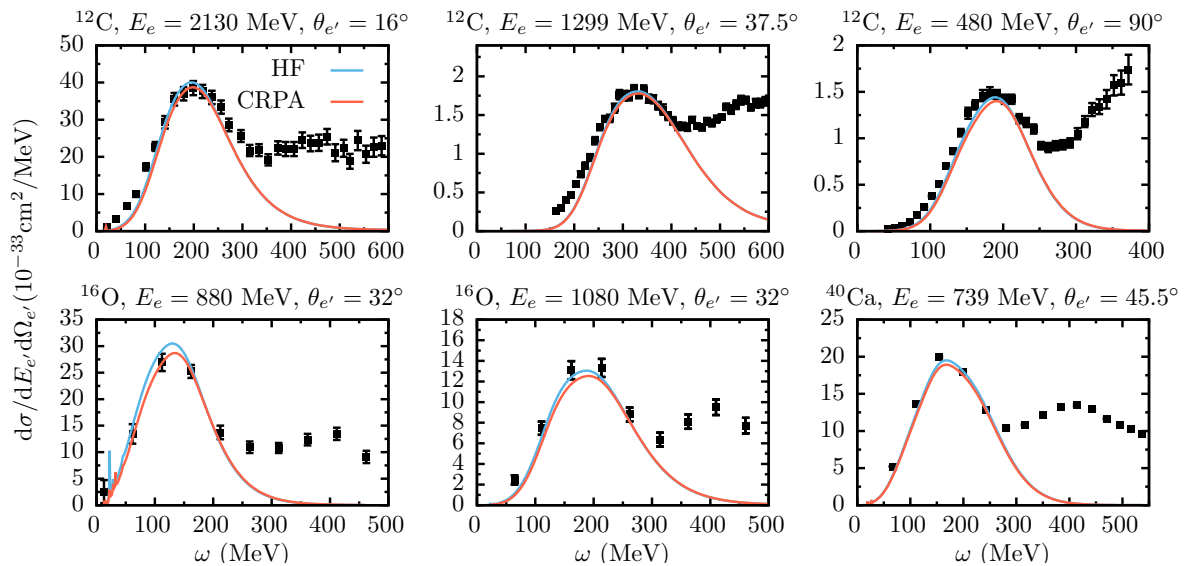


FIG. 1: Double differential (e, e') cross section with ^{12}C , ^{16}O and ^{40}Ca as target nuclei. Data are from Refs. [10–14].

only considers the QE channel, while the measurements include contributions such as Δ excitations and two-particle knockout, our numerical calculations provide a fair agreement with the data in the kinematic range presented here. The difference between the HF and CRPA results are sizable for $Q^2 \leq 0.25$ (GeV/c) 2 , see Ref. [7]. For the results presented here, which account for higher Q^2 values, the HF and CRPA cross sections are comparable.

SHORT-RANGE CORRELATIONS

To account for SRCs in neutrino-nucleus scattering, we rely on a model developed for exclusive as well as semi-exclusive electron-nucleus scattering cross sections [15–18]. This work is a first step in the extension of this model towards the weak sector.

The correlated wave functions $|\Psi\rangle$ are constructed by applying a many-body correlation operator $\hat{\mathcal{G}}$ to the uncorrelated wave functions $|\Phi\rangle$

$$|\Psi\rangle = \frac{1}{\sqrt{\mathcal{N}}} \hat{\mathcal{G}} |\Phi\rangle, \quad (9)$$

with $\mathcal{N} = \langle \Phi | \hat{\mathcal{G}}^\dagger \hat{\mathcal{G}} | \Phi \rangle$ the normalization constant. In the construction of the correlation operator, one is guided by the features of the one-boson exchange nucleon-nucleon force. In this work, only the central and tensor part of the correlation operator are considered,

spin-isospin correlations will be included in future work,

$$\widehat{\mathcal{G}} = \widehat{\mathcal{S}} \left(\prod_{i < j}^A [1 + \widehat{l}(i, j)] \right), \quad (10)$$

with

$$\widehat{l}(i, j) = -\widehat{g}(i, j) + \widehat{t}(i, j) \quad (11)$$

$$= -g_c(r_{ij}) + f_{t\tau}(r_{ij}) \widehat{S}_{ij}(\vec{\tau}_i \cdot \vec{\tau}_j), \quad (12)$$

where $\widehat{\mathcal{S}}$ is the symmetrization operator, \widehat{S}_{ij} the tensor operator $\frac{3}{r_{ij}^2} (\vec{\sigma}_i \cdot \vec{r}_{ij}) (\vec{\sigma}_j \cdot \vec{r}_{ij}) - (\vec{\sigma}_i \cdot \vec{\sigma}_j)$, $g_c(r_{ij})$ the central correlation function and $f_{t\tau}(r_{ij})$ the tensor correlation function. In the calculations presented in this work we used the central correlation function parameterization by Gearhaert and Dickhoff [19] and the tensor correlation function by Pieper *et al.* [20]. Ref. [21] provides arguments and evidence to support the fact that these correlation functions can be considered realistic.

When calculating transition matrix elements between correlated states $|\Psi\rangle$, one can shift the effect of the correlations towards the transition operators and calculate matrix elements between uncorrelated states $|\Phi\rangle$ with an effective transition operator. In the IA, the many-body nuclear current operator $\widehat{J}_\lambda^{\text{nucl}}$ can be written as a sum of one-body currents $\widehat{J}_\lambda^{[1]}(i)$. To account for SRCs, the current in Eq. 4 is replaced with an effective current

$$\langle \Psi_f | \widehat{J}_\lambda^{\text{nucl}} | \Psi_i \rangle = \frac{1}{\mathcal{N}} \langle \Phi_f | \widehat{\mathcal{G}}^\dagger \widehat{J}_\lambda^{\text{nucl}} \widehat{\mathcal{G}} | \Phi_i \rangle = \frac{1}{\mathcal{N}} \langle \Phi_f | \widehat{J}_\lambda^{\text{eff}} | \Phi_i \rangle, \quad (13)$$

with

$$\widehat{J}_\lambda^{\text{eff}} = \left(\prod_{j < k}^A [1 + \widehat{l}(j, k)] \right)^\dagger \sum_{i=1}^A \widehat{J}_\lambda^{[1]}(i) \left(\prod_{l < m}^A [1 + \widehat{l}(l, m)] \right). \quad (14)$$

Relying on the short-range behavior of the correlations, the effective current is approximated as

$$\widehat{J}_\lambda^{\text{eff}} \approx \sum_{i=1}^A \widehat{J}_\lambda^{[1]}(i) + \sum_{i < j}^A \widehat{J}_\lambda^{[1],\text{in}}(i, j) + \left[\sum_{i < j}^A \widehat{J}_\lambda^{[1],\text{in}}(i, j) \right]^\dagger, \quad (15)$$

where the first term is the nuclear current in the IA, and the second term is a two-body current which is the product of a one-body current and a correlation operator

$$\widehat{J}_\lambda^{[1],\text{in}}(i, j) = \left[\widehat{J}_\lambda^{[1]}(i) + \widehat{J}_\lambda^{[1]}(j) \right] \widehat{l}(i, j). \quad (16)$$

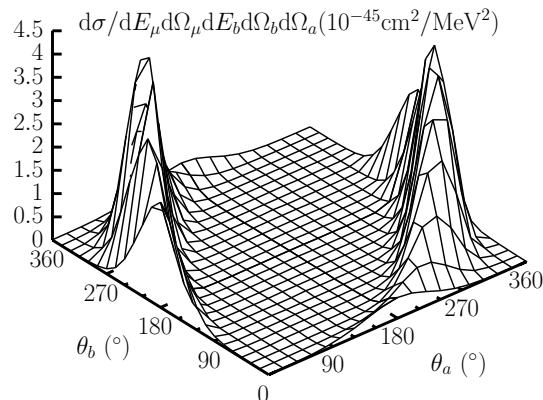


FIG. 2: Exclusive $^{12}\text{C}(\nu_\mu, \mu^- N_a N_b)$ cross section at $E_{\nu_\mu} = 750$ MeV, $E_\mu = 550$ MeV, $\theta_\mu = 15^\circ$ and $T_p = 50$ MeV with outgoing nucleons in the lepton scattering plane.

This model is used to study the effect of SRCs on the quasielastic double differential neutrino-nucleus scattering cross section. Due to the two-body structure of the effective operator, the SRCs influence the $1p1h$ as well as the $2p2h$ channel.

FIG. 2 shows the result of an exclusive cross section calculation. A striking feature of the displayed cross section is the dominance of back-to-back nucleon knockout, reminiscent of the 'hammer events' seen by the ArgoNeuT collaboration [22]. This feature is independent of the interacting lepton or the type of two-body interaction [16, 23].

The contribution of the $2p2h$ channel to the double differential cross section involves an integration over the phase space of the undetected nucleons as outlined in Refs. [15, 23]

$$\frac{d\sigma}{dE_\mu d\Omega_\mu}(\nu_\mu, \mu^-) = \int dT_b d\Omega_b d\Omega_a \frac{d\sigma}{dE_\mu d\Omega_\mu dT_b d\Omega_b d\Omega_a}(\nu_\mu, \mu^- N_a N_b). \quad (17)$$

In FIG. 3, double differential CRPA $^{12}\text{C}(e, e')$ calculations are compared with the model including SRCs in the $1p1h$ and $2p2h$ channels. The CRPA suppression in the QE-region is visible as well as the increase of the cross section in the dip-region due to the two-particle knockout of short-range correlated pairs. FIG. 4 compares the influence of long- and short-range correlations, accounting for one- and two-particle knockout, on the mean-field $^{12}\text{C}(\nu_\mu, \mu^-)$ cross section, for three kinematics relevant for accelerator-based neutrino-oscillation experiments. Both models result in a decrease of the cross section at the QE-peak.

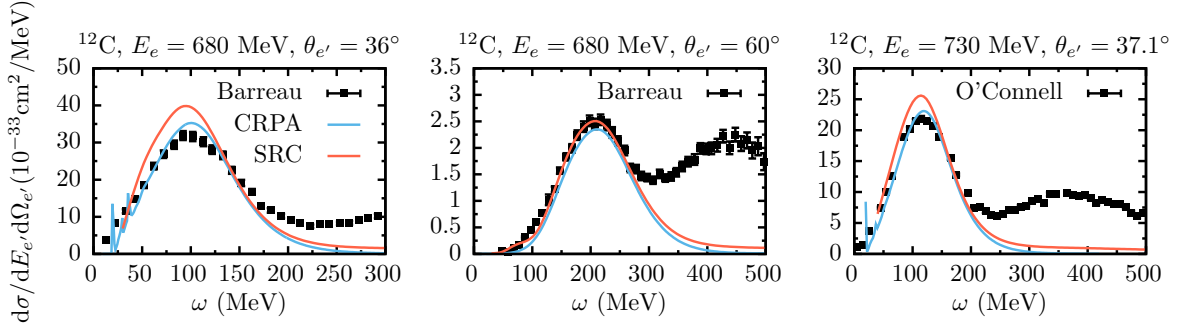


FIG. 3: Double differential $^{12}\text{C}(e, e')$ cross section for three kinematics. Data are from Refs. [12, 24].

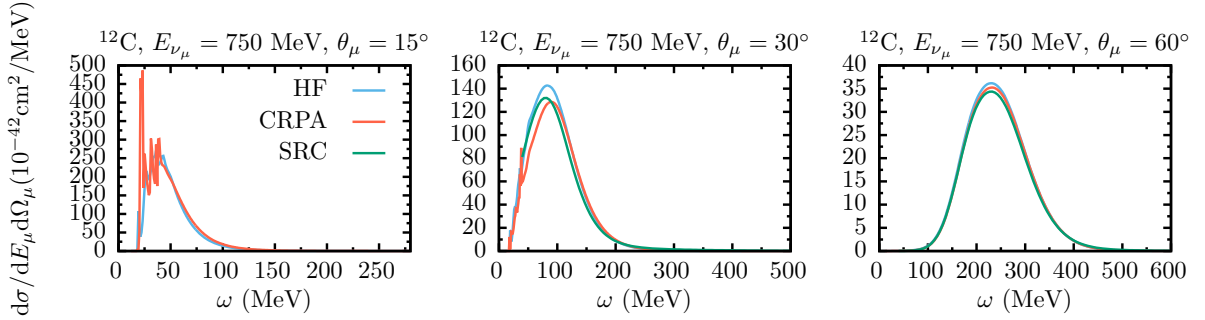


FIG. 4: Double differential $^{12}\text{C}(\nu_\mu, \mu^-)$ cross section for three kinematics.

SUMMARY

We have presented a discussion of long- and short-range correlations in quasielastic charged-current neutrino-nucleus scattering. We confronted our numerical results with double-differential inclusive (e, e') electron scattering data and calculated double differential (ν_μ, μ^-) neutrino-nucleus scattering cross sections at energies relevant for recent measurements. A fair agreement with electron-scattering data was reached in the region where the quasielastic channel is expected to dominate. Furthermore, the framework allows for the prediction of exclusive cross sections, which might provide deeper insight in neutrino experiments detecting the nuclear final state.

This work was supported by the Interuniversity Attraction Poles Programme P7/12 initiated by the Belgian Science Policy Office and the Research Foundation Flanders (FWO-Flanders). The computational resources (Stevin Supercomputer Infrastructure) and services used in this work were provided by Ghent University, the Hercules Foundation and the Flemish Government.

* Presented at NuFact15, 10-15 Aug 2015, Rio de Janeiro, Brazil [C15-08-10.2]

† Electronic address: Tom.VanCuyck@UGent.be; Speaker

‡ Electronic address: Vishvas.Pandey@UGent.be

§ Electronic address: Natalie.Jachowicz@UGent.be

- [1] J. Ryckebusch, M. Waroquier, K. Heyde, J. Moreau, and D. Ryckbosch, Nucl.Phys. **A476**, 237 (1988).
- [2] J. Ryckebusch, K. Heyde, D. Van Neck, and M. Waroquier, Nucl.Phys. **A503**, 694 (1989).
- [3] N. Jachowicz, S. Rombouts, K. Heyde, and J. Ryckebusch, Phys.Rev. **C59**, 3246 (1999).
- [4] N. Jachowicz, K. Heyde, J. Ryckebusch, and S. Rombouts, Phys.Rev. **C65**, 025501 (2002).
- [5] N. Jachowicz, K. Vantournhout, J. Ryckebusch, and K. Heyde, Phys. Rev. Lett. **93**, 082501 (2004).
- [6] V. Pandey, N. Jachowicz, J. Ryckebusch, T. Van Cuyck, and W. Cosyn, Phys.Rev. **C89**, 024601 (2014).
- [7] V. Pandey, N. Jachowicz, T. Van Cuyck, J. Ryckebusch, and M. Martini, Phys. Rev. **C92**, 024606 (2015).
- [8] J. Engel, Phys. Rev. **C57**, 2004 (1998).
- [9] S. Jeschonnek and T. W. Donnelly, Phys. Rev. **C57**, 2438 (1998).
- [10] D. Bagdasaryan *et al.*, YERPHI-1077-40-88 (1988).
- [11] R. Sealock *et al.*, Phys.Rev.Lett. **62**, 1350 (1989).
- [12] P. Barreau *et al.*, Nucl.Phys. **A402**, 515 (1983).
- [13] M. Anghinolfi *et al.*, Nucl.Phys. **A602**, 405 (1996).
- [14] C. Williamson *et al.*, Phys.Rev. **C56**, 3152 (1997).
- [15] V. Van der Sluys, J. Ryckebusch, and M. Waroquier, Phys.Rev. **C51**, 2664 (1995).
- [16] J. Ryckebusch *et al.*, Nucl.Phys. **A624**, 581 (1997).
- [17] S. Janssen, J. Ryckebusch, W. Van Nespén, and D. Debruyne, Nucl.Phys. **A672**, 285 (2000).
- [18] J. Ryckebusch, W. Cosyn, and M. Vanhalst, J.Phys. **G42**, 055104 (2015).
- [19] C. C. Gearhaert, *unpublished*, PhD thesis, Washington University, St. Louis, 1994.
- [20] S. C. Pieper, R. B. Wiringa, and V. Pandharipande, Phys.Rev. **C46**, 1741 (1992).
- [21] M. Vanhalst, J. Ryckebusch, and W. Cosyn, Phys.Rev. **C86**, 044619 (2012).

- [22] ArgoNeuT, R. Acciarri *et al.*, Phys.Rev. **D90**, 012008 (2014).
- [23] J. Ryckebusch, M. Vanderhaeghen, L. Machenil, and M. Waroquier, Nucl.Phys. **A568**, 828 (1994).
- [24] J. O'Connell *et al.*, Phys.Rev.Lett. **53**, 1627 (1984).

Coherent elastic scattering between neutrinos and nuclei*

Bruno Miguez[†]

*Instituto de Física “Gleb Wataghin”
Universidade Estadual de Campinas, Unicamp
13083-970 Campinas, SP, Brazil*

Orlando L. G. Peres

*Instituto de Física “Gleb Wataghin”
Universidade Estadual de Campinas, Unicamp
13083-970 Campinas, SP, Brazil and
The Abdus Salam International Centre for Theoretical Physics,
Strada Costiera 11, 34014 Trieste, Italy.*

(Dated: April 6, 2016)

Abstract

In the limit of low momentum transfer for neutrino nuclei elastic scattering is expected to observe a coherent superposition that increases the nucleus cross section. This effect was already observed for scattering for electrons, but due to experimental difficulties it have never been verified in neutrino scattering. The next generation of dark matter detectors probably will be sensitive to this interactions.

A study of the expected signal produced by coherent elastic scattering for neutrinos from different sources (solar, atmosphere, diffuse flux from supernovae, reactors and accelerators) was made. Considering a conservative threshold 1 keV, as a detectable nuclear recoil, the most promising source to be observed is the 8B neutrinos produced in the Sun, with an expected rate of 100 events/(ton·year). Another promising source is the reactor, but the use of this source is quite dependent of the possible distance between reactor and detector. For a detector far 1 km from the reactor it is expected 10 events/(ton·year), but if be possible decrease this distance for 100 m the rate would be increased to 1000 events/(ton·year).

INTRODUCTION

The coherent elastic scattering is the consequence of constructive interference on the interaction of neutrinos and nuclei. It is expected that when the transferred momentum (Q) is small when compared with the nucleus radius (R_0), $QR_0 \lesssim 1$, the neutrino loses the capacity to distinguish among individual nucleons and interact with the atom nucleus as a whole, increasing his cross-section [1, 2]. The equation that describes the neutrino-nucleus coherent elastic scattering as a function of nuclear recoil (T) and incident neutrino energy (E_ν) is:

$$\frac{d\sigma}{dT} = \frac{G_F^2}{4\pi} M \left(1 - \frac{MT}{2E_\nu^2} \right) \frac{Q_w^2}{4} F^2(Q^2) \quad (1)$$

where G_F is the Fermi Constant and M is the nuclear mass. This equation includes a term, $Q_w = N - Z * (1 - 4\sin^2\theta_W)$, that describes the coherent superposition of nucleons cross-section (N is number of neutrons and Z is the number of protons and $\sin^2\theta_W \simeq 0.231$ is the weak mixing angle) and a form factor, $F(Q^2) = \frac{3}{QR_0} e^{-\frac{(Qs)^2}{2}} \left(\frac{\sin(QR_0)}{(QR_0)^2} - \frac{\cos(QR_0)}{QR_0} \right)$, to describe the loss of coherence with increasing momentum transfer ($R_0^2 = (1.2A^{1/3})^2 - 5s^2 \text{ fm}^2$

and $s = 0.5$ fm are constants from adopted nuclear model). The form factor can be described as a function of the transferred momentum using the relation $Q^2 = 2MT = E_\nu^2(1 + \cos\theta)$.

ATMOSPHERIC NEUTRINOS AND DIFFUSE FLUX FROM SUPERNOVAE NEUTRINOS

Atmospheric neutrinos are produced by cosmic ray interactions in the atmosphere [3]. Neutrinos from diffuse flux from supernovae are a stationary flux originated on the superposition of bursts emitted by all supernovae [4]. As can be seen in Fig. 1, both categories present relatively low fluxes, making difficult their detection. Recently, they attracted more interest once they can imitate the WIMP expected signal in direct search for dark matter [5].

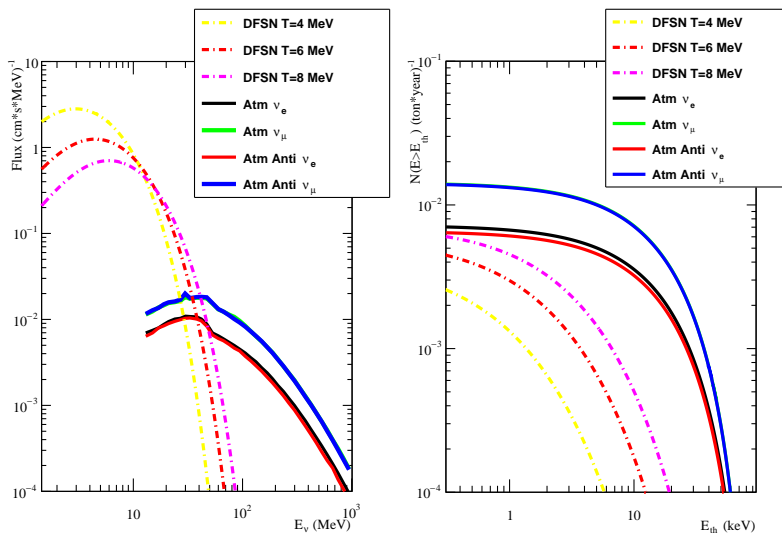


FIG. 1: Fluxes and expected number of events over threshold for atmospheric neutrinos and diffuse flux from supernovae neutrinos.

SOLAR NEUTRINOS

Solar neutrinos are produced in the nuclear reaction in the solar core and quickly reach the Earth. Their fluxes are relatively large, but their energies go just up to ~ 20 MeV, what limitates theirs detection once the maximum nuclear recoil (T_{max}) for a nucleus with mass (M) produced by a neutrino with energy E_ν is given by $T_{max} = E_\nu^2/M$, as showed in Fig. 2.

In this work was used the fluxes from Bahcall Website (<http://www.sns.ias.edu/~jnb/>) and the monoenergetic fluxes are not considered.

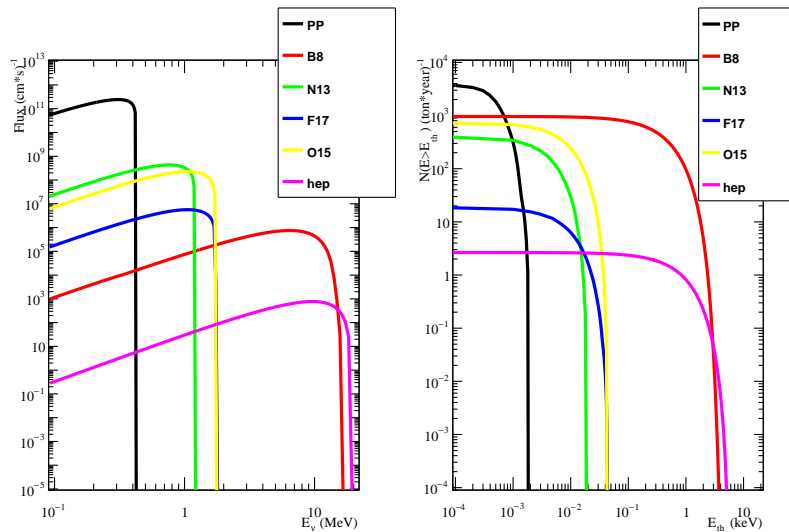


FIG. 2: Fluxes and expected number of events over threshold for solar neutrinos.

REACTOR NEUTRINOS

An preliminary extension of this study was made considering reactor neutrinos. These sources have their fluxes quite dependent of the used setup (distance, power, etc). In this work, to estimate a rate of coherent elastic scattering on xenon due to reactor neutrinos was used the neutrino spectrum presented in [6], considering also 100% ^{235}U composition, 5 GW thermal power and 1 km of distance between the reactor and the detector. The results are showed in Fig. 3.

CONCLUSIONS

It is expected that neutrino-nuclei coherent elastic scattering be observed soon. The improvement in detection techniques allows to observe nuclear recoils with energies in order of 1 keV in ton scale detectors. The neutrino background represents a limit on the sensitivity that direct dark matter detectors can reach, once they can interact through coherent elastic scattering with nuclei. In this work we reproduced the results in [5] with good agreement and extended the study to neutrinos from reactors and accelerators.

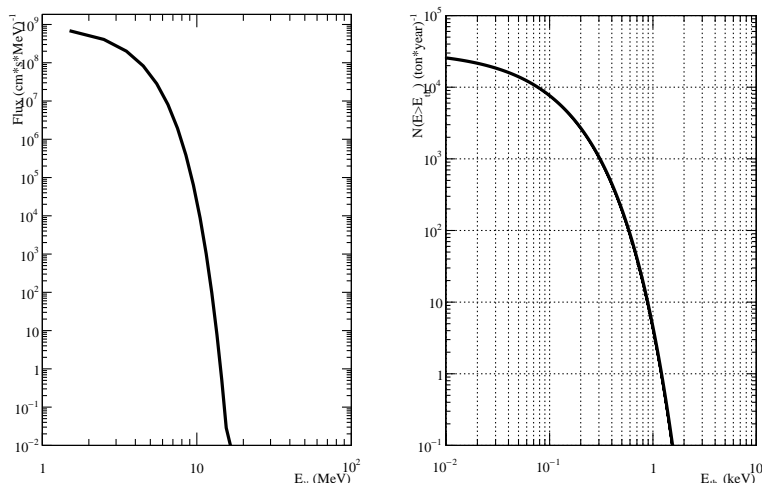


FIG. 3: Fluxes and expected number of events over threshold for reactor neutrinos.

The best source to detect neutrino-nuclei coherent elastic scattering considering a threshold of 1 keV should be the solar neutrinos from ${}^8\text{B}$ with ~ 100 events/(ton·year). Another good source should be the reactor, but in this case the viability is too much dependent of setup, mainly the distance. The case showed in Fig. 3 presents a rate of ~ 10 events/(ton·year), but this number can be increased up to ~ 1000 events/(ton·year) if the detector could be placed 100 m far from reactor.

We would also like to thank FAPESP, CAPES, CNPq and Unicamp for several financial supports. O.L.G.P. thanks the support of FAPESP funding grant 2012/16389-1. The authors thanks the support of FAPESP funding grant 2015/12505-5..

* Presented at NuFact15, 10-15 Aug 2015, Rio de Janeiro, Brazil [C15-08-10.2]

† bmiguez@ifi.unicamp.br; Speaker

- [1] D. Z. Freedman, Physical Review D **9**, 1389 (1974).
- [2] A. J. Anderson *et al.*, Phys. Rev. **D84**, 13008 (2011).
- [3] T. K. Gaisser and M. Honda, Ann. Rev. Nucl. Part. Sci. **52**, 153 (2002).
- [4] S. Ando and K. Sato, New J. Phys. **6**, 170 (2004).
- [5] J. Billard, L. Strigari, and E. Figueroa-Feliciano, Phys. Rev. **D89**, 023524 (2014).
- [6] H. Murayama and A. Pierce, Phys.Rev. **D65**, 013012 (2002).

Understanding CCQE events in MicroBooNE*

Andrew P Furmanski for the MicroBooNE collaboration[†]

University of Manchester

(Dated: June 15, 2016)

Abstract

Understanding nuclear effects in neutrino interactions, particularly on argon, will be critical for the future success of neutrino oscillation experiments. One channel that potentially allows these effects to be probed is the CCQE-like channel where a single muon and no pions are produced. Liquid argon time projection chambers allow unprecedented resolution of the hadronic side of neutrino interactions on heavy nuclei. Different models and generators make very different predictions for the kinematics and multiplicity of protons in these interactions, and MicroBooNE will be able to collect enough data in the first year of running to begin probing this previously unmeasured part of phase space.

MICROBOONE

MicroBooNE is a 170 ton (87 ton active) liquid argon TPC in the Booster Neutrino Beam at Fermilab. The bubble-chamber quality images allow for extremely good particle identification, calorimetry, and a low threshold for tracking heavy particles such as protons. This makes it the ideal place to study nuclear effects in neutrino interactions. Figure 1 shows a schematic of the MicroBooNE detector.

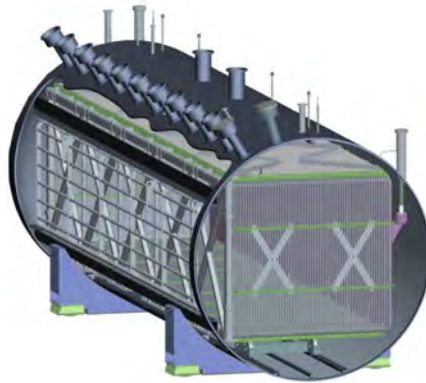


FIG. 1: Schematic showing the MicroBooNE cryostat with the TPC placed inside. The booster neutrino beam enters from the far end of the detector.

PREVIOUS EVIDENCE FOR CORRELATIONS

From electron scattering experiments, there is significant evidence for correlations between nucleons in nuclei. Recently ArgoNeuT observed a number of interesting “hammer” events [1] - a single muon accompanied by a pair of back-to-back protons (shown in figure 2). The observation of back-to-back protons is indicative of nucleon-nucleon correlations being observed for the first time in neutrino scattering. Unfortunately due to the small size and short exposure of ArgoNeuT the results are very statistically limited. MicroBooNE will collect an order of magnitude more events than ArgoNeuT in the CCQE regime.

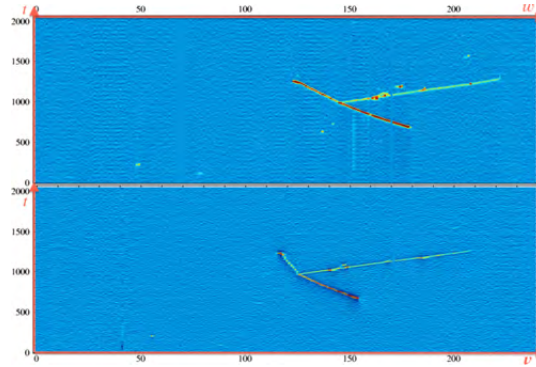


FIG. 2: An event display from the ArgoNeuT [1] experiment, showing a single muon and a pair of back-to-back protons. This is known as a “hammer” event.

GENERATORS AND MODELS

Two generators are considered in this study. The first is GENIE version 2.8.6 [2, 3], which is commonly used in the neutrino physics community. All GENIE parameters were left at their default values. Importantly, the default GENIE settings use the Bodek-Ritchie Relativistic Fermi Gas nuclear model and no nucleon-nucleon correlations.

The second generator considered was NuWro version 11q [4]. NuWro has many options for nuclear models. For this study, the Benhar Spectral Function nuclear model was selected, as this model includes nucleon-nucleon correlations. In addition the Nieves model for meson-exchange current (MEC) interactions was enabled. Other parameters were left at their default values.

PREDICTED EVENT RATES

Figure 3 shows the predicted muon momentum spectrum for the two models. The distributions are very similar. However figures 4 and 5 show the predictions for the number of protons and the angle between 2 protons (for the topology with exactly 2 protons). Large differences are seen in these variables.

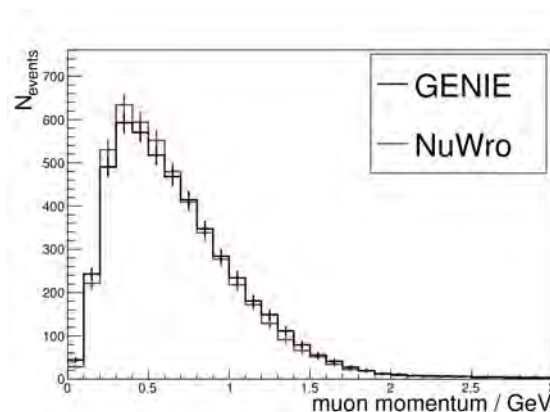


FIG. 3: Muon momentum distribution for all $CC0\pi$ events. The distributions are very similar despite large differences in the models used.

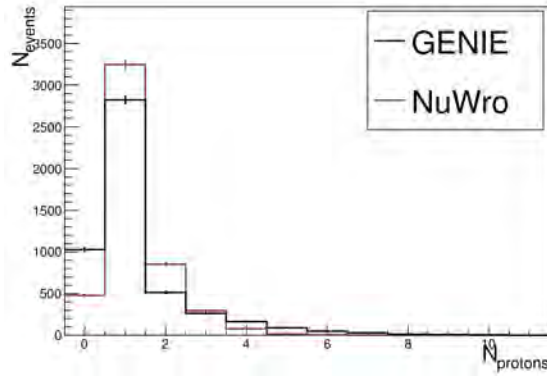


FIG. 4: Number of protons above 200 MeV/c momentum for all CC0 π events. Large differences can be seen in all bins.

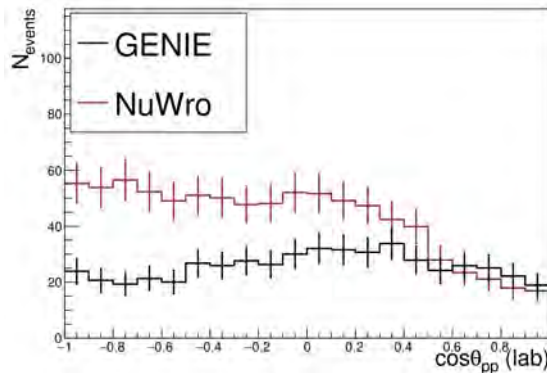


FIG. 5: Proton-proton angle for CC0 π events with exactly two protons above 200 MeV/c momentum. NuWro shows enhancement in the back-to-back region, due to MEC events.

CONCLUSIONS

Nuclear effects, such as nucleon-nucleon correlations, can have a large effect on the multiplicity and kinematics of protons leaving the nucleus in a neutrino interaction, even when the muon kinematics are relatively unchanged. In particular, models which incorporate nucleon-nucleon correlations and multinucleon interactions tend to predict larger proton pair opening angles than those models without these effects. Using a high-statistics event sample in a liquid argon TPC such as MicroBooNE, it will soon be possible to begin to explore these effects in neutrino interactions.

* Presented at NuFact15, 10-15 Aug 2015, Rio de Janeiro, Brazil [C15-08-10.2]

† andrew.furmanski@manchester.ac.uk

- [1] R. Acciarri, C. Adams, J. Asaadi, B. Baller, T. Bolton, C. Bromberg, F. Cavanna, E. Church, D. Edmunds, A. Ereditato, S. Farooq, B. Fleming, H. Greenlee, G. Horton-Smith, C. James, E. Klein, K. Lang, P. Laurens, R. Mehdiyev, B. Page, O. Palamara, K. Partyka, G. Rameika, B. Rebel, M. Soderberg, J. Spitz, A. M. Szelc, M. Weber, T. Yang, and G. P. Zeller. Detection of back-to-back proton pairs in charged-current neutrino interactions with the argoneut detector in the numi low energy beam line. *Phys. Rev. D*, 90:012008, Jul 2014.
- [2] C. Andreopoulos et al. The GENIE Neutrino Monte Carlo Generator. *Nucl. Instrum. Meth.*, A614:87–104, 2010.
- [3] Costas Andreopoulos, Christopher Barry, Steve Dytman, Hugh Gallagher, Tomasz Golan, Robert Hatcher, Gabriel Perdue, and Julia Yarba. The GENIE Neutrino Monte Carlo Generator: Physics and User Manual. 2015.
- [4] C. Juszczak, J. A. Nowak, and J. T. Sobczyk. Simulations from a new neutrino event generator. *Nuclear Physics B - Proceedings Supplements*, 159(0):211 – 216, 2006.

QCD dynamic effects in the neutrino absorption by the Earth's interior at IceCube neutrino energies and above*

V. P. Gonçalves^{1,2} and D. R. Gratieri^{3,4†}

¹ *Department of Astronomy and Theoretical Physics,
Lund University, 223-62 Lund, Sweden.*

² *Instituto de Física e Matemática,
Universidade Federal de Pelotas, Caixa Postal 354,
CEP 96010-900, Pelotas, RS, Brazil*

³ *Escola de Engenharia Industrial Metalúrgica de Volta Redonda,
Depto de Ciências Exatas, Universidade Federal Fluminense,
CEP 27255125 - Volta Redonda, RJ - Brazil and*

⁴*Instituto de Física Gleb Wataghin - UNICAMP, 13083-859, Campinas, SP, Brazil*

Abstract

We investigate how the uncertainties in $\sigma^{\nu N}$ due the different QCD dynamic models would modify the neutrino absorption while they travel across the Earth. We compare the predictions of models based on the solution of the linear DGLAP equations at small- x and large- Q^2 with those which impose the Froissart bound at large energies, taking into account the unitarity effects in the neutrino - nucleon cross section. Our results indicate that the probability of absorption and the angular distribution of neutrino events are sensitive to the QCD dynamics at ultra high energies.

INTRODUCTION

The observation of ultra high energy (UHE) neutrino events at PeV by the IceCube Collaboration marks the birth of neutrino astronomy [1, 2]. However to interpret the experimental results is fundamental to take into account that the attenuation of the neutrino beam in route to a detector is strongly dependent on the high energy behaviour of the neutrino - nucleon cross section ($\sigma^{\nu N}$), which determines the opacity of the Earth to incident neutrinos. As discussed by several authors in the last years, [3–10], at ultra high energies, the neutrino-nucleon cross section provides a probe of Quantum Chromodynamics (QCD) in the kinematic region of very small values of Bjorken- x and large virtualities Q^2 , which was not explored by the HERA measurements of the structure functions [11]. The results from Ref. [7] shown that the solution of the linear Dokshitzer - Gribov - Lipatov - Altarelli - Parisi (DGLAP) equation [12] at small - x and large Q^2 obtained in Ref. [13], denoted FJKPP hereafter, provides an upper bound for the behaviour of $\sigma^{\nu N}$ at ultra high energies. In contrast, the solution proposed in Ref. [14], denoted BBMT hereafter, which imposes that $\sigma^{\nu N}$ satisfies the Froissart bound at high energies, can be considered a lower bound. As demonstrated in Ref. [7], models which taken into account of the non - linear effects to the QCD dynamics predict high energy behaviours between these extreme scenarios. In this contribution we review the results obtained in Ref. [10] where we have extended these previous studies for the analysis of the probability of neutrino absorption by the Earths interior at ultra high energies and determined the theoretical uncertainty present in this quantity. For completeness we also present the predictions obtained the CT10 parametrization [15] for the parton distributions (PDFs), derived using the DGLAP evolution equations, which allows us to estimate the uncertainty present in the global fits as well as those associated to

the extrapolation of the PDFs in a kinematical range beyond that probed by HERA.

FORMALISM AND RESULTS

Neutrino DIS is described in terms of charged current (CC) interaction, which proceed through W^\pm exchange, and is written as

$$\sigma_{\nu h}^{CC}(E_\nu) = \int_{Q_{min}^2}^s dQ^2 \int_{Q^2/s}^1 dx \frac{1}{xs} \frac{\partial^2 \sigma^{CC}}{\partial x \partial y}, \quad (1)$$

where E_ν is the neutrino energy, $s = 2ME_\nu$ with M the hadron mass, $y = Q^2/(xs)$. Also, the differential cross section is given by

$$\frac{\partial^2 \sigma_{\nu h}}{\partial x \partial y} = \frac{G_F^2 M E_\nu}{\pi} \left(\frac{M_W^2}{M_W^2 + Q^2} \right)^2 \left[\frac{1 + (1-y)^2}{2} F_2^h(x, Q^2) \frac{y^2}{2} F_L^h(x, Q^2) + y(1 - \frac{y}{2}) x F_3^h(x, Q^2) \right] \quad (2)$$

where $h = p$ or A , with A the atomic number, G_F is the Fermi constant and M_W denotes the mass of the charged gauge boson. In the QCD improved parton model the structure functions F_2 , F_L and F_3 are calculated in terms of quark and gluon distribution functions. For completeness we include in our calculations the anti electron neutrino resonant scattering with electrons in the medium [16].

In Fig. 1 (a) we compare the antineutrino cross-section as given by antineutrino-electron resonant scattering with the CC neutrino-nucleon cross-section. We see that the former is only important in the region around the resonance, defined by $(M_W - 2\Gamma_W)/2m_e^2 \approx 5.7 \text{ PeV} \leq E_\nu \leq (M_W + 2\Gamma_W)/2m_e^2 \approx 7 \text{ PeV}$. The shaded band is due to the propagation of the uncertainty present in the data fits as well as those associated to the extrapolation of the PDFs in a kinematical range beyond that probed by HERA. We obtain that both models based on linear dynamics, GQRS [4], FJKPP and CT10, predicts a strong growth of CC neutrino-nucleon cross-section when compared with the Froissart based model BBMT, being the difference of a factor of two at $E_\nu = 10^{11} \text{ GeV}$ and increases to ≈ 5 at $E_\nu = 10^{13} \text{ GeV}$.

Following [4] we define the the probability of neutrino interact while crosses the Earth as

$$P_{Shad}^j(E_\nu) = exp \left\{ -N_A \sigma_{\nu_j}(E_\nu) \int_0^{r_f(\theta)} \rho_i(r) dr \right\}, \quad (3)$$

where j represents each final state of resonant scattering, or the CC neutrino-nucleon interaction. In this work we use the density profile from [17]. At this point we integrate

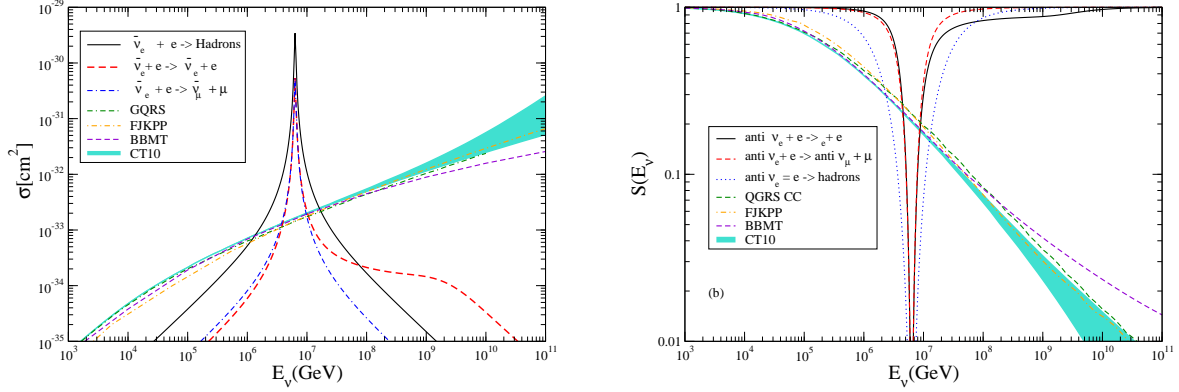


FIG. 1: (a): Comparison between CC neutrino-nucleon cross-section for the hadronic models we discuss and the antineutrino-electron resonant cross-section for the different final states relevant in this analysis. (b): Comparison of function $S(E_\nu)$ as given by Eq. (4) for the different νN interaction models we probe as well $\bar{\nu}_e e^-$ resonant scattering.

Eq. (3) with respect to the zenith angle, and define the absorption function for the neutrinos while it crosses the Earth as

$$S^i(E_\nu) = \int_{-1}^0 d\cos(\theta_\nu) P_{shad}^i(E_\nu) = \int_{-1}^0 d\cos(\theta_\nu) \exp \left\{ -N_A \sigma_{\nu_i}(E_\nu) \int_0^{r(\theta)} \rho_i(r) dr \right\}, \quad (4)$$

where $i = e, N$. The integration over zenith angle tends to smear the absorption effects, as we can see if Fig. 1 (b), where the width of Glashow resonance absorption is reduced significantly. On the other hand we have that the difference between the FJKPP (CT10) and BBMT predictions increases for higher neutrino energy and becomes a factor 2 at $E_\nu \approx 10^{10}$ GeV, with the BBMT one being an upper bound. This difference of a factor 2 between the predictions has a strong impact in the analysis and interpretation of the possible few events that should be observed at such UHE.

As a summary of our main conclusions, in this contribution we have estimated the impact of the current uncertainty in the description of νN interactions at ultra high energies in the absorption of neutrinos crossing the Earth until the detectors. Our results indicated that the the probability of absorption is sensitive to the treatment of the QCD dynamics at ultra high energies. We also verified that, as this probability is proportional to the distance travelled by neutrinos and the net quantity of nuclear matter they crosses, the angular distribution of neutrino events should be modified when we impose a Froissart-like behaviour at neutrino-

nucleon cross-section. Such results have direct implication in the determination of sources of UHE neutrinos below the horizon of IceCube neutrino observatory and in the analysis of the neutrino events in future experiments.

Acknowledgments

This work was partially financed by the Brazilian funding agencies CNPq, CAPES and FAPERGS.

* *Presented at NuFact15, 10-15 Aug 2015, Rio de Janeiro, Brazil [C15-08-10.2]*

† `barros@ufpel.edu.br, drgratieri@id.uff.br`

- [1] M.G. Aartsen *et al.* IceCube Collaboration. *Phys. Rev. Lett.* **111**, 021103 (2013)
- [2] M. G. Aartsen *et al.* IceCube Collaboration. *Science* **342**, no. 6161, 1242856 (2013).
- [3] R. Gandhi, C. Quigg, M. H. Reno and I. Sarcevic, *Astropart. Phys.* **5**, 81 (1996)
- [4] R. Gandhi, C. Quigg, M. H. Reno and I. Sarcevic, *Phys. Rev. D* **58**, 093009 (1998)
- [5] N. Armesto, C. Merino, G. Parente and E. Zas, *Phys. Rev. D* **77**, 013001 (2008)
- [6] A. Cooper-Sarkar and S. Sarkar, *JHEP* **0801**, 075 (2008); A. Cooper-Sarkar, P. Mertsch and S. Sarkar, *JHEP* **1108**, 042 (2011)
- [7] V. P. Goncalves and P. Hepp, *Phys. Rev. D* **83**, 014014 (2011).
- [8] V. P. Goncalves and D. R. Gratieri, *Phys. Rev. D* **88**, no. 1, 014022 (2013).
- [9] V. P. Goncalves and D. R. Gratieri, *Phys. Rev. D* **90**, no. 5, 057502 (2014).
- [10] V. P. Goncalves and D. R. Gratieri. *Phys. Rev. D* **92**, 113007 (2015).
- [11] G. Wolf, *Rept. Prog. Phys.* **73**, 116202 (2010)
- [12] V.N. Gribov and L.N. Lipatov, *Sov. J. Nucl. Phys.* **15**, 438 (1972); G. Altarelli and G. Parisi, *Nucl. Phys.* **B126**, 298 (1977); Yu.L. Dokshitzer, *Sov. Phys. JETP* **46**, 641 (1977).
- [13] R. Fiore, L. L. Jenkovszky, A. Kotikov, F. Paccanoni, A. Papa and E. Predazzi, *Phys. Rev. D* **68**, 093010 (2003); *Phys. Rev. D* **71**, 033002 (2005); R. Fiore, L. L. Jenkovszky, A. V. Kotikov, F. Paccanoni and A. Papa, *Phys. Rev. D* **73**, 053012 (2006).
- [14] E. L. Berger, M. M. Block, D. W. McKay and C. I. Tan, *Phys. Rev. D* **77**, 053007 (2008); M. M. Block, P. Ha and D. W. McKay, *Phys. Rev. D* **82**, 077302 (2010)
- [15] H. L. Lai, M. Guzzi, J. Huston, Z. Li, P. M. Nadolsky, J. Pumplin, and C.-P. Yuan, *Phys. Rev. D* **82**, 074024 (2010).
- [16] S. L. Glashow, *Phys. Rev.* **118**, 316 (1960).
- [17] A. M. Dziewonski, D. L. Anderson, *Physics of the Earth and Planetary Interiors*, **25** 297 (1981).

Computation of atmospheric neutrino production*

G. V. Stenico[†]

Instituto de Física Gleb Wataghin - UNICAMP, 13083-859, Campinas SP, Brazil

O. L. G. Peres[‡]

Instituto de Física Gleb Wataghin - UNICAMP,

13083-859, Campinas SP, Brazil and

The Abdus Salam International Centre for Theoretical Physics,

Strada Costiera 11, 34014 Trieste, Italy.

(Dated: March 31, 2016)

Abstract

Atmospheric neutrinos are created by the interactions of primary cosmic rays, mainly composed by protons, with the nuclei in the atmosphere. The energy spectrum of cosmic rays, from 200 MeV up to about 10^{20} eV, is approximately proportional to a power-law $E^{-\alpha}$. We computed atmospheric neutrinos flux from about 1 GeV to about 1 TeV, whose cosmic ray flux is sufficiently high to generate an observable flux of atmospheric neutrinos. After, we compared the results with numerical calculations and we accomplished good agreement with semi-analytical methods. As an original work, we extended the calculations including a neutrino-neutrino-scalar vertex that it will modify the rate of neutrino production compared with Standard Model prediction. We observe that this new interaction have a equal production of electron and muon neutrinos that in principle can be tested in present and future atmospheric neutrino experiments.

PACS numbers: 13.85.Tp, 14.60.St, 14.80.Va

Keywords: neutrinos, particle physics, particle cascade equations

INTRODUCTION

We start with a differential flux of protons given by

$$\phi_N(E) \simeq \phi_N(E = 1\text{GeV}) \left(\frac{E}{\text{GeV}} \right)^{-\alpha} \quad (1)$$

where $\phi_N(E = 1\text{GeV}) \simeq 1.8 \times 10^4 \frac{\text{nucleons}}{\text{m}^2 \text{ sr s GeV}}$ and $\alpha = 2.7$ to describe the processes of absorption, scattering and decay of secondary particles produced until neutrino creation. In a one-dimensional approximation, the evolution in the atmosphere of the flux ϕ_j of a cosmic ray of type j is given by the cascade equation [1].

$$\frac{d\phi_j(E, t)}{dt} = -\frac{\phi_j(E, t)}{\lambda_j(E)} - \frac{d\phi_j(E, t)}{d_j(E, t)} + \sum_k S_{k \rightarrow j}(E, t), \quad (2)$$

where t is so-called *slant depth*, measured in units of g/cm^2 . $\lambda_j(E)$ in g/cm^2 is the *interaction length* which describes the disappearance of the particle j due to interactions with atmosphere, $d_j(E, t)$ describes the decay of the particle in g/cm^2 and it is called *decay length* and $S_{k \rightarrow j}(E, t)$ describes the generation of a secondary particle j due to the interaction of a particle k with atmosphere (*source term*). We use the Cascade Equation (2) to compute

flux of particles in the atmosphere, using a power law for the initial protons, to describe evolution of the proton flux in function of energy and slant depth. Proton interactions resulted in pions, which are the most light and abundant mesons produced in this interactions. Pions decay into neutrinos and charged leptons, mainly muons, which decay into electrons and neutrinos.

RESULTS

The results are in Figure (1). In Figure (1a), we compare the calculations with the work of Gaisser *et al* who use the same proton flux as input, but performed numerical calculations. We digitalized the curves from Ref.[2] and compare with our results for the particles: proton (which is the same for both calculations), pion, muon and muon neutrino fluxes. The dashed and solid curves are for Gaisser *et al* and our work, respectively. We accomplish a reasonably good agreement for neutrino fluxes and less for muons and pion fluxes. In Figure (1b), we show our results for the energy dependence. Notice that all energies the flux of muon neutrinos is bigger than electron neutrinos. In our computation there is a equality between neutrino and antineutrino fluxes.

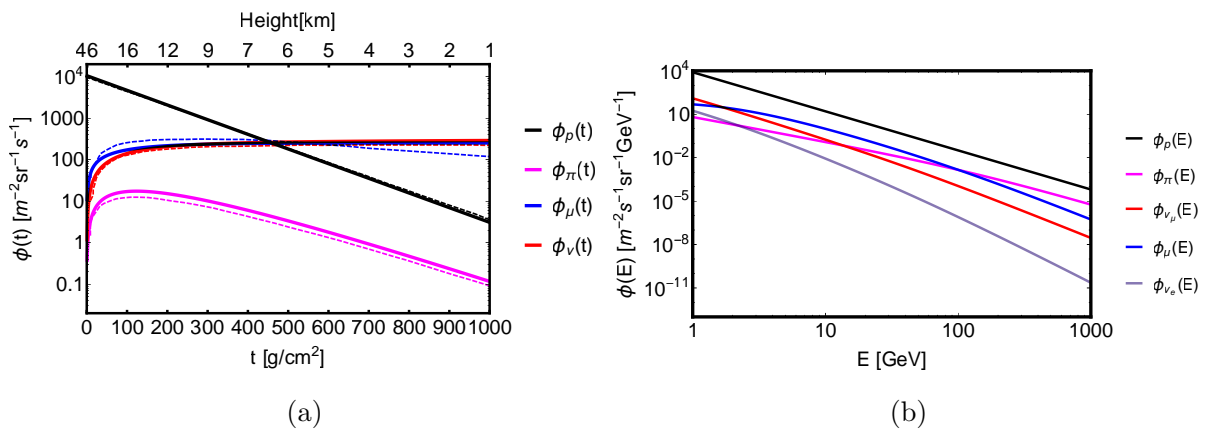


FIG. 1: (a) Integral fluxes of cosmic rays with $E > 1$ GeV as a function of the slant depth. (b) Energy spectra of particles produced in the atmosphere at slant depth = 100 g/cm^2 due to a primary proton with a power-law energy spectrum.

Since we have the particle energy spectra (with only interactions of Standard Model), we will observe how the neutrino flux changes if we consider an exotic decay in the flux.

MAJORON COUPLING AND $\pi \rightarrow l\nu\chi$ DECAY CHANNEL

Majoron (χ) is a massless Goldstone boson that arises in extended gauge theories that have spontaneous symmetry breaking. The Yukawa coupling of majoron to neutrino is given by [3]

$$\mathcal{L}_{\nu\chi} = \frac{1}{2} \sum_{l'l'} g_{ll'} \bar{\nu}_l (i\gamma^5 \chi) \nu_{l'} \quad (3)$$

where $g_{ll'}$ is the majoron-neutrino coupling, $\bar{\nu}_l$ and $\nu_{l'}$ are neutrino spinors, and l, l' go over e, μ and τ . Majoron has not been observed yet, but majoron theory can be tested if we consider exotic decays with majoron as final particle and evaluate the branching ratio between exotic and known process to constrain the limits of $g_{ll'}$ coupling constant. As pion decay is the main source of neutrinos in Earth atmosphere, we calculated the exotic process $\pi \rightarrow l\nu\chi$ and compare with conventional decay to observe the changes in the process with majoron addition. The result is shown in Figure (2).

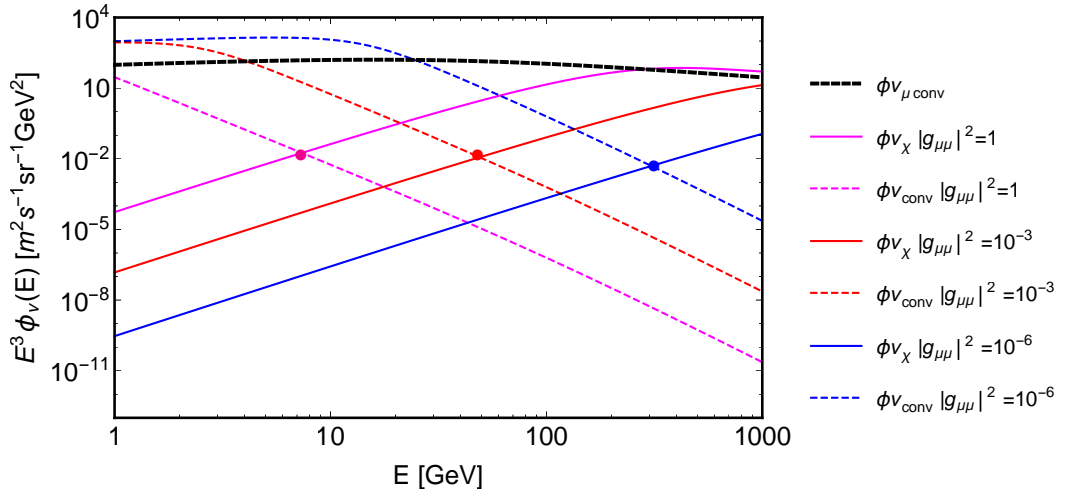


FIG. 2: Energy spectra of neutrinos from pion decay. Dashed lines are the neutrino fluxes from pion conventional decay, now normalized by the two channels: $\Gamma_{\pi \rightarrow \mu\nu} + \Gamma_{\pi \rightarrow \mu\nu\chi}$. Black dashed line is neutrino flux with no majoron emission (spectrum in Fig. 1b) and solid lines are neutrino flux from majoron emission to three different values for $|g_{\mu\mu}|^2$. Dots show the energies which conventional and exotic flux are identical.

We see that the renormalized fluxes depend on energy and coupling constant $|g_{\mu\mu}|^2$, so it

is possible put limit on it by observing in which energies the exotic flux start to be significant and compare with experimental data provided i.e. by *ICECUBE* and *SuperKamiokande*.

CONCLUSIONS

In this work, we concluded that using semi-analytical method for calculating atmospheric neutrino flux we had a good agreement with numerical results, that it is time consuming. We also compute the contribution the exotic decay channel for pion decay and we compare with the conventional one. We have found that we have appreciable changes in the muon neutrino flux that for higher enough energies most of neutrinos came from this exotic decay. From this we can put a limit on $|g_{\mu\mu}|^2$ coupling from the atmospheric neutrino data from ICECUBE and SuperKamiokande experiment.

ACKNOWLEDGEMENTS

G.V.S. would like to thank FAPESP (contract no. 2014/00347-3) for the Master scholarship and CAPES for financial support. We would also like to thank FAPESP funding through the grant no. 2012/16389-1.

* *Presented at NuFact15, 10-15 Aug 2015, Rio de Janeiro, Brazil [C15-08-10.2]*

† `gstenico@ifi.unicamp.br`

‡ `orlando@ifi.unicamp.br`

- [1] P. Lipari, *Astroparticle Physics* **1**, 195 (1993), ISSN 0927-6505, URL <http://www.sciencedirect.com/science/article/pii/0927650593900226>.
- [2] T. K. Gaisser and T. Stanev, *Phys. Lett.* **B592**, 228 (2004), the Review of Particle Properties 2004.
- [3] V. Barger, W. Y. Keung, and S. Pakvasa, *Phys. Rev. D* **25**, 907 (1982), URL <http://link.aps.org/doi/10.1103/PhysRevD.25.907>.

Fermilabs Neutrino Beamlines, a Short History and the Current Status*

Craig D. Moore[†]

Fermilab

(Dated: March 23, 2016)

Abstract

Neutrino experiments need high intensity due to the small cross section that neutrinos have with matter. This normally leads to concerns about targets and horns. There is not so much concern for the LBNF Primary beam and a large reason is the success of the present NuMI Beam and we will discuss how the Booster Neutrino Beam (BNB) lead the way for the efficient operation of the NuMI Beamline. The main components of the efficient operation are: Large aperture compared to the size of the beam, automatic checking of beamline parameters using a Beam Permit System, and finally an automatic beamline tuning system which is generically called Autotune.

INTRODUCTION

An overview of the Fermilab Accelerator complex is given in figure 1. Both a short baseline neutrino program and a long baseline neutrino program are supported. Schematic depictions of these programs are given in figures 2 and 3.

As indicated both near detectors see neutrinos from the other beam lines.

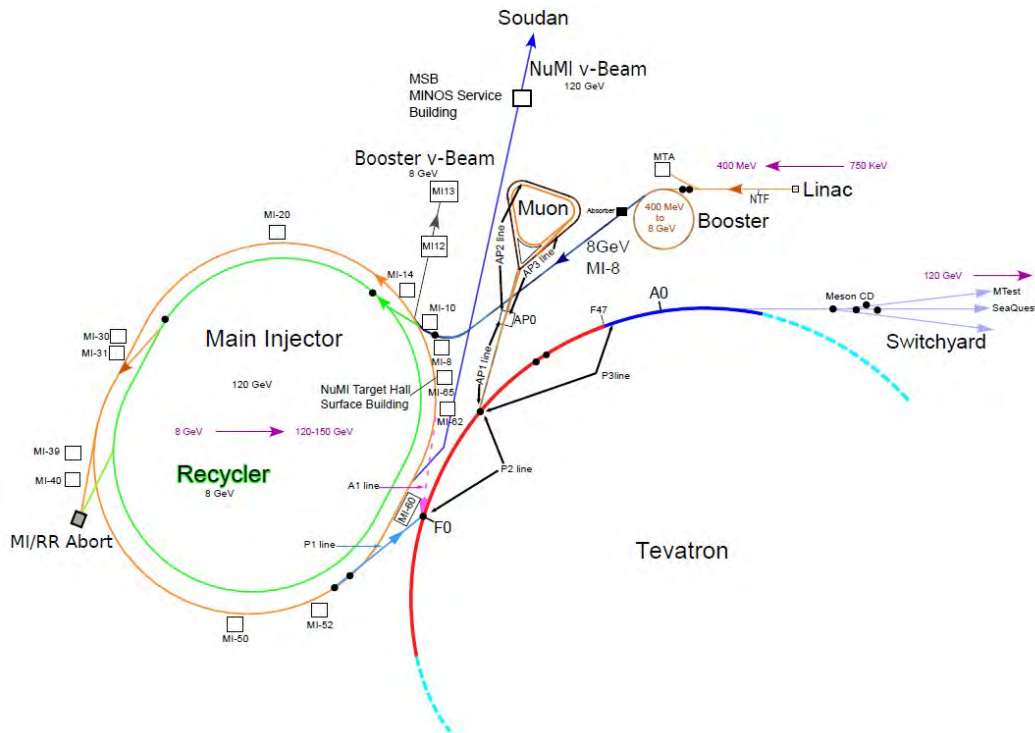


FIG. 1: Fermilab Accelerator Complex

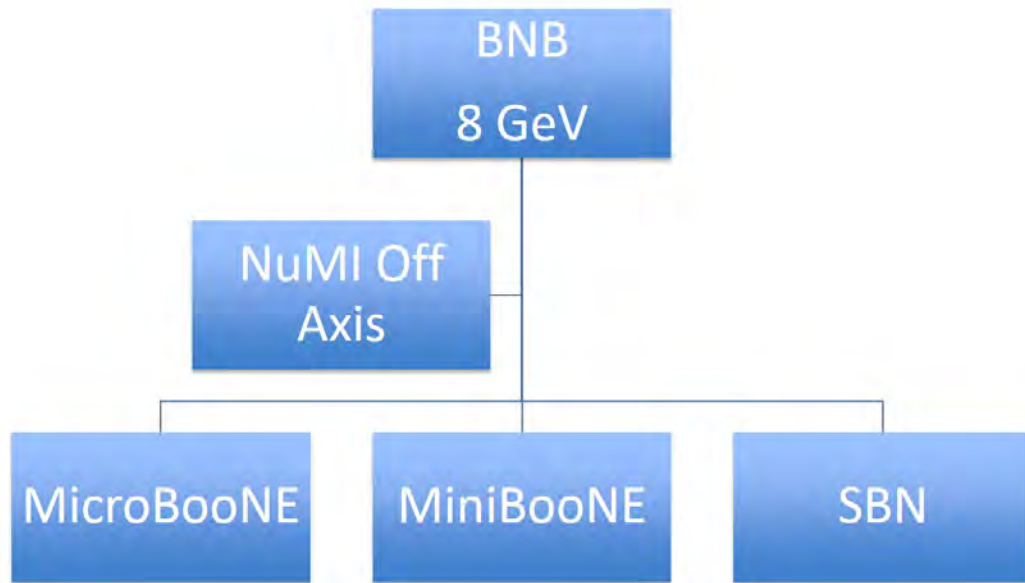


FIG. 2: A schematic depiction of the Short Baseline Program

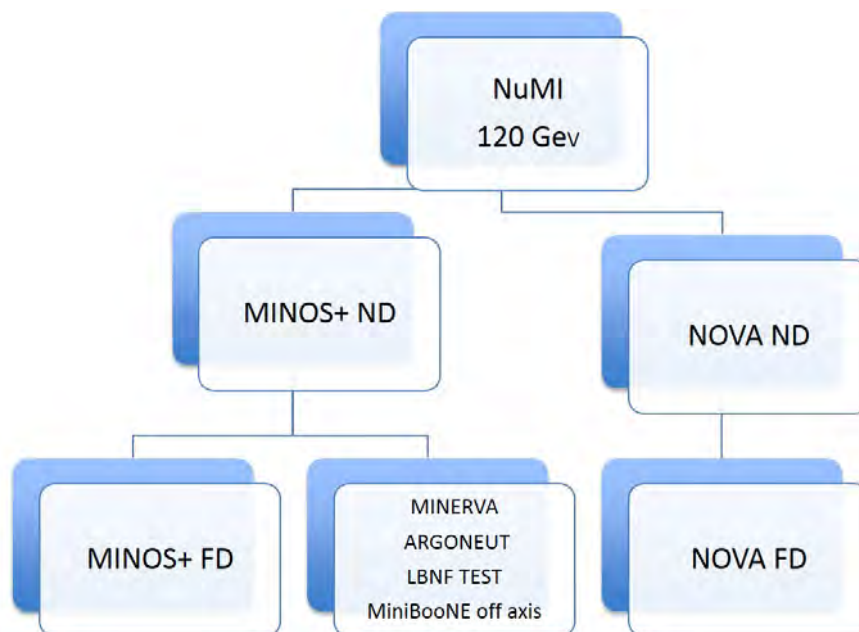


FIG. 3: A schematic depiction of the Long Baseline Program

BOOSTER NEUTRINO BEAM (BNB)

The BNB was constructed to send beam to the MiniBooNE experiment and that experiment took more intensity in a year than was delivered during 17 years of Fixed Target Running. The experiment can run at $18000 \frac{\text{pulses}}{\text{hour}}$ at $5E12$ protons per pulse. Due to the

large intensity per hour and the rapid repetition rate much care was devoted to dealing with the radiation issues associated with these large intensities. Early on it was decided to utilize magnets, which had a large aperture, and the beamline was designed to ensure that the clearance of the aperture was large with respect to the size of the beam at the aperture location. Due to the rapid repetition rate of the beam an automated correction system (Autotune) was used to find and correct minor beam wandering, which is difficult to do manually because of the 5 Hz rate. Finally a MiniBooNE Beam Permit System was installed that is able to check various digital and analogue information against nominal values on a pulse-by-pulse basis.

Since turning on the BNB has transported $2.3E21$ protons and the horns have pulsed half-a-billion times.

NUMI BEAMLIN

Because of ground water issues NuMI losses were even more of a concern than BNB. A brute force solution was adopted in that the beamline was designed with a larger acceptance than the largest beam emittance that could be accelerated the Main Injector. Of course the beam could still be steered into an aperture restriction so an Autotune program was needed and due to operational considerations the NuMI Autotune was more sophisticated than the one used by BNB. The NuMI Beam Permit System checks more than 250 items. These loss control systems lead to a fractional beam loss prior to the target profile monitor of $3E - 7$. Far detector considerations implied we needed to have excellent accuracy and stability of targeting. We achieve angular stability of +15 microradians and a positional stability of +100 microns.

There were several changes for the NOvA medium Energy Run. The experiment requested a movement of the second horn to improve the desired flux at their far detector. In order to deal with the increased intensity several changes were made in the target area: a new baffle with 13 mm diameter was installed, a new and more robust target was installed and additionally the beam spot size was increased to 1.3 mm rms in both directions to reduce the stress on the target.

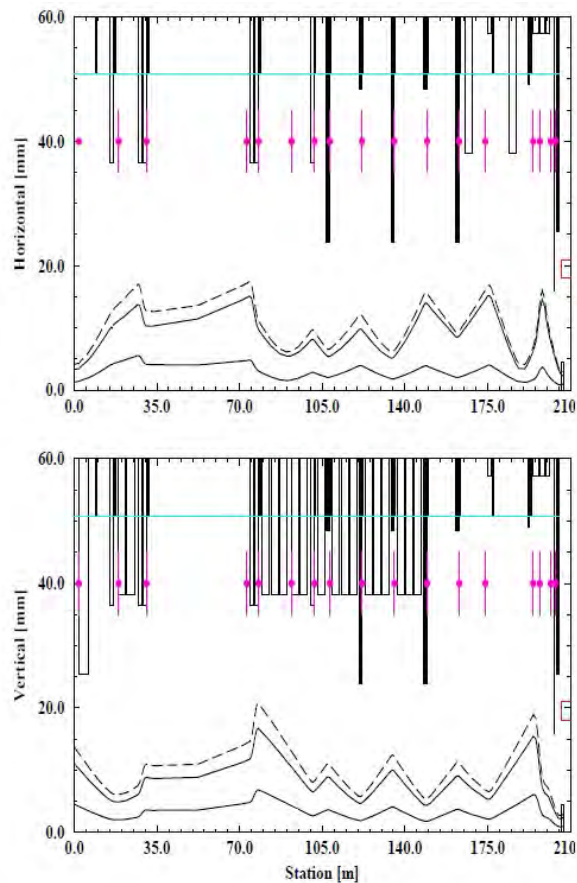


FIG. 4: Beam envelope and apertures. The lower beam envelope is the one sigma and the upper two traces are 95% and 99% with momentum folded in. The assumed emittances were 20π and $\frac{dp}{p}$ of .1%. The line indicates the total loss monitor coverage and the dots indicate the location of individual loss monitors.

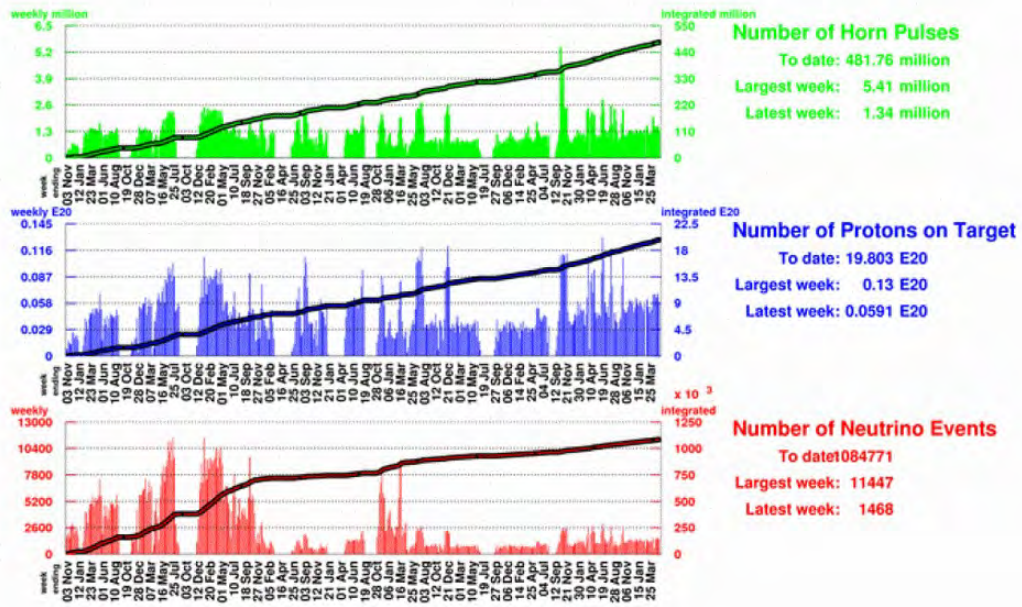


FIG. 5: 2002 – 2012 performance plots.

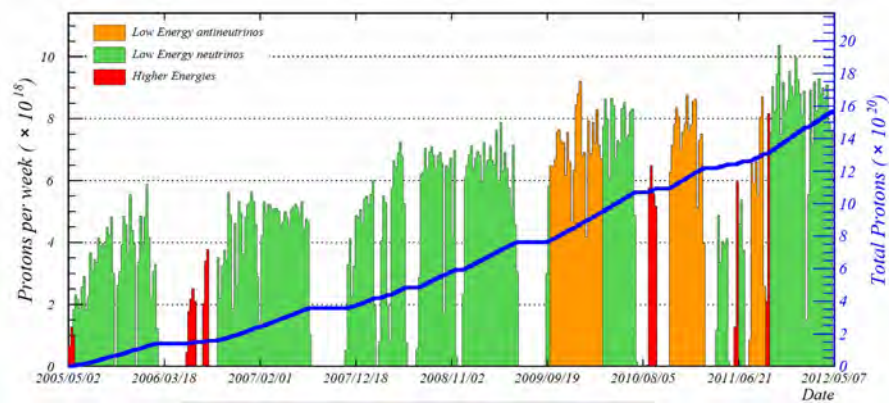


FIG. 6: The cumulative POT on the NuMI Target over the MINOS run. The total POT was $1.56E21$ in various beam configurations. Green is neutrino, orange is antineutrino and red is special runs (e.g. horn off).



FIG. 7: NOvA Protons on Target

HORN STATUS

In the recent past we have had Horn 1 failures on both NuMI and BNB.

For NuMI, horn PH1-04 had a stripline fracture after about 30M pulses, which is believed to have been the result of a design change. PH1-05 is a ready 700 kW design horn however it shares the same stripline design as PH1-04 and one might expect a similar lifetime. There is a strong preference to modify this horn before installation. PH1-03 was designed as a 400 kW horn but it does not have the same stripline design as PH1-04. There are some modifications that can be rapidly implemented to increase the allowable power towards the 700 kW level. These include enhanced downstream water-cooling to reduce stripline flag and contact terminal temperatures along with using an air diverter to supply more air-cooling to stripline flags. PH1-03 was installed and all NuMI experiments are running. The current plan is to study and modify the PH1-05 stripline to enhance fatigue lifetime. It is possible that there would be a preventative horn replacement in the FY16 shutdown but this is to be determined. The situation for NuMI horn 2 is much better due in part to the fact that there is less radiation at its location. There has been one Horn 2 failure (PH2-01) however PH2-02 has well over 60 M pulses and shows no problems. The spare situation is quite well in hand with PH2-03 as a ready spare and PH2-04 very close to completion.

BNB-2 had over 400 M pulses when it was decided to change it out for BNB-3. BNB-2 had plugged water spray nozzles and two leaking water supply manifolds that were previously valved out. There were many challenges some of which were the result of the long running period and the resultant corrosion of movable parts. An important change was the design of a new rad-hard positioning platform, which will make future changes much easier. Also an upgraded RAW skid and pre-target instrumentation were installed. At present BNB does not have a spare horn but over 90% of the hardware has been procured for BNB-4. It is expected that BNB-4 will be completed in the latter part of FY16.

TARGET STATUS

There have been no BNB target failures and parts exist to make a target for BNB-4. However there have been several failures of the Low Energy (LE) targets used in the MINOS running and also an indication of target degradation. This degradation is shown in figure 8 and figure 9 shows the historical POT. There is no sign of neutrino yield degradation for the first NOvA medium energy target MET-01 and this is checked on a weekly basis with plots similar to figure 8. Since the POT on MET-01 is similar to the POT on NT-02 we are encouraged. It may be that NT-02 had a still not understood problem. The lab is in good shape with spare medium energy targets. MET-02 is a ready spare with 3 Be fins (out of 48) to investigate how Be acts with respect to graphite. MET-03 is almost complete and MET-04 and MET-05 are projected to finish in FY16.

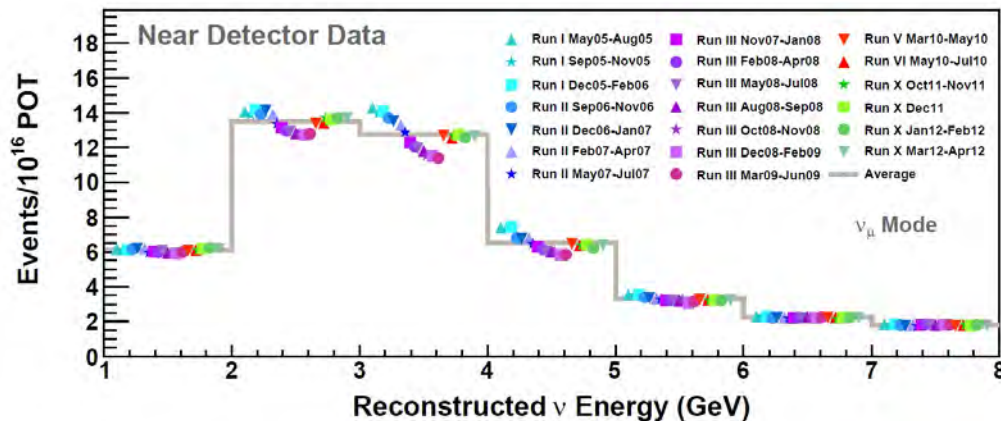


FIG. 8: All time MINOS LE reconstructed Neutrino Spectrum. The solid line is the POT weighted average spectrum over the whole data taking period while the points represent the data for specific runs. The significant drop in the 2nd, 3rd, and 4th bins is due to NT02 target degradation.

CURRENT STATUS

Both neutrino beamlines are up and running after the summer shutdown. For the BNB, MicroBooNE and MiniBooNE are running and there are three small experiments DCTPC, ANNIE, and SCIBATH. Studies are under way to upgrade the facility for the upcoming Short Baseline program. The NuMI beamline is delivering neutrinos for NOvA, MINOS+, MINERVA, and test setup for LBNF with the goal of safely and efficiently delivering 700 kW.

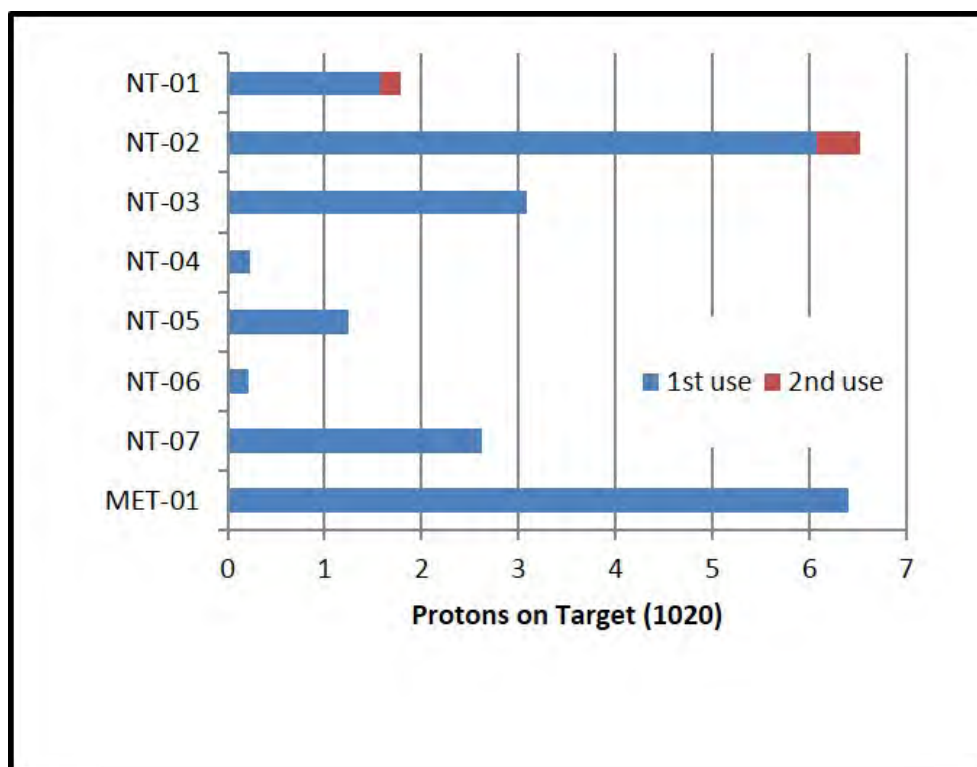


FIG. 9: Protons on target for the NuMI LE targets and the first NOvA medium energy target.

* Presented at NuFact15, 10-15 Aug 2015, Rio de Janeiro, Brazil [C15-08-10.2]

† cmoore@fnal.gov

**The status of nuSTORM and its production of
non-conventional ν_μ beams***

Alan D. Bross[†]

Fermi National Accelerator Laboratory

(Dated: March 25, 2016)

Abstract

Neutrino beams produced from the decay of muons in a racetrack-like decay ring (the so called Neutrino Factory) provide a powerful way to study neutrino oscillation physics and, in addition, provide unique beams for neutrino interaction studies. The Neutrinos from STORed Muons (nuSTORM) facility uses a neutrino factory-like design. Due to the particular nature of nuSTORM, it can also provide an intense, very pure, muon neutrino beam from pion decay. This so-called “Neo-conventional” muon neutrino beam from nuSTORM makes nuSTORM a hybrid neutrino factory. In this paper we describe the facility and give a detailed description of the neutrino beam fluxes that are available and the precision to which these fluxes can be determined. We then present sensitivity plots that indicated how well the facility can perform for short-baseline oscillation searches and show its potential for a neutrino interaction physics program. Finally, we comment on the performance potential of the “Neo-conventional” muon neutrino beam optimized for long-baseline neutrino-oscillation physics.

OVERVIEW

The nuSTORM facility is the simplest implementation of the Neutrino Factory concept [1]. Our studies have assumed that 120 GeV/c protons impinge on a conventional solid target to produce pions. The pions are collected with a magnetic horn and quadrupole magnets and they are then transported to, and injected into, a storage ring. The pions that decay in the first straight (production straight) of the ring can yield muons that are captured in the ring. The circulating muons then subsequently decay into electrons and neutrinos. The storage ring design is optimized for 3.8 GeV/c muon central momentum. This momen-

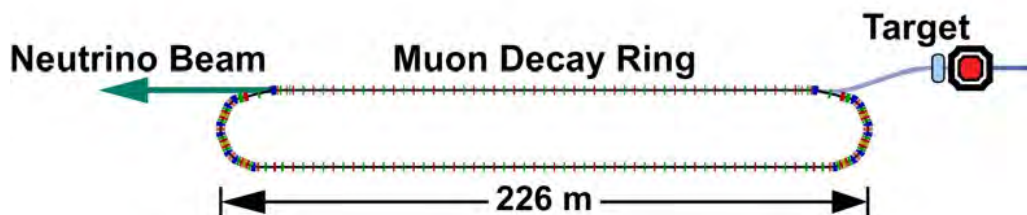


FIG. 1: Schematic of the facility

tum was selected to maximize the physics reach for both short-baseline ν oscillation and ν interaction physics. See Figure 1 for a schematic of the facility. The facility can deliver beams of $\vec{\nu}_e$ and $\vec{\nu}_\mu$ from the decay of the stored μ^\pm beam, but since pions are injected into the ring and decay to produce the stored muon beam, $\vec{\nu}_\mu$ beams from pion decay are also delivered [2–5]. With these beams, experiments can be carried out that:

- Search for sterile neutrinos with unmatched sensitivity;
- Serve future long- and short-baseline neutrino-oscillation programs by providing measurements of $\vec{\nu}_e N$ and $\vec{\nu}_\mu N$ scattering cross sections with percent-level precision; and
- Have the potential to study long-baseline ν oscillation physics.

The pion beam (5 ± 1.0 GeV/c) is brought out of the target station and transported to the injection point of the decay ring, which we have called the ‘‘Orbit Combination Section’’ (OCS), where a large dispersion is introduced in order to combine the pion and muon reference orbits. Figure 2 gives a schematic of this concept. In the ‘‘production straight

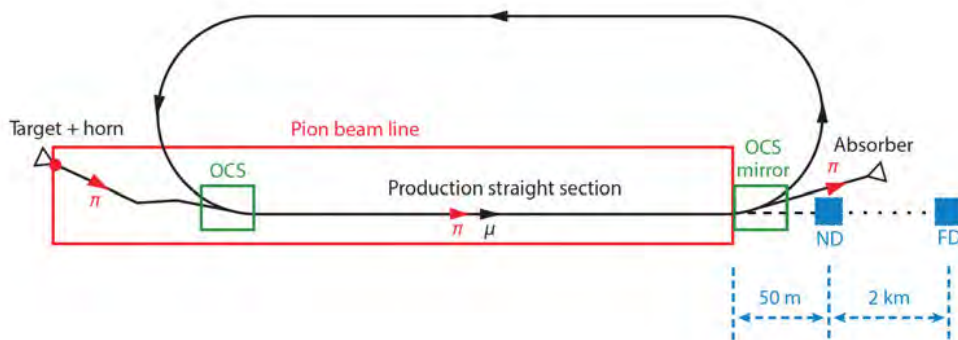


FIG. 2: Schematic of pion injection into the nuSTORM ring.

section’’, approximately 50% of the pions decay into muons, a fraction of which are captured within the ring’s acceptance. The figure-of-merit for the baseline nuSTORM design is that 8×10^{-3} muons are stored in the ring per proton on target. The decay ring straight-section FODO cells were designed to have betatron functions β_x, β_y (the Twiss parameters) optimized for beam acceptance and neutrino beam production (small divergence relative to

the muon opening angle ($1/\gamma$) from $\pi \rightarrow \mu$ decay). At the end of the production straight there is a mirror of the OCS which removes the pions that have not decayed, along with muons in the pion momentum band, the forward decays, and transports these particles to a beam absorber. With a beam absorber depth of ~ 3.5 m, all the pions are absorbed, but the muons produce an intense, pulsed low-momentum muon beam (10^{10} /pulse with $100 \leq P \leq 300$ MeV/c) exiting the back of the absorber.

The nuSTORM ring (see Figure 3) is a compact racetrack design (480 m in circumference) based on large aperture, separate function magnets (dipoles and quadrupoles). The ring is configured with FODO cells combined with DBA (Double Bend Achromat) optics. The production straight is 185 m long. Since the arcs are set for the central muon momentum of 3.8 GeV/c, the pions remaining at the end of the straight will not be transported by the arc, making it necessary to guide the remaining pion beam into an appropriate absorber. Another OCS, which is just a mirror reflection of the injection OCS, is placed at the end of the decay straight. It extracts the residual pions and the muons which are in a 5 ± 0.5 GeV/c momentum band. These extracted muons will enter the absorber along with pions and can be used to produce the intense low-energy muon beam.



FIG. 3: Racetrack ring layout. Pions are injected into the ring at the Orbit Combination Section (OCS). Similarly, extraction of pions and muons at the end of the production straight is done using a mirror image of the OCS.

NEUTRINO FLUXES, EVENT RATES AND SBL OSCILLATION SENSITIVITY

Knowledge of the neutrino flux remains a significant source of systematic error for both neutrino interaction and oscillation experiments. The neutrino beams produced at nuSTORM can be determined with excellent precision with the use of conventional beam diagnostics tools to understand the parent particle distributions, from which the neutrino flux can then be precisely calculated. In order to determine the neutrino beams available at the

nuSTORM facility, an ensemble of particles produced in a MARS [6] simulation of the target and horn were tracked using G4Beamline [7] from the downstream face of the horn and then through the transfer line and injection into the decay ring via the OCS. The particles' energy and 4-momenta in the G4Beamline tracking were then used to determine the neutrino flux at an arbitrary distance from the end of the production straight. This methodology was used to both determine the flux from the decay of circulating muons (those that decayed in the production straight) and from pions that decayed in the production straight. The calculation of the flux in this way presents a real-case flux determination based upon a modeled lattice and beam instrumentation. The errors on the binned flux are dependent solely on the knowledge of the particle trajectories and momentum distribution obtained by the beam diagnostics. A combination of instrumentation performance predictions and simulations indicate that the flux error will be below 1%. The simulated flux from the stored muon beam (for an exposure of 10^{21} POT) is given in Figure 4 (left) at the near detector position and at the 2km far detector in Figure 4 (right). The simulated flux from the pion beam is shown at

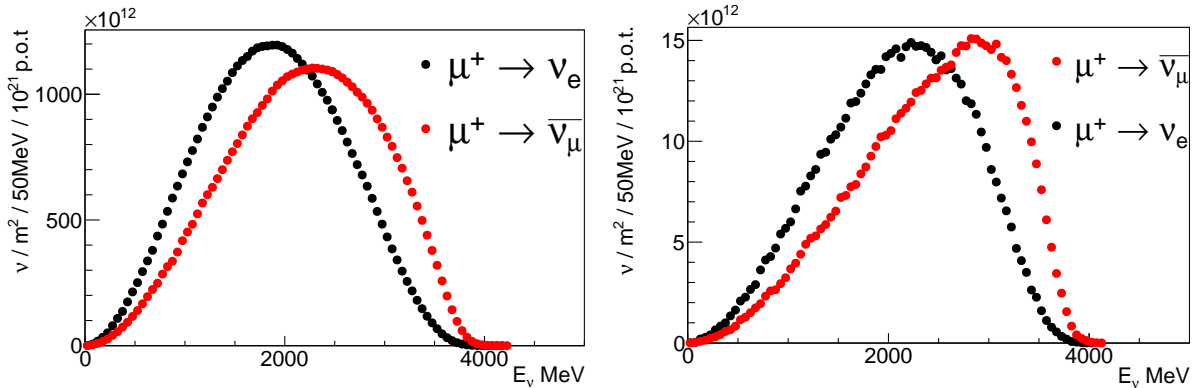


FIG. 4: Neutrino flux from μ decay at the near detector (left) and at the far detector (right)

the near detector position in Figure 5 (left) and at the 2km far detector position in Figure 5 (right). As can be seen in the Figure 5, nuSTORM produces an extremely pure ν_μ beam. Based on the flux calculations given above, the total number of neutrino interactions for a 100T detector at the 50m near position (exposure of 10^{21} POT) can be determined and is shown in Table I. With a flux precision of $\leq 1\%$ and with the statistics given in this table, nuSTORM offers unprecedented opportunities for the study of neutrino (both $\bar{\nu}_\mu$ and $\bar{\nu}_e$) interaction physics. Table II gives the event rates seen at a 1 kT SuperBIND detector [3] at 2 km from the end of the production straight. Rates assuming no short-baseline oscillation

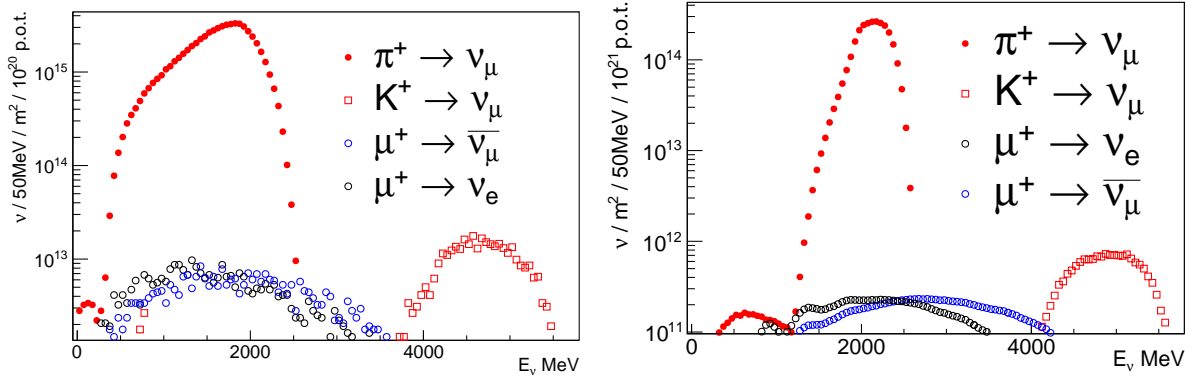


FIG. 5: Neutrino flux from π decay at the near detector (left) and at the far detector (right)

TABLE I: Event rates at 50 m from the end of the decay straight per 100 T for 10^{21} POT.

μ^+ stored		μ^- stored	
Channel	kEvents	Channel	kEvents
ν_e CC	5,188	$\bar{\nu}_e$ CC	2,519
$\bar{\nu}_\mu$ CC	3,030	ν_μ CC	6,060
ν_e NC	1,817	$\bar{\nu}_e$ NC	1,002
$\bar{\nu}_\mu$ NC	1,174	ν_μ NC	2,074

π^+ injected		π^- injected	
Channel	kEvents	Channel	kEvents
ν_μ CC	41,053	$\bar{\nu}_\mu$ CC	19,939
ν_μ NC	14,384	$\bar{\nu}_\mu$ CC	6,986

TABLE II: Event rates at 2 km per 1.3 kT for 10^{21} POT for the no oscillation scenario and one with 1 sterile neutrino.

μ^+ Stored		
Channel	No Oscillation	Oscillation
$\nu_e \rightarrow \nu_\mu$	0	288
$\nu_e \rightarrow \nu_e$	188,292	176,174
$\bar{\nu}_\mu \rightarrow \bar{\nu}_\mu$	99,893	94,776
$\bar{\nu}_\mu \rightarrow \bar{\nu}_e$	0	133

π^+ Injected		
Channel	No Oscillation	Oscillation
$\nu_\mu \rightarrow \nu_\mu$	915,337	854,052
$\nu_\mu \rightarrow \nu_e$	0	1,587

and an oscillation scenario following a 3+1 scenario (3 standard neutrinos and 1 sterile neutrino) are given. The nuSTORM facility also provides the opportunity to perform searches for sterile neutrinos with unmatched sensitivity and breadth. In Figure 6 we show the exclusion plot for ν_μ appearance that is obtainable using a $\bar{\nu}_e$ beam from μ^+ decay normalized to 10^{21} POT and using the SuperBIND detector.

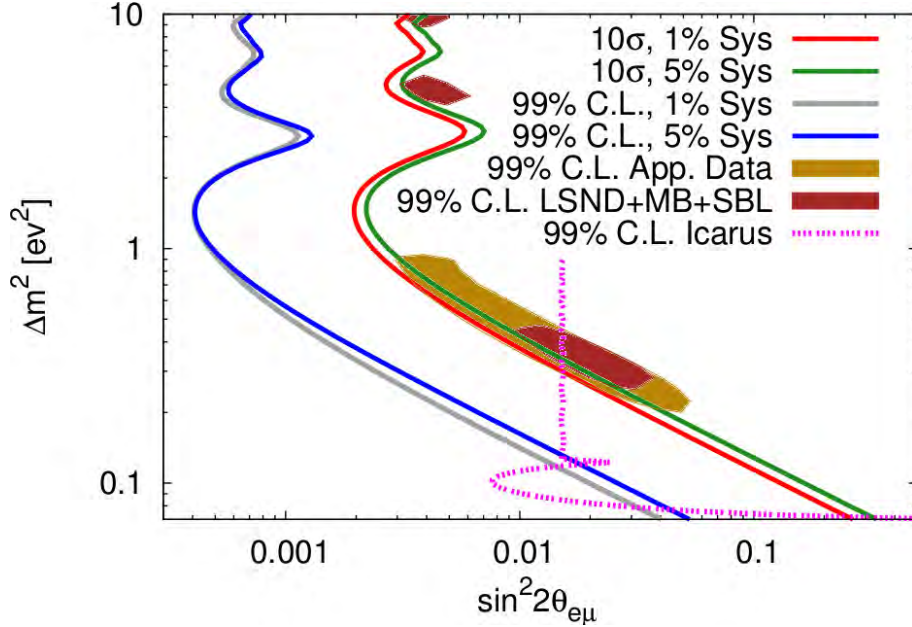


FIG. 6: The sensitivity of a ν_μ appearance experiment to a short baseline oscillation due to a sterile neutrino at nuSTORM assuming a 3+1 model. Both the 10σ significance and 99% confidence level contours are shown for two different scenarios for the systematic uncertainties; one in which the total systematic uncertainty is 1% of the beam normalization and a second when the systematic uncertainty is a factor of 5 times larger. The 99% contours generated from the fit to the MiniBooNE and LSND data is shown with the brown dotted line (Evid. Data), while the fit to all available appearance data is shown with the black dotted line (App. Data). The 99% exclusion contour from Icarus is also shown.

OPTIMIZATION OF THE NUSTORM PION BEAM LINE FOR LONG-BASELINE OSCILLATION PHYSICS

If the decay ring of nuSTORM is tilted, beams could be used for a long-baseline neutrino oscillation experiment. We have investigated this option, but have determined that the flux available from pion decay in the production (injection) straight is too small to be useful. We then considered a configuration that was optimized for the production of a $\bar{\nu}_\mu$ beam from pion decay. We removed the capability for a stored muon beam, considering only a pion injection line (from the target to the end of the production straight). This concept of producing neutrinos from an instrumented pion beam line, nuPIL, is shown in Figure 7. In this configuration, the injection OSC, the arcs and the return straight are removed (no

ring) and the lattice design is only optimized to transport pions in a momentum band of 5 ± 1 GeV/c. Since the straight is no longer required to transport both pions and muons (with a lower momentum), the compromises needed to do so are no longer incorporated and pion transport is more efficient. In this case, a simplified mirror OSC is used to extract the remaining pions (and some muons as described above) to a beam absorber. This pion injection beam line would, of course, need to be tilted at an appropriate angle. Figure 8

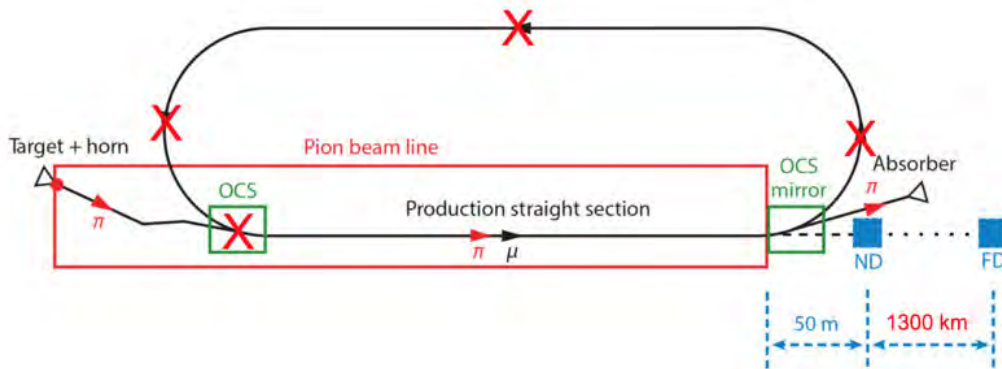


FIG. 7: Schematic of the pion injection line. The red Xs indicate the components removed from the nuSTORM configuration.

(left) shows the ν_μ flux/yr obtained at 1300 km for this configuration. This is for 1.47×10^{21} POT. Also shown is the flux that would be obtained for nuSTORM and, for reference, the current optimized flux for DUNE [8]. This configuration shows that nuPIL produces $\simeq 40X$ the flux of nuSTORM. The flux does fall short of what is obtained at DUNE, but the beam systematics will be greatly reduced since effects due to uncertainties in secondary particle production, proton-beam targeting stability, target degradation/stability and horn stability can be removed by in situ measurement of the pion flux (via beam line instrumentation) in the production straight. In addition, the wrong-flavor neutrinos ($\bar{\nu}_\mu$ in the ν_μ beam and vice versa) and the high-energy component of the $\bar{\nu}_\mu$ beam are essentially entirely suppressed in this neutrino beam line design. In order to increase the flux, we are investigating a lattice design utilizing Fixed-Field Alternating Gradient (FFAG) optics with a much larger pion momentum acceptance than the FODO design. See Figure 8 (right).

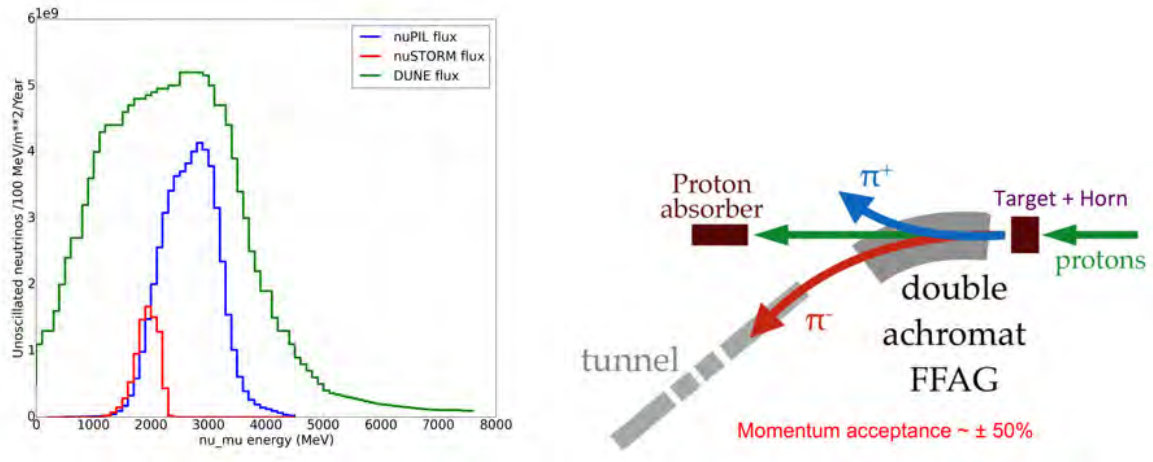


FIG. 8: Left: The neutrino flux (ν_μ from pion decay at a distance of 1300 km for nuSTORM and nuPIL. The baseline flux for DUNE is shown for comparison. Right: A schematic of the concept to extend the nuPIL FODO design to a FFAG lattice.

CONCLUSIONS

In this article we have summarized the status and capabilities of the nuSTORM facility. We have also shown how one component of the facility (the pion injection line) could be re-optimized solely for the production of $\bar{\nu}_\mu$ from π^\pm decay, producing a neutrino beam with very small flux uncertainties.

* Presented at NuFact15, 10-15 Aug 2015, Rio de Janeiro, Brazil [C15-08-10.2]

† bross@fnal.gov; Work supported by DOE under contract DE-AC02-07CH11359

- [1] S. Geer, Phys. Rev. **D57**, 6989 (1998), [Erratum: Phys. Rev.D59,039903(1999)], hep-ph/9712290.
- [2] D. Adey, R. Bayes, A. Bross, and P. Snopok, Ann. Rev. Nucl. Part. Sci. **65**, 145 (2015).
- [3] D. Adey et al. (nuSTORM) (2013), 1308.6822.
- [4] A. Liu, D. Neuffer, and A. Bross, Nucl. Instrum. Meth. **A801**, 44 (2015).
- [5] A. Liu, A. Bross, and D. Neuffer, Nucl. Instrum. Meth. **A794**, 200 (2015).
- [6] N. V. Mokhov, K. K. Gudima, C. C. James, M. A. Kostin, S. G. Mashnik, E. Ng, J. F. Ostiguy, I. L. Rakhno, A. J. Sierk, and S. I. Striganov, Radiat. Prot. Dosim. **116**, 99 (2005),

nucl-th/0404084.

- [7] K. B. Beard, T. J. Roberts, and P. Degtiarenko, Conf. Proc. **C0806233**, MOPD017 (2008).
- [8] C. Adams et al. (LBNE) (2013), 1307.7335, URL <http://www.osti.gov/scitech/biblio/1128102>.

**The European Spallation Source Neutrino Super Beam for CP
Violation discovery***

Marcos Dracos[†]

IPHC, Université de Strasbourg, CNRS/IN2P3, F-67037 Strasbourg, France

(Dated: December 21, 2015)

Abstract

After measuring the last neutrino mixing angle and founding it to have a relatively large value, neutrino Super Beams became very competitive on discovering a CP violation in the leptonic sector. This large value also, despite the lower statistics, favours the second oscillation maximum for this discovery because of its enhanced sensitivity to the CP violation parameter δ_{CP} . A possible Super Beam operated at the second oscillation maximum could be produced using the very powerful proton linac of the European Spallation Source under construction in Lund, Sweden. Indeed, the 5 MW proton power of this linac could provide enough muon neutrinos to operate the facility at the second oscillation maximum. The performance of this facility on CP violation discovery is presented in this paper. This facility could also produce a copious number of muons, which could be used by other facilities as nuSTORM, the Neutrino Factory or a future muon collider.

INTRODUCTION

The relatively large value of the last neutrino mixing angle θ_{13} opens the door to new discoveries as a possible CP violation in the leptonic sector and the determination of the neutrino mass hierarchy using conventional neutrino facilities. Indeed, neutrino beams produced using the traditional method of hitting a target with a proton beam and producing mesons decaying into neutrinos, can again be used for these researches. The only condition is that the used proton beams must be very powerful compared to the proton drivers already used in neutrino physics. It also comes out that for the measured θ_{13} value, the sensitivity to CP violation is significantly higher at the second oscillation maximum than the first one [1]. The neutrino/antineutrino asymmetry is of the order of $0.3 \sin \delta_{CP}$ on the first oscillation maximum while this value is $0.75 \sin \delta_{CP}$ at the second one. On top of that, at the second oscillation maximum the interference term of the $\nu_{\mu} \rightarrow \nu_e$ oscillation probability is dominant compared to the “solar” and “atmospheric” term [2]. These arguments show that measurements at the second oscillation maximum will be less affected by systematic errors than those done at the first maximum.

To exploit the second oscillation maximum capabilities the baseline between the neutrino production point and the far detector must be relatively large, or the energy of the neutrinos must be relatively low or both. Increasing the distance will necessitate more and more powerful proton beams in order to get enough statistics in relatively short time (less

than 10 years of facility operation). Using the European Spallation Source [3] linac under construction (first beam expected by 2019 while a full power and full energy proton beam is expected by 2023) in Lund, Sweden, expected to have a proton power of 5 MW and energy of 2 GeV, enough neutrinos can be obtained placing the far detector at a distance of about 500 km, in order to cover a large fraction of the δ_{CP} values with a confidence level of 5σ . A full proposal done by the ESS ν SB group of how to use the ESS proton beam to add, on top of the neutron facility, a neutrino facility, can be found in [4].

THE NEUTRINO FACILITY AT ESS

Some modifications are necessary in order to add the neutrino facility on top of the neutron one at ESS. These modifications are mainly needed because of the too long proton pulses delivered by the linac for the neutrino facility. Indeed, the proton pulses at the present design are of 2.86 ms, while for the neutrino facility they have to be reduced at the level of few μ s, duration affordable by the hadron collector (horn) placed after the neutrino target to collect the charged pions. To reduce the duration of the proton pulses an accumulator ring with a circumference of the order of 400 m has to be added before sending the beam to the target. A fast extraction of the proton beam accumulated in the ring can be performed after.

Not been able to introduce new protons in the accumulator while other protons already circulate in due to space charge effects, H^- ions have to be accelerated in the linac instead of protons. The electrons of the ions can be stripped at the entrance of the accumulator using a classical carbon foil (as done at SNS [5]) or a laser technique.

The adopted target/horn station is the one proposed by the EURO ν Design Study in the Super Beam option [6, 7]. In this configuration, in order to mitigate the high power of the proton beam, four target/horn systems are used pulsed alternatively. The pion decay tunnel is relatively short compared to other facilities due to the low pion energy. The length of this tunnel is of the order of 25 m, which can be easily filled with He instead of vacuum in order to avoid a window between the target/horn station and the decay tunnel.

Fig. 1 presents the obtained neutrino (positive horn polarity) and antineutrino (negative horn polarity) beams at a distance of 100 km for 200 days of continues operation. The proton intensity is 1.1×10^{15} protons/pulse. Table I summarizes the obtained neutrino

beam composition. The muon neutrino beam is quite pure especially in the neutrino mode. A 0.5% electron neutrino contamination is observed in both modes. Efforts are done to use this contamination to measure the electron neutrino cross-section in a near detector. In case this is possible it will considerably reduce the systematic errors for the CP violation search.

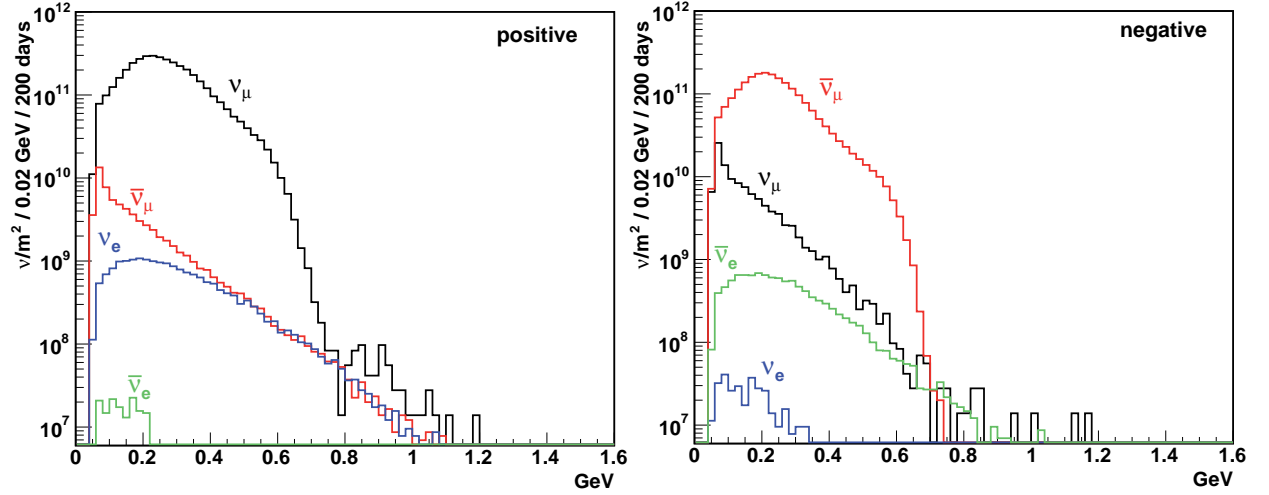


FIG. 1: Neutrino fluence as a function of energy at a distance of 100 km on-axis from the target station, for 2.0 GeV protons and positive (left) and negative (right) horn current polarities, respectively.

TABLE I: Number of neutrinos per m^2 crossing a surface placed on-axis at a distance of 100 km from the target station during 200 days for 2.0 GeV protons and positive and negative horn current polarities.

	positive		negative	
	$N_\nu (\times 10^{10})/\text{m}^2$	%	$N_\nu (\times 10^{10})/\text{m}^2$	%
ν_μ	396	97.9	11	1.6
$\bar{\nu}_\mu$	6.6	1.6	206	94.5
ν_e	1.9	0.5	0.04	0.01
$\bar{\nu}_e$	0.02	0.005	1.1	0.5

PHYSICS PERFORMANCE

Using the neutrino spectra of Fig. 1 and GLOBES [8, 9] package, the physics performance of the neutrino facility in terms of CP violation discovery has been evaluated. Fig. 2 presents the δ_{CP} fraction coverage versus the distance to the far detector for 3σ and 5σ confidence level. This has been extracted assuming the utilization of MEMPHYS Water Cherenkov megaton detector [10, 11] and 5% (10%) systematic error for the signal (background). To estimate this performance several proton energies have been used on top of the default one of 2 GeV since it is possible to upgrade the linac to deliver higher energy protons.

The best performance is obtained for a distance between 350 km to 550 km reaching a maximum of 60% δ_{CP} coverage. An active mine exists at a distance of 540 km at the location of Garpenberg, Sweden, where the far detector can be installed in a depth of more than 1000 m.

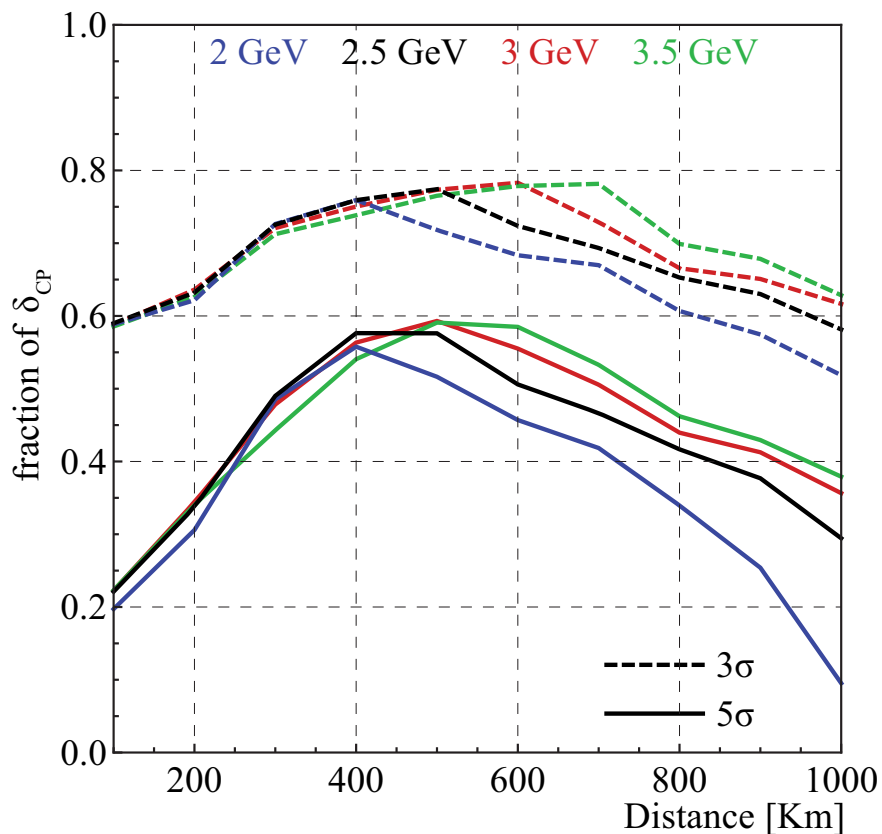


FIG. 2: The fraction of the full δ_{CP} range as function of the baseline. The lower (upper) curves are for CP violation discovery at 5σ (3σ) significance.

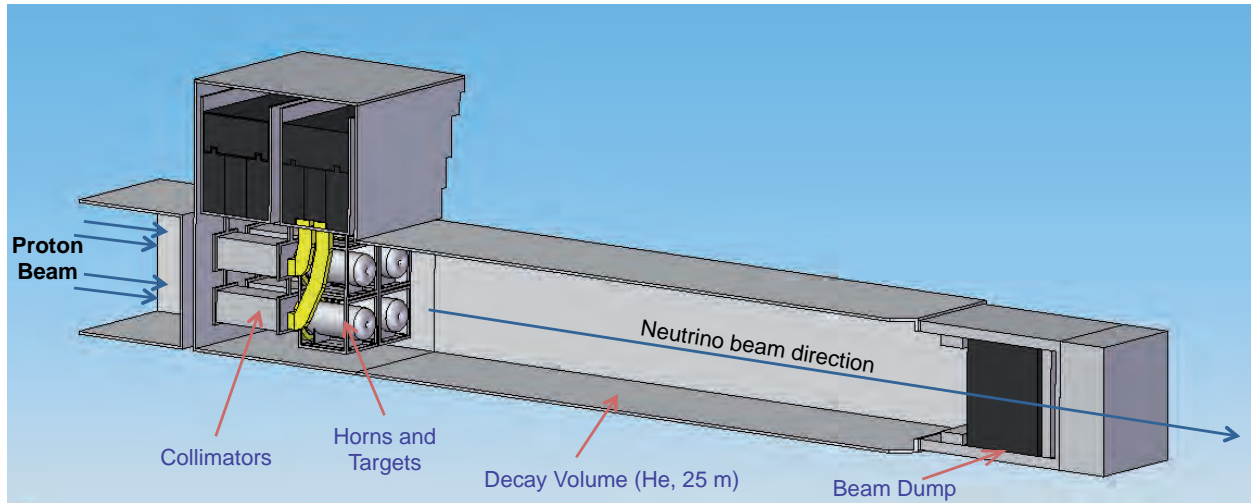


FIG. 3: Schematic view of the target/horn station.

MUON PRODUCTION

The same neutrino facility can be used to produce a copious number of muons. In fact, these muons are produced for free in the decay tunnel together with the muon neutrinos by the decay of pions and could be collected at the level of the neutrino facility beam dump (Fig. 3). These muons could be used by a low energy nuSTORM [12] facility to measure neutrino cross-sections at the energies where this neutrino facility will be operated. They could also be useful for 6D muon cooling experiments and in an ultimate stage they could be used to operate a Neutrino Facility or a muon collider.

A specific device under study could be used to extract these muons and inject them in a beam pipe. Fig. 4 and 5 present the impacts of remaining pions and produced muons at the surface of the beam dump. In the pion distribution one can distinguish four spots induced by the four targets and horns while for the muons coming from the pion decays these spots are more diluted. The big majority of these particles is concentrated in a surface of $2 \times 2 \text{ m}^2$ that constitutes a difficulty for their extraction and injection in a beam pipe. Considering a surface of 1 m^2 centered in the middle of these distributions or centered on one of the pion or muon spots, one could collect about 3.6×10^{20} pions and 4.1×10^{20} muons per year.

The mean value of the momentum of pions and muons is 0.7 GeV and 0.46 GeV, respectively (Fig. 6 and 7). For these energies, the mean free path of pions is of the order of 40 m after which they will decay to give some more muons. The mean free path for the muons is

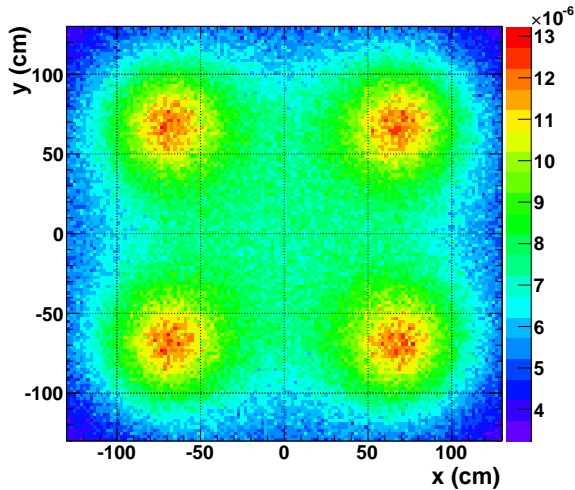


FIG. 4: Impacts of pions on the surface of the beam dump (normalized per proton).

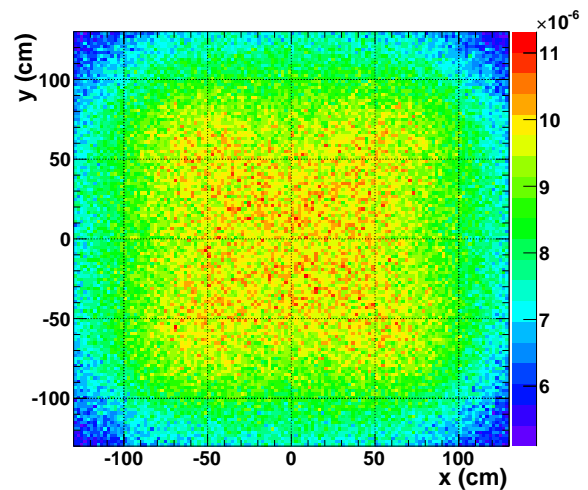


FIG. 5: Impacts of muons on the surface of the beam dump (normalized per proton).

2.9 km which is enough to send them in a ring, as the one foreseen for nuSTORM, where they can decay in straight sections to produce muon and electron neutrinos to be used to measure cross-sections.

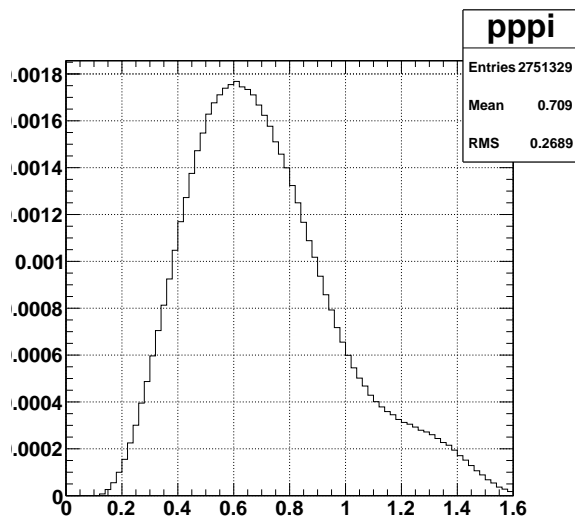


FIG. 6: Momentum of remaining pions at the level the beam dump (normalized per proton).

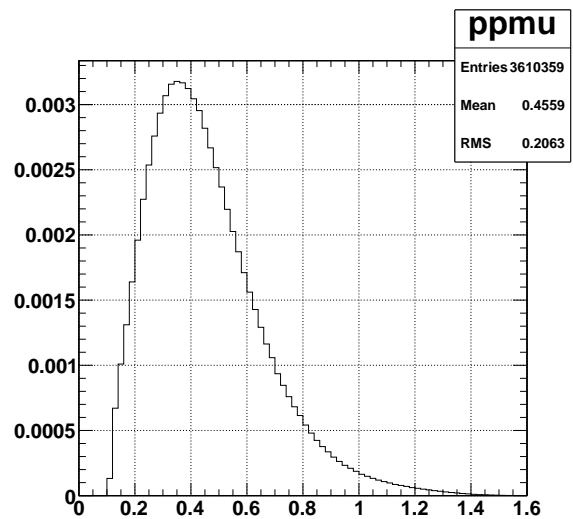


FIG. 7: Muon momentum at the level of the beam dump (normalized per proton).

While for nuSTORM muon beam an iron absorber is needed to lower the muon momentum to a mean value of 400 MeV in order to perform 6D muon cooling experiments (of which success could lead to the construction of a Neutrino Factory and a muon collider), for

ESSnuSB the muon momentum is directly around the required values. nuSTORM plans to collect in the region between 200 MeV/c and 500 MeV/c about 4.3×10^{17} muons per year while the ESSnuSB facility could provide more than 2.5×10^{20} muons per year for the same momentum range.

CONCLUSION

The proposed ESSnuSB neutrino facility operated on the ESS proton linac at the same time than the neutron facility, has very competitive performance in terms of CP violation discovery in the lepton sector. This facility, operated at the second oscillation maximum, can cover up to 60% of the δ_{CP} range with a confidence level of 5σ . The megaton far Water Cherenkov detector used by this projects also has a rich astroparticle physics program.

A byproduct of this facility is the production of a copious muon number. These muons could be used in a low energy version of nuSTORM to measure neutrino cross-sections at the energies interested by the neutrino oscillation program of the facility. 6D muon cooling experiments could also use these muons for studies which could open the way to the construction of a Neutrino Factory and a muon collider.

ACKNOWLEDGMENTS

The author would like to thank all ESSnuSB colleagues and particularly Pilar Coloma, Enrique Fernandez-Martinez, Tord Ekelof and Nikolaos Vassilopoulos for their help, plots and valuable discussions.

* *Presented at NuFact15, 10-15 Aug 2015, Rio de Janeiro, Brazil [C15-08-10.2]*

† `marcos.dracos@in2p3.fr`; Speaker

- [1] S. J. Parke, “Neutrinos: Theory and Phenomenology,” *Phys. Scripta T* **158**, 014013 (2013) [arXiv:1310.5992 [hep-ph]].
- [2] P. Coloma and E. Fernandez-Martinez, “Optimization of neutrino oscillation facilities for large θ_{13} ,” *JHEP* **1204**, 089 (2012) [arXiv:1110.4583 [hep-ph]].

- [3] The European Spallation Source, <http://europeanspallationsource.se/>, ESS Technical Design Report, Release 1.0, Nov. 2012.
European Spallation Source Project <http://ess-scandinavia.eu>
- [4] E. Baussan *et al.* [ESSnuSB Collaboration], “A Very Intense Neutrino Super Beam Experiment for Leptonic CP Violation Discovery based on the European Spallation Source Linac: A Snowmass 2013 White Paper,” Nuclear Physics B, Volume 885, August 2014, Pages 127-149, arXiv:1309.7022 [hep-ex].
- [5] Spallation Neutron Source, <http://neutrons.ornl.gov/facilities/SNS/>
- [6] T. R. Edgecock, O. Caretta, T. Davenne, C. Densham, M. Fitton, D. Kelliher, P. Loveridge and S. Machida *et al.*, “The EUROnu Project,” Phys. Rev. ST Accel. Beams **16** (2013) 021002 [arXiv:1305.4067 [physics.acc-ph]].
- [7] E. Baussan *et al.* [EUROnu Super Beam Collaboration], “The SPL-based Neutrino Super Beam,” arXiv:1212.0732 [physics.acc-ph].
- [8] P. Huber, M. Lindner and W. Winter, Comput. Phys. Commun. **167** (2005) 195 [hep-ph/0407333].
- [9] P. Huber, J. Kopp, M. Lindner, M. Rolinec and W. Winter, Comput. Phys. Commun. **177** (2007) 432 [hep-ph/0701187].
- [10] A. de Bellefon, J. Bouchez, J. Busto, J. -E. Campagne, C. Cavata, J. Dolbeau, J. Dumarchez and P. Gorodetzky *et al.*, “MEMPHYS: A Large scale water Cherenkov detector at Frejus,” hep-ex/0607026.
- [11] L. Agostino *et al.* [MEMPHYS Collaboration], “Study of the performance of a large scale water-Cherenkov detector (MEMPHYS),” JCAP **1301**, 024 (2013) [arXiv:1206.6665 [hep-ex]].
- [12] P. Kyberd *et al.* [nuSTORM Collaboration], arXiv:1206.0294 [hep-ex].

Prospects for Precision Neutrino Cross Section Measurements*

Deborah A. Harris[†]

Fermilab

(Dated: March 21, 2016)

Abstract

The need for precision cross section measurements is more urgent now than ever before, given the central role neutrino oscillation measurements play in the field of particle physics. The definition of precision is something worth considering, however. In order to build the best model for an oscillation experiment, cross section measurements should span a broad range of energies, neutrino interaction channels, and target nuclei. Precision might better be defined not in the final uncertainty associated with any one measurement but rather with the breadth of measurements that are available to constrain models. Current experience shows that models are better constrained by 10 measurements across different processes and energies with 10% uncertainties than by one measurement of one process on one nucleus with a 1% uncertainty. This article describes the current status of and future prospects for the field of precision cross section measurements considering the metric of how many processes, energies, and nuclei have been studied.

INTRODUCTION

The need for precision cross section measurements is more urgent now than ever before given the requirements of current and future oscillation experiments. These experiments need to measure precisely the oscillation probabilities for neutrinos ranging from 600 MeV to several GeV, using targets ranging from carbon and oxygen to argon and steel. The neutrino energy that is available for any detector technology to measure depends not only on the specific process that the neutrino underwent on a particular nucleon, but also the effect of the nuclear environment on that process.

The nuclear environment can change the cross section from that of a bare nucleon process in several ways. For example, nucleons are not simply in a non-interacting relativistic Fermi Gas when they interact with the exchange boson, they are often interacting with each other. In addition, the final state particles that exit the bare nucleon process can lose energy on the way out of the nucleus, or even undergo charge exchange and leave the nucleus at a different energy and a different charge than the one produced in the bare nucleon process.

Oscillation experiments try to address this challenge using a battery of measurements: first, hadron production measurements and a detailed beamline simulation are needed to provide an accurate prediction of the initial flux of the neutrinos as a function of energy. Second, most oscillation experiments will use a (suite of) near detector(s) to try to measure

the neutrino event rate as a function of energy before oscillations have taken place. There is usually an emphasis on having at least part of the near detector include the same nuclei that make up the far detector to reduce uncertainties due to these nuclear effects. However, the amount of energy lost in that nucleus affects the overall neutrino energy scale and will not cancel between the near and far detectors in a measurement of the neutrino mass squared splittings.

External cross section measurements are another important component of an oscillation experiment's strategy for making far detector predictions. For example, T2K uses external cross section measurements from MiniBooNE and MINERvA at higher energies in its fit for oscillation parameters [1]. Until we as a field can produce neutrino interaction models (and associated generators) which can faithfully reproduce cross section measurements, experiments will use what they have on hand and try to determine uncertainties accordingly. The more ways we can test and improve models by providing precision cross section measurements, the better those models will eventually be, and the better the oscillation parameters will be measured.

CURRENT STATUS

Given the needs of oscillation experiments it is worth examining the breadth of measurements have been made so far as well as what measurements are potentially available given the data that has been taken. The important issues for each energy and interaction channel are not only the flux, detector mass, and acceptance that are available, but what uncertainties are achievable on those quantities. Given the few-GeV neutrino energies that are in use by current oscillation experiments, it is most important to measure (and ultimately model) the charged-current quasi-elastic process (CCQE), charged and neutral pion production, coherent pion production, and to a lesser extent deep inelastic scattering (DIS). Since it is sometimes difficult to separate those different processes in any one detector technology, a total charged-current cross-section measurement (referred to as CCINCL in Tab. I) can also be useful to help constrain models. Although the nuclear effects were first seen in DIS in charged leptons [2], there is no guarantee that even if we completely understood all of those effects for charged leptons, that we could then predict how the nucleus would affect these other processes, or even DIS for neutrino scattering.

The energies available range from the 600 MeV narrow band beam at T2K's near detector complex, to the 1 GeV Booster Neutrino Beam, through the NuMI Beamline's broad band energies peaked at 3 GeV and 6 GeV. By using hadron production measurements from HARP, the Booster Neutrino Beam absolute ν_μ ($\bar{\nu}_\mu$) flux uncertainties were dominated by a 14.7% (17.5%) flux uncertainty in π^+ (π^-) production [3, 4]. The T2K neutrino flux uncertainties are approximately 12% at the peak off axis neutrino energy, and are also dominated by hadronic interactions [1]. The MIPP experiment [5] has produced measurements of charged pion and kaon production off the NuMI target which should result in significantly lower total flux uncertainties for both NOvA [6] and MINERvA, and MINERvA's flux uncertainties at the time of NuFact'15 were approximately 12% [7], again dominated by the uncertainties in pion production [8].

The neutrino target nuclei available today range from carbon (in scintillator oil or solid scintillator), to oxygen (in Water Cerenkov), to argon (liquid argon time projection chambers) and finally iron (scintillator-steel tracking calorimetry). These detectors have all been placed in neutrino beams, and some have also been placed in test beams of charged hadrons and electrons, in order to better measure detector response. Most recently, MINERvA has released results on its scintillator detector responses to pions and protons ranging from 0.4 to 2 GeV [9] and the LArIAT test beam program [10] has been collecting data on a Liquid Argon TPC in that same beamline. The typical precision on the absolute energy scale that MINERvA achieved was between 3-4% from this program.

The current coverage of neutrino experiments in terms of energy ranges and target nuclei can be shown in Tab. I.

UPCOMING RESULTS

Although there have been several new results on cross sections since the 2014 NuFact conference, the current data still have many potential channels and kinematics to explore. In addition, the MicroBooNE experiment started operations in a 1 GeV broad band neutrino beam just after the 2015 NuFact conference took place, and will be able to shed more light on the puzzles that exist on pion production because of its improved resolution of pion kinematics using a Liquid Argon Time Projection Chamber, compared to MiniBooNE's resolution using an oil Cerenkov detector.

TABLE I: This table shows the channels that have been measured as a function of target nucleus and process. The entries that are names of experiments correspond to data sets that are being taken now, or if in italics, data sets that are projected to be available in the future.

Target	Peak Neutrino Energy				
	700MeV	1GeV	2 GeV	3 GeV	6 GeV
CH_2		CCQE [11, 12] π^\pm, π^0 prod. [13, 14]	NO ν A		
CH	CCQE [15] Coherent [19]	CCQE [16]		CCQE [17, 18], Coherent [8] π^\pm, π^0 prod. [20, 21]	MINER ν A
H_2O	T2K			MINER ν A	MINER ν A
Ar		MicroBooNE <i>SBND</i>		CCINC [22], Coherent [23], CC-no π [24]	<i>CAPTAIN</i> <i>MINERνA</i>
Fe		CCINCL ratio [25]		CCQE [26], π prod., coherent, CCINCL [27] CCINCL Ratios [28] DIS Ratios [29]	MINER ν A
Pb				CCINCL and DIS ratios [28, 29]	MINER ν A

T2K

The T2K near detector suite allows for both on-axis measurements using a broad band beam at 3 GeV, as well as off axis measurements using a narrow band beam at about 700 MeV. The on-axis detector, in particular the central module which allows for proton and some pion identification, will be able to do exclusive-channel cross sections, including a measurement of charged current coherent pion production and 0 pion production on Carbon. The off-axis detector suite affords a much broader range of final state channels and target nuclei. For example, T2K expects to have results out shortly on both neutral and charged pion production, as well as electron neutrino measurements. The variety of near detector components means that T2K is also planning to measure oxygen and lead to carbon cross-section ratios.

MINERvA

There are several new measurements from MINERvA that are presented elsewhere in these proceedings. Reference [30] includes a first measurement of the electron neutrino quasi-elastic cross section, which shows that at least to the level of the statistical precision of the data, the electron neutrino cross section is consistent with that of muon neutrinos as a function of momentum transferred to the nucleus. In addition, a first measurement of the ratios of neutrino DIS cross sections between C, Fe, and Pb and CH is given in Ref. [31]. Other expected results that will come from MINERvA's Low Energy (3 GeV) data set is a charged current quasielastic double differential cross section, and pion production cross sections for neutrinos and antineutrinos both, as described in Ref. [32, 33] respectively.

In the future, MINERvA expects to provide measurements using its Medium Energy (6 GeV) data set, which is in progress. The increased flux, cross section, and accumulated protons on target in this beam will mean that the channels that have already been measured on CH (plastic scintillator) can be measured on the solid nuclear targets (C, Fe, Pb) at interesting ($\sim 10\%$ or better) precision.

NOvA

NOvA has already accumulated an impressive near detector data set comprising more than 2 million charged current neutrino interactions [34]. These statistics will allow NOvA to map out both the quasi-elastic and total charged current cross sections at 2 GeV on CH_2 in great detail. Given the muon neutrino statistics, the electron neutrino charged current statistics in NOvA will also be at the tens of thousands of events, and in fact the measurements there will be limited by the uncertainty in the flux, and the detector energy scale. Both of these are expected to improve over time and with the incorporation of hadron production measurements.

FUTURE PROSPECTS

Given the suite of measurements expected from the current operating program, the path forward is clear. Given the DUNE far detector technology of Liquid Argon Time Projection Chambers, and the broad band of energies expected at DUNE, high statistics data on argon

nuclei between 0.5 through 6 GeV is clearly needed, for both neutrino and antineutrino interactions.

In order to best constrain models of neutrino interactions on argon, however, comparisons between argon and other nuclei are also in demand, again in both neutrino and antineutrino beams. Although at the time of this writing the MINERvA experiment has a large sample of neutrino events across nuclei ranging from helium to lead, antineutrino statistics have yet to be accumulated. Two of the future experiments described below (SBND and CAPTAIN MINERvA) will aim to make measurements on argon in broad band beams that can be compared to measurements on carbon made in the same neutrino beam. The two experiments, by spanning both the below and above few-GeV neutrino energies, will be able to study nuclear effects across a range of channels and a range of energies.

Finally, the cross section measurements on electron neutrinos are particularly sparse: to date there are a few total cross section measurements [35, 36], and at the time of this writing only one charged current quasi-elastic measurement [30].

1 GeV Liquid Argon Measurements

The Booster Beamline at Fermilab is home to a suite of new Liquid Argon TPC experiments [37]: MicroBooNE, located at 470 m from the booster beamline target and at 61 ton fiducial mass, will provide the first measurements at these energies on an argon target. The Short Baseline Near Detector (SBND) at only 110m from the target and at 110 ton fiducial mass, will collect an estimated 5.2 million muon neutrino charged current events over the expected exposure of 6.2×10^{20} protons on target (POT). In addition SBND will also be able to collect some 38 thousand charged current electron neutrino interactions to study. These measurements will help expand the fields understanding of the nuclear effects that are critical at 1 GeV, a picture that was first painted by MiniBooNE's broad range of interaction measurements on carbon in the same beamline. Because of the energies of this beamline, both the quasi-elastic and single pion production channels can be accessed. Comparisons to MiniBooNE's measurements on CH_2 can provide some handles, although the reconstruction capabilities of the two detector technologies are very different.

3-6 GeV Liquid Argon Measurements

Just as the MicroBooNE and SBND measurements will greatly expand the reach of the MiniBooNE measurements on carbon by enabling cross section ratios to be measured at high precision at 1 GeV, the CAPTAIN MINERvA experiment will do the same thing at the higher energies of 3-6 GeV where the DUNE experiment expects most of its far detector events. This experiment will put a 6 ton Liquid Argon TPC (CAPTAIN) in front of the MINERvA detector to collect on the order of a million charged current interactions on Argon in an exposure of 6.2×10^{20} POT [38]. These can be directly compared to the statistics collected on MINERvA's scintillator target, which is of comparable fiducial mass and reconstruction capabilities. Because of the higher energy of the NuMI beamline where CAPTAIN MINERvA sits, the experiment will have access to not only the quasi-elastic and single pion production, but also to multi-pion final states and Deep Inelastic Scattering.

Narrow Band Measurements on Water

The NuPRISM experiment is a completely different strategy compared to the previous two experiments. Rather than comparing cross sections across different nuclei in a broad-band neutrino beam, NUPRISM aims to map out cross sections in several different monochromatic neutrino beams [39]. These beams are “created” by comparing interaction rates at different angles with respect to the T2K beamline. Those angles are available by building a large cylinder of water that can be instrumented to collect cerenkov light from neutrino interactions at very well-defined angles. This experiment takes advantage of 2-body kinematics and the existence of the T2K beamline to create whatever neutrino energy spectrum would be of interest, simply by adding or subtracting data taken at slightly different angles. This proposal has been presented to the J-PARC Physics Advisory Committee.

CONCLUSIONS

There has been impressive progress on precision cross sections in the past year, where progress has been made not only by collecting substantial data sets on very fine grained detectors in intense beams, but also with significantly better understanding of neutrino fluxes and detector responses through auxiliary measurements. Harvesting the data that has been

taken will mean a wealth of cross section measurements that have uncertainties at the 10% level or better, assuming systematics can be kept under control. The clear places where the field is missing precision measurements is in electron neutrino cross sections, antineutrino measurements, and comparisons between argon and other nuclei at several different energies. There are several new efforts underway to help address these shortcomings, and while the field may never get to the one or two per cent precision level for any absolute cross section, having a broad range of energies, processes, and nuclei will be key to creating a precise model of neutrino interactions.

This work was supported by the Fermi National Accelerator Laboratory under US Department of Energy contract No. DE-AC02-07CH11359. Partial support was also provided by the American Physical Society through the Brazil-U.S. Professorship/Lectureship Program.

* *Presented at NuFact15, 10-15 Aug 2015, Rio de Janeiro, Brazil [C15-08-10.2]*

† `dharris@fnal.gov`

- [1] K. Abe et al. (T2K), *Phys. Rev. Lett.* **112**, 181801 (2014), 1403.1532.
- [2] P. Norton, *Rept. Prog. Phys.* **66**, 1253 (2003).
- [3] A. Bolshakova et al. (HARP-CDP Group), *Eur. Phys. J.* **C62**, 293 (2009), 0901.3648.
- [4] A. A. Aguilar-Arevalo et al. (MiniBooNE), *Phys. Rev.* **D79**, 072002 (2009), 0806.1449.
- [5] J. M. Paley et al. (MIPP), *Phys. Rev.* **D90**, 032001 (2014), 1404.5882.
- [6] D. S. Ayres et al. (NOvA) (2004), hep-ex/0503053.
- [7] J. Park et al. (MINERvA) (2015), 1512.07699.
- [8] A. Higuera et al. (MINERvA), *Phys. Rev. Lett.* **113**, 261802 (2014), 1409.3835.
- [9] L. Aliaga et al. (MINERvA), *Nucl. Instrum. Meth.* **A789**, 28 (2015), 1501.06431.
- [10] W. Foreman (LArIAT), in *Meeting of the APS Division of Particles and Fields (DPF 2015) Ann Arbor, Michigan, USA, August 4-8, 2015* (2015), 1511.00305, URL <http://inspirehep.net/record/1402345/files/arXiv:1511.00305.pdf>.
- [11] A. A. Aguilar-Arevalo et al. (MiniBooNE), *Phys.Rev.Lett.* **100**, 032301 (2008), 0706.0926.
- [12] A. A. Aguilar-Arevalo et al. (MiniBooNE) (2013), 1301.7067.
- [13] A. A. Aguilar-Arevalo et al. (MiniBooNE), *Phys. Rev.* **D83**, 052007 (2011), 1011.3572.
- [14] A. A. Aguilar-Arevalo et al. (MiniBooNE), *Phys. Rev.* **D83**, 052009 (2011), 1010.3264.

- [15] K. Abe et al. (T2K), Phys. Rev. **D92**, 112003 (2015), 1411.6264.
- [16] K. Abe et al. (T2K), Phys. Rev. **D91**, 112002 (2015), 1503.07452.
- [17] L. Fields, J. Chvojka, et al. (MINERvA Collaboration), Phys.Rev.Lett. **111**, 022501 (2013), 1305.2234.
- [18] G. Fiorentini, D. Schmitz, et al. (MINERvA Collaboration), Phys.Rev.Lett. **111**, 022502 (2013), 1305.2243.
- [19] M. Hasegawa et al. (K2K), Phys.Rev.Lett. **95**, 252301 (2005), hep-ex/0506008.
- [20] B. Eberly et al. (MINERvA), Phys. Rev. **D92**, 092008 (2015), 1406.6415.
- [21] T. Le et al. (MINERvA), Phys. Lett. **B749**, 130 (2015), 1503.02107.
- [22] R. Acciarri et al. (ArgoNeuT), Phys. Rev. **D89**, 112003 (2014), 1404.4809.
- [23] R. Acciarri et al. (ArgoNeuT), Phys. Rev. Lett. **113**, 261801 (2014), [Erratum: Phys. Rev. Lett.114,no.3,039901(2015)], 1408.0598.
- [24] R. Acciarri et al. (ArgoNeuT), Phys. Rev. **D90**, 012008 (2014), 1405.4261.
- [25] K. Abe et al. (T2K), Phys. Rev. **D90**, 052010 (2014), 1407.4256.
- [26] P. Adamson et al. (MINOS), Phys. Rev. **D91**, 012005 (2015), 1410.8613.
- [27] P. Adamson et al. (MINOS), Phys. Rev. **D81**, 072002 (2010), 0910.2201.
- [28] B. G. Tice et al. (MINERvA), Phys. Rev. Lett. **112**, 231801 (2014), 1403.2103.
- [29] J. Mousseau et al. (MINERvA) (2016), 1601.06313.
- [30] J. Wolcott et al. (MINERvA) (2015), 1509.05729.
- [31] A. Bravar, Presented at NuFact 2015 (2015), Deep Inelastic Scattering at MINERvA .
- [32] A. Ghosh, these Proceedings (2015), Quasi-elastic measurements at MINERvA.
- [33] M. Carneiro, these proceedings (2015), Pion and kaon production at MINERvA.
- [34] J. Bian (NOvA), in *Meeting of the APS Division of Particles and Fields (DPF 2015) Ann Arbor, Michigan, USA, August 4-8, 2015* (2015), 1510.05708, URL <http://inspirehep.net/record/1399048/files/arXiv:1510.05708.pdf>.
- [35] J. Blietschau et al. (Gargamelle), Nucl. Phys. **B133**, 205 (1978).
- [36] K. Abe et al. (T2K), Phys. Rev. Lett. **113**, 241803 (2014), 1407.7389.
- [37] L. Camilleri, AIP Conf. Proc. **1680**, 020004 (2015).
- [38] A. Higuera, these proceedings (2015), CAPTAIN (BNB and the CAPTAIN/MINERvA Physics Programs).
- [39] S. Bhadra et al. (nuPRISM) (2014), 1412.3086.

MICE Demonstration of Ionization Cooling*

J.-B. Lagrange[†]

Imperial College London, UK/Fermilab, USA

J. Pasternak

Imperial College London, UK/ISIS-RAL-STFC, UK

on behalf of the MICE collaboration

(Dated: March 22, 2016)

Abstract

Muon beams of low emittance provide the basis for the intense, well-characterised neutrino beams necessary to elucidate the physics of flavour at the Neutrino Factory and to provide lepton-antilepton collisions at energies of up to several TeV at the Muon Collider. The International Muon Ionization Cooling Experiment (MICE) will demonstrate ionization cooling, the technique by which it is proposed to reduce the phase-space volume occupied by the muon beam at such facilities. In an ionization-cooling channel, the muon beam passes through a material (the absorber) in which it loses energy. The energy lost is then replaced using RF cavities. The combined effect of energy loss and re-acceleration is to reduce the transverse emittance of the beam (transverse cooling). A major revision of the scope of the MICE project was carried out over the summer of 2014. The revised project plan, which has received the formal endorsement of the international MICE Project Board and the international MICE Funding Agency Committee, will deliver a demonstration of ionization cooling. The design of the cooling demonstration experiment will be described together with the cooling performance of the revised configuration.

INTRODUCTION

Stored muon beams have been proposed as the source of neutrinos at the Neutrino Factory and as the means to deliver multi-TeV lepton-antilepton collisions at the Muon Collider [1]. In such facilities the muon beam is produced from the decay of pions produced by a high-power proton beam hitting a target. The tertiary muon beam occupies a large volume in phase space. To optimise the muon yield while maintaining a suitably small aperture in the muon-acceleration systems requires that the muon-beam phase space be reduced (cooled) prior to acceleration. The short muon lifetime makes traditional cooling techniques unacceptably inefficient when applied to muon beams. Ionization cooling, in which the muon beam is passed through material (the absorber) and subsequently accelerated, is the technique by which it is proposed to cool the beam [2, 3].

A full demonstration of ionisation cooling can be considered in two parts:

- A study of the properties that determine the lattice cooling performance,
- Demonstration of transverse emittance reduction with longitudinal re-acceleration.

Cooling performance depends on the initial beam emittance, momentum, absorber material and β_{\perp} at the absorber which is studied in MICE Step IV [4]. Once material properties have been fully characterised at Step IV, sustainable ionisation cooling must be demonstrated. This requires restoring the energy lost by the muons passing through the absorber in RF cavities. The experimental configuration with which the MICE collaboration will study ionization cooling has been revised in the light of the recommendations of the US Particle Physics Projects Prioritization Panel and subsequent national and international reviews of the project. This process culminated in November 2014 when the project was formally rebaselined to deliver the configuration presented in this paper. The schedule for the rebaselined project shows that the initial demonstration of ionization cooling will be performed by the end of US fiscal year 2017, while preserving MICE measurements at Step IV [4]. This paper describes the lattice configuration adopted for the MICE demonstration of ionization cooling and presents its performance.

LATTICE CONFIGURATION

The so-called “DEMO” lattice that will be used for the demonstration of ionization cooling is shown in Fig. 1. It consists of two single RF cavities, one primary (65 mm) LiH absorber, and two secondary (32.5 mm) LiH secondary absorbers. The cooling cell is formed of the central lithium-hydride (LiH) absorber sandwiched between two focus-coil (AFC) modules. The emittance is measured upstream and downstream of the cooling channel by solenoidal spectrometers. Further instrumentation upstream and downstream of the magnetic channel serves to select a pure sample of muons passing through the channel and to measure the phase at which each muon passes through the RF cavities. The layout of the experiment has been optimised to maximise the reduction in transverse emittance using the primary (central) and secondary LiH absorbers, while keeping minimum the non-linear effects. With this configuration, a small betatron function at the position of the primary absorber can be achieved together with an acceptable beam size at the position of the 201 MHz cavities. The phase advance of the cooling cell has been chosen between two half integer resonances to minimize the chromatic effects due to the large momentum spread of the beam, leading to strong non-linearities. The spectrometer solenoids (SSs) house high-precision scintillating-fibre tracking detectors (trackers) [5] in a uniform field of

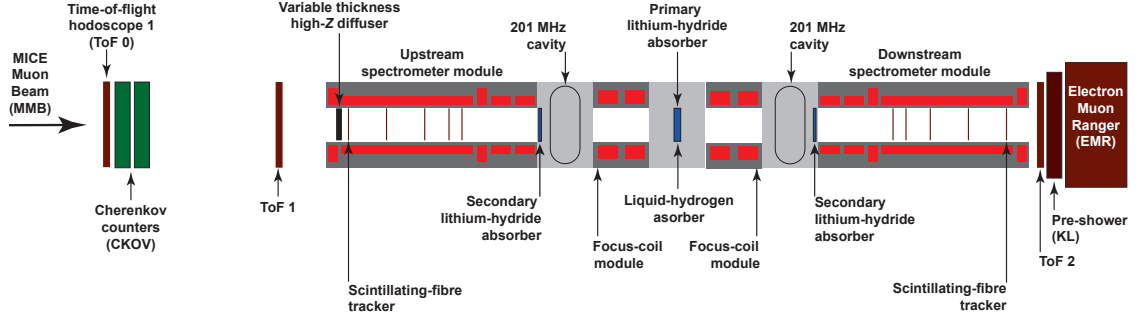


FIG. 1: Layout of the lattice configuration for the MICE Cooling Demonstration (DEMO lattice).

TABLE I: Design parameters of the DEMO lattice.

Parameter	Value
$L_{SS \rightarrow AFC}$ (mm)	2607.5
$L_{AFC \rightarrow AFC}$ (mm)	1678.8
$L_{RFmodule \rightarrow AFC}$ (mm)	784.0
RF Gradient (MV/m)	10.3
No. RF cavities	2
No. primary absorbers	1
No. secondary absorbers	2

4T. The trackers will be used to reconstruct the trajectories of individual muons before and after they pass through the cooling cell. The reconstructed tracks will be combined with the information from the instrumentation upstream and downstream of the channel to measure the muon beam emittance with a precision of 0.1%.

The parameters of the lattice are presented in Tab. I. Bellows around each cavity module have been added in order to allow easy cavity module inspection.

The resulting solenoidal magnetic field on axis is shown in Fig. 2 for the three planned settings (140 MeV/c, 200 MeV/c and 240 MeV/c). Vertical lines locate the positions of the centre of the AFC modules (red), the primary absorber (burgundy) and the secondary absorbers (blue). In the “[+ + - -]” configuration shown, the downstream AFC and SS modules are powered in the opposite sense to the upstream AFC and SS so that the field changes sign at the absorber. This is a desirable feature for studying the cancellation of

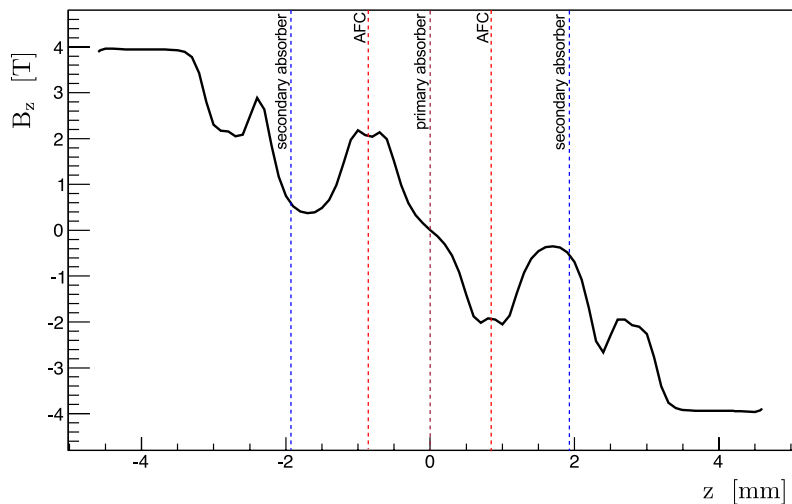


FIG. 2: B_z on-axis in $[++--]$ polarity for the DEMO lattice design for 200 MeV/ c configuration.

canonical angular momentum through the lattice.

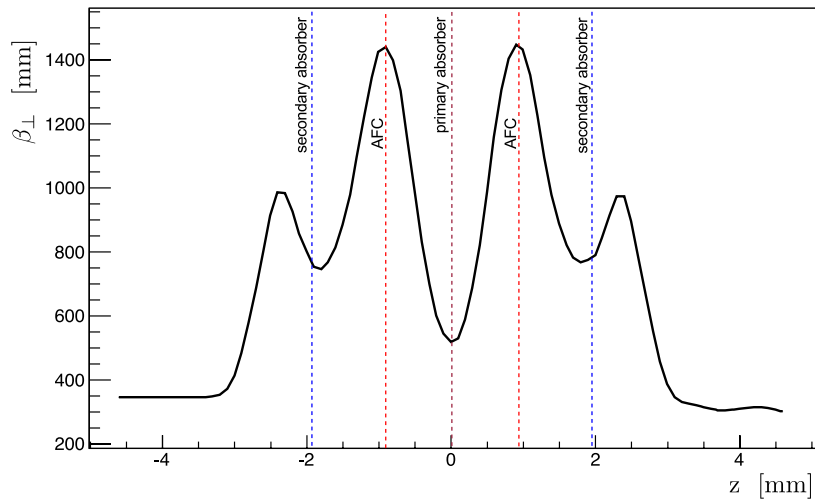
Secondary absorbers

The secondary LiH absorbers (SAs) are introduced between the cavities and trackers in order to minimise the exposure of trackers to dark-current electrons originating from the RF cavities. Such electrons produce correlated background to the muon tracks in the trackers.

The SAs also increase the net transverse cooling effect. The positions for SAs were carefully selected as a compromise between the requirement of a small value of beta at absorbers and the ability to remove the absorbers remotely to allow studies of the bare magnetic lattice.

Radiation shutters

Retractable, lead radiation shutters will be installed on rails between SSs and the RF modules to protect the trackers against dark-current induced radiation during cavity conditioning. The SAs will be mounted on a rail system and will be located between the cavities and the lead shutters. Both mechanisms will be moved using linear Piezo-electric motors that operate in vacuum and in magnetic field.

FIG. 3: β_{\perp} for 200 MeV/ c configuration in the DEMO lattice.TABLE II: Beta-function values at relevant positions for an initial beam at 200 MeV/ c in the DEMO lattice design.

Parameter	Value
β_{\perp} at primary absorber (mm)	520
β_{\perp} at secondary absorbers (mm)	780
β_{\max} at AFC (mm)	1450

Optics parameters

The betatron function evolution shown in Fig. 3 is matched for an initial 200 MeV/ c beam. The Courant Snyder parameters in each Tracker are matched to the constant 4 T solenoidal field and a small beta waist in the central absorber is achieved. This matching takes into account the change in energy of the muons as they pass through the cooling cell by adjusting currents in the upstream and downstream FCs and in the matching coils in the SSs independently while maintaining the field in the tracking volumes at 4 T. Beta values at relevant positions are summarised in Tab. II.

TABLE III: General parameters of the initial beam in the different simulations

Parameter	Value
Particle	muon μ^+
Number of particles	10000
Longitudinal position [mm]	-4612.1
Central energy [MeV]	228.0
Gaussian transverse distribution	
α_{\perp}	0
β_{\perp} [mm]	339.0
Gaussian longitudinal distribution	
Longitudinal emittance [mm]	20
Longitudinal β [mm]	11
Longitudinal α	-0.7

COOLING PERFORMANCE

MAUS code

Simulation to evaluate the performance of the lattice has been done using the official simulation and reconstruction software of MICE called MAUS (MICE Analysis User Framework). In addition to simulation, MAUS also provides a framework for any subsequent data analysis. MAUS is used for both offline analysis and also to provide fast real-time detector reconstruction and data visualization during MICE running.

MAUS is written in Python (primarily for top level code provided to the user) and C++ (lower level code used for performance). GEANT4 is used to support simulation by providing beam propagation and detector responses, ROOT is used for data visualization and as a data storage format.

Tracking and analysis

Tracking has been done for different configurations. Parameters of the initial beam used for the different simulations are summarized in Table III.

TABLE IV: Acceptance criteria for analysis.

Parameter	Muon accepted
Radius at upstream tracker (mm)	≤ 150.0
Radius at downstream tracker (mm)	≤ 150.0
Particle	muon μ^+

Table IV lists the acceptance criteria required by all analyses presented here, which exclude muons that do not appear within the active region of the trackers and limit particles to positive muons only (as muons may decay).

A muon passing through two 32.5 mm secondary LiH absorbers and one 65 mm primary LiH absorber would lose $\langle \Delta E \rangle = 18.9$ MeV. Including losses in the SciFi trackers and windows, this increases to 24.3 MeV. The RF gradient achievable in two cavities is insufficient to replace the energy lost in the absorber, therefore a comparison of beam energy with and without RF is required. With RF an energy deficit of $\langle \Delta E \rangle = 19$ MeV would be observed. This measurable difference would confirm that, were more RF cavities or higher RF gradient available, the transverse emittance reduction would be sustainable.

200 MeV/c configuration performance

Energy is lost in the upstream tracker and first secondary absorber before being partially restored in the first RF cavity ($z \approx -1600$ mm). Further energy is lost in the primary absorber, partially restored in the second RF cavity, and then lost in the final secondary absorber. The reduction in transverse emittance, with RF, is shown in Figure 4. The beam is subject to non-linear effects in regions of high β_{\perp} , which causes limited emittance growth. Nonetheless, a reduction in emittance is observed between the upstream and downstream trackers ($z \approx \pm 3500$ mm). The DEMO lattice achieves a reduction of ≈ 5.6 %.

Figure 5 shows the fractional change in emittance with respect to the initial emittance.

SUMMARY

The MICE collaboration is now on track to deliver its demonstration of ionization cooling by 2017. The demonstration will be performed using lithium-hydride absorbers and with

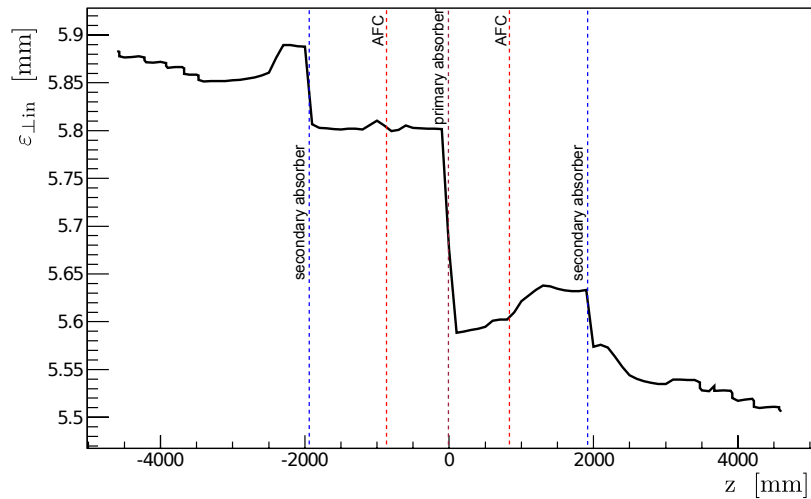


FIG. 4: Emittance reduction of an initial $\varepsilon = 6$ mm beam for the DEMO lattice design in the 200 MeV/ c configuration.

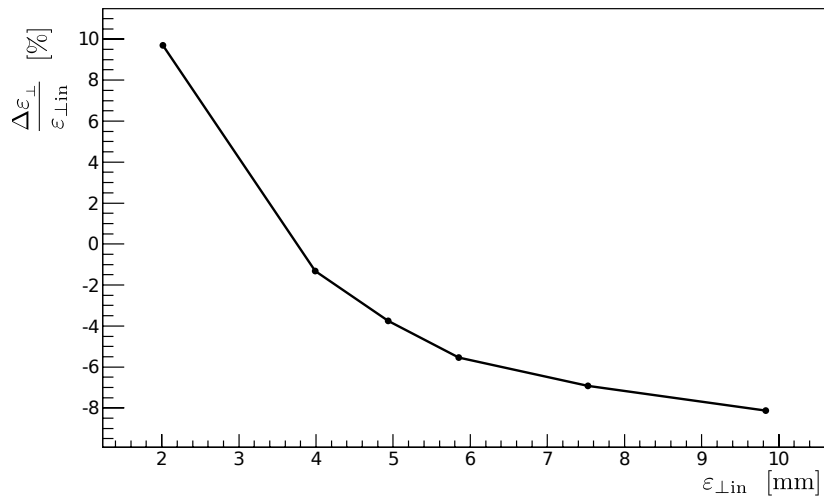


FIG. 5: Fractional change in emittance as a function of initial emittance for the DEMO lattice design in the 200 MeV/ c configuration.

acceleration provided by two single, 201 MHz, cavity modules. The equipment necessary to mount the experiment is either in hand like the superconducting magnets and instrumentation or at an advanced stage of preparation such as the single-cavity modules. The DEMO configuration has been shown to deliver the performance required for the detailed study of the ionization-cooling technique.

The demonstration of ionization cooling that MICE will provide is essential for the provision of the intense, well characterised muon beams required to elucidate the physics of flavour at the Neutrino Factory or to deliver multi-TeV lepton-antilepton collisions at the Muon Collider. The successful completion of the MICE programme will therefore herald the establishment of a new technique for particle physics.

* *Presented at NuFact15, 10-15 Aug 2015, Rio de Janeiro, Brazil [C15-08-10.2]*

† `j.lagrange@imperial.ac.uk`; Speaker

- [1] S. Geer, *Phys. Rev. D* **57**, 6989 (1998).
- [2] A. Skrinsky and V. Parkhomchuk, *Sov. J. Part. Nucl.* **12**, 223 (1981).
- [3] D. Neuffer, *Part. Accel.* **14**, 75 (1983).
- [4] D. Rajaram et al., in *Proc. of IPAC2015 Conf.* (2015).
- [5] M. Uchida, in *Proc. of IPAC2015 Conf.* (2015).

Neutrinos from Pion Beam Line, nuPIL*

J.-B. Lagrange[†]

Imperial College London, UK/FNAL, USA

J. Pasternak

Imperial College London, UK/ISIS-RAL-STFC, UK

A. Bross and A. Liu

FNAL, USA

(Dated: March 22, 2016)

Abstract

LBNF-DUNE (Long Baseline Neutrino Facilities – Deep Underground Neutrino Experiment) is a project based at Fermilab to study neutrino oscillations. The current baseline regarding the neutrino production considers the conventional approach: a high energy proton beam hits a target, producing pions that are collected by a horn and that decay in a decay pipe. An alternative solution, called nuPIL (neutrinos from a Pion beam Line) consists of using a beam line to guide the pions to clean the beam and to put instrumentation to monitor it. This paper presents the concept and the first preliminary results.

INTRODUCTION

The LBNF decay pipe points toward detectors placed at the Sanford Underground Research Facility (SURF) in South Dakota, about 1300 km away, so the tunnel is tilted with a vertical angle of 5.8 deg. To maximise the flux, the target is also tilted and a hill needs to be built to transport the primary proton beam so it hits the target with the correct angle. The resulting pions are focused by two horns and are injected into the 4 m-diameter and 204 m-long pipe. The pipe is also filled with helium to minimize pion interactions in transit. In this configuration, the flux is indeed maximised, however radiation safety requires that the high power beam should be shielded by a $\tilde{6}$ m of concrete surrounding the pipe, which makes a total excavation of a 16 m-diameter tunnel over 204 m. Furthermore, since all forwarding particles would enter the decay tunnel, kaon decays and wrong-sign pion decays will also produce neutrinos that can reach the detector, creating a background signal.

Another solution would be the use of a pion beam line, as presented in Fig. 1. The primary proton beam would hit the target on the surface, then a horn would collect the resulting pions. They would be transported in a 5.8 deg beam line bend and then injected into a decay beam line. This approach has several advantages:

- the pions would go through a charge selection process in the bend, providing a clean neutrino beam,
- most of the kaons would decay in the bend, getting rid of this background at the detector,

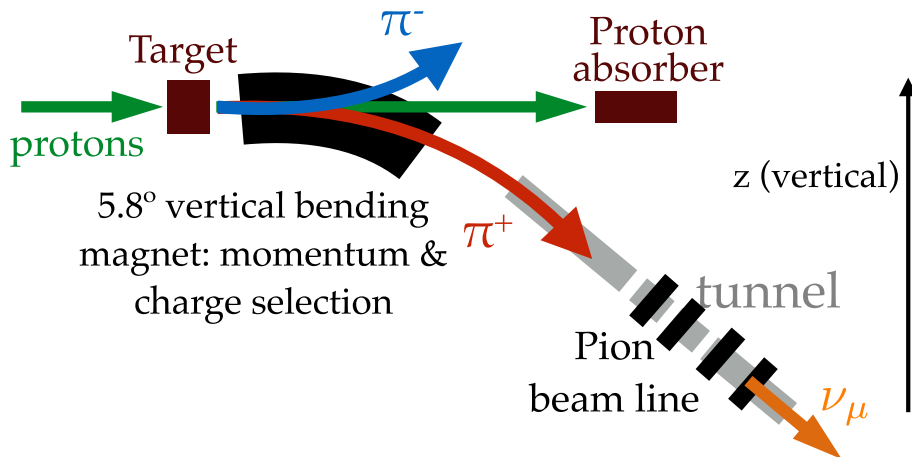


FIG. 1: Scheme of the nuPIL concept.

- instrumentation can be installed in the decay beam line, giving the possibility to have access to an actual measurement of the flux,
- since the target is not tilted, the hill is not needed,
- the remaining high energy protons would go straight in the bending part and thus remain on the surface, simplifying the radiation safety in the decay tunnel,
- the wrong sign pions could be collected in the bending part for cross-section measurements and sterile neutrinos search (i.e. nuSTORM [1]).

This approach had been investigated previously in the nuSTORM project [2, 3], but the resulting neutrino flux was too small to become an interesting possibility. However, increasing the length of the decay line to 204 m (like in the baseline scenario) and getting rid of both the chicane and the possibility to have a circulating muon beam, the number of pions can be greatly increase. Furthermore, the use of scaling Fixed Field Alternating Gradient (FFAG) magnets could also increase the momentum acceptance. This paper will present the preliminary results of the nuPIL concept.

FODO SOLUTION

The design of a pion beam line to transport as many pions as possible between 3.5 GeV/c and 10.5 GeV/c has been done with large aperture separate function magnets (dipoles and quadrupoles) to accommodate the pion distribution coming out of the horn that had been

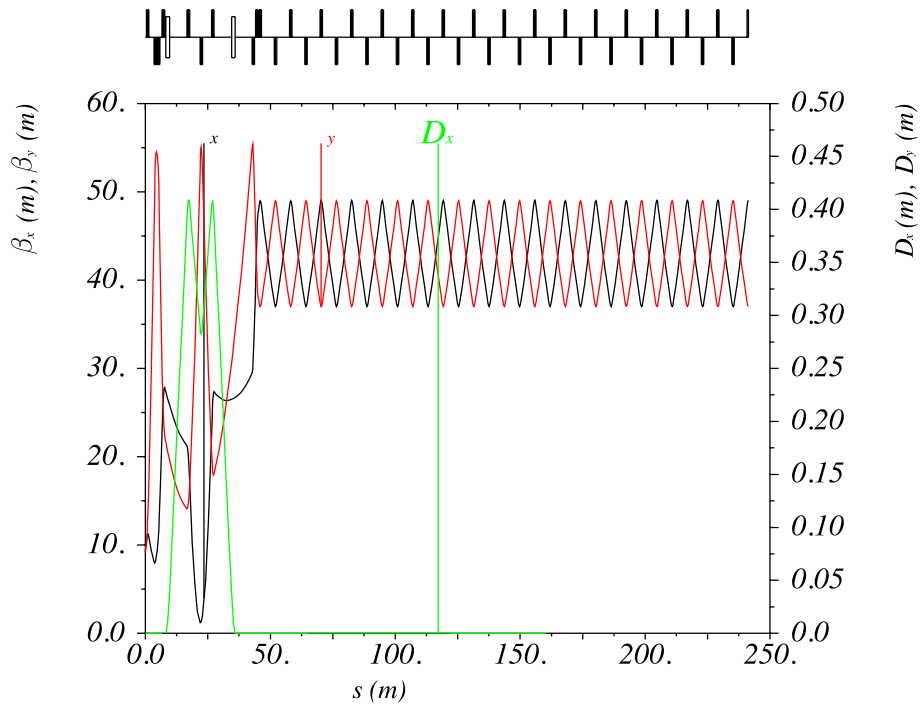


FIG. 2: linear parameters of the FoDo solution.

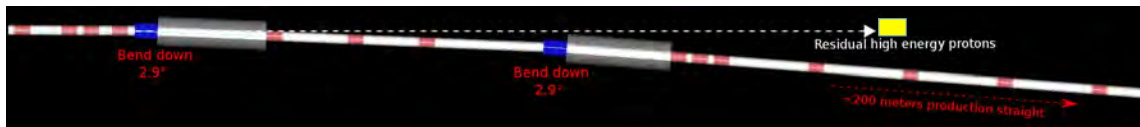


FIG. 3: FODO solution tracked in G4BL.

optimized for nuSTORM [4] into a small divergence beam in the decay line. The beta and dispersion function of the whole beam line is presented in Fig. 2. The bending section is around 40 m-long, and the straight section is around 200 m long. Tracking has been done in G4beamline with decay. The geometry can be seen in Fig. 3 and the resulting flux in blue in Fig. 4. No wrong-sign pions (π^-) has survived the bending part, so the resulting flux is very clean. The flux has been greatly increased compare to the nuSTORM flux (in red in Fig. 4). The horn was optimized for 5 GeV/c pions $\pm 10\%$, and a proper optimization of the horn for 7 GeV/c pions $\pm 50\%$ could increase the flux.

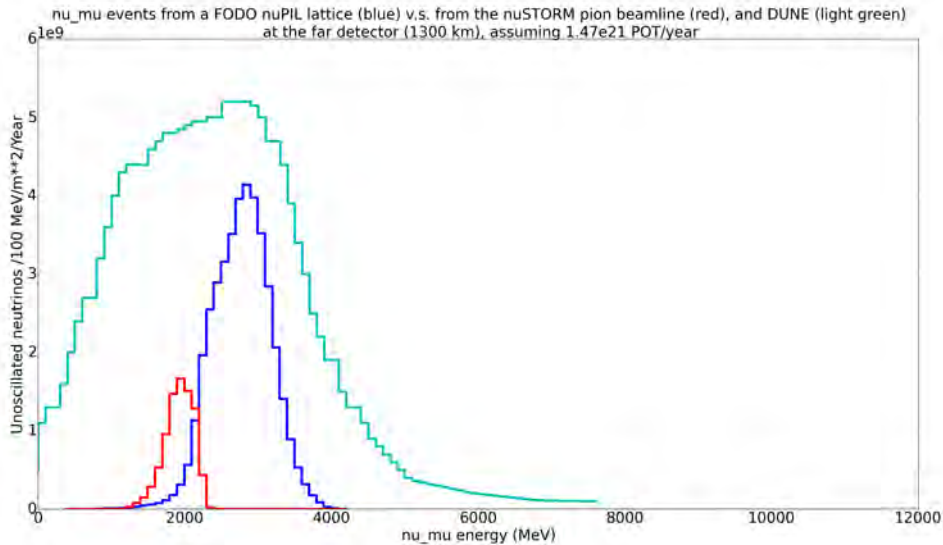


FIG. 4: Neutrino flux in the FODO solution.

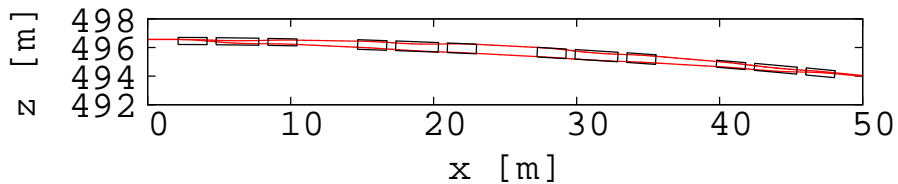


FIG. 5: FFAG double achromat bending beam line with trajectories of 3.5 GeV/c and 10.5 GeV/c in red.

FFAG BEAM LINE

The transport of such a large momentum spread beam seems difficult with separated function magnets, especially in the bending section. The use of achromatic FFAG magnets is being investigated to significantly increase the momentum acceptance of the line. A double achromat FFAG beam line with a 5.8 deg. bend has been designed and tracked using Runge Kutta code. The aim of this bend is to inject the surviving beam into large aperture quadrupole magnets forming the decay line. The FFAG bend is presented in Fig. 5. The dispersion function has been computed centered around 7 GeV/c in tracking and can be seen in Fig. 6. The magnetic field for the maximum momentum is presented in Fig. 7, and shows that the magnets are within the normal conducting range.

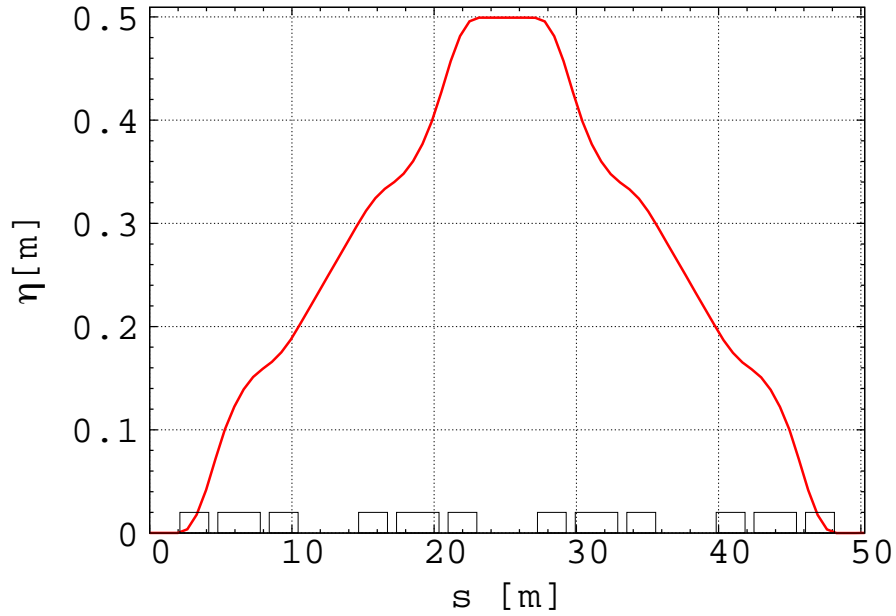


FIG. 6: dispersion function in the FFAG double achromat bend at 7 GeV/c.

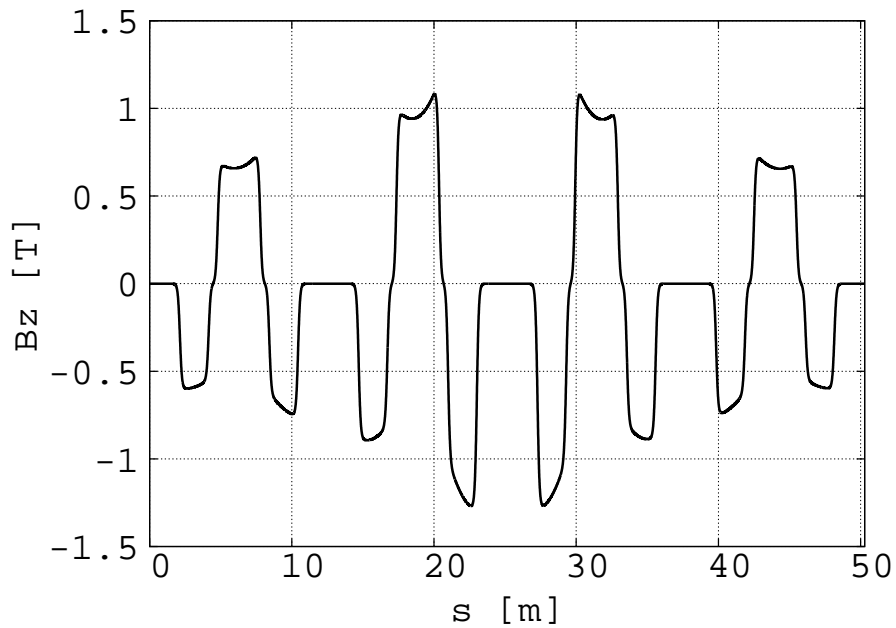


FIG. 7: Magnetic field for 10.5 GeV/c in the FFAG double achromat bend.

The survival of a large momentum range has been investigated by tracking 10000 particles within a water bag distribution. The unnormalized emittances are 2000 mm·mrad in both transverse planes, and the momentum is uniformly distributed around 7 GeV/c $\pm 50\%$. The survival rate at the end of the bend is 80%, with losses mainly seen at the extrema momenta

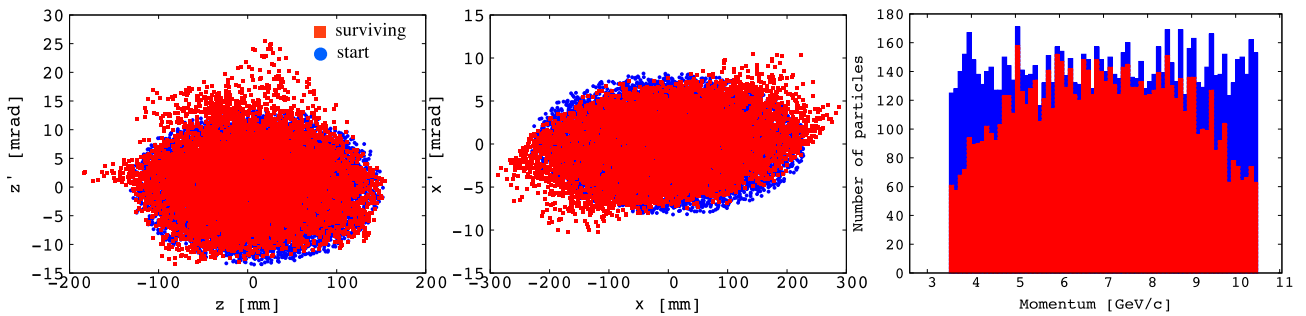


FIG. 8: Start (in blue) and surviving (red) pions π^+ after the FFAG double achromat bend in the bending phase space plane (left), in the non-bending phase space plane (center), and the momentum distribution (right).

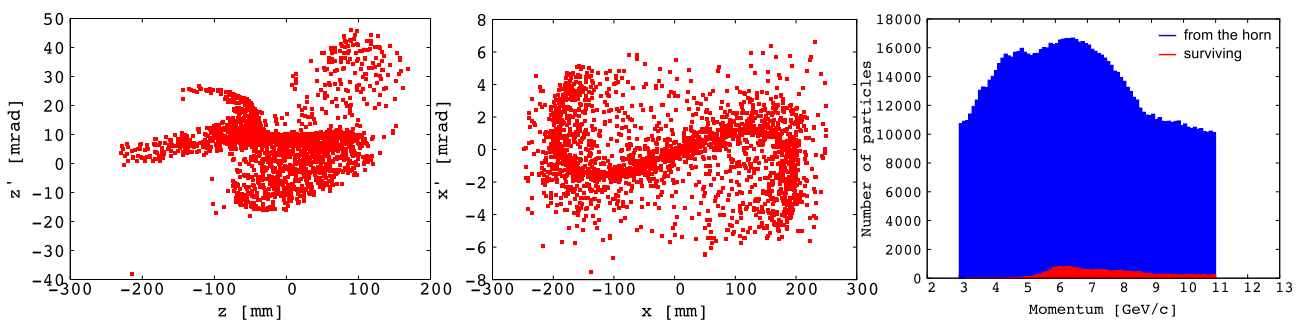


FIG. 9: Start (in blue) and surviving (red) pions π^- after the FFAG double achromat bend in the bending phase space plane (left), in the non-bending phase space plane (center), and the momentum distribution (right).

due to the limitation of the good field region. The results of the tracking are presented in Fig. 8.

The survival of the wrong-sign pions has also been investigated by tracking the distribution coming from the nuSTORM horn in the Runge Kutta code. The survival rate of the 1.1×10^6 initial particles is 2.38%, and the results of the tracking are presented in Fig. 9. The background coming from this beam is expected to be very small.

CONCLUSION AND FUTURE PLANS

The nuPIL concept aims to deliver a clean neutrino flux for the DUNE experiment. Preliminary results are promising and the physics reach looks interesting. Furthermore, this configuration for LBNF gives several possibilities of upgrades, with a cost-effective

implementation of nuSTORM and an experiment for demonstration of a 6D muon cooling ring.

* *Presented at NuFact15, 10-15 Aug 2015, Rio de Janeiro, Brazil [C15-08-10.2]*

† `j.lagrange@imperial.ac.uk`; Speaker

- [1] D. Adey et al. (nuSTORM) (2013), 1308.6822.
- [2] J.-B. L. et al., in *Nuclear and Particle Physics Proceedings* (2015).
- [3] A. B. et al., in *Proc. of nuFACT15* (2015).
- [4] A. Liu, A. Bross, and D. Neuffer, *Nucl. Inst. Meth. A* **794**, 200 (2015).

MICE: The Trackers and Magnets*

M.A.Uchida[†]

Imperial College

(Dated: April 5, 2016)

Abstract

The Muon Ionization Cooling experiment (MICE) has been designed to demonstrate the reduction of the phase space volume (cooling) occupied by a muon beam using the ionization-cooling technique. This demonstration will be an important step in establishing the feasibility of muon colliders and Neutrino Factories for particle physics. The emittance of the beam will be measured before and after the cooling cell (or absorber) using a solenoidal spectrometer. Each spectrometer is instrumented with a high precision scintillating-fibre tracking detector (Tracker), which are immersed in a uniform magnetic field of 4 T. The cooling cell sits in an alternating focus coil magnet (AFC) which has two coils, axially aligned, that can be powered so that the fields oppose “Flip mode” or align “Solenoid mode”, to a maximum B_z of ~ 3 T. The status of the Trackers and magnets are described here.

INTRODUCTION: MICE

The Muon Ionization Cooling Experiment (MICE) [1–3], under development at the Rutherford Appleton Laboratory in the UK, aims to demonstrate ionization cooling of muons for the first time. Ionization cooling is the process of reducing the beam emittance (phase space) while maintaining the longitudinal momentum of the beam. Muons are produced with

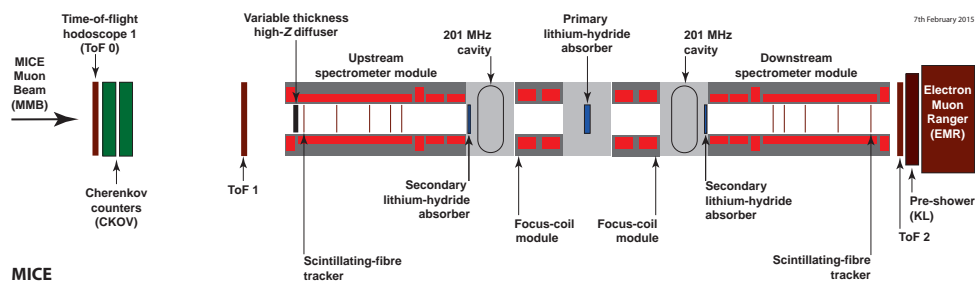


FIG. 1: Schematic of the International Muon Ionization Cooling Experiment (MICE), with the beam entering from the left.

a large emittance, which must be reduced before re-acceleration. Muon beams are produced at the front end of a Neutrino Factory (NF) [4] with an emittance of 15–20 mm·rad, which must be reduced to 2–5 mm·rad. A Muon Collider [5] requires further cooling, reducing the emittance to 0.00025 mm·rad in the transverse plane, and 70 mm·rad in the longitudinal plane [6]. Due to the short muon lifetime stochastic cooling techniques are unsuitable for muon beams, and hence ionization cooling is the only process that can efficiently reduce the emittance of a muon beam within its lifetime.

The MICE experiment shown in Figure 1 will pass a muon beam through a low- Z material (absorber), where the muons lose both longitudinal and transverse momentum through ionization energy loss (cooling). The lost longitudinal momentum is then restored using accelerating RF cavities that follow the absorber. Along with this cooling, however, there is a heating effect produced as a result of multiple scattering through the system, therefore, the net cooling is a balance between these two effects. This is described in Eq. 1, where the first term on the right hand side represents cooling and the second term heating:

$$\frac{d\epsilon_n}{ds} \sim -\frac{1}{\beta^2} \left\langle \frac{dE_\mu}{ds} \right\rangle \frac{\epsilon_n}{E_\mu} + \frac{1}{\beta^3} \frac{\beta_\perp (0.014\text{GeV})^2}{2E_\mu m_\mu L_R}. \quad (1)$$

$\frac{d\epsilon_n}{ds}$ is the rate of change of normalised-emittance within the absorber; β , E_μ and m_μ the ratio of the muon velocity to the speed of light, energy, and mass respectively; β_\perp is the lattice betatron function at the absorber; and L_R is the radiation length of the absorber material.

MICE aims to reduce the normalised emittance of the muon beam by a few percent and to measure the reduction with a precision of 0.1%. To do this each muon will be measured individually by an upstream and downstream high precision scintillating fibre tracking detector (Tracker). The Trackers are contained within super-conducting spectrometer solenoids (SSs) which produce a uniform 4 T field. The muon beamline has been commissioned and the beams have been shown by direct measurement with MICE particle detectors to be adequate for cooling measurements, the beam was experimentally studied paying particular attention to the rate, particle composition and emittance; the Trackers are built, fully tested, installed and are undergoing commissioning and calibration. MICE is surrounded by a partial return yolk (PRY) so as to minimise any stray magnetic field from the experiment.

MICE Step IV, shown in Figure 2 will begin data taking this year. It will test the full

system but without RF cavities to accelerate the beam (and will have only one absorber). Step IV will reduce overall beam emittance and measure it, but will not restore longitudinal momentum and so it will not allow for sustainable cooling demonstration.

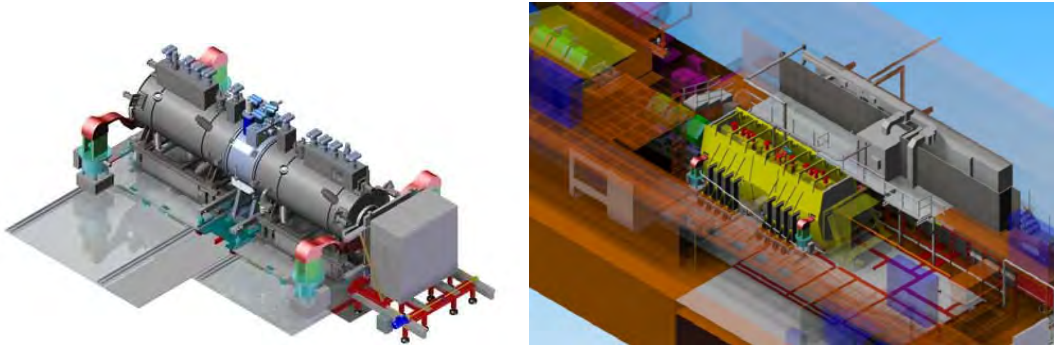


FIG. 2: Left: Step IV of the MICE Experiment, showing the AFC absorber module (Central blue magnet) which contains the absorber, the two SS magnets either side (in grey) which contain the Trackers and the DS PID detectors (Grey square). Right: Rendering of Step IV cooling channel in the MICE Hall including the PRY (yellow).

The final stage (see Figure 1), the Demonstration of ionization Cooling will include the RF cavities and additional absorber modules. Construction is scheduled for completion in 2017.

THE TRACKERS

The emittance of the MICE beam will be measured before and after cooling using two high-precision scintillating-fibre tracking detectors (Trackers), each sitting within a superconducting solenoid magnet (SS) which produces a uniform magnetic field of 4 T. They are designed to measure normalised emittance reduction with a precision of 0.1%.

The Trackers (one shown in Figure 3) are 110 cm in length and 30 cm in diameter. There are five stations per Tracker, held in position using a carbon-fibre space-frame, at varying separations in z of 20–35 cm. This ensures that the azimuthal rotation of track position from one station to the next differs, this difference being important in resolving ambiguities at the pattern-recognition stage. Each Tracker is instrumented with an internal LED calibration system and four 3D hall probes.

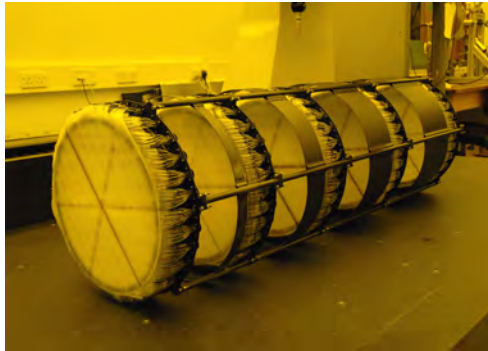


FIG. 3: Photograph of one of the MICE Trackers, showing the 5 stations and the 3 doublet planes of scintillating fibres at 120° angles (the central fibres of plane can be seen as darker lines traversing the station).

The Tracker stations consists of three doublet layers of $350\ \mu\text{m}$ scintillating fibres, these layers are arranged such that each is at an angle of 120° to the next (as can be seen Figure 3). This arrangement ensures that there are no inactive regions between adjacent fibres. Bundles of seven fibres are grouped into a single readout channel. (This reduces the number of readout channels, while maintaining position resolution). The Trackers have a spatial resolution per doublet layer of $470\ \mu\text{m}$ and an expected light yield of ~ 10 photo-electrons.

Tracker Alignment

In order for the Trackers to measure the beam emittance with the required precision, it is essential that their relative positions and those of their stations are well understood. To this end the relative positions of the five Tracker stations were measured using a coordinate measuring machine (CMM) as part of the QA during construction and the Trackers are mechanically aligned inside the bore of each SS which in turn is surveyed into position in the MICE hall; the Upstream and Downstream Trackers must be aligned to one another, and to the magnetic and beam axes and the internal positions of the Tracker stations checked. The relative positions of the trackers are determined using through-going muons from data-taking without field.

Mechanical Alignment of the Trackers

Each Tracker is mechanically aligned inside the bore of its SS (superconducting solenoid) using a specifically designed ‘alignment jig’ (shown in Figure 4). The jig allows the Tracker to be positioned inside the bore, with respect to the SS (which is then surveyed in the hall), to an accuracy of ~ 25 microns in theta and z .

The alignment jig has a semicircular section with three reflectors mounted onto it to allow the central vertical fibre of the Tracker stations to be positioned at true vertical, with no rotational offset which would affect particle track reconstruction. Once this is in place inside the bore, a long shaft section of the jig is used to allow the z position (along the beamline) of the Tracker to be fixed. Since the SS is a series of coils designed to create a homogeneous field in the region of the Tracker, it is essential that the Trackers are positioned in this appropriate region in z . The long shaft section of the jig is extended to the correct position in z and theta (already determined) and bolted into place. The jig, with the exception of the shaft, is then removed and the Tracker is inserted into the bore at the correct theta and z , now set by the jig shaft (which is then also removed).



FIG. 4: Technical drawing of the MICE Tracker alignment jig; showing the semicircular section for rotational (theta) alignment (far left); the shaft for positioning in z (far right) which determines how far into the bore the Tracker is inserted; and the mount for the survey balls (centre).

The SS magnets themselves are surveyed into position in the MICE experimental hall to ± 1 mm. Once in position, they can be moved in order to centralise the magnetic axis.

Upstream To Downstream Tracker Alignment

The relative positions of the Trackers are determined using a through going beam of straight track muons of a range of momenta and emittance (the magnets are off, thereby allowing the muons to follow straight tracks through the Trackers). The path of the muons will be affected by the Earth's magnetic field ($\sim 250 \mu\text{m}$ deflection between the first US tracker and the last DS Tracker planes for a $300 \text{ MeV}/c$ beam and $\sim 300 \mu\text{m}$ for a $200 \text{ MeV}/c$ beam), multiple scattering and fields due to magnetic material along the experiment, and hence these effects must be accounted for when modelling the expected path (in the case of perfect alignment) of the beam through the Trackers. To reduce the effect of multiple scattering the absorber is removed.

Events with a single, five-point track in both the upstream and downstream Trackers are selected and the Tracker relative alignment is performed using the residuals between the downstream track parameters and the parameters of the upstream track extrapolated to the reference surface of the downstream Tracker. The Tracker-to-Tracker alignment residuals, based on data from the Kalman fit, are shown in Figure 5[7]. Multiple Coulomb scattering combined with the uncertainty on the extrapolated track parameters combine to yield a significant spread in track position residuals. The width of the residual distributions are consistent with expectations based on simulation.

THE MAGNETS

The Upstream SS magnet, followed by the absorber focus coil magnet(s) (AFC) (that surround the absorber(s)) and the Downstream SS combine to form the magnetic axis of the experiment. These magnets are installed and surveyed into the hall and commissioning has begun.

Field Mapping

The magnetic fields of each of the superconducting solenoids were measured ("mapped") to record the magnetic field and determine the alignment of the coils within the cryostats. The field was measured using a disc carrying seven three-axis Hall probes spaced by 30 mm apart radially. The disc was moved longitudinally and rotated within the warm bore of the

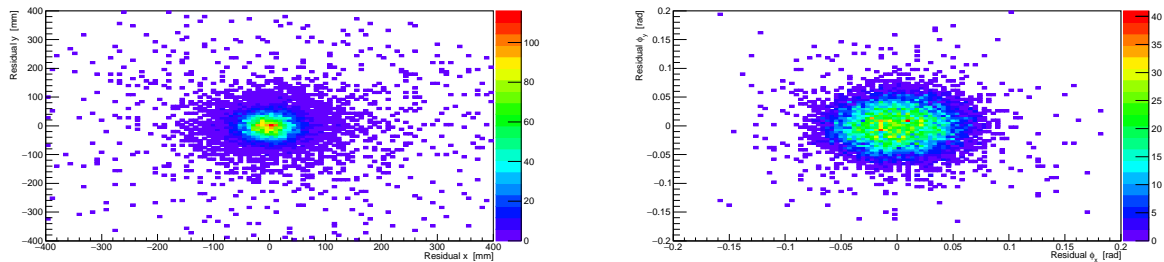


FIG. 5: Left panel: x, y position reconstruction residuals showing US to DS Tracker alignment performed using the MAUS Kalman filter. The residuals are calculated between propagated upstream tracks and the reconstructed downstream tracks. Right panel: The residuals for the ϕ_x - ϕ_y angles, where the ϕ_x angle describes the rotation in the x-z plane and ϕ_y shows the x-y plane. Performed using the MAUS Kalman filter between propagated upstream tracks and the reconstructed downstream tracks.

magnet. The axis of travel of the disc was surveyed with respect to fiducial marks on the cryostats. The positions of the Hall probes were known to about two tenths of a millimetre in the coordinate system defined by the magnet's fiducial marks.

The field components were measured typically every 20 mm to 50 mm longitudinally and every 20 to 45 degrees in azimuth. The probes recorded the radial, azimuthal and longitudinal field components in the coordinate system of the mapper disc. The Maxwell relation $\nabla \times \mathbf{B} = 0$ was used to correct the measured radial and azimuthal components for small radial misalignments of the probes (i.e. small rotations around the longitudinal axis). These components (and probe positions) were then converted to transverse Cartesian components in the mapper coordinate system. Figure 6 shows the fields measured in one of the spectrometer solenoids and one of the focus-coil modules.

The magnetic axis of each module was obtained by the implicit use of $\nabla \cdot \mathbf{B} = 0$. At each longitudinal position, z , simple linear fits of B_s versus s , where $s \equiv x$ or y in the mapper system, were made. The slopes, $k(z) = \partial B_s / \partial s \equiv -(1/2) \partial B_z / \partial z$, and intercepts, $B_o(z)$, from these fits were then used in a global fit over all longitudinal positions to find the equation of the magnetic axis in the mapper system:

$$B_o(z) = -k(z)s_o - \alpha k(z)z + \alpha_s B_z ; \quad (2)$$

where α_s and s_o are respectively the slope and intercept of the axis in the s - z projection

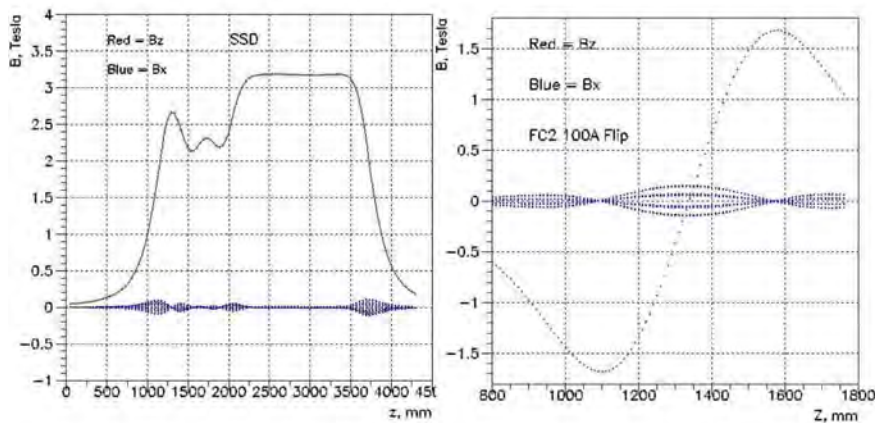


FIG. 6: Longitudinal, z , and transverse, x , fields in one of the spectrometer solenoids (left) and one of the focus-coil modules in flip-mode (right).

and the last term allows for the angle between the longitudinal mapper axis and the true magnetic axis.

The mapper survey was then used to transform the magnetic axis in the mapper system to the fiducial system of the the cryostat and finally, after the modules had been installed, into the MICE Hall coordinate system. The overall accuracy of this procedure was estimated to be better than 0.3 mm in each transverse coordinate.

CONCLUSIONS

MICE will demonstrate ionization cooling of a muon beam for the first time (reducing the beam emittance through ionization energy loss with partially restored longitudinal momentum by RF acceleration). The emittance of the beam will be measured before and after cooling using two Trackers positioned either side of the cooling channel. The Trackers sit in a 4 T magnetic field created by superconducting solenoid (SS) magnets. All magnets and detectors necessary for MICE Step IV are installed and are undergoing commissioning. It is essential to align all elements of the Tracker as precisely as possible. The Trackers are aligned mechanically to 25 microns and using through going straight track muon data. Initial results show that the Tracker alignment is consistent with expectations based on simulation. The magnetic fields of each of the superconducting solenoids were measured (“mapped”) to record the magnetic field and determine the alignment of the coils within the cryostats.

* *Presented at NuFact15, 10-15 Aug 2015, Rio de Janeiro, Brazil [C15-08-10.2]*

† `m.a.uchida@imperial.ac.uk`; On behalf of the MICE Collaboration

- [1] M. Bogomilov et al. (MICE), JINST **7**, P05009 (2012), 1203.4089.
- [2] M. Bogomilov et al. (MICE) (2015), arXiv:1511.00556.
- [3] D. Adams et al. (MICE), JINST **10**, P12012 (2015).
- [4] R. J. Abrams et al. (The IDS-NF) (2011), arXiv:1112.2853.
- [5] M. M. Alsharo'a et al., Phys. Rev. ST Accel. Beams **6**, 081001 (2003), URL <http://link.aps.org/doi/10.1103/PhysRevSTAB.6.081001>.
- [6] R. Palmer et al. (2007), arXiv:0711.4275.
- [7] This analysis was performed with data taken in October 2015 and hence was not included in the original conference talk, but is included here for completeness

LBNF Neutrino Beam*

James Strait[‡]

Fermi National Accelerator Laboratory[‡]

P.O. Box 500, Batavia,

IL 60510-0500, USA

on behalf of the LBNF/DUNE Team

(Dated: March 22, 2016)

[‡] Operated by Fermi Research Alliance, LLC under Contract No. De-AC02-07CH11359 with the United States Department of Energy

Abstract

The Long-Baseline Neutrino Facility will provide a high-power, broad band, tuneable neutrino beam at Fermilab to illuminate the Deep Underground Neutrino Experiment's liquid argon detector at the Sanford Underground Research Facility 1,300 km from Fermilab and near detector on the Fermilab site. The reference design uses a NuMI-type target-horn system, and a 194 m long, 4 m diameter, helium-filled decay pipe. The system is designed to accommodate a 1.2 MW beam from the Fermilab Main Injector, and all components which cannot be replaced later are designed for 2.4 MW. Studies are under way which hold the promise to improve the neutrino flux spectrum and substantially increase the reach for determination of CP violation and the neutrino mass ordering.

INTRODUCTION

The Long-Baseline Neutrino Facility (LBNF) will enable a world-leading experimental program[1, 2] in neutrino physics, nucleon decay and astroparticle physics to be carried out by the DUNE Collaboration[3]. LBNF[4] comprises: 1) Underground and surface facilities at the Sanford Underground Research Facility (SURF) capable of hosting a modular LAr TPC of fiducial mass ≥ 40 kt (~ 70 kt liquid mass)[5], to be built and operated by the DUNE Collaboration; 2) Cryostats, refrigeration and purification systems to operate the detectors; 3) A high-power, broad-band, tunable, sign-selected neutrino beam at Fermilab; and 4) Underground and surface facilities to host the DUNE near detector[5]. LBNF is a DOE/Fermilab hosted project with international participation. DUNE is a fully-international collaboration with members from 26 countries on five continents.

The LBNF neutrino beam will be driven by the proton beam from the Fermilab Main Injector. In parallel with the construction of LBNF, the PIP-II upgrade[6] of the Fermilab accelerator complex will increase the proton beam power for neutrinos up to 1.2 MW, and allow >1 MW operation for proton beam energies between 60 and 120 GeV. The LBNF beamline is designed to accommodate potential future upgrades to 2.4 MW. Figure 1 summarizes the beam-power parameters to which LBNF is designed.

Parameter	Protons per cycle	Cycle Time (sec)	Beam Power (MW)
≤ 1.2 MW Operation - Current Maximum Value for LBNF			
Proton Beam Energy (GeV):			
60	7.5E+13	0.7	1.03
80	7.5E+13	0.9	1.07
120	7.5E+13	1.2	1.20
≤ 2.4 MW Operation - Planned Maximum Value for LBNF 2nd Phase			
Proton Beam Energy (GeV):			
60	1.5E+14	0.7	2.06
80	1.5E+14	0.9	2.14
120	1.5E+14	1.2	2.40

FIG. 1: Main Injector beam-power related parameters with the PIP-II upgrade (top half) and a possible doubling of beam power beyond PIP-II (bottom half).

THE LBNF BEAM DESIGN

The LBNF neutrino beam is driven by protons from the Fermilab Main Injector (MI). Figure 2 shows the layout of the beamline on the Fermilab site. The proton beam is extracted at MI-10, directed up and over a man-made embankment, and then directed downward at a 10% slope towards SURF. The proton beam strikes a target, which produces a shower of secondary particle which are focused by a two-horn system. The secondary particles enter a 194 m long, 4 m diameter decay pipe in which pions and kaons decay to produce the neutrino beam. An absorber at the end of the decay pipe removes un-decayed mesons and protons that are transmitted by the target. Muons range out in the rock downstream of the absorber. With the primary beamline on an embankment, the target hall complex is placed at grade level, easing access and situating this high-radiation environment well above the aquifer. The decay pipe is mainly in glacial till and enters bedrock only at the downstream end, making for more economical construction than in a deeper design.

The target hall complex, including the target-horn system and upstream end of the decay pipe is shown in Fig. 3. The reference beam design uses NuMI-type horns and a NuMI-like target and baffle system[7]. The target chase is longer and wider than is necessary to accommodate the reference design shown, to allow for more advanced target-horn systems which can increase the neutrino flux substantially, as discussed below.

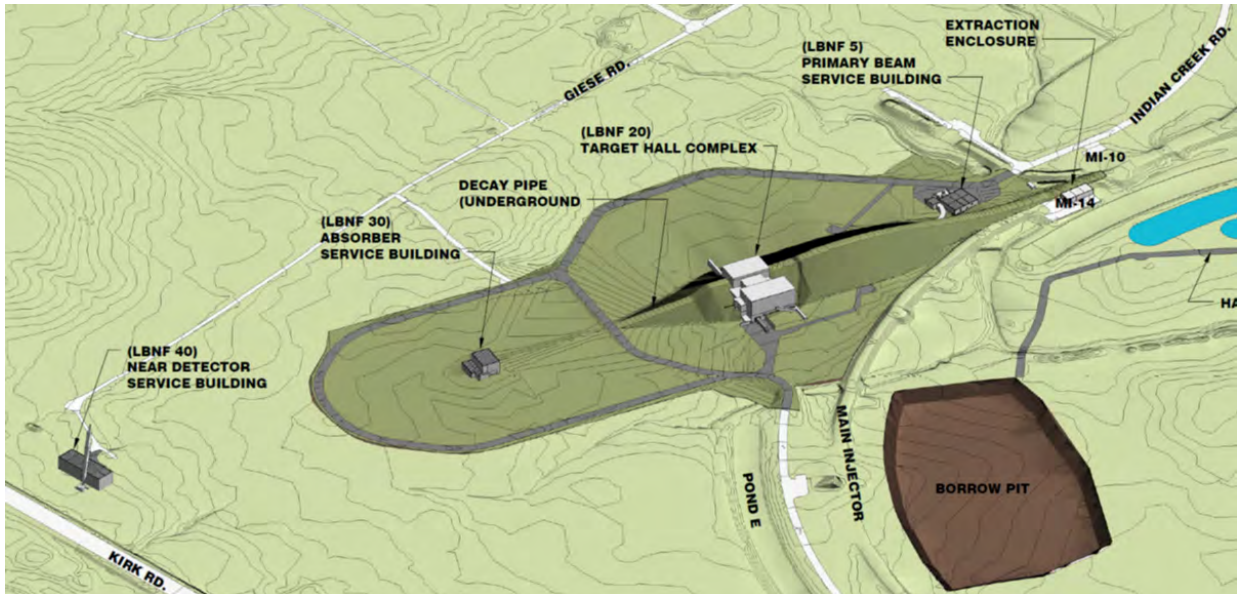


FIG. 2: Overview of the LBNF beamline on the Fermilab site.

The LBNF beamline utilizes a segmented graphite target, very similar to the NuMI design. However, the width of the rectangular target has been increased from 7.4 mm to 10 mm to accommodate the larger beam size that is necessary to allow the target to survive the higher power 1.2 MW beam and the number of cooling tubes has been doubled. A transverse section of the LBNF Target is shown in Fig. 4.

Figure 5 is a longitudinal section of the first horn, showing the placement of the target. The LBNF horn conductors are identical to the NuMI design, but they will be operated at a higher current of 230 kA to increase the neutrino flux. A new power supply is required to generate a narrower 0.8 ms pulse to compensate for the greater beam heating and higher peak current. The spacing between the two horns is 6.6 m from the upstream end of horn 1 to that of horn 2 (see Fig 3), which is set to maximize the flux at the first oscillation maximum (~ 2.4 GeV) and to the extent possible at the second maximum.

The target chase is air filled and cooled by a combination of air and water. The decay pipe is helium filled, requiring a thin window between the two environments. This window is mounted on the upstream end of a reduced-diameter “snout” at the upstream end of the decay pipe, as shown in Fig. 3, and is designed to be replaceable using remote handling techniques. The decay pipe is a closed, helium-filled volume which is cooled by air flowing through an annular gap between an inner and outer pipe, as shown in Fig. 6. The cooling air is returned in a closed loop through four smaller pipes placed just outside the decay pipe

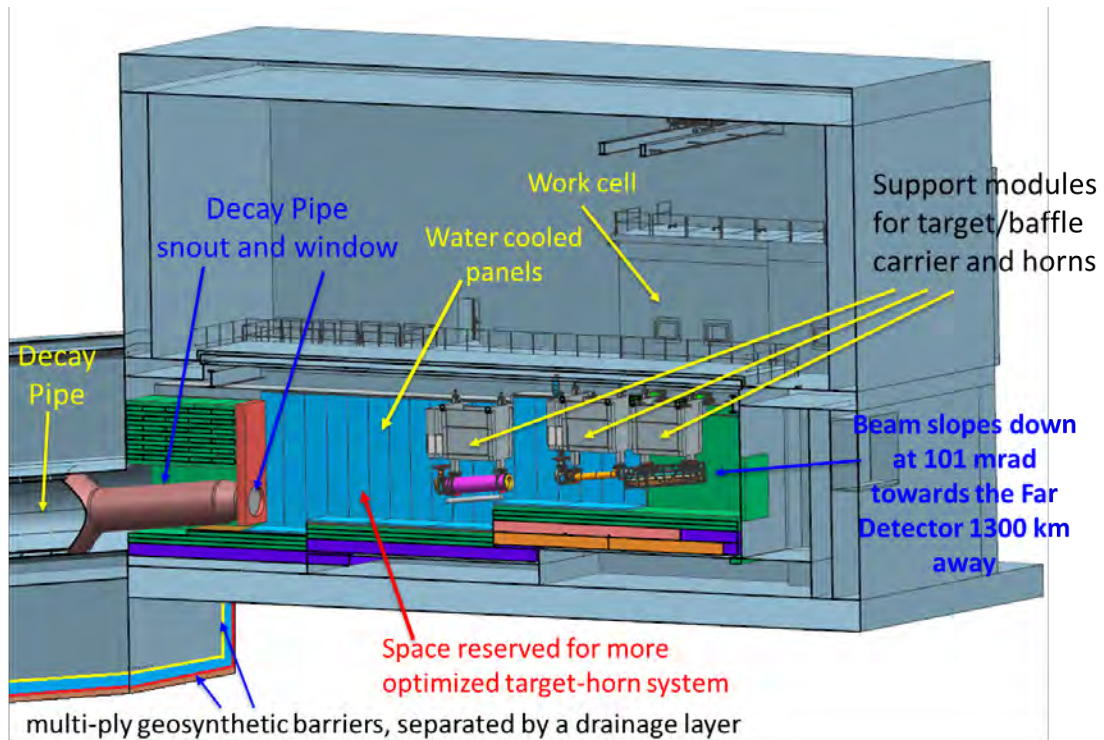


FIG. 3: The LBNF neutrino beamline target hall and upstream end of the decay pipe.

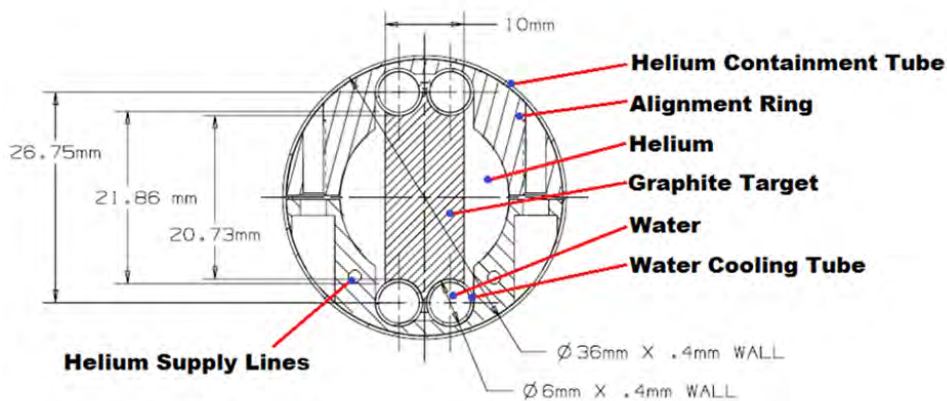


FIG. 4: Cross-section of the LBNF target.

itself. The decay pipe is surrounded by massive concrete shielding with a minimum radial thickness of 5.6 m, to accommodate up to a 2.4 MW beam. The shielding is surrounded by a water-proof geomembrane system to keep the concrete dry and separated from ground water. Beam heat is intercepted by a set of air cooling tubes, as indicated in Fig. 6, to maintain the geomembrane at an acceptable temperature even with a 2.4 MW beam.

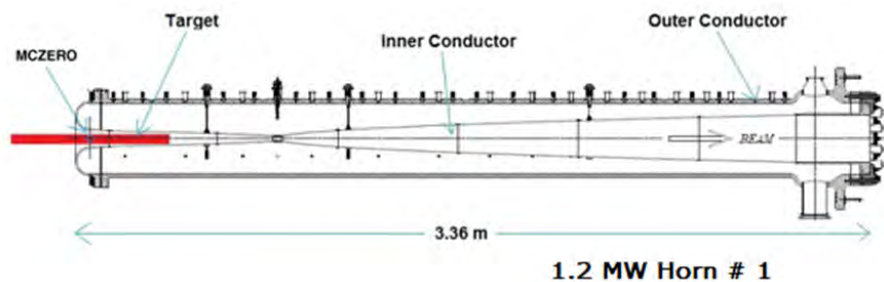


FIG. 5: The reference design horn 1 and target.

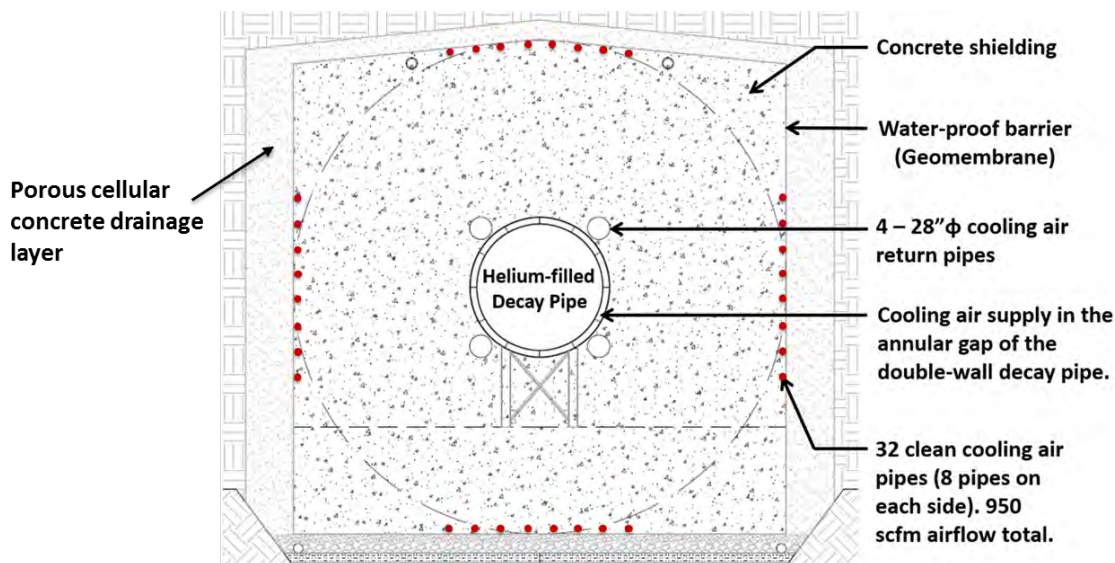


FIG. 6: Cross-section of the LBNF decay pipe.

Almost one-third of the proton beam power is deposited in the absorber. In addition, the absorber must be able to handle an accident condition in which two pulses of the full proton beam hit it. The absorber is made with a core of replaceable water-cooled aluminum blocks, surrounded by forced-air cooled steel and concrete shielding. A “spoiler” and sculpted aluminum blocks in the upstream part of the absorber serve to lower the average density and spread the showers transversely to reduce the peak average power density and peak energy density in an accident. Extensive MARS modeling has been done to validate the design. This modeling revealed that the muon plume downstream of the absorber is sufficiently intense at high beam power as to be a concern for groundwater activation. To protect the groundwater, a 30 m long steel absorber (“kern”) is placed downstream of the absorber hall. It, together with the absorber hall itself, are surrounded by the same geomembrane system

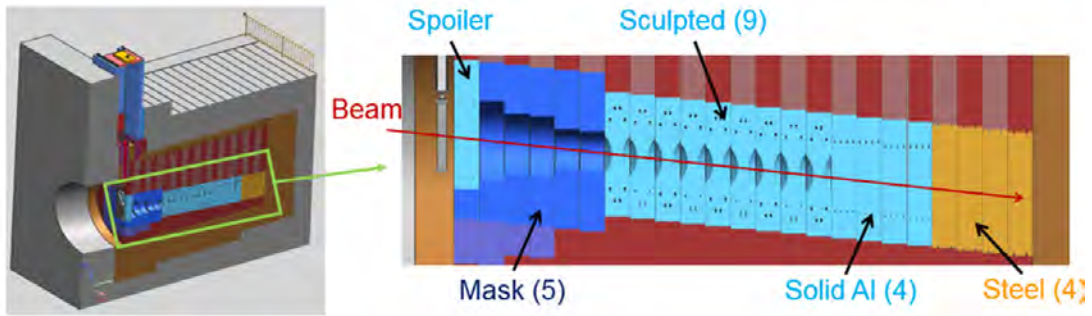


FIG. 7: The LBNF beam absorber.

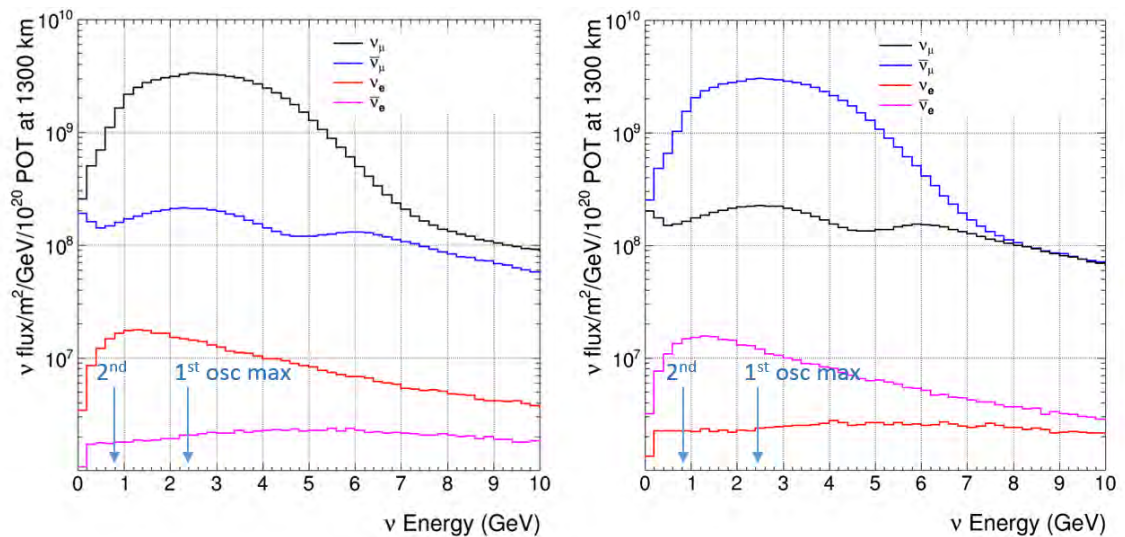


FIG. 8: Neutrino spectra for the reference beam design for positive horn current (left) and negative horn current (right).

used to separate the decay pipe from the groundwater.

All components of the neutrino beamline are designed to accommodate a 1.2 MW beam at 120 GeV. Those parts which cannot practically be changed later are designed for 2.4 MW. These include: the sizes and the shielding of all enclosures; the primary beamline components; the decay pipe shielding, cooling system and downstream window; the beam absorber; remote handling equipment; and the radioactive water system piping.

The neutrino spectra generated by the reference beam configuration are shown in Fig. 8. The ν_μ spectrum peaks near the first oscillation maximum. At the second maximum, the flux is about 1/3 that at the peak and coupled with the lower cross-section at lower energy, the event rate at the second maximum is expected to be about 10% that at the first maximum.

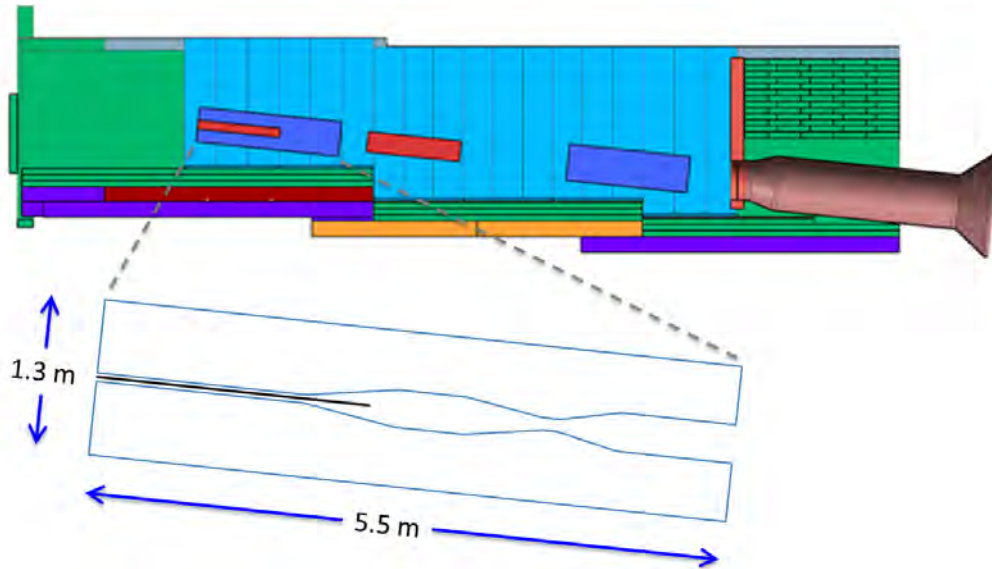


FIG. 9: The optimized target-horn system in the LBNF target chase. The red rectangles indicate the size and positions of the two reference design horns; the blue rectangles show the optimized horn system. The shape and size of the first horn is indicated in the lower part of the figure.

OPTIMIZATION OF THE BEAM DESIGN

A number of studies have been done to improve the spectrum to increase CP violation and mass hierarchy sensitivity. These include varying the proton beam energy, the horn currents, the decay pipe dimensions, and the target material, dimensions and position. Following work done in the LAGUNA-LBNO Design Study[8], a genetic algorithm has been used to optimize the dimensions of a horn 1 with a new shape and a horn 2 of the NuMI shape but with the length and radial dimensions independently varied. The spacing between the horns and the target position, length and diameter were also varied. The algorithm optimized the system parameters to maximize the minimum significance for CP violation determination ($\sqrt{\Delta\chi^2}$) over 75% of the range of δ_{CP} . This optimization favors a more complex shape for horn 1, substantially longer and larger diameter horns (e.g. horn 1 goes from 3.4 m to 5.5 m long), and a longer target ($2\lambda \rightarrow 5\lambda$), as shown in Fig. 9.

The ν_μ spectrum generated by this beam design is compared with the reference design as well as several other configurations in Fig. 10. The “Enhanced Reference” design uses the reference design (NuMI) horns, but with a thinner, shorter cylindrical beryllium target placed 25 cm upstream of horn 1. The effect of varying the decay pipe length and diameter

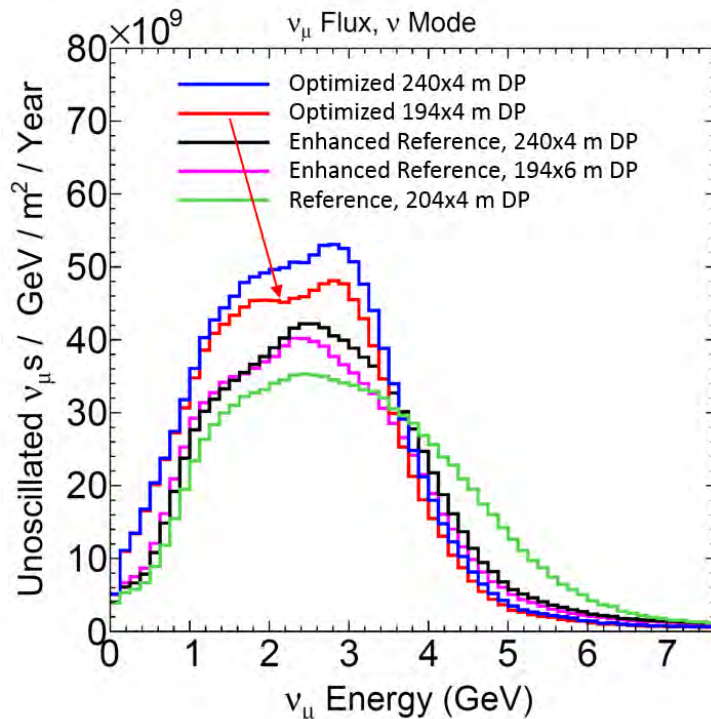


FIG. 10: Comparison of the optimized neutrino flux spectrum with the reference design and several other configurations.

are also shown. An 80 GeV proton beam is assumed in all cases. The optimized design utilizing the reference decay pipe dimensions gives about 30% more flux at the first oscillation maximum and almost 100% more flux at the second maximum. It also reduces the high-energy tail, which contributes little to the ν_e appearance signal but does contribute to the background from neutral current and ν_τ appearance events. The optimized beam reduces the time necessary to achieve a given sensitivity for CP violation or mass hierarchy determination by 30-40% as presented in [9].

Further work is required on optimization of the target-horn system. Engineering is needed to determine the feasibility of the horn designs chosen by the genetic algorithm. The physics impact of splitting the complex horn 1 design from the genetic algorithm into two closely-spaced horns is being evaluated. The phase space for horn design should be more broadly considered, including other evaluation criteria, e.g. ν_τ appearance. Alternate designs and materials for the target could be explored. R&D is required to develop designs that will work at 2.4 MW.

SUMMARY

The LBNF neutrino beam design is well developed and is based on designs and experience with the NuMI neutrino beam. All systems are designed for up to 1.2 MW operation with proton beam energy between 60 and 120 GeV, and systems that cannot be replaced later are designed for 2.4 MW. Initial studies show that a more optimized target-horn system can have a big impact on the physics reach of DUNE, and there may be room for further improvement.

* *Presented at NuFact15, 10-15 Aug 2015, Rio de Janeiro, Brazil [C15-08-10.2]*

† `strait@fnal.gov`; Speaker

- [1] LBNF/DUNE Collaboration, *Conceptual Design Report, Volume 1: The LBNF and DUNE Projects*, Tech. Rep. DUNE-doc-180 (2015).
- [2] LBNF/DUNE Collaboration, *Conceptual Design Report, Volume 2: The Physics Program for DUNE at LBNF*, Tech. Rep. DUNE-doc-181, arXiv:1512.06148 (2015).
- [3] <http://www.dunescience.org>.
- [4] LBNF/DUNE Collaboration, *Conceptual Design Report, Volume 3: Long-Baseline Neutrino Facility for DUNE*, Tech. Rep. DUNE-doc-182 (2015).
- [5] LBNF/DUNE Collaboration, *Conceptual Design Report, Volume 4: The DUNE Detectors at LBNF*, Tech. Rep. DUNE-doc-183, arXiv:1601:02984 (2015).
- [6] P. Derwent *et al.*, *Proton Improvement Plan-II*, Tech. Rep. Project X-doc-1232 (2013).
- [7] K. Anderson *et al.*, “The NuMI Facility Technical Design Report,” <http://lss.fnal.gov/archive/design/fermilab-design-1998-01.pdf> (1998).
- [8] The LAGUNA-LBNO Consortium, “Conceptual Design of a Conventional Neutrino Beam from CERN to Pyhäsalmi,” http://laguna.ethz.ch:8080/Plone/deliverables/laguna-lbno-284518-deliverables/conceptual-design-of-a-conventional-neutrino-beam-from-cern-to-pyhasalmi/at_download/file (2014).
- [9] J. Strait *et al.*, “DUNE Physics,” *Presented at the XVII International Workshop on Neutrino Factories and Future Neutrino Facilities*, (2015).

**A non-conventional neutrino beamline for the measurement of
the electron neutrino cross section***

A. Berra, M. Prest

*Dep. of Physics, Univ. of Insubria and INFN,
Como and Sezione di Milano-Bicocca, Milano, Italy*

S. Cecchini, F. Cindolo, G. Mandrioli, N. Mauri, L. Patrizzii, M. Pozzato, G. Sirri

INFN, Sezione di Bologna, Bologna, Italy

C. Jollet, A. Mereaglia

IPHC, Université de Strasbourg, CNRS/IN2P3, Strasbourg, France

L. Ludovici

INFN, Sezione di Roma, Rome, Italy

A. Longhin, A. Paoloni, F. Pupilli, L. Votano

Lab. Nazionali di Frascati dell'INFN, Frascati (RM), Italy

L. Pasqualini

Dep. of Physics, Univ. of Bologna and INFN, Sezione di Bologna, Bologna, Italy

F. Terranova[†]

*Dep. of Physics, Univ. of Milano-Bicocca and INFN,
Sezione di Milano-Bicocca, Milano, Italy*

E. Vallazza

INFN, Sezione di Trieste, Trieste, Italy

(Dated: March 22, 2016)

Abstract

Absolute neutrino cross section measurements at the GeV scale are ultimately limited by the knowledge of the initial ν flux. In order to evade such limitation and reach the accuracy that is needed for precision oscillation physics ($\sim 1\%$), substantial advances in flux measurement techniques are requested. We discuss here the possibility of instrumenting the decay tunnel to identify large-angle positrons and monitor ν_e production from $K^+ \rightarrow e^+ \nu_e \pi^0$ decays. This non conventional technique opens up opportunities to measure the ν_e CC cross section at the per cent level in the energy range of interest for DUNE/HK. We discuss the progress in the simulation of the facility (beamline and instrumentation) and the ongoing R&D.

INTRODUCTION

A precise measurement of neutrino interaction cross sections will play a key role in the next generation of oscillation physics experiments and will impact significantly on the CPV and mass hierarchy (MH) reach of long baseline facilities (see e.g. [1]). This is particularly evident for ν_e cross sections since $\nu_\mu \rightarrow \nu_e$ transitions (and their CP conjugate) represent the main observable to measure the CP phase and determine the sign of Δm_{31}^2 (MH).

In the last ten years, an intense experimental programme has been pursued, employing both the near detectors of running long-baseline experiments and dedicated cross section experiments [1]. This programme already provided a wealth of new data on absolute and differential cross section both with inclusive (CC and NC) and exclusive final states identification. These data challenge current theoretical interpretations of neutrino interaction on nuclei at the GeV scale and boosted the development of several new models and a systematic comparison of existing approaches [2].

Modern cross section experiments are swiftly reaching the intrinsic limitations of conventional neutrino beams. In these beamlines, both the ν_e and ν_μ flux is inferred by a full simulation of meson production and transport from the target down to the beam dump and is validated by external data (hadro-production data, online monitoring of the protons on target and muon current after the beam dump). Employing dedicated hadro-production experiments (replica targets) the uncertainty on the neutrino flux can be reduced to $\sim 10\%$ and additional improvements in the 5-10% scale are still possible [3].

On the other hand, reaching the per cent scale requires a change of paradigm in the

techniques employed to determine the neutrino flux similar to the one recently proposed by the nuSTORM Collaboration [4].

A technique with a similar aim as nuSTORM and specifically focused on ν_e cross sections has been considered in [5]: a beamline with focused and sign-selected secondaries at 8.5 GeV that are transported down to an instrumented decay tunnel where electron neutrinos are produced by the three body decay of K^+ (K_{e3} , i.e. $K^+ \rightarrow e^+ \nu_e \pi^0$). Inside this non conventional decay tunnel, large angle positrons are identified by purely calorimetric techniques. The mean energy and momentum bite ($\pm 20\%$) of the transfer line is optimized to enhance the ν_e components from K_{e3} and suppress to a negligible level the ν_e contamination from muon decays. This beamline provides an intense source of electron neutrinos for the study of ν_e CC interactions. It exploits an observable (the positron rate) that can be directly linked to the rate of ν_e at the far detector through the three body kinematics of K_{e3} . The positron rate in the decay tunnel allows for the *direct* monitoring of the ν rate at source and provides a per cent measurement of the flux.

The proposal put forward in [5] must be validated through a dedicated R&D. The most relevant items are the design and optimization of the beamline, the choice of the technology for the positron monitoring and the evaluation of the systematic budget. In this talk, we report on the progress of such R&D, the results achieved in the last few months and the plans for the future.

YIELD AT THE TARGET AND TRANSFER LINE

High precision ν_e cross section measurements based on K_{e3} decays can be performed employing conventional beamlines with primary protons impinging on a target, producing secondary hadrons which are captured, sign selected and transported further down to the instrumented decay tunnel (see Fig. 1).

Secondary meson yields for this facility were evaluated with FLUKA 2011 [6] to simulate primary proton interactions on a 110 cm long (about 2.6 interaction lengths) cylindrical beryllium target of 3 mm diameter. Graphite and INCONEL targets are being simulated, too. For the momentum range and transfer line acceptance of interest for this study, the secondary yields at the target grow linearly with the primary proton energy. The yields have been computed simulating proton energies of relevance for the J-PARC Proton Synchrotron

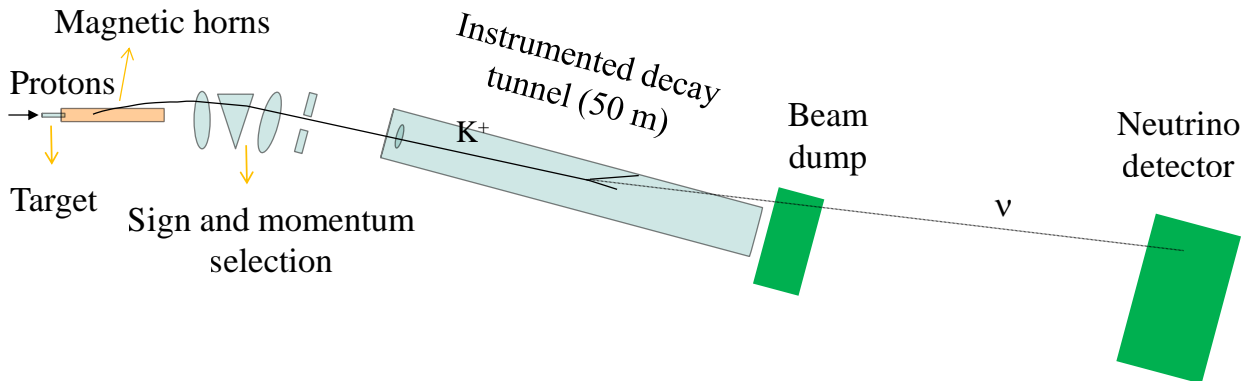


FIG. 1: Layout of the facility (not to scale).

(30 GeV), the Fermilab Main Injector (120 GeV) and the CERN SPS (450 GeV).

An end-to-end simulation of the focusing and transfer line is not available yet and will be the subject of upcoming R&D work. Following [5], fluxes at the entrance of the decay tunnel are estimated considering the phase space xx' , yy' of pions and kaons in a momentum bite of $8.5 \text{ GeV}/c \pm 20\%$ at 5 cm downstream the 110 cm long target. All secondaries within an emittance $\epsilon_{xx'} = \epsilon_{yy'} = 0.15 \text{ mm rad}$ are focused assuming a typical horn focusing efficiency of 85% [4].

Table I summarizes the results. The second and third columns show the pions and kaons per proton-on-target (PoT) transported at the entrance of the decay tunnel. The fourth column shows the number of PoT in a single extraction spill to obtain 10^{10} pions per spill. The last column shows the number of integrated protons on target that are needed to collect $10^4 \nu_e$ charged current events on a 500 tons neutrino detector. These proton fluxes are well within the reach of the above-mentioned accelerators both in terms of integrated PoT (from 5×10^{20} at 30 GeV to 5×10^{19} at 450 GeV) and protons per spill (2.5×10^{12} to 3×10^{11}).

E_p (GeV)	π^+/PoT (10^{-3})	K^+/PoT (10^{-3})	PoT for a 10^{10} π^+ spill (10^{12})	PoT for 10^4 ν_e CC (10^{20})
30 [J-PARC]	4.0	0.39	2.5	5.0
120 [Fermilab]	16.6	1.69	0.60	1.16
450 [CERN]	33.5	3.73	0.30	0.52

TABLE I: Pion and kaon yields at (8.5 ± 1.7) GeV/c. The rightmost column is evaluated assuming a 500 ton neutrino detector located 50 m after the beam dump.

PROTON EXTRACTION SCHEME

The results of the previous Section combined with the maximum particle rate sustainable by the instrumentation of the decay tunnel (see below) fix the main constraint on the length of the proton spill extracted from the accelerator. For a maximum particle rate of 500 kHz/cm², this constraint corresponds to an upper limit to the average number of PoT per second:

$$\text{PoT/s} < 1.5 \times 10^{14} \quad (1)$$

For instance, assuming 450 GeV protons extracted from the SPS (third line of Table I), a 2 ms (10 ms) spill requires less than 3×10^{11} PoT/spill (1.5×10^{12} PoT/spill). This operation mode is unpractical for high energy machines (e.g. the SPS) where the number of protons circulating in the lattice exceeds 10^{13} but the repetition rate is O(0.1) Hz. These machines must hence resort to (resonant) slow extraction modes. Two options are currently under investigation:

- **Slow extraction modes:** a 1 s slow extraction mode similar to the one devised for SHiP at the CERN-SPS [7]. It is the classical solution envisaged for the “tagged neutrino beams” [8, 9] and it fulfills the constraint of Eq. (1) even in the occurrence of complete depletion of the protons accumulated in the lattice (4.5×10^{13} for the CERN-SPS). It comes with two significant drawbacks: it prevents the use of magnetic horns and challenges the cosmic background reduction of the neutrino detector. Still, due to the relatively low flux needed for cross section measurements compared with standard oscillation experiments, static focusing systems based on FODO/FFAG [10] represent a viable option for this facility.

- **Multiple slow resonant extractions:** Slow extractions of limited duration (10 ms, a few thousands turns) repeated frequently (~ 10 Hz) can be envisaged to deplete the lattice at the end of the acceleration phase. For instance, in the standard operation mode of the CERN-SPS [7], particles are extracted during a flat top of 4.8 s inside the 15 s full acceleration cycle (super-cycle). This mode corresponds to a 30% duty cycle. Assuming 4.5×10^{13} accumulated protons in the lattice, full depletion is achieved with 30 extractions of 10 ms (1.5×10^{12} PoT per extraction) repeated every 160 ms. The feasibility of this kind of schemes for the particular case of the CERN-SPS is under investigation.

In both cases, assuming full depletion mode (i.e. the accelerator running in dedicated mode for the neutrino experiment) the integrated exposure requested in Table I to perform the cross section measurement is reached in ~ 200 days (~ 1 year considering a standard 200 days/y effective livetime).

INSTRUMENTED DECAY TUNNEL

In conventional low energy neutrino beams, the decay tunnel is located just after the horn and therefore accepts neutral and wrong sign particles, together with high energy protons. Doses and rates are therefore not suitable for additional instrumentation. In the facility considered here (Fig. 1) the decay tunnel is located at the end of the transfer line, while neutrals and protons are dumped before the bending dipoles. In addition, the positrons produced by kaon decays have a polar angle that is much larger than muons from $\pi^+ \rightarrow \mu^+ \nu_\mu$ decays. Additional instrumentation can hence be located just in the outer radius of the tunnel. Undecayed pions, transported protons and muons from pion decay will reach the beam dump without intercepting the outer walls of the decay tunnel and, hence, will not contribute to the rates. This is assured by the above constraint on the emittance: if the entrance windows of the secondaries in the tunnel and the spread in polar angle is smaller than the muon production angle from pion decay (4 mrad for 8.5 GeV pions), all particles (but decayed kaons) will reach the beam dump without additional focusing units inside the tunnel. In [5], a 50 m long tunnel with 40 cm inner radius and a ± 5 cm entrance windows with polar angles smaller than 3 mrad has been considered. The precise values are under evaluation in the framework of the end-to-end simulation of the transfer line.



FIG. 2: Test prototype for the light readout system of the calorimeter based on SiPM embedded in the shashlik module.

The most critical issue is the identification of the detector technology that can be used to instrument (a fraction of) the evacuated (<1 mbar) decay tunnel. As for the general study performed in [5], the detector must be able to stand a maximum rate of 500 kHz/cm² and provide charged pions/positron misidentification and photon veto at few percent level. Radiation hardness must be assured at the level of > 1.3 kGy. Shashlik calorimeters with fast fiber readout and longitudinal segmentation (sampling every $4 X_0$) complemented by a plastic scintillator photon veto offer a compact and cost effective solution, which has already been proved to be radiation hard at the >5 kGy level [11]. Both ionizing and non ionizing (neutron) doses are low enough to allow for the use of solid state photosensors (SiPM) embedded inside the module of the calorimeters. Each SiPM reads separately a WLS fiber of the module and the outputs of multiple SiPM's are summed up. Full simulation of this setup is in progress and, for modules of $3 \times 3 \times 10$ cm² size (sum of 9 SiPM), preliminary results confirm the positron identification capability estimated for a generic calorimeter in [5]. The embedding of the SiPM inside the modules to achieve longitudinal segmentation without loss of compactness and with negligible dead zones has been tested in summer 2015 with an early prototype (Fig. 2) at CERN PS. The test demonstrated that nuclear counter effects are negligible and the embedding does not introduce significant deterioration of the energy response with respect to standard fiber bundling [12].

EVENT RATES AND SYSTEMATICS CONTRIBUTIONS

The high momentum (8.5 GeV) secondaries selected in the transfer line produce a neutrino beam at the end of the decay tunnel that is enriched in ν_e from kaon decays and depleted in ν_e from muon decay in flight (DIF). For the parameters of [5], the ν_e/ν_μ flux ratio at the neutrino detector is independent of the proton energy and it is:

$$\frac{\Phi_{\nu_e}}{\Phi_{\nu_\mu}} = 1.8 \% (\nu_e \text{ from } K_{e3}) \ ; \ \frac{\Phi_{\nu_e}}{\Phi_{\nu_\mu}} = 0.06 \% (\nu_e \text{ from DIF}).$$

The mean energy of the neutrinos interacting at the far detector (ν_e CC events) is 3 GeV with a FWHM of ~ 3.5 GeV. This region covers the entire range of interest for the next generation long baseline experiments. Unlike conventional neutrino beams, a facility that is able to monitor the positron production at the decay tunnel can provide a flux estimate that does not depend on prior information on the proton intensity and secondary yields. A summary of the most relevant contributions is given in Tab. II. Current activities focus on the evaluation of the sub-dominant contributions due to the instrumentation response in the decay tunnel.

CONCLUSIONS

The knowledge of the flux at source in conventional neutrino beams dominates the precision of neutrino cross section measurements in short baseline experiments. In order to reach a per cent accuracy, a breakthrough in the experimental techniques employed to estimate the flux is needed. The technique we are investigating is particularly well suited for the measurement of the ν_e cross section - a key ingredient to establish CP violation in the leptonic sector - and it is based on the monitoring of large angle positrons originating from $K^+ \rightarrow e^+ \nu_e \pi^0$. We discussed the most relevant technical challenges and ongoing R&D both for the design of the beamline and for the instrumentation of the decay tunnel. In particular, we identified a specific detector option based on shashlik calorimetry that is suitable for the instrumentation of the decay tunnel and fulfills the requirements of PID capability, pile-up mitigation and radiation hardness.

* Presented at NuFact15, 10-15 Aug 2015, Rio de Janeiro, Brazil [C15-08-10.2]

Uncertainty	Conv. This		
kaon (pion) production yield	X		
kaon/pion ratio	X		
protons-on-target	X		
statistical error on monitored e^+	X	<0.1%	
geometrical efficiency	X	X	survey (<0.5%)
3 body kinem. and K^+ mass	X	X	< 0.1%
phase space at tunnel entrance		X	measured on-site
BR of K_{e3}	X		
$e/\pi/\gamma$ separation		X	measured with test beams and on-site with control samples
calorimeter response stability		X	on-site monitoring and calibration
residual gas in beampipe		X	negligible at 0.1 mbar

TABLE II: Main contributions to flux uncertainty for conventional (“Conv.”) neutrino beams and for this facility (“This”). “X” indicates whether the contribution is relevant or is by-passed by the monitoring of the positrons.

[†] francesco.terrano@cern.ch; Speaker

- [1] 10th International Workshop on Neutrino-Nucleus Interactions in the Few-GeV Region (NuInt15), Osaka 16-21 Nov 2015 (2015).
- [2] O. Benhar, P. Huber, C. Mariani, and D. Meloni (2015), arXiv:1501.06448.
- [3] A. Bravar, Talk at NuFact 2015 (these Proceedings) (2015).
- [4] D. Adey et al. (nuSTORM Collaboration) (2013), arXiv:1308.6822.
- [5] A. Longhin, L. Ludovici, and F. Terranova, Eur. Phys. J. **C75**, 155 (2015), arXiv:1412.5987.
- [6] G. Battistoni, S. Muraro, P. R. Sala, F. Cerutti, A. Ferrari, S. Roesler, A. Fasso, and J. Ranft, AIP Conf. Proc. **896**, 31 (2007).
- [7] G. Arduini et al., CERN EN-DH-2014-007 (2014), available at <http://ship.web.cern.ch/ship/>.
- [8] P. Denisov et al., IHEP 81-98 (1981).
- [9] L. Ludovici and F. Terranova, Eur. Phys. J. **C69**, 331 (2010), arXiv:1004.2904.

- [10] J. Lagrange, Talk at NuFact 2015 (these Proceedings) (2015).
- [11] V. Poliakov, Talk at 1st SHIP Workshop, 11 June 2014 (2014), available at <https://indico.cern.ch/event/303892/>.
- [12] A. Berra et al. (2016), in preparation.

Studies on pion/muon capture at MOMENT*

Nikolaos Vassilopoulos[†]

IHEP, CAS, Beijing, China

(Dated: March 25, 2016)

Abstract

MOMENT (a muon-decay medium-baseline neutrino beam facility) in China is proposed to provide a low energy neutrino beam with $\langle E_\nu \rangle > 240$ MeV induced by muons in order to explore the leptonic CP-violation. In order to provide those neutrinos a continuous working CW linac will provide protons with 1.5 GeV of kinetic energy and 15 MW of power. A Hg-jet which interacts with the proton beam is placed inside a superconductive solenoid which captures the produced charged pions. In this article, an optimization study is presented for the capture solenoid system concerning the proton beam, the Hg-jet target and the applied adiabatic magnetic fields parameters in order to maximize the collection of pions and therefore intensify the neutrino beam.

SIMULATION REPRESENTATION

In this study, optimizations are performed on the pion capture system of the MOMENT project [1–3] with the aim to maximize the yields of the pions and muons along their transport line. The proton beam, Hg-jet and their interactions, and the solenoids are simulated with FLUKA Monte Carlo [4, 5]. The main capture solenoid MCS and the following adiabatic section are represented only by the magnetic field applied inside their empty volume. The shields and the magnets are simulated as a common area where the particles are stopped.

The configuration of the primary proton beam and the Hg-jet target should be engineered in a manner that the two collide at a very small angle such as the interactions to happen for at least two nuclear interaction lengths, because of the helical trajectory of the beam protons albeit with very low curvatures and also any engineering constraints. That system has also to be tilted at a small angle with respect to the solenoid axis in order to avoid the absorption of the pions from the target due to their helical trajectories [6, 7]. In this simulation, the proton beam has a Gaussian profile and interacts fully over the target symmetry axis.

Different tilting-angles, radii and lengths for the target, and different sizes for the beam are studied in order to find the optimum parameters or to understand their range where the pion and muon yields are maximized in the case of different technical criteria in the future. Particles are recorded at the end of the adiabatic taper section. Similar studies have been performed at the Neutrino Factory project [8, 9].

TABLE I: Parameters simulated, the baseline ones are highlighted in bold numbers.

Proton Beam		
E_{kin} (GeV)	σ (cm)	<i>divergence</i> (mrad)
1.5 , 2, 2.5	0, 0.05, 0.1 , 0.15, 0.2	0
Hg-jet		
θ_{tilt} (mrad)	L (cm)	r (cm)
0, 40, 80, 100, 120, 140, 180, 220	15, 20, 25, 30 , 35, 40	0.3, 0.4, 0.5 , 0.6, 0.8, 1, 1.2

TABLE II: Particles exiting the Hg-jet per p.o.t., produced by FLUKA with 10^6 p.o.t.

$E_{kin} = 1.5$ GeV, $L = 30$ cm, $r = 0.5$ cm							
π^+	π^-	K^+	K^-	μ^+	μ^-	n	p
0.12	$7.4 \cdot 10^{-2}$	$7.8 \cdot 10^{-5}$	0	$2 \cdot 10^{-4}$	$4.3 \cdot 10^{-5}$	12.4	1.4

SYSTEM PARAMETERS, SELECTION AND ADIABATIC MAGNETIC FIELDS

The baseline proton beam and target parameters used in these studies are presented in Table I while the pion, muon, neutron and proton yields for two interaction lengths of Hg (30 cm) are presented in Table II. The latter shows that low pion yields are produced due to the low energy of the proton beam.

The aim of the capture system is to have a peak magnetic field inside the main capture solenoid MCS of $B_0 = 14$ T and the following adiabatic taper section to vary from 14 T to 3 T in order to capture pions that will eventually decay to muons with an $\langle E_\mu \rangle$ of $300 \text{ MeV} \pm 50\%$ [1]. Fig. 1 shows the transverse momentum of the π^+ versus their momentum and the band of pions that will give that muon beam. It also shows the different bands of pions for different MCS-radii. It is clear that the higher the radius the higher the yield and the momentum of the pions [10]. The MCS-radius of 20 cm is chosen for these studies.

The figure of merit for the optimizations are the yields of selected pions with momenta between $0.228 < P(\text{GeV}/c) < 0.776$ and selected muons with momenta between $0.107 < P(\text{GeV}/c) < 0.438$ at the end of the taper. The muons and the neutrinos have an average energy of 57% and 43% respectively of the pion when their directions are the same.

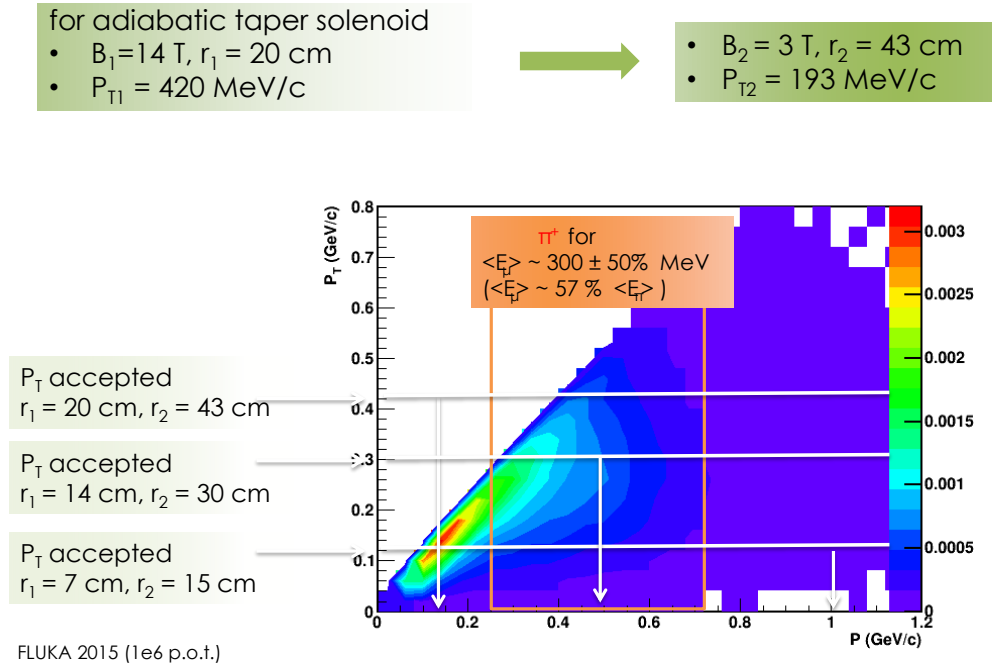


FIG. 1: P_T of π^+ s versus their momentum for a proton beam with $E_{kin} = 1.5 \text{ GeV}$. The pions which produce the muon beam with an average energy $\langle E_\mu \rangle$ of $300 \text{ MeV} \pm 50\%$ are being located within the orange borders. Arrows indicate the selected P_T for different MCS-radii of $r_1 = 7, 14$ and 20 cm . The final radius r_2 of the taper from 14 T to 3 T is also written.

Adiabatic fields

In the initial studies a constant field of 14 T was applied all over the MCS then substituted by a Gaussian which gives a more realistic field simulation at the edges of the MCS shown in Fig. 3. The field peak of 14 T is applied at the centre of target (at $z_0 = -16 \text{ cm}$ in FLUKA's geometry) and is reduced by 7% after $\pm\lambda_I$ as the response of a field proposed for the Neutrino Factory studies [6] or by 1% as one proposed for MOMENT [11]. Moving the target by $\pm\lambda_I/4$ does not alter the particle yields [10].

The MCS is matched with an adiabatic taper at $z = z_1 = 0 \text{ cm}$ in the geometry. The matching is done between the Gaussian field and an adiabatic field represented by a polynomial function as described in [6, 7]. Then the field is reduced to 3 T along the length of

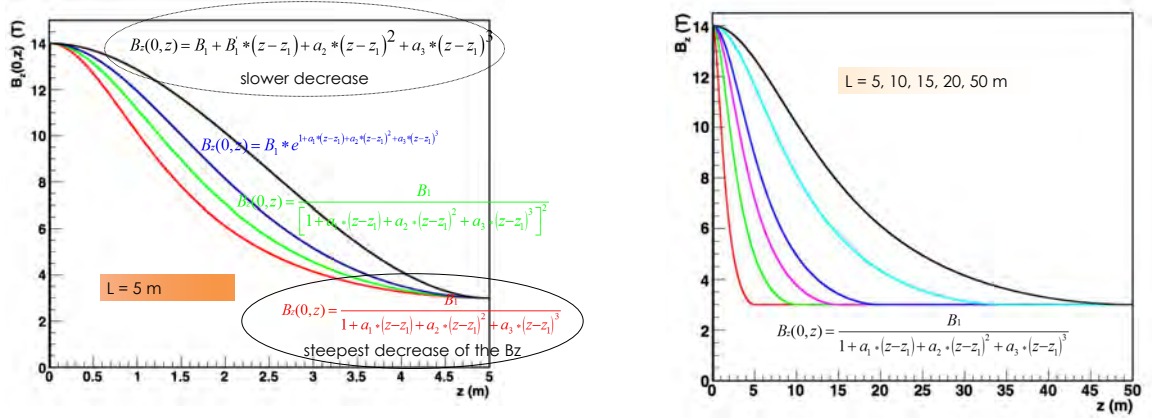


FIG. 2: Functions of adiabatic solenoidal fields for a 5 m taper solenoid (left-plot). The inverse polynomial is chosen and is plotted for different taper lengths (right-plot).

the taper. Therefore the transverse momentum is reduced at the expense of an increased helical radius for the transported charged particles. In Fig. 2, different fields with different responses are presented for a 5 m long adiabatic taper. In these studies, the first degree inverse polynomial function with the fastest decrease response is used:

$$B_z(r = 0, z) = \frac{B_1}{1 + a_1(z - z_1) + a_2(z - z_1)^2 + a_3(z - z_1)^3} \quad (1)$$

This field when matched with the Gaussian is decreasing monotonically as shown in Fig. 3.

The magnetic field in FLUKA implemented for the axial and radial components by the first order terms as shown in the following equations:

$$B_z(r, z) \approx B_z(0, z), \quad B_r(r, z) \approx -\frac{r}{2} \frac{\partial B_z(0, z)}{\partial z} \quad (2)$$

The particle yields have been studied for several adiabatic taper lengths [10] but in this proceeding only the results of the 5 m and the 50 m are shown. The 5 m section is a realistic representation of the solenoids where the particles are mostly pions (75%) at the end, while the 50 m one is considered as an idealistic where the particles are almost muons (90%). The adiabatic tapers are approximated by 5 cones with their radii following the conservation of the magnetic flux ($\Phi = B\pi r^2$). Their representation in FLUKA is shown in Fig. 4.

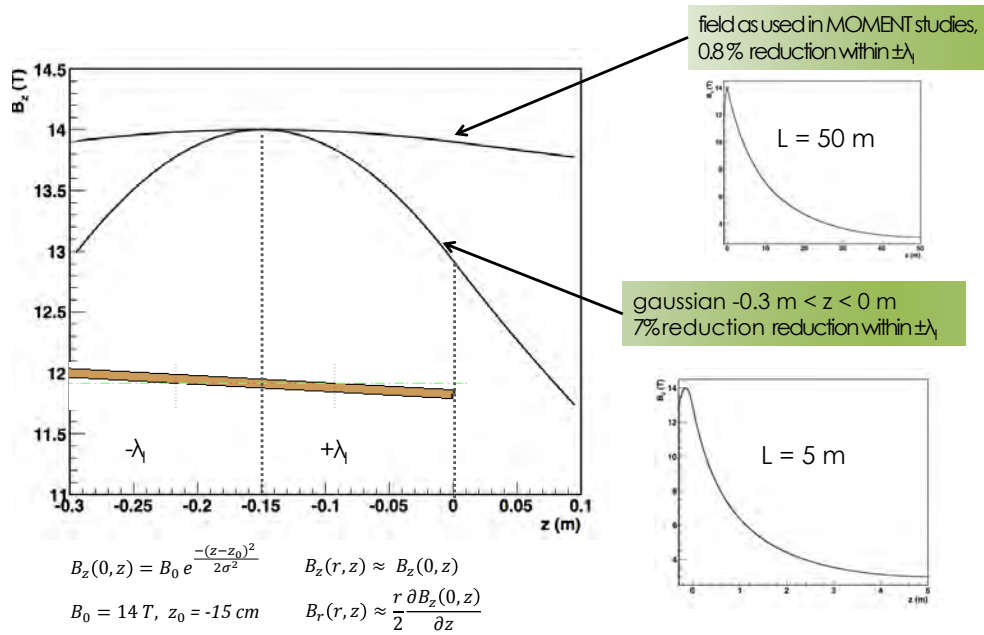


FIG. 3: Representations in FLUKA of the Gaussian field for the main capture solenoid and the studied tapers of 5 m and 50 m lengths.

TARGET TILTING

Different tilts of the target axis with respect to the main capture solenoid symmetry axis are studied by keeping the rest beam and target parameters the same. This is done in order to determine the best angle where the absorption of the captured pions is kept at minimum. In Fig. 5, the yields as function of the tilting-angle are shown for the pions (plus the muons) and only for the muons for the 5 m and 50 m tapers respectively. The tilting-angle pattern is similar with an optimum value seen at 100 mrad. In Fig. 6, the same is shown, now for the separated π^+ , π^- and μ^+ , μ^- . The comparison between the Fig. 5 and the Table II for the 5 m taper indicates that the capture efficiency of the pions is almost 50%.

Protons

Protons have also helical trajectories in the solenoids. The ones with high momenta ($> 1.5 \text{ GeV}/c$) have trajectories with large helical wavelengths and could be separated from

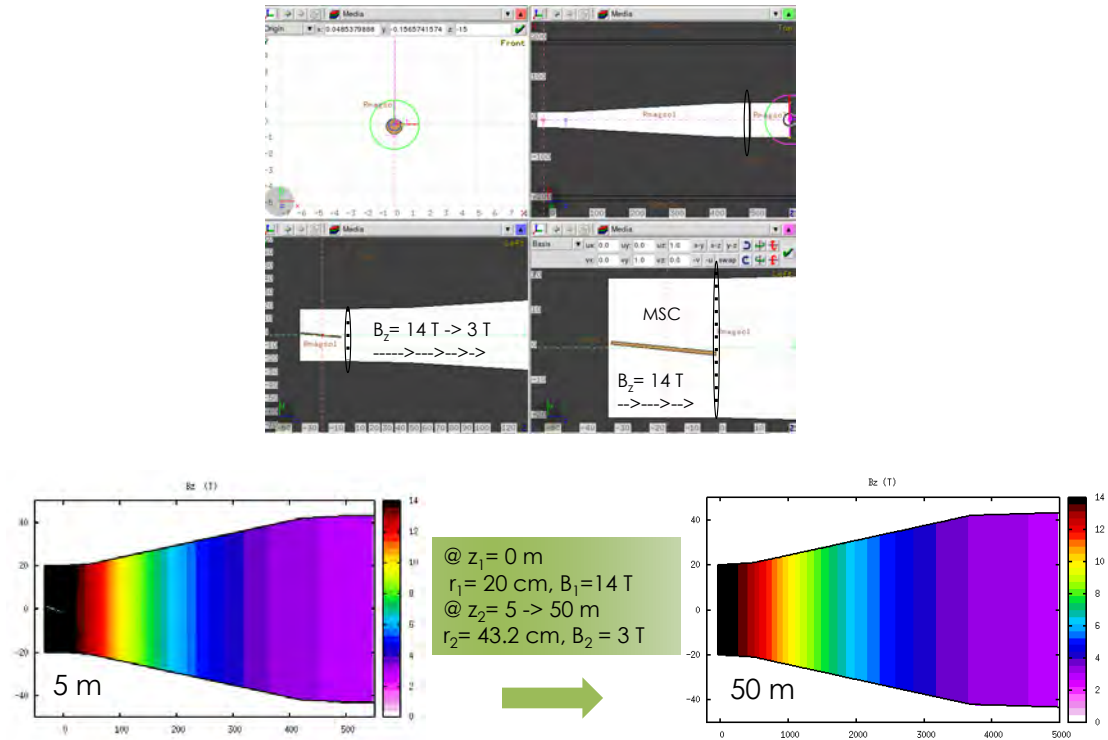


FIG. 4: Geometry representation in FLUKA for the Main Capture Solenoid and the adiabatic tapers of 5 m and 50 m lengths. The intensity of their field is also shown.

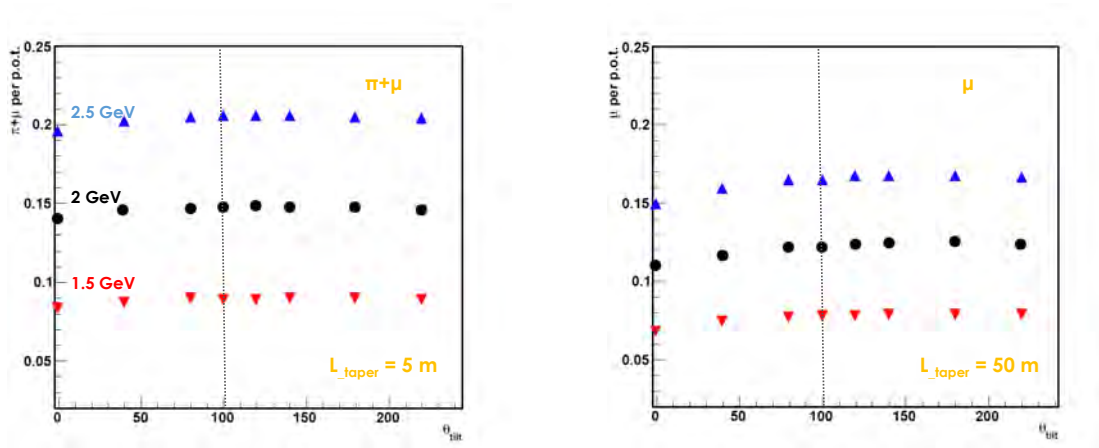


FIG. 5: Particle yields at the end of the 5 m (left-plot) and 50 m (right-plot) as function of the target tilting-angle (in mrad) for proton beams with $E_{kin} = 1.5, 2$ and 2.5 GeV/c.

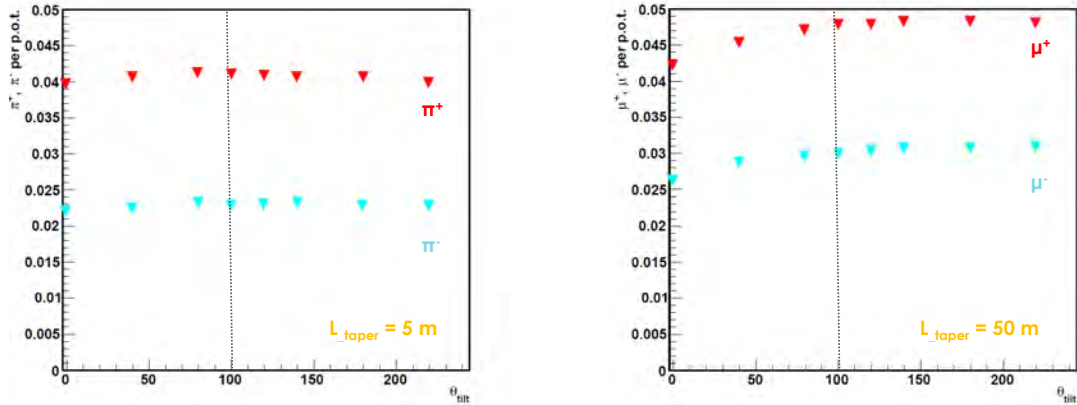


FIG. 6: π^+ , π^- and μ^+ , μ^- yields for the 5 m (left-plot) and 50 m (right-plot) taper solenoids respectively as function of the target tilting-angle (in mrad) for proton beam with $E_{kin} = 1.5$ GeV/c.

the selected pions as shown in these proceedings [12]. In the opposite way, protons with momenta similar to the selected pions are transported along with them. The yield for the former is reduced while for the latter remains similar as function of the tilting-angle [10].

TARGET RADIUS AND LENGTH

Different target radii and lengths are studied by having the target tilt fixed at 100 mrad and by keeping the rest baseline parameters the same. As result, the target thickness could be increased by few millimetres while its length could be decreased or increased by a few centimetres depending on the Hg-jet configuration without decreasing the yields of the particles. This is shown in Fig. 7 and Fig. 8.

Beam size

Variations of Beam sizes between $\sigma = 0$ mm to 2 mm have shown that the particle yields are decreasing for values higher than 1 mm while the rest parameters are kept at their baseline values [11]. This effect is similar to the variation of the target radius where the yield is decreasing for lower values due to the smaller interaction region.

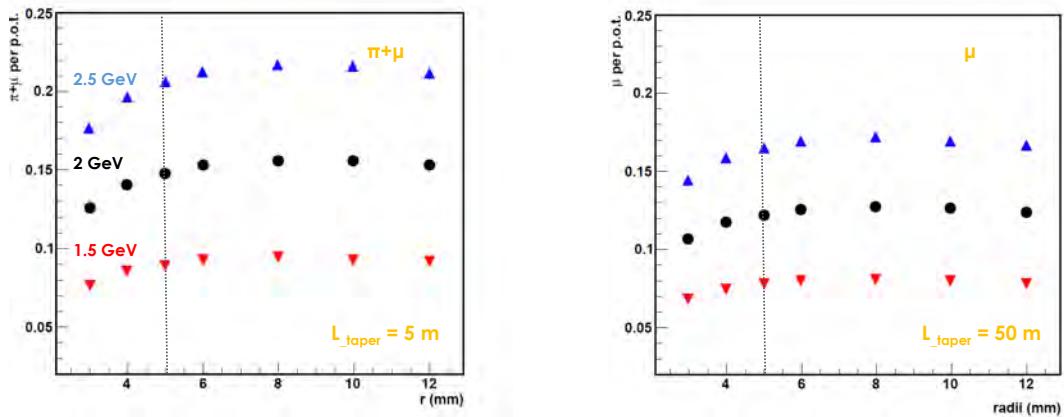


FIG. 7: Particle yields for the 5 m (left-plot) and 50 m (right-plot) taper solenoids respectively as function of the target radii for proton beams with $E_{kin} = 1.5, 2$ and 2.5 GeV/c.

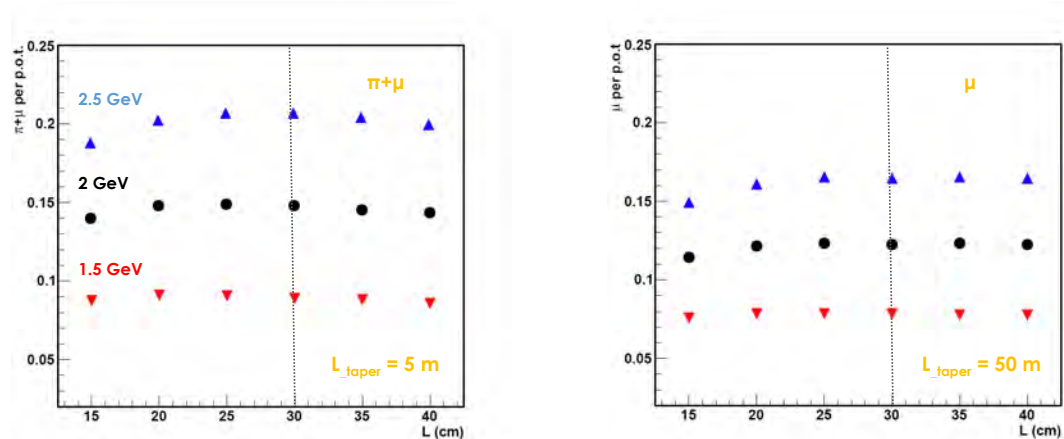


FIG. 8: Particle yields for the 5 m (left-plot) and 50 m (right-plot) taper solenoids respectively as function of the target lengths for proton beams with $E_{kin} = 1.5, 2$ and 2.5 GeV/c.

CONCLUSION

In this study the yields of selected pions and muons at the end of the adiabatic taper are used as a figure of merit in order to find the right values or ranges for the beam and the target parameters. These first results show that a tilting-angle of 100 mrad, a radius greater than 0.5 cm, and a length greater than 25 cm for the Hg-jet target could be used. The thickness of the target is relevant to the beam size, and for the baseline radius of 0.5 cm it should not be greater than about $\sigma = 0.1$ cm.

Further studies are being performed in order to cross-check the results with different

Monte Carlos, to study in detail the configuration of the capture system as the relevant angle between the beam and the target, the shielding, and finally to look for alternative targets [11], to be presented in the future.

The author would like to thank Professor Ye Yuan for their valuable discussions on the capture solenoid system parameters and design.

* Presented at NuFact15, 10-15 Aug 2015, Rio de Janeiro, Brazil [C15-08-10.2]

† vassilopoulos@ihep.ac.cn; Speaker

- [1] J. Cao et al., Phys. Rev. ST Accel. Beams **17**, 090101 (2014), 1401.8125.
- [2] J. Tang, *Moment synergies with other projects*, these proceedings.
- [3] Y. Yuan, *Moment as multiple neutrino sources*, this workshop, URL <https://indico.fnal.gov/getFile.py/access?contribId=117&sessionId=16&resId=0&materialId=slides&confId=8903>.
- [4] T. Bhlen et al., Nuclear Data Sheets **120**, 211 (2012).
- [5] A. Ferrari, P. Sala, A. Fasso, and J. Ranft, *Fluka: a multi-particle transport code* (2005).
- [6] K. McDonald, *Analytic forms for an adiabatic tapered solenoid gaussian* (2010), URL <http://puhep1.princeton.edu/mumu/target/taper.pdf>.
- [7] K. Paul and C. Johnstone, *Optimizing the pion capture and decay channel* (2004), URL http://www.hep.princeton.edu/~mcdonald/mumu/target/Paul/paul_muc0289.pdf.
- [8] M. Bogomilov et al., Phys. Rev. ST Accel. Beams **17**, 121002 (2014).
- [9] K. McDonald et al., in *Proceedings, 5th International Particle Accelerator Conference (IPAC 2014)* (2014), p. TUPRI008, URL <http://accelconf.web.cern.ch/AccelConf/IPAC2014/papers/tupri008.pdf>.
- [10] N. Vassilopoulos, *Studies on pion/muon capture at moment*, this workshop, URL <https://indico.fnal.gov/getFile.py/access?contribId=118&sessionId=16&resId=1&materialId=slides&confId=8903>.
- [11] Y. Yuan, N. Vassilopoulos, and G. Zhao, personal communication, (Target Group-MOMENT).
- [12] C. Meng, *Protons after bombarding the target at moment*, these proceedings.

**Cosmological bounds of sterile neutrinos in a
 $SU(3)_C \otimes SU(3)_L \otimes SU(3)_R \otimes U(1)_N$ model as dark matter candidates***

Cesar Peixoto Ferreira,[†] Marcelo Moraes Guzzo,[‡] and Pedro Cunha de Holanda[§]

Universidade Estadual de Campinas - Unicamp

(Dated: April 2, 2016)

Abstract

We study sterile neutrinos in an extension of the standard model, based on the gauge group $SU(3)_C \otimes SU(3)_L \otimes SU(3)_R \otimes U(1)_N$, and use this model to illustrate how to apply cosmological limits to thermalized particles that decouple while relativistic. We analyse the cosmological limits imposed by N_{eff} and dark matter abundance on these neutrinos. Assuming that these neutrinos have roughly equal masses and are not Cold Dark Matter, we conclude that the N_{eff} experimental value can be satisfied in some cases and the abundance constraint implies that these neutrinos are hot dark matter.

INTRODUCTION

The existence of Dark Matter is one of the most important discoveries in Cosmology in the last century . The Standard Model of Particle Physics(SM) doesn't have a viable candidate for dark matter. We study one extension, proposed by Dias et al[1], is the so-called 3L3R extension, based on the gauge group $SU(3)_C \otimes SU(3)_L \otimes SU(3)_R \otimes U(1)_N$ and in it, 3 sterile - under $SU(2)_L$ - neutrinos appear, which seems to be good Warm Dark Matter candidates.

We try to impose cosmological constraints into these sterile neutrinos, with the determination of its abundance and impact on N_{eff} (the effective number of neutrino species). Our intent is to illustrate to particle physicists how to use cosmological limits in particle physics models.

THE 3L3R MODEL

The 3L3R model can be considered an extension of the 3-3-1 extensions, and the introduction of a $SU(3)_R$ group makes the seesaw mechanism for neutrino masses possible. The leptons in the 3L3R transforms in the following way:

$$\begin{aligned}\Psi_{aL} &= (\nu_{aL}, l_{aL}, N_{aL})^T \sim (\mathbf{1}, \mathbf{3}, \mathbf{1}, -1/3), \\ \Psi_{aR} &= (\nu_{aR}, l_{aR}, N_{aR})^T \sim (\mathbf{1}, \mathbf{1}, \mathbf{3}, -1/3),\end{aligned}$$

where $a = e, \mu, \tau$ are the three leptonic families, and $N_{a[L,R]}$ are new neutrinos that transforms as triplets of the $SU(3)_L$ and $SU(3)_R$ groups, respectively.

It's possible to apply the seesaw mechanism, which gives the following mass matrix for the left handed neutrinos:

$$M_{\nu'_L} = -\frac{\Lambda_M}{4\Lambda_D^2} \begin{pmatrix} y^D (y^M)^{-1} (y^D)^T \nu_{\eta L}^2 & 0 \\ 0 & g^D (g^M)^{-1} (g^D)^T \nu_{\chi L}^2 \end{pmatrix}. \quad (1)$$

$M_{\nu'_L}$ is a 6×6 block diagonal matrix. The upper block gives the active neutrinos mass, and the lower the sterile neutrinos mass.

COSMOLOGICAL CONSTRAINTS

The prediction of the model of 3 new keV scale sterile neutrinos should have an impact in cosmological observables. We use two of them: N_{eff} (effective number of neutrinos) and abundance.

The N_{eff} constraint is a parameter related to the radiation energy density at a given temperature, and is defined as:

$$\rho_R = \rho_\gamma \left[1 + \frac{7}{8} \left(\frac{4}{11} \right)^{4/3} N_{eff} \right]. \quad (2)$$

Usually, N_{eff} is written as $N_{eff} = 3 + \Delta N_{eff}$, and ΔN_{eff} measures the excess of radiation ('Dark Radiation'), beyond active neutrinos. Suppose that the sterile neutrinos decouple at a temperature T_D with g_{si} entropic degrees of freedom. Right before the active neutrino decoupling, $g_s = 2 + (7/8)(2.2 + 3.2) = 10.75$ (when e, e^+ , photons and neutrinos are coupled). Then its possible to deduce that,

$$\Delta N_{eff} = \left(\frac{10.75}{g_{si}} \right)^{4/3} \quad (\text{per sterile neutrino species}), \quad (3)$$

Experimentally, we adopt the value $N_{eff} = 3.28 \pm 0.28[2]$.

RESULTS

We analyse three different cases, with different N_{aL} decoupling temperatures: (1) $T_D \in [105, 140 \text{ MeV}]$, (2) $T_D \in [140, 200 \text{ MeV}]$, (3) $T_D \in [200, 220] \text{ MeV}$. We adopt $T_{Had} = 200 \text{ MeV}[3]$. We have:

- Case 1: $g_{si} = 14.25 \implies \Delta N_{eff} = 0.69$. (per neutrino species)

- Case 2: $g_{si} = 17.25 \implies \Delta N_{eff} = 0.53$. (per neutrino species)
- Case 3: $g_{si} = 61.75 \implies \Delta N_{eff} = 0.097$. (per neutrino species)

So at the 1σ level, case 1 is excluded, case 2 admits one sterile neutrino only, and in case 3 all three neutrinos are possible. The limits to the g_D and g_M are given in Figure 1.

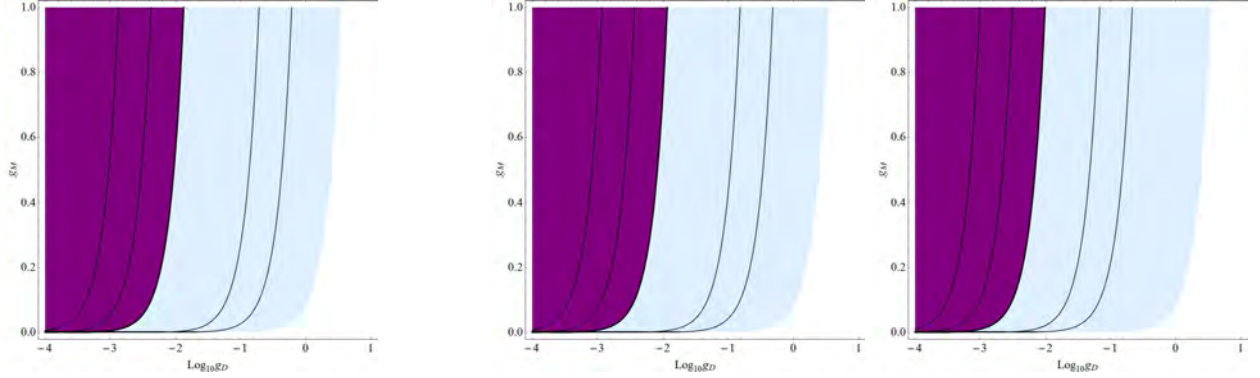


FIG. 1: Allowed regions of parameter space for g_D and g_M . Left: Case 1 ($\nu_{\chi'_L} = 5.7$ TeV). Center: Case 2 ($\nu_{\chi'_L} = 7.2$ TeV). Right: Case 3 ($\nu_{\chi'_L} = 9.3$ TeV). Cases 1 and 2 have only one neutrino, and case 3 has three. In each graphic, from left to right, the first three isolines gives the values of g_D and g_M for $\xi = 0.01$, $\xi = 0.1$ and $\xi = 1$. The last two isolines gives values for which the sterile neutrino mass is $m_{N_{aL}} = 1$ keV and $m_{N_{aL}} = 10$ keV, respectively.

In tables 1 and 2 we give limits on the mass of these sterile neutrinos, and the maximum allowed value for g_D in each scenario. Since these candidates are Hot Dark Matter, another

TABLE I: Values of the allowed neutrinos mass for each scenario and neutrino energy fraction of Dark Matter(ξ).

Cases					
Case 1 (one neutrino)		Case 2 (one neutrino)		Case 3 (three neutrinos)	
ξ	$m_{N_{aL}}(\text{eV})$	ξ	$m_{N_{aL}}(\text{eV})$	ξ	$m_{N_{aL}}(\text{eV})$
0.01	0.14	0.01	0.17	0.01	0.21
0.1	1.45	0.1	1.76	0.1	2.1
1	14.56	1	17.62	1	21.03

different limit can be imposed. It is possible to deduce that the sterile neutrinos affect the neutrino sum masses as $\sum_a (n_{N_{aL}}/n_\nu) m_{N_{aL}} \leq 0.17$ eV.

For case 2, $(n_{N_{aL}}/n_\nu) = 0.62$ and allows only one neutrino, and case 3 has $(n_{N_{aL}}/n_\nu) = 0.17$ and 3 neutrinos. For $\xi = 0.01$, we have:

TABLE II: Maximum allowed value for g_D in each scenario, with $g_M = 1$ and $\nu_{\chi'_L} = 5.7$ TeV (case 1), $\nu_{\chi'_L} = 7.2$ TeV (case 2) and $\nu_{\chi'_L} = 9.3$ TeV (case 3).

ξ	Cases		
	Case 1 (1 neutrino)	Case 2 (1 neutrino)	Case 3 (3 neutrinos)
0.01	1.3×10^{-3}	1.1×10^{-3}	9.8×10^{-4}
0.1	4.2×10^{-3}	3.6×10^{-3}	3.1×10^{-3}

- Case 2: $\sum_a (n_{N_{aL}}/n_\nu) m_{N_{aL}} = 0.62 \times 0.17 \approx 0.11$ eV.
- Case 3: $\sum_a (n_{N_{aL}}/n_\nu) m_{N_{aL}} = 0.17 \times 3 \times 0.21 \approx 0.11$ eV.

So for both cases the bound given above is satisfied.

Both cases obey the cosmological bounds applied with $\xi = 0.01$ and, although unable to answer the DM problem, are not ruled out as HDM candidates.

CONCLUSIONS

We imposed the N_{eff} and abundance constraints on sterile neutrinos that arise in the 3L3R model. Although we focused our analysis on this particular model, the results obtained are quite general and already known in cosmology: Stable thermalized keV particles overclose the Universe, and in this situation they are only possible if they are light (HDM) and constitutes only a small fraction of the Universe energy density.

* Presented at NuFact15, 10-15 Aug 2015, Rio de Janeiro, Brazil [C15-08-10.2]

† cesarpf@ifi.unicamp.br; Speaker

‡ guzzo@ifi.unicamp.br

§ holanda@ifi.unicamp.br

- [1] Alex G. Dias, C. A. de S. Pires, and P. S. Rodrigues da Silva, Phys. Rev. D **82**, 035013 (2010).
- [2] Ryan J. Cooke et al. 2014. *The Astrophysical Journal*(apJ) **781** 31
- [3] J.Lesgourgues et al. *Neutrino Cosmology*, Cambridge University Press, 2013. pp. 392

Progress on Cherenkov Reconstruction in MICE*

Daniel M. Kaplan,[†] Michael Drews, Durga Rajaram, and Miles Winter
Illinois Institute of Technology, Chicago, Illinois 60616, USA

Lucien Cremaldi, David Sanders, and Don Summers
University of Mississippi, Oxford, Mississippi 38677, USA

(Dated: December 10, 2015)

Abstract

Two beamline Cherenkov detectors (Ckov-a,-b) support particle identification in the MICE beamline. Electrons and high-momentum muons and pions can be identified with good efficiency. We report on the Ckov-a,-b performance in detecting pions and muons with MICE Step I data and derive an upper limit on the pion contamination in the standard MICE muon beam.

INTRODUCTION

The international Muon Ionization Cooling Experiment (MICE) [1] is designed to measure muon ionization cooling [2]. Cooling is needed for neutrino factories based on muon decay ($\mu^- \rightarrow e^- \bar{\nu}_e \nu_\mu$ and $\mu^+ \rightarrow e^+ \nu_e \bar{\nu}_\mu$) in storage rings [3] and for muon colliders [4].

Two high-density aerogel threshold Cherenkov counters [5], located just after the first Time of Flight counter (TOF0) in the MICE beamline, are used in support of muon and pion particle identification. The measured [6] refractive indices of the aerogels in the counters are $n_a = 1.069 \pm 0.003$ in Ckov-a and $n_b = 1.112 \pm 0.004$ in Ckov-b. The corresponding momentum thresholds for muons (pions) are at 280.5 (367.9) and 217.9 (285.8) MeV/c, respectively. Light is collected in each counter by four 9354KB eight-inch UV-enhanced phototubes and recorded by CAEN V1731 500 MS/s flash ADCs (FADCs).

EVENT HANDLING AND CALIBRATION

A charge-integration algorithm identifies charge clusters $q_i, i = 1-8$ in the FADCs where the ADC value crosses a threshold, marking times t_1 and t_2 at the threshold crossings, approximating the pulse beginning and end times. The time t_{max} at the cluster signal maximum is found. The charges are converted to a photoelectron count pe_i , by subtracting a pedestal q_{0i} and then normalizing by the single photoelectron charge q_{1i} for each phototube. For all $q_i > 0$, the total charge, arrival time, t_1 , and t_{max} are stored per event.

The asymptotic $\beta=1$ light yield $N_{\beta=1}$ in each counter is measured using the electron peak in MICE calibration-beam runs, giving 25 and 16 photoelectrons (pe's) in Ckov-b and Ckov-a, respectively, for a nominal run. The photoelectron yields versus momentum are displayed in Fig. 1. The observed muon thresholds, 213 ± 4 and 272 ± 3 MeV/c, are in reasonable agreement with the expectations given above. The average number of photoelectrons for normal incidence in the counters can be predicted from the Cherenkov angle $\cos \theta_c = 1/n\beta$, and, near threshold $\beta_{th} = 1/n$,

$$N_{pe} = N_{\beta=1} \times \sin^2 \theta_c = N_{\beta=1} \times (1 - (p_{th}/p)^2). \quad (1)$$

As seen in Fig. 2, the photoelectron spectra for μ, π are observed to be Poisson-like with tails from electromagnetic showers and delta rays produced as the particle traverses TOF0 and the aerogel radiator. Secondary electrons from these processes above about 1 MeV/c produce Cherenkov light 5–6% of the time for each particle passage. For small- N_{pe} signals, the measured spectra contain more zero-pe events than expected from pure Poisson-like behavior $P_0(x) = e^{-x}$, $x = \langle N_{pe} \rangle$.

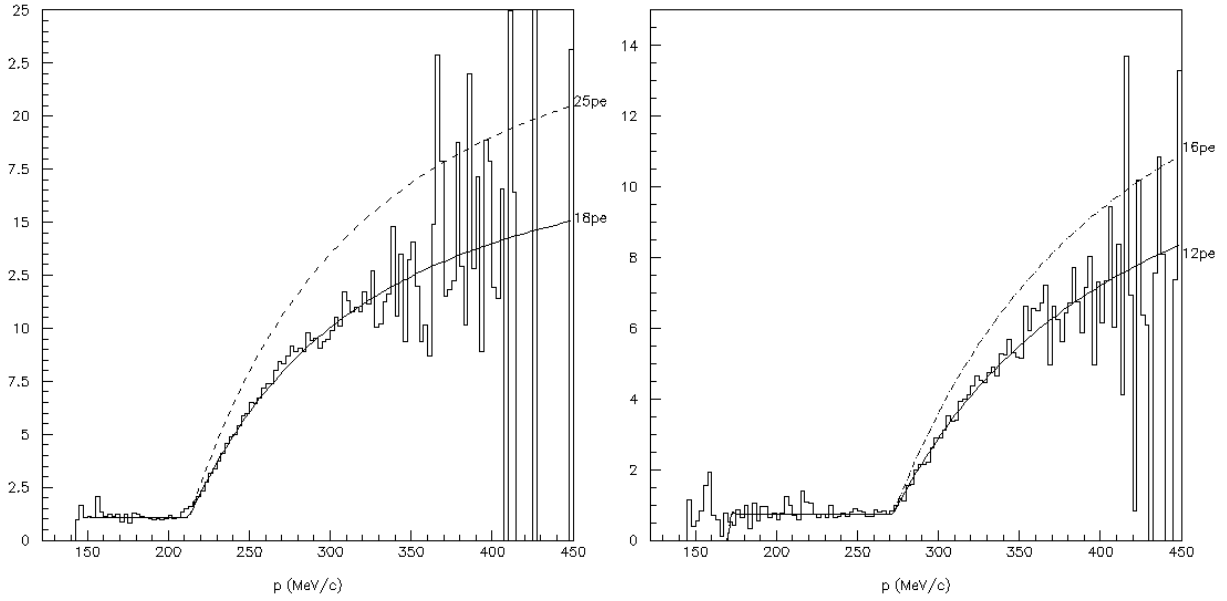


FIG. 1: Photoelectron (N_{pe}) curves versus momentum for muons in (left) Ckov-b and (right) Ckov-a. The $N_{\beta=1}$ values are about 75% of the values predicted from the asymptotic photoelectron spectrum of $\beta = 1$ electrons (labeled at right)—not unexpected since for electrons TOF0 acts effectively as a “preshower” radiator.

BEAM PARTICLE SPECTRA

The “D1” and “D2” dipoles in the MICE beamline [1] predominantly control the beam momentum and particle types transmitted into the MICE spectrometer. In the $p_{tgt} \approx p_{D1} \approx p_{D2}$ setting (calibration mode), the beamline transports a mixture of decay/conversion electrons, decay muons, and primary pions. For $p_{tgt} \approx p_{D1} \approx 0.5p_{D2}$, backward muon decays from the decay solenoid (DS) are selected. G4beamline [7] Monte Carlo runs indicate that a small leakage of primary pions through the D2 selection magnet can occur at the $\sim 1\%$ level [8]. Both these high-momentum pions and their decay muons should be observable in both Ckov-a and Ckov-b. Ckov-a can be used effectively to select the high-momentum π, μ events that are just over threshold [9].

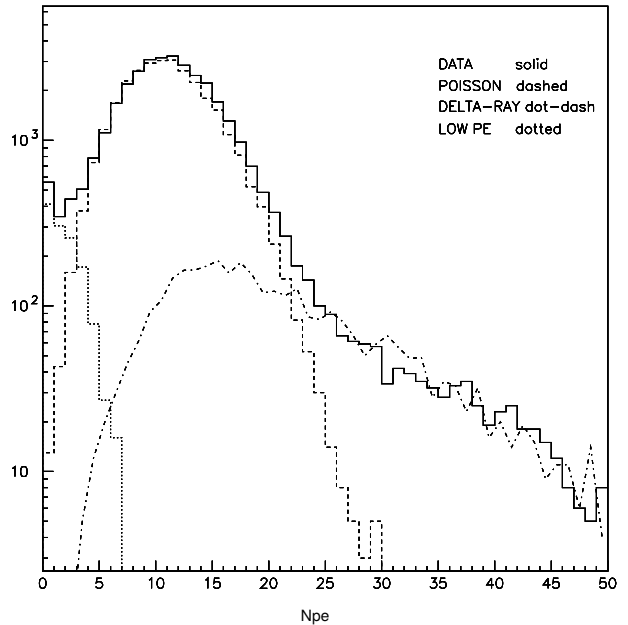


FIG. 2: Typical photoelectron spectrum seen for muons or pions above threshold in Ckov-b (solid histogram), together with model fit components: Poisson (dashed), delta-ray tail (dot-dash), and anomalous low- N_{pe} component (dotted).

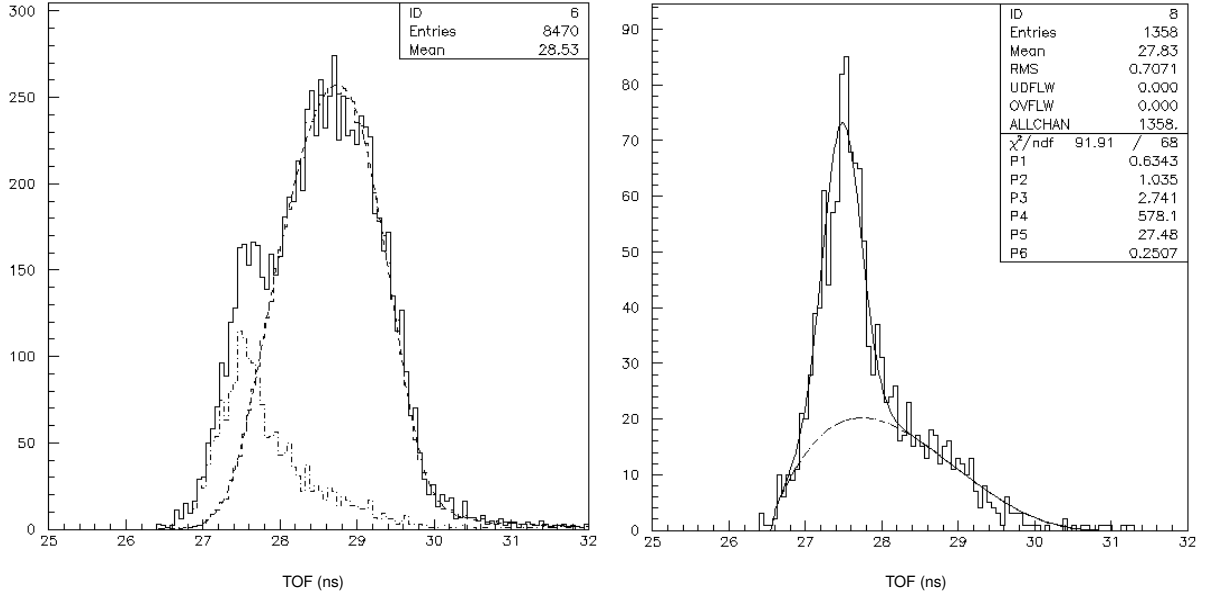


FIG. 3: Time-of-flight spectrum from TOF0 to TOF1 with (left) $pea > 2$ cut (solid) and $peb > 8$ cut (dot-dash), with shape of muon spectrum superimposed (dashed); and (right) $pea > 2$ and $peb > 10$ cuts. The peb requirements greatly reduce the delta-ray contribution. Fast π - μ are identified as the satellite peak centered at 27.6 ns.

ANALYSIS

Unambiguous identification of particle species using the Cherenkov detectors (measuring velocity) would require a momentum measurement from the MICE tracker, which was not available in Step I data. Muons and pions are thus indistinguishable here by the Cherenkov effect. In the following analysis we look for high-momentum π or μ that trigger Ckov-a. An additional cut on the number of photoelectrons in Ckov-b serves to suppress the $\approx 6\%$ of slow “background” events that pass the Ckov-a cut due to delta-ray emission.

We analyzed 120k Step I muon events with $p_{tgt} = 400$ MeV/ c and $p_{D2} = 237$ MeV/ c (the “standard” muon beam settings). We also analyzed 35k muon events with $p_{tgt} = 500$ MeV/ c and $p_{D2} = 294$ MeV/ c . In Fig. 3 we cut away the electron signal (by requiring $tof > 26.4$ ns) and also make a Ckov-a $N_{pe} > 2$ cut. The shoulder centered at 27.6 ns is made up of fast muons and pions triggering in Ckov-a and at TOF1. The background events centered approximately at $tof = 28$ ns are from particles with momenta below threshold in Ckov-a, but giving $N_{pe} > 2$ Ckov-a light by delta-ray emission. This background is consistent with the expected 6% contamination level. The $tof = 27.6$ ns peak corresponds to $p_{\mu} = 277$ MeV/ c or $p_{\pi} = 363$ MeV/ c , both above threshold in Ckov-a.

Fast muons and pions will leave considerable light in Ckov-b. According to Eq. 1 about 10 pe will be produced in Ckov-b at $p_{\mu} = 270$ MeV/ c . The probability for simultaneous delta-ray detection in *both* Ckov-a *and* Ckov-b will be about $0.06^2 = 3.6 \times 10^{-3}$. In Fig. 3 (right) we add a Ckov-b $N_{pe} > 10$ cut. The delta-ray background is substantially reduced

to about 500 events. A fit to Gaussian signal and phase-space background of the form ($x \equiv$ time of flight) $f = N(\sqrt{2\pi}\sigma)^{-1}e^{-(x-x_0)^2/2\sigma^2} + B(x-x_{lo})^\alpha(x_{hi}-x)^\beta$ gives 539 ± 34 signal events. When corrected for efficiency [9] we obtain $N = 1002 \pm 56$ events. By varying the fitting parameters we find a ± 101 -event systematic (syst) uncertainty [9]. The fast π - μ fraction is thus $R_{\mu\pi} = (1002 \pm 56 \pm 101)/118,793 = [0.84 \pm 0.05 \text{ (stat)} \pm 0.09 \text{ (syst)}]\%$.

If we assume pessimistically that all fast π - μ are pions, we can obtain upper limits on the pion fraction: $R_{\mu\pi} < 0.97\%$ (90% CL) and $R_{\mu\pi} < 1.00\%$ (95% CL). Any Bayesian model would require some prior knowledge of the pion-to-muon ratio in the beam. Estimating this (based on the G4beamline simulation) to be about 1/20 (or about 50 pions) allows us to estimate the fraction of pions in the beam to be $\pi/\mu \simeq 50/119,000 = 0.04\%$ —indeed very small, surpassing the MICE design requirements.

* Presented at NuFact15, 10-15 Aug 2015, Rio de Janeiro, Brazil [C15-08-10.2]; work supported by U.S. DOE via the MAP Collaboration.

† Electronic address: kaplan@iit.edu; presenter

- [1] M. Bogomilov *et al.*, JINST **7** (2012) P05009; D. Adams *et al.*, Eur. Phys. J. **C73** (2013) 2582; D. Adams *et al.*, arXiv:1510.08306; M. Bogomilov *et al.*, arXiv:1511.00556.
- [2] D. Neuffer, arXiv:1312.1266; D. Neuffer, AIP Conf. Proc. **441** (1998) 270; R. B. Palmer *et al.*, Phys. Rev. ST Accel. Beams **8** (2005) 061003; P. Snopok *et al.*, Int. J. Mod. Phys. **A24** (2009) 987; J. C. Gallardo and M. S. Zisman, AIP Conf Proc. **1222** (2010) 308; M. Chung *et al.*, Phys. Rev. Lett. **111** (2013) 184802; C. Yoshikawa *et al.*, IPAC-2014-TUPME016; D. Stratakis and R. B. Palmer, Phys. Rev. ST Accel. Beams **18** (2015) 031003; J. G. Acosta *et al.*, COOL-2015-MOPF07.
- [3] D. G. Koshkarev, CERN-ISR-DI-74-62 (1974); D. Cline and D. Neuffer, AIP Conf. Proc. **68** (1980) 856; D. Neuffer, IEEE Trans. Nucl. Sci. **28** (1981) 2034; S. Ozaki, R. B. Palmer, M. S. Zisman *et al.*, BNL-52623 (2001); M. M. Alsharo'a *et al.*, Phys. Rev. ST Accel. Beams **6** (2003) 081001; S. Choubey *et al.*, arXiv:1112.2853; D. Adey *et al.*, Phys. Rev. **D80** (2014) 071301.
- [4] C. M. Ankenbrandt *et al.*, Phys. Rev. ST Accel. Beams **2** (1998) 081001; J. G. Gallardo *et al.*, Snowmass 1996, BNL-52503; R. B. Palmer *et al.*, Nucl. Phys. Proc. Suppl. **51A** (1996) 61; D. Neuffer and R. Palmer, Conf. Proc. C940627 (1995) 52; A. V. Tollestrup, Conf. Proc. C9610311 (1996) 221; A. M. Sessler, Phys. Today **51N3** (1998) 48.
- [5] L. Cremaldi *et al.*, IEEE Trans. Nucl. Sci. **56** (2009) 1475; D. A. Sanders, Conf. Proc. C090504 (2009) 1696.
- [6] L. Cremaldi *et al.*, “Examination of Matsushita High Density Aerogel,” MICE-NOTE-149, Sept. 2006, <http://mice.iit.edu/micenotes/public/pdf/MICE0149/MICE0149.pdf>.
- [7] T. J. Roberts *et al.*, Conf. Proc. C0806233 (2008) WEPP120.
- [8] Pions leaking through D2 produce high-momentum decay muons in the MICE beam—a different production mechanism than that of the nominal MICE beam, which comes from pion decays *upstream* of D2.
- [9] More details of the analysis may be found in L. Cremaldi *et al.*, MICE Note 473 (2015), <http://mice.iit.edu/micenotes/public/pdf/MICE0473/MICE0473.pdf>.

Connections between $g - 2$, EDMs, CLFV and LHC

Paride Paradisi*

*Dipartimento di Fisica ed Astronomia "G. Galilei",
Univarsita' degli Studi di Padova, and Istituto Nazionale di Fisica Nucleare,
Sezione di Padova, Via Marzolo 8, 35131 Padova, Italy*

(Dated: January 29, 2016)

Abstract

We present a concise review of the status of charged lepton flavor violation (cLFV) in scenarios beyond the SM. We emphasize that the current experimental resolutions on cLFV processes are already testing territories of new physics (NP) models well beyond the LHC reach. On the other hand, with the expected sensitivities of next-generation experiments, cLFV will become the most powerful probe of NP signals at our disposal. Finally, the interrelationship among leptonic $g - 2$, EDMs and cLFV will turn out to be of outmost importance to disentangle among different NP scenarios.

INTRODUCTION

The origin of flavor remains, to a large extent, an open problem. However, significant progress has been achieved in the phenomenological investigation of the sources of flavour symmetry breaking which are accessible at low energies, ruling out models with significant misalignments from the SM Yukawa couplings at the TeV scale.

The search for LFV in charged leptons is probably the most interesting goal of flavour physics in the next years. The observation of neutrino oscillations has clearly demonstrated that lepton flavour is not conserved. The question is whether LFV effects can be visible also in other sectors of the theory, or if we can observe LFV in processes that conserve total lepton number. The most promising LFV low-energy channels are probably $\mu \rightarrow e\gamma$, $\mu \rightarrow eee$, $\mu \rightarrow e$ conversion in Nuclei as well as τ LFV processes which will be further investigated at the Super-Belle machine. The future sensitivities of next-generation experiments are collected in table I.

Moreover, the flavour-conserving component of the same diagrams generating $\mu \rightarrow e\gamma$ induces non-vanishing contributions to the anomalous magnetic moment of leptons as well as to the leptonic EDMs. In this context, the current anomaly for the muon ($g - 2$),

LFV Process	Present Bound	Future Sensitivity
$\mu \rightarrow e\gamma$	5.7×10^{-13} [1]	$\approx 6 \times 10^{-14}$ [2]
$\mu \rightarrow 3e$	1.0×10^{-12} [3]	$\approx 10^{-16}$ [4]
$\mu^- \text{Au} \rightarrow e^- \text{Au}$	7.0×10^{-13} [5]	?
$\mu^- \text{Ti} \rightarrow e^- \text{Ti}$	4.3×10^{-12} [6]	?
$\mu^- \text{Al} \rightarrow e^- \text{Al}$	–	$\approx 10^{-16}$ [7?]
$\tau \rightarrow e\gamma$	3.3×10^{-8} [8]	$\sim 10^{-8} - 10^{-9}$ [9]
$\tau \rightarrow \mu\gamma$	4.4×10^{-8} [8]	$\sim 10^{-8} - 10^{-9}$ [9]
$\tau \rightarrow 3e$	2.7×10^{-8} [10]	$\sim 10^{-9} - 10^{-10}$ [9]
$\tau \rightarrow 3\mu$	2.1×10^{-8} [10]	$\sim 10^{-9} - 10^{-10}$ [9]
Lepton EDM	Present Bound	Future Sensitivity
d_e (e cm)	8.7×10^{-29} [11]	?
d_μ (e cm)	1.9×10^{-19} [12]	?

TABLE I: Present and future experimental sensitivities for relevant low-energy observables.

reinforces the expectation of detecting $\mu \rightarrow e\gamma$ within the reach of the MEG experiment. Once some clear deviation from the SM is established, the next most important step is to identify correlations among different non-standard effects that can reveal the flavour-breaking pattern of the new degrees of freedom providing, at the same time, a powerful tool to disentangle among different New Physics scenarios. The above program represents one of the most exciting proofs of the synergy and interplay existing between the LHC, i.e. the *high-energy frontier*, and high-precision low-energy experiments, i.e. the *high-intensity frontier*.

LEPTONIC $g - 2$, EDMS AND LFV: A MODEL-INDEPENDENT ANALYSIS

The physics responsible for neutrino masses and mixing might or might not be related to the physics related to cLFV. On general grounds, we can say that:

- neutrino masses might be naturally explained within see-saw scenarios which introduce heavy right-handed Majorana neutrinos typically at the grand-unification (GUT) scale. These scenarios can also explain the baryon-antibaryon asymmetry in the universe through the leptogenesis mechanism. The new interactions of the model generally violate lepton-number $L = L_e + L_\mu + L_\tau$ (LNV).
- In the Standard Model (SM) with massive neutrinos, where the only source of LFV is coming from the operators responsible for the neutrino masses, the LFV effects are loop suppressed and proportional to the GIM factor $(m_\nu/M_W)^4$, therefore, completely negligible. For instance, it turns out that $\text{Br}(\mu \rightarrow e\gamma) \sim 10^{-54}$.
- On the other hand, generic models for new physics (NP) at the TeV scale contain new sources for LFV (but not necessarily for LNV), leading to decay rates accessible with future experiments.

From the low-energy point of view, these observations can be accounted for by considering the SM as an effective theory and extending its Lagrangian,

$$\mathcal{L}_{\text{eff}} = \mathcal{L}_{\text{SM}} + \frac{1}{\Lambda_{\text{LNV}}} \mathcal{O}^{\text{dim-5}} + \frac{1}{\Lambda_{\text{LFV}}^2} \mathcal{O}^{\text{dim-6}} + \dots \quad (1)$$

Here, the dimension-5 operator responsible for the neutrino masses is uniquely given in terms of the lepton doublets L^i and the Higgs doublet H in the SM,

$$\mathcal{O}^{\text{dim-5}} = (g_\nu)^{ij} (\bar{L}^i \widetilde{H})(\widetilde{H}^\dagger L^j)^c + \text{h.c.} \quad (2)$$

and the misalignment between the flavour matrix g_ν and the Yukawa coupling matrix Y_E in the charged-lepton sector leads to a non-trivial mixing matrix U_{PMNS} for neutrino oscillations.

For instance, within scenarios with right-handed Majorana neutrinos (type-I see saw), one can identify $g_\nu/\Lambda_{\text{LNV}} = Y_\nu M^{-1} Y_\nu^T$, where Y_ν is the Yukawa matrix in the neutrino sector, and M the Majorana mass matrix.

Examples for a dimension-6 operator are

$$\mathcal{O}^{\text{dim-6}} \ni \bar{\mu}_R \sigma^{\mu\nu} H e_L F_{\mu\nu}, \quad (\bar{\mu}_L \gamma^\mu e_L) (\bar{f}_L \gamma^\mu f_L), \quad (\bar{\mu}_R e_L) (\bar{f}_R f_L), \quad (3)$$

where $f = e, u, d$ and the first dipole-operator leads to LFV decays like $\mu \rightarrow e\gamma$ while the second and third ones generate, at the leading order, only processes like $\mu \rightarrow eee$ and $\mu \leftrightarrow e$ conversion in Nuclei. Obviously, the underlying dipole-transition $\mu \rightarrow e\gamma^*$ with a virtual γ also contributes to $\mu \rightarrow eee$ and $\mu \leftrightarrow e$ conversion in Nuclei.

In particular, within NP theories where the dominant LFV effects are captured by the dipole-operator, the following model-independent relations hold

$$\frac{\text{BR}(\ell_i \rightarrow \ell_j \ell_k \bar{\ell}_k)}{\text{BR}(\ell_i \rightarrow \ell_j \bar{\nu}_j \nu_i)} \simeq \frac{\alpha_{e\ell}}{3\pi} \left(\log \frac{m_{\ell_i}^2}{m_{\ell_k}^2} - 3 \right) \frac{\text{BR}(\ell_i \rightarrow \ell_j \gamma)}{\text{BR}(\ell_i \rightarrow \ell_j \bar{\nu}_j \nu_i)},$$

$$\text{CR}(\mu \rightarrow e \text{ in N}) \simeq \alpha_{\text{em}} \times \text{BR}(\mu \rightarrow e\gamma), \quad (4)$$

and therefore, the current MEG bound $\text{BR}(\mu \rightarrow e\gamma) \sim 5 \times 10^{-13}$ already implies that $\text{BR}(\mu \rightarrow eee) \leq 3 \times 10^{-15}$ and $\text{CR}(\mu \rightarrow e \text{ in N}) \leq 3 \times 10^{-15}$.

However, it is worth stressing that in many NP scenarios non-dipole operators, such as those shown in eq. 3, provide the dominant sources of LFV effects. Therefore, in such cases, $\mu \rightarrow eee$ and $\mu \leftrightarrow e$ conversion in Nuclei represent the best probes of LFV.

Dipole transitions $\ell \rightarrow \ell'\gamma$ in the leptonic sector are accounted for by means of the effective Lagrangian

$$\mathcal{L} = e \frac{m_\ell}{2} \left(\bar{\ell}_R \sigma_{\mu\nu} A_{\ell\ell'} \ell'_L + \bar{\ell}'_L \sigma_{\mu\nu} A_{\ell'\ell}^* \ell_R \right) F^{\mu\nu} \quad \ell, \ell' = e, \mu, \tau. \quad (5)$$

Starting from eq. (5), we can evaluate LFV processes, such as $\mu \rightarrow e\gamma$,

$$\frac{\text{BR}(\ell \rightarrow \ell'\gamma)}{\text{BR}(\ell \rightarrow \ell' \nu_\ell \bar{\nu}_{\ell'})} = \frac{48\pi^3 \alpha}{G_F^2} \left(|A_{\ell\ell'}|^2 + |A_{\ell'\ell}|^2 \right). \quad (6)$$

The underlying $\ell \rightarrow \ell'\gamma$ transition can generate, in addition to LFV processes, also lepton flavor conserving processes like the anomalous magnetic moments Δa_ℓ as well as leptonic electric dipole moments (EDMs, d_ℓ). In terms of the effective Lagrangian of eq. (5) we can write Δa_ℓ and d_ℓ as

$$\Delta a_\ell = 2m_\ell^2 \text{Re}(A_{\ell\ell}), \quad \frac{d_\ell}{e} = m_\ell \text{Im}(A_{\ell\ell}). \quad (7)$$

On general grounds, one would expect that, in concrete NP scenarios, Δa_ℓ , d_ℓ and $\text{BR}(\ell \rightarrow \ell'\gamma)$, are correlated. In practice, their correlations depend on the unknown flavor and CP structure of the NP couplings and thus we cannot draw any firm conclusion.

Parametrizing the amplitude $A_{\ell\ell'}$ as $A_{\ell\ell'} = c_{\ell\ell'}/\Lambda^2$, where Λ refers to the NP scale, we can evaluate which are the values of Λ probed by $\mu \rightarrow e\gamma$. We find that

$$\text{BR}(\mu \rightarrow e\gamma) \approx 10^{-12} \left(\frac{500 \text{ TeV}}{\Lambda} \right)^4 \left(|c_{\mu e}|^2 + |c_{e\mu}|^2 \right), \quad (8)$$

and therefore, for $c_{\mu e} \sim 1$ and/or $c_{e\mu} \sim 1$, we are left with $\Lambda > 500 \text{ TeV}$.

Since the anomalous magnetic moment of the muon $a_\mu = (g - 2)_\mu/2$ exhibits a $\sim 3.5\sigma$ discrepancy between the SM prediction and the experimental value [13] $\Delta a_\mu = a_\mu^{\text{EXP}} - a_\mu^{\text{SM}} = 2.90(90) \times 10^{-9}$, it is interesting to monitor the implications for $\text{BR}(\ell \rightarrow \ell'\gamma)$ assuming that such a discrepancy is due to NP. In particular, we find that

$$\begin{aligned} \text{BR}(\mu \rightarrow e\gamma) &\approx 10^{-12} \left(\frac{\Delta a_\mu}{3 \times 10^{-9}} \right)^2 \left(\frac{\theta_{e\mu}}{2 \times 10^{-5}} \right)^2, \\ \text{BR}(\tau \rightarrow \ell\gamma) &\approx 10^{-8} \left(\frac{\Delta a_\mu}{3 \times 10^{-9}} \right)^2 \left(\frac{\theta_{\ell\tau}}{5 \times 10^{-3}} \right)^2. \end{aligned} \quad (9)$$

where $\theta_{\ell\ell'} = \sqrt{|c_{\ell\ell'}|^2 + |c_{\ell'\ell}|^2}/c_{\mu\mu}$. Therefore, we learn that the a_μ anomaly can be accommodated while satisfying the $\text{BR}(\mu \rightarrow e\gamma)$ bound only for extremely small flavor mixing angles $\theta_{e\mu}$.

Similarly, from eq. 7, we find that $d_e \simeq 10^{-24} \times [\text{Im}(c_{ee})/\text{Re}(c_{\mu\mu})] e$ cm whenever $\Delta a_\mu \approx 3 \times 10^{-9}$. Therefore, also the electron EDM exceeds the current experimental bound by many orders of magnitudes unless there exists a dynamical mechanism suppressing the relevant CP violating phases.

SPECIFIC NP MODELS

The phenomenology of cLFV observables has been worked out in a number of well motivated NP scenarios. Among the most important questions are (i) which are the best probes among cLFV processes for any given NP model, (ii) how the predictions compare with the present/foreseen experimental bounds, (iii) what the constraints are on new sources of LFV and new-particle masses, (iv) what are the correlations among different LFV observables.

Concerning the latter point, it should be stressed that 1) ratios for branching ratios of processes such as $\mu \rightarrow e\gamma$ and $\tau \rightarrow \mu\gamma$ would provide a direct access to the flavor structure of the NP model while 2) a comparative analysis of processes with the same underlying flavor transition (such as $\mu \rightarrow e\gamma$ and $\mu \rightarrow eee$) would provide information about the operators which are generating potential LFV signals.

In the following, we briefly discuss two classes of NP models: supersymmetric (SUSY) extensions of the SM and strongly interacting models based on the partial-compositeness paradigm.

SUSY models

In SUSY models, new sources for LFV stem from the soft SUSY-breaking sector since the lepton and slepton mass matrices are generally misaligned. The leading effects for cLFV processes arise from sneutrino-chargino and slepton-neutralino loops. In the generic MSSM, it is useful to stick to the mass-insertion approximation, assuming small off-diagonal entries in the slepton mass matrices $(\delta_{AB}^{ij})_f = (m_{\tilde{A}\tilde{B}}^2)_{ij}/m_{\tilde{\ell}}^2$, where $A, B = L, R$ and $m_{\tilde{\ell}}$ is an average slepton mass.

A scenario which has received particular attention after the discovery of the Higgs-like boson at the LHC is the so-called “disoriented A-terms” scenario [14]. The assumption of disoriented A-terms is that flavor violation is restricted to the trilinear terms

$$(\delta_{LR}^{ij})_f \sim \frac{A_f \theta_{ij}^f m_{f_j}}{m_{\tilde{f}}} \quad f = u, d, \ell, \quad (10)$$

where θ_{ij}^f are generic mixing angles. This pattern can be obtained when the trilinear terms have the same hierarchical pattern as the corresponding Yukawa matrices but they do not respect exact proportionality. A natural realization of this ansatz arises in scenarios with partial compositeness [15], where also the SM flavor puzzle can be accounted for. Interestingly, the structure of eq. (10) allows us to naturally satisfy the very stringent flavor bounds of the down-sector thanks to the smallness of down-type quark masses. On the other hand, sizable A-terms help to account for a Higgs boson with mass around 125 GeV while keeping the SUSY scale not too far from the TeV.

The bounds from the lepton sector can be satisfied under the (natural) assumption that the unknown leptonic flavor mixing angles are of the form $\theta_{ij}^\ell \sim \sqrt{m_i/m_j}$ [15]. In particular, we get the following predictions [16]

$$\begin{aligned} \text{BR}(\mu \rightarrow e\gamma) &\approx 6 \times 10^{-13} \left| \frac{A_\ell}{\text{TeV}} \frac{\theta_{12}^\ell}{\sqrt{m_e/m_\mu}} \right|^2 \left(\frac{\text{TeV}}{m_{\tilde{\ell}}} \right)^4, \\ d_e &\approx 4 \times 10^{-28} \text{Im} \left(\frac{A_\ell \theta_{11}^\ell}{\text{TeV}} \right) \left(\frac{\text{TeV}}{m_{\tilde{\ell}}} \right)^2 e \text{ cm}, \\ \Delta a_\mu &\approx 1 \times 10^{-9} \left(\frac{\text{TeV}}{m_{\tilde{\ell}}} \right)^2 \left(\frac{\tan \beta}{30} \right). \end{aligned} \quad (11)$$

where we have assumed that the only possible sources of CP violation arise from A terms, as well. These estimates are fully confirmed by the numerical analysis shown in fig. 1 which has been obtained by means of the following scan: $0.5 \leq |A_e|/\tilde{m} \leq 2$ with $\sin \phi_{A_e}=1$, $\tilde{m} \leq 2$ TeV, $(M_2, \mu, M_1) \leq 1$ TeV and $10 \leq \tan \beta \leq 50$ [16].

It is interesting that disoriented A-terms can account for $(g-2)_\mu$, satisfy the bounds on $\mu \rightarrow e\gamma$ and d_e , while giving predictions within experimental reach [16].

Composite Higgs Models

Besides low-energy supersymmetry, a class of attractive SM extensions addressing the gauge hierarchy problem is provided by composite Higgs models [17, 18], where fermion masses and mixing angles are described by partial compositeness [19]. Light fermions obtain hierarchical masses from the mixing between an elementary sector and a composite one.

As a toy model, let us consider, for each SM fermion, a pair of heavy fermions allowing a Dirac mass term of the order of the compositeness scale and a mixing term with the SM fields [20]

$$\mathcal{L}_Y = - \sum_{i,j=1}^3 \left(\bar{\ell}_{Li} \Delta_{ij} L_{Rj} - \tilde{e}_{Ri} \tilde{\Delta}_{ij} \tilde{E}_{Lj} \right) + h.c. \quad (12)$$

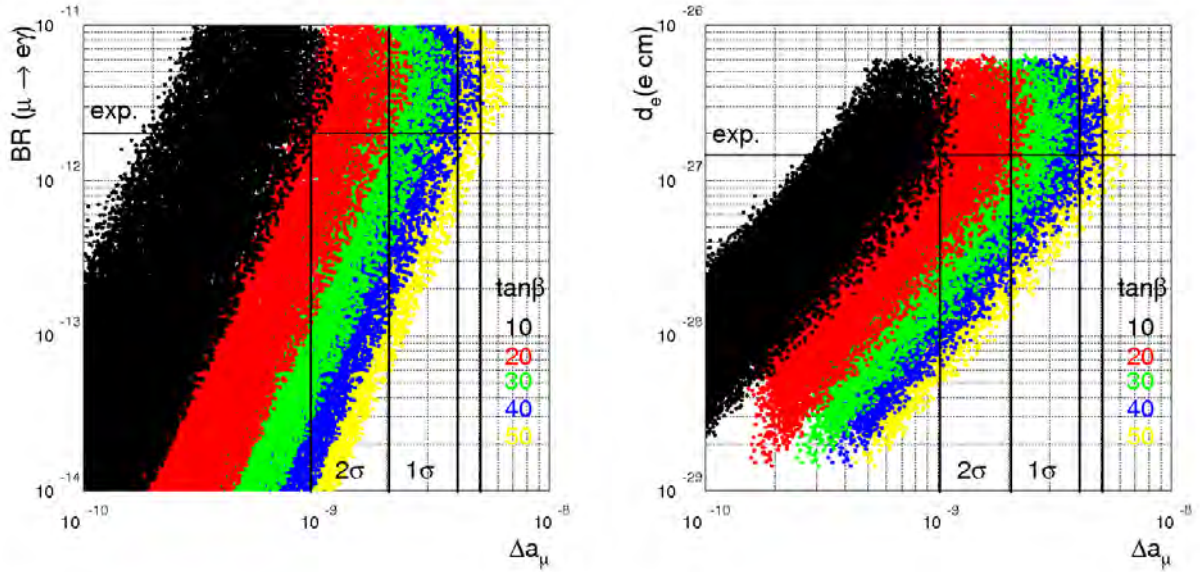


FIG. 1: Predictions of the disoriented A-term scenario [16]. Left: $\mu \rightarrow e\gamma$ vs. Δa_μ . Right: d_e vs. Δa_μ .

$$- \sum_{i=1}^3 \left(\bar{L}_i m_i L_i + \bar{\tilde{E}}_i \tilde{m}_i \tilde{E}_i \right) \quad (13)$$

$$- \sum_{i,j=1}^3 \left(\bar{L}_{Ri} \varphi Y_{Lij}^* \tilde{E}_{Lj} + \bar{L}_{Li} \varphi Y_{Rij}^* \tilde{E}_{Rj} \right) + h.c. \quad (14)$$

The first line represents the mixing between the elementary composite sectors, the second line contains Dirac mass terms for the fermions of the composite sector and the third line shows the Yukawa interactions which are restricted to the composite sector only with $1 \leq |Y_R^*|, |Y_L^*| \leq 4\pi$. By integrating out the composite sector under the assumptions $m_i = m$, $\tilde{m}_i = \tilde{m}$ and $\tilde{m}, m \gg v$, we get the SM-like Yukawa interaction

$$\mathcal{L}_Y^{eff} = -\bar{\ell}_L \varphi \hat{y}_\ell^{SM} \tilde{e}_R + \dots \quad y_\ell^{SM} = X Y_R^* \tilde{X}^\dagger \quad , \quad (15)$$

where $X \equiv \Delta m^{-1}$, $\tilde{X} \equiv \tilde{\Delta} \tilde{m}^{-1\dagger}$ and dots stand for contributions of higher order in v/m . The remarkable feature of this pattern is that hierarchical fermion masses and mixing angles can be explained by the mixing matrices X and \tilde{X} , even in the presence of anarchical matrices Y_R^* and Y_L^* . At the one-loop level, summing over the h, Z and W amplitudes, we get the main contribution to the electromagnetic dipole operator:

$$A_{\ell\ell'} \sim \frac{1}{16\pi^2} \frac{1}{m\tilde{m}} \left(X Y_R^* Y_L^* \tilde{X}^\dagger \right)_{\ell\ell'} \quad . \quad (16)$$

If Y_R^* and Y_L^* are anarchical matrices we see that, in general, y_ℓ^{SM} and $A_{\ell\ell'}$ are not diagonal in the same basis. From the present bounds on $BR(\mu \rightarrow e\gamma)$ and d_e we find that, with reasonable assumptions on the mixing matrices X and \tilde{X} , we need $m/\langle Y \rangle$ and $\tilde{m}/\langle Y \rangle$

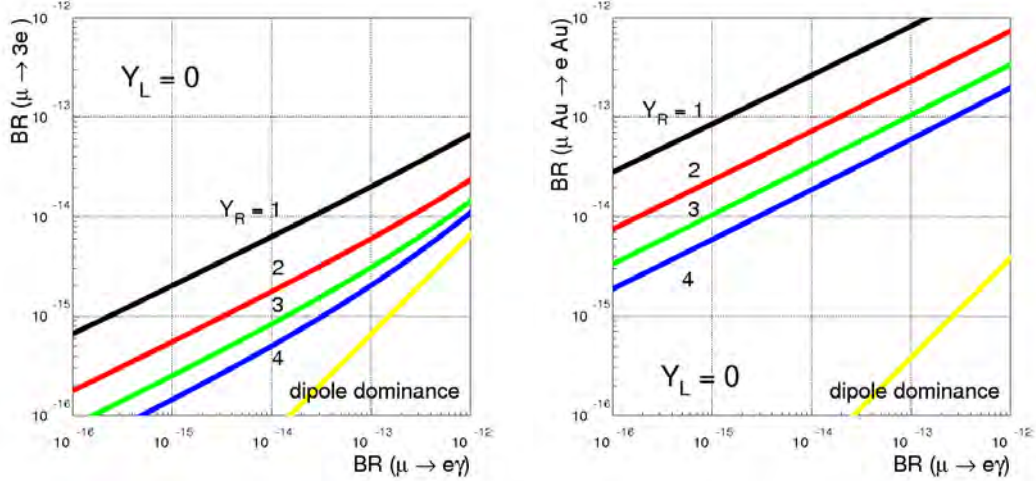


FIG. 2: Branching ratio of $\mu \rightarrow 3e$ (left) and $\mu^- Au \rightarrow e^- Au$ (right) versus the branching ratio of $\mu \rightarrow e\gamma$ for $Y_L^* = 0$. The case of dominance of the dipole operator is shown in yellow.

well above 10 TeV, $\langle Y \rangle$ denoting an average absolute value of the Yukawa matrices. If we postulate that $Y_L^* = 0$, charged lepton masses do not vanish while the leading order contribution (16) does and we find [21]

$$\text{BR}(\mu \rightarrow e\gamma) \approx 3 \times 10^{-13} \left(\frac{1.5 \text{ TeV}}{m} \right)^8 |Y_R^*|^8, \quad (17)$$

where Y_R^* now stands for an average element of the anarchic matrix Y_{Rij}^* , implying that $\mu \rightarrow e\gamma$ saturates its current experimental bound for $m \approx 1.5 \text{ TeV}$ and $Y_R^* \approx 1$.

A quite similar behavior is expected for the electron EDM. Indeed, setting $Y_L^* = 0$ and assuming $\mathcal{O}(1)$ CP-violating phases, it turns out that [21]

$$\frac{|d_e|}{e} \approx 10^{-28} \text{ cm} \left(\frac{3 \text{ TeV}}{m} \right)^4 Y_R^{*4}. \quad (18)$$

Moreover, it turns $\mu \rightarrow 3e$ and $\text{BR}(\mu^- Au \rightarrow e^- Au)$ are dominated by non-dipole operators and the correlation of eq. (4) is significantly violated as it is explicitly shown in fig. 2. This is a relevant result, as within composite Higgs models with $Y_L^* \neq 0$, as well as in supersymmetric scenarios, eq. (4) holds to an excellent approximation. In particular, we find [21]

$$\text{BR}(\mu \rightarrow 3e) \approx 5 \times 10^{-13} \left(\frac{1 \text{ TeV}}{m} \right)^4 |Y_R^*|^2, \quad (19)$$

$$\text{BR}(\mu^- Au \rightarrow e^- Au) \approx 4 \times 10^{-13} \left(\frac{3 \text{ TeV}}{m} \right)^4 |Y_R^*|^2, \quad (20)$$

and therefore $\mu^- Au \rightarrow e^- Au$ is a better probe than $\mu \rightarrow 3e$ of the scenario in question.

CONCLUSIONS

Despite of the fact that the origin of flavor remains a major open problem, significant progress has been achieved in the phenomenological investigation of the sources of flavour symmetry breaking which are accessible at low energies, ruling out models with significant misalignments from the SM Yukawa couplings at the TeV scale.

The search for LFV in charged leptons is probably the most interesting goal of flavour physics in the next years (see table I). The observation of neutrino oscillations has clearly demonstrated that lepton flavour is not conserved. The question is whether LFV effects can be visible also in other sectors of the theory. The most promising LFV low-energy channels are probably $\mu \rightarrow e\gamma$, $\mu \rightarrow eee$, $\mu \rightarrow e$ conversion in Nuclei as well as τ LFV processes. The current experimental resolutions on cLFV processes are already testing territories of new physics (NP) models well beyond the LHC reach. On the other hand, with the expected sensitivities of next-generation experiments, cLFV will become the most powerful probe of NP signals at our disposal and the interrelationship among leptonic $g-2$, EDMs and cLFV will be of outmost importance to disentangle among different NP scenarios.

ACKNOWLEDGMENTS

This work was supported by the ERC Advanced Grant No.267985 *Electroweak Symmetry Breaking, Flavour and Dark Matter: One Solution for Three Mysteries (DaMeSyFla)*.

* `paride.paradisi@pd.infn.it`; Paride Paradisi

- [1] J. Adam et al. (MEG), Phys. Rev. Lett. **110**, 201801 (2013), 1303.0754.
- [2] A. M. Baldini et al. (2013), 1301.7225.
- [3] U. Bellgardt et al. (SINDRUM), Nucl. Phys. **B299**, 1 (1988).
- [4] A. Blondel et al. (2013), 1301.6113.
- [5] W. H. Bertl et al. (SINDRUM II), Eur. Phys. J. **C47**, 337 (2006).
- [6] C. Dohmen et al. (SINDRUM II), Phys. Lett. **B317**, 631 (1993).
- [7] C. Collaboration, <http://comet.kek.jp/Documents.html> (????).
- [8] B. Aubert et al. (BaBar), Phys. Rev. Lett. **104**, 021802 (2010), 0908.2381.
- [9] K. Hayasaka (Belle, Belle-II), J. Phys. Conf. Ser. **408**, 012069 (2013).
- [10] K. Hayasaka et al., Phys. Lett. **B687**, 139 (2010), 1001.3221.
- [11] J. Baron et al. (ACME), Science **343**, 269 (2014), 1310.7534.
- [12] G. W. Bennett et al. (Muon (g-2)), Phys. Rev. **D80**, 052008 (2009), 0811.1207.
- [13] F. Jegerlehner and A. Nyffeler, Phys. Rept. **477**, 1 (2009), 0902.3360.
- [14] G. F. Giudice, G. Isidori, and P. Paradisi, JHEP **04**, 060 (2012), 1201.6204.
- [15] B. Keren-Zur, P. Lodone, M. Nardecchia, D. Pappadopulo, R. Rattazzi, and L. Vecchi, Nucl. Phys. **B867**, 394 (2013), 1205.5803.
- [16] G. F. Giudice, P. Paradisi, and M. Passera, JHEP **11**, 113 (2012), 1208.6583.

- [17] B. Bellazzini, C. Cski, and J. Serra, *Eur. Phys. J.* **C74**, 2766 (2014), 1401.2457.
- [18] G. Panico and A. Wulzer, *Lect. Notes Phys.* **913**, pp. (2016), 1506.01961.
- [19] D. B. Kaplan, *Nucl. Phys.* **B365**, 259 (1991).
- [20] R. Contino, T. Kramer, M. Son, and R. Sundrum, *JHEP* **05**, 074 (2007), hep-ph/0612180.
- [21] F. Feruglio, P. Paradisi, and A. Pattori, *Eur. Phys. J.* **C75**, 579 (2015), 1509.03241.

Update on the AlCap Experiment*

Benjamin E. Krikler[†]
Imperial College London
(Dated: April 18, 2016)

Abstract

The AlCap experiment studies the emission products following muon capture on an aluminium nucleus. Such a measurement is important in the context of the up-coming muon-to-electron conversion experiments, COMET and Mu2e, which will both use an aluminium stopping target. Despite this, and the potential nuclear and astrophysical implications, the existing range of measurements is incomplete, with the majority of measurements on proton and neutron emissions already some 40 years old.

AlCap first ran in 2013, and will have run twice more by the end of 2015. It is a joint effort by the Mu2e and COMET collaborations.

INTRODUCTION

Both the COMET experiment at J-PARC [1, 2] and the Mu2e experiment at Fermilab [3], aim to improve the search for muon-to-electron conversion by around four orders of magnitude compared to the current limit, set by the SINDRUM-II experiment [4]. Such an increased sensitivity is achieved by the use of a pulsed muon beam and a relatively light stopping target, made of aluminium. Significant background suppression can be achieved since the lifetime of the muon in aluminium is 864 ns, compared to the typical beam flash time of 200 ns. However, this poses an issue for the next generation of μ - e conversion experiments since the stopping of negative muons in aluminium has not been well studied.

In particular, whilst the decay of a muon bound to a nucleus can be relatively well theoretically modelled [5], the nuclear capture of the muon is much harder due to the complexity of the nuclear environment. Captured muons cause emission of various particles, through both prompt and nuclear relaxation mechanisms, which in general can be written as:

$$\mu + N(A, Z) \rightarrow \nu_{\mu} + N^*(A, Z - 1) \quad (1)$$

$$N^*(A, Z - 1) \rightarrow N(A', Z') + X \quad (2)$$

where X is any combination of additional final state particles, such as protons, neutrons, photons, deuterons, alpha particles and so on.

Although producing a 105 MeV electron following muon capture is highly unlikely, the emission of these final state particles causes several additional difficulties in the design and operation of COMET and Mu2e for several reasons. Firstly, neutral particles such as neutrons and photons can cause difficulties for any electronics systems near the detectors. Emitted neutrons can also create fake vetoes in the active Cosmic Ray Veto systems which are based on scintillating bars that a neutron recoil could trigger. If the neutron flux were too high, shielding of the veto system and more radiation-hard electronics might be required. On the other hand, the charged particle emissions will increase the detector occupancy. Since low energy protons are strongly ionising they can blind large parts of the detector to any signal electron. Controlling these particles would require some additional absorbing material between the target and the detector, the downside of this being that any signal electron will also be affected essentially reducing the resolution of the detector. It is important then that the rates and energies of the emitted particles be well understood in order to optimise the designs of the upcoming μ - e conversion experiments.

As a joint collaboration between COMET and Mu2e, AlCap therefore aims to measure:

- the emitted charged particle rates and spectra down to 2.5 MeV with a 5-10 % resolution,
- X-ray and gamma spectra and the relative intensities in the various peaks,
- the neutron spectrum and rate from 1 to 10 MeV.

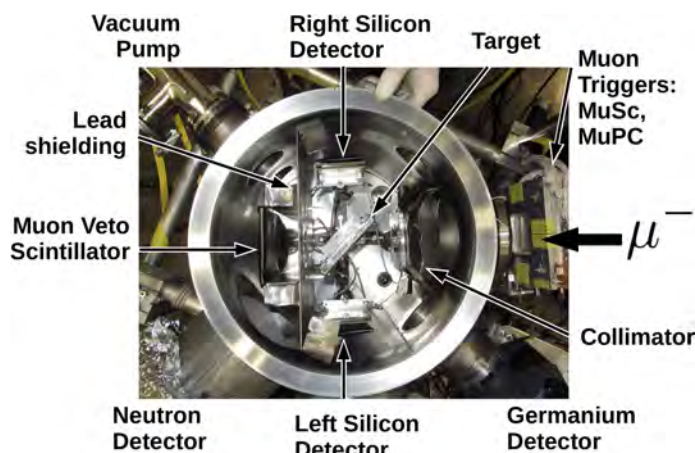
Work towards these goals has been split between three separate runs, each taking place at the Paul Scherrer Institute (PSI), near Zurich. The first run, Run 2013, took place during the winter of 2013, focussed on charged particle emission but also ran some preliminary neutron measurements. Two runs will have taken place during 2015 with the first, Run 2015a, held in June and focussed primarily on neutral particle emissions (photons and neutrons). Finally, Run 2015b will run during November 2015 and repeat and improve the charged particle measurement from Run 2013.

RUN 2013: CHARGED PARTICLES

The 2013 run dealt primarily with measuring the charged particles emitted following muon capture, and took place from mid-November to the end of the year using the piE1 beamline of the Swiss Muon Source ($S\mu S$) at the Paul Scherrer Institute (PSI). A brief description is provided here whilst more information is provided in [6, 7].

The primary aim for this run was to obtain the emission rates and distributions for low energy protons, deuterons, tritons and alphas particles. To reduce the amount of scattering of the charged capture products both the aluminium target and detector systems were placed in a vacuum and the target size kept to a thickness of less than 1 mm. At such a thickness a beam momentum of around 30 MeV was expected to be roughly optimal to stop all muons in the target. At this energy the muon rate in the piE1 beam was roughly 3-6 kHz, running in a continuous mode.

Fig. 1 shows the experimental set-up for this run. The muon beam reaches the target by passing through several beam monitors (namely, a scintillator paddle, muSc, and a scintillator paddle with a hole centred on the beam axis, muScA, which together with the muSc



(a) Setup

Dataset	Target	Run Time (hrs.)
Al50	50 μm Al.	50
Al100	100 μm Al.	17
Si16	65 μm Si.	8
SiR2 (Active)	1.5 mm Si.	8

(b) R13 Datasets

FIG. 1: Experimental set-up and acquired datasets from Run 2013. See text for a full description of the experiment set-up.

defined an on-axis muon entering the chamber, and finally a proportional wire chamber which gave a measurement of the beam profile before the chamber), entering the vacuum chamber through a light-sealed mylar window and passing a lead collimator.

The stopping target was mounted at 45° to the beam to reduce the amount of target material the charged daughter products would have to pass through before reaching the two charged particle detectors, which sat to the left and right at 90° with respect to the beam direction at the target position. Behind the stopping target sat another scintillator paddle to veto muons that did not stop in the target. All the remaining surfaces that faced the beam were covered in lead so that secondaries from capture of scattered muons could be removed by a prompt-time cut, since the muon lifetime in lead is only 75 ns.

Each of the two charged particle telescopes consisted of a pair of silicon detectors and a punch-through scintillator paddle. The first of the silicon detectors was only about $65\ \mu\text{m}$ in thickness and divided into 4 quadrants, whilst the second was a single silicon detector of thickness of 1.5 mm. Information on both the particle's identity and energy can be obtained using a coincidence between the thick and thin silicon detectors. Although a vacuum pressure of around 10^{-2} Pa would have been sufficient to reduce multiple scattering, to prevent arcing between the quadrants of the thin silicon detector the vacuum was maintained at below 10^{-4} Pa.

Finally, outside of the vacuum chamber were placed a germanium detector to measure the X-ray and gamma spectrum as well as liquid scintillator neutron detectors.

The 64 or so detector channels were digitised on a mix of custom-built Flash ADCs and CAEN digitizers. All of the silicon detector outputs were passed through both fast and slow analogue filters to provide better time and energy resolution of the individual pulses. Each channel was then operated in a self-trigger mode within a DAQ-active gate that was initiated by the global DAQ system. The DAQ-active gate lasted 112 ms and typically had a dead-time between gates of about 10 ms.

Datasets

Several different datasets were obtained with both silicon and aluminium targets. Fig. 1b gives a summary of the different datasets obtained in the 2013 run.

Runs dedicated to calibration, background measurements and other cross checks were also performed. These included the use of one of the silicon packages as an active target, which was used both to tune the beam and as a means to cross-check aspects of the analysis.

Preliminary Analysis

Stopped Muon Normalisation

When negative muons come to a stop in a material they become bound to the nucleus. An electromagnetic cascade down to the lowest energy atomic orbital takes place over very short time scales, with the emission of characteristic X-rays corresponding to the transition energy between the muonic atom energy levels. To determine the number of stopped muons during the run, the X-rays from this cascade were observed using the external germanium detector. In particular, the $2p-1s$ line was used, since it has the highest relative intensity and is well

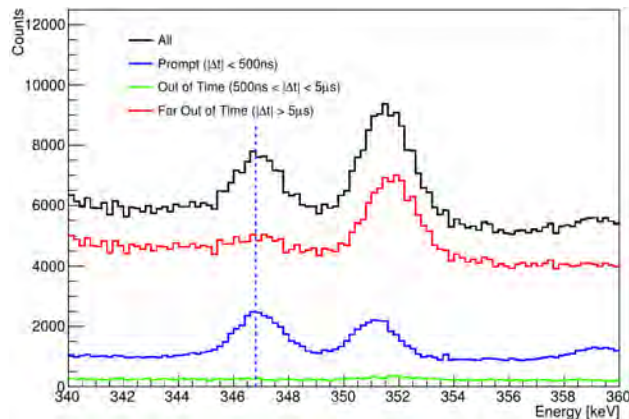


FIG. 2: A close up of the $2p-1s$ transition line at around 347 keV used for the normalisation of stopped muons for the A1100 dataset. The blue solid line shows x-rays coming within 500 ns of muon entering the chamber as determined by the muSc entrance scintillator that was fitted with two Gaussians and a linear background. The second peak at around 352 keV is believed to be a combination of X-rays coming from the radioactive decay chain of lead and thallium.

separated from any nearby background peaks. A prompt timing cut was made between the germanium detector and the incoming muon scintillator paddle (muSc) to remove accidental backgrounds. The same muon pile-up protection cut was also applied as described below for the charged particle analysis. Fig. 2 shows the X-ray spectrum from the A1100 dataset around the $2p-1s$ peak. The peak was fitted with a Gaussian plus a linear background and the area under the peak extracted. The detector's acceptance was found using an Eu-152 source and cross checked with a Monte Carlo simulation, and the efficiency at a given energy was obtained by an empirical fit to calibration data. The observed value was scaled by this to give the total number of muons stopped during a run.

Charged Particle Measurement status

For particles stopping in the thick silicon, a coincident hit in the thin allowed for a measurement of both the particle's dE/dx and its total energy. These two values taken together provide for particle identification as shown for simulated data in Fig. 1a. Variation in the dE/dx due to different angles of incidence was small, given the distance from the target to the detector and was estimated to be around 10%, far less than the separation of the different bands. This set-up allowed for the distinction of protons, deuterons, tritons and alpha particles, over a range of energies from about 2 to 10 MeV. So far only the proton band has been analysed although it is thought that sufficient data was taken to estimate an integrated rate for at least deuteron emission.

The selection criteria for detecting a charged particle used the following cuts: coincidental hits in both thin and thick silicon (to remove accidental backgrounds and noise pulses); coincidence with a Muon-like hit in the muSc (to ensure the particles came from a muon a hit in the muSc must have occurred within $10 \mu\text{s}$ and have an amplitude corresponding to the typical energy deposited by a muon); no other muon hit in muSc within $10 \mu\text{s}$ (removes the mis-identification of protons coming from close-arriving muons, which would complicate

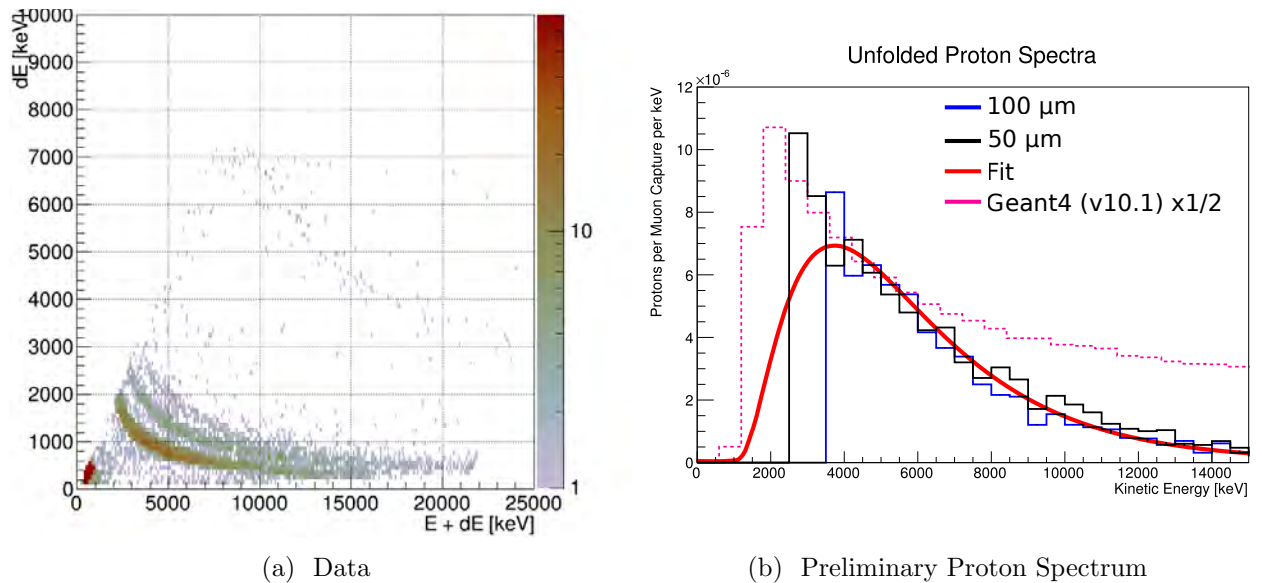


FIG. 3: Charged particle analysis and preliminary results. (a) Bands corresponding to the observation of different particle species at one of the silicon detectors. (b) The preliminary unfolded proton emission spectra from the two aluminium datasets of R2013. Only the range between 3.5 and 10 MeV is considered reliable, since outside of this range the unfolding of the different datasets does not seem stable. The uncertainty on each bin is still under analysis, so no error bars are shown here. Additionally the spectrum produced by standard Geant4 (v10.1) is shown, scaled by a factor 1/2.

the normalisation and timing distributions); time since muSc hit must be greater than 100 ns (removes scattered muons and protons coming from capture in the lead shielding or collimator).

Once a hit is identified as coming from a charged particle emitted after capture in the stopping target, particle identity cuts are applied based on either a geometrical cut on the dE/dx plot or using a probability that the event was from the desired particle, based on a Monte Carlo simulation. Fig. 3a shows the raw spectrum obtained after applying the above cuts for one of the silicon telescopes.

Preliminary results

Once the raw spectrum has been acquired, to obtain the ‘true’ spectrum following muon capture and account for scattering in the target and the detector’s acceptance, a Bayesian unfolding procedure is applied using the RooUnfold tool-kit [8]. The total response matrix for the combined target-detector system was found using a Monte Carlo simulation based on Geant4 [9]. For protons below around 2.5 MeV the acceptance drops to zero since below this energy they are unable to penetrate the target and thin silicon detector. Above around 4 MeV the response becomes roughly linear.

This procedure has been successfully applied to the aluminium datasets, however, for the active target runs using the silicon detector as the target, the statistics have been too low to perform a successful unfolding and so analysis of those datasets cannot continue. This is

unfortunate as it could in principal provide a good cross check of the unfolding process since more information on the distribution at the target is known. This is an area that future runs will address.

Fig. 3b shows the unfolded spectra where it can be seen that approximate agreement is found from around 3 to 10 MeV between the different 50 μm and 100 μm aluminium datasets. This region has been fitted with the same function as previously used by the COMET and Mu2e collaborations [10], which is empirically motivated and given by the equation:

$$f(x) = \left(1 - \frac{T_{\text{th}}}{x}\right)^{\alpha} \exp\left(-\frac{x}{T_0}\right), \quad (3)$$

where T_{th} is a threshold energy, expected to relate to the Coulomb barrier and Fermi energy of nucleons in the intermediate nucleus, α is a shape parameter that controls the form of the spectrum around the emission threshold, and T_0 should be related to the thermal energy associated with the nucleons in the free-Fermi gas nuclear model.

Based on this fit, the total proton emission rate per muon capture is estimated to be around $3.3 \pm 0.4\%$ although it must be stressed that this is a preliminary value with the final analysis and error assessment still ongoing. At this stage, the leading systematic errors are due to the unfolding process, misalignment in the geometry, uncertainties in the muon stopping distribution and beam profile at the target, and energy calibration of the silicon detectors. Each of these issues will be addressed directly by improvements in the upcoming Run 2015b.

The impacts of this measurement are already being felt for both COMET and Mu2e. Mu2e is re-optimising their proton absorber whilst for COMET Phase-I it has been removed. Furthermore, it is clear that the built-in modelling of muon capture in Geant4 needs improving, since it produces a much harder spectrum with a rate about 7 times too large, as shown by the overlay of the preliminary fitted AlCap spectrum to that from Geant4 in Fig. 3b.

RUN 2015A: NEUTRAL PARTICLES

Although the 2013 run did include neutron and X-ray detectors, the need for a vacuum chamber and thin target complicated the neutral particle measurement and reduced the final statistics. To improve the situation a two week run dedicated to measuring the neutral particle products without the vacuum chamber and with a thicker stopping target took place in June 2015. This used the piE5 beamline also at PSI, and future home to the Mu3e experiment [11]. With the thicker stopping target, a higher muon beam momentum of about 36 MeV/c could be used which increased the muon rate to about 10 kHz.

Setup

Unlike the charged particle run, no vacuum chamber was needed for the neutral particle measurement. As such, detectors were placed facing a central stopping target directly which improved acceptance and reduced backgrounds from scattered muons. Neutrons from the muon stopping target were observed by two liquid scintillator neutron detectors, whilst a

germanium detector measured the muonic X-rays and gammas. A LYSO array was also included in the set-up to monitor very hard gamma rays from the capture process.

As well as the removal of the vacuum chamber and the thicker target, several other improvements from the 2013 run were included. In particular, better ADCs increased the DAQ stability and a continuous input test pulse has improved the time calibration of signals. Furthermore, the neutron detectors had been calibrated before the run at the Triangle Universities Nuclear Laboratory (TUNL), in North Carolina, USA.

The data taken from Run 2015a is summarised in Table I. As well as measuring neutrons and photons from muon capture on aluminium, some time was dedicated to other targets. In particular, titanium, which is an alternative stopping target material for COMET and Mu2e, was studied as well as lead and water to understand potential backgrounds for this measurement.

Activation Study

The current baseline for COMET and Mu2e uses the prompt X-ray spectrum from the electromagnetic cascade of the stopped muon to estimate the number of stopped muons. However, one alternative idea is to look at X-rays coming from decays of the radioactive magnesium isotope Mg-27, left from muon capture. This might suffer fewer backgrounds than the prompt X-ray spectrum and so might be more reliable. To confirm this method a target was activated and monitored with a second germanium detector away from the beam area.

Analysis

Analysis of this run is in its very first stages, primarily focussed on data quality checks at this time. Nonetheless, the reconstruction of the neutron energy spectrum is moving along.

Firstly, since the liquid scintillator neutron detectors respond to both photons and neutrons, a separation routine must be developed to distinguish the two incoming particles. Pulse Shape Discrimination was used, where the ratio of the integral over an initial portion of the pulse to the integral over the full length indicates the cause of the pulse as a neutron or photon. Since photons in general deposit more energy in the tail of the pulse, the two particles can be separated which can be seen from Fig. 4a for the aluminium dataset of Run2015a.

TABLE I: Datasets acquired during R2015a

Target	Target Thickness (mm)	Approximate Exposure (hours)
Aluminium	2	42
Titanium	1.1	24
Lead	1.5	9
Water	~ 6 (not uniform)	4.5
Empty	-	3

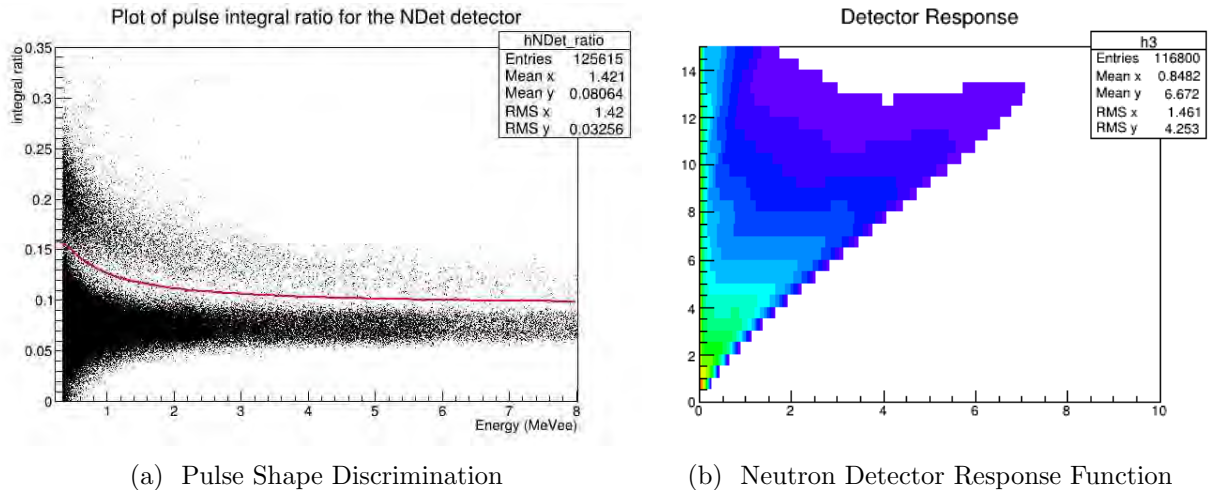


FIG. 4: Progress on analysis of the Neutron detectors. (a) Pulse shape discrimination showing separation between gammas (below red line) and neutrons (above red line) in the neutron detector. (b) The response function for the neutron detector obtained from the TUNL neutron beam.

Uncovering the neutron spectrum is further complicated by the fact that the observed energy is actually that of a nuclear recoil from a neutron reaching the detector. Unfolding must therefore be performed to recover the real neutron spectrum from the observed energy spectrum, using the response and acceptance of the detectors, based on simulation and calibration runs. The response matrix as a function of input energy can be seen in Fig. 4b.

Analysis of the other detectors is also under way, with the germanium detector being studied using the techniques developed for the 2013 run. The LYSO array is being studied externally to the AICap collaboration.

RUN 2015B: CHARGED PARTICLES

In November of this year, the charged particle measurement will be repeated and refined. In particular, an extra silicon detector with 1.5 mm thickness will be added to the two silicon telescopes which should increase the range for the total energy measurements up to about 25 MeV. To reduce our systematic uncertainties on the muon stopping distribution a scanning beam-monitor device will measure the beam profile at the target position during dedicated runs. Furthermore, a thinner active silicon target will improve the certainty of the stopping depth and distribution as well provide for a more rigorous cross-check of the unfolding procedures.

SUMMARY

In summary, future μ - e conversion searches need much improved knowledge of the muon capture process in order to predict and protect against the various daughter particles that can be produced. In particular for aluminium, the stopping target of choice for both Mu2e and COMET, the momentum spectrum and rates of both charged and neutral particle

emissions must be measured.

The AlCap experiment is a joint effort by COMET and Mu2e to make such a measurement. The first run in 2013 successfully observed the proton spectrum from about 4 to 10 MeV finding the total emission rate to be about 3 % per capture, with a relative uncertainty of about 10 % although analysis is on-going. A second run took place in June 2015 focussed on neutral particles and used a simpler set-up than the 2013 run which had required a vacuum to reduce scattering of the charged particles in air. Thicker stopping targets were used, allowing for higher beam energy and therefore a higher muon rate. Analysis of this data is only in its earliest stages at this time. Nevertheless for the analysis of the neutron spectrum, separation of neutrons from photons has been demonstrated and the detector response function and calibration has been obtained.

Finally, a third run in November 2015 will take place to improve the 2013 results by increasing the statistical sizes, extending the observed energy range and reducing systematic uncertainties.

ACKNOWLEDGEMENTS

I would like to thank the AlCap collaboration for the opportunity to present this work at NuFact as well as the STFC (UK) and the IoP's Research Student Conference Fund for funding the trip.

* Presented at NuFact15, 10-15 Aug 2015, Rio de Janeiro, Brazil [C15-08-10.2]

† benjamin.krikler07@imperial.ac.uk; On behalf of the AlCap collaboration

- [1] The COMET Collaboration, Tech. Rep., KEK (2015), URL http://www-lib.kek.jp/cgi-bin/kiss_prepri.v8?KN=201524001&OF=8.
- [2] B. E. Krikler, *An Overview of the COMET Experiment and Its Recent Progress* (2015), NuFact 2015.
- [3] L. Bartoszek et al. (Mu2e) (2014), 1501.05241.
- [4] W. H. Bertl et al. (SINDRUM II Collaboration), *Eur.Phys.J.* **C47**, 337 (2006).
- [5] A. Czarnecki, M. Dowling, X. G. i. Tormo, W. J. Marciano, and R. Szafron, *Phys.Rev.* **D90**, 093002 (2014), 1406.3575.
- [6] AlCap Collaboration, *Study of muon capture for muon to electron conversion experiments*, http://muon.npl.washington.edu/exp/AlCap/R-13-03.1_BV44.pdf, Accessed: 28-October-2015.
- [7] R. P. Litchfield (AlCap), *PoS NUFACT2014*, 095 (2015), 1501.04880.
- [8] T. Adye, in *Proceedings of the PHYSTAT 2011 Workshop, CERN, Geneva, Switzerland, January 2011, CERN-2011-006, pp 313-318* (2011), pp. 313-318, 1105.1160, URL <http://inspirehep.net/record/898599/files/arXiv:1105.1160.pdf>.
- [9] S. Agostinelli, J. Allison, K. Amako, J. Apostolakis, H. Araujo, P. Arce, M. Asai, D. Axen, S. Banerjee, G. Barrand, et al., *NIM in PRS A* **506**, 250 (2003), ISSN 0168-9002.
- [10] E. V. Hungerford, Tech. Rep., Department of Physics, University of Houston, Houston, Texas (1994).
- [11] A. Blondel, A. Bravar, M. Pohl, S. Bachmann, N. Berger, et al. (2013), 1301.6113.

An Overview of the COMET Experiment and Its Recent Progress*

Benjamin E. Krikler[†]
Imperial College London
(Dated: April 17, 2016)

Abstract

Forbidden in the Standard Model, Charged Lepton Flavour Violation is a strong probe for New Physics. The COMET Experiment will measure one of these processes: that of COherent Muon to Electron Transitions, where a muon converts to an electron in the presence of a nucleus without the emission of any neutrinos. COMET aims to improve the current limit on this process by four orders of magnitude. Being built in two phases at J-PARC, Tokai, Japan, COMET will first take data in 2018, where it should achieve a factor 100 improvement on present limits. This report gives an overview of μ - e conversion and the COMET experiment as well as a summary of the recent progress in construction and design.

INTRODUCTION

Lepton flavour conservation has been a key ingredient in our description of the world of particle physics since the first experiments showed a muon to decay to an electron only if accompanied by the emission of two other massless (or so they thought) fermions. Tests of the validity of this conservation have continued, through searches for neutrinoless muon decay to an electron accompanied by either a photon, an electron-positron pair, or in the presence of an atomic nucleus.

The COMET experiment will search for the last of these processes, in COherent Muon to Electron Transitions, where the nucleus is additionally left unchanged. COMET is being built at the Japanese Proton Accelerator Research Centre (J-PARC), in Tokai, Japan and will first take data in 2018, during Phase-I. Phase-II shall follow at the beginning of the next decade, and aims to improve the sensitivity to the μ - e conversion process by four orders of magnitude compared to the present limit. The following sections gives an overview of muon-to-electron conversion, an outline of the COMET experiment as a whole, and a summary of the recent progress in its construction and design.

THE MUON-TO-ELECTRON CONVERSION PROCESS

Muon-to-electron conversion occurs as the neutrinoless decay of a muon in the presence of an atomic nucleus. Since no neutrinos are emitted, and if the nucleus is left unchanged, the process is essentially a two-body interaction such that the energy of the out-going electron has a fixed value, E_e , given by the equation:

$$E_e = M_\mu - E_{\text{Binding}} - E_{\text{Recoil}} \quad (1)$$

where M_μ is the mass of the muon, E_{Binding} is the binding energy of the original muon-nucleus system, and E_{Recoil} is the recoil energy of the nucleus. The last two terms are small compared to the muon mass, so that the μ - e conversion signal occurs close to 105 MeV and is well separated from electrons of Standard Model muon decay (with neutrino emission), which for a free muon can only achieve energies up to half the muon mass.

Further background suppression can be achieved using timing information of the process, which is fixed to the lifetime of the muonic atom. In aluminium, the target of choice for COMET, the lifetime of the muon is about 864 ns, whilst the signal energy is $E_e = 104.97$ MeV.

To remove uncertainties in the initial muon wavefunction, the conversion rate is typically normalised to the rate of muon nuclear capture. The current limit on μ - e conversion comes

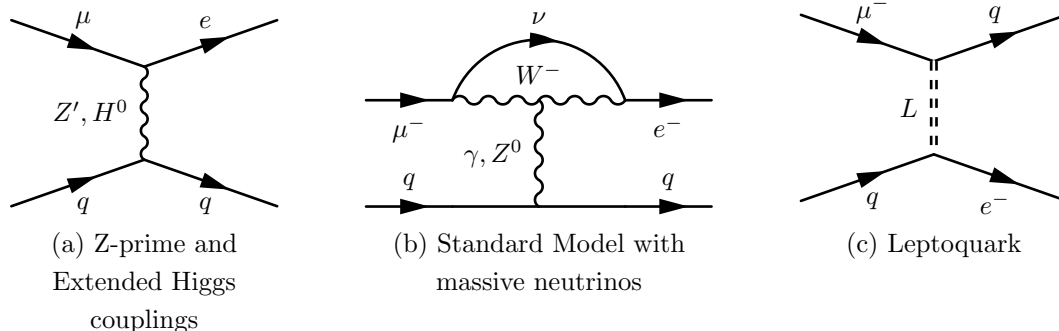


FIG. 1: Example Feynman diagrams that give rise to μ - e conversion. The dipole term with a SM neutrino in (b), whilst allowed in the SM with neutrino oscillations, is heavily GIM suppressed.

from the SINDRUM-II experiment [2], which used a gold target and set a 90% confidence limit on the Conversion Rate (C.R.) at 7×10^{-13} . COMET will be built in a staged approach hoping to improve this limit (but using an aluminium target) by about two orders of magnitude at each stage. The Single-Event-Sensitivity (SES) is the figure of merit for a μ - e conversion experiment's ability to observe the signal process. It is equivalent to the minimum value of the conversion rate where the experiment can still expect to see one signal event during the run. For COMET Phase-I, our SES is 3×10^{-15} , which should improve to 3×10^{-17} for Phase-II.

In principle, neutrino oscillations alone produce this sort of charged lepton flavour violation through penguin diagrams like that shown in Fig. 1b. However, if this were the only mechanism, the process would be highly GIM suppressed by the tiny mass squared difference of the neutrinos to conversion rates of order $\mathcal{O}(10^{-54})$. As a corollary, if New Physics is to be seen it must be well beyond both the Standard Model and even neutrino oscillations. There is no dearth however of models that give measurable conversion rates, including leptoquarks, Z -primes, extended Higgs couplings, supersymmetry, and of course heavy neutrinos [11] as shown in Fig. 1.

THE COMET EXPERIMENT

The COMET beamline and detectors are built to provide an intense, low energy muon beam, whilst minimizing all backgrounds. Key backgrounds include: intrinsic ones which occur when negative muons stop in a target, processes related to impurities in the beam, detector effects such as particle misidentification and pile-up, and cosmic backgrounds.

Using a delayed-time detector window, shown schematically in Fig. 2a with a pulsed proton beam removes most of the beam related backgrounds. Proton bunches of 100 ns produce a beam flash of about 200 ns (Fig. 2b) at the stopping target and by filling every second bucket in the J-PARC Main Ring (MR), a bunch separation of $1.17 \mu\text{s}$ can be achieved. Since the muon lifetime in aluminium is 864 ns, a high suppression of beam related backgrounds can be achieved, provided the extinction factor, which quantifies the number of protons in between bunches, can be kept low. Extinction factors of around 10^{-9} were originally thought necessary, but in late 2014 extinction levels of around 10^{-12} were measured at J-PARC [10].

The intrinsic backgrounds for COMET are any process involving a negative muon stopping in the target and resulting in an electron close to 105 MeV. This includes radiative

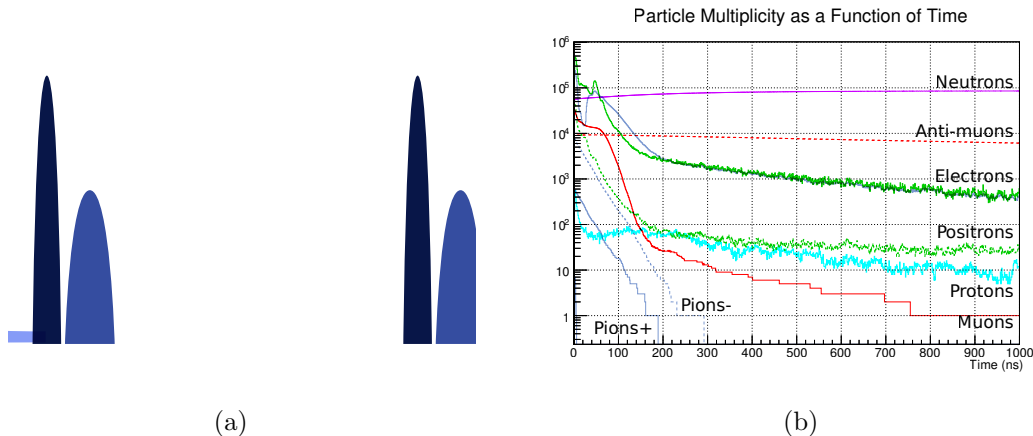


FIG. 2: Timing structures in COMET. (a) Schematic of the bunch structure and time-gated detector window used to reduce prompt beam-related backgrounds. (b) Simulated particle fluxes, integrated over the entire experiment and produced by protons at $t = 0$. The y-axis is in arbitrary units, but normalised to give the correct relative flux for each particle type.

muon capture followed by pair-production from the photon (either internally or externally) and the Standard Model decay of the bound muon. Of the two, the bound muon decay is expected to dominate. Whilst electrons from free muon decay cannot be produced above half the muon mass (in the muon rest frame), a high-energy tail arises from the nuclear recoil, and whilst it falls steeply above 55 MeV, it remains significant compared to the limit on the conversion rate. Since only the energy can be used to distinguishing such electrons from μ - e conversion electrons COMET requires a high precision particle detector and a minimal material budget for the stopping target. Reducing the stopping target length, however, must be offset by the decrease in the muon stopping rate, which favours a thicker target, and makes a low energy muon beam desirable. Furthermore, muons above 77 MeV/ c are undesirable since they can produce electrons with signal-like energies.

To achieve a low energy, high intensity muon beam with few impurities COMET uses two novel approaches: capturing backwards emitted pions and muons from the production target using superconducting solenoid fields, and a combination of bent solenoids, vertical dipole fields and collimators along the muon beam transport. Both of these remove the high-energy components of the beam whilst maintaining a high muon intensity, and the long decay length of the bent transport solenoids additionally improves beam purity since most pions will decay.

COMET Phase-II

Fig. 3b shows a schematic of the configuration for Phase-II. From this it can be seen that the muon transport beamline captures pions coming backwards from the production with respect to the proton beam, which itself enters from the top-left corner of the image. In Phase-II, this secondary beam is then transported around 180° of bent solenoid (with a small straight section in the middle for possible collimators and field matching). The beam is then directed on to the stopping target which is made of 200 μm thick aluminium disks, and followed by a beam blocker that should absorb any beam that does not stop in the target. Electrons produced in the target are then collected by a graded magnetic field, and transported around a second section of bent solenoid with a much larger aperture. The

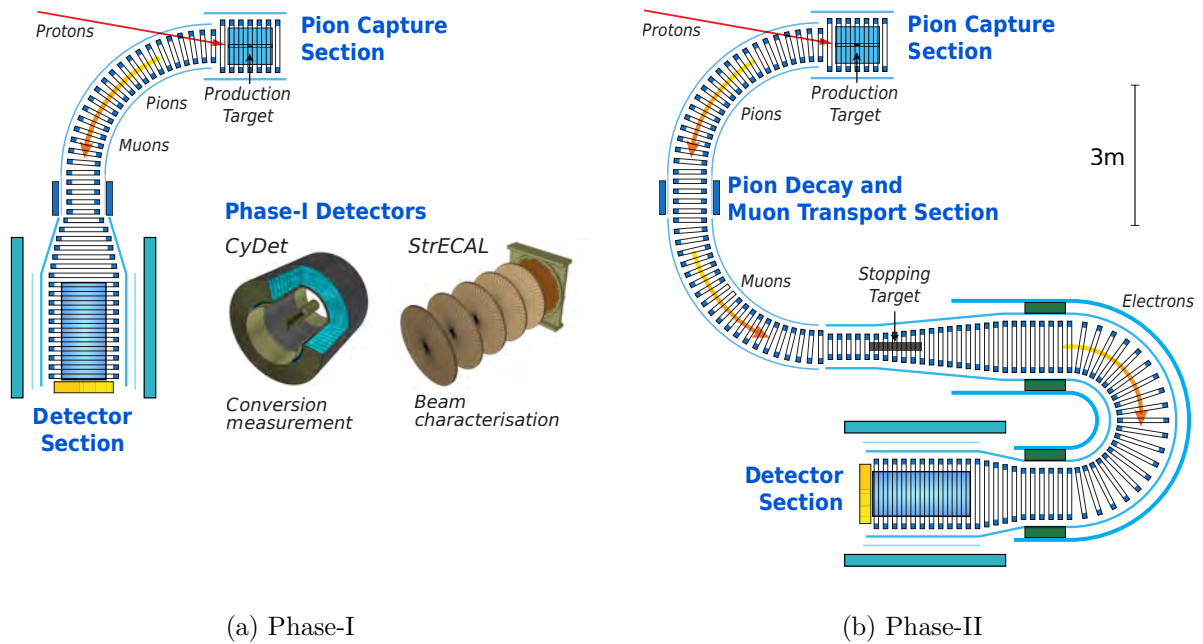


FIG. 3: The COMET experiment in the two different phases. (a) The Phase-I beamline configuration, which is identical to Phase-II up to the first 90° of the bent muon transport solenoid and excluding the production target. (b) The Phase-II beamline then moves the detector solenoid back, extends the muon transport beamline, and adds an extra bent solenoid between the stopping target and detector.

dipole field along this region is tuned to remove low energy electrons from decay-in-orbit and other charged particles coming from the stopping target. Additionally, having no line-of-sight between the target and the detector helps reduce backgrounds from neutral particles such as photons from radiative muon capture. Finally, the electrons enter the detector system formed by a series of straw tracker planes and a crystal electromagnetic calorimeter (ECAL).

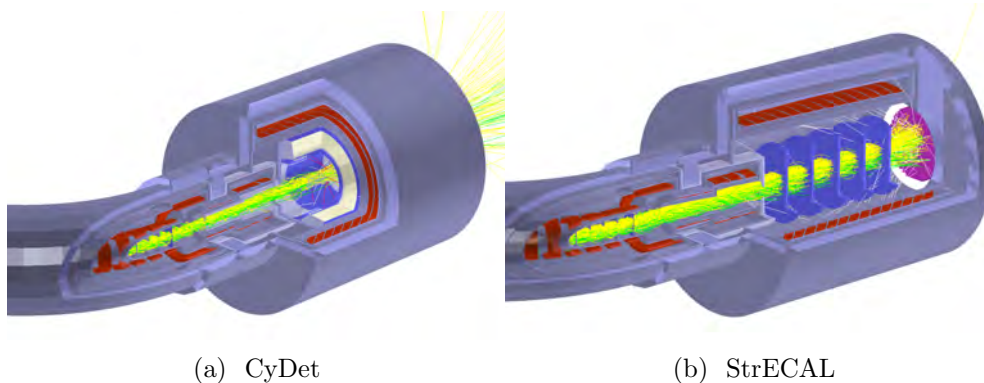


FIG. 4: Simulated event displays for the two different Phase-I detectors. Track colour shows the particle ID: electrons (yellow), muons (green), photons (white), protons (red).

COMET Phase-I

Given the number of new techniques being employed for COMET Phase-II there are many uncertainties associated with the expected production yields, beamline dynamics and consequently the final background rates. It was therefore decided to take a staged approach, such that COMET Phase-I will build the production target and first 90° of muon transport beamline. Phase-I will operate two different configurations, either to perform beam characterisation or to make a μ - e conversion measurement, aiming for a hundred-fold improvement on the limits set by the SINDRUM-II experiment. Fig. 3a illustrates the beamline that will be used for Phase-I, showing how the first 90° for Phase-II will be built at this stage. To be able to both study the beam properties and measure $\mu^- + N \rightarrow e^- + N$ at Phase-I, two different detector systems will be used as shown in Fig. 4.

CONSTRUCTION AND ON-GOING RESEARCH AND DEVELOPMENT

Facility Construction

Fig. 5 shows two images of the construction of the COMET facility. The COMET building joins on to the existing Hadron Hall at J-PARC and contains the experiment area on the lowest level, a staging and craning area on the first and second floor, and offices and control rooms on the top floor. In January 2015, the fifteenth COMET collaboration meeting was held in J-PARC and KEK where the collaboration were able to view the nearly finished building. By March 2015, the first beamline components were being installed, starting with the first 90° of bent muon transport solenoid that will be used for Phase-I.

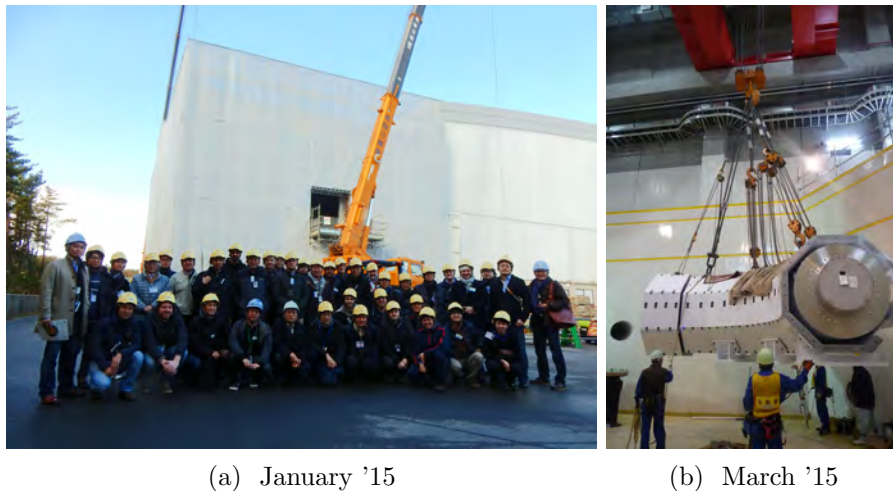


FIG. 5: Construction of the COMET building and beamline. (Fig. 5a) The COMET collaboration in front of the nearly finished COMET Experiment Building at the 15th collaboration meeting in January 2015. (Fig. 5b) Installation of the first 90° of the bent muon transport solenoid in March 2015.



FIG. 6: Preparation of various components of the CyDet detector. The outer and inner walls have been purchased (left) and wire stringing has begun (right).

The CyDet: a Cylindrical Detector for the Phase-I Physics Measurement

In order to achieve the desired two orders of magnitude improvement over SINDRUM-II at Phase-I, the detector needs to be blind to most of the beam flash, and the large number of low-energy electrons produced by bound muon decay in the target. The detector known as the CyDet (Cylindrical Detector) will be tasked with this measurement. It combines a Cylindrical Drift Chamber (CDC) with two rings of Cherenkov Hodoscope and Scintillation counters which provide a trigger and t_0 for each event.

Contained in a co-axial solenoidal field, the inner radius of the CDC is tuned such that the detector is blind to most of the beam flash, which will enter and remain in the region close to the solenoidal axis given its relatively low momentum. The same is true for the bulk of the bound muon decay spectrum, the majority of which has momentum less than 60 MeV. Given the stopping target diameter and the 1 T field magnitude in the detector, the inner wall of the CDC is set to 60 cm which means electrons with less than 60 MeV coming from the target are unable to reach the detector. Fig. 4a shows an event display from a simulation of the CyDet with the beam flash from a single proton bunch passing through it.

Construction of the CDC is well under way with about 40% of all wires already strung. In total 150 days are expected to be needed to complete wire stringing, which should finish in November when tensioning checks can be performed before transportation to the COMET facility. In the meantime, tests using prototype versions have been on-going using both cosmic rays and electron beams at Tohoku University in Japan. Additionally, significant work is under way to study the use of a purely track-based trigger, which could allow the triggering hodoscopes to be removed and higher beam rates supported.

The StrECAL: a Straw Tube Tracker and Crystal ECAL Detector

The StrECAL, consisting of several Straw Tube Tracker stations (five in Phase-I, but possibly more for Phase-II) followed by an ECAL is able to measure both momentum and energy of particles over the full cross section of the beam as is shown in Fig. 4b. As such, in Phase-I it will predominantly be used to profile the beam and understand the impurity

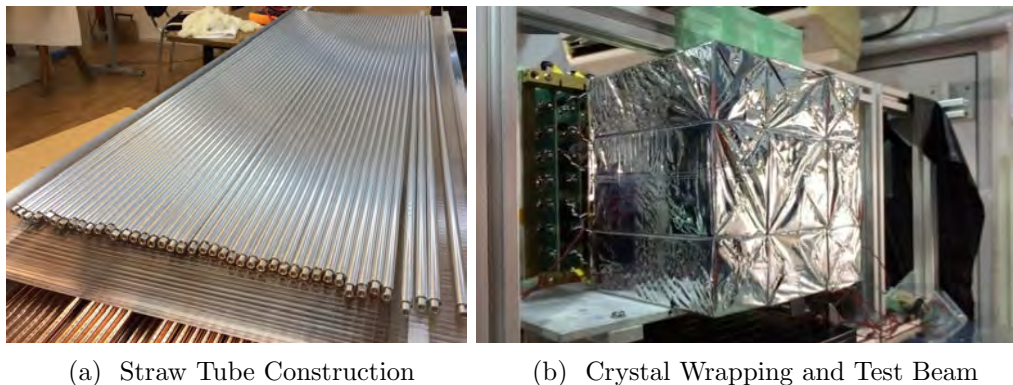


FIG. 7: Preparation of various components of the StrECAL detector. (a) Production of 2500 aluminised-Mylar has been completed and a prototype detector has been prepared for beam and cosmic tests. (b) Crystals for the ECAL wrapped and mounted for characterisation and resolution studies in an electron beam.

rate, momentum distributions, transport beam optics, and additionally the production target distributions. Furthermore, by building, testing and running the StrECAL in Phase-I, significant understanding of the detector can be progressed in anticipation of Phase-II.

For the Straw Tube Tracker, straw production for Phase-I was recently completed, with 2500 tubes being made in total. The straws use the single-seam welding procedure developed for NA62 [4] which is able to reduce the straw thickness whilst maintaining mechanical strength.

In parallel, work on the ECAL is well under way. The decision to use LYSO (Lutetium Yttrium Sulphate) was taken in February 2015 and procurement has already begun with 200 crystals expected to have been purchased by the end of the fiscal year. Despite its increased cost, LYSO was chosen over GSO due to its increased light yield and response time which lead to an improved energy resolution and greater robustness against pile-up. These properties have been tested and confirmed in dedicated beam tests at PSI, Zurich and at Tohoku University in Japan. Each crystal is $2 \times 2 \times 12$ cm which is about 10 radiation lengths for an electron at 105 MeV and in total, by Phase-II, about 2272 crystals will be used. Avalanche photodiodes (APDs) will be mounted to each crystal which will then be wrapped in Teflon tape and grouped into modules of 2×2 crystals to be wrapped in aluminised Mylar.

Simulation, Offline Software and Expected Backgrounds

Simulating the COMET experiment is no easy task, given that some 10^{19} Protons are expected to be stopped in the production target at Phase-I whilst to achieve the desired sensitivity fewer than one background events should occur. This means the simulation needs to be both highly efficient and highly detailed, with accurate modelling of the geometry and material properties, magnetic fields, and underlying physics processes.

However, the current modelling of hadronic processes is such that there is large disagreement between different models for the pion and muon yield in the backwards direction at the production target from protons with 8 GeV kinetic energy. To improve the situation, data from the HARP experiment [3] and some input from the MuSiC [12] experiment has been used, in addition to running with multiple different hadronic production models, including

Geant4 (QGSP_BERT_HP) [9], MARS [8], Fluka [1] and PHITS [5].

In addition, there are limitations in the description of the physics of bound muons. For muon nuclear capture, whilst the branching fraction is known to be about 61% for a stopped negative muon in aluminium [7] the rates for subsequent charged or neutral particle emission are not well known. The AlCap experiment [6] will measure daughter particles and the results from this experiment are feeding back in to the COMET simulation. At the same time, default Geant4 does not accurately reflect the most recent theoretical calculation of the electron spectrum for bound muon decay, instead using only a rather crude parametrisation to adapt the distribution from free muon decay spectrum. Custom physics modelling is therefore being included to address these issues.

The simulation chain begins with the production target, where any of the codes listed above can be used, then moves on to the beam and detector simulations which is based on Geant4. Energy deposits produced at this stage can then either be fed directly into a detector and electronics response package, or via a resampling package that allows a smaller set of proton events to be robustly resampled and smeared in time. The COMET Software includes all these aspects (and more) and recently reached its first stable release in April this year. Since then, two large scale productions have taken place.

DEVELOPMENTS SINCE NUFACT 2015

Since the NuFact conference in August, significant progress has been made on several fronts. For the CDC, wire stringing was completed in November, and wire tensioning measurements are well under way.

Several beam test programs have been carried out including a test at PSI to look at novel particle identification (PID) methods using the ECAL, and separate Straw Tracker and CDC prototype tests at Tohoku University, Sendai, Japan.

On the simulation side, custom muon physics has been completely implemented, including the bound muon decay spectrum and preliminary results from the AlCap experiment. Additionally, there have been significant improvements to the geometry and field calculations, which are shown in Fig. 8.

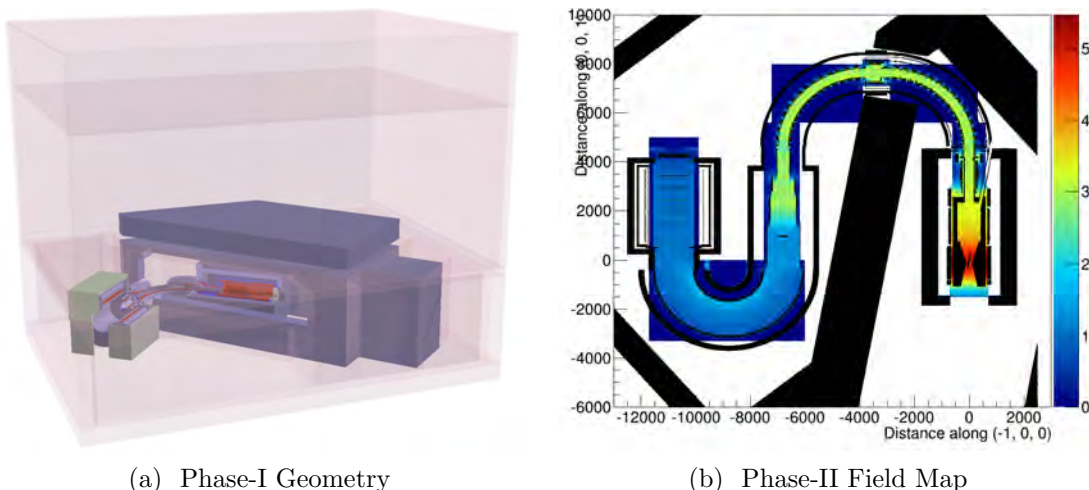


FIG. 8: (a) The current representation of the geometry for Phase-I. (b) The magnetic field magnitude for Phase-II (colour, units are Tesla) with a slice through the geometry overlaid (black).

SUMMARY

The process of muon to electron conversion is a highly sensitive probe for new physics beyond the Standard Model. The COMET experiment will make the first measurement of this process since the SINDRUM-II experiment in 2006. Using several new techniques including a pulsed proton beam, backwards capture of pions and muons from the production target, and bent solenoids combined with tuned dipole fields and collimators allow for Phase-II's four-orders-of-magnitude improvement to the signal sensitivity compared with SINDRUM-II. Given the uncertainties associated with such novel approaches, COMET will first run Phase-I with a reduced transport beamline and two dedicated detectors, with data taking beginning in 2018, and an expected sensitivity of 3×10^{-15} . Progress is well under way, in particular, for the building and facility construction, delivery of the first beamline sections, detector development, and offline software.

ACKNOWLEDGEMENTS

I would like to thank the COMET collaboration for giving me the opportunity to present at NuFact and providing feedback on the presentation and this report. Additionally I would like to thank the STFC (UK) and IoP's Research Student Conference Fund for funding my participation.

* Presented at NuFact15, 10-15 Aug 2015, Rio de Janeiro, Brazil [C15-08-10.2]

† benjamin.krikler07@imperial.ac.uk; On behalf of the COMET collaboration

- [1] A. Ferrari et al. FLUKA: A multi-particle transport code (Program version 2005). 2005.
- [2] W. H. Bertl et al. A Search for muon to electron conversion in muonic gold. *Eur.Phys.J.*, C47:337–346, 2006.
- [3] M. G. Catanesi et al. The HARP detector at the CERN PS. *Nucl. Instrum. Meth.*, A571:527–561, 2007.
- [4] F. Hahn et al. NA62: Technical Design Document. Technical Report NA62-10-07, CERN, Geneva, Dec 2010.
- [5] H. Iwase et al. Development of General-purpose Particle and Heavy Ion Transport Monte Carlo Code. *Journal of Nuclear Science and Technology*, 39(11):1142–1151, 2002.
- [6] B. E. Krikler. Update on the alcap experiment. *NuFact 2015*, 2015.
- [7] D. Measday. The nuclear physics of muon capture. *Physics Reports*, 354(45):243 – 409, 2001.
- [8] N. V. Mokhov. The MARS code system user's guide version 13(95). *FERMILAB-FN-0628*, 1995.
- [9] S. Agostinelli et al. Geant4 - a simulation toolkit. *NIM in PRS A*, 506(3):250 – 303, 2003.
- [10] The COMET Collaboration. COMET Phase-I: Technical Design Report. Technical report, KEK, May 2015.
- [11] W. Altmannshofer et al. Anatomy and phenomenology of fnc and cpv effects in susy theories. *Nuclear Physics B*, 830(12):17 – 94, 2010.
- [12] Y. Hino et al. A Highly intense DC muon source, MuSIC and muon CLFV search. *Nuclear Physics B (Proceedings Supplements)*, 253-255:206–207, 2014.

Searches for Charged Lepton Flavor Violation with the ATLAS Detector at the LHC*

Craig Blocker on behalf of the ATLAS Collaboration[†]

Brandeis University

(Dated: April 19, 2016)

Abstract

ATLAS has searched for charged lepton flavor violation in several processes, including decays of Standard Model particles ($H \rightarrow \mu\tau$ and $Z \rightarrow e\mu$) and beyond the Standard Model physics (Z' or $\tilde{\nu}$ decay, $\tilde{t} \rightarrow lb$, neutralino decay in R-parity-violating supersymmetry theories, decays of Quantum Black Holes, and decays of heavy Majorana neutrinos). No significant excess of events over Standard Model expectations is seen and limits are set.

INTRODUCTION

Neutrino oscillations show that lepton flavor is not a good symmetry of Nature. An important and interesting question is whether charged leptons also exhibit lepton flavor violation (LFV).

ATLAS looked for several possible signatures of charged lepton flavor violation, including Higgs $\rightarrow \mu\tau$; $Z \rightarrow e\mu$; Z' or $\tilde{\nu} \rightarrow e\mu$, $e\tau$, or $\mu\tau$; \tilde{t} decay in a B-L R-parity violating (RPV) supersymmetry (SUSY) theory; multilepton events or displaced vertices in RPV SUSY; decays of Quantum Black Holes; and production of heavy, Majorana neutrinos. No excess of events over Standard Model (SM) expectations was seen and limits were set. Some of these limits are compatible with or exceed limits on couplings from precision, low-energy experiments.

LHC AND THE ATLAS EXPERIMENT

The Large Hadron Collider (LHC) collides protons with protons at high energy. All the results in this article are from 20.3 fb^{-1} of data with a center-of-mass energy of 8 TeV taken during 2012 with the ATLAS detector.

ATLAS [1] is one of four major detectors at the LHC. It is a general purpose detector with roughly cylindrical symmetry. The inner tracking volume consists of silicon strip detectors, silicon pixel detectors, and transition radiation detectors surrounded by a 2 T superconducting solenoid. Outside the solenoid and in the endcap regions are lead-liquid Argon electromagnetic calorimeters followed by steel-scintillator hadronic calorimeters. Outside the calorimeters is the muon spectrometer consisting of trigger chambers, three layers of precision tracking chambers, and superconducting magnets giving a toroidal field.

The physics objects most important for the analyses presented here are electrons, muons, jets, and missing transverse momentum. Electrons are identified from a track in the inner detector associated with energy deposited in the electromagnetic calorimeter consistent with an electron. Muons are combined inner tracks and muon spectrometer tracks. Jets are identified from local energy clusters in the calorimeters by the anti- k_t algorithm with a distance parameter of 0.4. The missing transverse momentum vector is the negative of the sum of the momentum vectors in the plane transverse to the beam of the physics objects (electrons, muons, photons, and jets) and any energy clusters in the calorimeters not associated with these objects. The magnitude of the missing transverse momentum vector is known as the missing transverse energy (E_T^{miss}).

HIGGS $\rightarrow \mu\tau$

The observation of the Higgs boson completes the Standard Model (SM) but also raises many important questions, including “Is this the SM Higgs?” Observation of non-SM decays, such as LFV decays, would be direct evidence for physics beyond the SM.

Possible LFV Higgs decays include $H \rightarrow e\mu$, $H \rightarrow e\tau$, and $H \rightarrow \mu\tau$. The decay $H \rightarrow e\mu$ is constrained to have a branching ratio less than about 10^{-8} from low energy results limits on $\mu \rightarrow e\gamma$, but the decay $H \rightarrow \mu\tau$ could be as large as $\sim 10\%$ and not be in conflict with low energy limits (Ref. [2] and references therein).

ATLAS searched for the decay $H \rightarrow \mu\tau$ [2] in events with a muon with transverse momentum $p_T > 26$ GeV and a hadronic tau decay with $p_T > 45$ GeV. Two signal regions and two control regions (one for $W + \text{jets}$ and one for $t\bar{t}$ and single-top production) were defined based on the transverse masses of the muon- E_T^{miss} and $\tau_{\text{had}}-E_T^{\text{miss}}$ systems, the number of jets, and the number of b-tagged jets. The number of events in each region were simultaneously fit to constrain the backgrounds and search for a possible signal.

The data along with the SM expectations and a possible Higgs signal are shown in Figure 1 for the two signal regions combined. No significant excess of events was seen, and a 95% confidence level (CL) limit was placed on the $H \rightarrow \mu\tau$ branching ratio of 1.92%, compared to an expected limit of 1.24%.

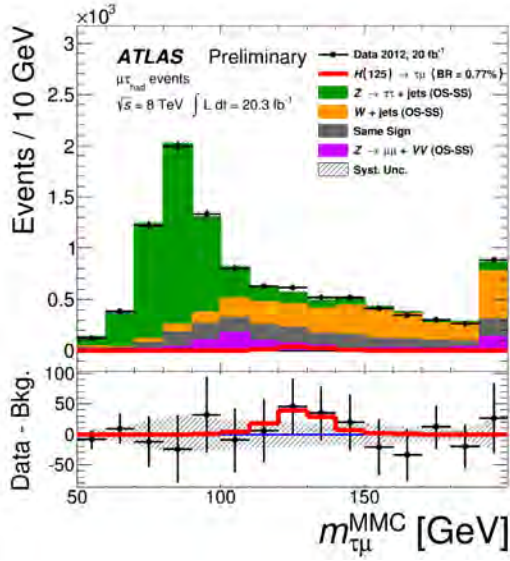


FIG. 1: The $\mu\tau$ invariant mass distribution for the combined signal regions showing the data, SM expected background, and a potential Higgs decay for $BR = 0.77\%$ (taken from Ref. [2]).

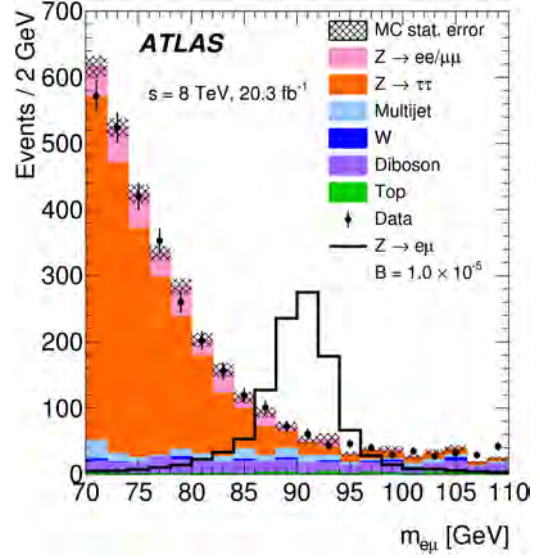


FIG. 2: The $e\mu$ invariant mass after all selections showing the data, expected backgrounds, and a potential signal for a branching ratio of 10^{-5} (taken from Ref. [3]).

$Z \rightarrow e\mu$

A search for the LFV decay $Z \rightarrow e\mu$ was done [3]. Events were required to have exactly one electron with $p_T > 25$ GeV and exactly one muon with $p_T > 25$ GeV and opposite sign. Events with a jet with $p_T > 30$ GeV or $E_T^{\text{miss}} > 17$ GeV were rejected.

The resulting $e\mu$ invariant mass distribution (Figure 2) was fit to a background distribution plus a signal contribution. No significant signal contribution was found, and the limit on the branching ratio was determined to be $BR(Z \rightarrow e\mu) < 7.5 \times 10^{-7}$ at the 95% CL. This improves upon the previous limit from LEP of 1.6×10^{-6} but is not as low as the inferred limit of $\sim 10^{-12}$ from limits on the decay $\mu \rightarrow eee$.

Z' or $\tilde{\nu} \rightarrow e\mu, e\tau, \text{ or } \mu\tau$

ATLAS searched for production of a resonance decaying to $e\mu, e\tau, \text{ or } \mu\tau$ [4]. A spin-0 resonance was modeled as an RPV sneutrino. A spin-1 resonance was modeled as a Z' with the same couplings to quarks as the Z boson.

For this search, only 1-prong hadronic tau decays were used. The missing transverse

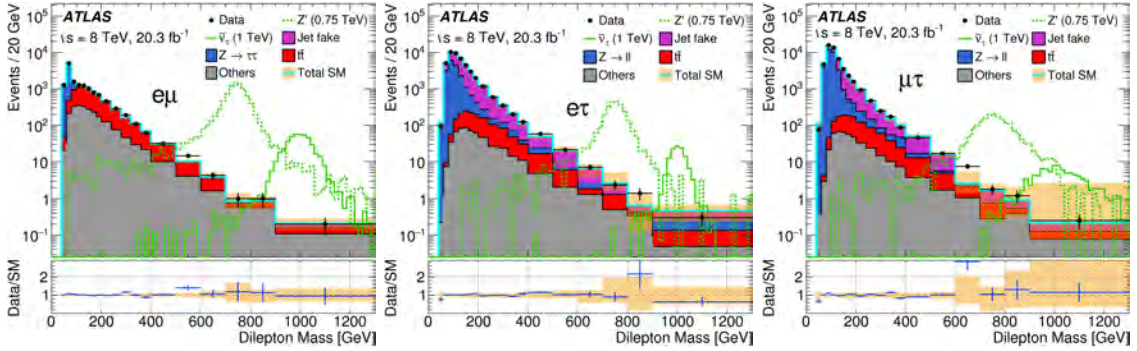


FIG. 3: The $e\mu$, $e\tau$, and $\mu\tau$ invariant mass distributions showing the data, expected SM backgrounds, and potential signals (taken from Ref. [4]).

momentum vector and the assumption that the neutrino in the tau decay is collinear with the visible tau decay products was used to correct the tau's momentum, which significantly improved the dilepton invariant mass resolution.

Events were selected with two leptons of different flavor and opposite sign. Each lepton had $p_T > 25$ GeV. The dilepton invariant masses distributions are shown in Figure 3. No significant excesses above the SM expectations were seen, and the limits on cross sections times branching ratios at the 95% CL are shown in Figure 4.

In RPV SUSY, the sneutrino couples only to down-like quarks, d and s in this case. The coupling dependences and model assumptions are different for the ATLAS resonance search than for low-energy experiments, but the ATLAS limits are comparable or better than those from low-energy experiments for all the tau modes and for $s\bar{s} \rightarrow \tilde{\nu} \rightarrow e\mu$. The low-energy limits from μ - e conversion ($K_L \rightarrow e\mu$) are about an order of magnitude better than those from ATLAS for the production of $e\mu$ via $d\bar{d}$, $d\bar{s}$, or $s\bar{d}$.

STOP SQUARK $\tilde{t} \rightarrow \ell b$

A possible extension of supersymmetry is the addition of an R-parity violating (RPV) B-L U(1) symmetry which violates lepton number but not baryon number (Ref. [5] and references therein). In one such model, the stop squark \tilde{t} is the lightest SUSY particle and decays to $b\ell$, where ℓ is a charged lepton.

ATLAS searched for \tilde{t} pair production followed by decay to either $b\ell$ or $b\mu$ [5], giving events with two b-tagged jets and dileptons (ee , $\mu\mu$, or $e\mu$) of opposite sign. Events with

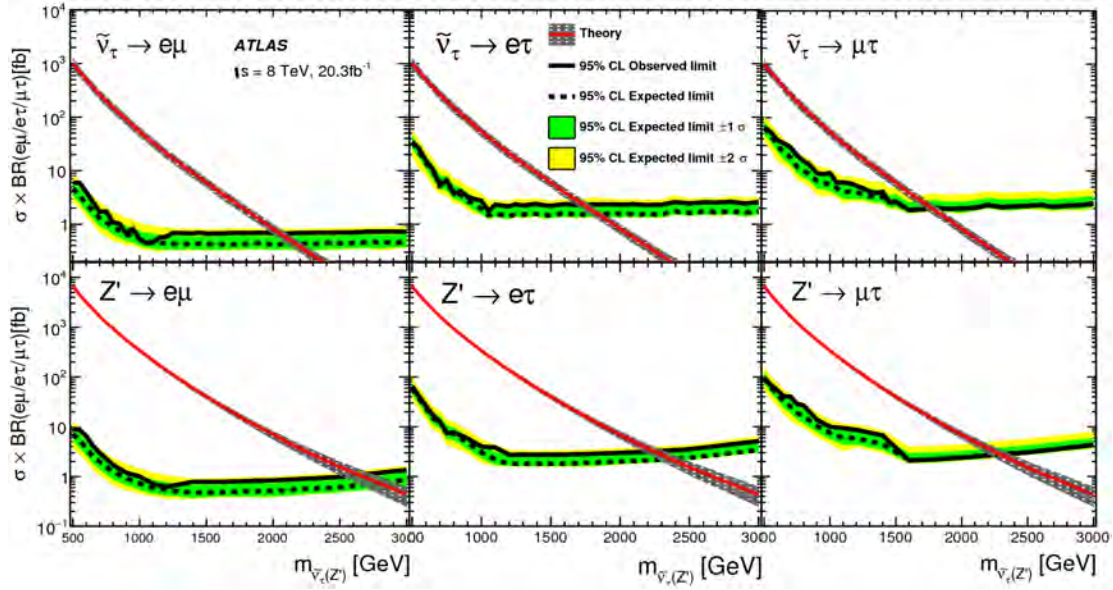


FIG. 4: The 95% CL limits on the cross section times branching ratio for $\tilde{\nu}$ (top) or Z' (bottom) decaying to $e\mu$, $e\tau$, or $\mu\tau$ (taken from Ref. [4]).

same flavor leptons with an invariant mass consistent with the Z mass were rejected. The jet-lepton pairing that gave the smallest difference between the masses of the two lepton-jet combinations was chosen. The lepton-jet invariant masses, their difference, and H_T (the scalar sum of the transverse momenta of the two b-jets and the two leptons) were used to define two signal regions and several control regions. Two events were observed, consistent with SM expectations. The 95% CL regions in the $\text{BR}(\tilde{t} \rightarrow b\tau)$ versus $\text{BR}(\tilde{t} \rightarrow be)$ plane (the sum of the branching ratios to be , $b\mu$, and $b\tau$ was constrained to one) is shown in Figure 5 for various \tilde{t} masses.

MULTILEPTON EVENTS AND DISPLACED VERTICES IN RPV SUSY

In RPV SUSY, the lightest supersymmetric particle (LSP) (assumed to be a neutralino $\tilde{\chi}$ here) is not stable. ATLAS searched for neutralino decays with leptons ($\tilde{\chi} \rightarrow \ell\ell\nu$, $q\bar{q}\ell$, or $q\bar{q}\nu$) [6]. The neutralinos were assumed to be pair-produced either via gluinos ($q\bar{q} \rightarrow \tilde{g}\tilde{g} \rightarrow q\bar{q}\tilde{\chi}q\bar{q}\tilde{\chi}$) or squarks ($q\bar{q} \rightarrow \tilde{q}\tilde{q} \rightarrow q\tilde{\chi}\bar{q}\tilde{\chi}$), leading to events with multiple leptons.

Events with 4ℓ , $3\ell\tau$, $2\ell 2\tau$, 3ℓ , or $\ell^\pm\ell^\pm$ were selected, where ℓ is e or μ . Any event consistent with coming from $Z \rightarrow \ell\ell$, $\ell\ell\gamma$, or $\ell\ell\ell\ell$ was rejected. The numbers of observed events were compatible with SM expectations, and 95% CL limits were placed on various

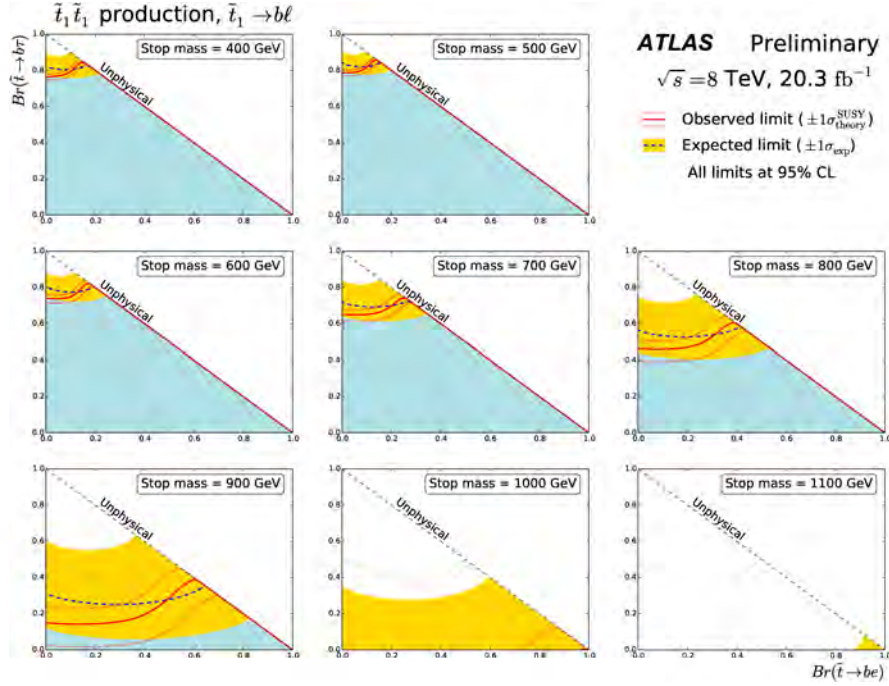


FIG. 5: Observed and expected limits on the \tilde{t} leptonic branching ratios for various \tilde{t} masses. The areas under the solid red curves are excluded at the 95% CL. The dashed lines are the expected limits (taken from Ref. [5]).

production mechanisms dependent on the gluino or squark mass. An example limit plot is shown in Figure 6, showing the limits on the gluino mass assuming $m_{\tilde{\chi}}/m_{\tilde{g}} = 0.1$ and using the lll and $l^{\pm}l^{\pm}$ events as a function of the neutralino branching ratios to taus for left-handed ($BR(\tau_L)$) and right-handed ($BR(\tau_R)$) superfields.

If the RPV SUSY couplings are sufficiently small, the LSP may live sufficiently long to give a displaced secondary vertex. ATLAS searched for displaced vertices with either one lepton (e or μ) or two leptons (ee , $\mu\mu$, or $e\mu$) [7]. Observed events were consistent with SM expectations. Limits depend on SUSY masses, the production mechanism, SUSY parameters. An example cross section limit is shown in Figure 7.

QUANTUM BLACK HOLES

In theories with large extra dimensions, it is possible to produce Quantum Black Holes at the LHC (Ref. [8] and references therein). For black holes, only quantum numbers associated with local gauge invariance (such as charge and color) are expected to be conserved, allowing for violation of both lepton flavor and lepton number. ATLAS searched for Quantum Black

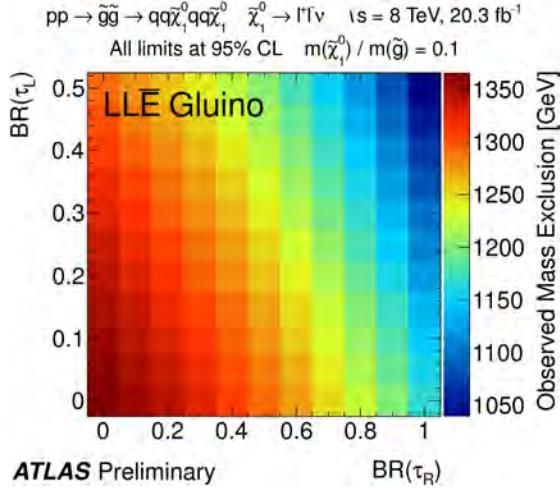


FIG. 6: Limits on the gluino mass assuming $m_{\tilde{\chi}_1^0}/m_{\tilde{g}} = 0.1$ and using $\ell\ell\ell$ and $\ell^\pm\ell^\pm$ events (taken from Ref. [6]).

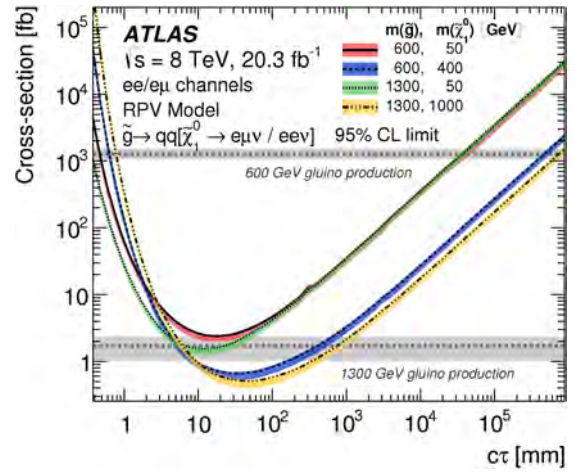


FIG. 7: Limit on the cross section as a function of $c\tau$ for displaced vertices with ee or $e\mu$ (taken from Ref. [7]).

Holes decaying to a lepton (e or μ) plus a jet [8]. Figure 8 shows the e -jet and μ -jet invariant mass distributions for the data, expected SM backgrounds, and potential Black Hole signals. Limits were placed on the cross section times branching ratio as a function of the model parameter M_{th} (Figure 9).

ATLAS also searched for Black Holes in other modes that have LFV in the model but where it would not be manifest in the signal [9, 10].

HEAVY MAJORANA NEUTRINOS

A very important question in neutrino physics is whether they are Dirac or Majorana particles. In some theories, such as those with a see-saw mechanism or left-right symmetric models, the partner to a Majorana neutrino is expected to be heavy (Ref. [11] and references therein). Furthermore, different flavor heavy neutrinos can in principle mix, giving rise to lepton flavor violation.

ATLAS searched for heavy neutrinos in events with two same-sign leptons ($e^\pm e^\pm$ or $\mu^\pm \mu^\pm$) with at least two jets that might be produced in processes such as those shown in Figure 10 [11]. No excess of events was seen over SM expectations, and limits were placed at the 95% CL. The limits depend on the mode and the masses of the additional gauge bosons in the model. An example of an excluded region in the mass of the heavy neutrino (m_N) versus the mass of a right-handed W (m_{W_R}) plane for the $\mu\mu$ is shown in Figure 11.

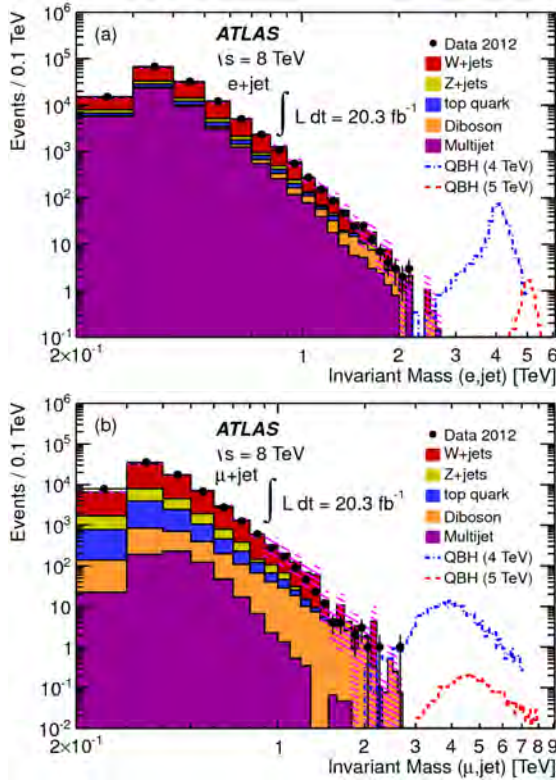


FIG. 8: Invariant mass distributions for e -jet (left) and μ -jet (right) showing the data, SM backgrounds, and potential Black Hole signals (taken from Ref. [8]).

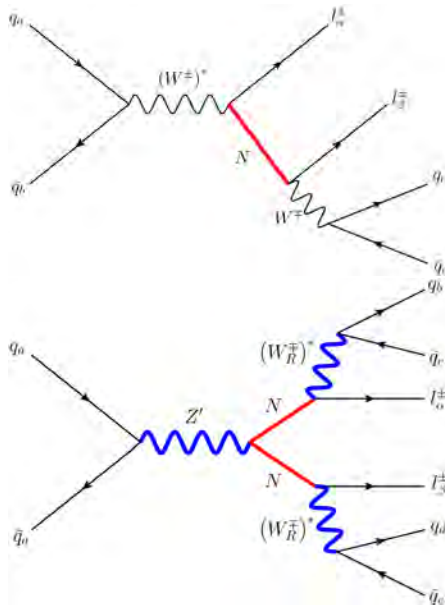


FIG. 10: Possible processes for producing same-sign dilepton events via heavy neutrinos (taken from Ref. [11]).

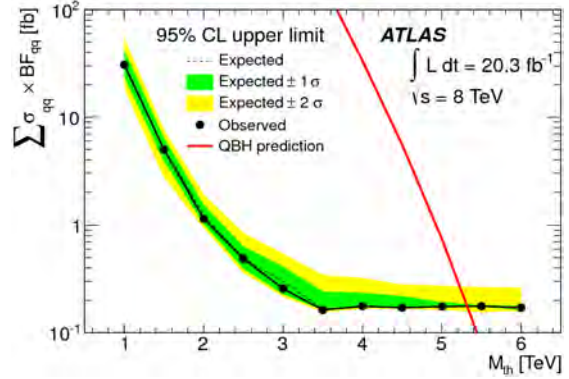


FIG. 9: Limit on the cross section times branching ratio for production of a Black Hole decaying to lepton + jet as a function of the model parameter M_{th} (taken from Ref. [8]).

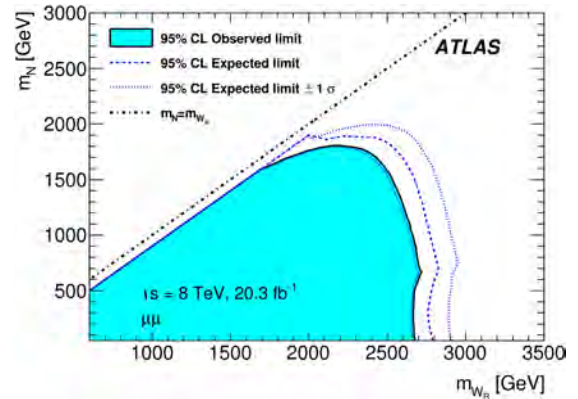


FIG. 11: Excluded region in the heavy neutrino mass versus right-handed W mass plane for the $\mu\mu$ mode (taken from Ref. [11]).

CONCLUSIONS

ATLAS has searched for LFV signatures in both SM particle decays (H and Z) and in processes from beyond the SM physics. No excess of events over SM expectations was seen, and limits were placed, some of which are comparable or better than those from precision, low-energy experiments. Since the coupling dependences and model assumptions for limits from the LHC and from low-energy experiments are often different, these measurements complement each other.

* *Presented at NuFact15, 10-15 Aug 2015, Rio de Janeiro, Brazil [C15-08-10.2]*

† blocker@brandeis.edu; Speaker; ATLAS Collaboration

- [1] ATLAS Collaboration, “The ATLAS Experiment at the CERN Large Hadron Collider,” *JINST* **3**, S08003 (2008).
- [2] ATLAS Collaboration, “Search for lepton-flavour-violating $H \rightarrow \mu\tau$ decays of the Higgs boson with the ATLAS detector,” accepted by EPJC (2015), arXiv:1508.03372 [hep-ex].
- [3] ATLAS Collaboration, “Search for the lepton flavor violating decay $Z \rightarrow e\mu$ in pp collisions at $\sqrt{s} = 8$ TeV with the ATLAS detector,” *Phys. Rev. D* **90**, 072010 (2014), arXiv:1408.5774 [hep-ex].
- [4] ATLAS Collaboration, “Search for a Heavy Neutral Particle Decaying to $e\mu$, $e\tau$, or $\mu\tau$ in pp collisions at $\sqrt{s} = 8$ TeV with the ATLAS Detector,” *Phys. Rev. Lett.* **115**, 031801 (2015), arXiv:1503.04430 [hep-ex].
- [5] ATLAS Collaboration, “A search for B-L R -parity-violating scalar top decays in $\sqrt{s} = 8$ TeV pp collisions with the ATLAS experiment,” ATLAS-CONF-2015-015, <http://cdsweb.cern.ch/record/2002885> (2015).
- [6] ATLAS Collaboration, “Constraints on promptly decaying supersymmetric particles with lepton-number- and R -parity-violating interactions using Run-1 ATLAS data,” ATLAS-CONF-2015-018, <http://cdsweb.cern.ch/record/2017303> (2015).
- [7] ATLAS Collaboration, “Search for massive, long-lived particles using multitrack displaced vertices or displaced lepton pairs in pp collisions at $\sqrt{s} = 8$ TeV with the ATLAS detector,” *Phys. Rev. D* **92**, 072004 (2015), arXiv:1408.5774 [hep-ex].
- [8] ATLAS Collaboration, “Search for Quantum Black Hole Production in High-Invariant-Mass Lepton+Jet Final States Using pp Collisions at $\sqrt{s} = 8$ TeV and the ATLAS Detector,” *Phys. Rev. Lett.* **112**, 091804 (2014), arXiv:1311.2006 [hep-ex].
- [9] ATLAS Collaboration, “Search for microscopic black holes in a like-sign dimuon final state using large track multiplicity with the ATLAS detector,” *Phys. Rev. D* **88**, 072001 (2013), arXiv:1308.4075 [hep-ex].
- [10] ATLAS Collaboration, “Search for microscopic black holes and string balls in final states with leptons and jets with the ATLAS detector at $\sqrt{s} = 8$ TeV,” *JHEP* **1408**, 103 (2014), arXiv:1405.4254 [hep-ex].
- [11] ATLAS Collaboration, “Search for heavy Majorana neutrinos with the ATLAS detector in pp collisions at $\sqrt{s} = 8$ TeV,” *JHEP* **1507**, 162 (2015), arXiv:1506.06020 [hep-ex].

The Muon $g - 2$ Experiment at Fermilab*

Kevin R. Lynch^{1,2,†}

(The Fermilab Muon $g - 2$ Collaboration)[‡]

¹*Department of Earth and Physical Sciences,
York College, City University of New York,
94-20 Guy R. Brewer Blvd, Jamaica, NY 11451 USA*

²*The Graduate Center, City University of New York,
365 Fifth Avenue New York, NY 10016 USA*

(Dated: April 18, 2016)

Abstract

There remains a tantalizing discrepancy between the Standard Model prediction for the muon $g - 2$, and the value measured by the Brookhaven E821 Experiment. This discrepancy has driven designs for multiple experiments. Here I present current progress on the construction of the Fermilab E989 experiment which will improve on the Brookhaven experiment by a factor of four, to a combined uncertainty of 0.14 ppm.

INTRODUCTION

Understanding the anomalous magnetic moment of the muon has consumed the energies of generations of physicists, from the likes of Dirac and Schwinger, down to the present day. Advances in the theory and measurement of $g - 2$ have fed off each other and have productively informed all other subfields of particle and nuclear physics.

The most recent chapter closed at the Brookhaven National Laboratory (BNL) in the United States at the turn of the century, followed by publication of the final report of the Muon $g - 2$ Experiment E821 [1]. This experiment reached an ultimate combined uncertainty of 0.54 ppm. This precision is sufficiently high to access the very small electroweak contributions present at second order. Parallel developments at the same precision have

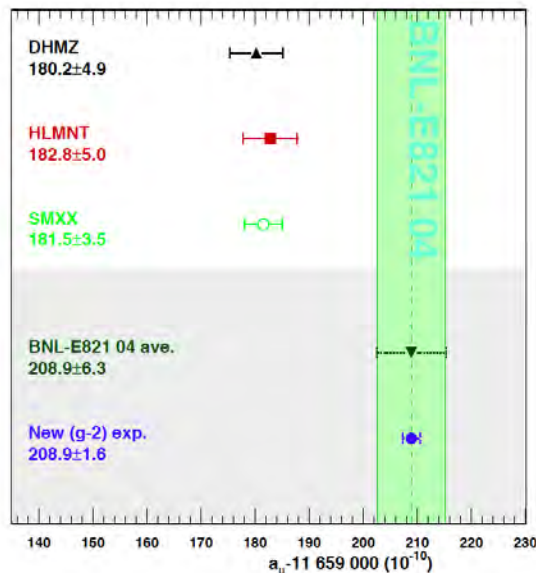


FIG. 1: This plot summarizes the current discrepancy between the consensus Standard Model theory prediction for the muon anomaly and the BNL E821 experimental result.

been required in the theory. Consensus among contributors to the ongoing theory efforts makes it appear likely that the results of E821 show a discrepancy from the Standard Model prediction, at the level of 3.6 standard deviations; see Figure 1.

This unresolved state-of-affairs fairly begs for significant continued effort on both the theoretical and experimental fronts. The US High Energy Physics community has recognized the importance of this measurement: Recommendation 22 in the recent report of the Particle Physics Project Prioritization Panel (P5) [2] recommends completing the Fermilab E989 Muon $g - 2$ project under all funding scenarios. Here, I describe the current progress on bringing this next generation storage ring experiment to the data taking stage. Other contributions in this workshop present progress on a radically different method for measuring the muon magnetic anomaly at the Japan Proton Accelerator Research Center (JPARC).

THE METHOD

Modern electron g -factor experiments have dramatically improved uncertainties by going to smaller experiments with very large observation times on individual particles in cyclotron traps [3]. The brief muon lifetime prevents that approach, so muon experiments have by necessity proceeded by a different path: the last four precision $g - 2$ experiments all utilized storage ring techniques, to measure time dependent ensemble spin precession. Understanding this method is key to understanding the design of the experiment.

Muon beams are naturally highly polarized: muons are born in a two-body decay of spin-zero pions via the $V - A$ (left-handed) weak interaction. As neutrinos are only observed in left-handed chirality, angular momentum conservation demands that all muons have the same spin orientation. In the case of muon $g - 2$, we maximize and utilize that beam ensemble polarization to effect our measurement.

To produce a muon beam, a proton beam impinges upon a pion production target. Those pions are collected, momentum selected, and transported through a decay channel, along which they decay to muons. Those muons are then injected into a storage ring with an extremely uniform magnetic field. For those muons which are stored in the ring, the momentum will precess at the cyclotron frequency

$$\omega_C = \frac{eB}{mc\gamma},$$

while the spin undergoes both Larmor and Thomas precession

$$\omega_S = \frac{geB}{2mc} + (1 - \gamma)\frac{eB}{mc\gamma} .$$

The difference between these two frequencies,

$$\omega_a = \omega_S - \omega_C = \frac{g - 2}{2} \frac{eB}{mc} = a_\mu \frac{eB}{mc} ,$$

is known as the anomaly frequency. Measuring all quantities in this expression (in particular, ω_a and B) gives the anomaly directly.

In practice, things are of course not so simple. Muons will not remain in a storage ring with only a single uniform magnetic field. This field will retain particles by focusing in the plane perpendicular to the field, but will do nothing to prevent vertical losses (along the field direction). Since we want an extremely uniform magnetic field across the entire volume of stored muons, we can not use magnetic fields to perform vertical focusing. Instead, we utilize an electrostatic quadrupole focusing system; the induced horizontal defocusing is overcome by the magnetic field.

In the presence of vertical motions and the electric fields, our previous expression relating ω_a to a_μ must be modified:

$$\vec{\omega}_a = \frac{e}{mc} \left[a_\mu \vec{B} - \left(a_\mu - \frac{1}{\gamma^2 - 1} \right) \vec{\beta} \times \vec{E} - a_\mu \frac{\gamma}{\gamma + 1} (\vec{\beta} \cdot \vec{B}) \vec{\beta} \right] ,$$

The first term in the square brackets is our original result. The second encodes the effect of the electrostatic quadrupoles. The final term comes from the vertical momentum component. Since the deviations from the horizontal plane will be small, let me ignore the final term for now; in the experiment, we must correct for the vertical motions, but this *pitch correction* is small and well controlled. The key insight here is that the electric field effects vanish for a particular “magic” value of the momentum, given by

$$\gamma_{\text{magic}} = \sqrt{1 + \frac{1}{a_\mu}} .$$

For muons this corresponds to a momentum $p_{\text{magic}} = 3.091 \text{ GeV}/c$. Producing large numbers of muons at this momentum demands only quite modest proton beam energy; at Fermilab, we will use an 8 GeV beam. Of course since there is a distribution of momenta in the stored beam, corrections must be applied to the final result; again, this *E-field correction* turns out to be small and well controlled.

Key to the experiment then is measurement of ω_a . The chiral structure of the weak interactions gives us direct access to the spin direction, at least on a statistical basis. In the three body decay of the muon, the electron is not emitted isotropically. In the rest frame of the muon, with the spin aligned along a coordinate axis, the differential decay distribution for the electron momentum direction is given (in units of the dimensionless electron energy $y = E_e/E_{\max}$) by

$$\frac{d^2\Gamma_{\mu^\pm}}{dyd\Omega} = n(y) (1 \mp a(y) \cos \theta) ,$$

with $n(y) = y^2(2 - y)$ and $a(y) = (2y - 1)/(3 - 2y)$. This results in the highest energy positrons (electrons) being emitted preferentially parallel (anti-parallel) to the muon spin orientation. In the lab frame the combination of spin precession and energy dependent asymmetry is observed as a sinusoidal variation in the observed number of positrons (electrons) above a threshold energy

$$f(t) = N_0(E_{\text{thresh}})e^{-t/\tau} [1 + A(E_{\text{thresh}}) \cos(\omega_a t + \phi)] \quad (1)$$

This threshold is chosen to maximize the statistical power of the collected data, which is proportional to the asymmetry $A(E)$ (rising with energy) and the square of the observed number of electrons $N(E)$ (falling with energy); $A(E)$ and $N(E)$ are the integrals of $a(y)$ and $n(y)$ from the chosen threshold to E_{\max} . During analysis, we will provide a multi-level blinding process to the analysis so that neither the Collaboration as a whole, nor the analyzers individually, will be able to steer (whether intentionally or not) the analysis toward a “preferred” value.

To extract the anomaly, we must know the absolute value of the magnetic field distribution, integrated over the storage volume, in addition to ω_a . A number of pulsed NMR probes, including fixed, plunging, and traveling, are used to measured the proton Larmor precession frequency in the field

$$\omega_P = \frac{eB}{2m_P} g_p$$

Like the ω_a analysis, this frequency is also hidden by a blinding procedure, further protecting from unintentional bias.

The combination of ω_a and ω_P allows calculation of a_μ .

$$a_\mu = \frac{\omega_a/\omega_P}{\mu_\mu/\mu_P - \omega_a/\omega_P} , \quad (2)$$

TABLE I: A summary of the ω_a systematics in both the BNL E821 and expected improvements for the FNAL E989 experiment [4].

Category	E821 [ppb]	E989 Improvement Plans	Goal [ppb]
Detector Gain changes	120	Better laser calibration	
		low-energy threshold	20
Pileup	80	Low-energy samples recorded	
		calorimeter segmentation	40
Lost muons	90	Better collimation in ring	20
Coherent Betatron Oscillations	70	Higher n value (frequency)	
		Better match of beamline to ring	< 30
Field and pitch corrections	50	Improved tracker	
		Precise storage ring simulations	30
Total	180	Quadrature sum	70

where the ratio of magnetic moments was measured at the Los Alamos National Laboratory (LANL) in the United States utilizing the same spherical calibration probe used in the E821 NMR calibration procedure.

IMPROVING THE SYSTEMATICS

To improve the overall error relative to E821 by a factor of four will require improvements not only in statistics (a factor of at least twenty), but also systematics. In the BNL experiment, systematic errors contributed 0.28 ppm, and statistics 0.46 ppm, to the final, combined 0.54 ppm result.

When discussing improvements to the systematics, it helps to recall that we are performing two parallel measurements - ω_a and ω_P - and we divide our systematic studies along these lines. We intend to improve substantially on both of these, to better than 0.1 ppm in each category. The major ω_a systematics are illustrated in Table I, and ω_P systematics in Table II.

What do we need to do to reach these goals? Since it is impossible to discuss the

TABLE II: A summary of the ω_P systematics in both the BNL E821 and expected improvements for the FNAL E989 experiment [4].

Category	E821 [ppb]	Main E989 Improvement Plans	Goal [ppb]
Absolute field calibration	50	Special 1.45 T calibration magnet with thermal enclosure; additional probes; better electronics	35
Trolley probe calibrations	90	Plunging probes that can cross calibrate off-central probes; better position accuracy by physical stops and/or optical survey; more frequent calibrations	30
Trolley measurements of B_0	50	Reduced position uncertainty by factor of 2; improved rail irregularities; stabilized magnet field during measurements*	30
Fixed probe interpolation	70	Better temperature stability of the magnet; more frequent trolley runs	30
Muon distribution	30	Additional probes at larger radii; improved field uniformity; improved muon tracking	10
Time-dependent external magnetic fields	–	Direct measurement of external fields; simulations of impact; active feedback	5
Others †	100	Improved trolley power supply; trolley probes extended to larger radii; reduced temperature effects on trolley; measure kicker field transients	30
Total systematic error on ω_p	170		70

experimental requirements along with all of our plans in the short space available here, I choose to concentrate on just a few issues. It should be understood, however, that much more work has been done to date than I have room to discuss.

Implementation details

The FNAL implementation of the experiment is an evolutionary upgrade of the E821 model. The majority of the major devices, in fact, have been transplanted from BNL to FNAL, and form the backbone of the experiment. Despite this, nearly all of the subsystems are undergoing major upgrades in functionality and/or precision to meet the stringent new requirements.

At FNAL, the experiment is part of a larger muon physics program - which includes the muon-to-electron conversion (Mu2e) search experiment - in a new Muon Campus facility close to Wilson Hall. The $g - 2$ experiment occupies the new MC1 experimental hall and is served by a new beamline. Proton delivery to the muon campus requires modest upgrades to the accelerator complex which are compatible with the ongoing neutrino program. Protons will continue to be accelerated by the Booster ring to 8 GeV. Bunches will be extracted from the Booster and transported to the Recycler ring. After extraction from the Recycler, the protons will impinge on an upgraded production target in the AP0 hall - occupying the former Tevatron antiproton production facility. Pions will be focused by a lithium lens and momentum selected by a pulsed dipole; these devices served the antiproton program and required significant upgrades to operate reliably with the more demanding $g - 2$ pulse rates. Pions will be sent to the Delivery ring - which will serve as part of an 800 m long decay line, effectively eliminating pions from the beam - and will be extracted after one turn for delivery to the $g - 2$ storage ring. Upgrades to the Delivery ring (the former antiproton Debuncher) are designed to accommodate both single-turn muon extraction for $g - 2$ and resonant proton extraction for Mu2e. Extracted beam will traverse a new line to the $g - 2$ Storage Ring, which was moved - with much fanfare - from BNL to FNAL in the summer of 2013 [5].

Once the muons have reached the storage ring, the work of the accelerator physicists gives way to the particle physicists. Of course, the beam must be transported from the outside to the inside of the ring; the storage volume is a torus with radius 7.11 m, with an

unobstructed circular cross sectional of diameter 90 mm. Over this region, the storage field, averaged over azimuth and the weighted by the muon storage distribution, must be uniform to better than 1 ppm. To reach the storage region, the fringe fields must be cancelled without destroying the field uniformity in the neighboring storage region. This key task is the job of a superconducting magnetic inflector. The baseline design for the FNAL experiment is to refurbish and reuse the E821 inflector. This device is a truncated double cosine magnet with an external superconducting shield that both maintained a field free channel within the fringe field of the storage ring and reduced the impact of the injection channel field on the storage field at the required level. Despite the success of this device, some design choices - in particular, that windings cover the ends of the beam channel - significantly impact the efficiency of beam injection. Significant R&D is ongoing to design a new inflector with open ends and a wider bore as a possible option should scope contingency be available at a later date.

The exit of the E821 inflector is centered 77 mm from the center of the storage region. Without additional work, the muon ensemble would not store. The task of moving the beam on-orbit is handled by three fast kicker modules, each consisting of a pair of plates and a high voltage, high-speed pulse forming network. The current sheets created during the kick locally suppress the magnetic field by an amount sufficient to deflect magic momentum muons by 10.8 mrad, sufficient to move the distribution onto the nominal orbit. New fast kicker modules are being designed for the FNAL effort, based on a Blumlein triaxial transmission line design. This should enable a significantly shorter, higher amplitude current pulse, improving storage efficiency. Simultaneously, the new design will retain significant margin to allow a higher kick for compatibility with the proposed increase in the inflector bore, which will shift the centroid of the muon bunch further outward radially, requiring a stronger kick deflection.

As mentioned in the overview above, maintaining a stored beam requires electrostatic quadrupole fields for vertical focusing. This is accomplished by a four quadrant system, which will be largely reused. A number of upgrades are in progress to improve various aspects of the system. Of perhaps greatest importance, the system will be operated at a higher field index to move the frequency of coherent betatron oscillations far away from the second harmonic of the $g - 2$ oscillation frequency. Second, during injection, the BNL muon beam passed through the first outer quadrupole plate and insulating supports; ongoing

redesign of this part of the system should significantly reduce losses resulting from scattering.

The decay electrons have lower energy than the muons, with correspondingly smaller orbital radii in the magnetic storage field. Therefore, decay positron paths will curve inward, towards the center of the ring. The magnet yoke is C-shaped, with the open side toward the ring center, and the beam vacuum vessel is scalloped to minimize scattering during the inward spiral. Twenty-four segmented PbF_2 calorimeters will be located symmetrically around the ring. The output signal waveforms from each segment will be digitized and stored. Offline processing produces the energy and time histograms needed to fit the physics and extract ω_a .

Analysis improvements

In E821, oscillation spectra were constructed from individual event timings, the so called “T-method” of analysis. The output signals from the calorimeters were waveform digitized, zero suppressed, and the over-threshold samples were stored in onboard RAM until read out by the data acquisition system. Individual pulses were fit to a template, below threshold pulses were rejected, and histograms were built. Construction cost and memory limitations were severe constraints when the digitizer modules were designed necessitating this approach.

In the intervening years, the impact of Moore’s law on transient and persistent data storage, network data transmission, and computation resources, have been very large, while the physics have changed little. These gains permit us to reimagine the entire data collection and processing scheme. We building a new set of highly segmented calorimeters, and custom waveform digitizers which will be able to store and readout every sample during the measurement period, for every segment of every calorimeter. Advances in parallel and distributed computation and in high speed networks promise significantly higher throughput data acquisition and offline analysis systems.

Access to the full data record for each channel enables fabulous possibilities undreamed of at the E821 design stage. We intend to again pursue the T-method, but access to the full data stream enables many improvements in the areas of threshold and pedestal stability tracking, as well as vast improvements in pileup reconstruction. In addition, the full data stream permits a new integrated charge collection, or “Q method” approach. Here, we integrate data from all data samples from early to late, and fit the resulting oscillatory

signal. Because this method sums over all data samples, it is impacted differently by various systematic errors. The complementarity of these two methods combined with the blinded analysis will provide significant strength to our final result.

IN CONCLUSION

As of this workshop, the Fermilab Muon $g - 2$ Project had reached a number of important milestones: the ring had been shipped from BNL to FNAL and installed in the new MC1 experiment hall at the Fermilab Muon Campus. As the workshop got underway, the storage ring superconducting magnets had just been energized for the first time in fourteen years, validating the condition of the full system; a few small issues had been discovered and fixes were being planned and scheduled, and the field shimming plans for 2015 were being finalized. A host of other construction and R&D activities were underway at many Laboratory and University sites both inside and outside the USA. Under the current budget profile, the experiment will begin full commissioning and data taking at the beginning of calendar year 2017, followed by three years of data taking.

The speaker's work on the Muon $g - 2$ effort is supported by the U.S. Department of Energy, Office of Science, Office of High Energy Physics under Award Number DE-FG02-13ER41931.

* *Presented at NuFact15, 10-15 Aug 2015, Rio de Janeiro, Brazil [C15-08-10.2]*

† `klynch@york.cuny.edu`; Speaker

‡ URL: <http://muon-g-2.fnal.gov/>

- [1] G. W. Bennett et al. (Muon G-2), *Phys. Rev.* **D73**, 072003 (2006), [hep-ex/0602035](http://arxiv.org/abs/hep-ex/0602035).
- [2] Particle Physics Project Prioritization Panel (P5) (2014), URL http://science.energy.gov/~media/hep/hepap/pdf/May-2014/FINAL_P5_Report_053014.pdf.
- [3] D. Hanneke, S. Fogwell, and G. Gabrielse, *Phys. Rev. Lett.* **100**, 120801 (2008), 0801.1134.
- [4] J. Grange et al. (Muon g-2) (2015), 1501.06858.
- [5] Fermi National Accelerator Laboratory, *The Big Move* (2013), URL <http://muon-g-2.fnal.gov/bigmove/>.

The Mu2e Experiment at Fermilab*

Kevin R. Lynch^{1,2,†}

(The Fermilab Mu2e Collaboration)[‡]

¹*Department of Earth and Physical Sciences,
York College, City University of New York,
94-20 Guy R. Brewer Blvd, Jamaica, NY 11451 USA*

²*The Graduate Center, City University of New York,
365 Fifth Avenue New York, NY 10016 USA*

(Dated: April 18, 2016)

Abstract

The Mu2e Experiment at Fermilab will search for the coherent, neutrinoless conversion of a muon to an electron in the field of an atomic nucleus. Such charged lepton flavor violating events have never been observed, but are predicted to occur in many Beyond the Standard Model scenarios at rates accessible to our experiment. I outline the physics and key issues for the experiment, our progress on design and construction to date, and prospects for the future.

INTRODUCTION

The Mu2e effort holds a prominent place in the near term future of the U.S. High Energy Physics program. In fact, the recent report of the Particle Physics Project Prioritization Panel (P5) - which advises the U.S. Government on HEP community priorities - advises completion of the Mu2e Experiment under all budget scenarios considered [1]. With a project baseline cost of \$270 million, this involves a significant investment of available resources; why, then, this level of interest?

Although charged lepton flavor violation (CLFV) has never been observed experimentally, we know that it must occur: neutrino flavor oscillations coupled with loops guarantees the existence of CLFV; see Figure 1. However, even with the most optimistic parameter values in the PMNS neutrino mixing matrix U , the Standard Model rate prediction is tiny

$$\text{Br}(\mu \rightarrow e\gamma) = \frac{3\alpha}{32\pi} \left| \sum_{k=2,3} U_{\mu k}^* U_{ek} \frac{\Delta m_{1k}^2}{M_W^2} \right|^2 < 10^{-54} .$$

There is no conceivable experiment which could observe a branching ratio this small. While this initially seems disappointing, it is a major opportunity in disguise as *any* experimental observation of CLFV becomes incontrovertible evidence for new physics Beyond the Standard Model (BSM)!

Searches for CLFV have a long and distinguished history of guiding both theorists and experimentalists in elucidating the foundations of particle physics. For at least seventy years, there has been a long line of experiments searching for violations in both meson and lepton decays. Early non-observation of $\mu \rightarrow e\gamma$ at the 10% level laid rest to the notion that the muon was simply an electromagnetic excitation of the electron [2]. Later, the non-observation of the same signal at the 10^{-8} level proved that muon and electron neutrinos were distinct species [3].

Today, CLFV searches form their own cottage industry: there are numerous ongoing searches in many meson and tau channels at the LHC, while there are a number of significant efforts worldwide in muon decays. A large number of these efforts were represented at this workshop. In $\mu \rightarrow e\gamma$, the MEG search at PSI has pushed down nearly to the limits of their sensitivity [4], while the Mu3e developments at PSI promise a very sensitive search for $\mu^+ \rightarrow e^+e^+e^-$ [5]. Neutrinoless conversion provides perhaps the most promising avenue for large sensitivity improvements, with at least three ongoing efforts at advanced stages of development: DeeMee [6] and COMET [7] at the JPARC, and the Mu2e Experiment at Fermilab [8].

The conversion experiments have a major kinematic advantage over MEG and Mu3e: in the latter experiments, the signal electrons of interest are hard to distinguish from the bulk of electrons from the vast background of Michel electrons from normal muon decay. In contrast, because the conversion signal comes from the two body decay of a heavy muonic atom, the signal electrons are monochromatic with an energy roughly that of the muon mass. This puts the signal well above the vast bulk of the background, and just beyond the high energy recoil tail from normal muon decay in orbit (DIO). Herein lies the advantage of the conversion channel, and the experiments are designed to take advantage of this kinematic separation.

In terms of accessing new physics, the conversion process has an additional advantage, as it can be driven by more different types of physics than other channels. For instance, because of the final state photon, the $\mu \rightarrow e\gamma$ channel can only be driven by dipole type interactions in the low energy effective theory. By contrast, conversion can be driven by both dipole interactions and four fermion processes. This gives the conversion process significantly deeper reach into heretofore unexplored energy regimes. In Figure 3, we show the reach of

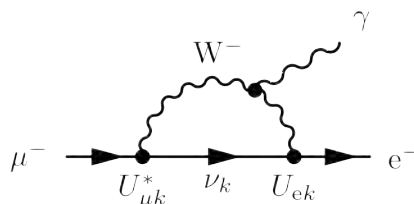


FIG. 1: A Standard Model source of charged lepton flavor violating $\mu \rightarrow e\gamma$ arises from neutrino flavor oscillations within loops; these events have an unmeasurably small branching ratio.

History of $\mu \rightarrow e\gamma$, $\mu N \rightarrow eN$, and $\mu \rightarrow 3e$

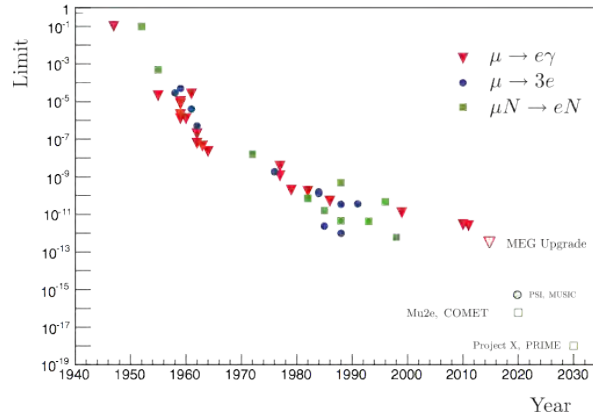


FIG. 2: The history of CLFV searches in muon decay stretch over seventy years and many decades in rate.

both MEG and Mu2e in terms of the model of de Gouvêa and Vogel [9]. This model has two terms in the CLFV Lagrangian, corresponding to dipole and four fermi interactions, and the dimensionless parameter κ interpolates between the dipole and fermi limits

$$\mathcal{L}_{\text{cLFV}} = \frac{1}{\kappa + 1} \frac{m_\mu}{\Lambda^2} \bar{\mu}_R \sigma_{\alpha\beta} e_L F^{\alpha\beta} + \frac{\kappa}{\kappa + 1} \frac{1}{\Lambda^2} \bar{\mu}_L \gamma_\alpha e_L (\bar{u}_L \gamma^\alpha u_L + \bar{d}_L \gamma^\alpha d_L) ,$$

where Λ is the scale of the new physics contributions. Because amplitudes scale as the Lagrangian, and rates scale with the square of the amplitudes, the conversion rate scales with the fourth power of Λ . By improving the sensitivity to conversion by four orders of magnitude, both COMET and Mu2e will improve our energy reach by an order of magnitude compared to the SINDRUM-II experiment [10] across the entire parameter space, to perhaps as high as 10^4 TeV, well in excess of processes directly accessible at even the LHC.

THE DESIGN OF MU2E

The known atomic, nuclear, and particle physics processes of the negatively charged muon drive the design of the experiment. For a high statistics search, we must bring a large quantity of muons to rest in a stopping target that can be observed by a precision detector. Negative muons are brought to rest in the stopping target by well understood electromagnetic scattering and energy loss processes, thermalize, and are captured into atomic orbitals of the target atoms. They act like heavy electrons and rapidly cascade to the $1s$ ground state

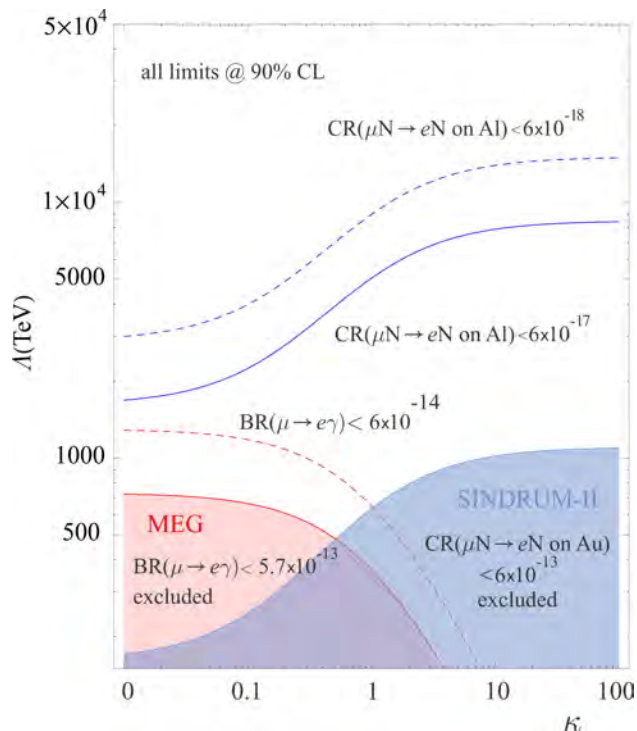


FIG. 3: Here we plot the sensitivity in terms of new physics energy scale reach for the model of de Gouvêa and Vogel; the left side of the plot corresponds to dipole transition dominated CLFV physics, while the right side corresponds to fermi contact interactions.

through a series of well understood level transitions, with the corresponding emission of well-characterized hard photons. Once in the ground state, the muons will either perform a Michel-like Decay in Orbit (DIO), or capture on the nucleus. The ratio of DIO to capture depends on the target nucleus, and is well characterized for all interesting target materials; for aluminum in particular, this ratio is roughly 40:60.

The process of conversion itself produces a monochromatic electron with energy roughly the muon mass (slightly reduced of course by the small electron mass, atomic binding energy, and nuclear recoil). This signal energy is essentially identical to the endpoint for the rapidly falling DIO spectrum. DIO, of course, has a four body final state: the decay electron, the recoiling nucleus, and a pair of neutrinos. In the limit that the neutrinos are born at rest, the kinematics of DIO and conversion are the same. To conclusively observe any conversion events requires high intrinsic detector resolution, requiring an extremely low mass design to minimize the energy loss and multiple scattering leading to resolution smearing. Additionally, as the rate near the end point is many orders of magnitude below the rate at

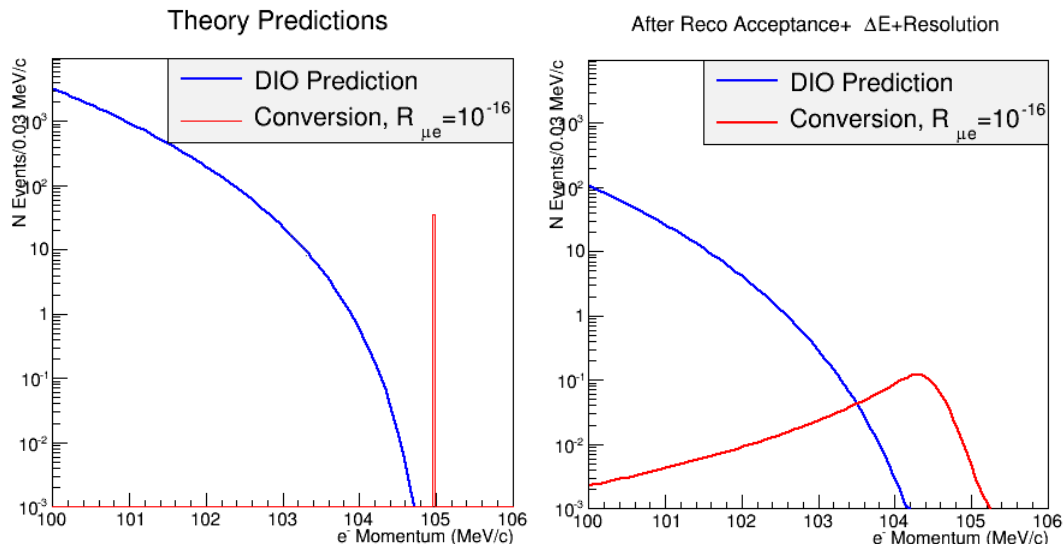


FIG. 4: A schematic illustration of the effects of resolution smearing on the observed spectrum of conversion event candidates; the left hand plot is the ideal physics case, while the right hand plot has the effects of detector physics included. It is clear that minimizing distortion of the signal peak requires a low mass detector system.

the Michel peak, there is a major issue with dynamic range that any detector must overcome.

In addition to the intrinsic DIO background, there are potentially severe backgrounds from beam sources, primarily pion capture products. Because of the physics processes involved, these backgrounds are prompt with the arrival of the beam particle. The standard solution to reducing such prompt contamination is a pulsed primary beam followed by a pause before opening the “live window” for data collection.

THE MU2E IMPLEMENTATION

The Mu2e Experiment is under construction at the Fermi National Accelerator Laboratory in Batavia, Illinois in the United States. Along with the Fermilab Muon $g - 2$ Experiment, Mu2e will occupy the new Muon Campus facility close to Wilson hall, forming the core of a muon program for at least the next decade. Proton delivery to the Muon Campus has required modest upgrades to the accelerator complex, upgrades which are compatible with the continuation of the ongoing Fermilab neutrino program. For Mu2e, protons will be accelerated by the Booster ring to 8 GeV, and transported to the Recycler ring where they will be rebunched and stacked into the Delivery Ring (the former antiproton

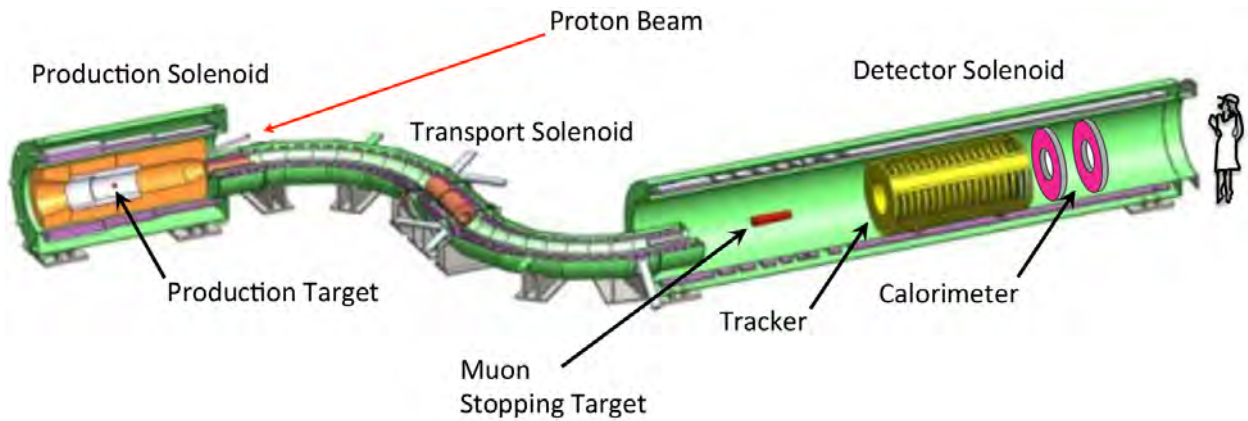


FIG. 5: The Mu2e Apparatus, showing cutaways of the three solenoids.

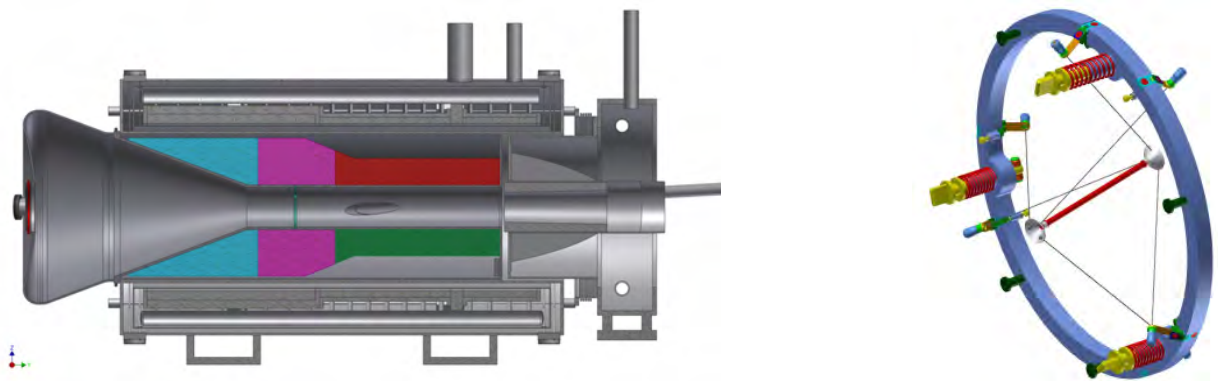


FIG. 6: The left-hand rendering shows the design of the Mu2e Production Solenoid; here, the TS is off to the right, and the proton beam enters from right, just above the centerline. The right-hand picture shows a blowup of the pion production target mounted in its “bicycle wheel” support structure.

Debuncher). Protons will be slow extracted for delivery to the Mu2e production target in a new experiment hall that is currently under construction. This full chain requires additional RF equipment in the Recycler, a reconfiguration of the Delivery Ring, as well as the construction of a new beamline from the Delivery Ring to the Mu2e experiment hall on the Muon Campus.

The Mu2e apparatus will separate the production of muons from observation of their decays; see Figure 5. Muons will be produced within the *Production Solenoid* (PS) and their decays will be observed by a suite of detectors within the *Detector Solenoid* (DS). An “S”-shaped *Transport Solenoid* (TS) will be responsible for muon beam transport between the other solenoids.

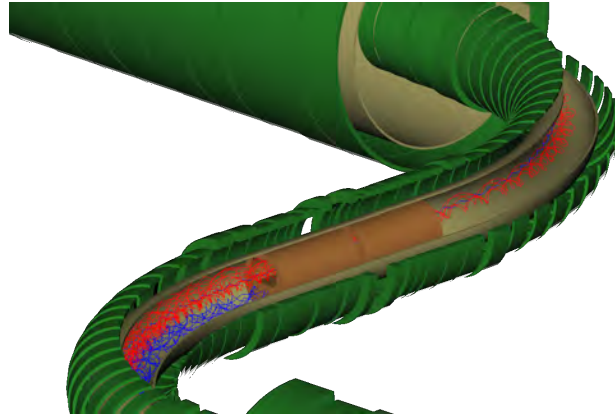


FIG. 7: The Mu2e Transport Solenoid contains an asymmetric collimator to eliminate the positively secondary beam; vertical drift in a curved solenoid separates particles of opposite charge, allowing us to sign select our beam.

The PS (see Figure 6) produces a backward moving muon beam to dramatically reduce beam related backgrounds. The proton beam enters slightly off axis, in the gap between the PS and TS. The production target is pencil-sized tungsten rod, held in place by a “bicycle wheel” support system, and cooled by direct radiation to the vacuum. The stainless steel vacuum vessel holding the production target is surrounded by a bronze and water heat and radiation shield to protect the PS superconducting coils from both heat load and radiation damage. The PS endcap provides windows for passing the spent beam to a downstream proton beam stop, along with a maintenance window to allow for target changes. Because of the heavy activation of the target and PS, target changes will be performed by a robotic remote handling system. The field in the PS is graded from 4.5 T at the proton-downstream end to 2.5 T at the entrance to the TS. This graded field acts both as a mirror increasing muon acceptance, as well as sweeping particles towards to TS to prevent long-lived storage of secondaries within the PS that could later escape and arrive in the DS during the live window.

The “S”-shaped solenoid TS sweeps muons from the PS to the DS. The field is also graded inside TS, again to ensure that particles do not become trapped in long-lived orbits. The solenoid is curved to ensure that there is no line-of-sight path between the production target and the detectors to reduce contamination by neutral particles. The entrance to and exit from the TS are occupied by collimators to define the acceptance of the channel. The most interesting aspect of this design is the effect a curved solenoid has on charged particle

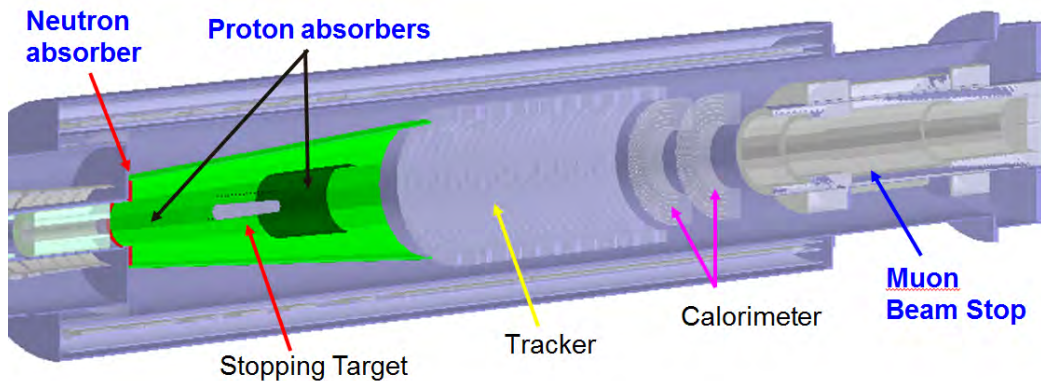


FIG. 8: A rendering of the Mu2e Detector Solenoid, showing the internal arrangement of muon stopping target foils, detectors, and supporting devices.

trajectories: charged particles drift in the non-bend direction (vertically in our case), with particles of opposite sign drifting in opposite directions. This naturally charge separates the beam in the vertical direction. We insert an asymmetric collimator in the central straight section to sign select on negative muons; see Figure 6. The recurved section past the central collimator moves the beam back on-axis at the entrance to the DS.

The Detector Solenoid forms the heart of the experiment; see Figure 8. As the beam enters the DS, it first encounters a series of aluminum stopping target foils. These are mounted within a graded magnetic field region; again, the grade reflects decay products towards the downstream end of the DS, increasing the acceptance of the detector systems. Beyond the stopping target, the field becomes uniform over the detector train. The primary measurement device is a low-mass, straw-tube electron tracker; with a wall thickness of only $15\ \mu\text{m}$, the tracker has a high-side resolution of less than $180\ \text{keV}$, thanks to the low mass design. The dynamic range issues are solved by simply not measuring electrons in the peak of the DIO distribution: the tracker has a central hole along its axis that passes particles below $55\ \text{MeV}/c$ without measurement. Following the tracker is a scintillating crystal calorimeter, made from two annular disks. The calorimeter provides a redundant energy measurement to the tracker, as well as powerful particle ID capability, and independent trigger and track seeding capabilities. The final major component mounted within the DS is a muon beam stop, which intercepts and absorbs the beam particles that are not stopped by the target foils, and decay products below measurement threshold. A four layer scintillating plastic Cosmic Ray Veto system surrounds the top and sides of the DS to virtually eliminate cosmic

ray muons that could fake conversion signals; to reduce the rate from one per day to less than 0.1 event during the three year duration of the experiment, this system must operate at a 99.99% detection efficiency.

While the bulk of the Mu2e experiment is designed for the detection of conversion events, that's only half the equation (literally!). To measure the conversion *rate* (or branching ratio), we have to normalize the number of conversion candidates to some proxy for the total number of muon stops. This is the job of the final detector, the *Stopping Target Monitor* (STM). The baseline design is for a High Purity Germanium detector that will view through very small solid angle the stopping target foils, and will count the characteristic atomic cascade transition x-rays. Given acceptance and efficiency measures for both the conversion event counting and the cascade x-ray counting, we can determine the ratio of conversions to nuclear capture events; our final result will be the *conversion ratio*

$$R_{\mu e} = \frac{\mu^- + A(Z, N) \rightarrow e^- + A(Z, N)}{\mu^- + A(Z, N) \rightarrow \nu_\mu + A(Z - 1, N)} .$$

For a three year run, we expect less than half a background event in the signal window; our goal for single event sensitivity is 2.5×10^{-17} , a four order of magnitude improvement over the SINDRUM II result. For a conversion ration $R_{\mu e} \sim 10^{-15}$, we will see fifty conversion events during the run.

RECENT PROGRESS AND FUTURE PROSPECTS

The Mu2e Project and Collaboration are making progress on design, reviews, procurement, and construction across the many subsystems comprising the experiment. Two significant milestones occurred in the spring of 2015: U.S. Department of Energy Critical Decision 2 approval of the project baseline design and cost, and Critical Decision 3b approval to begin construction of the experiment hall. The formal groundbreaking for that hall occurred during the Collaboration Meeting in April. The Project and Collaboration are working diligently to prepare for the many subsystem technical reviews leading up to the Critical Decision 3c review in early 2016, which will authorize construction of the rest of the experiment. The baseline schedule has commissioning slated for early 2021, followed by at least three years of data taking.

As mentioned earlier, because the Standard Model does not predict observable levels of

CLFV, the value of μ_2e is high whether or not we see a signal. In either case, a future extension of the experiment - μ_2e -II - is under active study. If we do see a signal in our first run, an upgraded experiment run with multiple different target materials could help elucidate the physics sources responsible for CLFV. If we do not see a signal in our first run, an upgrade will allow us to improve our sensitivity and probe higher energy scales. In either case, the result from μ_2e combined with other CLFV experiments and direct searches at the LHC will help point us in the right direction to define the next Standard Model.

Acknowledgements

The speaker's work on the μ_2e effort is supported by the U.S. Department of Energy, Office of Science, Office of High Energy Physics under Award Number DE-FG02-13ER41931, by a contract with the μ_2e Project Office at Fermilab, and by a PSC-CUNY Award, jointly funded by The Professional Staff Congress and The City University of New York.

* *Presented at NuFact15, 10-15 Aug 2015, Rio de Janeiro, Brazil [C15-08-10.2]*

† `klynch@york.cuny.edu`; Speaker

‡ URL: <http://mu2e.fnal.gov/>

- [1] Particle Physics Project Prioritization Panel (P5) (2014), URL [\url{http://science.energy.gov/~media/hep/hepap/pdf/May-2014/FINAL_P5_Report_053014.pdf}](http://science.energy.gov/~media/hep/hepap/pdf/May-2014/FINAL_P5_Report_053014.pdf).
- [2] E. P. Hincks and B. Pontecorvo, *Phys. Rev.* **73**, 257 (1948).
- [3] G. Danby et al., *Phys. Rev. Lett.* **9**, 36 (1962).
- [4] J. Adam et al. (MEG), *Phys. Rev. Lett.* **110**, 201801 (2013), 1303.0754.
- [5] N. Berger (μ_3e), *Nucl. Phys. Proc. Suppl.* **248-250**, 35 (2014).
- [6] M. Aoki (DeeMe), *PoS ICHEP2010*, 279 (2010).
- [7] Y. G. Cui et al. (COMET), KEK-2009-10 (2009).
- [8] L. Bartoszek et al. (μ_2e), FERMILAB-TM-2594, FERMILAB-DESIGN-2014-01 (2014), 1501.05241.
- [9] A. de Gouvea and P. Vogel, *Prog. Part. Nucl. Phys.* **71**, 75 (2013), 1303.4097.
- [10] C. Dohmen et al. (SINDRUM II), *Phys. Lett.* **B317**, 631 (1993).

The MuLan Experiment: Measuring the muon lifetime to 1 ppm*

Kevin R. Lynch^{1,2,†}

(The MuLan Collaboration)

¹*Department of Earth and Physical Sciences,
York College, City University of New York,
94-20 Guy R. Brewer Blvd, Jamaica, NY 11451 USA*

²*The Graduate Center, City University of New York,
365 Fifth Avenue New York, NY 10016 USA*

(Dated: April 18, 2016)

Abstract

The MuLan Collaboration has measured the lifetime of the positive muon to 1 ppm. Our result now drives the world average. Within the Standard Model framework, this permits a determination of the Fermi Constant to 0.5 ppm. I present our measurement method, our published results, and prospects for future improvements in the technique.

INTRODUCTION

The Standard Model of particle interactions is a triumph of modern physics. We find extremely impressive agreement between theoretical predictions and measurements in the realms of atomic physics, nuclear structure, high energy interactions, and astrophysics and cosmology. These theoretical predictions, of course, are based on precision measurements of a small number of fundamental input parameters. The electroweak sector of the model, in particular, rests on three very well measured values: the fine structure constant, α_{em} , the mass of the neutral weak gauge boson, M_{Z^0} , and the Fermi constant, G_{F} .

Striking improvements have occurred in the last decade in measuring these three fundamental inputs. The Gabrielse group at Harvard has measured the fine structure constant at the 0.37 ppb level [1], while the combination of the four LEP experiments has determined the Z^0 mass to 23 ppm [2]. After extensive analysis of data collected in 2006 and 2007, the MuLan Collaboration published its final results, which give the first major improvement in our knowledge of the Fermi Constant in twenty years [3, 4].

The Fermi constant sets the strength of the weak $V - A$ interaction, and can be cleanly extracted at high precision from a measurement of the free muon lifetime [5]

$$\frac{1}{\tau_{\mu}} = \frac{G_{\text{F}}^2 m_{\mu}^5}{192\pi^3} \left(1 + \sum_i q_i \right). \quad (1)$$

Here, we see the $V - A$ prediction factorized into a pure weak contact contribution (encoded in G_{F}), plus a sum over non-weak corrections (the q_i). These include the massive phase space integrals (q_0), and QED and hadronic loops. This extracted value of the Fermi constant must then be connected with the weak interaction physics of interest - usually the Standard Model - through a loop expansion.

At the close of the twentieth century, extracting G_{F} from the muon lifetime was limited by theory - only q_0 and q_1 were known. The uncalculated higher order terms were esti-

mated to contribute 30 ppm, compared with a world averaged experimental uncertainty of 18 ppm. In 1999, van Ritbergen and Stuart [6] succeeded in calculating the second order QED corrections (q_2) in the limit of massless electrons, reducing the theory uncertainty to the sub-ppm level. On the heels of this result followed multiple proposals to improve the experimental uncertainties to comparable levels, culminating in the independent MuLan and FAST experiments at the Swiss Muon Source at the Paul Scherrer Institut (PSI) in Villigen Switzerland. Both efforts initially pursued 1 ppm measurements of the muon lifetime. In addition to extracting the Fermi constant, improved direct measurement of the free muon lifetime is critical for comparisons with bound muon lifetimes used in the extraction of nuclear physics parameters; see the talk on the MuCap experiment by B. Kiburg in these proceedings.

EXPERIMENTAL METHOD

Previous experiments have generally utilized low rate, “one at a time” methods: a beam of muons is focused on a stopping target, with average target occupancy of fewer than one muon. This approach does not scale to a 1 ppm measurement, where we need to record in excess of 10^{12} individual decays to reduce the statistical uncertainties. Instead, MuLan pursued a method with high stopping target occupancy, namely a pulsed source that permits us to perform many muon lifetime measurements simultaneously.

To this end, we developed a high-rate (7 MHz) beam tune in the $\pi E3$ beam line at PSI, and constructed a fast electrostatic kicker to chop the beam [7]. We collected polarized muons on a fixed stopping target for a $5 \mu s$ (two muon lifetime) accumulation period, and then deflected the beam away from the target during the next $22 \mu s$ (ten lifetime) measurement period.

The stopping target was surrounded by a large acceptance, point symmetric, high granularity detector. The detector had a truncated icosahedral, or “soccer ball”, geometry; each hexagonal (pentagonal) face consisted of six (five) triangular dual layer plastic scintillators, connected through short light guides to fast photomultiplier tubes. The upstream and downstream pentagonal faces were not instrumented, to permit the entry of the beam transport corridor upstream, and the exit of beam electrons downstream. To reduce background contamination, we demanded a coincidence between the inner and outer tiles of each pair. For

the data collected in our 2006 and 2007 run periods, the PMTs were instrumented with custom, high-rate waveform digitizers (WFDs). The entire system was controlled and read out with a customized data acquisition system based on the MIDAS framework [8]. In all, we recorded 340 channels of PMT “physics” signals, along with a number of other diagnostic and monitoring channels. The result of the data acquisition was a set of lifetime spectra which, after application of a set of well controlled, data driven corrections, could be fit to a simple functional form where the ultimate goal was the measurement of τ_μ at the ppm level.

MAJOR SYSTEMATIC ERRORS

Systematics, not statistics, were the core concern for our 10^{12} event data sets. As such, the experiment was designed from the ground up to minimize or eliminate systematic errors. The main class of errors were those that systematically skewed count rate efficiency early-to-late in the measurement period. Any such errors could directly contribute to a shift between the fitted lifetime and the actual lifetime, usually without any diagnostic problems in the quality of fit parameters. There are a large number of effects that we identified, either from fundamental physics or from finite instrumental precision, which needed to be addressed; a few are recounted here.

Timing shifts

Rate dependencies (particularly in the PMTs) are known to cause small timing shifts of order a few picoseconds. We directly monitored this effect with a laser reference system. We illuminated a subset of the detector tiles, as well as an independent reference counter located well away from the detector, with a regular fast laser pulse. The laser pulses were injected at a very low rate, and independent of the state of the data acquisition cycle. They therefore uniformly populated the measurement period, leading only to a very small increase in the flat background. A systematic time shift on the detector would be measured as a change in the time difference with the reference counter. No measurable shifts were seen.

Additionally, we searched for timing shifts with a parallel “randoms” experiment. With an additional pair of tiles located away from the detector, we observed the decays of a radioactive source. This measurement should see a flat time spectrum across the observation

period; no deviation was observed.

Gain shifts

Any rate dependencies in the PMT gain or discriminator thresholds would manifest as a change in counting efficiency. With the WFDs, we could directly monitor the average amplitude response from the laser system, comparing the amplitude response with that of the reference counter. No measurable gain shifts were seen.

Beam-off backgrounds

The background term in the fit function arises primarily from muon arrivals during the beam off period and irreducible cosmic ray events. To minimize the number of these out-of-time arrivals, our beam kicker was designed to operate with a 25 kV potential difference between the plates, providing a beam extinction around 900. To eliminate any early-to-late variation in the background at the ppm level, the extinction (and hence the voltage difference) must be regulated at better than the 1 V level. This stability was achieved early on [7].

Pileup

In our experiment, pileup was the loss of counts or time shifting of counts due to the finite pulse time resolution of our detector. To combat this, our detector was a highly segmented design, with 170 dual layer tiles built from fast plastic scintillator to minimize event occupancy in each channel. Even with our high beam rate, the time structure and beam extinction ensured that the average measurement period occupancy of each channel was less than 0.1 hits per beam cycle. Combined with the good time resolution for pulse timing available with the WFDs, this reduced the pileup losses to about 10^{-4} . We had to understand these effects at roughly the 0.1% level to eliminate this as a dominant systematic.

In principle, we could have determined the effects of pileup processes on the lifetime spectrum, and modified our fitting function to account for them. The dominant contribution, an $\exp(-2t/\tau_\mu)$ term, has long been understood and applied in previous experiments.

Unfortunately, this dramatically reduces the statistical power for a given number of decays: the dominant pileup term alone reduces the statistical precision by a factor of two. Since pileup events were rare, however, we could directly reconstruct the pileup contributions from the data. This is possible because we could determine how various classes of events nearby in time in a single channel will lead to time shifts or event losses. We call our statistical reconstruction method the *shadow window reconstruction* procedure. While the details of its application depend on the details of the pulse reconstruction algorithm, we can easily describe the flavor of the pileup reconstruction.

Consider the dominant pileup term: what we call *normal pileup*. In this case, two decay events pass through a single channel within the resolution time of the pulse reconstruction. In this case, the reconstruction will “see” only one event - we have a small but finite dead-time. Since the probability of the individual events happening in the same time window are independent, it follows that this probability is the same as that of two events happening in the same time window, but in *different* measurement periods. The number of times the latter occurs matches the number of times events have been lost.

The correction procedure, then, was applied in the following way. First, we reconstructed every pulse we could find in the raw data. Then, we applied an *artificial deadtime* cut to remove nearby events, and put all the remaining events into a *pileup contaminated* histogram. We also built a second, *pileup correction* histogram by applying the approach discussed above: if we saw an event in observation period 1, we looked in the same window (the *shadow window*) of observation period 2. If we found an event in that second window, we also added an entry to the correction histogram. The sum of the contaminated and correction histograms should represent the true, uncontaminated lifetime spectrum. In addition to normal pileup, we considered additional pileup corrections from other sources, including (among others) three simultaneous events, timing jitter, and the accidental time coincidence of uncorrelated singles hits on an inner and outer tile pair.

The pileup correction procedure was repeated for many values of the artificial deadtime cut. The lifetime for each of all the corrected spectra will agree with each other if the procedure has accounted for all relevant pileup effects. For our final results, a small residual correlation between artificial deadtime and fitted lifetime of 0.008 ppm/ns remained after pileup correction. No conclusive source for this discrepancy was identified, but we showed that it was stable and linear with artificial deadtime; we extrapolated the correction to zero

deadtime to produce our final lifetime. We assigned a systematic uncertainty of 0.2 ppm for pileup corrections.

Muon polarization effects

Muon beams are naturally highly polarized: muons are born from the two body decay of spin-zero pions via the chiral weak interaction. Since the muon neutrino is only available in left-handed form, angular momentum conservation demands that all the muons have the same chirality. The large ensemble spin polarization can be either a blessing or a curse, depending on the application. In the case of MuLan, it carried the potential for disaster. If the ensemble maintains any of its polarization after stopping in the target, then 1. the component perpendicular to any local magnetic field will precess and decay with time, and 2. the parallel component will decay (longitudinal relaxation) with a different lifetime. Either effect could lead add an additional, unknown component to the spectrum for any individual detector tile.

We took a number of steps to both control and measure the size of these effects. The key observation is that detectors on opposite sides of the stopping target should have seen effects that cancel, up to (unavoidable) small differences in positioning, acceptance, and efficiency. The detector was designed to maximize the point symmetry, and opposing tiles were chosen to have closely matched efficiencies. To the extent possible, materials and construction of the elements surrounding the stopping target were chosen to minimize acceptance differences. Additionally, we performed systematic studies with stopping targets that maintain the residual polarization, such as silver, in order to measure the departures from design symmetry.

The physics targets were chosen to minimize the residual polarization, but in different ways. For the 2006 running period, we chose the ferromagnetic alloy Arnokrome-3 (AK3); the high internal fields cause many precession cycles between muon arrivals which “scrambled” the ensemble of spins. This picture was confirmed both with dedicated muon spin resonance studies and with analysis of point symmetric detector tile asymmetries. For 2007, we chose crystalline quartz in a strong applied field (of order 150 G). In quartz, a large fraction of the stopped muons are bound in muonium; the muon spin precesses a thousand times faster in muonium than does a free muon. The applied field then performs the same

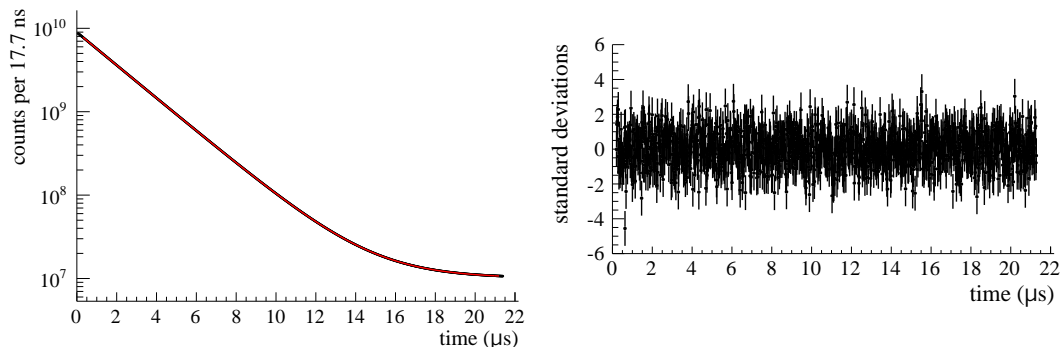


FIG. 1: A fit to the entire AK3 data set. The fits for the entire data sample began at $1 \mu\text{s}$ after the end of injection. We also display the residuals to the fit, showing no observable structure.

depolarization as the AK3 internal fields, for both the muonium and remaining free muons. Analysis of the efficacy of this target in reducing polarization effects showed that it gave us good measurement of and control over the polarization systematic.

THE STATUS OF MULAN

The experiment ended data collection with our 2007 run period. For both the 2006 and 2007 run periods, we analyzed in excess 10^{12} decay events. In addition to the dedicated systematic studies discussed above, we performed many consistency checks over subsets of the data, including various kicker, beam, and target conditions, discriminator threshold settings, artificial deadtimes, etc. Lifetime fits over various exclusive subsets were all consistent within statistics. Fit start and stop time scans revealed no structure in the residuals, suggesting that no time dependent effects of any significance were missed.

The final fit function for the AK3 (2006) data set was the same three parameter fit function: $f(t) = N \exp(-t/\tau) + B$. For the quartz (2007) data, fits were performed on individual tiles with a multiparameter function that accounted for measurable residual polarization effects that canceled in the sum of all data. All of the significant systematic errors for both run periods (both correlated and uncorrelated) are presented in Table I.

The results of this 2006 and 2007 run periods were published in 2010 [3], with the results

$$\tau_{\mu}(2006) = 2\,196\,979.9 \pm 2.5(stat) \pm 0.9(syst) \text{ ps} \quad (2)$$

TABLE I: Sources of systematic uncertainties on the muon lifetime measurements in the R06/R07 running periods. The uncertainties listed in single-column format are common uncertainties and those listed in two-column format are uncorrelated uncertainties. The last two rows are the combined systematic uncertainties and the overall statistical uncertainties for the 2006 and 2007 datasets.

Uncertainty	R06	R07
	(ppm)	(ppm)
Kicker stability	0.20	0.07
μ SR distortions	0.10	0.20
Pulse pileup	0.20	
Gain variations	0.25	
Upstream stops	0.10	
Timing pick-off stability	0.12	
Master clock calibration	0.03	
Combined systematic uncertainty	0.42	0.42
Statistical uncertainty	1.14	1.68

and

$$\tau_{\mu}(2007) = 2\,196\,981.2 \pm 3.7(stat) \pm 0.9(syst) \text{ ps.} \quad (3)$$

The combined result

$$\tau_{\mu}(\text{MuLan}) = 2\,196\,980.3 \pm 2.1(stat) \pm 0.7(syst) \text{ ps} \quad (4)$$

is obtained from the weighted average of the two individual values with the appropriate accounting for the correlated uncertainties. A comparison of these results in the context of previous muon lifetime experiments is plotted in Figure 2.

Using our value of the muon lifetime, we can extract the Fermi constant

$$G_{\text{F}}(\text{MuLan}) = 1.166\,378\,7(6) \times 10^{-5} \text{ GeV}^{-2} \text{ (0.5 ppm).} \quad (5)$$

This result represents a thirty-fold improvement over the 1999 PDG value obtained before the vRS theoretical work and the lifetime measurements pre-dating MuLan. The error in

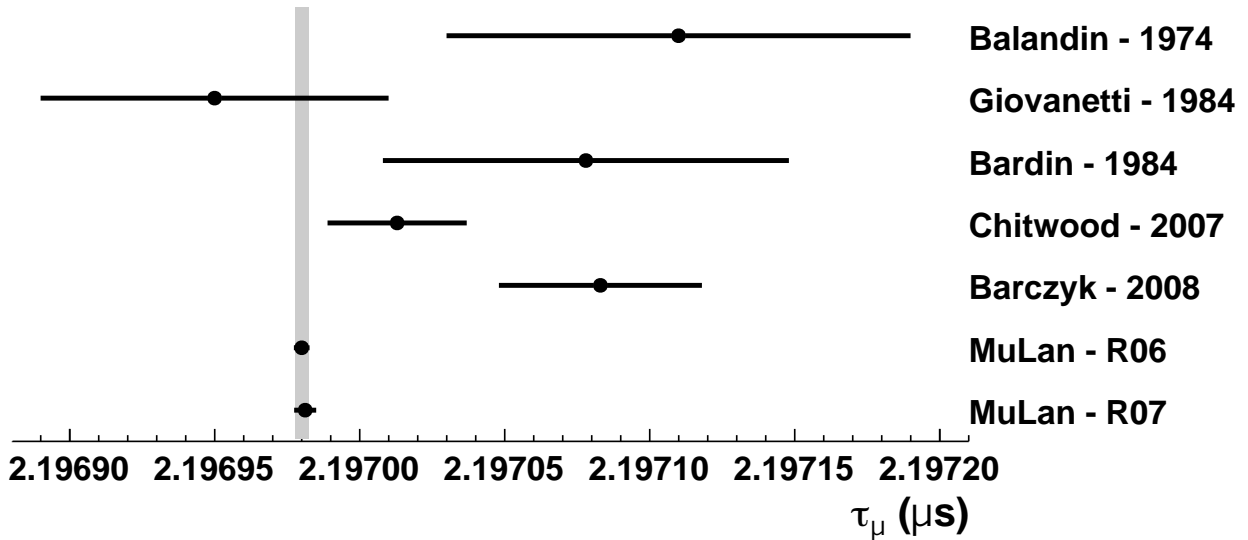


FIG. 2: A history of muon lifetime results. The narrow vertical bar shows the world averaged experimental muon lifetime, including our results.

G_F of 0.5 ppm is dominated by the 1.0 ppm uncertainty of the muon lifetime measurement with additional contributions of 0.08 ppm from the muon mass measurement and 0.14 ppm from the theoretical corrections.

FUTURE PROSPECTS

One goal of this workshop was to outline the prospects for new experiments at future neutrino sources. Although the MuLan experiment is finished and the detector has been dismantled, the techniques we used could be scaled up to provide continued improvements in the measurement of τ_μ and G_F should that prove valuable in the future. MuLan was statistics limited, but a new generation of lifetime experiment would need to take careful notice of the dominant systematics in our effort. Presumably a new experiment would run with much higher stopped muon rates, requiring greater detector coverage, segmentation, and uniformity to maximize the control of systematics given by the point symmetry of the detector. Special care will need to be taken to better understand pulse pileup corrections, and there will be need to better control or correct detector gain stability early-to-late in the measurement period. Finally, a more comprehensive understanding of muon polarization effects will be required. The extraction of the Fermi constant from the muon lifetime is

currently dominated by experimental uncertainty; with some modest improvements, we could likely bring the experimental contribution closer to parity with the theory contribution. A similar back-and-forth between theory and experiment in this measurement has a long history of productively enhancing our field.

* *Presented at NuFact15, 10-15 Aug 2015, Rio de Janeiro, Brazil [C15-08-10.2]*

† `klynch@york.cuny.edu`; Speaker

- [1] D. Hanneke, S. Fogwell, and G. Gabrielse, *Phys. Rev. Lett.* **100**, 120801 (2008), 0801.1134.
- [2] *Phys. Rept.* **427**, 257 (2006), hep-ex/0509008.
- [3] D. M. Webber et al. (MuLan), *Phys. Rev. Lett.* **106**, 041803 (2011), [*Phys. Rev. Lett.*106,079901(2011)], 1010.0991.
- [4] V. Tishchenko et al. (MuLan), *Phys. Rev.* **D87**, 052003 (2013), 1211.0960.
- [5] T. van Ritbergen and R. G. Stuart, *Nucl. Phys.* **B564**, 343 (2000), hep-ph/9904240.
- [6] T. van Ritbergen and R. G. Stuart, *Phys. Rev. Lett.* **82**, 488 (1999), hep-ph/9808283.
- [7] M. J. Barnes and G. D. Wait, *IEEE Trans. Plasma Sci.* **32**, 1932 (2004).
- [8] V. Tishchenko et al., *Nucl. Instrum. Meth.* **A592**, 114 (2008), 0802.1029.
- [9] D. B. Chitwood et al. (MuLan), *Phys. Rev. Lett.* **99**, 032001 (2007), 0704.1981.
- [10] A. Barczyk et al. (FAST), *Phys. Lett.* **B663**, 172 (2008), 0707.3904.

g-2 J-PARC (E34)*

M. Otani, for the J-PARC E34 collaboration[†]

KEK, Tsukuba, Japan

(Dated: April 20, 2016)

Abstract

The muon anomalous magnetic moment $(g-2)_\mu$ and electric dipole moment (EDM) are sensitive to new physics beyond Standard Model of elementary particle physics. The E34 experiment aims to measure $(g-2)_\mu$ and EDM with a precision of 0.1 ppm and a sensitivity to 10^{-21} e-cm, respectively, whereas current precision is 0.54 ppm and upper limit is 10^{-19} e-cm. We achieve the goal with high intensity proton beam at J-PARC and newly developed novel technique of the ultra-cold muon beam. The ultra-cold muon is generated from the thermal muonium production by the silica aerogel followed by the laser ionization, and then accelerated up to 300 MeV/c. The muon is injected to the super-conducting storage magnet supplying 3 T field and the decay positron is detected by the silicon detector. This paper reports current status of the each experimental component.

INTRODUCTION

Though the discovery of Higgs at LHC completed the particles predicted in Standard Model (SM) of elementary particle physics, some observations such as dark matter existence indicate new physics beyond SM at some energy scale or interaction scale. One of the clues for new physics is anomaly of the muon anomalous magnetic moment $(g-2)_\mu$; There is a $\sim 3\sigma$ discrepancy between the SM prediction and the experimental value measured by E821 with a precision of 0.54 ppm [1]. Measurement with higher precision (0.1 ppm) is necessary to confirm this anomaly.

It should be also mentioned that measurements up to now rely on the technique of the magic momentum. Because the muon beam generated from the secondary pions in flight has large emittance, focusing with electric field in addition to the magnetic field is necessary in storage ring. The anomalous spin precession vector of muon is written by

$$\vec{\omega} = -\frac{e}{m} \left[a_\mu \vec{B} - \left(a_\mu - \frac{1}{\gamma^2 - 1} \right) \frac{\vec{\beta} \times \vec{E}}{c} + \frac{\eta}{2} (\vec{\beta} \times \vec{B} + \frac{\vec{E}}{c}) \right] \quad (1)$$

where e is elementary charge, m is muon mass, a_μ is anomalous magnetic moment, γ is the Lorentz Factor, β is the ratio of particle velocity to the speed of light c , and η is electric dipole moment. The second term depending on the electric field is eliminated when the muon momentum is 3.094 GeV/c, so called magic momentum. Measurement with a new method should be surveyed for verification of the $(g-2)_\mu$ anomaly.

The muon electric dipole moment (EDM) is also sensitive to new physics because it is strongly suppressed in SM (10^{-38} e-cm), and violates CP symmetry assuming the CPT theorem. In addition to that, there is a possibility that anomaly of $(g-2)_\mu$ can be explained by finite EDM with an order of 10^{-20} e-cm [2], whereas current direct limit is 1.9×10^{-19} e-cm [3].

The E34 experiment [4] aims to measure $(g-2)_\mu$ with a precision of 0.1 ppm and search for EDM with a sensitivity to 10^{-21} e-cm by utilizing high intensity proton beam at J-PARC and newly developed novel technique of the ultra-cold muon beam. Figure 1 shows the experimental setup. The experiment utilizes the proton beam from the 3 GeV Synchrotron ring to Materials and Life Science facility (MLF). The proton beam is injected to the graphite target. The generated surface muons are extracted to one of the muon beamline of H-line. Surface muons stop in the muonium (μ^+e^- , Mu) production target of the silica aerogel and then form thermal muoniums. The paired electron in the muonium is knocked out by laser and thermal muon (3 keV/c) is generated. Then the muon is accelerated up to 300 MeV/c and injected to the storage ring supplying 3 T. The decay positron is detected by the silicon strip tracker and the spin precession frequency is obtained from variation of counting rate of the decay positron. Thanks to the ultra-cold beam ($\sigma_{pT}/p = 10^{-5}$) where p_T is the transverse momentum of the beam particles, the electric focusing is not necessary anymore. Eq. 1 becomes

$$\vec{\omega} = -\frac{e}{m} \left[a_\mu \vec{B} + \frac{\eta}{2} (\vec{\beta} \times \vec{B}) \right] \quad (2)$$

The anomalous magnetic moment and EDM are perpendicular each other. Therefore these can be measured simultaneously.

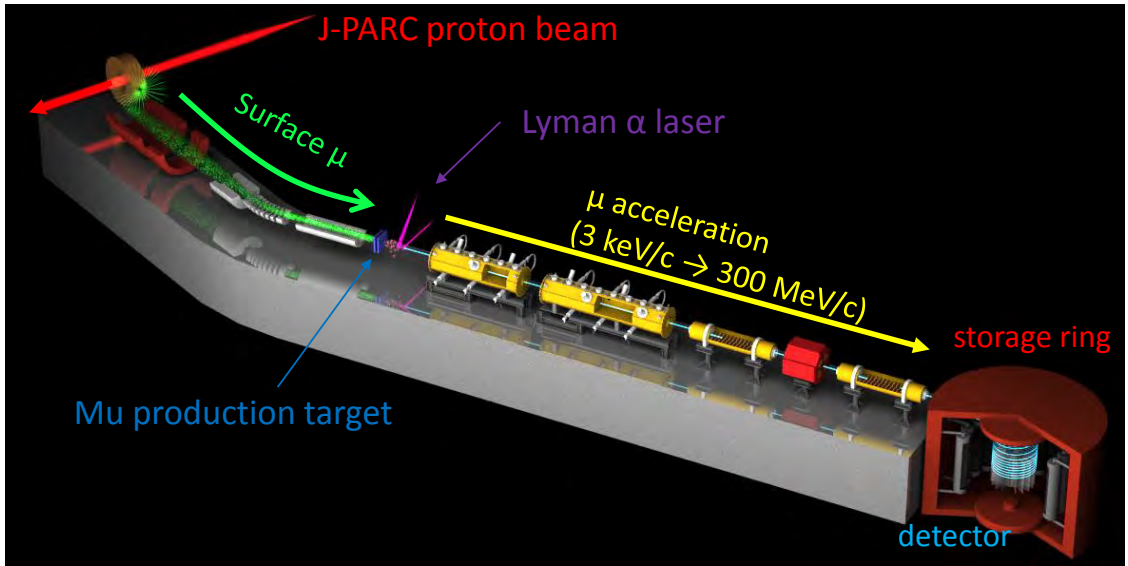


FIG. 1: Schematic view of E34

We are planning to start the experiment in 2019 and developing each experimental component. This paper reports current status of the each component.

MUONIUM PRODUCTION TARGET

Hot tungsten foil is widely used and developed as a muonium production target [5, 6]. It has a high production efficiency but the generated muon has a high energy due to the high temperature of the tungsten (2100 K). The silica aerogel is also known as a Mu production target [7]. The aerogel can be used in the room temperature and energy of the generated muons satisfies our requirement ($p=3$ keV/c). The production efficiency, however, was smaller than our requirement.

Our previous measurement with silica aerogel [7] reveals that the diffusion length of muonium in the silica aerogel is $30 \mu\text{m}$ which is much shorter than the muon stopping distribution of several millimeters. It indicates that the aerogel with a sub-millimeter structure can emit muoniums to outside the target more easily.

According to this indication, the silica aerogel with sub-millimeter structure was fabricated by using femto-meter laser. The surface area was covered by a triangular pattern of holes of the $270 \mu\text{m}$ diameter with equal spacing of $300 \mu\text{m}$, $400 \mu\text{m}$ (Fig. 2) and $500 \mu\text{m}$. Measurement of the muonium emission from the laser ablated aerogel was performed at the TRIUMF M15 beamline in 2013 [8, 9]. Figure 3 shows the timing distribution of the reconstructed decay positrons downstream of the laser ablated aerogel with equal spacing of $300 \mu\text{m}$ with comparison to that from the silica aerogel without ablation. It is obvious that more emission rate is achieved with laser ablated aerogel, at least eight times higher than the one without the laser ablation. We can achieve the statistical precision of 0.36 ppm for $(g-2)_\mu$ in 2×10^7 s of data taking time by using this target. We are planning to perform further developments towards higher efficiency at the J-PARC muon beamline.

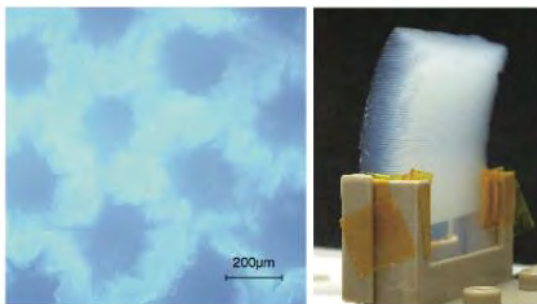


FIG. 2: (Left) Photo of surface on the laser ablated aerogel target. (Right) Whole picture of the target. The muon beam incidents from left and Mu is exiting from right surface. Ref. [8]

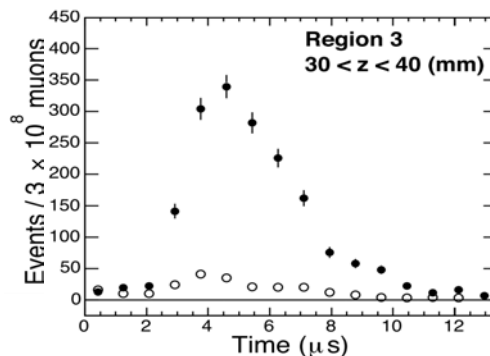


FIG. 3: Time distribution of positrons in near the target surface for flat aerogel (open circles) and laser ablated aerogel (close circles). No background has been subtracted. Ref. [8].

IONIZATION LASER

Emitted thermal muonium is ionized by the two wavelengths of laser: 122 nm to excite a muonium from 1S ground state to 2P state and 355 nm to ionize from 2P. The latter is generated as a third harmonic of 1062.78 nm and the former is generated using a four-wave mixing technique in Kr gas (Lyman- α). Figure 4 shows the schematic diagram of the laser system. The system has been developed in the J-PARC U-line and the Lyman- α laser was succeeded to be fired on August 2014 (Fig. 5). Now the development towards higher power is on-going. More detail discussions can be found elsewhere [10].

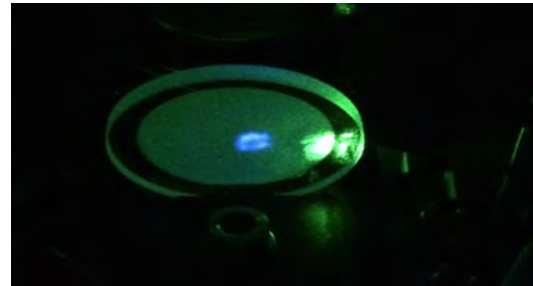
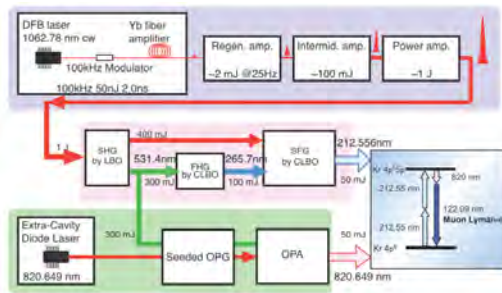


FIG. 4: Schematic diagram of the laser system.

FIG. 5: Demonstration of the Lyman- α generation at the J-PARC MUSE U-line.

In addition to developments in J-PARC, ultra-slow muon production with the laser ablated silica aerogel will be investigated in RIKEN-RAL port3. Beam commissioning has been conducted from September 2015.

MUON ACCELERATION

Because muon has a finite lifetime, the muon should be accelerated in a sufficiently short period of time to suppress the decay loss. To realize fast acceleration, a muon LINAC dedicated for our experiment is being developed (Fig. 6). Since velocity (β) of a muon largely varies during acceleration, several types of RF cavities should be adopted to realize sufficiently effective acceleration along with β . Three types of cavities are adopted after RFQ: inter-digital H-mode (IH) for low β (< 0.27), disk and washer (DAW) for middle β ($0.27 < \beta < 0.7$), and disk loaded structure for high β ($0.7 > \beta$) section.

It is planned to utilize the spare RFQ structure from J-PARC proton LINAC (Fig. 7). The electric field of the RFQ is proportional to the mass of the particle to be handled and the RFQ can be operated with $\sim 1/9$ of the field strength for the J-PARC proton LINAC operation in principle. The transmission efficiency is estimated to be 76.8% including decay

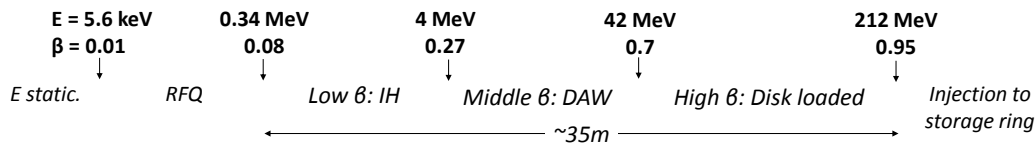


FIG. 6: Overview of the muon LINAC.

loss (19%) and the normalized rms transverse emittance for x (y) is estimated to be 0.294 (0.166) π mm mrad with PARMTEQ [11]. The offline test of the RFQ was performed at J-PARC in July 2015. The RFQ was successfully operated with nominal power of 4.2 kW. The Micro Channel Plate detector for the accelerated muon detection was connected to the RFQ and measured background. It was shown that there is no background related to the RF operation [12].

The muon acceleration test with RFQ is under planning in 2016 in the actual experimental area. The equipments for the test such as electrostatic lens were transported from RIKEN-RAL port3 [6] to the J-PARC MLF experimental hall. All the equipments were re-assembled as shown in Fig. 8, with which measurement of the slow muon production is scheduled in 2016. Other studies towards the acceleration test such as the H-line design can be found elsewhere [13].



FIG. 7: Photo of the RFQ for muon acceleration.

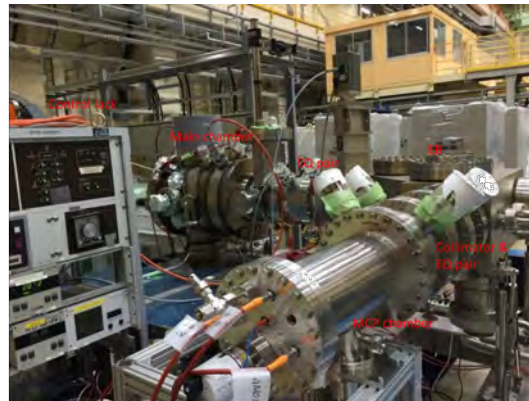


FIG. 8: Photo of slow muon beamline assembled in J-PARC MLF.

The IH cavity consists of a cylindrical cavity and two ridges that are mounted on the top and bottom of cavity. To operate it as an accelerator with the TE111 mode, drift tubes are mounted alternately on the top and bottom ridges via stems. To realize fast acceleration,

Alternative Phase Focusing (APF) method is adopted. According to the simulation study, the prototype of the IH cavity was fabricated (Fig. 9). The resonant frequency is measured to be 323.48 MHz which is consistent to the designed value. Further optimization of the cavity design is in progress based on the prototype result.

DAW is one of coupled-cavity linacs. It has highly effective shunt impedance and strong coupling between acceleration and coupling mode. The optimization of the cell design was performed (Fig. 10) and can be found elsewhere [12, 14, 15].

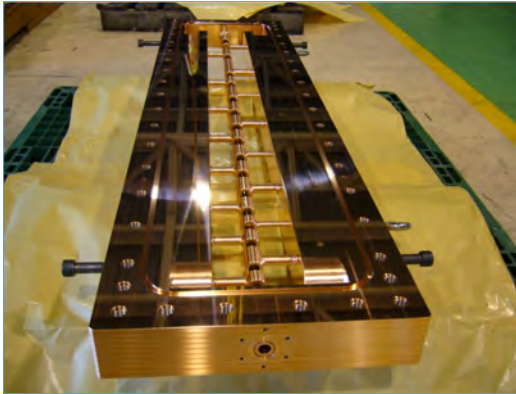


FIG. 9: Photo of the IH prototype in Tokyo Institute of Technology.

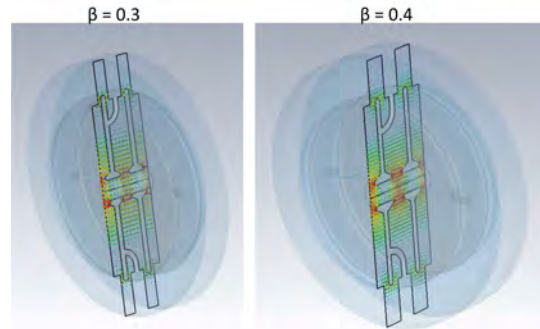


FIG. 10: Three dimensional model and calculated field of the acceleration mode of the DAW cavity in CST MW Studio.

Injection and storage magnet

Because the radius of the beam orbit in the storage magnet is only 33.3 cm, the same apparatus as previous experiment, a devise called an inflector and kicker, can not be used in our experiment. That's why a three dimensional spiral injection scheme is adopted. In order to match the acceptance of the spiral injection estimated by the simulation, the transport beamline was designed. According to this design, small-scale beamline and solenoid magnet was constructed to demonstrate the injection and storage with electrons. All the apparatuses were assembled (Fig. 11) and the measurement with electrons is being performed.

The storage magnet consists of four super-conducting coils supplying injection field, focusing field and main field of 3 T with local uniformity of 1 ppm. The solenoid magnet is being designed in collaboration with a private company. In order to achieve high homogeneity of the magnetic field below 1 ppm, the error field is corrected by shimming with iron pieces inside the magnet bore and superconducting shim coils. The correction scheme

with iron pieces was demonstrated with the magnet for the MuSEUM experiment [16] which supplies 1.7 T in this demonstration. Figure 12 shows the field residual after shimming. It was succeeded to get local uniformity with less than 1 ppm.

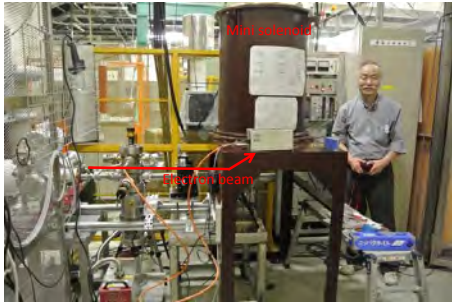


FIG. 11: Small-scale beamline and solenoid magnet to demonstrate the three dimensional spiral injection and storage.

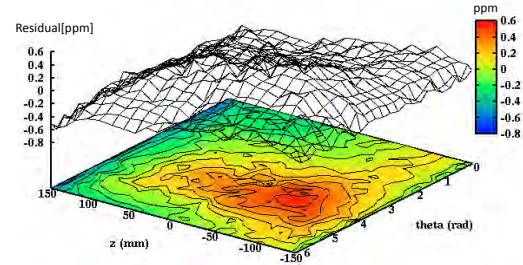


FIG. 12: Field residual after the shimming with iron pieces. Uniformity below 1 ppm in required region is successfully achieved.

Detector

The decay positron detector is required to be highly segmented and operated in 3 T. To satisfy these requirements, the silicon strip detectors are radially placed in the detection volume to efficiently detect the circular track of the positrons. The prototypes of the single silicon detector were produced (Fig. 13) according to the simulation study; the effective area is $102 \text{ mm} \times 72 \text{ mm}$ and strip pitch (width) is $100 \mu\text{m}$ ($27 \mu\text{m}$) for axial direction and $188 \mu\text{m}$ ($50 \mu\text{m}$) for radial direction on p-side. Basic parameters such as the inter-strip capacitance and the full depletion voltage satisfy our requirement [17].

Because the mean hit rate per silicon strip is very high due to the high intensity pulsed beam, the readout electronics should be capable to record data stably up to several MHz. The analog part of ASICs (SlitA) is being developed with a electronics simulation and some prototypes were produced (Fig. 14). The basic performances were measured with the 200 MeV/c positron beam at Tohoku University and decay positron from muon beam at J-PARC [18].

SUMMARY

Precise measurement of $(g - 2)_\mu$ is one of the promising paths to establish new physics beyond SM and muon EDM is sensitive to new physics because it is very suppressed in SM.

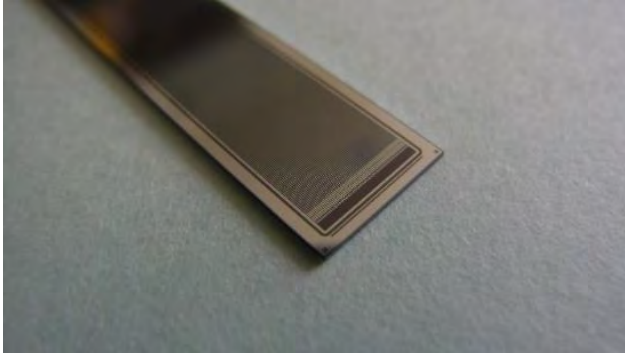


FIG. 13: Photo of the prototype of the silicon detector.

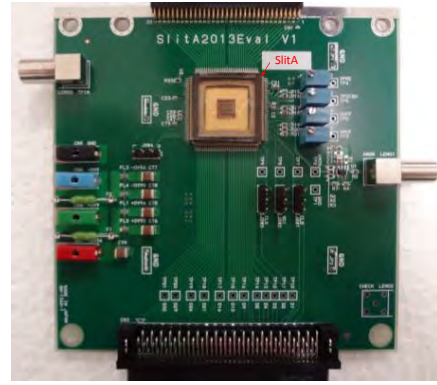


FIG. 14: Photo of the prototype of SlitA on an evaluation board.

E34 aims to measure $(g-2)_\mu$ and EDM with high precision and sensitivity with newly developed novel method of the ultra-cold muon beam. We successfully developed the muonium production target with higher production efficiency by utilizing laser ablated technique. The laser system has been developed in the J-PARC U-line and the Lyman- α laser was succeeded to be fired. The RFQ for initial acceleration and bunching of the cold muons is ready and following RF cavities are being designed. The prototypes of the silicon detector and readout electronics were produced and tested.

We submitted the Technical Design Report to the Program Advisory Committee (PAC) for Nuclear and Particle Physics Experiments at J-PARC and PAC for KEK IMSS MUSE to the aim of starting the experiment in 2019.

* Presented at NuFact15, 10-15 Aug 2015, Rio de Janeiro, Brazil [C15-08-10.2]

† masashio@post.kek.jp; Speaker

- [1] G.W. Bennett et al.: Phys. Rev. **D73** (2006) 072003
- [2] J.L. Feng, K. T. Matchev and Y. Shadmi: Nucl. Phys. **B613** (2001) 366
- [3] G.W. Bennett et al.: Phys. Rev. **D80** (2009) 052008
- [4] J-PARC E34 conceptual design report (2011)
- [5] A.P. Mills, Jr. et al.: Phys. Rev. Lett. **56** (1986) 1463
- [6] P. Bakule et al.: Nucl. Instrum. Meth. **B266** 335-346 (2008)
- [7] P. Bakule et al.: Prog. Theor. Exp. Phys., **103** (2013) C01
- [8] G.A. Beer et al.: Prog. Theor. Exp. Phys., **091** (2014) C01
- [9] R. Kitamura et al.: 025016, 10.7566/JPSCP.8.025016

- [10] N. Saito: Pulsed Coherent Lyman- α Resonance Radiation Generated by Two-Photon Resonance Four-Wave Mixing in Kr-Ar Gas, International Symposium on Science Explored by Ultra Slow Muon 2013
- [11] Y. Kondo et al.: Proc. of IPAC2015, THPF045 (2015)
- [12] M. Otani for the J-PARC E34 collaboration: Development of Muon LINAC for the Muon g-2/EDM Experiment at J-PARC, in these proceedings
- [13] M. Otani et al.: 025010, 10.7566/JPSCP.8.025010
- [14] M. Otani et al.: Biperiodic L-support DAW for Medium Beta for Muon g-2/EDM at J-PARC, PASJ **2014** (2014) SAP039
- [15] M. Otani et al.: Demonstration of muon acceleration and cavity design of the muon LINAC for J-PARC E34, PASJ **2015** (2015) WEOM02
- [16] Hiroyuki A. Torii et al.: 025018, 10.7566/JPSCP.8.025018
- [17] S. Nishimura et al.: Specification and evaluation of silicon strip sensor for the muon g-2/EDM experiment at J-PARC, In *TIPP 2014*
- [18] S. Nishimura et al.: Design of the positron tracking detector for the muon g-2/EDM experiment at J-PARC, in these proceedings

Recent results on lepton flavor violation from CMS*

Alexander Nehr Korn on behalf of the CMS Collaboration[†]

Physics Institute 3B, RWTH Aachen University

(Dated: January 27, 2016)

Abstract

Lepton flavor is a conserved quantity in the standard model of particle physics. It does not follow from an underlying gauge symmetry however, and from neutrino oscillation we know of its violation in the neutral sector. Charged lepton flavor violation induced by neutrino oscillation is heavily suppressed by the small neutrino and heavy gauge boson masses making its discovery extremely unlikely. Extensions of the standard model are able to enhance the branching fractions of such decays to levels observable at the LHC. Here, three searches for lepton flavor violation with the CMS experiment are presented: the decay of the Higgs boson into a muon and a tau lepton, and the decay of heavy resonances as well as the Z boson into an electron and a muon.

LEPTON FLAVOR VIOLATION IN HIGGS DECAYS

Introduction

Flavor-violating Yukawa couplings become possible for example in case the standard model (SM) is valid only until a finite scale [1]. Other possibilities for their introduction are theories with more than one Higgs doublet [2]. While the decay of the Higgs boson to an electron and a muon is strongly constrained by $\mu \rightarrow e\gamma$ searches ($\mathcal{B}(\text{H} \rightarrow e\mu) < \mathcal{O}(10^{-8})$), $\mathcal{B}(\text{H} \rightarrow e\tau)$ and $\mathcal{B}(\text{H} \rightarrow \mu\tau)$ are constrained to upper limits of only $\mathcal{O}(10\%)$ [1] making these channels especially interesting for a direct search.

Analysis

Based on an integrated luminosity of 19.7 fb^{-1} collected with the CMS detector [3] in pp collisions at $\sqrt{s} = 8 \text{ TeV}$, a search for lepton flavor violation (LFV) is performed in the two final states $\text{H} \rightarrow \mu\tau_e$ and $\text{H} \rightarrow \mu\tau_h$ where H corresponds to a standard model Higgs boson of mass $m_{\text{H}} = 125 \text{ GeV}$ and τ_e as well as τ_h denote the decays of tau leptons into electrons and hadrons [4]. The main background in the $\text{H} \rightarrow \mu\tau_e$ channel is $\text{Z} \rightarrow \tau\tau$ while subdominant background originates from jets misidentified as tau leptons in W+jets and multijet events. In the $\text{H} \rightarrow \mu\tau_h$ channel the latter is the dominant background and $\text{Z} \rightarrow \tau\tau$ as well as Z+jets are less important. These backgrounds are estimated using data-driven methods while smaller contributions from standard model $\text{H} \rightarrow \tau\tau$ decays as well as $t\bar{t}$ and diboson production are estimated by simulation. The simulation are normalized the integrated luminosity and theory calculation whereas for $t\bar{t}$ a control region in data is used. The signal is estimated using simulation and theory calculations.

Categorization, Mass Reconstruction and Event Selection

Depending on the final state, events are triggered by requiring a single muon ($H \rightarrow \mu\tau_h$) or a muon and an electron ($H \rightarrow \mu\tau_e$) fulfilling loose kinematic and identification criteria. The leptons in these two final states are then subject to tighter kinematic and identification requirements and must be isolated from other activity in the event. Events are further categorized based on the number of high energetic jets to enhance the sensitivity in the different production mechanisms. Signal events in the zero jet category are predominantly from Higgs bosons produced via gluon-gluon fusion while the two jet category is mostly populated by Higgs bosons produced through vector boson fusion. The one jet category contains signal events both from gluon-gluon fusion and production in association with a vector boson.

The variable of interest is the collinear mass (M_{col}) reconstructed from the muon, the visible part of the tau lepton and the component of the missing transverse energy pointing in the direction of the tau lepton. This technique is based on the collinear approximation which assumes that because the tau lepton mass is much smaller than that of the Higgs boson its decay products are highly boosted in the direction of the τ .

In order to reduce background contribution, discriminating variables are defined. These variables are based on the transverse momenta of the final state leptons, the transverse mass $M_T^\ell = \sqrt{2p_T^\ell E_T^{\text{miss}}(1 - \cos \Delta\phi)}$ of lepton ℓ ($= e, \mu, \tau$), and the azimuthal angles between the leptons and between one lepton and the missing transverse energy. p_T^ℓ denotes the transverse momentum of lepton ℓ , E_T^{miss} the missing transverse energy in the event, and $\Delta\phi$ the azimuthal angle between p_T^ℓ and E_T^{miss} . The selection criteria for these discriminants are chosen such that $S/\sqrt{S+B}$ is maximal. S and B are the number of expected signal and background events in the region $100 < M_{\text{col}} < 150 \text{ GeV}$, and $\mathcal{B}(H \rightarrow \mu\tau) = 10\%$. Furthermore, the jets in the vector boson fusion category must have an invariant mass $m_{jj} > 550 \text{ GeV}$ and must be separated by a pseudorapidity gap of $\Delta\eta > 3.5$. In order to reduce contamination from $t\bar{t}$, events with at least one b-tagged jet are vetoed in the $H \rightarrow \mu\tau_e$ channel.

Systematic Uncertainties

Normalization uncertainties range from 9–100% for the different background estimations while for the signal they are of the order of 10% depending on the parton density functions,

renormalization and factorization scales, and the modeling of both the underlying event and parton showering. Uncertainties from the trigger, identification and isolation of the individual leptons, luminosity and b-tagging range between 2 – 3% and are small compared to the others. Uncertainties affecting the shape of signal and background distributions come from the energy scale of hadronically decaying tau leptons (3%), the jet energy scale (3 – 7%) and the unclustered energy scale affecting the missing transverse energy (10%). The observation of a 1% shift of M_{col} between data and simulation in $Z \rightarrow \tau\tau$ events is associated with an uncertainty of 100%.

Results

A binned likelihood is used to extract the event yields of signal and individual backgrounds from the collinear mass distribution for every category and channel. Using these values, an observed upper limit on the branching fraction of $\mathcal{B}(\text{H} \rightarrow \mu\tau) < 1.51\%$ at 95% confidence level (CL) is set while $\mathcal{B}(\text{H} \rightarrow \mu\tau) < (0.75 \pm 0.38)\%$ is expected. The best fit value of the branching fraction is $\mathcal{B}(\text{H} \rightarrow \mu\tau) = (0.84_{-0.37}^{+0.39})\%$ corresponding to an excess of 2.4 standard deviations. These results are consistent with those obtained by the ATLAS collaboration [5]. Given the observed upper limit on the branching fraction, an upper limit on the flavor-violating Yukawa couplings $\sqrt{|Y_{\mu\tau}|^2 + |Y_{\tau\mu}|^2} < 3.6 \times 10^{-3}$ can be set at 95% CL [1]. The distribution of the combination of the collinear mass in all channels and categories is shown in figure 1 together with the 95% CL upper limits per channel and category and the constraints on the flavor-violating Yukawa couplings.

DECAYS OF HEAVY STATES TO ELECTRON-MUON PAIRS

Introduction

Several extensions of the standard model predict lepton-flavor-violating decays of heavy states to an electron-muon pair. This analysis describes a search for three of these models with the CMS experiment [6]. The first model is R-parity violating supersymmetry with a tau sneutrino ($\tilde{\nu}_\tau$) as the lightest supersymmetric particle decaying to the $e\mu$ final state [7]. The other models describe lepton flavor violation in decays of Z'/a' bosons [8] and quantum black holes (QBH) [9–11] to electron-muon pairs. Similar searches have also been performed by the CDF [12, 13] and D0 [14] collaborations at the Tevatron, and the ATLAS Collaboration [15] at the LHC.

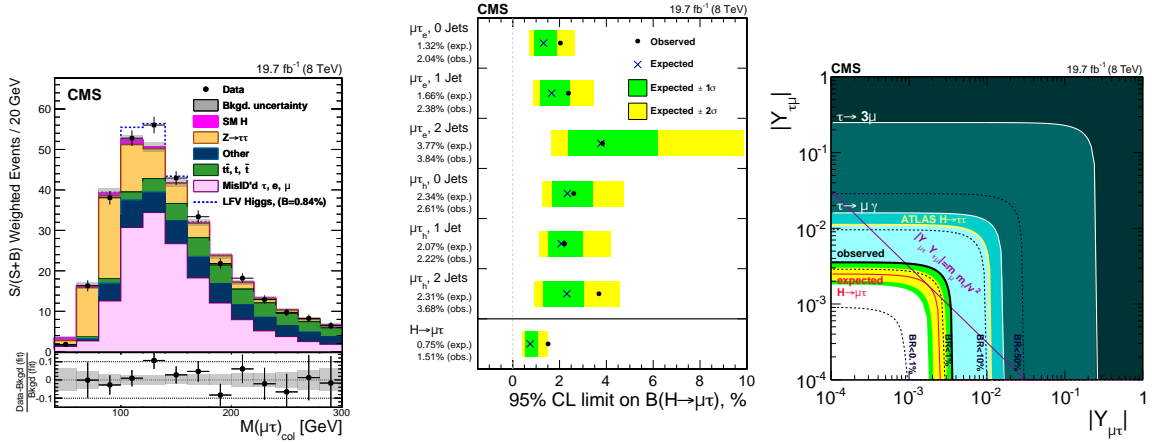


FIG. 1. Left: Distribution of M_{col} combined for all categories and channels individually weighted by $S/(S + B)$. Center: 95% CL upper limits on branching fractions split into categories and channels. Right: Constraints on $|Y_{\mu\tau}|$ and $|Y_{\tau\mu}|$. The red line depicts the expected limit together with its one and two sigma uncertainty bands in yellow and green, respectively. The solid black line shows the observed upper limit while the dashed black lines are reference values. The shaded regions come from null searches for the decays shown and the purple line shows the theoretical naturalness limit.

Analysis

In this search, an excess over the background expectation of electron-muon pairs with high invariant mass ($M_{e\mu} \geq 200$ GeV) is sought. The data sample used corresponds to an integrated luminosity of 19.7 fb⁻¹ collected in pp collisions by CMS at $\sqrt{s} = 8$ TeV. For this analysis $t\bar{t}$ is the dominant background at low invariant masses while above $M_{e\mu} \sim 1$ TeV also WW production becomes important. Other background processes are diboson (e.g., WZ, ZZ and $W\gamma$) as well as single-top production, $Z \rightarrow \tau\tau$, and W+jets, Z+jets and multijet production where jets are misidentified as leptons. While background from W+jets and multijet production is estimated using a data-driven technique, all other processes are modeled using simulation and normalized to theory calculations and integrated luminosity.

Event Selection

This analysis uses a single muon trigger to select events and then further requires at least one muon and one electron satisfying kinematic as well as identification and isolation requirements. Electrons are rejected if there is a muon with low transverse momentum in

its vicinity to reduce background from high p_T muons misidentified as electrons. If there is more than one electron-muon pair, the one with the higher invariant mass is chosen. The invariant mass distribution is shown in figure 2 (left). In order to keep this search as model independent as possible there are no further requirements imposed.

Systematic Uncertainties

The total systematic uncertainty on the background expectation lies between 10% and 35% increasing with the invariant mass. It includes uncertainties in the luminosity, lepton identification and isolation efficiencies, muon momentum as well as electron energy scale, parton distribution functions, cross sections, top- p_T , renormalization and factorization scale, and the limited amount of simulated events in the high invariant mass part of the distribution.

Results

No significant discrepancies between the SM expectation and the data collected by CMS are seen. The result is interpreted in terms of upper limits on different models: resonant tau sneutrino, Z'/a' and QBH production for different numbers of extra dimensions (see figure 2). While there is no sensitivity to lepton-flavor-violating Z'/a' decays when fixing the couplings to the upper bounds obtained in previous experiments [8, 16], yet, limits are set on the tau sneutrino mass depending on the couplings ($M_{\tilde{\nu}_\tau} < 1.21$ (2.11) TeV for $\lambda_{132} = \lambda'_{311} = 0.01$ ($\lambda_{132} = 0.05, \lambda'_{311} = 0.1$)) as well as on the threshold mass of quantum black holes depending on the number of extra dimensions ($M_{\text{th}} < 1.99 - 3.63$ TeV for $n = 0 - 6$). The exclusion limit on the tau sneutrino mass for coupling strengths $\lambda_{132} = 0.05, \lambda'_{311} = 0.1$ is similar to that obtained by the ATLAS collaboration [15].

LEPTON FLAVOR VIOLATION IN Z DECAYS

Introduction

Decays of the Z boson into leptons of different families are forbidden in the SM. Although neutrino oscillation does allow for non-zero branching fractions of lepton-flavor-violating decays, these fractions are unobservably small (e.g., $\mathcal{B}(Z \rightarrow e\mu) < 4 \cdot 10^{-60}$ [17]). Several supersymmetric models and models with massive Dirac or Majorana neutrinos are able to enhance these decay rates to observable levels [17, 18]. There are stringent indirect limits from low-energy $\mu \rightarrow 3e$ conversion experiments on the decay $Z \rightarrow e\mu$ [19, 20] which are

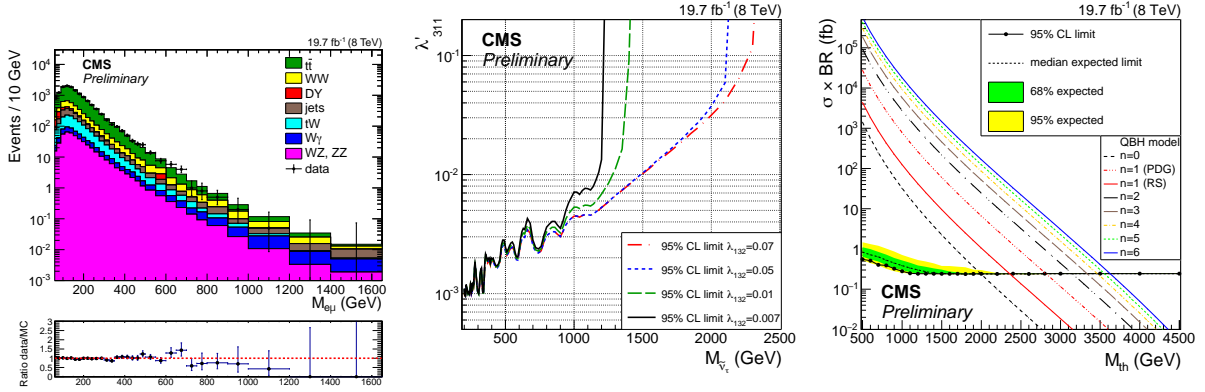


FIG. 2. Left: Invariant mass of electron-muon pairs passing the selection. ‘jets’ refers to the data-driven background estimate of W +jets and multijet production. Center: 95% CL limit contours in the $M_{\tilde{\nu}_\tau}$ - λ'_{311} plane. Regions above the curves are excluded. Right: 95% CL exclusion limit on the signal cross section times branching fraction for QBH production as a function of the threshold mass.

complemented by direct searches from the LEP experiments [21] and recently the ATLAS Collaboration [22].

Analysis

The analysis [23] looks for a deviation from the background expectation in the invariant mass distribution of electron-muon pairs at the Z pole using 19.7 fb^{-1} of data collected in pp collisions by CMS at $\sqrt{s} = 8 \text{ TeV}$. The main backgrounds come from dileptonic $t\bar{t}$ decays, WW production and $Z \rightarrow \tau\tau$. Other backgrounds are jets being misidentified as electrons or muons (e.g., from W +jets and multijet production) as well as single top and other diboson production (e.g., ZZ and WZ). Background from jets misidentified as leptons is estimated using a data-driven approach while the shapes of the other backgrounds are estimated using simulation. Simulated samples are normalized to calculated cross sections except in case of the top-antitop sample where a CMS cross section measurement is used. The signal is estimated using simulation and normalized to the production cross section of Z bosons and a branching fraction of 10^{-6} .

Event Selection

Events are preselected by an electron-muon trigger. Apart from basic kinematic as well as identification and isolation requirements on the electron and muon, the leptons must match

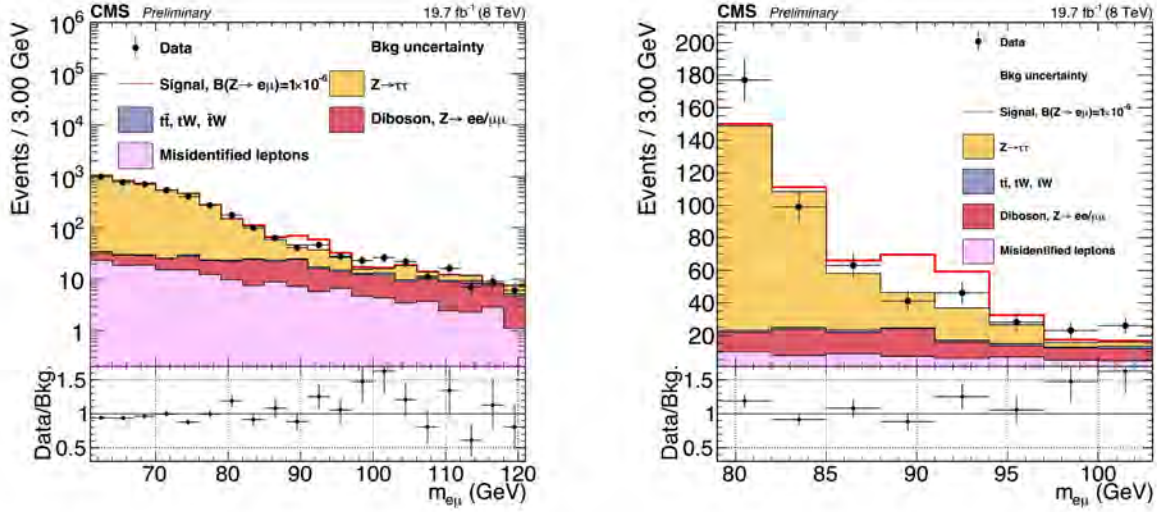


FIG. 3. Distributions of the invariant mass reconstructed from the electron and muon after the full selection for different mass ranges (left: 60 – 120 GeV, right: 79 – 103 GeV). The signal is stacked on top of the background estimate.

the trigger objects and further selection criteria are applied to reduce the large background from standard model processes. First, events with any second electron or muon are rejected in order to diminish background from diboson production and the invariant mass of the remaining events must satisfy $60 < m_{e\mu} < 120$ GeV. Second, three kinematic variables are used to control the main backgrounds. The first is the transverse momentum of the leading jet, the second the transverse mass of the muon M_T^μ and the third the transverse momentum of the Z reconstructed from the selected electron and muon. The requirements on the variables are determined by optimizing the discovery potential $S/\sqrt{S+B+\Delta B}$ in the signal region of 88 – 94 GeV with S and B being the signal and background yields, respectively, and ΔB representing the uncertainty in the background estimate. The distribution of the invariant mass after the full selection is depicted in figure 3.

Systematic Uncertainties

The dominant systematic uncertainty in the background estimate stems from the limited amount of simulated events (10.6%) followed by the normalization uncertainty (6.8%). Other uncertainties come from the electron energy and muon p_T scale as well as from influence of additional collisions in the same bunch crossing, the luminosity measurement and parton density functions (1 – 3%). Uncertainties in trigger, identification and isolation efficiencies

are small ($< 1\%$) as are uncertainties introduced by the jet energy scale and resolution as well as the missing transverse energy. For the signal estimate the systematic uncertainties mentioned above range between 0.1 and 3.3% with the normalization uncertainty being the dominant one.

Results

After the selection, 87 events are found in data within the mass range 88–94 GeV agreeing well with the background expectation of 83 ± 9 (stat.). Assuming a branching fraction of 10^{-6} , 43.8 ± 0.5 (stat.) signal events are expected. Using these numbers, an observed (expected) 95% CL limit on the branching fraction of $\mathcal{B}(Z \rightarrow e\mu) < 7.3 \cdot 10^{-7}$ ($6.7_{-2.0}^{+2.8} \cdot 10^{-7}$) is obtained which is similar to the result from the ATLAS Collaboration [22].

SUMMARY

The searches for lepton flavor violation in decays of the Higgs boson to a muon and a tau lepton and in decays of high mass resonances and the Z boson to electron-muon pairs have been presented. While a 2.4σ excess was observed in the process $H \rightarrow \mu\tau$, no evidence was found in the other searches. Thus, for lepton-flavor-violating Higgs and Z decays, upper limits were set on the respective branching fractions as well as on the Yukawa couplings in case of the Higgs. The absence of a signal in the high mass resonance search was interpreted in terms of three different standard model extensions and model dependent limits were set.

* *Presented at NuFact15, 10-15 Aug 2015, Rio de Janeiro, Brazil [C15-08-10.2]*

† alexander.nehrkorn@cern.ch

- [1] R. Harnik, J. Kopp, and J. Zupan, *JHEP* **03**, 026 (2013), arXiv:1209.1397 [hep-ph].
- [2] J. D. Bjorken and S. Weinberg, *Phys. Rev. Lett.* **38**, 622 (1977).
- [3] S. Chatrchyan *et al.* (CMS), *JINST* **3**, S08004 (2008).
- [4] V. Khachatryan *et al.* (CMS), *Phys. Lett.* **B749**, 337 (2015), arXiv:1502.07400 [hep-ex].
- [5] G. Aad *et al.* (ATLAS), “Search for lepton-flavour-violating $H \rightarrow \mu\tau$ decays of the Higgs boson with the ATLAS detector,” (2015), arXiv:1508.03372 [hep-ex].

- [6] *Search for Lepton Flavour Violating Decays of Heavy Resonances and Quantum Black Holes to electron/muon Pairs in pp Collisions at a centre of mass energy of 8 TeV*, Tech. Rep. CMS-PAS-EXO-13-002 (CERN, Geneva, 2015).
- [7] R. Barbier *et al.*, Phys. Rept. **420**, 1 (2005), arXiv:hep-ph/0406039 [hep-ph].
- [8] J. M. Frere, M. V. Libanov, E. Ya. Nugaev, and S. V. Troitsky, JETP Lett. **79**, 598 (2004), [Pisma Zh. Eksp. Teor. Fiz.79,734(2004)], arXiv:hep-ph/0404139 [hep-ph].
- [9] P. Meade and L. Randall, JHEP **05**, 003 (2008), arXiv:0708.3017 [hep-ph].
- [10] X. Calmet, W. Gong, and S. D. H. Hsu, Phys. Lett. **B668**, 20 (2008), arXiv:0806.4605 [hep-ph].
- [11] D. M. Gingrich, J. Phys. **G37**, 105008 (2010), arXiv:0912.0826 [hep-ph].
- [12] A. Abulencia *et al.* (CDF), Phys. Rev. Lett. **96**, 211802 (2006), arXiv:hep-ex/0603006 [hep-ex].
- [13] T. Aaltonen *et al.* (CDF), Phys. Rev. Lett. **105**, 191801 (2010), arXiv:1004.3042 [hep-ex].
- [14] V. M. Abazov *et al.* (D0), Phys. Rev. Lett. **105**, 191802 (2010), arXiv:1007.4835 [hep-ex].
- [15] G. Aad *et al.* (ATLAS), Phys. Rev. Lett. **115**, 031801 (2015), arXiv:1503.04430 [hep-ex].
- [16] J. M. Frere, M. V. Libanov, E. Y. Nugaev, and S. V. Troitsky, JHEP **03**, 001 (2004), arXiv:hep-ph/0309014 [hep-ph].
- [17] J. I. Illana and T. Riemann, Phys. Rev. **D63**, 053004 (2001), arXiv:hep-ph/0010193 [hep-ph].
- [18] J. M. Yang, Sci. China Phys. Mech. Astron. **53**, 1949 (2010), arXiv:1006.2594 [hep-ph].
- [19] U. Bellgardt *et al.* (SINDRUM), Nucl.Phys. **B299**, 1 (1988).
- [20] S. Nussinov, R. D. Peccei, and X. M. Zhang, Phys. Rev. **D63**, 016003 (2000).
- [21] R. Akers *et al.* (OPAL), Z.Phys. **C67**, 555 (1995).
- [22] G. Aad *et al.* (ATLAS), Phys. Rev. **D90**, 072010 (2014), arXiv:1408.5774 [hep-ex].
- [23] *Search for Lepton Flavor Violation in Z decays in pp collisions at sqrt(s)=8 TeV*, Tech. Rep. CMS-PAS-EXO-13-005 (CERN, Geneva, 2015).

Allowed rare pion and muon decays as tests of the Standard Model*

Dinko Počanić[†]

*Institute for Nuclear and Particle Physics,
University of Virginia, Charlottesville, VA 22904-4714, U.S.A.*

(PEN Collaboration)[‡]
(Dated: 20 December 2015)

Abstract

Simple dynamics, few available decay channels, and extremely well controlled radiative and loop corrections, make pion and muon decays a sensitive means for testing the underlying symmetries, the universality of weak fermion couplings, as well as for study of pion structure and chiral dynamics. We review the current state of experimental study of the allowed rare decays of charged pions: (a) electronic, $\pi^+ \rightarrow e^+\nu_e$, or π_{e2} , (b) radiative, $\pi^+ \rightarrow e^+\nu_e\gamma$, or $\pi_{e2\gamma}$, and (c) semileptonic, $\pi^+ \rightarrow \pi^0 e^+\nu$, or π_{e3} , as well as muon radiative decay, $\mu^+ \rightarrow e^+\nu_e\bar{\nu}_\mu\gamma$. Taken together, these data present an internally consistent picture that also agrees well with Standard Model (SM) predictions. However, even following the great strides of the recent decades, experimental accuracy is lagging far behind that of the theoretical description for all above processes. We review the implications of the present state of knowledge and prospects for further improvement in the near term.

MOTIVATION

Pion decay has provided an important testing ground for the weak interaction and radiative corrections from the beginnings of modern subatomic physics. The unexpected suppression of the direct electronic decay of the pion ($\pi \rightarrow e\nu$, or π_{e2}) led to an early examination of the nature of the weak interaction and to the prediction of a low branching fraction of $\sim 1.3 \times 10^{-4}$ [1] as a consequence of the $V-A$ nature of the weak interaction, through helicity suppression of the right-handed state of the electron. In the meantime, the extraordinary success of the Standard Model has opened significant opportunities for precision tests of its underlying symmetries, lepton and quark-lepton coupling universality, and a host of related issues through precision measurements of pion decays. We will address the specific motivation and physics reach for each channel separately below. A recent in-depth review of the subject is given in [2].

Muon decay, a purely leptonic electroweak process, serves a special role in the Standard Model because it calibrates the strength of the weak coupling. Its precise theoretical description, via the so-called Michel parameters [3], positions it uniquely to provide constraints on possible contributions outside the $V-A$ standard electroweak model. Below we discuss new results on the muon radiative decay $\mu^+ \rightarrow e^+\nu_e\bar{\nu}_\mu\gamma$, the only process that gives access to the decay parameter $\bar{\eta}$.

PION ELECTRONIC $\pi \rightarrow e\bar{\nu}$ DECAY (π_{e2})

At the tree level, the ratio of the $\pi \rightarrow e\bar{\nu}_e$ to $\pi \rightarrow \mu\bar{\nu}_\mu$ decay widths is given by [1, 4]

$$R_{e/\mu,0}^\pi = \frac{\Gamma(\pi \rightarrow e\bar{\nu}_e)}{\Gamma(\pi \rightarrow \mu\bar{\nu}_\mu)} = \frac{m_e^2}{m_\mu^2} \cdot \frac{(m_\pi^2 - m_e^2)^2}{(m_\pi^2 - m_\mu^2)^2} \simeq 1.283 \times 10^{-4}, \quad (1)$$

where the ratio of squared lepton masses for the two decays, comes from the helicity suppression by the $V-A$ lepton- W boson weak couplings. If, instead, the decay could proceed directly through the pseudoscalar current, the ratio $R_{e/\mu}^\pi$ would reduce to the second, phase-space factor, or approximately 5.5. More complete treatment of the process includes $\delta R_{e/\mu}^\pi$, the radiative and loop corrections, and the possibility of lepton universality violation, i.e.,

that g_e and g_μ , the electron and muon couplings to the W , respectively, may not be equal:

$$R_{e/\mu}^\pi = \frac{\Gamma(\pi \rightarrow e\bar{\nu}(\gamma))}{\Gamma(\pi \rightarrow \mu\bar{\nu}(\gamma))} = \frac{g_e^2 m_e^2 (m_\pi^2 - m_e^2)^2}{g_\mu^2 m_\mu^2 (m_\pi^2 - m_\mu^2)^2} (1 + \delta R_{e/\mu}^\pi), \quad (2)$$

where the “ (γ) ” indicates that radiative decays are fully included in the branching fractions. Improvements of the theoretical description of the π_{e2} decay have culminated in a series of calculations that have refined the SM prediction to a precision of 8 parts in 10^5 :

$$(R_{e/\mu}^\pi)^{\text{SM}} = \frac{\Gamma(\pi \rightarrow e\bar{\nu}(\gamma))}{\Gamma(\pi \rightarrow \mu\bar{\nu}(\gamma))} \Big|_{\text{calc}} = \begin{cases} 1.2352(5) \times 10^{-4} & [5], \\ 1.2354(2) \times 10^{-4} & [6], \\ 1.2352(1) \times 10^{-4} & [7]. \end{cases} \quad (3)$$

A comparison with equation (1) reveals that the radiative and loop corrections amount to almost 4% of $R_{e/\mu}^\pi$. However, the current experimental precision [8, 9]

$$(R_{e/\mu}^\pi)^{\text{EXP}} = 1.2327(23) \times 10^{-4}, \quad (4)$$

lags behind the theoretical one by more than an order of magnitude.

Because of the large helicity suppression of the π_{e2} decay, its branching ratio is highly susceptible to small non- $V-A$ contributions from new physics, making this decay a particularly suitable subject of study, as discussed in, e.g., [11–16]. This prospect provides the primary motivation for the ongoing PEN [17] and PIENU [18] experiments. Of the possible “new physics” contributions in the Lagrangian, π_{e2} is directly sensitive to the pseudoscalar one. At the precision of 10^{-3} , $R_{e/\mu}^\pi$ probes the pseudoscalar and axial vector mass scales up to 1000 TeV and 20 TeV, respectively [15, 16]. For comparison, Cabibbo-Kobayashi-Maskawa (CKM) matrix unitarity and precise measurements of several superallowed nuclear beta decays constrain the non-SM vector contributions to > 20 TeV, and scalar to > 10 TeV [8]. Although scalar interactions do not directly contribute to $R_{e/\mu}^\pi$, they can do so through loop diagrams, resulting in sensitivity to new scalar interactions up to 60 TeV [15, 16]. The subject was recently reviewed at length in [10]. In addition, $(R_{e/\mu}^\pi)^{\text{exp}}$ provides limits on masses of certain SUSY partners [14], and on neutrino sector anomalies [13].

The PEN experiment at PSI

Between 2008 and 2010, PEN, a collaboration of 7 institutions from USA and Europe, has carried out measurements of π^+ and μ^+ decays at rest at the Paul Scherrer Institute (PSI) with the aim to reach $\Delta R_{e/\mu}^\pi / R_{e/\mu}^\pi \simeq 5 \times 10^{-4}$, and is currently analyzing the data [17]. The PEN experiment uses an upgraded version of the PIBETA detector system, described in detail in [19], and previously used in a series of rare pion and muon decay measurements [2, 20–22]. The main component of the PEN apparatus, shown in Fig. 1, is a spherical large-acceptance ($\sim 3\pi$ sr) electromagnetic shower calorimeter. The calorimeter comprises 240 truncated pyramids of pure CsI, 12 radiation lengths (r.l.) deep. Beam particles entering the apparatus with $p \simeq 75$ MeV/ c are tagged in a thin upstream beam counter (BC) and, after a ~ 3 m long flight path in a 5 mm thick active degrader (AD) and a low-mass mini time projection chamber (mTPC), finally to reach a 15 mm thick active target (AT) where the beam pions stop. Decay particles are tracked non-magnetically in a pair of concentric

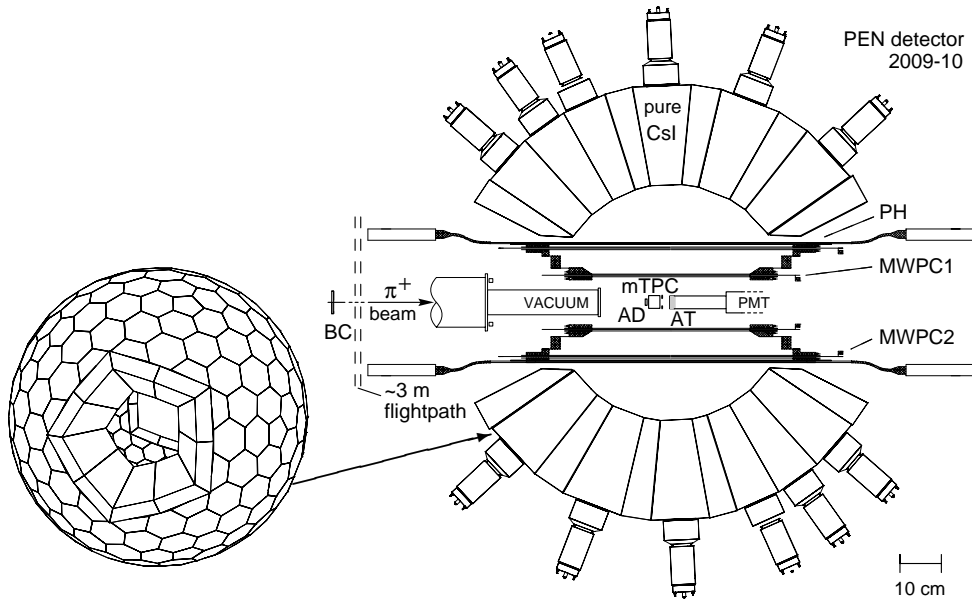


FIG. 1. Schematic cross section of the PEN apparatus: upstream beam counter (BC), 5 mm thick active degrader (AD), mini time projection chamber (mTPC), active target (AT), cylindrical multiwire proportional chambers (MWPC's), plastic hodoscope (PH) detectors and photomultiplier tubes (PMT's), 240-element pure CsI electromagnetic shower calorimeter and its PMT's. BC, AD, AT and PH detectors are made of plastic scintillator. For details on detector performance see [19].

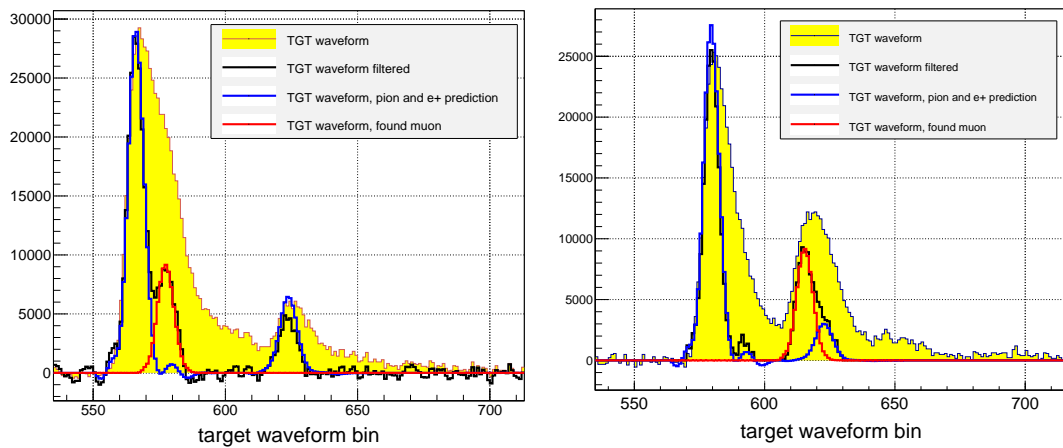


FIG. 2. Full and filtered active target (TGT) waveform in the PEN experiment for two challenging $\pi \rightarrow \mu \rightarrow e$ sequential decay events with an early $\pi \rightarrow \mu$ decay (left) and early $\mu \rightarrow e$ decay (right). The filtering procedure consists of a simple algebraic manipulation of the signal. To the naked eye both raw waveforms appear to have two peaks only. The separation of events with/without a muon signal depends critically on the accuracy of the predicted pion and positron signals.

cylindrical multiwire proportional chambers (MWPC1,2) and an array of twenty 4 mm thick plastic hodoscope detectors (PH), all surrounding the active target. The BC, AD, AT and PH detectors are all made of fast plastic scintillator material. Detector waveforms are digitized at 2 GS/s for BC, AD, and AT, and at 250 MS/s for the mTPC.

A key source of systematic uncertainty in π_{e2} measurements at rest has been the hard to measure low energy tail of the detector response function, caused by electromagnetic shower leakage from the calorimeter mostly in the form of photons, masked by the overwhelming $\pi \rightarrow \mu \rightarrow e$ background events. Other physical processes, if not properly identified and suppressed, also contribute events, mainly to the low energy part of the spectrum. They include: ordinary pion decay into a muon in flight, before the pion is stopped, with the resulting muon decaying within the time gate accepted in the measurement, and radiative decay events. The latter process is well measured, analyzed, and properly accounted for in the PEN apparatus. Shower leakage and pion decays in flight can only be well characterized if the $\pi \rightarrow \mu \rightarrow e$ chain can be well separated from the direct $\pi \rightarrow e\nu$ decay in the target. Therefore much effort has been devoted to digitization, filtering and analysis of the target waveforms [23], as illustrated in Fig. 2. The decay time histograms of the $\pi \rightarrow e\nu$ decay and $\pi \rightarrow \mu \rightarrow e$ sequence, shown in Fig. 3 for a subset of data recorded in 2010, illustrate best

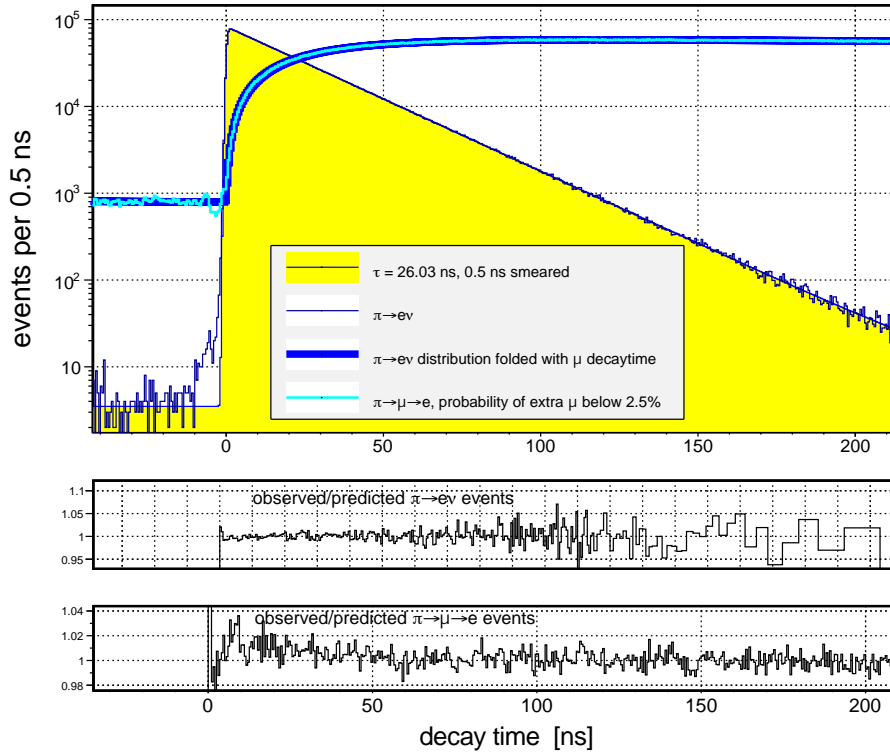


FIG. 3. Decay time histograms for a subset of 2010 PEN data: $\pi \rightarrow e\nu$ and $\pi \rightarrow \mu \rightarrow e$ events. The two processes are distinguished primarily by the total e^+ energy and by the absence or presence, respectively, of an extra 4.1 MeV (muon) in the target due to $\pi \rightarrow \mu$ decay. The π_{e2} data are shown with a pion lifetime $\tau_\pi = 26.03$ ns exponential decay function superimposed. The $\pi \rightarrow \mu \rightarrow e$ data, prescaled by a factor of $\sim 1/64$, are shown with the cut on the probability of $< 2.5\%$ for a second, pile-up muon to be present in the target at $t = 0 = t_{\pi\text{stop}}$. The turquoise histogram gives the $\pi \rightarrow \mu \rightarrow e$ yield constructed entirely from the measured $\pi \rightarrow e\nu$ data folded with the μ decay rate, and corrected for random muons; it perfectly matches the bold dark blue histogram. The two lower plots show the observed to predicted ratios for π_{e2} and $\pi \rightarrow \mu \rightarrow e$ events, respectively; the observed scatter is statistical in nature.

the quality of the PEN data. The $\pi \rightarrow e\nu$ data follow the exponential decay law over more than three orders of magnitude, and perfectly predict the measured $\pi \rightarrow \mu \rightarrow e$ sequential decay data once the latter are corrected for random (pile-up) events. Both event ensembles were obtained with minimal requirements (cuts) on detector observables, none of which bias the selection in ways that would affect the branching ratio. The probability of random $\mu \rightarrow e$ events originating in the target can be controlled in the data sample by making use of multihit time to digital converter (TDC) data that record early pion stop signals. With this information one can strongly suppress events in which an “old” muon was present in the target by the time of the pion stop that triggered the readout.

During the 2008-10 production runs the PEN experiment accumulated some 2.3×10^7 $\pi \rightarrow e\nu$, and more than 2.7×10^8 $\pi \rightarrow \mu \rightarrow e$ events, as well as significant numbers of pion and muon radiative decays. A comprehensive blinded maximum likelihood analysis is under way to extract a new experimental value of $R_{e/\mu}^\pi$. As of this writing, there appear no obstacles that would prevent the PEN collaboration to reach a precision of $\Delta R/R < 10^{-3}$. The PIENU experiment at TRIUMF, discussed below, has a similar precision goal.

The PIENU experiment at TRIUMF

The PIENU experiment at TRIUMF builds on the earlier measurements at the same laboratory [24], aiming at a significant improvement in precision through refinements of the technique used. Major improvements in precision in PIENU over the earlier TRIUMF TINA measurement derive from improved geometry and beamline, a superior calorimeter, as well as high-speed digitizing of all detector signals. The apparatus is described in detail in [9] and shown in Fig. 4. A $75 \text{ MeV}/c$ π^+ beam from the improved TRIUMF M13 beam line [25] is tracked in wire chambers, identified by plastic scintillators, and stopped in a 0.8 cm thick scintillator target. Fine tracking near the target is provided by two sets of single-sided silicon strip detectors located immediately upstream and downstream of the target assembly. The positrons from $\pi \rightarrow e\nu$ and $\pi \rightarrow \mu \rightarrow e$ decays are detected in the positron telescope, which consists of a silicon strip counter, two thin plastic counters, and an acceptance-defining wire chamber that covers the front of the crystal calorimeter. The calorimeter is 19 r.l. deep and consists of a large single crystal of NaI(Tl) surrounded laterally by an array of 97 pure CsI crystals. The solid-angle acceptance of the telescope counters is 20% of $4\pi \text{ sr}$. Thus, PIENU achieves better energy resolution than PEN, at the expense of lower solid angle coverage.

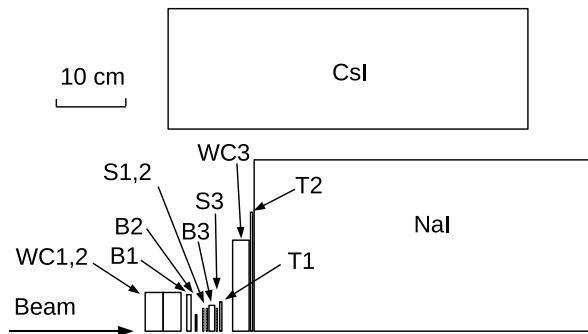


FIG. 4. Top half cross-section of the PIENU detector. The cylindrical NaI(Tl) crystal is surrounded by a cylindrical array of CsI crystals. For further details see [9] and references therein.

The PIENU experiment completed data acquisition in 2012, and is in the analysis stage as of this writing. The PIENU collaboration has recently published an analysis of 1/5 of their data [9] with the result

$$(R_{e/\mu}^\pi)^{\text{PIENU}} = 1.2344 (23)_{\text{stat}} (19)_{\text{syst}} \times 10^{-4}, \quad (5)$$

which is consistent with the previous world average [8] as well as with the Standard Model prediction of Eq. 3, and has the effect of reducing the previous world average uncertainty by almost a factor of two, as shown in Eq. 4.

PION RADIATIVE ELECTRONIC $\pi^+ \rightarrow e^+ \nu_e \gamma$ DECAY ($\pi_{e2\gamma}$)

The decay $\pi^+ \rightarrow e^+ \nu_e \gamma$ proceeds via a combination of QED (inner bremsstrahlung, IB) and direct, structure-dependent (SD) amplitudes [4, 26]. The strong helicity suppression of the primary non-radiative process, $\pi \rightarrow e\nu$, discussed above, also suppresses the IB terms, making the structure-dependent amplitudes measurable in certain regions of phase space [26, 27]. To describe the SD amplitude, standard $V-A$ electroweak theory requires only two pion form factors, F_A , axial vector, and F_V , vector (or polar-vector). The amplitudes F_A and F_V in principle depend on the 4-momentum transfer q^2 to the $e-\nu$ pair (or to the W boson); in $\pi_{e2\gamma}$ decay $q^2 \approx 0$ is a good approximation (“soft pion limit”). For a long time radiative pion decay measurements had access only to one structure dependent amplitude, the $SD^+ \propto (F_V + F_A)^2$, with weak or no sensitivity to $SD^- \propto (F_V - F_A)^2$. Therefore most evaluations took the value of F_V from the conserved vector current (CVC) hypothesis prediction based on the $\pi^0 \rightarrow \gamma\gamma$ decay width [26]. Recent PIBETA collaboration results [22] led to an order of magnitude improvement in the precision of the $\pi_{e2\gamma}$ branching ratio

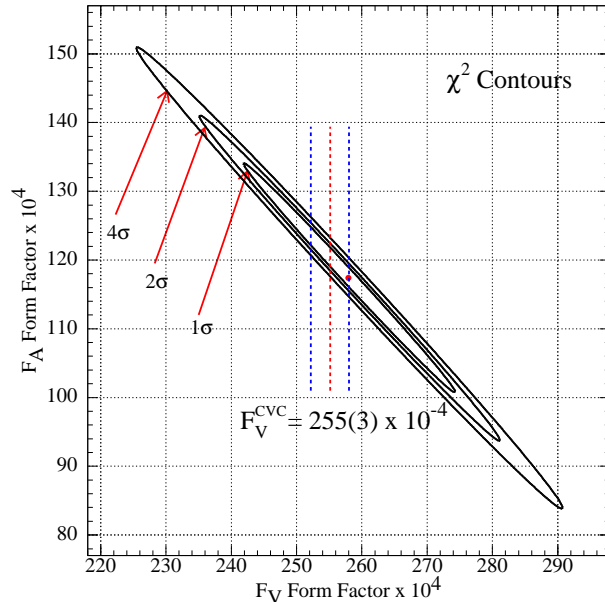


FIG. 5. PIBETA data: contour plot of loci of constant χ^2 for the minimum value χ_0^2 (red dot) plus 1, 2, and 4 units, respectively, in the F_A - F_V parameter plane. The range of the CVC prediction $F_V = 0.0255 \pm 0.0003$ is indicated by the dashed vertical lines. See [2, 22] for more details.

determination, as well as of F_A and F_V , and a first evaluation of the q^2 dependence of F_V . However, the measurement was most sensitive to the low p_ν segment of phase space which is strongly dominated by the SD^+ amplitude, resulting in a very narrow constraint on $F_V + F_A$, as shown in Fig. 5.

The PEN data analysis is expected to add significantly to the more than 60k PIBETA $\pi_{e2\gamma}$ event set, but with increased sensitivity to the SD^- amplitude due to better controlled backgrounds. Thus, the extremely skewed ellipse of Fig. 5 would give way to a more balanced set of limits, and, thus, an improved independent limit on F_V , as well as a further tightening of the limit on F_T , the long hinted-at tensor contribution [22]. It is worth noting that the ratio of F_A/F_V enters directly into the chiral perturbation theory lagrangian at the leading order through the $l_9 + l_{10}$ term [26], and is among the basic low energy chiral constants.

PION SEMILEPTONIC (BETA) $\pi^+ \rightarrow \pi^0 e^+ \nu$ DECAY (π_{e3})

Unlike π_{e2} , the extremely rare, $\mathcal{O}(10^{-8})$, pion beta decay is not suppressed; its low rate derives from the restricted phase space of final states, entirely due to the small difference between the π^\pm and π^0 masses. As a pure vector $0^- \rightarrow 0^-$ transition, it is fully analogous to the superallowed Fermi (SAF) nuclear beta decays; indeed it is the simplest realization of the latter, fully free of complications arising from nuclear structure corrections. SAF decays have historically led to the formulation of the CVC hypothesis, and have played a critical role in testing the unitarity of the Cabibbo-Kobayashi-Maskawa quark mixing matrix through evaluations of the V_{ud} element [8].

The $\sim 0.5\%$ PIBETA π_{e3} measurement [20] is the most precise one to date. Because it used π_{e2} decay events for normalization, this result will receive a slight improvement in precision once the PEN and PIENU results become available. Although not competitive with the SAF based V_{ud} , there are no plans to improve the PIBETA result precision until the current crop of experiments studying the more easily accessible neutron beta decay are completed (for a more detailed discussion of that topic see [28]). In the meantime, however, one can use the PIBETA π_{e3} branching ratio to evaluate $R_{e/\mu}^\pi$ by fixing V_{ud} to its very precise PDG 2014 recommended value of 0.97425 (22) [8] and adjusting $R_{e/\mu}^\pi$ until the extracted value of $V_{ud}^{\pi\beta}$ agrees. This exercise yields:

$$(R_{e/\mu}^\pi)^{\text{PIBETA}} = 1.2366 (64) \times 10^{-4}, \quad (6)$$

in good agreement with direct measurements reviewed in the above section on π_{e2} decay.

MUON RADIATIVE $\mu^+ \rightarrow e^+ \nu_e \bar{\nu}_\mu \gamma$ DECAY

A 2004 PIBETA set of ~ 0.5 M radiative muon events was recently analyzed; the relevant measured and Monte Carlo simulated spectra, including backgrounds, shown in Fig. 6, are in excellent agreement within the design acceptance of the spectrometer. The analysis yields a preliminary branching ratio for $E_\gamma > 10$ MeV, and $\theta_{e\gamma} > 30^\circ$:

$$B^{\text{exp}}(\mu^+ \rightarrow e^+ \nu_e \bar{\nu}_\mu \gamma) = 4.365 (9)_{\text{stat}} (42)_{\text{syst}} \times 10^{-3}, \quad (7)$$

which represents a 29-fold improvement in precision over the previous result [8], and is in excellent agreement with the SM value: $B^{\text{SM}} = 4.342 (5)_{\text{stat-MC}} \times 10^{-3}$. Minimum- χ^2

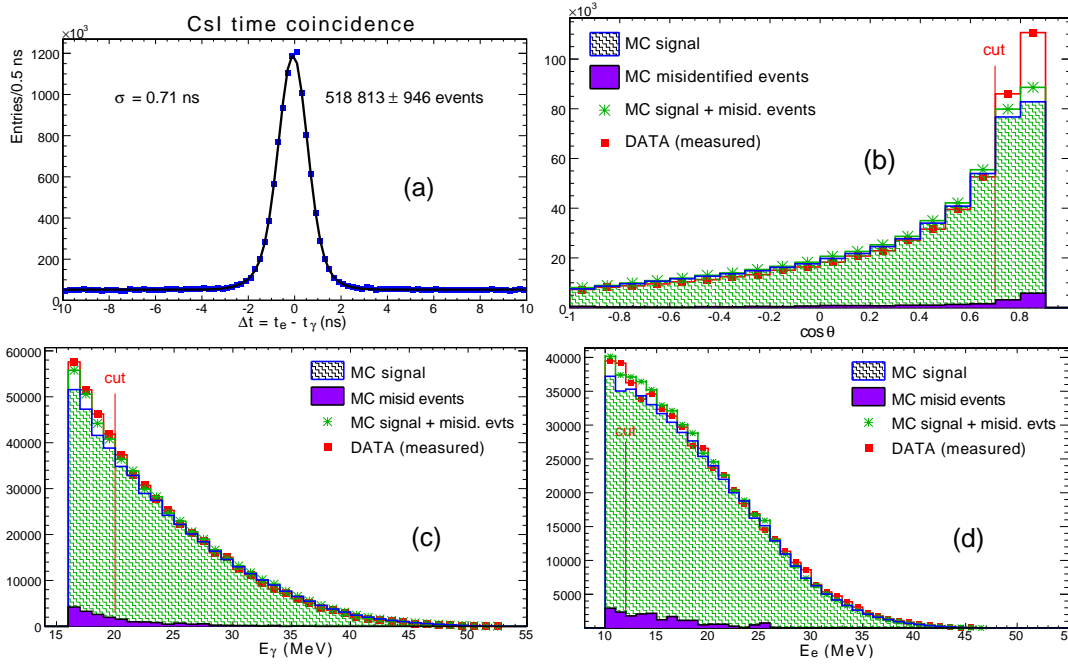


FIG. 6. PIBETA data: measured and simulated $\mu^+ \rightarrow e^+ \nu_e \bar{\nu}_\mu \gamma$ distributions of (a) $\Delta t_{e\gamma}$, (b) $\cos \theta_{e\gamma}$, (c) E_γ , and (d) E_{e^+} . Also shown are the misidentified Monte Carlo events (split-off secondary neutral showers), as well as bounds of cuts applied in the branching ratio analysis.

analysis of the most sensitive data subset (with roughly balanced systematic and statistical uncertainties) yields a preliminary value for the $\bar{\eta}$ parameter ($\bar{\eta}^{\text{SM}} \equiv 0$):

$$\bar{\eta} = 0.006 (17)_{\text{stat}} (18)_{\text{syst}}, \quad \text{or} \quad \bar{\eta} < 0.028 \quad (68\% \text{CL}), \quad (8)$$

a 4-fold improvement over previous limits [29]. Details of this analysis, including a discussion of the uncertainties, are given in [30] and [31].

CONCLUSIONS

Vigorous efforts are presently under way to measure precisely the branching ratios for allowed rare decays of the charged pion as well as of the muon. The experimental precision still lags by about an order of magnitude behind SM calculations. As that gap is narrowed, this field of research, complementary to collider searches, will realize its full potential for discovery or further improvement of the limits on various possible extensions of the Standard Model beyond the well established $V-A$ form. Specifically, a significant improvement of the precision of the π_{e2} branching ratio is expected from the full PEN and PIENU analyses which are forthcoming in the near future, with attendant limits on lepton universality and non- $(V-A)$ interaction terms.

This work has been supported by grants from the US National Science Foundation, the Paul Scherrer Institute, and the Russian Foundation for Basic Research.

* Presented at NuFact15, 10-15 Aug 2015, Rio de Janeiro, Brazil [C15-08-10.2]

[†] pocanic@virginia.edu; Speaker

- [‡] L. P. Alonzi, V. A. Baranov, W. Bertl, M. Bychkov, Yu. M. Bystritsky, E. Frlež, C. J. Glaser, V. A. Kalinnikov, N. V. Khomutov, A. S. Korenchenko, S. M. Korenchenko, M. Korolija, T. Kozlowski, N. P. Kravchuk, N. A. Kuchinsky, M. C. Lehman, D. Mekterović, E. Munyangabe, D. Mzhavia, A. Palladino, P. Robmann, A. M. Rozhdestvensky, I. Supek, P. Truöl, Z. Tsamalaidze, A. van der Schaaf, B. Vandevender, E. P. Velicheva, M. G. Vitz, V. P. Volnykh.
- [1] R. P. Feynman and M. Gell-Mann, *Phys. Rev.* **109**, 193 (1958).
 - [2] D. Počanić, E. Frlež and A. van der Schaaf, *J. Phys. G* **41**, 114002 (2014), arXiv:1407.2865.
 - [3] L. Michel, *Proc. Phys. Soc. London Sect. A* **63**, 514 (1950); C. Bouchiat and L. Michel, *Phys. Rev.* **106**, 170 (1957); T. Kinoshita and A. Sirlin, *ibid.* **108**, 844 (1957).
 - [4] For a detailed discussion of the fundamentals of the $\pi_{e2(\gamma)}$ decay see, e.g., D. A. Bryman, P. Depommier and C. Leroy *Phys. Rep.* **88**, 151 (1982).
 - [5] W. J. Marciano and A. Sirlin, *Phys. Rev. Lett.* **71**, 3629 (1993).
 - [6] M. Finkemeier, *Phys. Lett. B* **387**, 391 (1996).
 - [7] V. Cirigliano and I. Rosell, *Phys. Rev. Lett.* **99**, 231801 (2007).
 - [8] K. A. Olive *et al.* (Particle Data Group), *Chin. Phys. C*, **38**, 090001 (2014).
 - [9] A. Aguilar-Arevalo *et al.* (PIENU Collaboration), *Phys. Rev. Lett.* **115**, 071801 (2015).
 - [10] D. Bryman, W. J. Marciano, R. Tschirhart and T. Yamanaka, *Annu. Rev. Nucl. Part. Sci.* **61**, 331 (2011).
 - [11] R. E. Shrock *Phys. Lett. B* **96**, 159 (1980); *Phys. Rev. D* **24**, 5 (1981).
 - [12] O. U. Shanker *Nucl. Phys.* **B204**, 375 (1982).
 - [13] W. Loinaz, N. Okamura, S. Rayyan, T. Takeuchi, L.C.R. Wijewardhana, *Phys. Rev. D* **70**, 113004 (2004).
 - [14] M.J. Ramsey-Musolf, S. Su and S. Tulin, *Phys. Rev. D* **76**, 095017 (2007).
 - [15] B. A. Campbell and D. W. Maybury, *Nucl. Phys.* **B709**, 419 (2005).
 - [16] B. A. Campbell and A. Ismail, arXiv 0810.4918 (2008).
 - [17] <http://pen.phys.virginia.edu/> and links therein.
 - [18] <http://pienu.triumf.ca/> and links therein.
 - [19] E. Frlež, *et al.*, *Nucl. Instrum. Meth. A* **526**, 300 (2004).
 - [20] D. Počanić *et al.*, *Phys. Rev. Lett.* **93**, 181803 (2004).
 - [21] E. Frlež *et al.*, *Phys. Rev. Lett.* **93**, 181804 (2004).
 - [22] M. Bychkov, *et al.*, *Phys. Rev. Lett.* **103**, 181803 (2009).
 - [23] A. Palladino, PhD thesis, University of Virginia (2012).
 - [24] D. I. Britton *et al.*, *Phys. Rev. Lett.* **68**, 3000 (1992); D. I. Britton *et al.*, *Phys. Rev. D* **46**, R885 (1992).
 - [25] A. Aguilar-Arevalo *et al.* (PIENU Collaboration), *Nucl. Instrum. Meth. A* **609**, 102 (2009).
 - [26] For a detailed discussion see, e.g., J. F. Donoghue, E. Golowich and B. R. Holstein, *Dynamics of the Standard Model* (Cambridge, 1992).
 - [27] A. M. Bernstein and B. R. Holstein, *Rev. Mod. Phys.* **85**, 49 (2013).
 - [28] S. Baessler, J. D. Bowman, S. Penttilä and D. Počanić, *J. Phys. G* **41**, 114003 (2014).
 - [29] W. Eichenberger, R. Engfer, and A. van der Schaaf, *Nucl. Phys.* **A412**, 523 (1984).
 - [30] E. Munyangabe, Ph.D. thesis, University of Virginia, 2012.
 - [31] B. A. VanDevender, Ph.D. thesis, University of Virginia, 2005.

Search for the decay $\mu^+ \rightarrow e^+e^-e^{+\ast}$

Roman Gredig^{1,†}

(For the Mu3e Collaboration)[‡]

¹*University of Zurich*

(Dated: April 15, 2016)

Abstract

Mu3e is a proposed experiment to be built at the Paul Scherrer Institute searching for the charged lepton flavor violating decay $\mu^+ \rightarrow e^+e^-e^+$ with a sensitivity of $\mathcal{B} < 10^{-16}$, four orders of magnitudes lower than its predecessor SINDRUM [1]. The following proceeding gives an overview over the experiment and the current R&D efforts in building a silicon pixel tracker and time hodoscope consisting of scintillating fibers and tiles. The detector components and a read-out strategy for the whole experiment are described.

INTRODUCTION

In the standard model lepton flavor is conserved at tree level. The observation of neutrino oscillations by experiments such as SuperKamiokande [2], SNO [3], and KamLAND [4] is, however, a direct proof of lepton flavor violation (LFV). Charged LFV (CLFV) would lead to $\mu \rightarrow e$ and $\tau \rightarrow \mu$ transitions without neutrinos in the final state. In the standard model CLFV can only be induced by neutrino mixing (see Fig. 1 for the decay of interest here) but such processes are highly suppressed by the tiny neutrino masses. The resulting branching ratios are below 10^{-50} , way beyond the experimental sensitivity. The observation of CLFV would therefore directly signal physics beyond the standard model. Two examples are shown in Fig. 1 as well. Muon number violation has already been investigated in different channels (see Tab. I). When these processes would be observed their relative strengths would guide the attempts to identify the underlying mechanism. A new $\mu^+ \rightarrow e^+e^-e^+$ search has been proposed at the Paul Scherrer Institute (PSI) aiming at a hitherto unreached sensitivity down to $\mathcal{B} < 10^{-16}$ [5], four orders of magnitude more sensitive than reached by its 27 years old predecessor SINDRUM.

TABLE I: Experimental upper limits on the branching ratios B of LFV muon decays

Decay channel	Experiment	\mathcal{B} upper limit	Ref.
$\mu \rightarrow e\gamma$	MEGA	$1.2 \cdot 10^{-11}$	[6]
	MEG	$5.7 \cdot 10^{-13}$	[7]
$\mu \rightarrow eee$	SINDRUM	$1.0 \cdot 10^{-12}$	[1]
$\mu^- \text{Au} \rightarrow e^- \text{Au}$	SINDRUM II	$7 \cdot 10^{-13}$	[8]

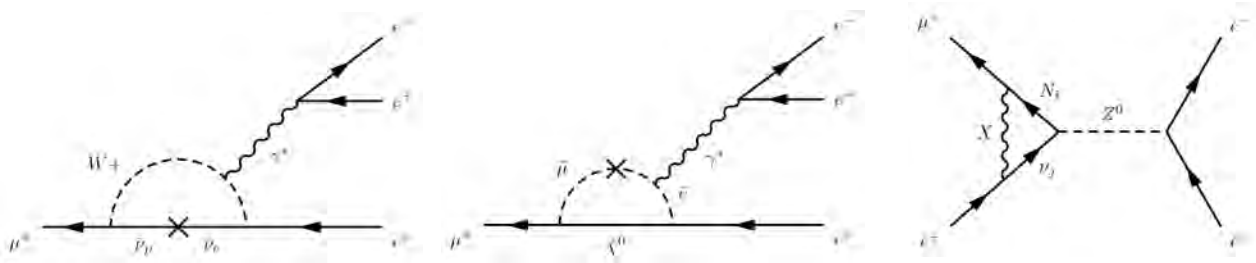


FIG. 1: Possible $\mu^+ \rightarrow e^+e^-e^+$ mechanisms. From the left: neutrino mixing allowed within the standard model, a supersymmetric contribution, and a penguin diagram in the little Higgs model.

DESIGN OF THE MU3E EXPERIMENT

A signal event in Mu3e are two positrons and one electron with common vertex, a vanishing sum of their momenta $\Sigma \vec{p}_i = 0$ and the muon mass as the total energy. The main challenge is the background suppression. An excellent momentum resolution of less than $0.5 \text{ MeV}/c$ is needed to identify the internal conversion background $\mu \rightarrow eee\nu\nu$ with a branching ratio $\mathcal{B} = 3.4 \cdot 10^{-5}$. In addition the combinatorial background needs to be suppressed by an excellent vertex locator, timing and momentum measurement.

The electron momenta are intended to be measured in a 1 T homogeneous magnetic field with silicon pixel detectors. Additional scintillating timing detectors are needed to suppress combinatorial background. The low momenta of the electrons ($p < 53 \text{ MeV}/c$) demand the reduction of the material in the active area to a minimum. Therefore the detector will be operated in a gaseous helium atmosphere. There will be a helium flow velocity of about 3 m s^{-1} to cool active components, as for example the silicon pixel sensors [9]. The readout FPGAs and timing detectors will be cooled by an additional liquid helium cooling system being outside the active area.

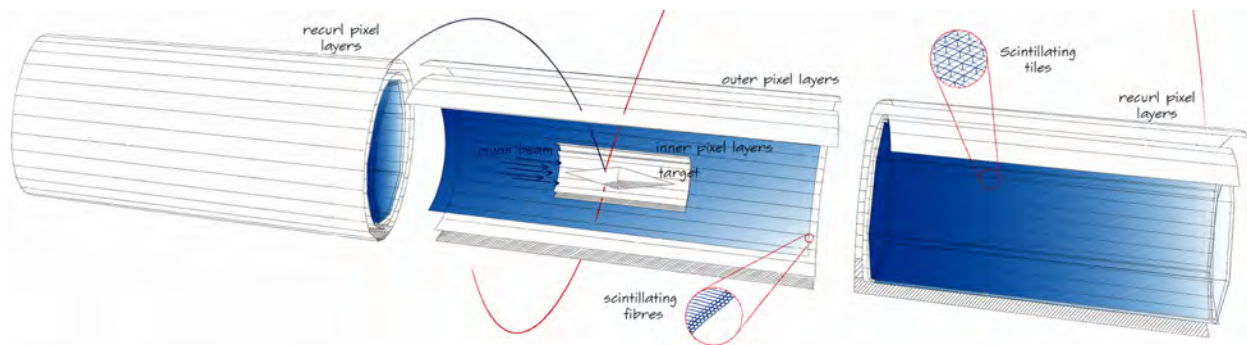


FIG. 2: Schematic of the central part of the Mu3e detector. The final detector consists of two more stations that are identical to the two stations on the side. Each station has a diameter of 17 cm and a length of 36 cm. The overall length of the final detector will be about 2 m.

A schematic of the experiment is shown in Fig. 2. The muons are stopped in a hollow double cone target in the middle of the detector. The target ensures a spread of the muon vertices to reduce the combinatorial background. The decay electrons propagate in a 1 T homogenous magnetic field. They pass the first two silicon pixel layers close to the target to identify the vertex and a second pair of pixel layers to specify the momentum. The momentum resolution precision depends in first order on the multiple scattering angle θ and the lever-arm Ω in a magnetic field to

$$\frac{\sigma_p}{p} \propto \frac{\theta_{MS}}{\Omega}. \quad (1)$$

A high lever arm by placing tracking stations at a large radius would increase the momentum resolution but also decrease the momentum acceptance. Therefore the electrons, after passing the second pair of trackers, propagate in the magnetic field until they curl back where they pass another pair of pixel layers. These layers are provided by two stations on each side of the central station. The momentum measurement with the recurling electrons

provides a momentum resolution of $0.5 \text{ MeV } c^{-1}$ while still having a wide momentum acceptance. Measuring the momentum with particles recurling close to an angle of π cancels out the error in momentum caused by multiple scattering at first order (Fig. 3).

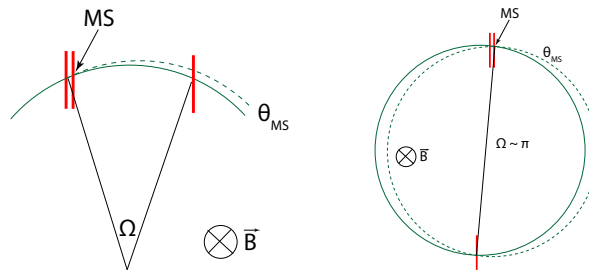


FIG. 3: Multiple scattering seen in the detector plane with the lever arm angle Ω (left) and the multiple scattering for a recurling particle (right).

Separating the decays requires additional timing detectors. The central part is extended with three layers of $250 \mu\text{m}$ thick scintillating fibers read out by silicon photomultipliers at both fibre ends. The outer stations have scintillation tiles close to the pixel sensors. The fibers require to have a time resolution below 1 ns while the tiles resolution needs to be better than 100 ps .

The modular structure allows to build and run the detector at different stages. In a first phase the detector will only consist of the central module and one recurl station at each side as shown in Fig. 2. The planned sensitivity goal is set at $\mathcal{B}(\mu \rightarrow eee) < 10^{-15}$. In a second phase each side of the detector will be expanded with an additional recurl station that allows to detect all recurling particles that are within the acceptance given by the central module. The second phase sensitivity goal is set at $\mathcal{B}(\mu \rightarrow eee) < 10^{-16}$. The feasibility of a beam intensity of $\sim 10^8$ muons per second has already been shown at PSI at the πE5 beamline fulfilling the requirements for the first phase. A new beamline providing $\sim 10^9$ muons per second as needed for the second phase is currently under investigation at PSI.

MONOLITHIC ACTIVE PIXEL SENSORS

With the Mu3e experiment a new pixel sensor technology will be introduced, the High Voltage Monolithic Active Pixel Sensor (HV-MAPS) [10]. The sensor consists of a depleted area biased with $\sim 70 \text{ V}$ enabling a fast $\mathcal{O}(1 \text{ ns})$ charge collection via drift. The digitization and the serial driver to write out the (zero suppressed) data are part of the chip itself. The data written consists of the hit pixel address and a time-stamp.

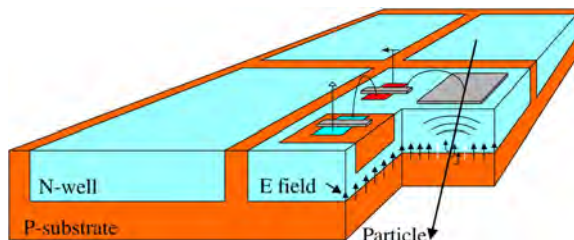


FIG. 4: Schematic view of HV-MAPS [10]

Each sensor-module consists of an active area of $2 \times 2 \text{ cm}^2$ with an individual pixel size of $80 \times 80 \mu\text{m}^2$. The sensor thickness will be less than $50 \mu\text{m}$. Together with a Kapton support structure of $25 \mu\text{m}$ and flexprint cables that provide supply voltage and readout data lines, the thickness will be about 1 permille radiation length X_0 . In the current prototype design (version 7) the chip already reaches a time resolution of $\sim 17 \text{ ns}$ with a pixel efficiency of $> 99 \%$. Using such small pixels the tracking resolution is dominated by multiple scattering and a smaller pixel size would not help improving the detector resolution. The HV-MAPS are produced by commercial CMOS technology leading to a rather cheap production technology as widely used in industrial processes. The current pixel R&D achieved a working chip at a still smaller active area of $2.9 \times 3.2 \text{ mm}^2$. A new series of chips is under commissioning that will have the proposed size of the active area.

TIME OF FLIGHT SYSTEM

Scintillating Fibres

The fibers at the central station of the detector will be placed close to the outer pixel layers. The photons generated in the fibers will be guided within the fibers out of the active area where they are detected at the fiber ends only. Each fiber has a diameter of $250 \mu\text{m}$ and a length of 30 cm . Three layers of fibers are glued together to 16 mm wide ribbons (see Fig. 5). These ribbons are placed close to the outer layers of the silicon pixel sensors. The scintillation light will be read out by silicon photomultipliers (SiPMs). Two readout schemes are currently discussed. Either an individual readout where each fiber is read out by an individual SiPM or a column wise readout where the fibre modules can be directly attached to 16 mm wide SiPM arrays. The SiPM technology allows to place up to about 4500 SiPMs dense enough to fit into the detector and they can be operated in a 1 T magnetic field environment.

Currently round and squared double cladding fibers are under investigation. First prototype R&D shows that squared fibers provide a time resolution better than 500 ps whereas the round fibers perform with about 1.5 ns . Several full size ribbons made with round shaped fibers have already been built and a tool for mass production has been developed.

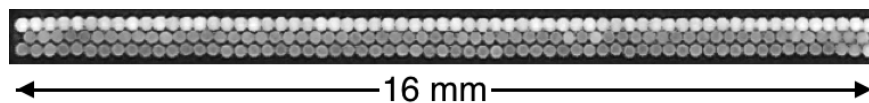


FIG. 5: Front view of a fibre ribbon prototype

Scintillating Tiles

The plastic scintillating tiles of the outer detector modules have a size of about $1 \times 1 \times 1 \text{ cm}^3$. Each station of the detector will have 3360 tiles where all are read out individually by a single SiPM. Thirtytwo tiles will be combined to submodules as shown in Fig. 6 left with two 4×4 tile arrays. Fifteen submodules together form a module of 480 channels. These modules are placed around the beam pipe (see Fig. 6, right) covering one station. For the

tiles the required time resolution better than 100 ps has already been proved by several test-beam measurements [11].

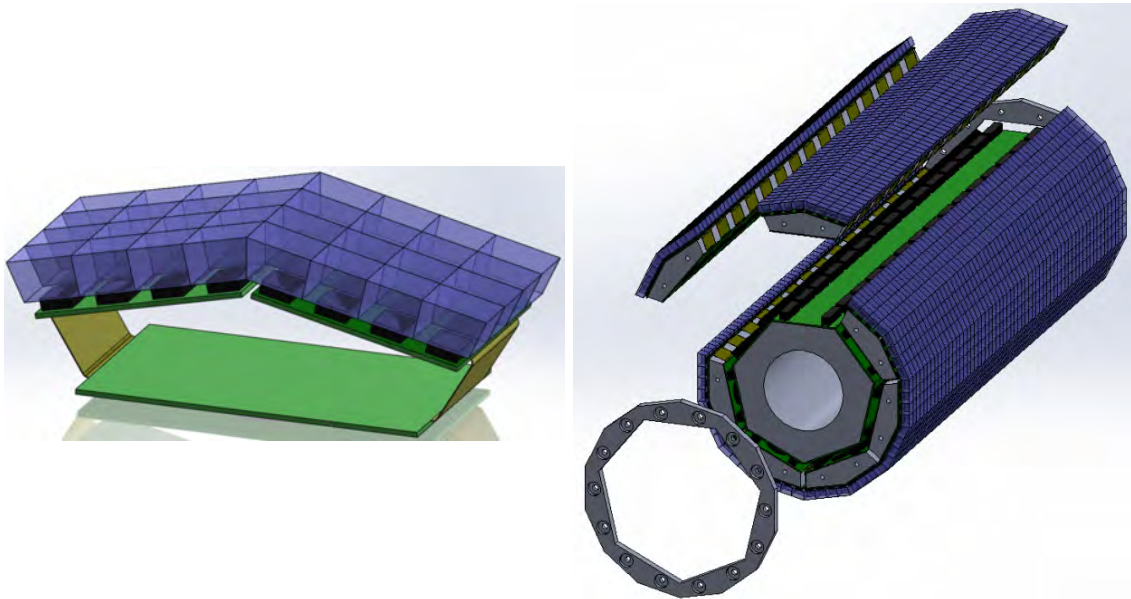


FIG. 6: *left*: submodule of the tile detector, *right*: explode view of a fully equipped detector station with seven modules [11]

Time of Flight System Readout

The baseline design uses the SiPM Timing Chip (STiC) [12] and a successor, the MuSTiC, that is a dedicated development for Mu3e. It will be used to read out the fibers and the tiles. The STiC chip is a mixed mode ASIC containing the analogue and digital part. For the analogue input two thresholds are used. The lower threshold specifies the timestamp of the input signal while the second threshold specifies the charge of the input signal by measuring the time over threshold. The intrinsic STiC time resolution has been measured being $\sigma_{\text{STiC}} < 30$ ps [13]. The STiC chip allows to vary the bias voltage within a window of 0.7 V. This allows to compensate the variations of the optimal SiPM bias voltage between different channels.

The STiC chip has been designed for a PET application with LYSO crystals where thousands of photons are expected. Also the tiles produce signals with ~ 1000 photons. Therefore the STiC chip can directly be used for the tile detector. For the fibers the STiC needs to operate with a few photons only. As SiPMs have high dark rates at low thresholds the main development for MuSTiC is to speed up the LVDS link to write out the data. The current design of the STiC and MuSTiC is not able to measure the time over threshold for signals containing a few photons only. Therefore additional R&D is needed to provide the feature for the fiber detector.

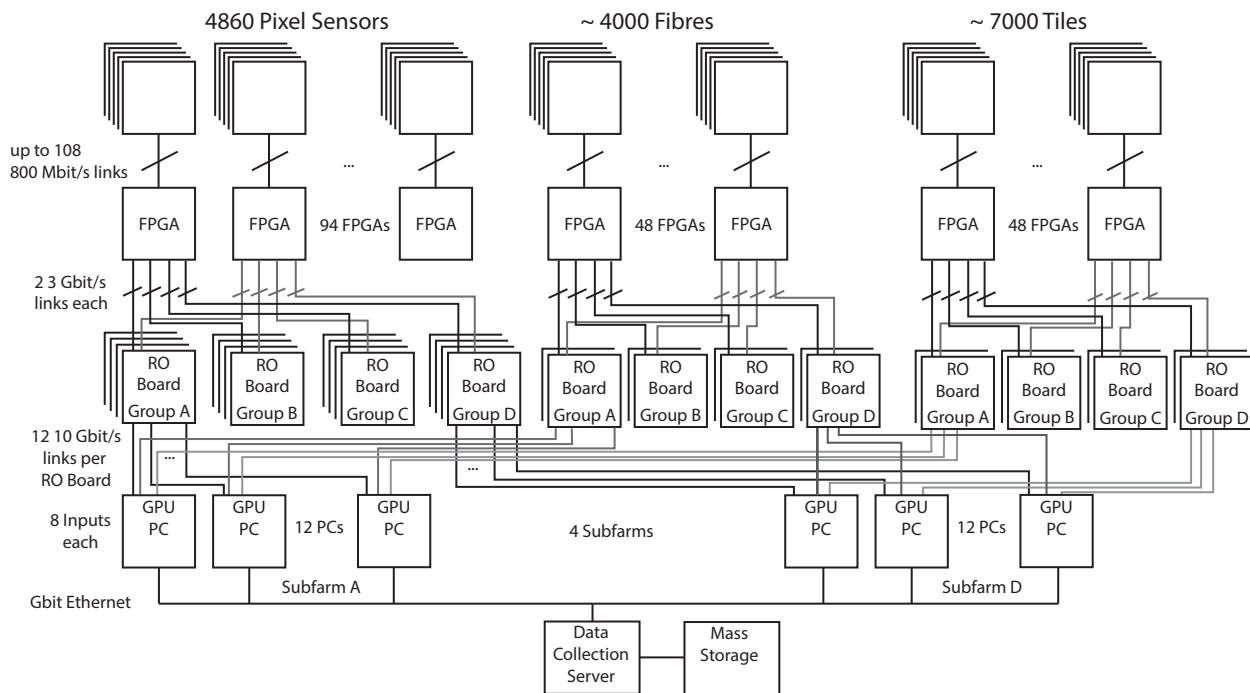


FIG. 7: Three staged readout scheme for Mu3e [14].

DATA ACQUISITION

The Mu3e experiment produces overall several Tbit s^{-1} of zero-suppressed data. Fig. 7 shows the readout of the experiment. The STiC chips from the tiles and fibres as the HV-MAPS pixel sensors provide digital differential LVDS links to the front-end FPGAs placed close to the detector. The front-end FPGAs merge and buffer data from the LVDS links and send them via optical links to the counting house. The optical links are not only needed to provide high enough bandwidth to transfer the data to the counting house but it also decouples the detector galvanically from the counting house electronics. The data is sent to the counting house by time slices to four different sub-farm FPGAs of the event filter farm in sequence. The sub-farm FPGAs are again connected to 12 computers for each sub-farm. In each computer a third FPGA rejects already tracks that are not coinciding in time. The rest of the data is sent to a graphics processing unit for reducing combinatorial background by reconstructing the muon vertex position. At the end the data written to tape will be reduced to less than 100 MB s^{-1} [14].

* Presented at NuFact15, 10-15 Aug 2015, Rio de Janeiro, Brazil [C15-08-10.2]

† rgredig@physik.uzh.ch; Speaker

‡ URL: <http://www.psi.ch/mu3e>

- [1] U. Bellgardt et al. (SINDRUM Collaboration), Nuclear Physics B **299**, 1 (1988).
- [2] Y. Fukuda et al. (Super-Kamiokande Collaboration), Phys. Rev. Lett. **81**, 1562 (1998).
- [3] Q. R. Ahmad et al. (SNO Collaboration), Physical Rev. Lett. **87**, 071301 (2001), 0106015.
- [4] K. Eguchi et al. (KamLAND Collaboration), Phys. Rev. Lett. **90**, 21802 (2002), 0212021.

- [5] A. Blondel et al., p. 104 (2013), 1301.6113.
- [6] M. L. Brooks et al. (MEGA Collaboration), *Phys. Rev. Lett.* **83**, 1521 (1999).
- [7] J. Adam et al. (MEG Collaboration), *Phys. Rev. Lett.* **110**, 201801 (2013).
- [8] W. Bertl et. al (SINDRUM II Collaboration), *European Physical Journal C* **47**, 337 (2006).
- [9] A. Herkert, Master's thesis, Heidelberg University (2015).
- [10] I. Perić, *Nucl. Instrum. Meth.* **582**, 876 (2007).
- [11] P. Eckert, Ph.D. thesis, Heidelberg University (2015).
- [12] T. Harion et al., *Journal of Instrumentation* **9**, C02003 (2014).
- [13] W. Shen et al., in *2013 IEEE Nuclear Science Symposium and Medical Imaging Conference (2013 NSS/MIC)* (IEEE, 2013), pp. 1–5.
- [14] D. Wiedner et al., *Journal of Instrumentation* **9**, C01011 (2014).

The Multiple Muon Charge Ratio in MINOS Far Detector*

C. M. Castromonte[†] and R. A. Gomes

Instituto de Física - Universidade Federal de Goiás, Brazil

M. C. Goodman and P. Schreiner

Argonne National Laboratory, Argonne, Illinois 60439, USA

(Dated: December 20, 2015)

Abstract

The charge ratio, $R_\mu = N_{\mu^+}/N_{\mu^-}$, for cosmogenic multiple-muon events observed at an underground depth of 2070 mwe has been measured using the MINOS Far Detector. The multiple-muon charge ratio is determined to be $R_\mu = 1.104 \pm 0.006(stat.)_{-0.010}^{+0.009}(syst.)$. This measurement serves to constrain models of cosmic ray interactions at TeV energies.

INTRODUCTION

Atmospheric muons are produced when primary cosmic ray nuclei interact near the top of the atmosphere to produce hadronic showers which contain pions and kaons. These secondary mesons can either interact in further collisions in the atmosphere or decay to produce atmospheric muons. Since the majority of primary cosmic rays are protons, there is an excess of positively charged mesons (K^+ , π^+) in the showers, and consequently, the atmospheric muon charge ratio for single muons is larger than unity. Due to the steeply falling primary cosmic ray energy spectrum, which follows an $E^{-2.7}$ power law, a single-muon event in a deep underground detector is more likely from the decay of a leading hadron than from a secondary hadron or later generation hadrons. Conversely, observation of a multiple muon event, one where two or more nearly parallel, time-coincident muon tracks are observed in the detector underground, must involve more than the decay of a single leading hadron. These muons are decay products of mesons which are generated in the hadronic core of the atmospheric cascade.

Precision measurements of R_μ in cosmic rays can be used to improve models of the interactions of cosmic rays in the atmosphere. In addition, measurements of the cosmic ray muon charge ratio from a few GeV to a few TeV are important for constraining calculations of atmospheric neutrino fluxes. These are of interest both for detailed measurements of neutrino oscillations in atmospheric neutrino experiments and also for calculations of backgrounds for neutrino telescopes.

THE MINOS FAR DETECTOR

The MINOS Far detector is a steel-scintillator sampling and tracking calorimeter located at a depth of 2070 m.w.e. in the Soudan Underground Laboratory, in Minnesota. The

detector consists of two supermodules separated by a gap of 1.15 m and has a total dimension of $8 \times 8 \times 31 \text{ m}^3$. The two supermodules contain a total of 486 octagonal steel planes, interleaved with 484 planes of extruded polystyrene scintillator strips. Each scintillator plane has 192 strips of width 4.1cm. The scintillator strips in alternating detector planes are oriented at $\pm 45^\circ$ to the vertical. Light from charged particles traversing the plastic scintillator is collected with wavelength shifting (WLS) plastic fibers embedded within the scintillator strips. The WLS fibers are coupled to clear optical fibers at both ends of a strip and are read out using 16-pixel multianode photomultiplier tubes (PMT's).

To measure the momentum of muons traversing the detector, the steel has been magnetized into a toroidal field configuration. In one magnetic field setting, negative muons resulting from interactions of neutrinos from the Fermilab NuMI beam are focused toward the center of the detector. This magnetic field orientation will be referred to as the forward field (FF) configuration. In the reverse field (RF) configuration, the coil current is reversed and positive muons are focused into the detector.

DATA ANALYSIS

The multiple muon sample used in this analysis was recorded between August 2003 and April 2012. During the data taking period, the detector run with both the FF and RF magnetic field configurations. Table I summarizes the number of muon tracks that pass each of the selection cuts. A sample of 312514 muons in multiple-muon events was obtained after all the cuts shown in Table I were applied. To eliminate biases from acceptance effects due to magnetic field, detector asymmetry and detector alignment, data taken in both magnetic field configurations is combined with a geometric mean (GM). Figure 1 shows the measured muon charge ratio as a function of the charge significance $(q/p)/\sigma(q/p)$ and BdL , for data collected in both magnetic field orientations respectively. Table II shows the measured muon charge ratio as a function of muon multiplicity for forward data (FF), reverse data (RF) and combined (GM) data sets. The obtained uncorrected charge ratio measurement is $R_{uncorr.} = 1.091 \pm 0.005(stat.)$

To obtain the true charge ratio of the multiple-muon events reaching the MINOS FD, $R_{uncorr.}$ must be corrected to account for the charge-separation efficiency, ε (which is obtained from Monte Carlo simulation). The corrected charge ratio, $R_{corr.}$, is related to the

TABLE I: Summary of the applied cuts. Each row shows the total number of muons in both field configurations remaining after all the applied cuts to data. The numbers in parenthesis show the percentage of muons remaining.

Cuts	Number of muons remaining	
Preselected tracks	8.35×10^6	(100%)
Analysis cuts		
parallel tracks ($< 5^\circ$)	7.31×10^6	(87.5%)
20 planes	5.88×10^6	(70.5%)
2 m track length	5.87×10^6	(70.3%)
downward-going track	5.86×10^6	(70.2%)
fiducial volume	5.75×10^6	(68.9%)
fit quality: $\chi^2/ndf < 2$	5.17×10^6	(61.9%)
Charge-sign quality cuts		
$(q/p)/\sigma(q/p) > 3$	1.08×10^6	(13.0%)
$BdL > 5 \text{ T}\cdot\text{m}$	3.12×10^5	(3.7%)

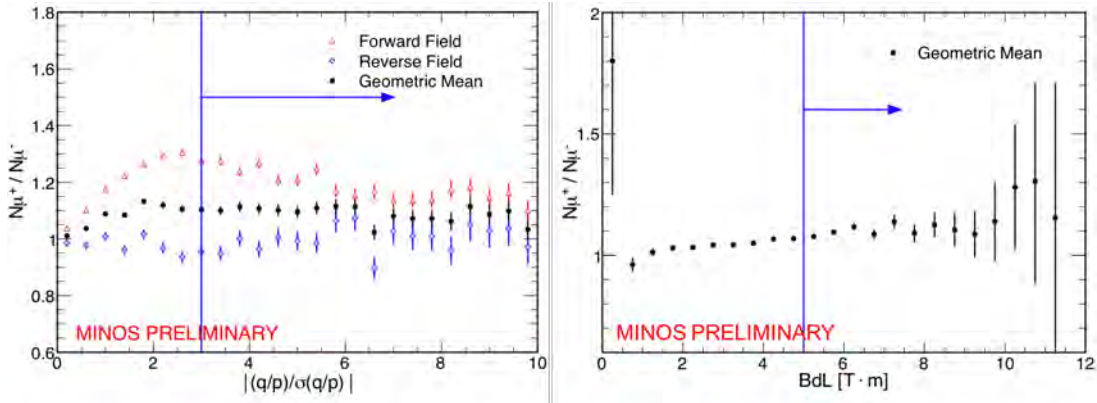


FIG. 1: Charge ratio for reconstructed multiple-muon tracks as a function of the charge significance (left), and BdL (right), after applying all the selection cuts. The vertical line denotes the minimum value for tracks used in the charge ratio measurement.

uncorrected GM, $R_{uncorr.}$, and the charge-separation efficiency, ε , by $R_{corr.} = \frac{R_{uncorr.} - (\frac{1-\varepsilon}{\varepsilon})}{1 - R_{uncorr.} \times (\frac{1-\varepsilon}{\varepsilon})}$.

The systematic error in the charge ratio measurement comes from the contribution of possible failure to cancel effects of magnetic field and alignment errors by reversing the magnetic field (bias) and dealing with reconstruction failures that tend to give a random charge determination (randomization). The multiple-muon charge ratio after charge efficiency correction is $R_{corr.} = 1.104 \pm 0.006(stat.)_{-0.010}^{+0.009}(syst.)$.

TABLE II: Measured muon charge ratio, $R_{uncorr.}$, as a function of muon multiplicity, M, for forward and reverse data, and the GM combination. Only statistical errors are shown.

M	Forward Field (FF)	Reverse Field (RF)	Geometric Mean (GM)
2	1.195 ± 0.005	1.025 ± 0.010	1.107 ± 0.006
3	1.157 ± 0.012	0.943 ± 0.020	1.044 ± 0.012
4	1.165 ± 0.021	0.929 ± 0.035	1.040 ± 0.022
5	1.210 ± 0.037	0.856 ± 0.055	1.018 ± 0.036
6	1.153 ± 0.057	0.882 ± 0.088	1.009 ± 0.056
7	1.192 ± 0.098	0.761 ± 0.121	0.952 ± 0.085
8	1.061 ± 0.149	0.692 ± 0.212	0.857 ± 0.145
9	1.000 ± 0.218	0.556 ± 0.310	0.745 ± 0.223
10	1.400 ± 0.580	0.500 ± 0.612	0.837 ± 0.541
All	1.187 ± 0.005	1.002 ± 0.008	1.091 ± 0.005

CONCLUSIONS

The calculated underground multiple-muon charge ratio ($R_{corr.}$) is lower than the single muon charge ratio measurements obtained by several experiments in the past [1]. This result gives support to the hypotheses about the decrease of the charge ratio for multiple-muon events mentioned in the Introduction, providing a better understanding of the mechanism of multiple-muon production in the atmosphere. The result is also consistent with the last OPERA multiple-muon charge ratio measurement [2].

* Presented at NuFact15, 10-15 Aug 2015, Rio de Janeiro, Brazil [C15-08-10.2]

† cesarc77@gmail.com; Speaker

[1] P. Adamson *et al.* (MINOS), Phys. Rev. D 83, 032011 (2011); P. Achard *et al.* (L3), Phys. Lett. B 598, 15 (2011); S. Haino *et al.*, Phys. Lett. B 594, 35 (2004); V. Khachatryan *et al.* (CMS), Phys. Lett. B 692, 83 (2010); T. Hebbeker and C. Timmermans, Astropart. Phys. 18, 107 (2002); P. Adamson *et al.* (MINOS), Phys. Rev. D 76, 052003 (2007); N. Agafonova *et al.* (OPERA), Eur. Phys. J. C 67, 25 (2010).

[2] N. Agafonova *et al.* (OPERA), Eur. Phys. J. C 74, 2933 (2014).

**Development of Muon LINAC for the Muon $g-2$ /EDM
Experiment at J-PARC***

M. Otani, for the J-PARC E34 collaboration[†]
KEK, Tsukuba, Japan
(Dated: December 9, 2015)

Abstract

We are developing a linac dedicated to the muon acceleration. It enables us to measure the muon anomalous magnetic moment with an accuracy of 0.1 ppm to explore beyond Standard Model of elementary particle physics. As a first step for demonstration of the muon acceleration, we are developing the source of slow muons with which RFQ acceleration is conducted. In order to cover the middle beta ($\beta \sim 0.3 - 0.7$) section of the muon LINAC, disk and washer coupled cell LINAC is employed and the DAW cell being designed now. This paper describes status of these developments.

INTRODUCTION

One of promising way to cast light on new physics beyond Standard Model is precise measurement of the muon anomalous magnetic moment $(g - 2)_\mu$ in which there is a discrepancy between the SM prediction and measurement. The E34 experiment aims to measure $(g - 2)_\mu$ with a precision of 0.1 ppm and search for EDM with a sensitivity to 10^{-21} e-cm by utilizing high intensity proton beam at J-PARC and newly developed novel technique of the ultra-cold muon beam.

We are developing a muon linac to accomplish the ultra-cold muon beam. First the thermal muon (30 meV) generated in the electric potential of 5.6 keV is injected to the radio-frequency quadrupole (RFQ). The spare for the J-PARC LINAC RFQ, so called RFQ II, will be used for the muon LINAC. After RFQ, Interdigital H-type (IH) DTL will be used to accelerate muon from $\beta = 0.08$ to 0.27. Then disk and washer (DAW) coupled cavity is employed to $\beta = 0.7$ and then disk loaded structure accelerates muons up to 212 MeV/c.

As a demonstration of the muon acceleration, we are planning to accelerate muons with electro-static field and RFQ II. Next section describes development of the muon source and RFQ for that test. Following section shows current status of the following RF cavity design, especially for DAW.

MUON ACCELERATION WITH RFQ

In order to conduct muon acceleration with RFQ, slow muon source is being developed. One of the promising candidates is negative muonium ($\mu^+e^-e^-$, Mu^-) or slow muon emission by injecting the surface muon beam to a thin metal foil. Previous experiment observed Mu^- and slow muon emission from an Al foil with average energy of 0.2 ± 0.1 keV and few keV, respectively, which can be injected to the RFQ II whose injection energy is 5.6 keV.

The measurement of the Mu^- or slow muon emission efficiency and its kinematics was proposed and approved in J-PARC MLF. Figure 1 shows the experimental setup of the measurement. Surface muons are injected into the Mu^- production target. The emitted Mu^- is accelerated and focused by the electro-static lens and transported to the detector chamber by following electro-static quadrupoles and electro-static deflector. The Micro-Channel-Plate (MCP) is used for counting and timing measurement of Mu^- and surrounding plastic scintillators for the decay-positron detection.

Figure 2 shows expected MCP timing distribution estimated by the GEANT4 simulation. In the simulation, the Mu^- signals are generated at the Mu^- target with kinetic energy of 0.2 keV and beam related backgrounds are estimated by injecting the beam muons towards the target. Backgrounds mainly consist of decay-positrons from the beam muons stopped around the target and the deflector, which can be reduced effectively by lead shields around the target chamber and the collimator located on downstream of the deflector. The signal to background ratio is estimated to be more than ten and clear separation between these can be achieved by observed timing as shown in Fig. 2.

The slow muon beamline has been assembled in J-PARC MLF. It was originally developed and operated in RIKEN-RAL port-3. It successfully demonstrated transportation of the slow muon beam. After shutdown of the beamline, some of the beamline components were moved

to J-PARC for the Mu^- measurement in summer 2014. Assembly and commissioning of all the equipments were completed by May 2015. Figure 3 shows one of the commissioning results of the beamline; an Al plate installed at the Mu^- target holder location is irradiated by UV light and then generated photo-electrons are accelerated and transported to the MCP detector location. The photo-electron events are observed successfully with nominal setup of the beamline components. Though current setup for Mu^- suffers background due to the field emission electrons from the electro-static lens electrodes, the setup for slow muon setup can be operated stably. Upgrade such as a magnetic equipment installation to separate the field emission electron from Mu^- is being discussed.

In conclusion, all the equipments are ready for slow muon measurement.

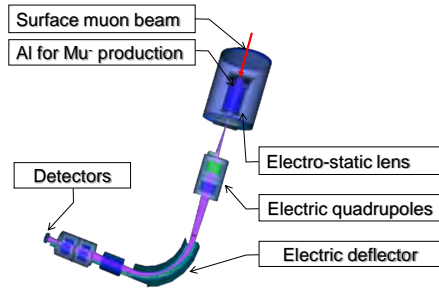


FIG. 1: Experimental setup for the Mu^- emission measurement at the J-PARC MLF muon beamline.

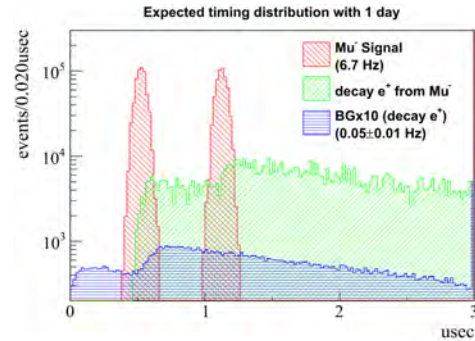


FIG. 2: Expected timing distribution estimated by the GEANT4 simulation.

In order to verify the RFQ II operation and measure the background from the RF field with MCP, the RFQ offline test was performed in June 2015 in the J-PARC LINAC building. Figure 4 shows photo of the RFQ offline test setup. The MCP detector chamber is connected to the RFQ downstream. Vacuuming is done with an ion pump and reach 10^{-6} Pa. The RFQ is powered on by low RF source and solid state amplifier up to 6 kW and 25 Hz repetition. The forward, reflection waves and RFQ internal power are monitored by power meters.

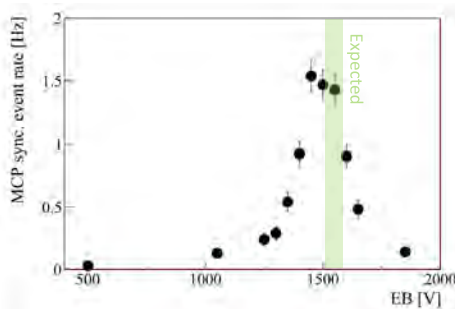


FIG. 3: Result of the beamline commissioning.



FIG. 4: Photo of the RFQ offline test at the J-PARC LINAC building.

Figure 5 shows the forward, reflection and pick-up power in RFQ with nominal power (5 kW) operation. Rising time is well consistent with expectation from Q factor. Figure 6 shows result of the MCP background measurement. Because the slow muon beam intensity in the first stage of the acceleration test is expected to be several counts per second, it is

necessary to measure background level with comparable accuracy to that. Though it was expected that there might be background events due to electron or X-ray excited by RF field, all the measurements are consistent each other within statistical error of about 0.1 Hz and no background events are observed.

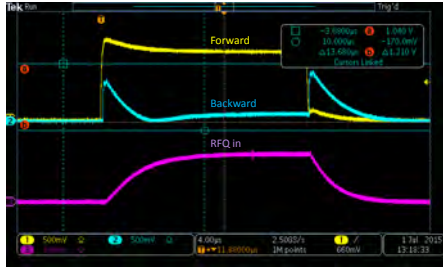


FIG. 5: Forward, reflection wave and pick-up power in RFQ with nominal power of 5 kW.

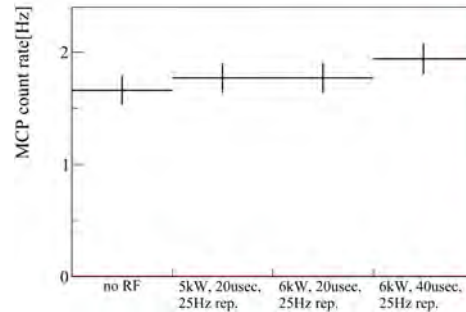


FIG. 6: Result of the MCP background measurement. All the measurements are consistent each other within statistical error.

In conclusion, RFQ is successfully operated and accelerated muons can be measured by MCP without beam related background.

DEVELOPMENT OF THE MIDDLE β SECTION

In the middle beta section ($\beta = 0.3 \sim 0.7$), the DAW cavity will be employed. It has high effective shunt impedance and high degree of coupling between adjacent RF cells. In order to solve the mode overlapping problem, a bi-periodic L-support structure is employed.

It is necessary to design our DAW cavity because muon acceleration is the first time in the world and the DAW cavity covering such a wide range of velocity is also the first time. In order to achieve higher acceleration gradient, the cavity design is optimized as follows. First, two dimensional model without the washer supports is optimized by calculating acceleration and coupling mode with SUPERFISH. Variable parameters are disk radius (T_d), disk thickness (T_d), washer radius (R_w) and gap between washer (G). Optimization process is done by the SIMPLEX algorithm and the optimization function is constructed with confluent condition ($f_a = f_b$), higher shunt impedance (Z_{TT}), and uniformity of the acceleration field. After optimization in two dimensional model three dimensional model with the washer supports is constructed based on the optimized dimensions with the 2-D code, with which resonant modes around operation frequency of 1.3 GHz are calculated in CST MICROWAVE STUDIO. Here the connection radius of the supports is decided to be the zero-electric point to minimize perturbation to the accelerating mode. In addition, the disk radius with and without the supports are slightly modified to recover the periodic feature of the acceleration field. The three dimensional model is also optimized by using same optimization function as two dimensional one. Finally the dispersion curve is investigated to check whether unfavored mode exists or not around the operation frequency. All the steps are repeated in several cavity lengths of $\beta\lambda/4$.

Figure 7, Fig. 8 and Tab. I show the dispersion curve, optimized model and optimized parameters, respectively, with $\beta = 0.3, 0.4, 0.5$ and 0.6 . Because of bi-periodic structure, some stop bands appear in $\pi/2$. Though TM11 mode is near to the operational frequency, the cavity is tuned in the optimization process so that the operational frequencies sit in the stop band at $\pi/2$. Though the dipole mode passband TE11 crossed the line where the phase

velocity matches the speed of muons, it is considered to be no problem because the muon beam current is negligibly small and transverse kick due to this mode is estimated to be much smaller than our requirement.

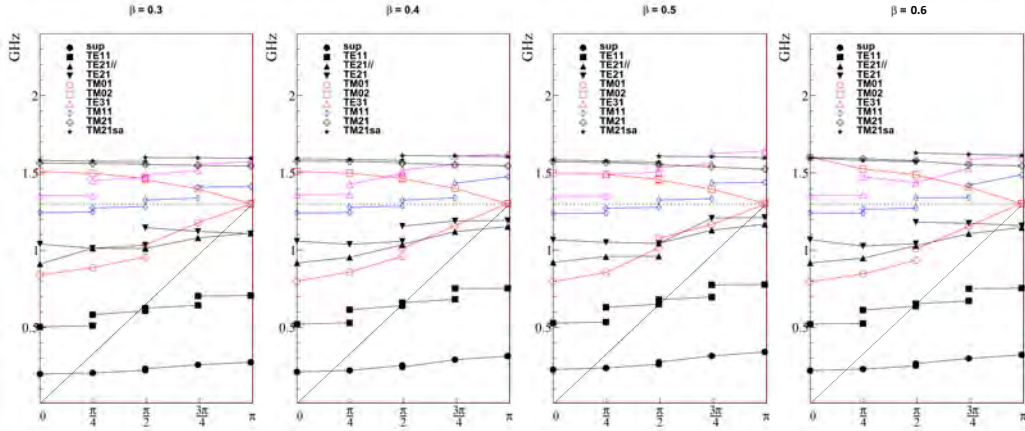


FIG. 7: Dispersion curve with optimized cavity in several β calculated by CST MICROWAVE STUDIO.

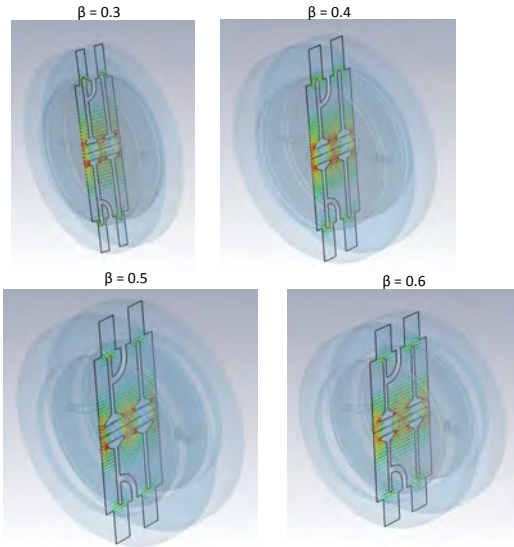


FIG. 8: Optimized three dimensional models in CST MICROWAVE STUDIO.

TABLE I: Parameters of the optimized DAW cavity.

β	0.6	0.5	0.4	0.3
L	$\beta\lambda/4$			
R_b [mm]	12			
R_n [mm]	2.6			
T_w [mm]	3.5			
θ [deg.]	30			
R_c [mm]	155	157	154	151
R_d [mm]	111.3	108.352	104.52	103.221
T_d [mm]	16.014	14.790	10.97	9.630
R_w [mm]	105.969	105.63	108.14	110.391
G [mm]	15.975	11.285	7.8976	6.148
f_a [GHz]	1.300	1.300	1.299	1.301
f_c [GHz]	1.299	1.301	1.302	1.301
ZTT[M Ω /m]	57.8	46.3	33.8	18.0

In conclusion, we completed design of the DAW cavity based on computer calculator. We are planning to fabricate a cold model made for measurement such as resonant frequencies.

* Presented at NuFact15, 10-15 Aug 2015, Rio de Janeiro, Brazil [C15-08-10.2]

† masashio@post.kek.jp; Speaker

Forbush event detected by CARPET on 2012 March*

Edith Tueros Cuadros[†]

Universidade Presbiteriana Mackenzie,

Centro de Rádio-Astronomia e Astrofísica Mackenzie - CRAAM, São Paulo, Brasil.

Emilia Correia[‡]

Instituto Nacional de Pesquisas Espaciais, INPE,

São José dos Campos, São Paulo, Brasil. and

Universidade Presbiteriana Mackenzie,

Centro de Rádio-Astronomia e Astrofísica Mackenzie - CRAAM, São Paulo, Brasil.

(Dated: January 23, 2016)

Abstract

We present a Forbush decrease (FD) event observed with CARPET cosmic ray detector operating at EL Leoncito (CASLEO San Juan, Argentinian) since 2006. The FD occurred from 8 to 16 on March 2012, it was caused by a couple of CMEs launched on 2012 March 7 associated with a X5 solar flare. CARPET data, after correcting by atmospheric variations, shows a FD with intensity $\sim 5\%$, which started just at the time of interplanetary shock that caused a intense geomagnetic storm. The FD event detected by CARPET showed a temporal evolution very similar to the one observed by Neutron Monitor of Rome detector. The onset of FD events occur few hours before geomagnetic storms, so statistic study of the correlation between their characteristics and storm intensity can be used to forecast geomagnetic activity level.

INTRODUCTION

The Earth's environment is constantly changing due the influence of solar phenomena, which is known as space weather. Solar flares and coronal mass ejections (CMEs) are responsible for significant disturbances in the nearby space (e.g. [1, 2]). Particularly CMEs are considered to be the cause of sudden decrease observed in the ground counting rates of galactic cosmic rays, these events are denominated Forbush Decrease (FD) [3]. The cosmic rays flux decrease is attributed to scattering of the galactic cosmic rays by the large scale magnetic structure of CMEs propagating in the Earth's nearby, which works as a shield. The FD normally starts in close association with interplanetary shocks, which occurs before geomagnetic storms, but the relation between FD and geomagnetic activity is complex. Geomagnetic storms require intense southward Interplanetary Magnetic Field (IMF), while cosmic ray flux is affected by large scale redistribution of IMF even when the CME is not passing nearby the Earth [4, 5]. In this work, we present a FD detected by CARPET cosmic ray detector operating in the Argentine Andes since 2006 [2]. The event was observed on 2012 March 8 and occurred in close association with a complex geomagnetic activity produced by the impact of two CMEs in the Earth's magnetosphere.

INSTRUMENTATION

CARPET detector was designed for the observation of the cosmic rays flux with energies in the range of 10^5 and -10^{12} eV. It is an important tool for the study of atmospheric, geomagnetic and solar phenomena. CARPET was installed in April 2006 at CASLEO, San Juan, Argentina, (site with magnetic rigidity of 11.8 GV and altitude of 2550 m). It is an array of 24 blocks of gas-discharge cylindrical Geiger counters. Each block consists of five upper and lower counters, separated by an 7 mm thickness aluminum absorber. Data is obtained in three mode signals, named: (a) UP and (b) LOW modes correspond to the total count rate of the 120 upper and the 120 lower counters, respectively, allowing detection of electrons and positrons with energies > 0.2 MeV, protons > 5 MeV, muons > 1.5 MeV and γ -rays > 0.02 MeV; and (c) TELESCOPE mode corresponds to the simultaneous particles detected by upper and lower counters allowing detection of electrons with energies > 5 MeV,

protons > 30 MeV and muons > 15.5 MeV [2, 6].

DATA ANALYSIS

Cosmic rays flux measured on ground is influenced by changes in the pressure and temperature, producing significant variations in the measurements. Thus, it is important to remove these influences from cosmic rays ground-based data, before studying its relation with any extraterrestrial phenomena [7].

Cosmic rays flux recorded by CARPET was corrected for atmospheric influence using the integral method applying the Equations 1 and 2. The following equations estimate the cosmic rays variations ΔI^{CP} and ΔI^{CT} due to changes in atmospheric pressure and temperature, respectively [8, 9]:

$$\Delta I^{CP} = \beta \Delta p \quad (1)$$

$$\Delta I^{CT} = \int_{h_0}^{h_f} \alpha(h') \Delta T(h') dh' + \alpha^G \Delta T(h_G) \quad (2)$$

where Δp is the pressure variation, β is the barometric coefficient, $\Delta T(h')$ is the temperature variation, $\alpha(h')$ is the temperature coefficient in the altitude h' , h_0 is the altitude where the atmospheric depth is close to zero ($h_0 \sim 111.0$ km), h_f equals to 14.0 km, $\Delta T(h_G)$ is the ground temperature deviation ($h_G = 2.5$ km) and α^G is the temperature coefficient on the ground.

Atmospheric pressure and temperature coefficients were calculated for the period of 2012 August 8. This period presents significant variations of the atmospheric pressure and temperature and extremely low geomagnetic activity.

Thus, it was calculated the pressure $\beta = -0.37\%/hPa$ and temperature $\alpha = -0.38\%/^{\circ}C$ coefficients and it was obtained the pressure-corrected CARPET cosmic rays data [9].

OBSERVATIONAL RESULTS

The FD event on 2012 March 8 and 9 occurred in association with a complex geomagnetic activity produced by the impact of two CMEs in the Earth's magnetosphere. The two CMEs were launched from the Sun early on March 7 during a GOES X5 solar flare; they were classified as full halo and present a velocity of ~ 2700 km/s and ~ 2000 km/s (http://cdaw.gsfc.nasa.gov/CME_list/). Figure 1 shows the corrected cosmic ray flux for the FD event detected by CARPET in TELESCOPE mode, which is compared with the flux detected by Neutron Monitor of Rome. Both detectors observed the FD event, which started in close association with the strong interplanetary shock that occurred at $\sim 12:00$ UT on 2012 March 8 (Figure 1c), and before the strong geomagnetic storm that maximum (Dst ~ -140 nT) was on 2012 March 9 (Figure 1d). The FD event shows similar variation in both instruments, starting just at the peak time of the interplanetary shock, reaching the minimum flux on March 9, and a slow recovering phase till \sim March 16. During the FD, cosmic rays flux decrease $\sim 4.9\%$ in CARPET detector and $\sim 8.5\%$ in Neutron Monitor of Rome detector.

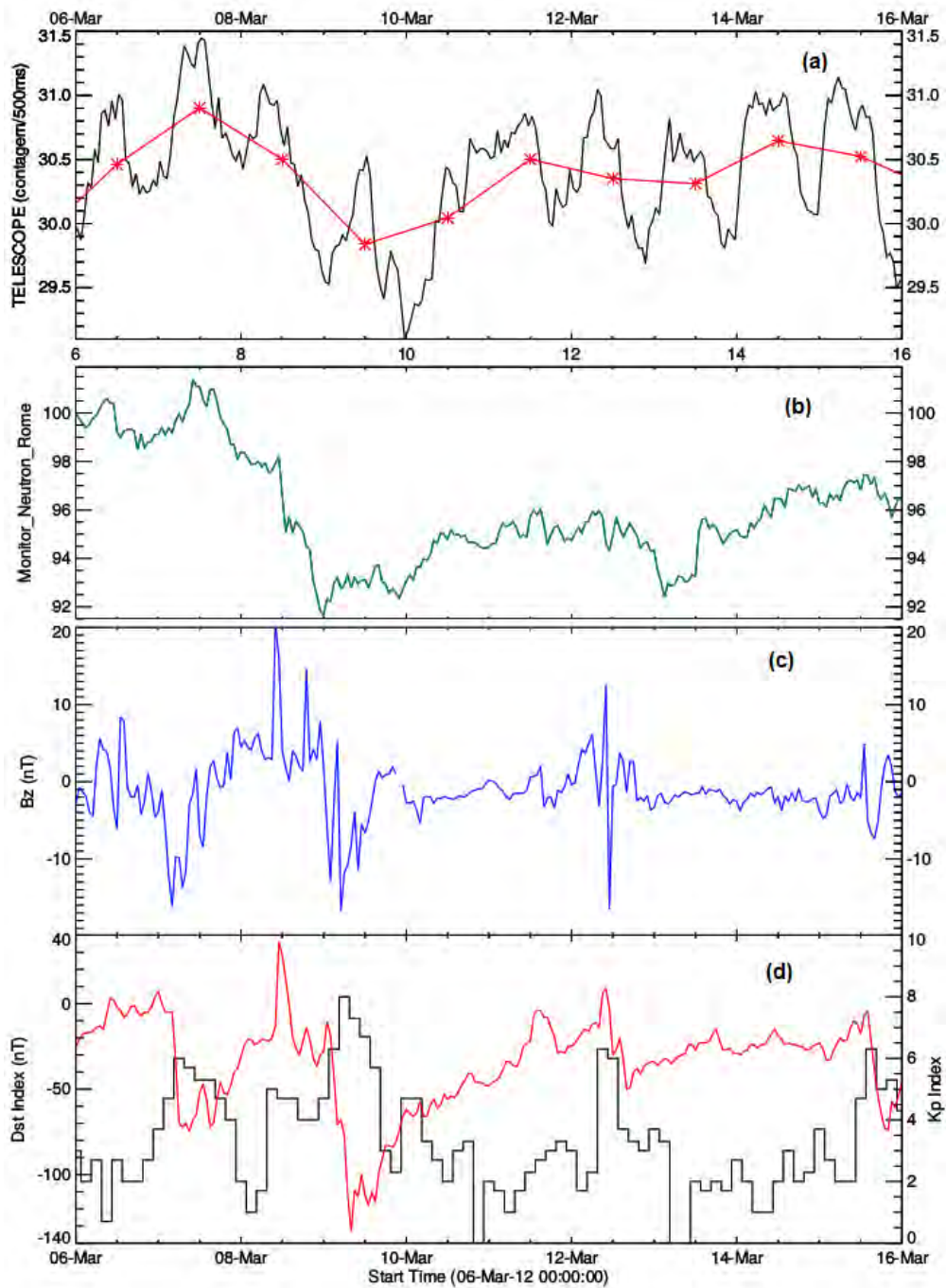


FIG. 1: Forbush Decrease occurred between 2012 March 8 and 10: (a) Corrected cosmic rays flux detected by CARPET TEL channel (red curve represents the flux integrated to 12 hours), (b) flux detected by Neutron Monitor of Rome (cyan curve), (c) interplanetary magnetic field (blue curve), and (d) KP index (black curve) and Dst (red curve) during.

CONCLUSIONS

CARPET detector installed at CASLEO has been used to study cosmic rays fluctuations in long and short term scales [2]. In this work, we presented the cosmic ray flux observed during a FD on 2012 March 8. CARPET TEL mode data used here was corrected by atmospheric pressure and afterwards by the temperature variations using the integral method [8, 9]. The results show the potential of CARPET to detect a FD. The onset Forbush Decrease events occurs before the main phase of the geomagnetic storm, indicating that could be used as a geomagnetic forecast index. Thus, the FD can provide in advance, valuable complementary information about geomagnetic storms, which can be used for space weather forecasting. To better characterize the FD and the associated geomagnetic storm intensity, it is necessary to perform a statistical study.

The authors thank FAPESP (Proc.2013/20876-8), CNPq (Proc. 550375/2002-3) agencies and the organizers for the support.

* Presented at NuFact15, 10-15 Aug 2015, Rio de Janeiro, Brazil [C15-08-10.2]

† edithtueros@gmail.com; Speaker

‡ ecorreia@craam.mackenzie.br

- [1] E. Echer, W. D. Gonzalez, F. L. Guarnieri, A. D. Lago, and L. E. A. Vieira, *Advances in Space Research* **35**, 855 (2005).
- [2] R. R. S. de Mendonca, *International Cosmic Ray Conference* **11**, 190 (2011).
- [3] S. E. Forbush, *Physical Review* **51**, 1108 (1937).
- [4] K. Kudela and R. Brenkus, *Journal of Atmospheric and Solar-Terrestrial Physics* **66**, 1121 (2004).
- [5] Badruddin and A. Kumar, **290**, 1271 (2015).
- [6] R. R. S. De Mendonça, J.-P. Raulin, F. C. P. Bertoni, E. Echer, V. S. Makhmutov, and G. Fernandez, *Journal of Atmospheric and Solar-Terrestrial Physics* **73**, 1410 (2011).
- [7] L. I. Dorman, ed., *Cosmic Rays in the Earth's Atmosphere and Underground*, vol. 303 of *Astrophysics and Space Science Library* (2004).
- [8] B. Famoso, P. La Rocca, and F. Riggi, *Physics Education* **40**, 461 (2005).
- [9] R. R. S. De Mendona, J. P. Raulin, E. Echer, V. S. Makhmutov, and G. Fernandez, *Journal of Geophysical Research: Space Physics* **118**, 1403 (2013), ISSN 2169-9402, URL <http://dx.doi.org/10.1029/2012JA018026>.

LIST OF PARTICIPANTS

Dr. ANJOS, João,	CBPF	BRAZIL
Prof. AOKI, Masaharu,	Osaka University	JAPAN
Dr. DE ANDRÉ, João Pedro A. M.,	Michigan State University	USA
Prof. BLOCKER, Craig,	Brandeis University	USA
Dr. BOGACZ, Alex,	Jefferson Lab	USA
Dr. BOLOGNESI, Sara	CEA Saclay	FRANCE
Dr. BONIFAZI, Carla	Instituto de Física – UFRJ	BRAZIL
Prof. BRAVAR, Alessandro	University of Geneva	SWITZERLAND
Prof. BROSS, Alan	Fermilab	USA
Mr. CACERES VERA, Gian Fredy R.	CBPF	BRAZIL
Dr. CARETTA, Ottone	RAL	UK
Mr. CARNEIRO, Mateus	CBPF	BRAZIL
Dr. CASTROMONTE, Cesar	CBPF	BRAZIL
Dr. CECCHI, Claudia	U. di Perugia e INFN Perugia	ITALY
Prof. CHEN, Mu-Chun	University of California, Irvine	USA
Dr. CHERDACK, Daniel	Colorado State University	USA
Prof. CHIMENTI, Pietro	UFABC	BRAZIL
Dr. COELHO, Joao	Tufts University	USA
Dr. DA MOTTA, Hélio	CBPF	BRAZIL
Dr. DIB, Claudio	U. T. Federico Santa Maria	CHILE
Prof. DODGE, Gail	Old Dominion University	USA
Dr. DRACOS, Marcos	IPHC-IN2P3/CNRS	FRANCE
Ms. DUFFY, Kirsty	University of Oxford	UK
Dr. FEUSELS, Tom	University of British Columbia	CANADA
Mr. FONSECA, Marllos	Univerdade Federal de Alfenas	BRAZIL
Dr. FURMANSKI, Andrew	University of Manchester	USA
Mr. GALINDO ORJUELA, Roger R.	U. T. Federico Santa Maria	CHILE
Prof. GALLAGHER, Hugh	Tufts University	USA
Dr. GHIANO, CHIARA	Universita di Genova, Italia	ITALY
Dr. GHOSH, Anushree	CBPF	BRAZIL
Prof. GIUSTI, Carlotta	University Pavia	ITALY
Mr. GOMES, Guilherme	Unicamp	BRAZIL
Prof. GOMES, Ricardo	UFG	BRAZIL
Dr. GRATIERI, Diego	UFF	BRAZIL
Mr. GREDIG, Roman	Physik-Institut UZH	SWITZERLAND
Prof. GRIGORIEV, Dmitry	Budker Institute of Nuclear Physics	RUSSIA
Mr. GÜNDÜZ, Mehmet	Ruhr-Uni Bochum	GERMANY
Dr. HARRIS, Deborah	Fermilab	USA
Prof. HARTZ, Mark	Kavli IPMU, U. of Tokyo/TRIUMF	JAPAN
Dr. HIGUERA, Aaron	University of Houston	USA
Dr. IWAI, Eito	KEK	JAPAN
Prof. JOO, Kyung Kwang	Chonnam National University	R. OF KOREA
Dr. KAMEDA, Jun	ICRR, University of Tokyo	JAPAN
Prof. KAPLAN, Daniel	Illinois Institute of Technology	USA
Dr. KIBURG, Brendan	Fermilab	USA
Prof. KOBAYASHI, Takashi	KEK/J-PARC	JAPAN
Dr. KOLOMENSKY, Yury	UC Berkeley and LBNL	USA
Mr. KRIKLER, Ben	Imperial College London	UK

Mr. KROLL, Mike	Ruhr-Uni Bochum	GERMANY
Prof. KUNO, Yoshitaka	Osaka University	JAPAN
Dr. LAGRANGE, Jean-Baptiste	Imperial College/Fermilab	UK
Dr. LI, Derun	LBNL	USA
Mr. LITTLEJOHN, Bryce	Illinois Institute of Technology	USA
Prof. LONG, Kenneth	Imperial College London	UK
Dr. LYNCH, Kevin	York College/CUNY	USA
Prof. MAHN, Kendall	Michigan State University	USA
Dr. MALYSHKIN, Yury	PUC Chile	CHILE
Dr. MARTINEZ CAICEDO, David	Illinois Institute of Technology	USA
Dr. MARTINI, Marco	Ghent University	BELGIUM
Prof. MCDONALD, Kirk	Princeton University	USA
Mr. MEGIAS VAZQUEZ, Guillermo D.	University of Seville, Spain	SPAIN
Dr. MENG, Cai	Institute of High Energy Physics	CHINA
Dr. MIGUEZ, Bruno	Unicamp – LNGS	BRAZIL
Dr. MINAKATA, Hisakazu	University of São Paulo	BRAZIL
Prof. MINAMINO, Akihiro	Kyoto University	JAPAN
Dr. MOORE, Craig	Fermilab	USA
Dr. MORFIN, Jorge G.	Fermilab	USA
Dr. MUHLBEIER, Thiago	PUC-Rio	BRAZIL
Dr. NAGASLAEV, Vladimir	Fermilab	USA
Dr. NAKAMURA, Satoshi	Osaka University	JAPAN
Mr. NEHRKORN, Alexander	Aachen University	GERMANY
Prof. NICOLA, Serra	University of Zurich	SWITZERLAND
Mr. NIRKKO, Martti	University of Bern	SWITZERLAND
Dr. NORMAN, Andrew	Fermilab	USA
Dr. NUNOKAWA, Hiroshi	PUC-Rio	BRAZIL
Dr. OLIVEIRA, Roberto	UNICAMP	BRAZIL
Prof. OREBI GANN, Gabriel	UC Berkeley / LBNL	USA
Dr. OTANI, Masashi	KEK	JAPAN
Dr. PALEY, Jonathan	Fermilab	USA
Prof. PALLADINO,	Vittorio Univ & INFN Napoli	ITALY
Dr. PALMER, Mark	Fermilab	USA
Dr. PAPA, Angela	Paul Scherrer Institut	SWITZERLAND
Dr. PARADISI, Paride	University of Padua	ITALY
Mr. PASQUINI, Pedro Simoni	Unicamp	BRAZIL
Dr. PASTERNAK, Jaroslaw	Imperial College/RAL-STFC	UK
Mr. PEIXOTO FERREIRA, Cesar	Unicamp	BRAZIL
Prof. PERES, Orlando Luis Goulart	UNICAMP	BRAZIL
Mr. PICORETI, Renan	UNICAMP	BRAZIL
Prof. POCANIC, Dinko	University of Virginia	USA
Dr. POPOVIC, Milorad	FNAL	USA
Dr. PRAKASH, Suprabh	Harish-Chandra Research Institute	INDIA
Mr. PRONOST, Guillaume	Subatech	FRANCE
Dr. QUIROGA, Alexander	PUC-Rio	BRAZIL
Dr. RAUT, Sushant	KTH Royal Institute of Technology	SWEDEN
Dr. SAMANA, Arturo	U. Estadual de Santa Cruz	BRAZIL
Prof. SANCHEZ, MaylyIowa	State University	USA
Mr. SCHOLZ, Bjorn	University Of Chicago	USA
Dr. SIRIGNANO, Chiara	University of Padova & INFN	ITALY

Dr. SNOPOK, Pavel	Illinois Institute of Technology	USA
Dr. SOLANO SALINAS, Carlos Javier	UNI, Peru	PERU
Prof. SOUSA, Alexandre	University of Cincinnati	USA
Dr. ST. JOHN, Jason	University of Cincinnati	USA
Dr. STRAIT, Jim	Fermilab	USA
Dr. STRATAKIS, Diktys	Brookhaven National Laboratory	USA
Dr. TAKAESU, Yoshitaro	University of Tokyo	JAPAN
Prof. TANG, Jingyu	Institute of High Energy Physics	CHINA
Dr. TERAOKA, Kazuhiro	Nevis Laboratories	USA
TERRANOVA, Francesco	U. of Milano-Bicocca and INFN	ITALY
Mr. TONG, Jianfei	Institute of High Energy Physics	CHINA
Ms. TUEROS, Edith	CRAAM	BRAZIL
Dr. UCHIDA, Melissa	Imperial College London	UK
Dr. UCHIDA, Yoshi	Imperial College London	UK
Mr. VAN CUYCK, Tom	Ghent University	BELGIUM
Ms. VARGAS, Danaisis	U. Estadual de Santa Cruz	BRAZIL
Dr. VASSILOPOULOS, Nikolaos	IHEP, Beijing	CHINA
Ms. VITTI STENICO, Gabriela	UNICAMP	BRAZIL
Dr. WAGNER, Stefan	CBPF	BRAZIL
Prof. WANG, Wei	Sun Yat-Sen University	CHINA
Dr. WHYTE, Colin	University of Strathclyde	UK
Ms. WURSTEN, Elise	University of Leuven	BELGIUM
Mr. YANG, Ye	Kyushu University / KEK	JAPAN
Prof. YUAN, Ye	IHEP, Beijing	CHINA
Prof. ZUKANOVICH FUNCHAL, Renata	University of São Paulo	BRAZIL